A MULTI-FREQUENCY STUDY OF AN X-RAY SELECTED SAMPLE OF ACTIVE GALACTIC NUCLEI

by

Bruce Alan Grossan

A. B. Physics, University of California at Berkeley, 1985

Submitted to the Department of Physics in Partial Fulfillment of the Requirements for the Degree of

Doctor of Philosophy
in Physics

at the
MASSACHUSETTS INSTITUTE OF TECHNOLOGY
September 1992

Signature of Author _____

Department of Physics
August 31, 1992

Certified by _____

Professor Hale V. D. Bradt
Thesis Supervisor

and _____

Ronald A. Remillard
Thesis Co-Supervisor

Accepted by _____

Professor George F. Koster
Chairman, Doctoral Committee

A MULTI-FREQUENCY STUDY OF AN X-RAY SELECTED SAMPLE OF ACTIVE GALACTIC NUCLEI

by
Bruce Alan Grossan
A. B. Physics, University of California at Berkeley, 1985

SUBMITTED TO THE DEPARTMENT OF PHYSICS IN PARTIAL FULFILLMENT OF THE REQUIREMENTS FOR THE DEGREE OF DOCTOR OF PHILOSOPHY

ABSTRACT

The LASS (Large Area Sky Survey) experiment, which flew aboard the HEAO-1 spacecraft, carried out a 2-20 keV survey of the sky during 1977–1978. The X-ray sources from this survey make up the LASS catalog (Wood et al. 1979). Optical counterparts have been identified for greater than 86 % of the LASS sources above a flux of ~0.95 μJy @ 5 keV (Remillard 1992b). The LASS error boxes, along with the more precise positions from the Modulation Collimator (MC) X-ray experiment (also aboard HEAO-1), subsequent X-ray imaging, and optical search techniques were all used to identify the LASS sources. From these identifications, a high-latitude ($|b| > 20°$), flux–limited (≥ 0.95 μJy) sample of 96 emission line Active Galactic Nuclei (AGN) have been selected for study. The sample is referred to as the LMA (for the LASS / MC identified sample of AGN). The objective of this work is to produce multi-frequency spectra of this sample of objects, in order to determine and interpret the statistical properties of the sample over nearly the full range of observable wavelengths.

Data were obtained for as much of the radio through hard X-ray (< 20 keV) spectrum as possible for each object in the LMA. Radio, near infra-red, and other measurements were taken from the literature, far IR fluxes were extracted from co-added observations from IRAS, UV spectra were obtained from the IUE archives, and original observations were performed (with the help of collaborators) in the radio, near IR, optical, UV, and X-ray to fulfill this goal.

Correlation studies of the continuum bands found poor correlations of X-ray and radio flux, good correlations for 12 and 25 μm flux with X-ray flux, excellent correlations for optical and near IR fluxes with X rays, and poor correlations of UV and X-ray fluxes. The correlations of fluxes in widely separated bands, along with the identification of thermal components on smaller frequency scales, suggest that AGN multi-frequency spectra are made up of an underlying component from the IR to the X-rays which is similar in most AGN, plus thermal components which vary widely from object to object. For objects without significant stellar contamination or reddening, the log slope from 1.25 μm to 5 keV has a mean of –1.04 with a standard deviation of 0.05 (~twice the typical measurement uncertainty). This result suggests that the underlying component has a small range of slopes centered near –1. In order to study the intrinsic distribution of blue bump strengths, broad-band spectral shapes and other spectral features were used to identify the presence of reddening and starlight contamination. The distribution of blue bump strength relative to the 1 μm flux, characterized by the log slope from the near IR to the UV, is found to vary significantly, with no observable dependence on luminosity. The near IR to UV log slopes from 20 objects diagnosed as un-reddened and uncontaminated by starlight range up to +0.12, and appear to approach a lower limit of –1. These results suggest that the blue-bump thermal component is superimposed on a ~ –1 log slope underlying component from 1.25 μm to the UV. In the objects with IR to UV log slopes near –1, the underlying continuum component is viewed directly because the thermal blue bump component is weak or absent.

Correlation studies of line and X-ray continuum flux yield a good correlation between the flux of [OIII], the strongest narrow emission line, and X-ray flux. The Balmer lines, however, do not show a strong correlation with X-ray flux. He I and Fe II emission in a band which includes 5200Å and 5320 Å

showed the best broad line correlations with X-ray flux. No significant correlation is observed between optical line flux and the UV continuum flux. However, all measured high-ionization UV line fluxes correlate very well with the simultaneously measured UV continuum. The good correlation of narrow [OIII] flux with X-ray flux is consistent with a simple picture for the narrow line region where a high-energy continuum, which is distributed over a large solid angle, and which is represented by the X-ray flux, photoionizes the gas in the narrow line region. If the UV continuum is assumed to originate in a disk, the correlation of UV line flux with the UV continuum flux, but not with the more isotropic X-ray flux, would suggest that UV line emission also originates in the disk. A very large spread in the value of broad line Balmer decrements (Hβ/Hα ~ 0.13 – 0.4) is observed among objects determined to be un-reddened ($E(B\text{-}V) \leq$ 0.03) by observation of their 2175 Å feature. If there were an intrinsic Balmer decrement for broad line regions in AGN, this spread would correspond to extreme values of reddening ($E(B\text{–}V)$>1 mag), therefore the broad line Balmer decrement is not useful in determining continuum reddening in most AGN.

Repeated observations of some of the LMA objects were used to assess the effects of variability on the conclusions above. The median fractional variability was found to be 29% in the UV, and 11% in the optical. A comparison of X-ray fluxes in the literature yielded an average fractional rms variability of 39%. A survey of the literature showed that variability greater than a factor of 2 was found to be rare in all but the IUE bands; such variations are insufficient to affect the correlations in luminosity discussed above, which have spreads of 1/2 to one decade. An X-ray observation of the object 1H0557-503 (PKS0558-504), yielded significant variation on a time scale ≤ 200 s, the fastest ever observed in a normal quasar. The inferred rate of change of luminosity ($dL/dt \approx 3.2 \times 10^{42}$ erg s^{-2}) is the first strong evidence that X rays from a normal quasar may be beamed.

The hard X-ray Luminosity Function (LF) of the LMA can be roughly described by a power law of slope -2.49 ± 0.02 from $10^{42} - 10^{48}$ erg s^{-1}, but the function steepens with increasing luminosity. Below 10^{42} erg s^{-1}, the LF flattens very significantly, and is not modeled well by a power law. The low-luminosity flattening has not been previously observed in the hard X-ray band, but has been reported in the soft X-ray EMSS sample (Maccacaro et al., 1991). The flatness of the LF at low L_X and the steepness of the LF at high L_X allows a more certain estimate of the contribution of AGN to the 2–10 keV diffuse X-ray background than available previously. Integration of the LF from $L_X = 8.9 \times 10^{41}$ to 2.17×10^{47} erg s^{-1} yields a contribution to the background of 26^{+8}_{-11} %. The X-ray LF of narrow lined objects can be described by a power law at low luminosities, with a log slope of -2.32 ± 0.19 from 10^{42} to $10^{43.5}$ erg s^{-1}. Above $10^{43.5}$ erg s^{-1}, however, the LF is truncated or becomes significantly steeper. The cumulative fraction of narrow-lined objects in the LMA for $L_X > 10^{43.5}$ erg s^{-1} is much lower (<1/5) than the total fraction reported for unbiased optical, IR, or radio samples. Either there is an intrinsic dependence of narrow-line fraction on X-ray luminosity, or hard X-ray selection is biased against detecting narrow-line AGN compared to broad-line AGN at high luminosities.

Thesis Supervisor: Dr. Hale V. D. Bradt
Title: Professor of Physics

Co-Thesis Supervisor: Dr. Ronald Remillard
Title: Research Scientist
Center for Space Research, MIT

ACKNOWLEDGEMENTS

I would like to thank my advisor Hale Bradt for sticking with my through a long and arduous thesis project. When others lost faith in me, he supported and encouraged me. He believed in me enough to send me half way around the world, to Japan, to do science. He provided every kind of support from encouraging words to funding for special tables to prevent wrist injury. My Co-thesis advisor, Ron Remillard, has been with me through the greatest difficulties in this long project, and I owe special thanks to him as well. Ron taught me telescopes and the night sky, the tools and territory of the astronomer. Particularly in these last few weeks, Ron has been instrumental in actually getting this behemoth signed and delivered. For all he has taught me, for many hours of reading, correcting, and suggesting, I owe him extra thanks.

Perhaps my greatest debt to anyone at MIT, however, is my debt to the students and staff of the Center for Space Research. These are the people I learned the most from, and who were the most willing to teach and help me. In roughly geographic order, those who have been of indispensable, personal and professional help include my office mates Wayne Lewis, Andrew Silber, Chris Becker, and Adam Nyman, CCD lab people Gerry Luppino (gone but not forgotten), Keith Gendreau, Rosemary Hanlon, and Pat Mock (who, when the chips are down, always comes through, but for no apparent reason). Sixth floor people of the past and present who deserve special thanks include Kathy Flannagan, Jeff Isaacson, Athul Pradan, Don Alvarez, and Bob Rutledge. Extra-special thanks goes to the resident non-native Hawaiian Eugene Magnier, my number one backboard for ideas, and my favorite Diva, Amy Lalime, who typed figure numbers and fed me lasagne at the most critical times during my thesis.

The only people who have put up with me for longer than anyone above deserve the greatest thanks. These are my Parents Rosalyn Grossan and Dr. Murray Grossan. My

mother's care packages and letters, and my father's encouragement and support were no less essential than anything else that helped me to finish this monster.

Bruce Grossan

Cambridge, 1992

QUOTATION

"Time is short and art is long."

-Goethe (Faust)

TABLE OF CONTENTS

LIST OF TABLES

LIST OF FIGURES

Chapter 1:

Chapter 2:

Chapter 3:

Chapter 4:

CHAPTER 1: INTRODUCTION

This chapter introduces the topic of AGN, and reviews previous studies of AGN from well-defined samples. The LASS/MC identified AGN sample is introduced, and the objectives of this study are summarized.

1. ACTIVE GALACTIC NUCLEI

1.1 Definition and Description

An Active Galactic Nucleus, or AGN, is any extragalactic object with substantial emission which cannot be explained by normal processes of stellar evolution, such as the emissions from novae, supernovae, star formation, or HII-regions. The most nearby examples of these objects occur in the central regions of visible galaxies, hence the name AGN. In this work, the term AGN will be taken to mean non-blazar, emission-line AGN, which make up the majority of AGN. Blazars are related objects which are characterized by linearly polarized optical continua. They are more variable than non-blazars and they may exhibit multi-frequency spectral shapes that are different than "normal" emission line AGN. These objects are outside the scope of this study. A good, up to date review of emission-line AGN is given in Urry (1988), which covers much of the material in these first two sections.

AGN emit roughly equal power per decade of frequency at observable frequencies higher than the radio band. They are intrinsically the most powerful objects in the known universe, with apparent luminosities of 10^{42} - 10^{47} erg s^{-1} in the hard X-ray band (defined here to be 2 - 10 keV) alone. The astounding energetics of AGN are

easiest to explain by processes involving accretion onto a black hole. Black holes transform the potential energy of an accreting particle into radiation with a theoretical limit of up to 10% of the rest mass energy of the particle (e.g., Fabian 1986). Considering the full bolometric luminosity of AGN, the average quasar could be powered by accreting ~ 10^{-3} to 10^{1} $M_{\odot}$ per year onto a black hole of ~ 10^{7}–10^{10} $M_{\odot}$ (O'Dell 1986). The AGN power source is known to be very compact, which is consistent with the model of accretion onto a super-massive black hole. Under assumptions of uniform, isotropic radiation, the minimum variation time scale of a source is equal to the light travel time across the object along the line-of-sight direction. Large variations in the flux of AGN have been observed in many cases on time scales of less than 10^{4} s, suggesting an emission region smaller than our solar system. The high luminosities, the production of high energy photons, the compact size, and the short variation time scales observed for AGN all support a model of accretion onto a supermassive black hole.

A special class of galaxies, defined by an intense point-like nuclear continuum and strong, very broad emission lines, was reported almost half a century ago (Seyfert, 1943). These objects are now known as Seyfert galaxies, and their classsification is discussed in section 1.4. The first quasars, the most luminous sub-class of AGN, were discovered to be the optical counterparts of radio sources (Schmidt 1963), and radio surveys have subsequently identified many such objects. Many Seyferts and nearby quasars have also been discovered by optical surveys of galaxies with luminous, compact nuclei (e.g. Arakelian 1975), or in spectral surveys of galaxies with an ultraviolet excess or prominent emission lines (Markarian 1967; Smith 1975).

1.2 AGN Continuum Emission

Figure 1 shows the multi-frequency spectra of two AGN, one with strong radio emission (a "radio-loud" object, the upper spectrum in the Fig. 1) and one with weak radio emission (a "radio-quiet" object, the lower spectrum in Fig. 1). The plot shows flux

per unit frequency times frequency (νF_ν) vs frequency (ν), referred to as a "spectral energy distribution". A spectrum with a log slope of -1 ($F_\nu \propto \nu^\alpha$, $\alpha = -1$) appears flat on such a plot. AGN have a *roughly* -1 slope above radio frequencies, so this type of plot provides a good graphical representation of their spectra. AGN multi-frequency spectra can be described by a radio component, a small Infra-Red (IR) bump (thermal emission from dust), an IR-Ultra Violet (UV) continuum (usually modeled with a power law function) superimposed with emission lines, a "blue bump" (possibly thermal emission from an accretion disk), and an X-ray power law, typically with a log slope ~ -0.7 in the hard (≥ 2 keV) X-ray band. Some of these components are represented schematically in Figure 1. About 10 - 20% of all AGN are radio-loud, and the spectral energy distribution of these objects remains roughly flat into the radio band, as shown in the upper panel of Figure 1. Radio-quiet AGN often have more than an order of magnitude less radio emission relative to other continuum components as shown in the lower panel of Figure 1.

Plausibility arguments can be made to account for the various continuum components, but the theoretical state of the art is far from building a self-consistent model to account for all the components above, to say nothing of motivating them from first principles.

In this section, the term "rising spectrum" refers to a positive slope on a νF_ν vs ν plot, and conversely for a falling spectrum. The low-frequency rise to a flat power law in the radio through IR part of the AGN spectrum is consistent with synchrotron radiation, probably from an extended component (Urry 1988). In the IR, thermal components are present. A good discussion of these components is given in Barvanis (1990). Contributions from cool dust in the host galaxy disk peak at around 60 μ (1.8×10^{12} Hz), and from warm nuclear dust, a peak at around 10 μ (3×10^{13} Hz) is observed. In general, the peaks observed are too broad to be from isothermal material, so the IR region

is usually modeled with dust emission from a range of temperatures (e.g. Neugebauer *et al.* 1985).

The near infra-red (NIR) through optical regions have contributions from several components. Nearly all AGN and quasars have a 1 μm (3×10^{14} Hz) rest wavelength "dust dip", of varying strength. This spectral feature is associated with thermal emission from dust near its sublimation temperature. Hotter dust, peaking at higher frequencies, cannot exist, causing an exponentially sharp cut-off near 1 μm. The combination of the cut-off of the dust component and the rising contribution with increasing frequency of other component(s) causes this inflection (Neugebauer *et al.* 1979). To model the relatively flat NIR-optical continuum, in addition to themal and emission line components, a non-thermal component is often invoked. Some workers use a relatively flat extension of an IR power law due to self-absorbed synchrotron emission (Edelson and Malkan 1986, see Fig. 1), others use a flatter power law attributed to free-free emission (Barvanis 1990). Starlight, usually observed in weak, nearby AGN, contributes a bump between about 0.4 and 3 μ ($1–8 \times 10^{14}$ Hz).

Toward the UV, the blue bump and the 3000Å bump (see Fig. 1) generally dominate the continuum. The 3000Å bump is a blend of Balmer continuum emission and FeII emission line multiplets which form an apparent continuum in a region as wide as 2000 – 4000 Å (see Fig. 1). One of the largest energy contributions from any component comes from a much broader spectral component, the so-called "blue bump". This bump rises with increasing frequency beginning somewhere between the near IR and the near UV (10,000–3000 Å) and dominates the UV. The bump is actually centered at higher energies, however, possibly somewhere in the unobservable EUV. Only the low frequency rise of this feature is observable in most objects. The high frequency end may have been observed in some objects with the strongest bumps, e.g. PG1211+143 (Bechtold *et al.* 1987). In this object, the steep rise of the bump in the UV region and its

steep fall to a flatter power law in the low energy X-ray band suggests that the peak flux density is located in the EUV (see Fig. 2). Shields (1978) suggested that the blue bump component in quasars could be thermal radiation from an accretion disk resulting from the superposition of blackbody emission at different disk radii. The fundamental motivation for such objects is to store and eject the angular momentum of the accreting material. The accreting material looses angular momentum via viscosity and spirals inward. At the same time, the angular momentum is transferred outward and is eventually ejected in the form of particles with high angular momentum. A combination of black bodies representing a range of temperatures of optically thick material has been fit to the observed spectra of AGN to the highest observable UV energies, with high-energy tails that may extend to soft X-ray energies (See, for example, Malkan and Sargent 1982, Bechtold et al. 1987). The simplest accretion disk models, which assume a thin disk, have the basic problem that they violate the Eddington limit strongly as their maximum temperature is increased to include the soft X-ray excess. The Eddington limit violation causes the disks to "puff up", and the model becomes internally inconsistent. Effects that have been ignored in simple pictures include electron opacity, gas and dust opacity, radiative transfer effects, thermal instabilities, disk thickening, inclination, and general relativistic effects for rotating black holes (Urry 1988). Further, the inclusion of some of these effects can be significant. Czerny and Elvis (1987) point out that electron opacity gives a high-energy tail at a lower temperature, which helps the Eddington limit problem. Sun and Malkan (1989) point out that relativistic effects in the inner disk can cause significant changes in the observed spectrum that are a strong function of inclination angle.

Despite the large body of work on the accretion disk model, it is not universally accepted. O'Dell, Scott, and Stein (1987) argue that the blue bump can also be explained by synchrotron radiation from a broken power law of electrons that has its origins in

relativistic processes among high-density protons; there have not been published fits of this model to data (Urry 1988).

A paper by McDowell et al. (1989) highlights the variation in strength of the blue bump. These authors find that some quasars have virtually no blue bump. The lack of a blue bump might suggest accretion without disks (*e.g.* spherical accretion), a high inclination angle of the disk, or extinction of the UV blue bump radiation by dust.

A smooth, pure power law is observed at hard (2-10 keV) X-ray energies. Large samples of AGN show only small dispersion about the mean log slope of this power law, –0.7 (Turner and Pounds 1989). Low energy X-ray spectra can be more complex, however. In the 0.2 - 4 keV band, radio-quiet objects tend to be steep, with log slopes of ~ –0.9, while radio-loud objects tend to be flatter, with log slopes of ~–0.5 (Wilkes and Elvis 1987). In addition, many AGN show evidence for a soft excess, a distinct power-law component with a steeper slope than the extrapolation of the high-energy power law which dominates below ~ 2 keV (Turner and Pounds 1989).

The physical origins of these components are not well understood. A discussion of the physical origins of the complex soft X-ray spectrum is beyond the scope of this work; however, see Urry (1988) and references therein. Turner and Pounds (1989) give a brief review of theoretical work on the production of the hard X-ray continuum, which is summarized here. Hard X-ray emission is most often attributed to the synchrotron self-Compton process, where photons from lower energy synchroton emission are upscattered by a relativistic electron population. This model can produce power laws of arbitrary slope by changing the parameters of the electron population, and is therefore not well constrained. Models have also been proposed where repeated Compton scattering of soft photons produces power laws at hard X-ray energies, however, there may be problems producing the correct range of hard X-ray slopes.

1.3 Multi-Frequency Nature of AGN

The *roughly* flat AGN spectral energy distribution (νF_ν vs ν space) of AGN dictates that all observable bands are of comparable importance energetically. This situation motivates a multi-frequency approach to the study of AGN. Each spectral band also gives a distinct view of the various aspects of AGN. Observations of the hard X-ray band allow us to view the processes close to the central engine without obscuration; the far IR bands also permit a less-obscured view, and allow detection of the radiation due to the heated obscuring material itself. Radio observations allow us to view emission by the ionized electron population of the AGN, possibly in jets and/or extended regions. The optical and UV spectral regions provide a view of the interaction of the continuum with line emitting and obscuring material, and possibly material in accretion disks. Even γ-rays (1-20MeV) have been observed from AGN (e.g. Shrader, 1992), allowing a view into relativistic energy processes (although these data are not available for most of the objects in this sample). A comprehensive analysis of all these bands together is necessary to yield the most complete input information and the most comprehensive constraints for physical models of AGN emission. This study explicitly emphasizes and exploits the multi-frequency nature of AGN as much as is possible with existing data.

1.4 Line Emission and Classification

As with any other topic in astronomy, this one is mired in tradition and terminology. As lists of AGN grew, the variety of the phenomena became evident and objects were classified according to the similarities in their optical spectra. Table 1, below, gives the classes of AGN and related objects, along with their defining optical characteristics. Figure 3 shows examples of optical spectra from each type. The optical classifications of these objects only reflect the different optical spectral appearances, not necessarily intrinsically distinct objects.

A good review of line emission phenomena is given in Osterbrock and Mathews (1986). References to the following discussion may be found in this work except where explicitly indicated otherwise. The X-ray / UV continuum is generally thought to photoionize material in the region near the nucleus to produce the emission lines observed in optical spectra. The Broad Line Region (BLR) lines are typically permitted lines of hydrogen, 1000 - 20,000 km s^{-1} full width at half maximum (FWHM). The spread in velocity is too large to be attributed to thermal motion; the widths of the lines must therefore be due to bulk motion. About 10–15 % of quasars have broad absorption lines which are blueshifted relative to nearby strong emission peaks, indicating outward radial flow. Other AGN line profiles, however, are consistent with models of inflow, chaotic motion, motion in an accretion disk, or possibly orbital motion (Netzer 1990), so no single BLR kinematic model is decisively favored for the majority of AGN.

The lack of strong forbidden-line emission from the BLR shows that the BLR contains relatively dense material, $N_H \sim 10^9 - 10^{11}$ cm^{-3}. These high densities, along with detailed photoionization calculations, suggest that the broad-line emitting gas is distributed in clouds, cooler than the ambient medium, at the densities quoted above (Osterbrock & Mathews 1986).

The best measurements of the distribution of broad-line material are made using a technique now called "echo-mapping". Gaskell and Sparke (1986) give a detailed description and application of this technique. The technique uses the time lag between continuum and line variations to determine the radial distribution of line emission. This technique is much more robust than simple variability time scale arguments, and allows us to say with certainty that BLR's occupy a region from ~ 10-40 light days (~3-12 $\times$ 10^{16} cm) in low-luminosity AGN (Horne, Welsh, and Peterson 1990; Gaskell and Peterson 1987). Some variations in the BLR size occur from object to object. Some

stratification of emission from different species may also be present within the BLR (Gaskell and Peterson 1987).

The narrow line region (NLR) is known to be much less dense than the BLR because of the presence of emission lines from "forbidden" transitions. In typical laboratory conditions the collisional de-excitation rate of these transitions is much more rapid than the rate of radiative decay, so the transitions are not observed and are said to be "forbidden". The observation of such lines immediately implies very low collision rates appropriate for extremely rarefied plasmas, and allows us to put upper limits on the density of the emission material. The characteristic density of the NLR region where [OIII] 5007Å, the strongest narrow line, is emitted is $< 5 \times 10^7$ cm^{-3}, the critical density for this line. Variability time scale arguments and imaging of the NLR in the closest Seyferts suggest a NLR size on the order of $10^{19} - 10^{20}$ cm (Netzer 1992). The width of the narrow lines is 500 – 1000 km s^{-1} FWHM, which is narrow compared to the broad-line width. However, these narrow lines are still broad compared to the lines from normal galaxies. Note that "broad lines" may have narrow components, as nothing prevents these species from radiating, if present, in the NLR. The strength of the narrow line components are usually small compared to the broad components. However, in some objects the narrow lines dominate the line emission. These objects are referred to here as "Type 2", or "narrow-lined" objects.

The density limits and size scales determined from optical spectra allow us to form a "cartoon" sketch of the AGN, as shown in Figure 4. Surrounding the putative black hole is the proposed accretion disk. Moving outward, we encounter the clouds of the BLR, a possible obscuring dust torus (discussed below), and the diffuse NLR. On this scale, everything depicted is unresolvable with current instruments except in the closest AGN, where the NLR is resolved.

1.5 Unified Models

Much recent work has attempted to explain the variety of AGN classes as essentially the same object viewed from different angles with different obscuration effects. The AGN in this study have been selected by hard (~2-20 keV) X-ray flux. Hard X-ray selection facilitates the study of obscured sources since hard X rays are less affected by absorption than the near IR - UV bands.

BLR obscuration models for Type 2 AGN lacking broad lines have been around a long time (e.g., Neugebauer et al. 1980). In these models, dust, possibly in a disk or torus, obscures the BLR from the observer. The narrow lines originate from outside the obscuring structure, and so are unaffected by it. The central continuum source is either only partially obscured or is scattered to the observer so that the continuum and narrow lines are similar to those in broad-line AGN. Antonucci and Miller (1985) reported the discovery of broad Hβ in scattered light in the well-known Seyfert 2 NGC 1068, and Miller and Goodrich (1987) have reported several more cases of obscured BLRs in Seyfert 2s, supporting this hypothesis.

Several schemes have been proposed where all types of AGN are intrinsically similar, with observed characteristics mostly accounted for by viewing angles, geometry, and obscuration. Barthel (1989) describes such a "unification model", where all AGN are divided into radio-loud (RL) and radio-quiet (RQ) objects, with relative broad line phenomenon explained by viewing-angle dependent obscuration, and radio phenomenon explained by orientation of the observer to a relativistic jet. First consider only radio-loud objects. This part of the model is motivated by the common radio morphology of most quasars, a dim core and a brighter lobe, with a hot spot at the leading edge of the lobe, an "edge dominated" morphology. The lobe and hot spot are interpreted as the result of a jet of relativistic electrons. The jet is emitted from the nucleus by an unspecified mechanism, collimated into a cone-like shape, and interacts with the surrounding medium to form the lobe and hot spot of radio emission. FRII radio

galaxies, classified by Fanaroff and Riley (Fanaroff & Riley 1974), are high-powered, double-lobed sources with a dim core. If one were to view such a source from an angle near the jet axis, relativistic beaming would enhance the brightness of the near lobe, and suppress the brightness of the far lobe, producing a single-lobed source, as is observed in many quasar radio maps. The Barthel (1989) model also includes a dust torus aligned about the symmetry axis of the jet. This torus would have little obscuring effects when viewed along the jet axis, but would obscure the BLR when the system is viewed far from the jet axis. In this way, RL quasars and RL Seyfert 1 galaxies are unobscured because they are viewed close to the jet axis, and RL Seyfert 2s and narrow-lined radio galaxies have their BLR's obscured by the molecular torus. This viewing angle also produces the correct radio morphology for the RL Seyfert 2's and radio galaxies. The addition of free electrons in the latter objects in the region above the obscuring torus would allow the observation of the BLR in light scattered by the electrons. Radio-quiet AGN are the same as the objects above, except their radio emission is extremely weak or absent. RQ quasars and Seyfert 1's are those objects observed near the axis of the torus. RQ Seyfert 2's correspond to Seyfert 1's viewed nearly perpendicular to the axis. Galaxies observed by the IRAS satellite to have powerful IR emission indicating nuclear activity, but which do not possess broad lines, may be powerful radio-quiet quasars viewed nearly perpendicular to the axis of the torus (Barthel 1989).

2 PREVIOUS AGN SURVEYS

2.1 Samples

Many samples of AGN have been studied previously, ranging from a few objects of interest to a particular author to huge compilations of observations. However, few of these samples are defined by a uniform selection criteria, and thus, few samples are complete with regard to uniform coverage over a region of the sky, or with regard to containing all objects down to a given flux or luminosity limit. Without well-defined and

complete samples, selection effects can bias the conclusions of a study. Each frequency band used for selection has its own properties which result in different sets of objects with different observational properties.

The Palomar Bright Quasar Survey (BQS) of Schmidt and Green (1983) was a search for objects with a strong UV excess. This survey yielded many emission-line AGN. The objects in the survey were selected by a comparison of images taken in the U photometric band to images of the same field in the B band. Objects with strong non-thermal continua stand out in such comparisons, hence the success at AGN detection. The sky coverage of the survey is 10,714 deg^2, and its flux limit is B = 16.6 with a total of 114 objects. Studies of subsets of this sample have been done in other wave bands (see, for example, Tananbaum, et al. 1986, for the soft X-ray properties of this sample, Kellermann et al. 1989 for the radio properties of the sample). The Faint Braccesi sample also used a UV excess selection criteria to form a complete sample with a much deeper flux limit, B = 19.8 mag, but for a much smaller region of the sky, 1.7 deg^2. Another type of survey, for example, the CTIO Michigan-Tollolo survey (Osmer and Smith 1980, Lewis, MacAlpine, and Weedman 1978) detected AGN with an objective prism, a technique which makes very low dispersion spectra of each object in a field, so that objects with strong optical emission lines will stand out. The chief selection effect of the UV excess surveys is their sensitivity to obscuration of AGN, as only the optically very bright objects with strong UV continuua are discovered. This bias results in a poor detection rate for narrow-lined objects, and especially for edge-on objects (Keel 1980, Kirhakos and Steiner 1990). Objective prism surveys are biased against objects with low emission line equivalent widths.

AGN are reported to have a bi-modal distribution in radio luminosity (Kellermann et al.), with one part of the population having orders of magnitude less energy emission per decade of frequency in the radio than in any other band, and the other part of the

population having roughly equal energy emission in all frequencies. These radio-quiet and radio-loud classes are believed to have different "intrinsic" properties (Barthel 1989). Radio selected samples of AGN detect only radio-loud objects, which make up the minority of all known or otherwise selected AGN. The most well-known and well-studied of these is a sub-sample of 33 objects from the 3CR (Revised 3rd Cambridge Catalogue of Radio Sources) optically identified as quasars (Schmidt 1968). The sample is said to be complete because all sources of radio emission are detected down to a limiting flux of 9 Jy at 178 MHz within the sample region, and all of these radio sources are optically identified to a limiting flux of approximately 18.4 mag in the V photometric band.

The Piccinotti Sample of AGN (Piccinotti et al 1982) consists of 23 Seyfert galaxies detected in a hard X ray (2-10 keV), all-sky (except for $|b| < 20°$, where b is the galactic latitude) survey with the A-2 instrument of the HEAO-1 satellite (Rothschild et al. 1979), to a limiting flux of 1.36 μJy at 5 keV. (This sample will be referred to hereafter as "the Piccinotti et al. sample"). All of the sources down to the X-ray flux limit of the survey have been identified. Quasars were not included in this sample. Hard X-ray measurements specifically study the very innermost regions of the nucleus, close to the black hole, where X rays are produced. The relative insensitivity of hard X rays to absorbing material between the observer and the AGN significantly reduces a possible bias against detecting obscured objects. The AGN X-ray source is compact and dominates the total X-ray emission from all but the weakest AGN. X-ray surveys are therefore not biased against objects with strong galaxy emission that might mask the nuclear emission in optical / UV surveys. The flux-limit introduces a bias toward nearby and high-luminosity objects, to be sure, but this is a well understood bias. Previous to this work, the Piccinotti et al. sample constituted the largest hard (> 2keV) X-ray selected sample meeting the criteria of large-area sky coverage and a uniform flux limit. Many individual studies of the Piccinotti et al. sample, or including this sample, have been carried out, but none have included nearly the full observable spectrum from the radio

through hard X-ray bands. The Piccinott et al. sample will be discussed in more detail in Chapter 7.

An interesting sample that has been recently studied is the subset of IRAS (Infra-Red Astronomical Satellite) detected objects with "warm" IR colors, flat spectral slopes from 60 to 25μm, suggesting strong non-thermal radiation. Optical identifications of such objects have yielded obscured and narrow-line objects with a high detection rate (De Grijp et al. 1985). Although this sample comes from a survey which had nearly all sky coverage, the identifications are not yet complete (Kailey and Lebofsky 1988 describe a sub-sample of these objects).

2.2 Multi-Frequency Observations

Many papers include interpretations of results from two frequency regimes for a sample of objects, but studies putting together all or several bands at once are rare. Early work in multi-frequency observations produced spectra for only a few of the brightest AGN. For example, Malkan (1983) studied six high red shift AGN with optical and UV data, rather poor near-IR data, and an Einstein IPC soft X-ray measurement of one of the objects. Such studies found that the combination of emission lines, a power-law continuum, and a superposition of black body spectra in the UV could roughly reproduce the multi-frequency spectra of the objects investigated. In the Malkan (1983) study, an attempt was made to interpret the range of black-body temperatures required to fit the spectrum in the context of theoretical models of accretion disks, but the models require significant assumptions that are not explicitly justified by observations. A series of papers by Wills and various co-authors (Wills et al., 1985, Netzer et al., 1985) reported detailed modeling of broad emission lines, in particular, to address the difficult problem of blended Fe II multiplet emission, which forms a "false continuum" in many parts of the AGN spectrum, particularly in the UV. These papers used exclusively UV and optical data. Recently, a paper by Barvanis (1990) highlighted the importance of dust

contributions to the AGN spectrum, particularly in the IR regime, both from the nucleus and perhaps associated with the host galaxy. This paper used only IR – near-UV data on a selection of radio quiet objects. Although the work above has increased our understanding, the de-convolution of AGN spectra is far from completely understood. Further, all the de-convolutions are empirically based, and have yet to be completely explained by physical models. Thus, there is a need to explore the application of these works to a large, well-defined sample with multi-frequency data.

3. THE X-RAY SELECTED SAMPLE

A hard X-ray selected, flux-limited, all-sky sample is well suited for group studies of AGN, because of the reduced bias against partially obscured objects, and because of the simple, single-component nature of hard X rays, discussed above. By comparison, the biases in optically or radio-selected AGN samples are much more complex.

Such a sample of galaxies is now available from the data from the sky survey of the HEAO-1 satellite's LASS (Large Area Sky Survey, or A-1) instrument. This instrument made three full scans of the sky, and was sensitive to hard (2-20 keV) X-rays, and is described in Wood et al. (1984). The Log (dN / dS) vs. Log dS curve, (where N is the cumulative number of sources detected with a flux greater than an instrumental flux S) of the survey, for sources detected at high galactic latitudes ($|b| > 20°$), is consistent with an isotropic distribution of sources down to a flux of 0.95 μJy at 5 keV. This demonstrates that the survey is complete to a limiting flux of 0.95 μJy, and allows the definition of a sample of AGN above this flux limit. More than 86% of the LASS sources with fluxes ≥ 0.95 μJy have been optically identified (Remillard et al. 1992). The optical identification program (described in Remillard et al. 1986) used a combination of the original LASS X-ray positions, superior X-ray positions from the Modulation Collimator (MC) experiment (see Gursky et al. 1985), optical search techniques, and X-ray imaging data. Ninety-six AGN have been optically identified at high galactic

latitudes ($|b| > 20°$) with flux greater than 0.95 μJy, and these objects form the flux-limited sub-sample to be studied in this work. This HEAO-1 (~2-20 keV X ray) LASS / MC identified sample of AGN will be referred to as the LMA sample. The LMA contains more than four times the number of objects in the Piccinotti sample, and the maximum luminosity in the LMA is nearly three orders of magnitude higher than that of the Piccinotti et al. sample. A variety of spectral classifications is present in the LMA, including Seyfert 1's, Seyfert 2's, quasars, and a variety of less standard classifications. A great variety of multi-frequency spectra is also represented in the LMA, including objects with the full range of blue bump strengths, a wide range of far IR slopes, and a wide range in radio loudness

4. OBJECTIVES

In this work, I present an atlas of multi-frequency spectra for the 96 AGN in the LMA sample. A few questions of central importance regarding the interrelations of continuum components, the nature of the blue bump, the relation of the emission lines to the continuum, the effects of reddening, and the X-ray luminosity function of AGN will be addressed with the data from the atlas.

The multi-frequency atlas contains radio detections for 54 AGN in the sample, IRAS detections in at least one frequency for 88 and upper limits for 7 more, Near-IR fluxes for 54, some optical data for every object, and IUE data which covers Lyα for 39 AGN. This collection of data constitutes one of the largest samples of multi-frequency spectra reported to date which includes data from radio, IRAS, near-IR, optical, IUE, and hard (~2-20) X-ray bands. The sample of multi-frequency spectra will be characterized statistically, and compared with other samples. Physical models for the spectra will be compared with the distribution of observed properties. Correlations will be performed on different continuum bands to determine the relationship between the various spectral

components, in order to understand how the mix of components in each band make up the observed multi-frequency spectra.

The strength of the blue bump will be investigated statistically among our sub-sample with IUE data. A set of diagnostics for reddening will be presented in an effort to study the intrinsic, rather than the apparent, bump strength. Correlations of bump strength with luminosity, radio loudness, and line emission will be investigated.

The relationship between the emission lines and the ionizing continuum will be investigated by searching for correlations between line and continuum fluxes, luminosities and slope. In particular, correlation tests will be performed on line emission and blue bump strength to determine the relationship between line emission and the continuum component thought to power it.

Reddening of AGN continua will be investigated by evaluating traditional means of reddening estimation, such as the Balmer decrement. Reddening will also be investigated using other indicators, including the 2175Å dust absorption feature in IUE spectra. A method for correcting the reddening using the 2175 Å feature will be discussed.

The X-ray luminosity function of AGN derived from the LMA will be presented. This function is of special interest because it is derived from a larger sample, with a greater variety of objects, than previous functions. A luminosity function will also be presented separately for the LMA narrow-line objects; this function will be the first hard X-ray luminosity function for narrow-line objects. The luminosity functions will be compared to search for differences between broad and narrow-line objects.

REFERENCES

Antonucci, R. R. J., and Miller, J. S. 1985, Ap J, 294, 158

Arakelian, M. A., 1975, Soobshch. Byurak. Obs., 47, 3

Barthel, P., 1989, Ap J, 336, 606

Barvanis, Richard, 1990, ApJ, 353, 419

Bechtold et al. 1987, ApJ, 314, 699

Carleton, N. P. et al., 1987 ApJ, 318, 595

Czerny, B., and Elvis, M. 1987, ApJ, 321, 243.

DeGrijp, M. H. K., Miley, G. K., Lub, J., and deJong, T., 1985, Nature, 314, 21

Edelson, R., and Malkan, M. A. 1986, ApJ, 308, 59

Fabian, A. C., in *The Physics of Accretion onto Compact Objects* (eds. Mason, K. O., Watson, M. G., and White, N. E.) p. 229, (Springer, Berlin, 1986)

Fanaroff, B. L., and Riley, J. M. 1974, MNRAS, 167, 31

Gaskell M.C.,and Peterson, B. M., 1987, ApJS, 65, 1

Gaskell, M.C., and Sparke, L. S. 1986, ApJ, 305, 175

Guilbert, P.W., and Rees, M. J. 1988, MNRAS, 233,475

Gursky, H. et al. 1978, ApJ, 223, 973

Horne, K., Welsh, W. F., and Peterson, B. M., 1991, ApJ, 367, L5

Keel, W. C., 1980, AJ, 85,198

Kailey, W., Lebofsky, M., 1988, ApJ, 326, 653

Kellermann, K. I., Sramek, R., Schmidt, MM., Shaffer, D. B., and Green, R. F., 1989, AJ 98, 1195

Kirhakos, S. D., and Steiner, J. E., 1990, AJ,99, 1722

Lightman, A. P. and White, T. R. 1988, ApJ, 335, 57

Maccacaro, T. Della Cecca, R., Gioia, I. M., Morris, S. L., Stocke, J. T., Wolter, A. 1991, ApJ, 374, 117

Malkan, M., ApJ, 1983, 268, 582

Malkan, M. A., and Sargent, W.L.W., 1982, Ap. J., 254, 22

McDowell et al., 1989 , ApJ, 345, L13-16

Miler, J. S., and Goodrich, B. F. 1987, Bull. A.A. S., 19, 695

Netzer, H. 1990, in Active Galactic Nuclei, ed. Blanford, R. D., Netzer, H., Woltjer, L., Springer-Verlag, New York

Netzer, H., Wamsteker, W., Wills, B., Wills, D., 1985, ApJ, 292, 143

Neugebauer, G., et al., 1980, Ap J, 238, 502

Neugebauer, G., Oke, J. B., Becklin, E. E., and Matthews, K. 1979, ApJ, 230, 79

O'dell, S. L. 1986, PASP, 98,140

O'Dell, S. L., Scott, H. A., and Stein, W. A. 1987, ApJ, 313, 164

Osterbrock and Mathews, 1986, ARA&A, 24,171

Piccinotti, G., Mushotzsky, Boldt, E. A., Holt, S.S., Marshall, F.E., Serlemitsos, P.J., Shafer, R. A., 1982 ApJ, 253, 485

Remillard, R. A., Bradt, H. V., Schwartz, D. A., Tuohey, I. R., 1992, preprint

Remillard, R., Schwartz, D. A., and Brissenden, R. J. 1988, in *A Decade of UV Astronomy with IUE* (Eur. Space Ag. spec. Pub. 281), p. 273

Remillard et. al., 1986, ApJ, 301, 742

Rothschild, R. et al., 1979, Space Sci. Instr., 4, 265

Seyfert, C. K., 1943, AJ, 97, 28

Schmidt, M., 1963, Nature, 197, 1040

Schmidt, M., 1968, ApJ, 151, 393

Schmidt, M., and Green, R.F., 1983, ApJ, 269, 352

Sun, W., & Malkan, M. A. 1989, ApJ, 346, 68

Turner, T. J., Pounds, K. A., 1989, MNRAS, 240, 833

Tannenbaum, H., Avni, Y., Green, R. F., Schmidt, M., Zamorani, G., 1986, ApJ, 305, 57

Urry, C.M., 1988, in Multiwavelength Astrophysics, Ed. France Cordova , (Cambridge Univ. Press), p. 279

Wills, B.J., Netzer, H., and Wills, D., 1985, ApJ , 288, 94

Wilkes, B., Elvis, M., 1987, ApJ, 323, 243

Wood, K., et al., 1984, ApJ Suppl., 56, 507

TABLE 1

AGN Classifications

Class	Optical Characteristic	Broad vs Forbidden Line Peak Heights
Seyfert Type 1	Strong, broad H emission lines	[OIII]/Hb ~ 1
Seyfert Type 2	Strong, narrow H emission lines	[OIII]/Hb >5
Quasars	Large L, entire object must be unresolvable point source	Emission lines similar to Sy 1s, but larger widths reported
LINERS (Low Ionization Nuclear Emitting Region, sometimes Seyfert Type 3)	Strong forbidden emission of singly ionized species	[SII]/Hβ ~ 1, much stronger than for the objects above.
NOT AGN, but related spectroscopically:		
Extragalactic HII regions	Forbidden lines strongest	[OIII]/Hβ >> 1

FIGURE CAPTIONS

Figure 1. Continuum components are shown for one radio-loud and one radio-quiet AGN, taken from Edelson and Malkan (1986). The top spectrum is from 3C273 a radio-loud object, and the lower spectrum is from MKN 335, a radio-quiet AGN. The best fit is shown as a heavy solid line. The spectra are not de-reddened, so power laws in the NIR-opt region The components included in the fit are: (dashed line) an IR power law, (dotted line) a near IR bump (warm dust and its cutoff at the sublimation temperature), (dot-dash line) starlight, (thin solid line) the 3000Å bump, (dot-dot-dash line) a UV blackbody to fit the blue bump.

Figure 2. The multi-frequency spectrum of PG1211+143 is presented in this figure. The blue bump is extremely prominent in this object, and the rise in the UV can be seen as well as the steep drop to a flatter power law in the X-ray band.

Figure 3. AGN Classes. Figure (a) is an object with both broad and narrow lines classified as a Seyfert type 1, similar to a quasar, but quasars often have broader lines. In (b) a Seyfert type 2 galaxy is shown, which lacks broad lines. Figure (c) is the spectrum of a LINER galaxy, with very weak Hβ , weak [OIII], and relatively much stronger Hα and strong [OI] and [NII]. Figure (d) shows a (high-excitation) Extragalactic HII region, which is not an AGN, for comparison. The strength of [OIII] dominates that of all other lines.

Figure 4. This "cartoon" sketch of the AGN shows the major components of the nucleus. The sketch is a side view, not to scale, in the plane of the dust torus and accretion disk (but co-alignment of the torus and disk is not required). Surrounding the continuum source are the proposed accretion disk, a proposed toroidal distribution of dust clouds, and, at much larger radii, the narrow line region. Note that if the AGN were viewed from the side of the figure, the BLR would be obscured, but if viewed from the top of the figure, the BLR would not be obscured.

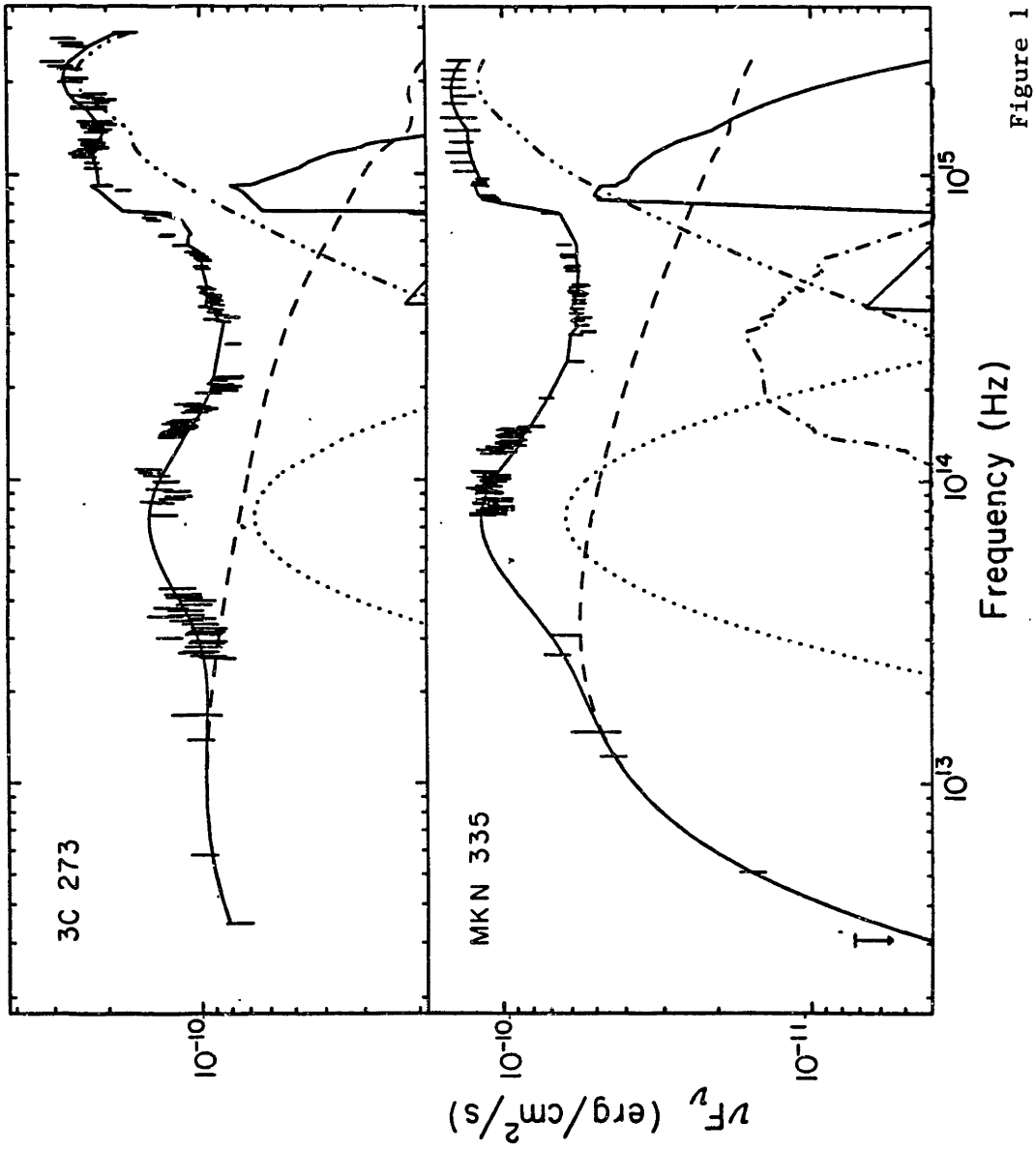
3C 273
MKN 335
10^{-10}
10^{-10}
10^{-11}
10^{13}
10^{14}
10^{15}
Frequency (Hz)
νF_ν (erg/cm^2/s)

Figure 1

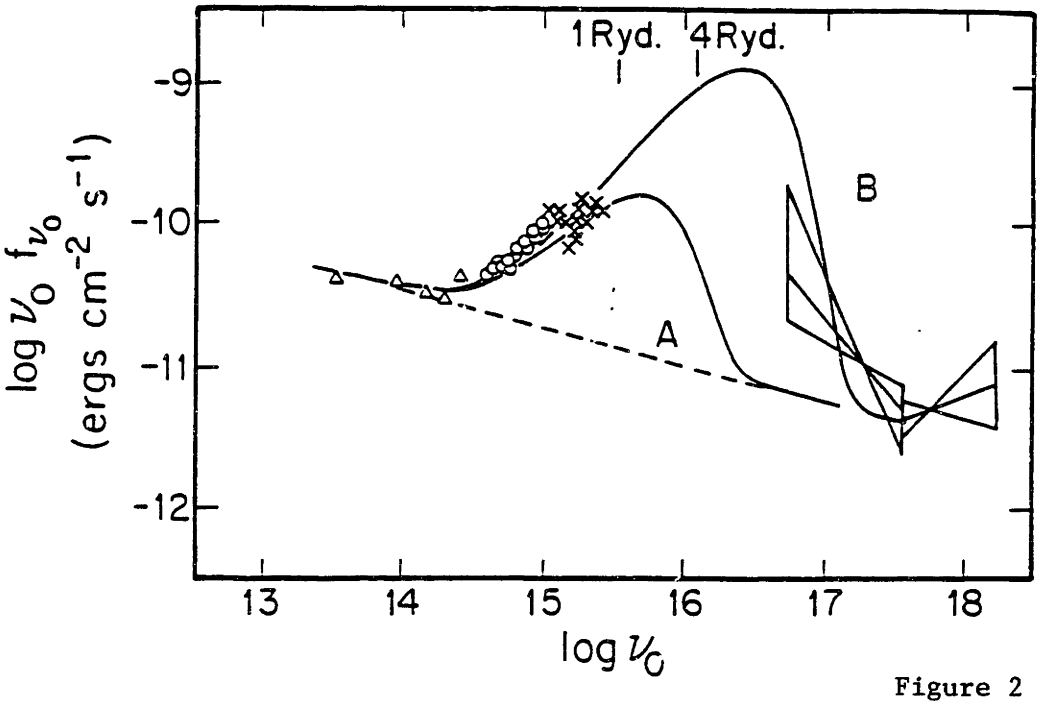
1Ryd.
4Ryd.
B
A
-9
-10
-11
-12
13
14
15
16
17
18
log ν_0 f_{ν_0}
(ergs cm^{-2} s^{-1})
log ν_0

Figure 2

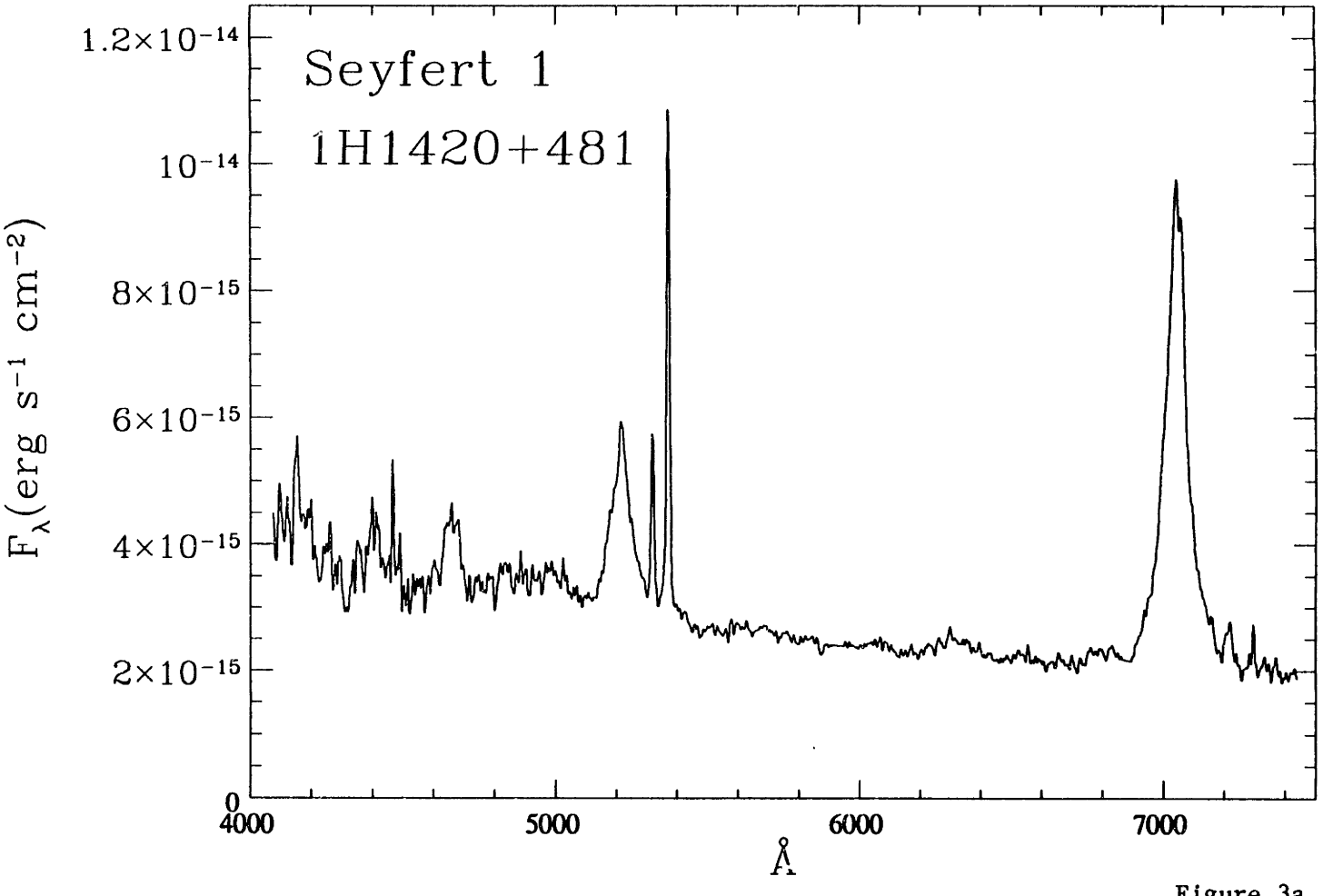
Seyfert 1
1H1420+481
F_λ(erg s^{-1} cm^{-2})
1.2×10^{-14}
10^{-14}
8×10^{-15}
6×10^{-15}
4×10^{-15}
2×10^{-15}
0
4000
5000
6000
7000
Å

Figure 3a

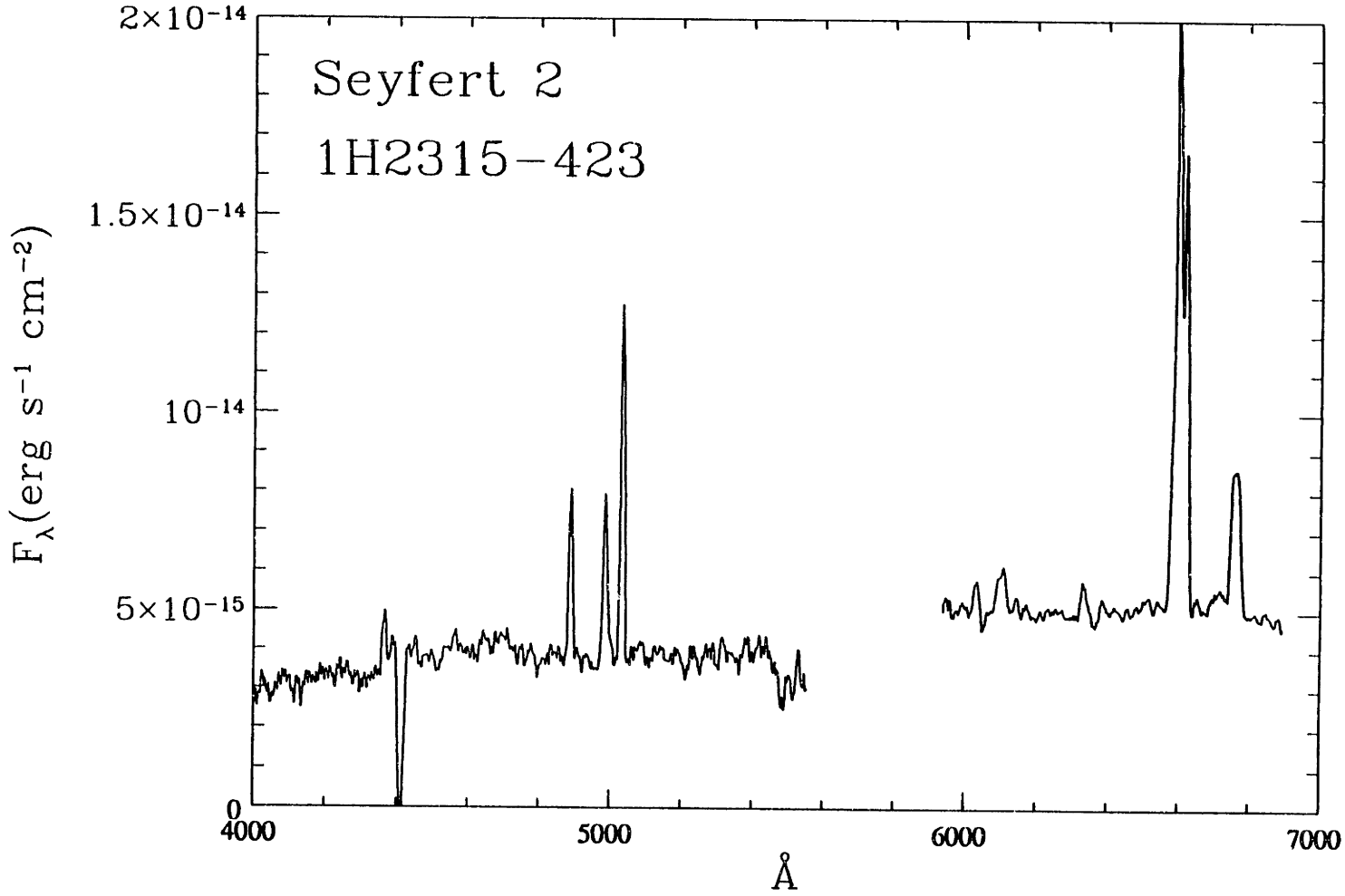
Seyfert 2
1H2315−423
2×10⁻¹⁴
1.5×10⁻¹⁴
10⁻¹⁴
5×10⁻¹⁵
0
F_λ(erg s⁻¹ cm⁻²)
4000
5000
6000
7000
Å

Figure 3b

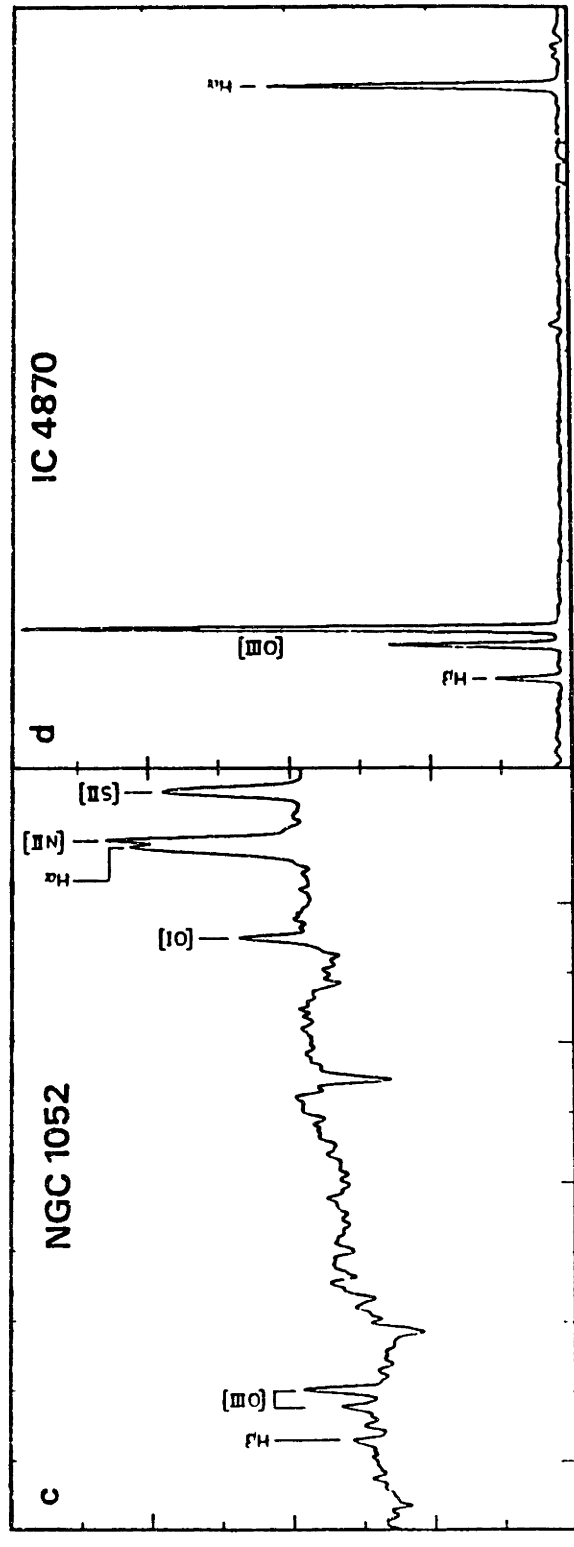

Figure 3c

Figure 3d

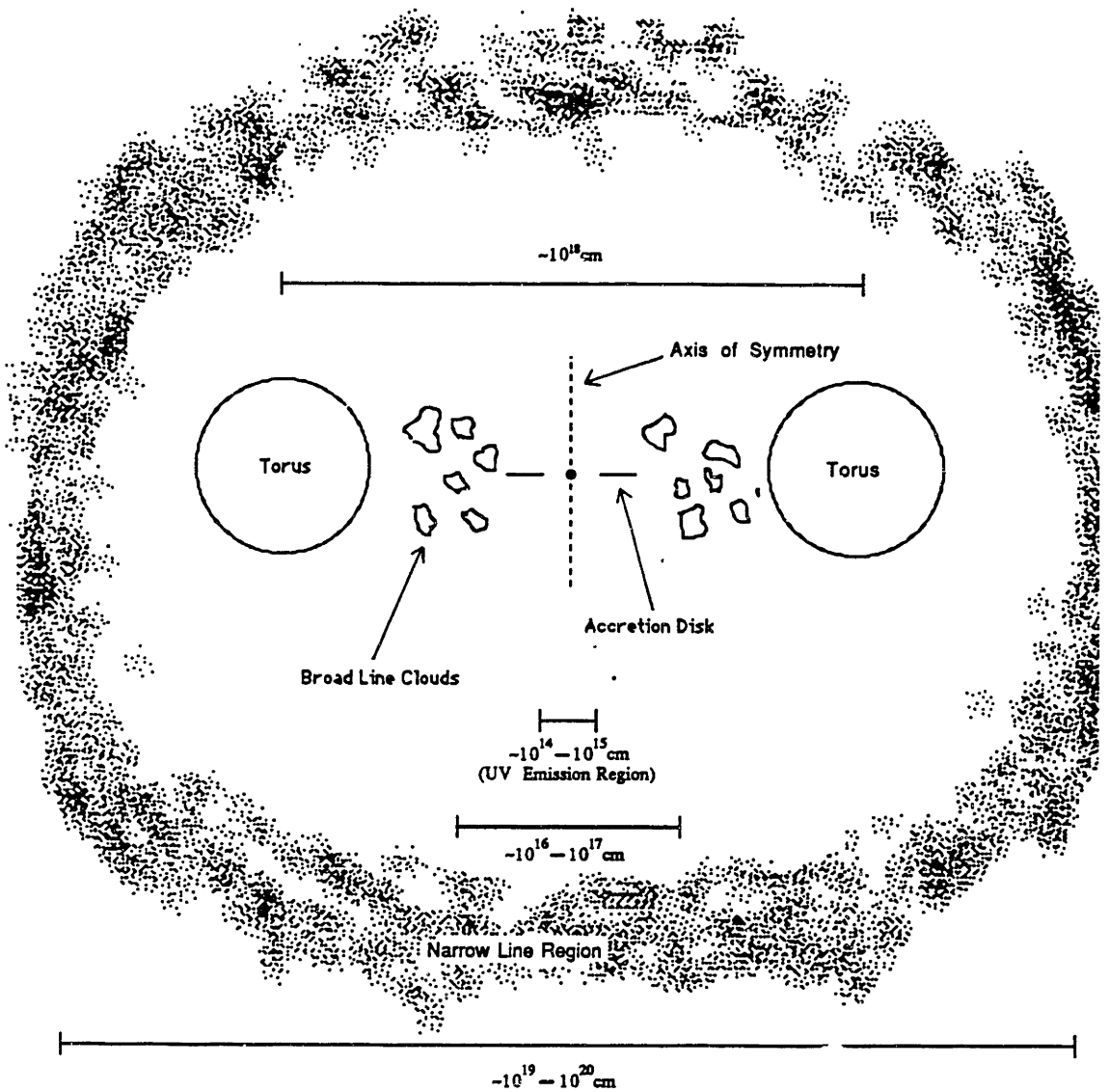

Cartoon Sketch of an AGN

(Side View)

Figure 4

CHAPTER 2:
SAMPLE DEFINITION AND OBSERVATIONS

The first section of this chapter gives a definition of the sample to be studied, the LASS / MC identified sample of AGN. The subsequent sections describe the additional observations from which the data at several other frequencies were derived and the techniques used to reduce them. Most of the measurements used in this study appear in tables at the end of this chapter.

1. DEFINING THE X-RAY SAMPLE

1.1 The LASS Catalog

The sample of galaxies studied herein has been selected from the catalog of X-ray sources from the LASS (Large Area Sky Survey, or HEAO A-1) instrument (Wood et al. 1984), which flew aboard the HEAO-1 satellite, launched in 1977. Subsequent identification efforts have allowed the definition of a nearly complete, all-sky, flux-limited sample of AGN. In this section, the sample definition is described, and the noise and completeness of the sample are evaluated.

The HEAO-1 instruments scanned the entire sky almost three times from 1977 to 1979; the LASS catalog covers only the first scan of the full sky, from August 1977 through February of 1978. (Two additional scans of the sky were performed, but they had inferior data due to the degradation of the LASS detectors, and the third scan was not

complete. These data are not used in this study.) The instrumentation used to perform the survey consisted of several modules, each a single proportional counter sensitive to ~2-20 keV X-rays and a mechanical collimator, described in Wood et al. (1984). Four "scan collimator modules" had large fields of view (1°×4° FWHM response) and two additional "fine collimator modules", had much smaller fields of view (1/2° × 1° FWHM response). These six modules provided data for the LASS catalog.

The LASS instrument scanned the sky along great circles perpendicular to the earth–sun line (i.e. scanning along ecliptic longitude). While in scanning mode, the satellite rotated at 3 revolutions per ~95 minute orbit; the scan path moved 1° per day, and the entire sky was scanned in six months. The scan collimator modules therefore had any given object in their field of view for at least ~ 8 days. The exposure for a given source depends on the ecliptic latitude of the source. The technique used by the NRL (Naval Research Laboratory) group to determine LASS fluxes and positions is as follows: The counts from the four scan modules were registered and summed over 1, 2, and 4 day intervals to form one-dimensional images of the sky. The four day sums were fit with the triangular collimator response function to locate prospective sources, then the one and two day sums were searched for sources that might have been missed in the four day sums. The background, source intensity, and position in the scan direction were determined in these first stage fits. In a second-stage process, the data from all the modules were summed in one-day intervals, and fit in the direction perpendicular to the scan direction to determine the location of each source. The fine module fits are forced to the positions determined by the scan module fits with this method. A stringent set of source acceptance criteria were applied to eliminate false sources. First, all sources were required to have at least 3 independent detections at > 3 σ significance in either set of modules. Second, the fluxes derived from the fine collimator modules had to be consistent with those of the scan collimator modules. In total, 842 celestial X-ray sources of all types were detected. The

fits yielded large rectangular error regions for each source position, typically ~1/2° × 1° for AGN near the flux limit of the sample (determined below).

1.2 The Identification Program

The MC instrument, (Modulation Collimator, or A-3 experiment; Gursky et al. 1985) which also flew aboard the HEAO-1 satellite, provided an array of precise positions for use in conjunction with the results from the LASS instrument. The combination of the LASS and MC positions together has facilitated the discovery of many new optical identifications for the LASS X-ray sources. The MC had a field of view which overlapped that of the LASS, and gave a pattern of multiple, small diamond-shaped error regions, each ~1'× 4' at the 90% confidence limit. The location of the X-ray source for any given LASS detection was therefore restricted to the region of overlap of the small MC diamonds and the large LASS error box, aiding in the optical identification process.

As of 1992 July, 86.5% of the sources from the LASS Catalog with a count rate ≥ 0.0036 LASS counts s^{-1} cm^{-2}, with $|b| > 20°$, and with a ratio of flux to LASS uncertainty ≥ 3.0 had been identified with optical sources and classified in Remillard et al (1992c). (The previous reference is a catalog of LASS identifications, in progress, but current versions are available on request). The program to identify the LASS sources is discussed in Remillard et al. (1986). Source identification usually began with general catalog searches for candidates' optical counterparts in the LASS and MC error regions. Catalogs of various classes of X-ray emitting objects and general survey catalogs at other frequencies were searched for candidates. Many sources were cross-checked with observations by imaging X-ray instruments with very precise positions. The Palomar or ESO plates were checked for bright stars, clusters, or prominent galaxies. Schmidt Photographic plates were also taken of regions near the X-ray source positions. The plates recorded two offset exposures, one each in the U and B bands. Candidate objects usually showed a bright UV excess compared to their B image on these plates. Finally, optical

spectra were taken to classify the candidates and secure the identifications. The majority of sources not in the galactic plane were identified as emission line AGN; clusters of galaxies were the next most common type of X-ray source. The painstaking AGN identification efforts, along with the crucial aid of the MC positions, are what make possible the definition and study of a flux-limited AGN sample from the LASS catalog.

1.3 The Flux Limit of the LASS Catalog

Remillard et al. (1992c) used the number vs. flux distribution of the LASS catalog to find the minimum flux above which all sources in the sky are detected. The behavior of the number vs flux distribution may be predicted in a simple way if one assumes a uniform distribution of sources of equal luminosity in a Euclidian universe. Given these assumptions, $N_i(S)$, the number of sources of luminosity L_i expected with a flux density of S or greater is given by:

(1.3.1) $$dN_i(S) = \rho_i \, dV(S)$$

where $V(S)$ is the volume of space within a distance $d(S)$such that the flux from each source is equal to S. The distance is given by the relation $4 \pi d^2(S) S = L_i$. From the latter expression and the Euclidian relation for volume $V(S) = 4/3 \pi d^3(S)$, we get:

(1.3.2) $$V(S) = 1/3 \, (4 \pi)^{-1/2} L_i^{3/2} S^{-3/2}, \text{ therefore,}$$

(1.3.3) $$dV(S) \propto L_i^{3/2} S^{-5/2} \, dS.$$

By substituting (1.3.3) into (1.3.1), we get $dN_i(S) \propto \rho_i L_i^{3/2} S^{-5/2} \, dS$. The differential number-flux relation for sources with luminosity L_i is then given by :

(1.3.4) $$dN_i(S)/ \, dS \propto \rho_i L_i^{3/2} S^{-5/2}$$

If one considers an ensemble of spatially uniformly distributed sets of sources, with each set of sources i of a different luminosity L_i:

(1.3.5) $$dN_{tot} / \, dS = \Sigma_i \, dN_i(S) / \, dS \propto \Sigma_i \rho_i L_i^{3/2} S^{-5/2} = S^{-5/2} (\Sigma_i L_i^{3/2} \rho_i),$$

where N_{tot} is the total number of objects of all luminosities combined. Therefore,

(1.3.6) $$dN_{tot} / \, dS \propto S^{-5/2}.$$

Any set of sources distributed uniformly in space will therefore have a dN/dS vs S curve with a log slope of –5/2. (The differential form of the number vs. flux distribution is generally preferred over the cumulative form for experimental purposes, as systematic errors tend to accumulate in the latter form.)

Survey instruments typically detect all sources down to some flux limit; below this limit, the probability of detection drops smoothly until a threshold is reached and no further sources are found. This effect is a natural consequence of finite detector area and Poisson fluctuations in the flux measurements. The Log dN/dS vs Log dS curve from the LASS catalog data, shown in Figure 1, demonstrates this behavior well. The effect is seen as a smooth fall off from the –5/2 slope as the flux approaches zero. Anisotropic source distributions were removed from this analysis by the exclusion of the region of the sky with $|b| < 20°$ to remove sources distributed in the plane of the Milky Way. In addition, several galactic bulge ($|b| > 20°$) X-ray binary systems were excluded, as was a region of the sky near the Magellanic Clouds. A fit of a –5/2 slope power law to this high-latitude portion of the LASS catalog is shown as a solid line in Figure 1. A good fit was obtained over the range of 0.0036 to 0.1044 LASS counts s^{-1} cm^{-2}. The data begin to fall off from the –5/2 slope below 0.0036 LASS counts s^{-1} cm^{-2} (marked with a dotted line in Figure 1). The next bin below this flux value is the first bin more than one sigma below the fitted line. This motivates the choice of 0.0036 LASS counts s^{-1} cm^{-2} as a conservative choice for the threshold of a flux-limited sample within the LASS catalog (Remillard 1989). Therefore, for fluxes equal to or greater than 0.0036 LASS counts s^{-1} cm^{-2}, nearly all sources were detected, assuming (nearly) the uniform, Euclidian behavior described above. There are 98 sources optically identified as AGN at $|b| > 20°$ above this limit (but additional constraints, discussed below, will modify this sample slightly).

The absolute flux calibration for AGN was determined by an intercomparison of AGN count rates from the LASS and the A-2 instrument (Mushotzky et al. 1980), another X-ray instrument aboard HEAO-1 with a similar energy response. The conversion was

determined to be approximately 263 μJy / LASS count s^{-1} cm^{-2} at 5 keV, for a power law spectrum, $F_\nu \propto \nu^\alpha$, with a log slope $\alpha \approx -0.7$. This empirical derivation of the flux conversion was necessary because the X-ray detectors of the LASS instrument lost all spectral resolution due to hardware failure. The net effect was that the LASS instrument behaved like a large X-ray photometer over a range of 1-20 keV. Several studies of AGN spectra have shown little scatter in the hard X-ray log slope, (Mushotzsky 1984, Turner & Pounds 1989, hereafter TP) with a mean value of -0.7 ± 0.17 (2-10 keV) (TP). This result validates Remillard's assumption of a –0.7 log slope used to determine the absolute flux calibration for AGN measured with the LASS instrument. The value of the flux limit of the sample, derived from the conversion above, is 0.95 μJy at 5 keV.

1.4 Detection, Flux, and Identification Quality

Flux Uncertainty

In order for the X-ray flux limit of the sample to be meaningful, the fluxes must be known to within a small uncertainty. The flux uncertainty has 2 separate components: one from measurement error, and the other from confusion noise. The contributions of these uncertainties are discussed separately below.

The LASS flux measurement errors, which are statistical uncertainties taken directly from the LASS catalog, were determined from the χ^2 contours of the source intensities and positions fit to each object. Due to unusual circumstances (proximity to extremely bright sources or unfavorable background conditions affecting the fits) the formal measurement errors on the X-ray fluxes for some sources are large. The distribution of signal to noise (i.e. the ratio of flux to the reported uncertainty) in the high-latitude, flux-limited sample (all source types), is given in Figure 2. It is clear from the figure that only a negligible fraction of sources have signal to noise values below 3. To enforce a rigid criterion on the acceptable errors in the flux values, a limit on measurement error of 3 σ will be applied. Only 2 AGN are rejected by this criterion. Removal of these

two AGN, 1H0426+051 and 1H1639-109, leaves 96 remaining objects. The remaining 96 identified AGN at $|b| \geq 20°$ make up the LMA (LASS / MC identified AGN) sample. The average signal to noise of the 5 sources at the flux limit (0.0036 LASS counts cm^{-2} s^{-1}) is 7.23.

In the region of the sky covered by this sample, there are approximately 6750 independent beam areas, each of 4 deg^2 (the scan collimator beam size is given because these modules dominate the fits for source positions and flux). More than one source can occur within one beam area. Confusion is the general term for the occurrence of multiple sources within the field of view of an instrument, and it can be a problem for the definition of a sample in two ways. First, two X-ray sources of flux less than the detection threshold in the same field of view may combine to appear as one source, leading to a spurious X-ray source detection. This effect will be discussed below. The second problem, confusion noise, is a related issue which affects the accuracy of flux measurements.

Confusion noise is due to the ensemble of unresolvable sources within the field of view of an instrument. The average contributions of these sources are effectively removed by background subtraction; the average background level is well determined, as it is fit over a large number of instrument fields of view (20° in scan longitude). Thus, only the fluctuations in the contribution of the unresolved sources within a single field of view are a problem. In Appendix I, a simple estimate is given of the confusion noise due to the sizes of the fields of view of the LASS detectors alone. This calculation was performed with the assumption that the Log dN/dS curve of the population of unresolved sources was described by the extrapolation of the –5/2 log slope power law determined by the LASS sample. The noise contribution due to Poisson fluctuations in the number of these sources within a single field of view was integrated to determine the resulting fluctuation in the measured flux. The estimated confusion noise for the LASS instrument yields a worst-case ratio of LASS flux / confusion noise of 3.62 at the flux limit. It should be noted that the confusion noise of the fine collimator modules is very small compared to that of the

scan collimator modules. All of the LASS catalog fluxes were consistent with the fine collimator detections, as required by the source acceptance criteria, which constrains the true confusion contribution. This additional constraint was not considered in the estimate given in Appendix I, and so the confusion level quoted above is an overestimate of the problem.

The total flux error was obtained from the quadrature sum of the measurement error and the confusion noise of the LASS instrument. Figure 3 shows the distribution of "total significance", the ratio of the total error to the reported LASS flux. From the figure it can be seen that only four objects have a total significance less than 3, demonstrating good integrity of the defining flux limit of the sample. Since the dynamic range of the X-ray luminosity in the objects in this sample is so large, about 5 orders of magnitude, even the few objects with the lowest significance are still useful for studies of the distribution of various properties in luminosity.

Identification Assessment

The source acceptance criteria, discussed above, make it unlikely that X-ray fluxes with unusually large systematic errors, or those due to random source or background fluctuations, would enter the sample. A different problem is that of spurious X-ray source detections where unresolved sources below the flux limit of the sample combine to appear as a single source. When such cases occur with only 2 or 3 bright sources, an optical observer would regard the HEAO-1 source as "confused". The effectiveness of the optical identification process in these cases can be evaluated by comparing the expected number of spurious X-ray detections to the number of optically confused sources. The details of this calculation are given in Appendix I. The resulting estimate is ~ 37 spurious detections. Remillard et al. (1992c) found that 24 LASS error boxes were likely to contain more than one X-ray source. These are probably the brightest of the unresolved sources affected by source confusion. Additional spurious X-ray source detections may be included among the

approximately 30 X-ray sources currently unidentified. These results suggest that the identification program described above is highly effective at identifying the ~ 10% of the sample that may be spurious.

The error boxes 1H0823+561, 1H0950+696, and 1H1219+301, were associated with AGN but were "confused" i.e., associated with two optical counterparts, one of which was an AGN. Examination of Einstein and EXOSAT observations of these objects established that the AGN fluxes were below the flux limit of the sample, and these AGN were not included among the 96 AGN investigated in this work.

The random coincidence of an AGN with an X-ray flux below the flux limit and an MC X-ray error region can cause an incorrect optical identification. The expected number of random coincidences is given by the probability of randomly finding AGN within the solid angle searched in the course of the identification of the flux-limited, high-latitude subsample. An average of 25 MC error regions, each 4 square arc minutes in area, were searched per source. The LASS flux-limited, high-latitude subsample contains 332 sources, but approximately 40 of these were not searched because they are either well-known identifications or because they exhibited spatially extended X-ray emission. The latter condition is a clear sign of the diffuse emission that arises from nearby clusters of galaxies. The total search area was approximately 7.9 deg^2. One can determine the surface density of possible AGN candidates by adding toge r the densities of Seyferts and quasars, which are reported separately. The surface density of quasars brighter than B = 18 is given by interpolating the tabulated surface densities given in Schmidt and Green (1973). The interpolation can be made with their expression, $d \text{ Log } N(<B) / dB = 0.90$, where $N(<B)$ is the number of sources per square degree brighter than a given B band magnitude. The surface density normalization is 0.014 AGN deg^{-2} at B=16.4 mag. Nearby, bright Seyfert galaxies, which are spatially extended, are not covered by this survey, as the faint source counts of Schmidt and Green (1973) are dominated by quasars. The total number of Seyfert galaxies brighter than $m_{pg} = 16$ mag found in UV excess

surveys is given (by extrapolation of previous results) to be 0.05 deg^{-2} (Remillard et al. 1986). This result may also be extrapolated to estimate the number of Seyfert galaxies above the limiting flux of the search for optical candidates.

The optical identifications of objects down to the LASS flux limit are complete to V=16.8 mag (Remillard 1992a). The average B–V for AGN is about 0.4 mag, so the limiting search magnitude is equivalent to approximately B=17.2 mag. Extrapolating the number of Seyfert galaxies to B=17.2 mag (which corresponds to $m_{pg} \approx 17.09$ mag; Zombeck 1990) with $N(>S) \propto S^{-3/2}$ yields 0.23 deg^{-2}. Interpolating the Schmidt and Green (1973) results, with the expression given above, yields a surface density of 0.073 quasars deg^{-2} for a limiting search magnitude of B=17.2 mag. Adding these surface densities together to estimate the number of chance coincidences of Seyferts and quasars yields 2.39 expected coincidences. A relatively small number of fields were searched to V=17.5. Extrapolating the counts above in the same manner to a limiting flux of B=17.9 yields 0.59 Seyferts deg^{-2} and 0.31 quasars deg^{-2} for a total of 7.11 expected coincidences. The actual number of chance coincidences probably lies somewhere in the range between 2.4 and 7.1. Such a small number of objects will have only a small effect on most of the statistical studies done in the following chapters. These numbers may be compared with the discovery of 3 quasars rejected as X-ray source counterparts (because of superior alternative candidates) found within MC error regions down to V=17.0, and 8 quasars within diamonds rejected down to V=17.6. The total predicted numbers of chance coincidences are roughly consistent, but the number of Seyferts appears to be overestimated, and the number of quasars appears to be under-estimated. The overall conclusion is that the number of chance occurrences of AGN within the allowed X-ray error regions is small, while the identification program provides further safeguards that reject spurious associations of LASS X-ray detections with faint quasars.

Optical Completeness

Out of a total of 332 objects in the flux-limited high-latitude LASS sample, approximately 287 optical counterpart identifications have been made. Therefore, the optical identifications are more than 86 % complete. More recent work with the IPC slew and ROSAT surveys has shown that the majority of the sources missed by previous optical search techniques are now being identified as faint BL Lac objects or stars with active coronae (Remillard 1992a). These objects were not identified using the LASS and MC error regions because there are too many active coronae candidates (V<11) to search effectively in the relatively large error regions of the LASS and the MC, and because some of the "new" BL Lac objects are optically faint (i.e. have much lower ratios of optical / X-ray flux). Few UV candidates with B > 17.5 have been studied. Therefore, statistical studies of the LMA sample are believed to be largely unaffected by the 45 unidentified sources.

1.5 The LMA Sample

The 96 AGN listed in Remillard et al. (1992c) with a flux ≥ 0.0036 LASS counts/s (0.95 μJy @ 5 keV) , with galactic latitudes $|b| > 20°$, and a ratio of LASS flux / LASS error > 3 make up the LMA. To within ~13% percent, the parent LASS sample can be said to be complete in terms of optical identifications down to the X-ray flux limit. The list of LMA sources, their HEAO-1 LASS, or "1H" names, their optical positions, red shifts, and X-ray fluxes are all given in Table 1. Note that the 1H names are made up of the right ascension (1950.0) in hours and minutes and the declination (1950.0) in decimal degrees of the center of the LASS error box; these designations are not the correct optical positions of the associated object. The fluxes and errors given in Table 1 are direct conversions of the count rates given in Wood et al. (1984) by the factor given above. An additional list is given for the narrow-line objects alone. The 23 sources with an optical counterpart

discovered by the LASS / MC identification program are specially footnoted, giving the discovery publication, which includes a finding chart. The total number of X-ray discovered or identified AGN from all sources is 32, 1/3 of the sample.

The composition of the sample is very heterogeneous. The range of z in the sample spans the range from 0.0033 to 1.56. The luminosity ranges from 6.65×10^{41} – 5.47×10^{47} ergs/s. Twelve objects are dominated by narrow-line flux. A large range in radio loudness (see Chapter 4) is represented, and many sources are very luminous in the infra-red and UV bands.

2. UV OBSERVATIONS

The IUE (International Ultraviolet Explorer) satellite has performed pointed observations of AGN since 1978, and the data from most of these observations are now publicly available. The satellite has an aperture of 0.45 m, and operates two separate instruments, the SWP and LWP (or their spares, the SWR and LWR) to record the spectral information from approximately 1150-2000Å and 2000-3200 Å respectively at 6-7 Å resolution for objects in the flux regime of AGN (Kondo 1987). The detectors are SEC Vidicons, which can saturate (usually the brightest emission lines) in a long exposure. The spectra are usually taken through an aperture 30 arc seconds in diameter. The reduction of the IUE data occurred at the Regional Data Analysis Facility at Goddard Spaceflight Center in Maryland, and used the standard techniques and calibrations provided for IUE guest observers. Table 2 gives a list of the data obtained for each object, the date of observation, the observer for original observations, and additional information described below. The majority of the IUE observations were extracted from the public archives. Original observations of 1H0557–503 and 1H2107–097, performed by my collaborators, are also reported in the table.

The final LWP and SWP spectra are first examined for a match in the continuum level in the region of overlap of the two spectra. If the continua of the two spectra do not

connect smoothly, then a note is made, as the object is a candidate for UV variability. The SW instrument always yields data of superior quality, so the LW instrument data in the overlap region is discarded unless no SWP spectrum is available.

Before the IUE data may be compared with other frequencies, it must be corrected for reddening due to material in the line of sight to the target object. This subject, including the determination of the amount of reddening material in the line of sight, is covered extensively in the next chapter. Next, the spectra are corrected to the rest frame of the objects, assuming a Hubble constant of $H_0 = 70$ km s^{-1} Mpc^{-1}. Data from IUE observations, after de-reddening and red shift correction, are presented on the multi-frequency plots (see Chapter 4) as discrete points representing the continuum. In this way, the noise in the continuum level is minimized by integration of many points and the emission lines are explicitly removed. The definition of these bands is given in Table 2, along with the integrated flux densities in each band for each object. The uncertainties given are the r.m.s. of the data in the interval.

3. OPTICAL OBSERVATIONS

The optical photometric data, given in table 3a, were obtained by myself and collaborators Ronald Remillard or Roger Brissenden at the times and observatories listed in Table 3b. While I was responsible for the majority of all data acquisition for all objects with $\delta > -20°$, all the data for objects south of this region were contributed by Ron Remillard and Roger Brissenden. Their data reduction procedures were nearly identical to mine, except where detectors other than CCDs were used. The data taken by them and described elsewhere are referenced and noted in the table. The reduction of the data taken by me is described below. The aperture size of all optical photometric measurements made within the collaboration are given in the table, as are the spectral resolution and wavelength range of all spectroscopic measurements. All photometric data in the near IR and optical, including data from the literature, were taken with Johnson system filters.

3.1 Photometry

I performed photometric measurements using the Michigan Direct Camera and the Thomson CCD detector on the McGraw-Hill 1.3 m telescope of the MDM (Michigan-Dartmouth-MIT) observatory. Each CCD image was bias subtracted and divided by a flat field image obtained by median averaging several normalized images of the sky during twilight, one for each filter. The photometry was reduced using the program VISTA by Todd Lauer of Princeton University Observatory, integrating the light in 15" square apertures. The net CCD counts were normalized to photometric magnitudes by observations of photometric standards from Landolt (1973, 1976). The 15" aperture size was chosen to insure that no significant flux was lost, insuring accurate photometry of both standards and objects. The uncertainties given in Table 3a are the standard deviation of three independent exposures per object added in quadrature with the standard deviation of the mean standard star calibration values. The calibration values were derived from the standard star measurements made throughout each observing run. The derived uncertainties and magnitudes were then converted to mJy units using the conversions given in Zombeck (1990), and de-reddened for analysis in the following chapters as described in the next chapter. The optical photometric measurements given in the table are not de-reddened for comparison purposes.

3.2 Spectroscopy

The goal of the spectroscopic observations was to make spectrophotometric measurements of all AGN in the sample from Hγ to Hα with sufficient resolution to study narrow lines. The motivation for the spectrophotometric measurements was to construct a flux-calibrated atlas of spectra for the sample. Such spectra would enable absolute flux comparisons of the continuum and emission lines with other studies.

I performed spectroscopic measurements at the MDM observatory on both the 1.3m and 2.4m telescopes, using the Mark III spectrograph and the Thomson CCD detector.

Previous spectra showed excellent resolution of narrow lines with large enough slits for accurate spectrophotometry with the 600 line/mm grisms, one blazed at ~6000Å and another blazed at 4600 Å for use with the bluest spectra. The actual FWHM resolution was better than 7Å for all wavelength ranges. With these gratings, the wavelength span of the spectrograph was ~ 1300Å, and three sets of exposures, each at separate configurations of the instrument, were required to cover the full range from Hγ to Hα. Because of the time necessary to re-configure the spectrograph, the exposure sets in the different wavelength ranges could not be taken sequentially. Such a procedure is vulnerable to changes in the weather between the exposure sets in the different wavelength ranges. The procedures for assuring spectrophotometric quality are discussed below.

In practice, the program was very ambitious, and due to weather problems, in the observing time allotted to the program, not all objects had their entire wavelength intervals observed in the same epoch. However, good coverage of most objects was obtained: flux calibrated spectra were obtained over the full wavelength range in a single observing run for 48 objects. An additional 15 objects were observed over the full wavelength range, but their spectra were not flux calibrated. Flux calibrated measurements of Hβ, OIII, and Fe II were made for a total of 69 objects. Table 3b gives the observation epoch, observatory, observer, wavelength coverage, and resolution for each measurement of each object. The line emission measurements are presented in Chapter 5.

All the spectra I obtained were recorded on a CCD, and reduced using IRAF software, described in Tody (1986). All frames were bias subtracted, but no flat-fielding was performed; the Thomson CCD used has unusually flat response characteristics. Flat-fielding the chip resulted in no significant improvement. Spectra were extracted from the two dimensional image using the IRAF task "apsum", with a variance-weighted extraction algorithm. The extraction aperture was selected so as to generously capture all the light above background from a bright standard star. After extraction, the spectra were wavelength calibrated using exposures of standard gas discharge lamps, air mass corrected,

and flux calibrated using observations of the standard stars of Oke (1974) and Stone (1977). After flux calibration, the spectra were averaged except where median averaging would remove artifacts due to cosmic rays.

Spectra of adjoining wavelength intervals were spliced together by first determining if they met criteria for good spectrophotometry, including connecting smoothly in the overlap region, and if so, they were averaged in the overlap region. Spectra which were not taken in the same observing epoch were not spliced Non-contemporaneous line emission measurements are used for the line studies in Chapter 5 if all spectra are obtained in spectrophotometric conditions and flux calibrated, however, ratios of emission lines from different spectra taken non-contemporaneously are not used. For spectra not taken in spectrophotometric conditions, only relative flux measurements are used.

4. IR OBSERVATIONS

4.1 Near IR DATA

K, H, and J band observations taken from the literature are given in Table 4a, and their references are given in Table 4b. Original observations by Roger Brissenden are also presented in Table 4a. Aperture sizes are given in Table 4c.

4.2 IRAS DATA

Observations at 12, 25, 60 and 100 μ were obtained from the survey of the IRAS satellite, which scanned the sky from February to November of 1983 (Neugebauer 1984). The various scans of the satellite at the optical position of each AGN were "co-added" together to obtain a one dimensional image of the region near the source along the scan direction of the satellite. The flux in each band was extracted with the program SCANPI, run by the staff of IPAC, for all the objects in the LMA. The resulting fluxes are given in Table 4c. The calibrations used in SCANPI agree with the IRAS Point Source Catalog to within 2%. The program SCANPI produces a plot of the source profiles, co-added using

average, median, or noise weighted averaging. For these choices of co-added data, a variety of flux values derived from profile fits and straightforward integration over a choice of apertures were given. Except in a few cases, the point spread function fits were of poor quality, so I chose aperture integration limits which best approximated a symmetric aperture set where the instrumental PSF would intersect the background. In the majority of all cases, the flux values from either aperture integrations or PSF fits were consistent for all methods of data averaging. In a few cases, particularly where the source was extended or when two sources contributed flux in the same field, some adjustments were made to the given fluxes and noise estimates. These adjustments are explained case-by-case in the notes in Table 4d. In these cases, the uncertainties given by SCANPI were added to the difference between the adjusted flux and the flux from the nominal aperture integrating the averaged data. Roger Brissenden (1989) provided the reduced IRAS fluxes for 5 objects, noted in the table, but no unusual techniques or adjustments were applied.

Of the 96 sources in the LMA, 88 were detected by IRAS at one wavelength or more, 7 additional objects were assigned 3 σ upper limits, and only one object was not observed by IRAS.

5. RADIO DATA

Except for a handful of objects, all the radio fluxes and upper limits have been taken from published observations or surveys. These data are given in Table 5a, with appropriate references in Table 5b. The data from observations by collaborators are described in Brissenden (1989), Remillard (1986), and Remillard (1992*d*), and are referenced where appropriate in Table 5b. Most of the objects without published fluxes are below the survey thresholds, but radio-quietness can still often be demonstrated with the upper limits derived from these surveys. For such objects, the surveys were searched for any sources within a small radius of the optical position of the AGN, usually 3', and if no sources were present, then the appropriate flux upper limit of the survey was used.

REFERENCES

Brissenden, R., 1989, Unpublished Thesis, Mt. Stromlo Observatory, ANU.

Brissenden et al., in progress (describes the discovery of 14 AGN).

Fabbiano, G., Trinchieri, G., and A., Macdonald, 1984, ApJ, 284, 65

Gursky, H. et al. 1978, ApJ, 223, 973

Hamuy, M., Maza, J., 1987, A&AS, 68, 383

Kondo, Y., ed., Scientific Accomplishments of the IUE, 1987, D. Reidel Publishing Co., pp ix-x.

Landolt, A. U., 1973, AJ, 78,959

Landolt, A. U., 1983, AJ, 88,439

Mushotzsky, R. F., Marshall, F. E., Boldt, E. A., Holt, S. S., and Serlemitsos, P. J. 1980, ApJ, 235, 377

Neugebauer, G., et al., 1984, ApJ, 278,L1

Oke, J.B., 1974, ApJ Suppl., 27, 21

Remillard, R.A., 1986, ApJ 301, 742

Remillard, R. A. 1989, private communication.

Remillard, R. A., 1992*a*, private communication.

Remillard, R. A., Bradt, H. V., Brissenden, R. J. V., Buckely, D. A. H., Roberts, W., Schwartz, D. A., Stroozas, B. A., & Tuohy, I. R. 1992*b* (To be submitted to AJ)

Remillard, R. A., Bradt, H. V., Schwartz, D. A., Tuohey, I. R., 1992*c*, Catalog of Identified LASS Sources, available upon request.

Remillard, R. A., Brissenden, R. J. V., Grossan, B., Bradt, H. V., Ohashi, T. 1992*d*, (in progress)

Schmidt, M., and Green, R. F. 1973, ApJ, 269, 352

Schwartz, D. A., Bradt, H., Buckley, D. Patterson, J., Remillard, R., Roberts, W., and Tuohy, I. 1985, Adv Space Res., 5,137

Stocke, et al., preprint submitted December 20 1990, to appear in ApJS.

Stone, R.P.S. 1977, ApJ, 218, 767

Tody, D., "The IRAF Data Reduction and Analysis System", 1986, Instrumentation in Astronomy VI, David L. Crawford, Editor, Proc. SPIE 627, 733

Turner, T. J., Pounds, K. A., 1989, MNRAS, 240, 833

Wood, K., et al., 1984, ApJ Suppl., 56, 507

Zombeck, M., Handbook of Space Astronomy and Astrophysics, 1990, Camb. Univ. Press., 2nd ed.

TABLE 1

THE LMA SAMPLE
(LASS / MC HARD X-RAY AGN SAMPLE)

AGN NAME[a]	RA (h ' ")	DEC (d)	(m)	(s)	LASS NAME[b]	Type[c]	z	X-ray [d] (μJy)	σ_{X-ray} (μJy)
III Zw 2	00 07 56.7	10	41	47	1H0014+111	1	0.09	1.63	0.39
EXO 0017.3-2538[e]	00 17 21.1	-25	38	42	1H0016-257	1	0.13	1.18	0.24
0048+291	00 48 53.1	29	7	46	1H0043+294	1	0.036	1.0	0.26
PG 0052+251	00 52 11.1	25	9	24	1H0048+250	1	0.154	2.08	0.37
MKN 352	00 57 8.6	31	33	27	1H0106+324	1	0.015	1.45	0.18
MKN 1152	01 11 21.9	-15	6	39	1H0113-148	1	0.052	1.60	0.18
NGC 526A	01 21 37.0	-35	19	32	1H0121-353	2	0.018	1.89	0.26
Fairall 9	01 21 51.2	-59	3	59	1H0122-590	1	0.045	1.87	0.21
B2 0138+39B	01 39 00.9	39	8	21	1H0140+393	1	0.08	0.947	0.24
H0147-537[f]	01 47 00.2	-53	43	21	1H0150-537	1	1.56	1.32	0.18
H0237-647[f]	02 13 20.9	-64	44	2	1H0217-639	1	0.074	1.21	0.29
NGC 985	02 32 10.5	-9	0	21	1H0227-094	1	0.043	0.947	0.16
2A0235-526	02 36 40.2	-52	24	28	1H0235-525	1	0.042	1.13	0.13
H0239-585[f]	02 39 14.4	-59	6	20	1H0239-585	1	1.36	0.947	0.18
H0300-124[f]	03 00 52.2	-12	25	12	1H0258-126	1	0.077	1.37	0.42
CTIO 0307-474	03 07 29.5	-47	26	41	1H0300-482	1	0.128	1.37	0.45
0316-346	03 16 07.6	-34	37	31	1H0311-348	1	0.265	1.16	0.24
H0355-826[f]	03 55 24.7	-82	39	10	1H0339-822	1	0.064	0.97	0.16
Fairall 1116	03 49 56.2	-40	36	52	1H0347-413	1	0.058	1.18	0.24
H0348-120[f]	03 50 26.3	-12	6	26	1H0355-116	1	1.52	1.97	0.21
PKS 0405-123	04 05 27.5	-12	19	32	1H0413-116	1	0.574	1.13	0.21
Fairall 303	04 29 30.8	-53	43	20	1H0435-531	1	0.04	1.39	0.24
H0439-272[f]	04 39 21.0	-27	14	3	1H0435-274	1	0.08	1.34	0.21
NGC 1667	04 46 10.2	-6	24	24	1H0445-060	2	0.015	1.05	0.21
MCG -01-13-025	04 49 14	-3	49	19	1H0448-041	1	0.013	1.92	0.18
Pic A	05 18 18.2	-45	49	48	1H0507-459	1	0.034	1.21	0.16
"H0510+031"[g]	04 59 30.9	3	27	44	1H0510+031	1	0.016	1.71	0.26
IR 0522-1212	05 21 47.4	-12	12	51	1H0523-118	1	0.049	1.16	0.13
3A 0557-383	05 56 21.2	-38	20	15	1H0555-384	1	0.0344	1.84	0.16
1H0557-503[h]	05 58 34.6	-50	26	55	1H0557-503	1	0.137	1.58	0.13
H0623-645[i]	06 22 54.2	-64	34	43	1H0620-646	1	0.128	1.13	0.11
MKN 6	06 45 43.4	74	29	7	1H0641+741	1	0.019	1.32	0.13
MKN 376	07 10 35.8	45	47	7	1H0659+453	1	0.056	1.87	0.21
IRAS F07144+4410[j]	07 14 26.0	44	10	56	1H0707+443	1	0.062	1.58	0.29
MKN 79	07 38 46.9	49	55	47	1H0744+499	1	0.0219	1.0	0.18
H0759+452[f]	07 59 16.4	45	10	28	1H0753+456	1	0.036	1.63	0.24
PG 0804+76	08 04 35.4	76	11	32	1H0758+762	1	0.10	1.1	0.16
MKN 705	09 23 20.0	12	57	3	1H0929+122	1	0.028	1.0	0.16
0942+095	09 42 49.1	9	50	5	1H0932+107	1	0.014	1.03	0.18
NGC 2992	09 43 17.6	-14	5	43	1H0946-144	2	0.007	2.58	0.21

H1002+427[f]	10 02 24.8	42	45	13	1H1003+428	1	0.257	1.16	0.16
NGC 3227	10 20 46.8	20	7	8	1H1017+202	1	0.0033	2.29	0.26
H1029–140[f]	10 29 26.9	–14	1	26	1H1032–142	1	0.09	1.05	0.18
H1039–074[f]	10 39 48.4	–7	24	52	1H1039–073	1	0.674	1.53	0.18
PG1121+422	11 21 52.1	42	16	54	1H1120+423	1	0.234	1.0	0.29
NGC 3783	11 36 33.0	–37	27	41	1H1135–372	1	0.0091	1.68	0.24
NGC 4151	12 08 01.0	39	41	2	1H1210+393	1	0.0033	2.08	0.24
3C 273	12 26 33.2	2	19	43	1H1226+022	1	0.158	3.39	0.29
AKN 374	12 29 33.1	20	26	3	1H1229+199	1	0.064	1.26	0.21
NGC 4593	12 37 04.6	–5	4	11	1H1238–050	1	0.009	2.21	0.34
NGC 4968	13 04 23.5	–23	24	31	1H1308–237	2	0.009	1.21	0.16
NGC 5033	13 11 09.2	36	51	30	1H1313+363	2	0.003	1.76	0.45
H1320+551[f]	13 20 48.9	55	11	8	1H1318+560	1	0.064	1.08	0.21
IR1321+058	13 21 48.6	5	52	43	1H1320+066	1	0.201	1.0	0.26
H1318+692[f]	13 18 45.0	69	16	45	1H1321+692	1	0.068	1.03	0.16
H1324–246[f]	13 24 27.5	–24	36	9	1H1325–246	1	0.041	1.0	0.18
MCG–6–30–15	13 33 01.7	–34	2	27	1H1334–340	1	0.0078	2.24	0.29
MKN 464	13 53 45.1	38	48	54	1H1341+402	1	0.051	1.71	0.24
IC 4329A	13 46 27.9	–30	3	41	1H1345–300	1	0.016	3.31	0.32
MKN 279	13 51 51.9	69	33	13	1H1350+696	1	0.031	1.6	0.11
NGC 5506	14 10 39.1	–2	58	27	1H1408–031	2	0.0061	0.97	0.13
NGC 5548	14 15 43.5	25	22	1	1H1415+255	1	0.0166	3.34	0.21
H1419+480[f]	14 19 38.4	48	1	6	1H1420+481	1	0.072	1.34	0.18
B2 1425+267	14 25 21.9	26	45	38	1H1422+273	1	0.366	1.0	0.13
MKN 478	14 40 04.6	35	38	53	1H1429+370	1	0.079	0.97	0.32
H1443+421[f]	14 43 44.1	42	6	52	1H1448+415	1	1.407	0.97	0.29
MKN 1392	15 03 25.9	3	53	59	1H1504+035	1	0.036	2.24	0.47
MKN 290	15 34 45.4	58	4	0	1H1530+585	1	0.029	1.1	0.13
1537–183[4]	15 37 28.6	–18	16	54	1H1538–182	1	0.024	1.0	0.13
H1537+339[f]	15 37 55.2	33	59	4	1H1540+338	1	0.33	2.08	0.34
MKN 876	16 13 36.2	65	50	37	1H1615+655	1	0.129	1.0	0.13
MKN 885	16 29 43.1	67	29	6	1H1630+673	1	0.026	1.45	0.29
UGC 10683B	17 02 24.7	–1	28	23	1H1703–013	1	0.031	1.79	0.16
3C 351	17 04 03.6	60	48	29	1H1704+605	1	0.371	1.18	0.26
MKN 506	17 20 45.6	30	55	30	1H1727+308	1	0.043	0.947	0.10
V 1803+676	18 03 37.4	67	37	54	1H1811+670	1	0.136	1.5	0.21
KUV1821+64	18 21 41.7	64	19	1	1H1820+643	1	0.297	1.47	0.13
Fairall 49	18 32 32.8	–59	26	39	1H1828–593	2	0.019	1.16	0.16
ESO 103–G35	18 33 22.0	–65	28	18	1H1832–652	2	0.013	1.53	0.16
H1839–786[h]	18 39 03.5	–78	35	6	1H1836–786	1	0.074	1.6	0.24
3C 390.3	18 45 37.5	79	43	6	1H1858+797	1	0.057	0.947	0.079
ESO 141–G55	19 16 57.0	–58	45	52	1H1911–589	1	0.0368	1.39	0.13
H1934–513[h]	19 34 14.8	–51	16	35	1H1927–516	1	0.04	1.13	0.21
Fairall 341	20 16 13.0	–52	47	0	1H2018–529	2	0.016	1.21	0.24
MKN 509	20 41 26.4	–10	54	16	1H2041–108	1	0.0352	2.76	0.32
H2106–099[h]	21 06 28.2	–9	52	29	1H2107–097	1	0.027	1.18	0.16
H2132–626[h]	21 32 33.2	–62	37	27	1H2129–624	1	0.059	1.18	0.21
NGC 7213	22 06 08.0	–47	24	38	1H2209–470	1	0.0059	1.71	0.24
NGC 7172	21 59 07.2	–32	6	43	1H2214–313	2	0.0085	0.97	0.21
AKN 564	22 40 18.3	29	27	46	1H2239+294	1	0.025	1.26	0.16
MR 2251–178	22 51 25.9	–17	50	54	1H2251–179	1	0.068	1.45	0.32
NGC 7469	23 00 44.2	8	36	16	1H2301+086	1	0.0167	2.58	0.26
MCG–2–58–22	23 02 07.1	–8	57	20	1H2303–089	1	0.0475	1.6	0.18
PG 2304+042	23 04 30.4	4	16	42	1H2303+039	1	0.042	1.42	0.29
NGC 7582	23 15 38.4	–42	38	38	1H2315–423	2	0.0053	2.47	0.21
NGC 7674	23 25 24.4	8	30	13	1H2320+084	2	0.029	1.32	0.29

References:
a. This column gives the popular name, except where an object was first identified as an optical counterpart as part of the A-3/LASS identification program (Remillard et al. 1992c). In this case, the IAU name is given, preceeded by "H", and a reference is given. See Veron for references to popular names. For more naming information, see Remillard et al. (1992c).
b. Name associated with the error box given in Wood et al. (1984).
c. Optical spectral line type. "1" is given if the broad line flux dominates at both Hβ and Hα, otherwise the type is "2".
d. LASS count rates converted to 5 keV flux density assuming a power law slope of –0.7, as given in Remillard et al. (1992c).
e. Giommi, P., et al., ApJ 1991, 378, 77
f. Remillard et al. (1992b)
g. See Veron (1989)
h. Remillard et al. (1986)
i. Brissenden et al. (in progress)
j. Argyle, R. W., Eldridge, P., MNRAS, 1990, 243, 504

NARROW LINE OBJECTS ONLY

AGN NAME	RA (h) (m) (s)	DEC (d)	(m)	(s)	LASS NAME	Type	z	X-ray μJy	Sigma(X)
NGC 526A	01 21 37.0	-35	19	32	1H0121-353	2	0.018	1.89	0.26
NGC 1667	04 46 10.2	-6	24	24	1H0445-060	2	0.015	1.05	0.21
NGC 2992	09 43 17.6	-14	5	43	1H0946-144	2	0.007	2.58	0.21
NGC 4968	13 04 23.5	-23	24	31	1H1308-237	2	0.009	1.21	0.16
NGC 5033	13 11 09.2	36	51	30	1H1313+363	2	0.003	1.76	0.45
NGC 5506	14 10 39.1	-2	58	27	1H1408-031	2	0.0061	0.97	0.13
Fairall 49	18 32 32.8	-59	26	39	1H1828-593	2	0.019	1.16	0.16
ESO 103-G35	18 33 22.0	-65	28	18	1H1832-652	2	0.013	1.53	0.16
Fairall 341	20 16 13.0	-52	47	0	1H2018-529	2	0.016	1.21	0.24
NGC 7172	21 59 07.2	-32	6	43	1H2214-313	2	0.0085	0.97	0.21
NGC 7582	23 15 38.4	-42	38	38	1H2315-423	2	0.0053	2.47	0.21
NGC 7674	23 25 24.4	8	30	13	1H2320+084	2	0.029	1.32	0.29

TABLE 2

IUE UV CONTINUUM MEASUREMENTS

LASS Name	[1]F_ν (mJy) 3030-3100 Å	[2]σ	F_ν (mJy) 2880-3030 Å	σ	F_ν (mJy) 2570-2720 Å	σ	F_ν (mJy) 2150-2325 Å	σ	F_ν (mJy) 1990-2050 Å	σ	F_ν (mJy) 1700-1860 Å	σ	F_ν (mJy) 1425-1520 Å	σ	F_ν (mJy) 1290-1360 Å	σ	F_ν (mJy) 1130-1170 Å	σ	[6]Exposure i.d. SW/LW
0014+111	0.00	12.00	0.00	4.54	2.77	0.50	2.03	0.54	2.15	3.06	1.29	0.50	1.15	0.51	1.39	0.57	0.80	0.20	1806/1687
0043+294	0.44	0.84	0.64	1.03	0.64	0.34	0.91	1.82	0.55	1.75	0.24	0.39	0.34	0.53	0.24	0.37	0.00	0.42	34724/14437
0048+250					3.01	1.96	2.58	1.00	2.21	1.29	3.01	3.38	2.04	1.78	1.98	0.42	1.66	0.26	19224/15214
0106+324	3.91	1.85	3.75	0.88	3.62	0.64	4.02	4.22	3.44	1.89	5.08	1.19	4.82	2.34	3.75	1.02	6.09	5.32	17961/14180
0113–148	0.71	1.75	0.39	0.54	0.27	0.24	0.35	0.60	0.15	0.67	0.20	0.27	0.09	0.34	0.07	0.23	0.13	0.37	30119/9953
0121–353	0.88	0.18	0.61	0.06	0.30	0.03	0.46	0.07	0.00	0.20	0.77	0.46							.../16117
0122–590	13.58	1.50	11.78	0.33	11.09	0.16	9.97	0.19	9.81	0.44	8.35	0.06	8.83	0.14	8.13	0.1	7.98	0.33	16890/13123
0122–590	12.87	1.88	7.371	0.10	7.827	0.06	6.52	0.12	6.765	0.26	6.51	0.01	6.544	0.03	5.442	0.09	5.06	0.21	28307/8081
0227–094	0.00	3.01	0.39	0.89	0.12	0.31	0.34	0.63	0.89	1.80	4.30	0.86	5.01	1.79	3.21	0.82	5.53	3.20	14689/11267
0235–525	0.74	0.45	0.07	0.10	0.05	0.07	0.81	0.25	0.00	0.73	0.98	0.04	0.91	0.08	0.93	0.08	2.70	0.38	15648/1410
0413–116									0.18	0.74	0.00	0.15	0.00	0.37	0.00	0.41	0.00	0.08	1356/1310
0413–116									2.09	1.12	1.52	0.16	1.73	0.38	1.53	0.44	1.11	0.17	21288/16976
[3]0557–503					13.51	0.25	9.74	0.11	10.28	0.29	9.67	0.14	8.46	0.09	8.76	0.11	10.20	0.14	
[4]0557–503					11.60	0.36	10.70	0.21	9.88	0.85	9.74	0.52	9.95	0.14	12.17	0.33	14.11	0.36	37604/16793
0641+741	5.24	3.55	1.31	1.25	0.79	0.57	1.00	0.93	0.03	1.61	0.11	1.10	0.24	0.81	0.41	0.72	0.41	2.07	10002/8711
0659+453	12.72	13.46	7.76	3.57	6.33	1.04	4.32	2.08	1.85	2.56	2.14	0.50	2.13	0.83	1.36	0.63	5.56	2.29	7163/6163
0659+453	4.85	2.17	3.58	1.41	2.98	0.54	2.55	1.42	1.94	2.66	1.23	0.48	1.10	0.65	0.61	0.57	1.66	0.97	34856/14575
0744+499	6.56	2.38	5.29	0.89	4.56	0.64	2.55	1.05	3.15	1.51	5.09	0.75	5.69	1.37	4.42	0.49	4.02	2.19	1364/1320
0758+762	6.40	5.99	4.92	0.52	3.75	0.58	3.83	2.53	3.15	0.50	2.56	0.42	2.59	0.52	2.24	0.39			17393/13645
0929+122											2.32	0.39	1.96	0.54	1.48	0.44	2.02	1.17	25826/...
0946–144	1.47	1.55	1.54	0.84	0.71	0.49	0.79	1.60	0.46	1.76	0.49	0.65	0.12	0.65	0.61	0.43	2.20	2.28	7214/9949
1017+202	5.28	1.35	5.08	1.11	3.11	0.50	1.87	1.47	1.32	1.75	0.58	0.29	0.36	0.35	0.14	0.17	1.03	3.24	21778/2416
1032–142													9.72	0.21	8.89	0.25	8.54	0.30	37590/...
1135–372	9.45	4.62	10.28	2.41	10.38	1.73	11.52	15.97	7.35	4.48	4.74	1.22	4.16	1.53	3.05	0.96	3.31	4.69	3509/3092
1135–372	15.22	2.68	16.46	2.50	15.84	1.56	14.33	6.08	12.06	6.53	6.53	0.75	6.29	1.41	4.74	1.09	3.73	4.85	21733/2405
1210+393	24.19	3.17	21.86	2.23	18.58	2.72	14.82	2.79	11.51	2.07	14.19	2.34	17.92	5.47	12.30	1.88	8.67	8.75	1372/1326
1210+393	10.61	2.49	9.81	0.95	7.44	1.23	6.96	4.40	3.64	4.41	0.18	0.66	0.95	1.33	0.21	0.75	0.83	5.42	28303/8194
1226+022					8.50	1.45	7.48	1.07	6.81	1.40	5.70	1.88	12.56	2.11	11.22	1.93	9.57	1.33	5116/4470
1226+022					16.67	1.79	12.67	1.24	11.85	1.60	10.91	2.39	9.00	0.81	9.44	0.89	8.07	0.73	16801/13057
1229+199	3.91	2.45	3.52	1.10	3.13	0.33	2.64	0.46	2.95	0.51	5.16	0.77	4.81	0.92	4.24	0.52	6.09	0.66	20142/16071

1238–050	4.91	1.65	4.70	0.90	3.76	0.53	3.01	2.37	1.52	1.25	1.51	0.44	1.41	0.67	0.89	0.21	0.45	1.08	2186/2731
1238–050	7.96	1.16	7.15	1.36	6.10	0.66	4.57	2.07	3.68	2.19	3.38	0.52	2.48	0.76	2.05	0.36	2.98	1.84	32523/12279
1345–300	1.41	0.41	1.02	0.32	0.56	0.19	0.56	0.85	0.07	0.61	0.45	0.27	0.34	0.33	0.17	0.24	0.00	1.21	9607/8380
1350+696	1.12	1.37	0.70	0.77	0.76	0.28	0.43	0.56	0.62	0.71	1.60	0.38	1.26	0.40	1.01	0.27	0.66	1.70	3497/3073
1350+696	3.02	1.10	2.75	0.87	2.74	0.32	2.28	1.25	2.13	1.66	1.00	0.33	1.56	1.23	0.71	0.40	0.00	0.94	22863/3232
1415+255	11.39	4.79	10.47	2.66	10.60	1.85	7.77	6.08	6.72	2.97	6.49	1.39	6.08	1.88	5.23	0.91	5.40	5.06	8752/7498
1415+255	10.97	1.04	10.22	1.82	9.86	0.57	6.58	2.11	6.53	2.53	6.42	0.50	6.28	1.69	5.01	0.68	4.40	1.56	19990/15950
1420+481	3.43	3.00	1.86	0.56	1.25	0.26	1.07	1.02	0.99	0.65	0.69	0.33	0.47	0.33	0.42	0.28	0.48	0.21	17265/1583
1420+481	2.95	2.02	2.49	0.73	1.97	0.23	1.56	0.41	1.32	0.62	1.22	0.82	0.68	0.26	0.59	0.21	0.69	0.15	18951/1760
1429+370	0.67	38.72	3.64	8.53	3.29	1.17	3.30	1.72	3.35	3.63	2.48	0.93	2.00	0.75	1.86	0.64	1.98	0.52	17170/13450
1429+370	10.13	52.11	1.23	8.61	2.44	0.96	2.41	1.29	3.42	3.44	1.66	1.18	1.95	2.01	1.60	1.78	3.18	1.72	22865/17396
1530+585	4.59	2.58	3.49	1.42	3.32	0.44	2.74	1.29	2.66	1.88	2.11	0.37	2.04	0.40	1.73	0.34	1.62	0.89	22862/3231
1530+585	3.76	0.83	3.45	0.75	3.45	0.36	3.01	1.22	3.05	1.48	2.32	0.39	2.42	0.60	1.95	0.30			24943/5245
1615+655					3.90	2.36	4.74	3.86	15.71	16.41	3.15	7.63	4.60	1.30	5.16	1.32	4.72	1.49	20801/16673
1704+605					0.54	0.02	0.48	0.01	0.50	0.01	0.49	0.03	0.46	0.01	0.37	0.02			18441/8711
1811+670					1.15	0.57	1.32	0.31	1.22	0.57	1.27	0.61	1.54	0.67	0.90	0.26	0.67	0.21	31032/10810
1820+643							4.09	0.56	3.74	0.45	3.93	0.79	2.65	0.18	2.64	0.15	2.30	0.34	31431/11294
1820+643							3.92	0.51	3.41	0.39	3.57	0.85	2.56	0.20	2.56	0.20	2.14	0.19	35516/14996
1828–593					6.04	0.67	2.11	0.25	2.57	0.15	4.18	0.75	3.44	1.16	5.82	4.61			.../9273
1836–786	0.24	0.95	4.79	0.31	4.09	0.10	4.38	0.19	4.78	0.78	3.20	0.13	3.37	0.17	1.97	0.13	4.02	0.22	25355/5453
1858+797	1.18	4.10	0.53	1.15	0.79	0.27	0.75	0.61	0.56	0.90	1.39	1.01	0.69	0.58	0.63	0.42	0.95	0.50	3478/3057
1858+797	2.03	1.22	1.45	1.12	1.19	0.28	0.82	0.74	0.96	1.03	0.32	0.19	0.61	0.37	0.32	0.20	0.58	0.43	10753/9435
1911–589	61.57	3.79	59.57	1.05	55.14	0.75	43.57	1.08	40.97	1.40	47.59	0.57	61.06	1.07	65.73	0.99	69.32	4.06	5514/4779
1911–589	27.17	1.70	31.35	0.41	35.90	0.38	45.59	0.88	46.15	1.20	34.52	0.33	35.59	0.61	34.95	0.60	34.13	2.30	16788/13043
2041–108	12.61	3.68	11.90	1.48	11.04	0.76	7.75	1.12	7.34	0.82	3.80	0.55	4.81	2.58	3.50	0.60	2.93	1.51	1743/1636
2041–108	17.75	2.27	15.44	2.77	14.79	1.21	12.07	2.92	10.45	3.35	9.32	0.59	9.31	1.73	8.07	1.22	5.31	1.69	5412/4651
[5]2107–097	10.75	1.31	8.95	1.13	7.49	0.62	5.96	1.65	3.14	3.07	3.34	0.49	3.52	0.82	2.98	0.82	1.52	0.62	1806/
2209–470	9.33	0.49	8.38	0.27	5.68	0.23	4.54	0.57	2.01	0.39	2.81	0.09	3.73	0.14	2.58	0.08	2.66	0.87	9099/7846
2209–470	10.80	0.60	7.53	0.15	5.19	0.15	3.86	0.29	3.52	0.76	2.63	0.07	2.70	0.12	3.03	0.08	3.72	0.97	10197/8944
2214–313	0.80	0.51	0.53	0.35	0.52	0.48	0.62	1.09	0.06	1.21									.../9261
2239+294	8.43	3.95	8.96	1.96	7.62	0.70	7.37	2.70	5.80	3.64	1.88	0.28	1.37	0.47	1.18	0.27	1.15	1.21	22031/2664
2251–179	1.36	11.92	3.61	2.71	3.39	0.80	2.79	0.98	2.72	2.04	1.83	0.56	2.95	1.29	2.12	0.89	1.80	0.72	3731/3316
2251–179	2.64	10.49	6.21	3.23	5.59	0.83	5.04	1.01	3.78	1.23	3.44	0.65	4.75	1.65	3.00	0.99	4.52	0.85	7485/6470
2301+086	6.91	1.63	8.06	2.24	7.32	0.85	6.20	1.60	5.33	1.25	6.54	0.57	6.16	0.93	5.35	0.50	4.19	1.68	1798/1680
2301+086	15.26	2.03	14.96	1.03	13.90	1.03	11.25	3.15	10.25	2.91	8.93	0.80	7.59	0.98	6.60	0.65	6.08	1.67	14095/10733
2303–089	7.75	4.58	7.69	1.65	6.34	0.70	4.97	0.78	3.62	0.75	13.65	2.70	18.13	4.64	12.40	1.46	11.91	4.66	7440/6432
2303–089	9.06	5.64	6.06	5.17	5.87	1.29	4.21	4.28	5.36	7.25	3.61	0.90	3.84	1.69	2.67	1.02	3.39	1.82	10856/9548
2315–423	9.48	1.31	7.57	0.37	4.40	0.27	2.47	0.46	4.69	0.88	0.32	0.08	0.18	0.07	0.01	0.07	1.13	0.35	3471/3051
2315–423	0.80	0.33	0.79	0.13	0.59	0.11	0.48	0.21	0.00	0.50	0.40	0.09	0.23	0.14	0.05	0.07			5353/4598

Notes to Table 2:

[1]Average background subtracted flux in emitted band indicated. 0.00 indicates that a flux << σ was measured.

[2]R. m. s. of band in previous column, in mJy.

[3]These data were acquired 1987 Sept. 21–22 by Ron Remillard.

[4]These data were collected by Hale V. D. Bradt on 1989 Nov. 15-16

[5]These data were taken 1988 May 18 by Roger Brissenden.

[6]This column gives the identification number of the short wavelength camera exposure, followed by, "/", and the identification number of the long wavelength camera exposure.

TABLE 3A
OPTICAL PHOTOMETRIC MEASUREMENTS

LASS Name	[1]Run / Ref.	U (mJy)	σ (mJy)	B (mJy)	σ (mJy)	V (mJy)	σ (mJy)	R (mJy)	σ (mJy)	I (mJy)	σ (mJy)
1H0014+111											
1H0016–257											
1H0043+294											
1H0048+250											
1H0106+324	s9			2.79	0.07	3.99	0.11	5.52	0.14	7.9	0.19
1H0113–148	s9			0.46	0.01	1.30	0.036	4.70	0.12	7.04	0.26
1H0121–353	Hamuy 85.8	0.94	0.02	2.63	0.05	5.62	0.16	7.49	0.18	10.61	0.22
1H0122–590				3.91	0.10	3.62	0.10	3.34	0.08	4.45	0.17
1H0140+393											
1H0150-535	Remillard 89.9	0.3	0.01	0.35	0.01	0.39	0.01	0.48	0.01	0.54	0.02
1H0217-639	Brissenden 89.1	0.67	0.04	1.46	0.13	1.99	0.17	2.62	0.21	3.39	0.77
1H0227–094	s9			5.06	0.12	5.9	0.17	8.05	0.2	9.94	0.25
1H0235–525											
1H0258–126											
1H0300–482											
1H0311–348											
1H0339–822	Brissenden 86.1	0.23	0.01	0.51	0.01	0.91	0.03	1.3	0.03	1.78	0.07
1H0347–413											
1H0355–116	Remillard 89.9					0.14	0.01				
1H0413–116	s9			2.57	0.06	3.68	0.1	4.31	0.11	4.76	0.18
1H0435–531											
1H0435–274	Remillard 89.11 (CTIO)	1.07	0.02	1.38	0.04	2.5	0.05	2.7	0.05	3.32	0.06
1H0445–060	s9			7.18	0.18	14.64	0.41	20.02	0.49	28.95	0.71
1H0448–041	s9			4.05	0.15	9.19	0.26	12.34	0.3	18.39	0.45
1H0507–459											
1H0510+031	s9			3.76	0.09	6.06	0.17	8.3	0.2	9.86	0.37
1H0523–118	s9			2.0	0.05	3.65	0.1	4.98	0.12	6.21	0.15
1H0555–384											
1H0557–503	Remillard 92	3.39	0.16	3.22	0.06	3.51	0.05	3.3	0.06	3.85	0.07
1H0620–646	Brissenden 89.1	1.29	0.08	1.28	0.03	1.76	0.03				
1H0641+741	s9			5.56	0.03	11.23	0.31	17.12	0.42	22.43	0.55
1H0659+453	s9			0.783	0.019	1.323	0.037	1.571	0.039	1.904	0.05
1H0707+443											
1H0744+499											
1H0753+456											
1H0758+762											
1H0929+122	Hamuy 85.4	2.74	0.07	3.63	0.1	5.57	0.16	6.96	0.1	9.67	0.2
1H0932+107											

1H0946–144	Hamuy 85.2	1.75	0.03	5.64	0.15	13.12	0.37	20.44	0.43	32.63	0.68
1H1003+428	Remillard 91.2					0.5	0.01				
1H1017+202	m9			13.07	0.1	21.67	0.17	32.1	0.32	41.76	0.28
1H1032-142	Brissenden 89.1	11.86	1.06	11.68	1.1	11.97	1.15	12.32	0.94	14.91	1.37
1H1039–073	Remillard 91.2					0.53	0.01				
1H1120+423	m9			1.6	0.03	1.57	0.03	1.46	0.02	1.89	0.01
1H1135–372	Hamuy 85.3	12.65	0.12	14.57	0.53	21.18	0.8	30.1	1.09	37.81	1.37
1H1210+393	m9			32.08	0.24	46.34	0.4	63.62	1.12	64.23	0.37
1H1226+022	m9			27.92	0.25	15.6	0.18	22.76	0.22	31.08	0.36
1H1229+199	m9			2.85	0.03	3.35	0.01	4.01	0.02	4.5	0.02
1H1238–050	m9			7.19	0.05	13	0.01	18.23	0.08	25.7	0.53
1H1308–237	m9			1.88	0.04	4.48	0.1	6.66	0.08	10.48	0.04
1H1313+363	m9			12.88	0.29	27.27	0.22	38.8	0.38	61.56	3.64
1H1318+560	s9			1.55	0.02	2.46	0.02	2.99	0.19	3.29	0.16
1H1320+066	Remillard 90.1					0.31	0.046				
1H1321+692	s9			0.53	0.02	0.79	0.02	0.99	0.01	1.26	0.02
1H1325–246	m9			0.84	0.02	1.6	0.04	2.17	0.03	3.03	0.05
1H1334–340	Hamuy 85.3	2.37	0.05	7.58	0.12	15.21	0.28	22.01	0.35	31.45	0.51
1H1341+402											
1H1345-300	Hamuy 85.2	1.81	0.02	5.85	0.09	13.37	0.25	24.13	0.39	35.78	0.58
1H1350+696	m9			3.29	0.07	5.5	0.04	8.23	0.08	9.73	0.05
1H1408–031	m9			2.22	0.03	4.41	0.05	4.73	0.06	5.81	0.05
1H1415+255	m9			13.44	0.11	16.47	0.14	22.24	0.21	23.94	0.16
1H1420+481	s9			2.28	0.02	3.01	0.03	3.66	0.04	4.37	0.04
1H1422+273	m9			1.336	0.03	1.073	0.03	1.17	0.029	1.28	0.048
1H1429+370	m9			4.94	0.04	5.54	0.04	5.79	0.06	6.64	0.05
1H1448+415						0.49	0.01				
1H1504+035	m9			2.22	0.02	3.74	0.03	5.03	0.05	6.4	0.04
1H1530+585	m9			3.09	0.05	4.06	0.06	5.15	0.05	5.49	0.03
1H1538–182											
1H1540+338	Remillard 89.4					0.71	0.10				
1H1615+655	m9			3.73	0.06	4.12	0.08	3.94	0.07	8.16	0.26
1H1630+673	m9 avg			1.74	0.01	3.65	0.03	5.05	0.04	7.26	0.04
1H1703-013	m9			0.52	0.01	1.5	0.04	2.58	0.04	4.41	0.1
1H1704+605	m9			2.08	0.03	2.14	0.03	2.41	0.02	2.62	0.02
1H1727+308	m9			1.52	0.04	2.87	0.05	4.07	0.04	5.32	
1H1811+670	m9 avg			0.73	0.003	0.88	0.025	0.88	0.022	0.83	0.02
1H1820+643	m9			8.26	0.08	7.11	0.03	7.71	0.06	9.23	0.09
1H1828–593											
1H1832–652	Hamuy 85.4	0.82	0.01	2.8	0.09	6.34	0.24	8.84	0.29	12.99	0.42
1H1836–786	Brissenden 87.4	1.83	0.03	1.92	0.04	2.48	0.05	3.04	0.05	3.82	0.12
1H1858+797											
1H1911–589	Hamuy 85.7	9.34	0.23	9.36	0.35	10.42	0.49	13.02	0.49	14.64	0.55
1H1927–516	Brissenden 87.4	1.64	0.03	1.67	0.04	2.1	0.06	2.62	0.07	3.03	0.06

1H2018–529											
1H2041–108	Hamuy 85.8	14	0.13	12.81	0.27	14.79	0.41	18.31	0.38	18.26	0.38
1H2107–097	m9			4.88	0.04	4.88	0.04	8.66	0.09	9.54	0.13
1H2129–624		2.28	0.06	2.37	0.07	3.24	0.12				
1H2209–470	Hamuy 85.9	9.25	0.09	31.87	0.66	65.16	1.83	93.45	1.94	136	2.83
1H2214–313	Hamuy 85.7	1.16	0.01	4.05	0.08	9.59	0.27	15.51	0.32	26.89	0.56
1H2239+294	s9			4.5	0.11	6.94	0.19	8.1	0.2	9.02	0.22
1H2251–179											
1H2301+086	s9			10.58	0.33	18.61	0.88	25.9	0.8	35.97	1.12
1H2303–089	Haumy 85.8	10.52	0.36	9.99	0.16	11.54	0.21	13.89	0.22	15.47	0.25
1H2303+039	Brissenden 84.8	0.47	0.01	0.94	0.02	1.95	0.04				
1H2315–423	Hamuy 85.8	3.42	0.03	9.54	0.2	18.62	0.52	29.01	0.6	43.01	0.9
1H2320+084											

[1]This column gives the run code, given in the Key to Observations, if observed within the collaboration. If photometry was taken from the literature, a reference is given, along with the year of the observation minus 1900. The abbreviation "avg" is used to indicate that more than one observation, performed within an interval of a few weeks, was averaged together.

References:
Hamuy - Hamuy, M., Maza, J., 1987, A&AS, 68, 383
Brissenden - Brissenden, R., 1989, Unpublished Thesis, Mt. Stromlo Observatory, ANU

TABLE 3B
OPTICAL OBSERVATION LOG

LASS NAME	B spectra[a]	V spectra[b]	R spectra[c]	Photometry[d]
1H0014+11i	O9, J1	J1	J1	N9 S9
1H0016–257	O9, N9	N9	N9	N9 S9
1H0043+294	O9B	J1	J1	S9
1H0048+250	N0	O9	O9,J1	N9 S9
1H0106+324	O9			S9
1H0113–148	O9			S9
1H0121–353	N9	N9	N9	N9
1H0122–590	N9	N9	N9	N9
1H0140+393	O9			
1H0150–535	O4	O4	O4	
1H0217–639		L6	L6	N9[V]
1H0227-094			O9	
1H0235–525	N9	N9	N9	N9
1H0239–585	D8	D8	D8	
1H0258–126	O9	O9		S9
1H0300–482	D8	D8	D8	
1H0311–348	L6	L6	L6	
1H0339–822	F6	F6	F6	
1H0347 –413	D8	D8	D8	
1H0355–116				
1H0413–116	N0	N0	F0	S9
1H0435–531	N9	N9	N9	N9
1H0435–274	N9	N9	N9	
1H0445–060	O9			S9
1H0448–041	O9,L6	O9, L6	L6	S9
1H0507–459	N9	N9	N9	N9
1H0510+031	F6	F6	F6	S9
1H0523–118	O9, F8, O4	O9, F8, O4	F8, O4	S9
1H0555–384	N9	N9	N9	N9
1H0557–503	F8, F4	F8, F4	F8, F4	N9
1H0620–646	F8	F8	F8	
1H0641+741	O9	O9		S9
1H0659+453	O9, M3[r]	M3[r]	M3[r]	S9
1H0707+443	N0	F0,N0	F0, N0	S9
1H0744+499			O9	S9,M9
1H0753+456				
1H0758+762			F0	N9
1H0929+122	O9			S9 M9
1H0932+107	O9	O9,J1	J1	S9S
1H0946–144	N0	M0	M0	
1H1003+428	Y1,D9,J9	D9,J9	F0	
1H1017+202	M9			N M9
1H1032–142	M9	M9,D9,F0	M9,D9,F0	C M9
1H1039–073		F0	F0	
1H1120+423	M9		J1	M9
1H1135–372				
1H1210+393	M9,	M0	M0	M9

1H1226+022	M9, M0	M9, M0		
1H1229+199	M9	M9	M9	C M9
1H1238–050	M9	M9, M0	M9, M0	C M9
1H1308–237	Y1	J0,J1	J1	M9
1H1313+363	M9	J0[r]	J0[r]	M9
1H1318+560	M9, J1, Y1	M9,J1	M9, J1	C M9
1H1320+066	F0	F0	F0	
1H1321+692	J0	J0, J1	J0, J1	
1H1325–246	F6	J0, F6	J0, F6	M9
1H1334–340		J1	J1	
1H1341+402	J0	J1	J0,J1	
1H1345–300	J0	J0, J1	J1	
1H1350+696	M9	M9	M9	C M9
1H1408–031	J0[r]			M9
1H1415+255	M9	M9, M0	M9, M0	C M9
1H1420+481	M9, Y1	M9	M9	C M9
1H1422+273	M9	M9		M9
1H1429+370	M9	M9	M9	C M9
1H1448+415	J0, Y1, F0,J1	F0,J1	J1	
1H1504+035	J0, F6	F6	F6	M9
1H1530+585	M9	M9,J0		M9
1H1538–182	J0, J1	J1,J9	J0, J1,J9	
1H1540+338	J9	J0, J9	F0	
1H1615+655	M9	M9	N9	N9 S9 M9
1H1630+673	M9	M9	M9	C M9
1H1703–013	M9	M9	J0	S9 M9
1H1704+605	M9	M9	.N9	N N9 M9
1H1727+308	M9	M9	M9	
1H1811+670	M9	M9	N9	N N9 S9 M9
1H1820+643	M9, D0, M3	M9, D0, M3	M9, F0	N9 M9
1H1828–593	N9	N9	N9	N9
1H1832–652	N9	N9	N9	N9
1H1836–786	M3	M3	M3	
1H1858+797	O9,J0[r]	J0[r]	J0[r]	
1H1911–589	N9	N9	N9	N9
1H1927–516	M3	M3	M3	
1H2018–529	N9	N9	N9	N9
1H2041–108	M9	M9, M0	M9, M0	C M9
1H2107–097	M9, M8	N0, D0, M9, M8	N0, D0, M8	S9, M9, M8
1H2129–624	M3	M3	M3	
1H2209–470	N9	N9	N9	N9
1H2214–313	N9	N9	N9	N9
1H2239+294	O9			N S9
1H2251–179	J0,O9	D0	D0, N9	S9 N9
1H2301+086	O9			N S9
1H2303–089	O9			N S9
1H2303+039	J0,O9, O4	O4	O4	S9
1H2315–423	N9	N9	N9	N9
1H2320+084	O9	O9		N S9

[a,b,c] Spectra were taken in multiple sections to cover Hα to Hγ. The wavelength regions of spectra have been named "B", "V", and "R", but have nothing to do with the traditional photometric band definitions, and cover the following approximate wavelength ranges: B spectra,~ 3860 – 5120Å, V spectra ~5000–6275Å, R spectra, ~6060– 7450, *except for objects with z > 0.10.* Some observations have different wavelength regions in their spectra, but completeness or deficiency of wavelength coverage is conveniently indicated by an observation code, or the absence of one, in the columns for these three wavelength intervals. For objects with z > 0.10, all band definitions are displaced by one column to the blue, ie. B ~ 5000–

6275Å, V ~6060– 7450, and R denotes any spectra considerably redder than 7450 Å. In this way, a blank in the R column for objects of $z > 0.10$ indicates that Hα was not measured.

[d] See Optical Key, below, for explanation of abbreviations.

[V] These photometry measurements include V band but do not cover B–I.

[r] Relative fluxes only; absolute fluxes are not available due to poor weather.

OPTICAL KEY:

Symbol	Epoch of observation / Telescope[a] / Observer[b]	Type of Observation	Resolution / Slit WIdth (If Spectra)	Aperture Size (If Photometry)
J1	1991 June MDM 1.3m RR	Spectra	6Å / 4.3"	
Y1	1991 January MDM 1.3m RR	Spectra	6Å / 4.3"	
D0	1990 December MDM 1.3m RR	Spectra	<12Å / 4.3"	
N0	1990 November MDM 1.3m RR	Spectra	6Å / 4.3"	
M0	1990 May CTIO 1.5m RR	photometry		10"
F0	1990 February MDM 2.4m RR	Spectra	10Å / 2.4"	
J0	1990 June MDM 2.4m	Spectra	7 Å / 2.4"	
M0	1990 May MDM 2.4m RR	Spectra	10Å / 2.4"	
N9	November 1989 CTIO 1.5m RR	photometry, spectra 3000–9000Å	15 Å	10"
O9	1989 October MDM 2.4m	BVspectra	6Å / 3.3"	
S9	1989 September MDM 1.3m	BVRI photometry		15"
M9	1989 May MDM 1.3m	BVR spectra, and BVRI photometry	6Å / 4.3"	15"
Y9	January 1989 MDM 2.4m RR	Photometry, spectra	10 Å / 2.4"	10"
D8	1988 December CTIO 4m RR	3000–9000A	10 Å	
M8	1988 May, Simultaneous with Ginga Observations (with RR)	Spectra and Photometry	<12 Å / 3.1"	15"
F8	1988 February ANU 2.3m RR	Spectra	6 Å / ~3.5"	
L6	1986 July AAT 3.9m RR	Spectra	<5500Å, 10Å, >5500Å, 20Å / ~3.5"	
F6	1986 February AAT 3.9m RR	spectra	<5500Å, 10Å, >5500Å, 20Å / ~3.5"	
N4	1984 November ANU 1m RR	Photometry		20"
O4	1984 October 3.9m AAT RR	spectra	10 Å / ~3.5"	
F4	1984 February AAT 3.9m RR	Spectra	10 Å / ~3.5"	
M3	1983 May AAT 3.9m RR	spectra	10 Å / ~3.5"	
Brisssenden	(all dates) ANU 2.3m RB	Photometry		10" diameter circle

[a]"MDM" referes to the Michigan–Dartmouth–MIT observatory atop Kitt Peak, AZ, with 1.3 m and 2.4 m telescopes, "AAT", the Anglo-Australian Telescope at Siding Spring Observatory, and "ANU", the telescopes of the Australian National University.

[b] Observers other than Bruce Grossan are identified by initials; RB for Roger Brissenden, RR for Ronald Remillard.

TABLE 4A

NEAR IR FLUX MEASUREMENTS

LASS NAME	1.25μ[a] (mJy)	$\sigma_{1.2}$	1.65μ (mJy)	$\sigma_{1.65}$	2.2μ (mJy)	$\sigma_{2.2}$	3.5μ (mJy)	$\sigma_{3.5}$	4.8μ (mJy)	$\sigma_{4.8}$	10.2μ (mJy)	$\sigma_{10.2}$
1H0014+111	9.3		11.3		21.0		36.0	4.0			44.0	9.0
1H0016–257												
1H0043+294												
1H0048+250	0.57	0.03	0.65	0.04	0.89	0.03	1.09	0.04			1.59	0.11
1H0106+324	9.6	0.77	11.2	0.9	14.0	1.12	15.0	0.15			17.0	8.0
1H0113–148	7.3	0.3	9.7	0.3	11.1	0.4	16.3	1.7	27.3	7.3		
1H0121–353	12.2	0.5	16.3	0.6	18.6	0.7	40.8	1.6	66	15.0		
1H0122–590	57.7	2	113	4.0	132	4.7	125	5.0	96	23.0		
1H0150–537												
1H0217–639	4.36	0.49	6.39	0.77	9.11	0.65						
1H0235–525	8.0	0.3	11	0.4	16.9	0.8	24.2	1.7				
1H0258–126												
1H0300–482												
1H0311–348												
1H0339–822	2.99	0.19	3.58	0.28	3.37	0.27						
1H0347–413												
1H0355–116												
1H0413–116												
1H0435–531												
1H0435–274												
1H0445–060												
1H0448–041	24.4	0.88	30.3	0.83	32.2	0.59						
1H0507–459												
1H0510+031	11.8	0.32	12.6	0.46	10.6	0.39						
1H0523–118	6.58	0.07	10.4	0.07	12.5	0.1	26.0	0.5			108	13.0
1H0555–384	10.0	0.6	19.2	1.5	38	3.0	113	9.0	116	25.0	347	45
1H0557–503	12.4	0.34	14.0	0.51	16.9	0.61						
1H0620–646												
1H0641+741	20.0	1.6	28.0	2.24	38	3.04	46.0	3.68			160	25.0
1H0659+453	14.7	1.18	21.0	1.68	34.0	2.72	55	44.0			77	13.0
1H0707+443												
1H0744+499	15.8	0.6	23.5	0.9	32.2	1.3	54.3	2.2	65.0	15.0	200	24
1H0753+456												
1H0758+762	0.95	0.03	1.11	0.03	1.4	0.03	1.71	0.04			2.07	0.07
1H0929+122												
1H0932+107												
1H0946–144	26.2	1.6	42.0	2.9	45.8	2.7	57.4	3.4	65	2.3	294	24
1H1003+428												
1H1017+202	54.7	1.9	69.5	1.0	68.8	1.3	78.3	4.4	72.0	27.0	260	60
1H1032–142												
1H1039–073												
1H1120+423												
1H1135–372	20.3	0.7	25.7	0.7	32.2	1.0	50.9	2.4			400	36

1H1210+393	98	4.0	138	3.0	167	4.0	325	10	449	34.0	900	120
1H1226+022	30.9	1.5	46.8	1.2	85	2.0	155	4.0			324	60
1H1229+199												
1H1238–050	32		45		54		81				320	70
1H1308–237											245	19
1H1313+363	89.3	2.7	106	1.6	84.2	1.9	48.7	2.8				
1H1318+560												
1H1320+066												
1H1321+692												
1H1325–246	5.75	0.41	6.88	0.78	6.3	1.11						
1H1334–340	23	0.9	35.1	0.7	43.5	1.0	87.7	4.5			286	14
1H1341+402												
1H1345–300	61.3	1.6	92	1.8	125	4.0	210	5.0	170	20	760	40
1H1350+696	19.0	1.52	24.0	1.92	23	1.84	32	2.56			76	12.0
1H1408–031	44.6	2.1	115	3.0	172	6.0	255	6.0	351	29.0	643	2
1H1415+255	34	1.5	45.7	1.2	55.6	1.4	98.6	3.7	100	21.0	164	33
1H1420+481												
1H1422+273												
1H1429+370	10	0.8	15	1.2	26	2.08	37	2.96			86	19
1H1448+415												
1H1504+035	12	0.75	14.6	1.16	14.2	0.76						
1H1530+585	0.86	0.03	0.98	0.03	1.15	0.03	1.34	0.03			48	25
1H1538–182												
1H1540+338												
1H1615+655	0.66	0.03	0.8	0.04	1.03	0.03	1.24	0.04			1.78	0.08
1H1630+673												
1H1703–013												
1H1704+605	0.45	0.04	0.52	0.04	0.74	0.04	1.16	0.06			1.6	0.1
1H1811+670												
1H1820+643												
1H1828–593												
1H1832–652	21.4	0.8	26	0.5	21.5	0.7	28.9	3.0				
1H1836–786	7.87	0.14	9.85	0.36	11.9	0.22						
1H1911–589	14.5	0.7	20.3	0.6	29	0.9	64	4.2			184	31
1H1927–516	5.39	0.1	6.27	0.11	6.97	0.13						
1H2018–529												
1H2041–108	28	2.24	35	2.8	56	4.48	88	7.04			140	20
1H2107–097	17.2	0.31	22.6	1.02	30.4	1.1						
1H2129–624	6.73	0.12	8.74	0.24	10.6	0.29						
1H2209–470	73		104		109		111		261	29		
1H2214–313	31.2	1.2	57.4	1.7	80.2	3.2	132	8.0	184	40	141	15
1H2239+294												
1H2251–179	11.4	0.8	22.7	1.0	27.8	0.9	18.2	2.8				
1H2301+086	58.9	1.6	86.9	2.5	102	3.0	159	5.0	259	33	690	50
1H2303–089	15.2	0.6	20.7	0.8	28.9	1.2	52.4	2.1	56	12		
1H2303+039	5.57	0.37	8.12	0.3								
1H2315–423	45.5	1.8	76.4	3.1	99.2	4.0	143	6.0			877	35
1H2320+084	14.0	0.6	21.0	0.97	31.6	1.46						

[a] This columnn gives the flux of each object in a band centered at the wavelength indicated at the head of the column. The next column gives the uncertianty in the measurement. The fluxes and uncertainties for other wavebands are given in the following pairs of columns. The standard J,H,K,L,M, and N filter bands were used for all measurements.

TABLE 4B
NEAR IR FLUX REFERENCES AND COMMENTS

LASS NAME	Near IR Reference / Comment.
1H0014+111	W
1H0016–257	
1H0043+294	
1H0048+250	N
1H0106+324	R
1H0113–148	W
1H0121–353	W
1H0122–590	W* More measurements are available, showing variability.
1H0150–537	
1H0217–639	
1H0235–525	W, RB 87 OCT
1H0258–126	
1H0300–482	
1H0311–348	
1H0339–822	87 OCT
1H0347 –413	
1H0355–116	
1H0413–116	
1H0435–531	
1H0435–274	
1H0445–060	
1H0448–041	RB 87 OCT
1H0507–459	
1H0510+031	RB 87 OCT
1H0523–118	H, Also Avail:RB 87 OCT
1H0555–384	W* 1–5μ fluxes are from '83 Feb. 7, 10–20μ are from '83 Feb.5.
1H0557–503	RB 87 OCT
1H0620–646	
1H0641+741	R
1H0659+453	R
1H0707+443	
1H0744+499	1*1-5μ 82 Oct15 10-20μ 84 Mar 7.
1H0753+456	
1H0758+762	N
1H0929+122	
1H0932+107	
1H0946–144	W
1H1003+428	
1H1017+202	W*1-5μ 79Mar8, 10-20μ 82 May 28.
1H1032–142	
1H1039–073	
1H1120+423	
1H1135–372	W*NC
1H1210+393	W*NC
1H1226+022	W
1H1229+199	
1H1238–050	W*NC
1H1308–237	

1H1313+363	
1H1318+560	
1H1320+066	
1H1321+692	
1H1325–246	87 May RB
1H1334–340	W*NC
1H1341+402	
1H1345–300	W*NC
1H1350+696	R
1H1408–031	W*NC Overlapping measurements show >–30% difference, suggesting variability.
1H1415+255	W*NC
1H1420+481	
1H1422+273	
1H1429+370	R
1H1448+415	
1H1504+035	87 May RB
1H1530+585	N, R(10)
1H1538–182	
1H1540+338	
1H1615+655	N
1H1630+673	
1H1703–013	
1H1704+605	N
1H1811+670	
1H1820+643	
1H1828–593	
1H1832–652	
1H1836–786	87 OCT RB, 87 May also avail, No significant variability
1H1911–589	1*NC
1H1927–516	87 OCT RB, 87 May also avail, No significant variability
1H2018–529	
1H2041–108	R
1H2107–097	87 OCT RB, 87 May also avail, No significant variability
1H2129–624	87 OCT RB, 87 May also avail, No significant variability
1H2209–470	W*- 10μ later but overlap shows no change.
1H2214–313	W*NC-10μ obtained later.
1H2239+294	
1H2251–179	M
1H2301+086	W*NC
1H2303–089	W
1H2303+039	W
1H2315–423	W
1H2320+084	L

NEAR IR FLUX REFERENCE KEY:

Symbol	Reference
W	Ward et. al . ApJ 315:74-91, 1987 April 1
M	MacAlry et al., A. J. 52:341-362, 1983 August. Used 7.9" aperture when avail.
H	Hill, G.J., Becklin, E.E., Wynn-Williams, C. G. , 1988, ApJ, 330, 737
R	Reike, 1978, 226, 550 - Note: 10.2μ actually 10.6μ
L	Lawerence et al., 1985, ApJ, 291,117
N	Neugebauer et al. ApJ Supp, 63, 615
RB	Brissenden, R., 1989, Unpublished Thesis, Mt. Stromlo Observatory, ANU

NEAR IR COMMENT KEY:

NC=Non-Contemoraneous. Unless noted, 1.2-4.8μ are all measured simultaneously, as are 10 – 20μ.
*=see reference for details.

TABLE 4C
IR MEASUREMENT APERTURE SIZES

	Near IR		
Reference / Observation	Aperture Size (") J band, 1.25μ	Aperture Size (") H band, 1.65μ	Aperture Size (") K band, 2.2μ
Brissenden	10	10	10

	Far IR			
Reference / Observation	Aperture Size (") 12μ	Aperture Size (") 25μ	Aperture Size (") 60μ	Aperture Size (") 100μ
IRAS	120	120	150	320

TABLE 4D
IRAS MEASUREMENTS

LASS NAME	[a]12μm (mJy)	σ12	[a]25μm (mJy)	σ25	[a]60μm (mJy)	σ60	[a]100μm (mJy)	σ100	[b]Warmth
1H0014+111	220	39	260	49	630	45	280	210	1.24
1H0016–257	170	36	350	44	UL	135	UL	255	
1H0043+294	140	32	180	45	1080	50	2520	190	0.50
1H0048+250	20	19	110	42	60	42	550	122	5.50
1H0106+324	420	26	150	31	140	48	180	130	3.21
1H0113–148	115	30	210	36	100	38	1000	131	6.30
1H0121–353	540	54	510	42	300	40	1380	200	5.10
1H0122–590	550	50	76	46	360	72	220	52	0.63
1H0140+393	1410	34	470	23	UL	270	UL	606	
1H0150–535	UL	53	UL	90	UL	90	UL	300	
1H0217–639	80	23	80	22	190	50	UL	173	1.26
1H0227–094	150	29	500	70	UL	1420	1840	160	
1H0235–525	70	30	80	14	38	27	510	100	6.32
1H0239–585	UL	52	UL	68			540	90	
1H0258–126	UL	80	UL	110	UL	90	UL	450	
1H0300–482	20	24	100	30	200	40	220	71	1.50
1H0311–348	UL	90	50	27	270	32	350	91	0.56
1H0339–822	70	14	110	15	90	24	UL	39	3.67
1H0347–413	120	40	120	30	160	32	350	80	2.25
1H0355–116	UL	90	UL	99	UL	114	UL	375	
1H0413–116	30	30	110	28	38	42	1290	299	8.68
1H0435–531	400	22	100	16	140	30	UL	100	2.14
1H0435–274	260	17	330	37	1030	37	1980	115	0.96
1H0445–060	590	34	660	62	6320	45	1584	172	0.31
1H0448–041	130	38	220	34	120	39	580	107	5.50
1H0507–459	50	33	100	25	UL	250	410	260	
1H0510+031	150	40	100	30	100	33	UL	280	3.00
1H0523–118	100	26	330	30	340	46	UL	970	2.91
1H0555–384	650	50	750	30	370	29	160	94	6.08
1H0557–503	100	21	90	18	220	24	340	87	1.23
1H0620–646	50	22	80	20	300	50	500	175	0.80
1H0641+741	310	33	680	20	1330	31	680	212	1.53
1H0659+453	310	31	580	28	1490	100	2420	192	1.17
1H0707+443	160	50	280	27	510	21	UL	375	1.65
1H0744+499	370	28	640	46	1630	46	4000	1000	1.18
1H0753+456	UL	100	UL	120	210	69	120	120	
1H0758+762	170	30	250	45	150	42	400	140	5.00
1H0929+122	310	53	240	63	520	37	910	146	1.38
1H0932+107	UL	93	UL	180	UL	126	UL	441	
1H0946–144	540	41	1480	250	1281	623	20690	169	3.47
1H1003+428	UL	129	UL	144	70	35	150	100	
1H1017+202	1030	23	1800	55	8910	60	18190	148	0.61
1H1032–142	210	50	130	65	320	100	UL	520	1.22
1H1039–073	UL	120	UL	60	UL	117	UL	480	
1H1120+423	UL	108	UL	72	UL	63	UL	345	

1H1135–372	940	24	2410	22	3440	45	5350	374	2.10
1H1210+393	2150	46	4810	37	6320	65	9480	400	2.28
1H1226+022	790	80	1160	60	2150	43	2950	102	1.62
1H1229+199	UL	85	530	61	60	38	UL	453	26.50
1H1238–050	450	90	910	69	3450	45	6140	100	0.79
1H1308–237	610	53	1420	38	2500	34	3020	256	1.70
1H1313+363	1750	180	2090	209	17350	65	50530	96	0.36
1H1318+560	UL	110	130	16	UL	345	UL	462	
1H1320+066	240	40	200	47	1260	38	530	104	0.48
1H1321+692	UL	66	80	35	190	29	UL	182	1.26
1H1325–246	100	30	UL	150	UL	170	UL	1860	
1H1334–340	290	30	990	55	1390	53	1880	190	2.14
1H1341+402	UL	102	UL	93	UL	186	UL	468	
1H1345–300	1060	26	2250	37	2170	27	2220	215	3.11
1H1350+696	240	20	470	24	1550	28	2720	59	0.91
1H1408–031	1310	28	4450	68	8780	76	8630	122	1.52
1H1415+255	300	51	780	36	1020	48	1850	110	2.29
1H1420+481	150	40	340	75	310	40	UL	309	3.29
1H1422+273	UL	153	UL	126	UL	141	UL	567	
1H1429+370	140	21	200	36	670	50	960	185	0.90
1H1448+415	UL	84	UL	93	180	60	UL	303	
1H1504+035	160	20	270	31	420	37	1310	75	1.93
1H1530+585	150	36	210	23	190	34	300	143	3.32
1H1538–182	10	54	110	61	840	47	1910	497	0.39
1H1540+338	70	23	UL	81	100	30	450	77	
1H1615+655	60	25	250	16	720	36	460	90	1.04
1H1630+673	70	16	70	17	260	37	650	120	0.81
1H1703–013	225	109	187	128	620	32	3140	1047	0.90
1H1704+605	40	22	140	16	170	24	UL	207	2.47
1H1727+309	UL	76	150	30	UL	90	315	150	
1H1811+670	50	12	60	13	UL	51	UL	315	
1H1820+643	250	23	820	410	1710	510	2050	98	1.44
1H1828–593	540	41	1650	36	3550	355	5370	530	1.39
1H1832–652	560	41	2290	22	2480	36	740	148	2.77
1H1836–786	100	18	160	22	400	35	820	250	1.20
1H1858+797	170	24	340	20	UL	320	UL	200	
1H1911–589	240	29	370	35	610	35	UL	1806	1.82
1H1927–516	170	30	80	22	210	40	UL	430	1.14
1H2018–529	110	28	296	98	910	40	870	95	UL.98
1H2041–108	340	29	740	47	1440	37	1440	123	1.54
1H2107–097	130	26	350	45	270	21	UL	1980	3.89
1H2129–624	150	31	290	29	470	47	420	121	1.85
1H2209–470	680	43	780	40	2890	44	9150	198	0.81
1H2214–313	470	33	770	39	6040	26	12790	78	0.38
1H2239+294	427	221	580	18	900	45	1290	217	1.93
1H2251–179	UL	56	100	31	360	64	110	154	0.83
1H2301+086	1540	42	5800	53	27670	29	35590	575	0.63
1H2303–089									
1H2303+039	UL	90	UL	160	140	29	790	126	
1H2315–423	2270	51	7500	38	51690	104	83480	229	0.44
1H2320+084	170	39	UL	39	310	42	UL	819	

[a]If no detection, then "UL" is entered in this column, and the uncertainty column gives the 3 σ upper limit.
[b]Warmth is defined as 3 × (25 μm flux) / (60 μm flux); a source with a warmth of 1 will just meet the IRAS "Warm Criterion", discussed in Chapter 4. See Chapter 4 for more details.

TABLE 4E

IRAS COMMENTS

LASS NAME	[a]IRAS Comments
1H0448–041	RB
1H0510+031	RB
1H0523–118	RB
1H0557–503	RB
1H1226+022	12μ background unusual
1H1238–050	12μ background poorly chosen
1H1313+363	Large 12,25 micron wings may indicate some extended emission.
1H1325–246	RB
1H1334–340	Extended emission at 100μ might be interfering with the AGN flux, so the total uncertainty was increased (in quadrature) by an estimate of extended flux.
1H1420+481	The 25μ flux was assigned a large uncertainty due to confusion with an additional source, an extended component, and/or bad background modeling.
1H1448+415	A large uncertainty was given at 60μ due to a poor background fit.
1H1703–013	The 12 μ co-added image has a 2nd source at -1.5 ', ~ 12/32 of 1st source; this quantity was subtracted from the total and added to the sigma. At 25μ, a 2nd source appears at -1.5'; 1/3 of this flux was subtracted. At 100μ an uncertainty of 30% is given due to poor background fit.
1H1820+643	Approximately 1/3 of the total flux at 25 μ is from a 2nd source 2' away. This flux was subtracted from the total and added to sigma. At 60μ the average of a point source fit and the integrated aperture flux was given; sigma = difference/2 was assigned. No 2nd source was present at 100μ.
1H1828–593	At 60 and 100μ sigmas are given as 10 % due to poor background fits.
1H2018–529	At 60μ 20% was subtracted from the total flux due to an unusual background; the same amount was added to the uncertainty.
1H2239+294	At 12μ a contribution from a nearby (<1' away) point source (30%of total flux) was subtracted and added to sigma.
1H2251–179	At 60μ the background is poorly determined; the average of the aperture and template fit fluxes is given; the difference was added to the uncertainty.

Note that the symbol "RB" means that the data were reduced by Roger Brissenden (Brissenden, R., 1989, Unpublished Thesis, Mt. Stromlo Observatory, ANU).

TABLE 5A

RADIO MEASUREMENTS

LASS NAME	[1]Parkes3.57cm (8.4GHz)	σ	6 cm flux in mJy (VLA 4.89 GHz)	σ	11cm (2.7GHz)	σ	20 cm flux in (1.49 GHz @ VLA)	σ	[2]Radio Loudness	UL Radio Loudness	[3]Log Slope
1H0014+111			184	10	230		296	15	78.08		–0.37
1H0016–257					UL	250				270.2	
1H0043+294			UL	90						33.78	
1H0048+250			0.42	0.07					0.26		
1H0106+324			UL	90						33.45	
1H0113–148			0.9	0.3			1.9	0.4	0.48		–0.62
1H0121–353			4	0.4			6	0.5	1.42		–0.34
1H0122–590					UL	250	UL	9		9.55	
1H0140+393			87	11					47.44		
1H0150–537					UL	250				523.86	
1H0217–639	UL	6									
1H0227–094			3						0.74		
1H0235–525					UL	250				34.90	
1H0239–585					UL	200				66.67	
1H0258–126			UL	0.11			UL	3		0.17	
1H0300–482					UL	250				112.0	
1H0311–348					UL	250				59.37	
1H0339–822	UL	6.6									
1H0347–413					UL	250				42.02	
1H0355–116	UL	250									
1H0413–116			1990		2360				306.3		–0.28
1H0435–531					UL	250					
1H0435–274					UL	250				18.33	
1H0445–060					21.2		47.9		1.89		
1H0448–041	UL	4.8	7.61	0.09			3.08	0.4	1.90		0.75
1H0507–459			15000		30000				14313		–1.14
1H0510+031	5.1	0.7	4.95	0.09			16.9	0.05	1.43		–1.02
1H0523–118	UL	7.5	1.16	0.11			UL	3.0	0.57		
1H0555–384			20	1.0			40	2.0	3.35		–0.58
1H0557–503	81	4.0			190		209	5.0	41.36		
1H0620–646							UL	20			
1H0641+741			91		150				17.23		–0.82

LASS NAME	[1]Parkes3.57cm (8.4GHz)	σ	6 cm flux in mJy (VLA 4.89 GHz)	σ	11cm (2.7GHz)	σ	20 cm flux in (1.49 GHz @ VLA)	σ	[2]Radio Loudness	UL Radio Loudness	[3]Log Slope
1H0659+453			1.8	0.11			4.01	0.35	1.05		–0.67
1H0707+443			34	6.0					8.93		
1H0744+499			4						0.70		
1H0753+456			UL	40							
1H0758+762			0.97	0.07					0.40		
1H0929+122			10.0	0.07					2.52		
1H0932+107			UL	72							
1H0946–144			77	5.0			206	10.0	14.55		–0.82
1H1003+428			UL	40							
1H1017+202			46.0	3.0			126		3.33		–0.84
1H1032–142					UL	250					
1H1039–073					UL	250				15.53	
1H1120+423			UL	0.25						38.06	
1H1135–372			16.0				23.0	2.0	1.08		–0.30
1H1210+393			152	19	200				4.68		–0.45
1H1226+022			43410		41440				1528		0.08
1H1229+199			0.3	0.07					0.11		
1H1238–050			2.0						0.27		
1H1308–237					UL	250					
1H1313+363			70	10	100		178		5.23		–0.59
1H1318+560			2.68	0.03			4.66	0.4	1.62		–0.46
1H1320+066			UL	72							
1H1321+692			UL	40						113.64	
1H1325–246	UL	6.6	1.75	0.25			1.37	0.06	0.80		0.20
1H1334–340			1.0	0.4			1.7	0.7	0.13		–0.44
1H1341+402			6.0				16		8.53		–0.81
1H1345–300			24	2.0			35	2.0	3.81		–0.31
1H1350+696			8.0						2.24		
1H1408–031			132		250		291	15.0	58.58		–1.05
1H1415+255			15.0		40		8.0		1.15		–1.62
1H1420+481			0.72	0.03			UL	1.62	0.37		
1H1422+273			80		170				52.76		–1.24
1H1429+370			0.8	0.11			4.46	0.35	0.17		–1.43

LASS NAME	[1]Parkes3.57cm (8.4GHz)	σ	6 cm flux in mJy (VLA 4.89 GHz)	σ	11cm (2.7GHz)	σ	20 cm flux in (1.49 GHz @ VLA)	σ	[2]Radio Loudness	UL Radio Loudness	[3]Log Slope
1H1448+415			184	10							
1H1504+035	UL	4.7	1.84	0.02			5.43	0.55	0.78		–0.90
1H1530+585			1.8	0.07					0.58		
1H1538–182					UL	600					
1H1540+338			UL	90						111.20	
1H1615+655			2.19	0.11			4.26	0.35	0.66		–0.55
1H1630+673			UL	27							
1H1703–013					UL	350				13.40	
1H1704+605			1210		2030				498.99		–0.85
1H1727+308			UL	25.0						421.42	
1H1811+670			UL	0.35							
1H1820+643			UL	25.0						11.62	
1H1828–593					UL	600				0.21	
1H1832–652					UL	250				2.65	
1H1836–786	UL	7.8								44.35	
1H1858+797			4480		6560				2521.40		–0.63
1H1911–589							UL	12.0			
1H1927–516	UL	5.8									
1H2018–529					UL	600				0.47	
1H2041–108			5.46	0.11			14.8	0.04	0.26		–0.83
1H2107–097	5.0	2.0	1.34	0.02			4.76	0.13	0.22		–1.05
1H2129–624	31.0	2.0					UL	20.0	17.0		
1H2209–470			228		190				8.92		0.30
1H2214–313			1.8	2.0			4.0	1.0	0.30		–0.66
1H2239+294			UL	90							
1H2251–179					UL	250					
1H2301+086			70		110		134	7.0	6.65		–0.75
1H2303–089			9.0				19.0	1.0	0.90		–0.62
1H2303+039	UL	12.3	0.5	0.02			1.01	0.07	0.46		–0.58
1H2315–423			69	5.0	190		166	9.0	9.54		–1.67
1H2320+084			UL	94			13.8	0.05	1.91		

[1]Table units are mJy.

[2]Radio Loudness = $F_{6\,cm} / F_B$ where the 6 cm flux and the B band optical flux have been transformed to the rest frame of the AGN.

[3]Log Slope = Log slope measured from 6 cm to 20 cm. See text for details.

TABLE 5B
RADIO COMMENTS

LASS NAME	Radio Comments and References
1H0014+111	Unger, V512, Unger
1H0016–257	PKS
1H0043+294	MGC
1H0048+250	K
1H0106+324	MGC
1H0113–148	Unger
1H0121–353	Unger
1H0122–590	PKS,WE
1H0140+393	MG
1H0150–537	PKS
1H0217–639	
1H0227–094	V982
1H0235–525	PKS
1H0239–585	PKS
1H0258–126	
1H0300–482	PKS
1H0311–348	PKS
1H0339–822	RB
1H0347–413	PKS
1H0355–116	V1036,1036
1H0413–116	V883,500
1H0426+051	Unger; MG 6cm = 3255; significant variability
1H0435–531	PKS
1H0435–274	PKS
1H0445–060	Condon
1H0448–041	
1H0507–459	V1143,1101
1H0510+031	
1H0523f–118	
1H0555–384	Unger
1H0557–503	V1143, RL 20cm and 57cm 87 May 8
1H0620–646	RB 88 Mar 13
1H0635–431	RB 88 Mar 28
1H0641+741	V511,511
1H0659+453	AB
1H0707+443	GC ; identified with 71427.0 1.6 +441127 19,
1H0744+499	V982
1H0753+456	GC
1H0758+762	K
1H0929+122	K
1H0932+107	MG
1H0946–144	UW
1H1003+428	
1H1017+202	GC,Veron 178
1H1032–142	PKS
1H1039–073	PKS

1H1120+423	K
1H1135–372	Veron 722, , Unger
1H1210+393	V917,224
1H1226+022	V713,500,WE
1H1229+199	K
1H1238–050	V983
1H1305+466	GC
1H1308–237	PKS
1H1313+363	GC,V, Condon
1H1318+560	
1H1320+066	MG
1H1321+692	GC
1H1325–246	RB
1H1334–340	UW,,UW
1H1341+402	WE
1H1345–300	V982, ,Unger
1H1350+696	V982
1H1359–421	V883,139
1H1408–031	V232,1022,Unger
1H1415+255	V1121,1026,WE
1H1420+481	
1H1422+273	V1022,1022
1H1429+370	AB
1H1448+415	GC
1H1504+035	RB
1H1513–400	
1H1530+585	K
1H1538–182	
1H1540+338	MGB
1H1615+655	AB; WE reported 3.03 at both 6 and 20cm.
1H1630+673	
1H1639–109	PKS
1H1703–013	PKS
1H1704+605	V713,500
1H1727+308	C
1H1811+670	WE
1H1820+643	
1H1828–593	PKS
1H1832–652	PKS
1H1836–786	RB
1H1858+797	V713, V500
1H1911–589	WE
1H1927–516	
1H2018–529	PKS
1H2041–108	AB, confirmed by Unger.
1H2107–097	RB Parkes 87 June 24, VLA taken May 8, 1988.
1H2129–624	RB Parkes and Fleurs 14 GHz 87 Jul 6
1H2209–470	V796,1138
1H2214–313	V984, Unger
1H2239+294	MGC
1H2251–179	PKS
1H2301+086	V178,224, Unger; MG
1H2303–089	V982, ,WE
1H2303+039	
1H2315–423	UW,V1138, UW
1H2320+084	MG

Note: References are given in order of the frequencies listed in the previous table. A Key to references is given on the next page.

Radio Key:

Symbol	Reference
C	Condon 1990 AJ, 73,359
WE	Wilkes and Elvis, ApJ, 1987,323, 243
U	Unger, S. W., Lawrence, A., Wilson, A. S., Elvis, W. Wright, A. I., 1987, MNRAS, 228,521
V(number)	Veron-Cetty, M.P., Veron, P., 1989,ESO Sci. Rept., No. 7; number = their reference.
UW	Ulvestad and Wilson, 1984, 285,439
MG	0.5 dgs - 19.5 deg.s, all RA, limit = f(dec); MIT Green Bank Survey I; Bennett, C. L., Lawrence, C.R., Burke, B. F., Hewitt, Mahoney, J., 1986, ApJS, 61, 1
MGB	2nd survey, 4-21 hrs RA, 17-39.15 deg.s, 90 mJy 5 sigma upper lim;1990, ApJS, 72, 621
MGC	3rd, 16.5hrs-5hrs., 17-39.15 deg.s, 90 mJy 5 sigma lower limit; 1990, ApJS
MGD	4th, 15.5-2.5hrs., 37-50.98 deg.s , 90mJy upperlim 5 sigma; ApJS, 1991, submitted
AB	Antonucci and Barvanis, 1988, 323, L13
PKS	Compendium of Parkes 2700 MHz observations, distributed by Alan Wright and Robina Otrucek, PKSCAT project, ATNF.
GC	Gregory and Condon, 1991, AJS 77,1 (cd-rom distribution)
K	Kellerman, K. I., Sramek, R., Schmidt, M., Shaffer,D. B., Green, R., 1989, AJ, 98,1195
RB	Brissenden, R., 1989, Unpublished Thesis, Mt. Stromlo Observatory, ANU

FIGURE CAPTIONS

Figure 1. The Log dN / dS vs Log S curve gives the distribution of fluxes of all sources, $|b| > 20°$, in the LASS Catalog. Note the departure from the slope of $-5/2$, indicated by the solid line, at 0.0036 LASS counts s^{-1} cm^{-2} ($\approx$0.95 μJy at 5 keV), the flux limit of the sample.

Figure 2. The distribution of measurement significance, the ratio of the LASS flux to the measurement error reported in the LASS catalog (Wood et al. 1984) is shown. Note that only a small fraction of the sample has a significance less than 3.

Figure 3. The distribution of estimated total error in the LMA fluxes is given. The total error estimate was obtained by adding the confusion noise estimate to the LASS catalog (Wood et al. 1984) measurement error in quadrature. Note, again, that only a small fraction of the sample has a significance less than 3.

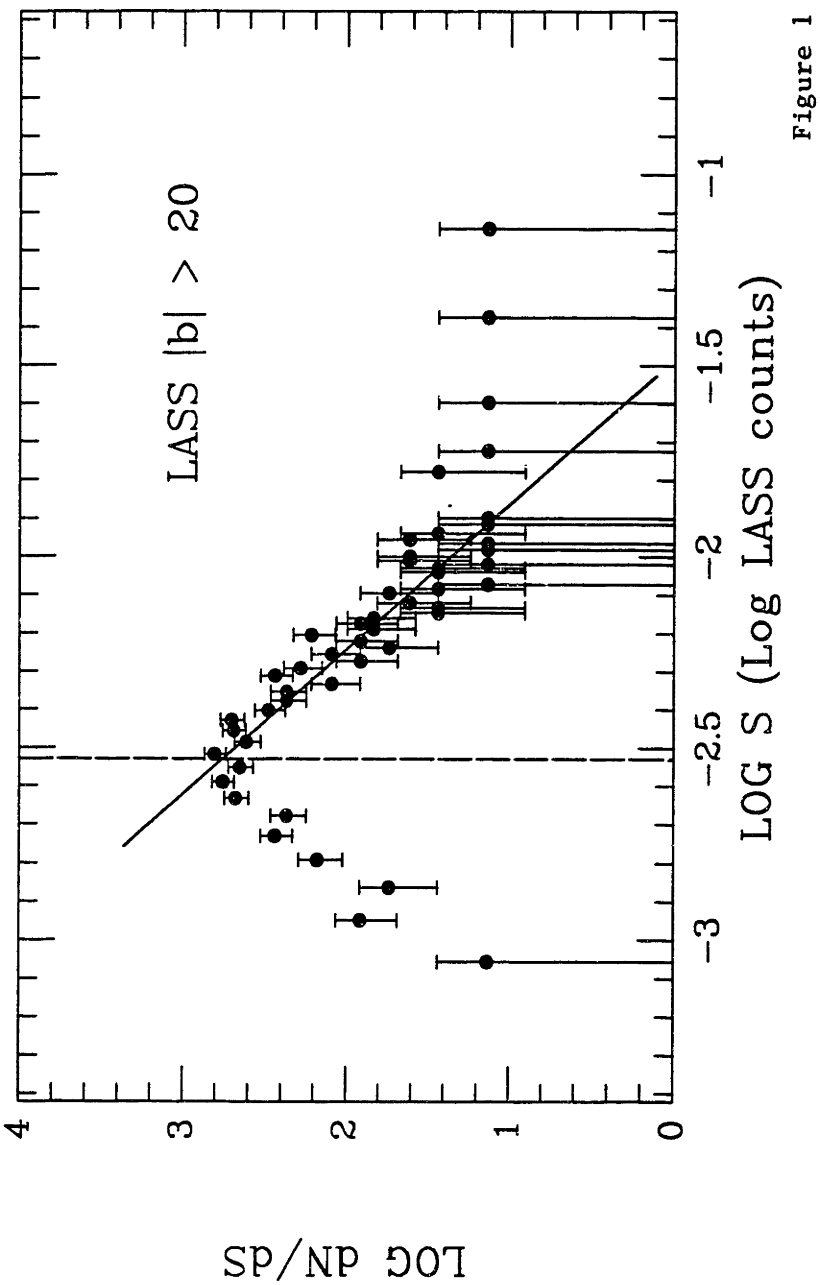

Figure 1

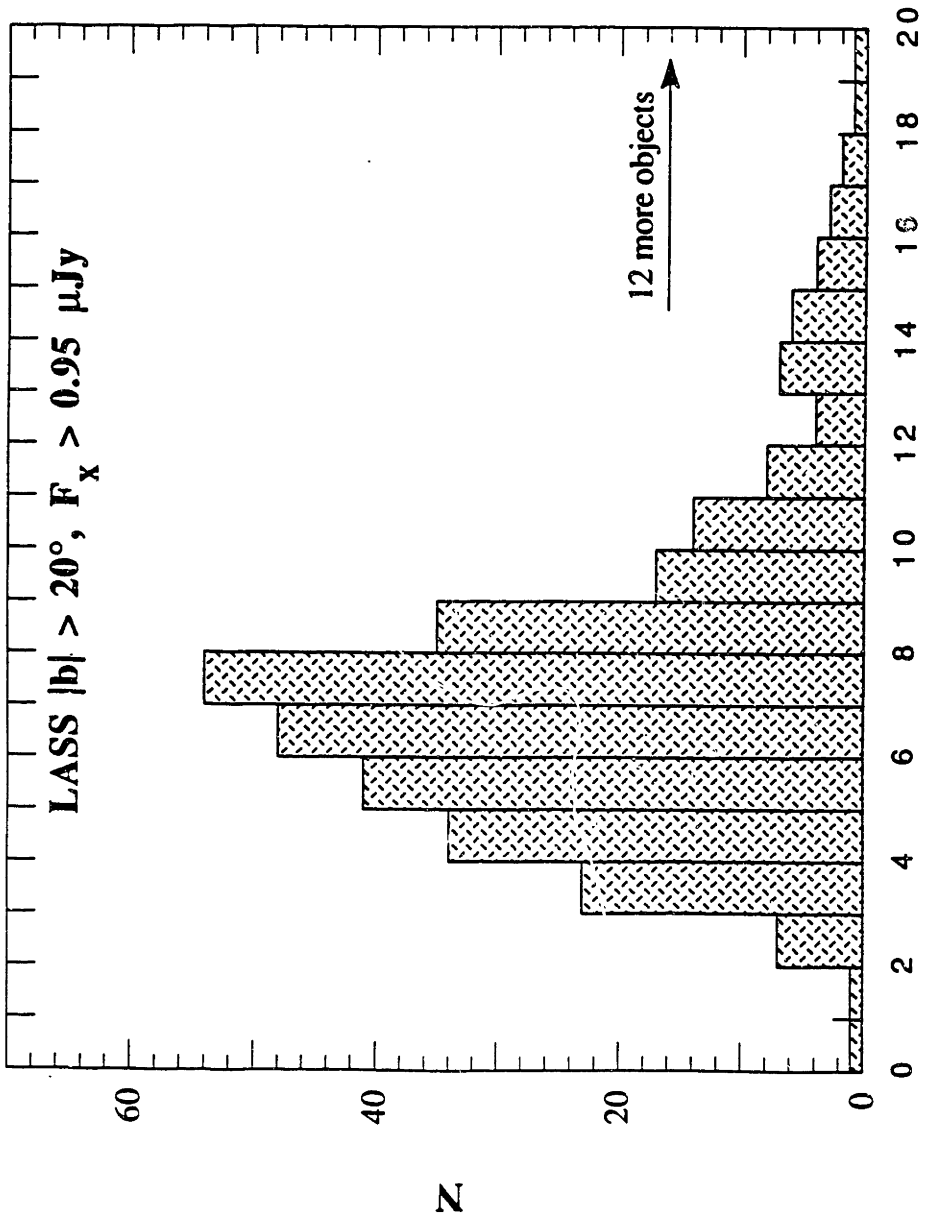
LASS |b| > 20°, F_x > 0.95 μJy
12 more objects
N
0
20
40
60
0
2
4
6
8
10
12
14
16
18
20
Flux / Measurement Noise

Figure 2

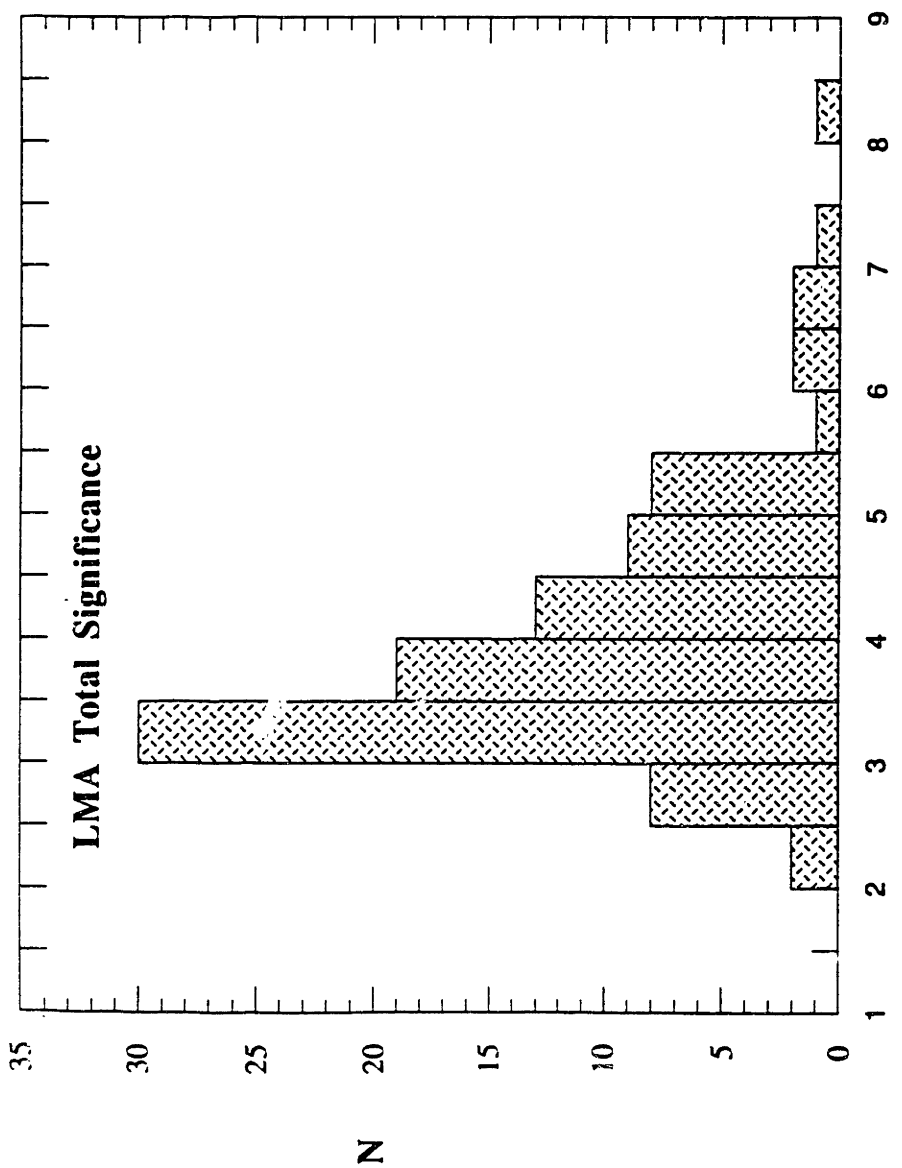
LMA Total Significance
N
Total Error / Flux
0
5
10
15
20
25
30
35
1
2
3
4
5
6
7
8
9

Figure 3

CHAPTER 3
REDDENING CORRECTION: H2107-097, AN ILLUSTRATIVE CASE

This chapter discusses reddening and its correction in AGN. The correction of reddening in the object 1H2107-097 is explained in detail as a illustrative example.

1. INTRODUCTION

Extinction refers to the sum of absorption and scattering due to dust and gas along the line of sight. Reddening refers to the effect of increasing extinction with higher frequency. More blue (and UV) light is scattered and absorbed by dust and gas than red (longer wavelength) light, so the spectrum we observe is said to be "reddened".

The average extinction function for interstellar material within our galaxy is given in Figure 1. The function was interpolated from data given in Savage & Mathis (1979). Extinction in magnitudes, A_λ, divided by $E(B-V)$, the difference in extinction between the B and V photometric bands, is plotted in the figure. $E(B-V)$ is essentially a measure of the column density of material along the line of sight. This parameterization is motivated by stellar astronomy, where the intrinsic $B-V$ of stars in often known, making $E(B-V)$ easy to calculate. The figure shows that the most significant extinction occurs in the UV. For a

typical high latitude observation of an AGN, the $E(B-V)$ due to material in the Milky Way is ~ 0.1. This level of extinction decreases the flux at V by a factor of 1.3, but at 1250 Å, the flux is depressed by a factor of 2.4. This explains why the measurement of intrinsic UV emission from AGN depends critically on reddening corrections. Because of the steepness of the extinction function, comparisons of UV measurements to other, less obscured, wave bands are particularly sensitive to extinction corrections. The log slope from the J band to the UV (1.25μm to ~ 1700Å), a measure of blue bump strength discussed in Chapter 4, is an example of a quantity highly sensitive to reddening. Careful correction for reddening is therefore essential in the multi-frequency studies presented in this work.

Since AGN are deep within the nuclei of their host galaxies, it is plausible that some absorption is taking place along the line of sight through these host galaxies or in the nucleus. In this case, to study the intrinsic emission from the AGN, it is necessary to correct for extinction both within the Milky Way and within the AGN and its host. This chapter will discuss the correction for absorption along the line of sight through our galaxy as well as the identification and correction of extinction in the host galaxy or AGN. (In the following discussion, no distinction is made between extinction within the nucleus and extinction outside of the nucleus in the host galaxy. Therefore, "extinction associated with the AGN" is understood from here on to refer to extinction from material in either region.

2. THE EXTINCTION FUNCTION

Reddening is caused by scattering and absorption by dust grains of size comparable to or smaller than the wavelength of light. Much of the description of this phenomenon has been empirical, rather than theoretical, since the effects depend on the typical distributions of dust particle sizes, dust composition, resonance absorption, and even particle surface effects (Savage & Mathis). In some representations, no less than six parameters are required to characterize the function (Van Steenberg & Shull 1988). However, the optical

region may be approximated by a λ^{-1} curve. The UV region has a much steeper component, and is dominated by an absorption feature attributed to graphite particles centered at 2175Å (1.38×10^{15} Hz) with a FWHM of ~480Å (Savage 1975). The position of the peak may vary by ± 50 Å in a few regions in the galaxy (Savage 1975), but this displacement is small compared to the width of the feature. Micro-features also exist in the reddening function (Savage and Mathis), but they are of small amplitude and have little effect on continuum measurements. They will therefore be ignored here.

The extinction function is determined for objects within the galaxy by comparing observations of reddened and relatively unreddened stars that have the same absorption lines. Significant differences in the reddening curve have been observed in small regions of the galaxy (Savage &Mathis). The differences in extinction curves are due to different mixes of gas and dust in the local environment of stars. Therefore, small regions with unusual reddening curves are unlikely to occur along lines of sight to AGN at high galactic latitudes; these lines of sight avoid the high stellar densities and dusty star-forming regions encountered in the plane of the galaxy. The line of sight for observations of extragalactic objects traverses relatively long distances, effectively averaging out any local varations in the *shape* of the extinction function. However, the column density of gas and dust, i.e., the *amount* of extinction, does vary along different lines of sight, particularly at different latitudes. Therefore, the average extinction curve within our galaxy may be used to "deredden" the spectrum of an AGN at high latitude if the value of $E(B-V)$ can be determined along the line of sight through the galaxy in the direction of the AGN.

3. REDDENING BY MATERIAL IN THE MILKY WAY

For a first approximation, the gas and dust in the galaxy can be described as being confined to an approximately flat disk with an effective thickness of ~250 pc for dust (Savage & Mathis) and roughly the same for gas, ~200 pc for HI (Zombeck 1990). The

line of sight distance through the gas and dust is therefore proportional to csc θ, where θ is the angle from symmetry axis of the disk.

The distribution of dust in the galaxy, however, has been measured to be patchy, and along some lines of sight it may be 5-10 times above or below the average (Savage & Mathis). This is what makes the assumption of a cosecant distribution a poor representation of the actual absorption. The dust along the line of sight can be determined, however, through its correlation with HI.

Measurements of 21 cm emission give the amount of HI in the line of sight within our galaxy. For small values of reddening, up to $E(B-V)$ ~0.1, there is a good correlation between the HI column and the dust absorbing column; for larger $E(B-V)$, Savage & Mathis show an increasing spread in the correlation. However, in a later survey of the interstellar medium with IUE observations, Van Steenberg & Shull (1988) emphasize that the gas (HI) to dust ratio is constant for all the $E(B-V)$ range they covered. I use the conversion of N_{HI}, the neutral hydrogen column density, to $E(B-V)$ of Van Steenberg & Shull, 5.2×10^{21} cm^{-2} mag^{-1}.

The 21 cm HI columns for the LMA objects are given in Table 1. These values were taken from Starke et al. (1992), and are typically good to ~ 10%. In the far south, where 21 cm measurement values are not available, there was no recourse but to estimate the HI column using a model with a csc θ angular dependence. An empirical fit to all available 21cm data in the direction of LMA objects yields the follwing approximate expression:

(3.0.1) $$N_{HI} \approx (3.52 \csc \theta - 1.744) \times 10^{20} \text{ cm}^{-2}.$$

The values of N_{HI} estimated using (3.0.1) are specially noted in the table.

The LMA sample objects were corrected for reddening due to material within the Milky Way as follows:

(3.0.2) $$F_V = (F_V)_{\text{raw}} 10^{(E(B-V) \times A_V / 2.5)}.$$

In this expression, F_ν is the flux density at the frequency ν, corrected for reddening within the Milky Way, $(F_\nu)_{raw}$ is the measured flux density at the frequency ν, and A_ν is the extinction per *E(B–V)* at the indicated frequency. Note that the de-reddening for material in the Milky Way is done in the observed frame, the frame of the local absorbing and scattering matter.

4. REDDENING BY MATERIAL ASSOCIATED WITH THE AGN HOST GALAXY

The morphology of Seyfert galaxies is predominantly spiral (Kirhakos and Steiner 1990), like our own galaxy. It is reasonable that these AGN hosts cause reddening in an amount similar to that within our own galaxy. The 21 cm measurements give us the E(B–V) to correct for reddening from HI in our own galaxy, but these measurements are not sensitive to material in the distant AGN or their hosts. Alternative methods must therefore be used to determine the reddening outside of our galaxy associated with each AGN.

It would be convenient if an intrinsic set of emission line parameters could be used to determine E(B–V). The physical conditions in a "Case B" optically thick recombination plasma (e.g. Lang 1974) are considered reasonable for the conditions in the BLR, and Case B models do reproduce the observed Lyα flux within a factor of 2. However, it has long been known that models using case B assumptions do not reproduce commonly observed ratios of Lyα / Hβ, referred to as "The Lyα / Hβ Problem" (Netzer, 1990). A variety of models have been used to predict the intrinsic ratio of successive Balmer lines, the "Balmer Decrement". This easily measured quantity could then used as an indicator of intrinsic reddening. However, as photoionization models became more sophisticated, it was found that a wide range of intrinsic conditions were required. The most recent papers conclude that the Balmer decrement is not a straightforward reddening indicator (e.g. Ward et al. 1989, Lawrence 1991), although they note that very steep decrements are associated with extremely reddened objects. In Chapter 5, the spread in the distribution of broad-line

Balmer decrements in un-reddened objects is shown to correspond to very large reddening values. The spread in intrinsic Balmer decrements is therefore too great to determine any but the most extreme (E(B–V) > 1 mag) reddening values. An alternative method to determine continuum reddening outside of our galaxy is therefore required. In the next section, I describe an alternative method used to determine the intrinsic reddening in the source 1H2107-097 and to correct for this reddening.

5. 1H2107-097: A CASE STUDY IN REDDENING

5.1 The 2175 Å Feature in 1H2107-097

The IUE (The International Ultraviolet Explorer satellite) spectrum of 1H2107-097, taken on 1988 May 18, appears in Figure 2. A gap appears where geocoronal Lyα was removed. No reddening corrections have been applied in this figure. A strong, broad dip in the continuum is present, stretching from ~1700 to ~2300 Å. The bottom of the dip is near 2175Å, coincident with the large feature in the extinction function.

There are several points that support the identification of this UV absorption feature. The longest-wavelength IUE spectral points connect smoothly to the optical spectrum. This agreement of the optical and UV spectra suggests that the flux calibrations of the spectra are correct. The IUE spectrum was taken in two separate exposures. The SWP spectrum, which spans 1150-1950 Å, connects smoothly to the LWP spectrum, which spans 1900-3200 Å (Boggess 1978) This smooth connection shows that the flux calibrations of these spectra are both correct, and that no features are introduced by a mis-match of the two spectra. Finally, similar behavior is also seen in independent observations of other objects.

Wu, Boggess, and Gull (1983) plot instrumental IUE spectra of four AGN, Mkn 279, Akn 120, ESO 141-G55, and Fairall 9, as F_ν vs ν, without having corrected them for reddening, and these objects all show this feature. In the F_ν vs ν representation, the onset of the feature is emphasized, occurring as a precipitous drop at ~1.3×10^{15} Hz (2300

Å). The feature in 1H2107-097 is easily noticeable in such a representation (not shown), and occurs at the same location. Further, the continuum dip in Akn 120, the largest among the AGN presented in Wu et al., is comparable in strength to that in 1H2107-097. The weaker features, such as that in ESO 141-G55, are due to absorption by material within our galaxy. However, the larger features, such as those of Akn 120 and 1H2107-097, are too strong to be caused by absorption within our galaxy. A "close-up" view of the 2175 Å region of 1H2107-097 is given in Figure 3, a plot of observed flux density vs the emitted wavelength at the AGN. Figure 3a shows the uncorrected spectrum, and Figure 3b is corrected for reddening due to the material in our galaxy along the line of sight to 1H2107-097. The column density along the line of sight within our galaxy to 1H2107-097, derived from 21cm measurements, is 4.96×10^{20} cm^{-2}. The figure shows that the feature persists after correction for reddening in our galaxy. The residual feature therefore suggests the presence of reddening material associated within 1H2107-097 itself.

The appearance of a dip-like feature can be produced by coincidental combinations of a steep continuum on the blue side of the feature and a broad emission line on the red side of the feature. The nearest broad emission feature which might contribute to this effect is the Fe II mound near 2400 Å. Examination of the Fe lines in this region in the spectra of other sources not believed to be reddened show that they occur in a bump from about 2270 Å - 2650 Å (full width at zero intensity) in the very strongest cases of UV Fe emission, such as in Mkn 290. The Fe II emission in these objects and in the models given in Wills, Netzer and Wills (1985; WNW hereafter) are not consistent with the dip observed in 1H2107-097, which rises steeply toward the red at a wavelength less than 2200 Å. Also, the spectrum of 1H2107-097, corrected for absorption due to material in our galaxy, does not rise dramatically to the blue. It is rather flat all the way out to Lyα, except for the blue side of the dip. It is therefore unlikely that Fe emission conspiring with the continuum could cause the drop, although the Fe emission might emphasize the red side of the 2175Å

dip. It is very likely that the residual feature (shown in Figure 3b) is due to reddening associated with the AGN itself.

5.2 Determination of Intrinsic Reddening

The first step to determining the reddening intrinsic to the AGN is to correct for the reddening due to material within our galaxy. In F_λ, this correction is given by:

(5.2.1) $$F_\lambda = (F_\lambda)_{raw}\, 10^{(E(B-V)\times A_\lambda / 2.5)}$$

where $(F_\lambda)_{raw}$ is the flux density of the uncorrected spectrum at the observed wavelength λ, F_λ is the flux density corrected for reddening, and A_λ is the extinction at the wavelength λ.

A reddened spectrum that shows a residual 2175Å feature can be corrected by applying increasing values of $E(B-V)$, in the rest frame of the AGN, until the feature vanishes. The subtlety to this procedure is that the appearance of the corrected spectrum, one from which the 2175Å feature has "vanished", is not well known. Below, I show that the shape of the continuum in the optical-UV region can be approximated by a power law. Given this assumption, a good estimate of the depth of the 2175 Å absorption feature can be obtained by de-reddening the measured continuum until the flux density at 2175 Å is consistent with the power law.

The UV-Optical AGN spectrum has been successfully modeled by WNW and Netzer et al. (1985) with a combination of line emission, a power-law model of an underlying continuum, blended Fe II emission, which forms an apparent continuum in much of the UV and optical regions, and Balmer continuum emission in the 2000-4000 Å region. (The fits were performed on the observed F_λ at the emitted wavelength, i.e., after the spectrum was shifted by a factor of 1/(1+z) in wavelength.) The power law continuum in these models was fitted only in Fe emission-free regions which were identified with extensive modeling of Fe II quantum levels, 1330-1380 Å, 1430-1460 Å, 5553Å-5664Å, 6750Å-6840Å, all in the emitted frame. In this way, contamination of the power law fits

from blended Fe II emission in the fit regions was avoided. In this work, a power law was fitted to the continuum of 1H2107-097 in the same regions used by WNW (also with fluxes shifted to the emitted wavelength). For a wide range of reddening corrections, the power law fits were not of good quality in the region immediately surrounding Hγ(4340 Å rest). In this region, the power law went above the apparent continuum. When points in the regions immediately surrounding Hγ were added to the fit, regions where WNW determined some, but relatively little, Fe emission was present, the quality of the fits improved. In the UV, the power law went above a low point immediately to the red of CIV(1550 Å rest) (as shown in Figure 3a). However, a previous spectrum of 1H2107-097 from the IUE archives does not show this feature, which suggests that it is spurious. The Fe-free regions determined by WNW plus the points in the regions immediately surrounding Hγ, 4247-4267 Å and 4416-4460 Å (emitted frame), were used in all fits described hereafter.

The spectrum was de-reddened in finite steps, fitting a power law at each step, iterating until the power law intersected the lowest continuum point in the dip region. This intersection occurs fortuitously near 2000Å, a region identified by WNW to have only small Fe II contributions. Because the power law modeling described above is done in the F_λ representation, and because the residual absorption occurs in the AGN rest frame, all operations below are performed on the flux density per unit wavelength at the observed wavelength λ_{obs} shifted to the wavelength $\lambda_{obs}/(1+z)$. In detail, the following procedures were performed on the wavelength shifted UV-Optical spectrum from 1988 May, corrected for Milky Way reddening :

1. The dip was fitted to a smooth function to reduce the difficulty of matching the dip and power law due to noise and real lines in the region. After removing emission lines, a Gaussian centered at 2175 Å was fitted *asymmetrically* from ~1650-2200Å, which is well clear of possible Fe II emission near 2400 Å. The fit was explicitly forced to 2175 Å rest because the reddening intrinsic to the AGN takes place in the AGN's frame (z =0.027).

2. For each guess of the correct value of $E_{int}(B-V)$, the reddening intrinsic to the source, the spectrum was de-reddened by that value (equation 5.2.1) and a new power law was fitted to the data.

3. This procedure continued iteratively with the goal of determining the reddening such that the power law would intersect the de-reddened continuum near its lowest point. It should be emphasized that the intersection of the actual data and the power law was sought. The Gaussian fit was used only to present a locally smooth version of the noisy data.

The power-law fit approached the lowest point of the continuum closest at $E_{int}(B-V) = 0.07$ mag. The match is inside the rms noise envelope of the continuum for values of $E_{int}(B-V)$ in the range (0.05–0.12) mag. Figure 3c, the "close-up" view of the 2175 Å feature, corrected as described above, shows a clear improvement in the smoothness of the continuum and the discrepancy between the power law fit (indicated as a dotted line) and the actual continuum. A good intersection of the power law fit and the actual data in the dip region is evident. The corrected optical-UV spectrum is presented in Figure 4; the fit points are indicated by small squares. The $E_{int}(B-V)$ value derived above, 0.07 mag, is of the same order as the reddening due to our galaxy, 0.104 mag. This seems reasonable if the host galaxy is morphologically similar to our own.

The method of de-reddening we present above is by no means a thorough solution to the reddening problem. However, in the previous literature, corrections for the Milky Way absorbing column are not always applied, and corrections for intrinsic reddening are usually ignored and never discussed; here the corrections are given to ~0.02 mag in $E(B-V)$. In this sense, the method presented is a useful first step in the reddening problem.

Discussion

The following discussion summarizes the assumptions and problems of the reddening correction method described above:.

The assumptions made in applying the reddening function as given above are first, that the measure of HI is a good indicator of the amount of dust in the Milky Way (i.e. that the dust to gas ratio is constant), and second, that the reddening function given is applicable to the material along the line of sight in both the Milky Way and at the AGN. The dust to gas ratio has been shown to be nearly constant for lines of sight out of the galaxy, which average over relatively long distances (Savage and Mathis), if they are within the range of reddenings considered here (Van Steenburg & Shull 1988). Further, it was argued that the shape of the extinction function should be similar for galaxies of similar morphological types. Can this argument be significantly flawed? In fact, significantly different extinction functions are known for some other galaxies, including the LMC (Nandy, et. al. 1984) and the SMC (Prevot, et al. 1984). In particular, the SMC has a much less pronounced 2175Å feature. However, these systems, classified as irregulars, are *very* different from our own galaxy. It is easy to imagine that different physical conditions resulting from the irregular morphology of these galaxies would result in different dust grain properties, and therefore a different extinction function. As noted above, the dominant morphology of emission line AGN is spiral type, similar to our own, which suggests a similar extinction function. If the amount of reddening is very large and the material is local to the active nucleus, the dust to gas ratio in the AGN could be investigated by a combination of the method presented above and the measurements of gas column density via X-ray spectral analysis.

An additional assumption was made above regarding the model fit to the spectrum. The optical-UV continuum must be well represented by an underlying power law plus emission lines for the results here to be correct. However, the wide success in fitting underlying power laws plus emission line models to other objects in this spectral region (e.g. WNW) supports the validity of these assumptions. The reasonable value of reddening determined and the satisfactory appearance of the 2175 Å region after correction with this value gives additional assurance that the method is sound.

6. REDDENING IN THE LMA

Significant intrinsic reddening was found via 2175 Å features for 3 objects in the LMA sample, 1H0744+499, 1H1415+255, and 1H2107-097, out of 32 IUE spectra of sufficient quality to identify a feature stronger than $E(B-V) \approx 0.03$ mag. The UV spectra of these objects in the 2175 Å region are shown in Figures 5a-c. A feature was also observed in an AGN which meets all the LMA criteria except the X-ray signal to noise criterion (discussed in Chapter 2), 1H0426+051, and this spectrum is also shown. Simultaneous UV and optical data were not available for any of these objects other than 1H2107–097. This is a significant concern, as UV variability of > factors of 2 in AGN is reported as ubiquitous by Kinney et al. (1991). Such a variation relative to the optical spectrum would not allow a reasonable fit of the optical–UV power law. In addition, the quality and availability of the UV and optical spectra did not allow the correction of any of the features of these objects other than 1H2107–097. Nonetheless, the identification of a residual 2175 Å feature in these objects shows that significant reddening occurred outside of our galaxy, almost certainly in the host galaxy or the AGN itself. The detection of the 2175 Å feature will be used as an important diagnostic tool for investigating the effects of reddening in the following chapters.

The observation of absorption features in < 10% of the LMA objects with high quality IUE spectra would seem to suggest that intrinsic reddening is rare. However, this conclusion is biased. Very reddened objects will not yield 2175 Å region IUE spectra with good signal to noise, because they will be faint. A robust conclusion about the incidence of reddening should only be drawn if good quality spectra of the 2175 Å region can be obtained for a sample of objects selected in some band relatively insensitive to reddening, such as radio, IR, or hard X-rays.

CONCLUSIONS

1. Spectral measurements in the UV including the 2175 Å region, along with simultaneous optical spectra, can be used to effectively detect and correct significant reddening in the AGN continuum. The first step is to correct for the reddening due to material in the Milky Way, with a measurement of the HI absorbing column from 21 cm measurements. This step is done in the observed frame. All remaining procedures operate on the spectrum corrected to the AGN rest frame, explicitly assuming the reddening takes place at the redshift of the AGN. A power law fit is made to the UV–optical continuum in regions specially selected to be free of line emission contributions, in order to define an underlying continuum. The spectrum is then iteratively corrected with the empirical reddening function until the observed continuum no longer shows signs of the 2175 Å feature and matches the power law fit. Although this method requires some assumptions about the intrinsic continuum, it provides a good means of checking for significant intrinsic reddening effects where previously no reliable method had been discussed in the literature.

2. In the absence of simultaneous UV and optical data, observations of the 2175 Å region alone provide a powerful diagnostic for reddening. The absorption feature must indicate the presence of dust along the line of sight to the AGN. All the AGN in the LMA sample for which IUE observations exist have been checked for a 2175 Å feature; thus the continuum measurements of these objects cannot have large errors due to undetected reddening, assuming a reddening function in the AGN host galaxy similar to the function in our galaxy.

3. Significant intrinsic reddening has been detected via residual 2175 Å features in only 3 out of 32 objects in the LMA sample observed by IUE with sufficient signal to noise to detect the 2175 Å feature. The best studied of the objects with an observable feature,

1H2107-097, required an additional reddening correction above that due to our galaxy of $E_{int}(B-V) = 0.07$ mag, for a total $E(B-V)$ of 0.17 mag.

REFERENCES

Boggess, A. *et al.* 1978, Nature, 275, 372

Kinney, A. L., Bohlin, R.C., Blades, and J.C., York, D. G., 1991, ApJS, 75, 645

Kirhakos, S. D., Steiner, J. E., 1991, AJ, 99, 1435

Lang, K. R., 1974, Astrophysical Formulae, Springer-Verlag, N.Y.

Lawrence, A., MNRAS 1991, 252,586

Netzer, N., Wamsteker, W., Wills, B., Wills, D., 1985, ApJ, 292, 143

Savage, B., Mathis, J., 1979, ARA&A, 17, 73

Stark, A. A., Gammie, C. F., Wilson, R. W., Bally, J., Linke, R. A., Heiles, C., & Hurwitz, M., 1992, ApJS, 79,77

Van Steenberg, M., and Shull, J., A Decade of UV Astronomy with IUE, Proc. Celebratory Symposium, GSFC, Greenbelt, MD 1988 April 12-15, publ. 1988, ESA SP-281, Vol. 2

Ward, M. J., Done, C., Fabian, A. C., Tennant, A. F., and Schafer, R. A., 1986, ApJ, 324, 767

(WNW) Wills, B.J., Netzer, H., and Wills, D., 1985, ApJ , 288, 94

Zombeck, M., Handbook of Space Astronomy and Astrophysics, 1990, Camb. Univ. Press., 2nd ed.

TABLE 1
REDDENING

RA (h m s)	Dec (d m s)	l^{II} (deg.s)	b^{II} (deg.s)	$^{a}N_H$ (10^{20} cm^{-2})	^{b}csc θ
00 07 56.7	+10 41 47.	106.98	-50.63	5.75	
00 17 21	-25 38 42.	45.13	-82.71	2.47	
00 48 53.1	+29 07 46.	122.97	-33.47	5.46	
00 52 11.1	+25 09 24.	123.91	-37.44	4.62	
00 57 08.6	+31 33 27.	125.02	-31.01	5.52	
01 11 21.9	-15 06 39.	147.05	-76.66	1.79	
01 21 37.	-35 19 32.	263.76	-79.46	2.12	
01 21 51.2	-59 03 59.	295.07	-57.83	...	2.42
01 39 .90	+39 08 21.	133.47	-22.44	5.88	
01 47 .20	-53 43 21.	284.86	-61.59	...	2.26
02 13 20.90	-64 44 02	289.08	-50.33	...	2.83
02 32 10.5	-09 00 21	-59.49	180.84	3.04	
02 36 40.2	-52 24 28.	271.64	-57.95	...	2.41
02 39 14.4	-59 06 20.	279.73	-53.04	...	2.66
03 52.20	-12 25 12.	193.70	-55.73	5.12	
03 07 29.5	-47 26 41.	259.00	-56.42	...	2.48
03 16 07.6	-34 37 31	235.21	-57.85	2.04	
03 55 24.7	-82 39 10	296.69	-32.31	...	4.85
03 49 56.2	-40 36 52.	244.63	-50.73	...	2.81
03 50 26.3	-12 06 26.	202.42	-44.95	3.51	
04 05 27.5	-12 19 32.	204.93	-41.76	3.74	
04 29 30.8	-53 43 20.	262.08	-42.17	...	3.50
04 39 21.	-27 14 03.	226.99	-39.33	2.51	
04 46 10.2	-06 24 24.	204.06	-30.13	5.50	
04 49 14.	-03 49 19.	201.88	-28.22	4.00	
05 18 18.2	-45 49 48.	251.60	-34.65	...	4.45
04 59 30.9	+03 27 44.	196.37	-22.31	7.74	
05 21 47.4	-12 12 51.	214.31	-24.81	9.1	
05 56 21.2	-38 20 15.	244.53	-26.36	3.79	
05 58 34.6	-50 26 55.	257.96	-28.57	...	5.62
06 22 54.2	-64 34 43.	274.31	-27.32	...	5.93
06 45 43.4	+74 29 07	140.33	26.11	6.57	
07 10 35.8	+45 47 07.	171.88	22.84	8.87	
07 14 26.	+44 10 56.	173.76	23.03	8.48	
07 38 46.9	+49 55 47.	168.60	28.38	5.72	
07 59 16.4	+45 10 28.	174.65	31.02	4.57	
08 04 35.4	+76 11 32.	138.28	31.03	3.07	
09 23 20.	+12 57 03.	219.05	40.00	3.43	
09 42 49.1	+09 50 05.	225.63	42.86	2.9	
09 43 17.6	-14 05 43.	249.71	28.78	5.15	
10 02 24.8	+42 45 13.	177.33	53.09	1.16	
10 20 46.8	+20 07 08.	216.99	55.45	2.26	
10 29 26.9	-14 01 26.	259.33	36.51	6.62	
10 39 48.4	-07 24 52.	256.36	43.22	3.75	
11 21 52.1	+42 16 54.	167.32	66.86	2.02	
11 36 33.	-37 27 41.	287.46	22.95	9.01	

12 08 01.	+39 41 02.	155.08	75.06	2.08	
12 26 33.2	+02 19 43.	289.95	64.36	1.81	
12 29 33.1	+20 26 03.	269.44	81.74	2.58	
12 37 04.6	-05 04 11.	297.48	57.40	2.35	
13 04 23.5	-23 24 31.	307.55	39.06	8.43	
13 11 09.2	+36 51 30.	98.06	79.45	1.06	
13 20 48.9	+55 11 08.	113.43	61.62	1.46	
13 21 48.6	+05 52 43.	324.40	67.11	2.31	
13 18 45.	+69 16 45.	119.08	47.89	1.56	
13 24 27.5	-24 36 09.	313.14	37.30	6.49	
13 33 01.7	-34 02 27.	313.29	27.68	4.3	
13 53 45.1	+38 48 54.	77.32	72.32	1.1	
13 46 27.9	-30 03 41.	317.50	30.92	4.4	
13 51 51.9	+69 33 13.	115.04	46.87	1.84	
14 10 39.1	-02 58 27.	339.15	53.81	3.76	
14 15 43.5	+25 22 01.	31.96	70.50	1.67	
14 19 38.4	+48 01 06.	88.57	62.89	1.72	
14 25 21.9	+26 45 38.	36.87	68.57	1.68	
14 40 04.	+35 38 53	59.23	65.04	1.01	
14 43 44.1	+42 06 52.	72.73	62.42	1.53	
15 03 25.9	+03 53 59.	2.75	50.26	3.76	
15 34 45.4	+58 04 0.	91.49	47.95	1.77	
15 37 28.6	-18 16 54.	349.58	28.75	7.85	
15 37 55.2	+33 59 04.	53.98	53.35	1.97	
16 13 36.2	+65 50 37.	98.27	40.38	2.89	
16 29 43.1	+67 29 06	99.40	38.26	4.08	
17 02 24.7	-01 28 23.	18.62	22.72	8.94	
17 04 03.6	+60 48 29.	90.08	36.38	2.33	
17 20 45.6	+30 55 30	54.17	31.50	3.26	
18 03 37.4	+67 37 54.	97.62	29.47	4.67	
18 21 41.7	+64 19 01.	94.00	27.42	3.98	
18 32 32.8	-59 26 39.	335.98	-21.34	...	7.93
18 33 22.	-65 28 18.	329.78	-23.18	...	7.20
18 39 03.5	-78 35 06.	315.74	-26.33	...	6.20
18 45 37.5	+79 43 06.	111.44	27.07	4.17	
19 16 57.	-58 45 52.	338.18	-26.71	...	6.09
19 34 14.8	-51 16 35.	346.96	-27.90	...	5.78
20 16 13.	-52 47 0.	345.93	-34.47	...	4.48
20 41 26.4	-10 54 16.	35.97	-29.86	3.93	
21 06 28.2	-09 52 29.	40.27	-34.94	4.96	
21 32 33.2	-62 37 27	331.14	-42.52	...	3.47
22 06 08.	-47 24 38.	349.59	-52.58	...	2.69
21 59 07.2	-32 06 43.	15.13	-53.07	1.69	
22 40 18.3	+29 27 46.	92.14	-25.34	6.10	
22 51 25.9	-17 50 54.	46.20	-61.33	2.78	
23 44.20	+08 36 16.	83.10	-45.47	4.83	
23 02 07.1	-08 57 20.	64.09	-58.76	3.47	
23 04 30.4	+04 16 42.	80.45	-49.51	5.19	
23 15 38.4	-42 38 38.	348.08	-65.70	...	2.12
23 25 24.4	+08 15 10.	88.97	-48.46	4.94	

[a] HI column density as given by the 21cm observations from -550 km/s to +550 km/s of Stark et al. (1992).

[b] "csc θ" denotes the approximate N_H value from a flat galactic disk approximation formula and the conversion of E(B-V) to N_H of Van Steenberg and Shull:

$N_H \approx 3.52 \csc|\theta| - 1.74$. This approximate figure is only given for objects farther south than the Stark et al. observations.

FIGURE CAPTIONS

Figure 1. This figure shows the extinction curve, a smooth interpolation of the data given in Savage & Mathis (1979). Note the extreme steepness of the function in the UV, and note the prominent feature centered near 2175 Å.

Figure 2. The IUE SW and LW (short and long wavelength spectrometers) spectra of 1H2107-097 are presented together with the geocoronal line removed. No reddening corrections have been applied. The feature marked "A" is instrumental. The apparent dip between this feature and CIV is also thought to be spurious.

Figure 3. This figure shows a "close-up" view of the region near 2175 Å in the IUE spectrum of 1H2107-097. The horizontal axis is the wavelength in the rest frame of the AGN. The bottom panel, (a), shows the "raw" spectrum uncorrected for reddening, the middle panel, (b), shows the spectrum corrected for the reddening due to material in our galaxy (as indicated by 21cm measurements), $E(B-V) = 0.104$ mag, and the top panel, (c), shows the spectrum de-reddened by 0.17 mag, the value determined by the method given in the text. In each panel, the dotted line gives the fit to a power law in the opt–UV region. See text for details of fit.

Figure 4. The combined UVoptical spectrum of 1H2107-097, after applying the de-reddening procedure described in the text, is presented in this figure. F_λ is plotted vs the wavelength in the rest frame of the AGN. The smooth line indicates the power law fit to the continuum, and the small squares indicate the fit points.

Figures 5a-c. These figures show the 2175 Å regions of two additional objects in the LMA sample for which significant 2175 Å features are observed, 1H0744+499 and 1H1415+255. 1H0426+051, which was observed as part of this work, is not in the LMA, but meets all the LMA criteria except the signal to noise criterion. Its spectrum was included for general interest. The observed flux corrected for reddening within the Milky

Way is plotted against the wavelength in the rest frame of the AGN. Smoothing was applied to all figures, but signicant noise remains. 1H0744 varied significantly between the SW and the LW camera exposures, so a fit could not be made to the continuum for correction. 1H1415 shows a significant dip in the 2175 Å region, but the noise, and Fe II and CIII] emission in this region precludes a good fit of the continuum for correction. 1H0426+051 shows a clear, deep residual 2175 Å feature.

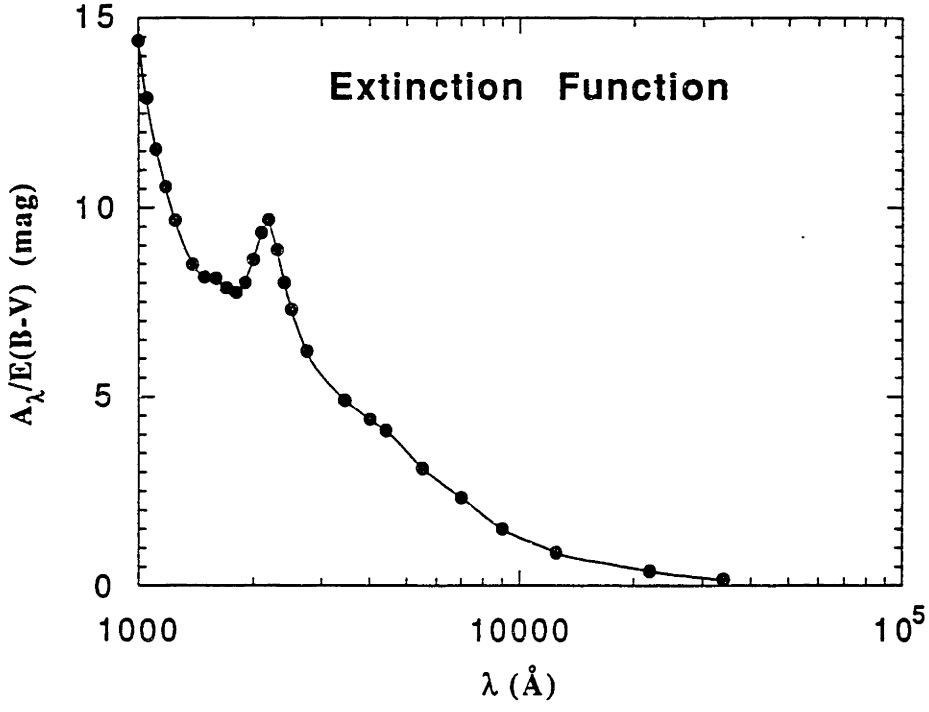
Extinction Function
15
10
5
0
1000
10000
10^5
$A_\lambda/E(B-V)$ (mag)
λ (Å)

Figure 1

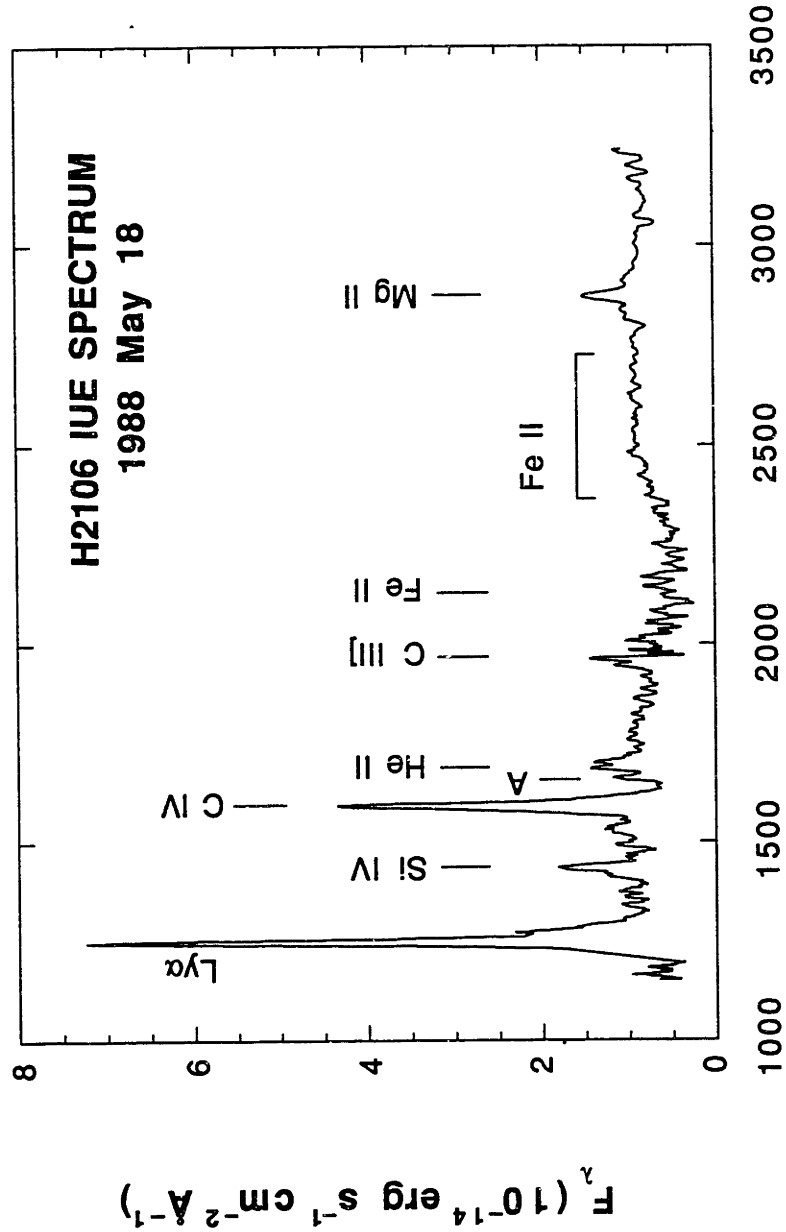
H2106 IUE SPECTRUM
1988 May 18
Lyα
Si IV
C IV
λ
He II
C III]
Fe II
Fe II
Mg II
0
2
4
6
8
1000
1500
2000
2500
3000
3500
λ (Å)
(Geocoronal line removed)
F_λ (10^{-14} erg s^{-1} cm^{-2} $Å^{-1}$)

Figure 2

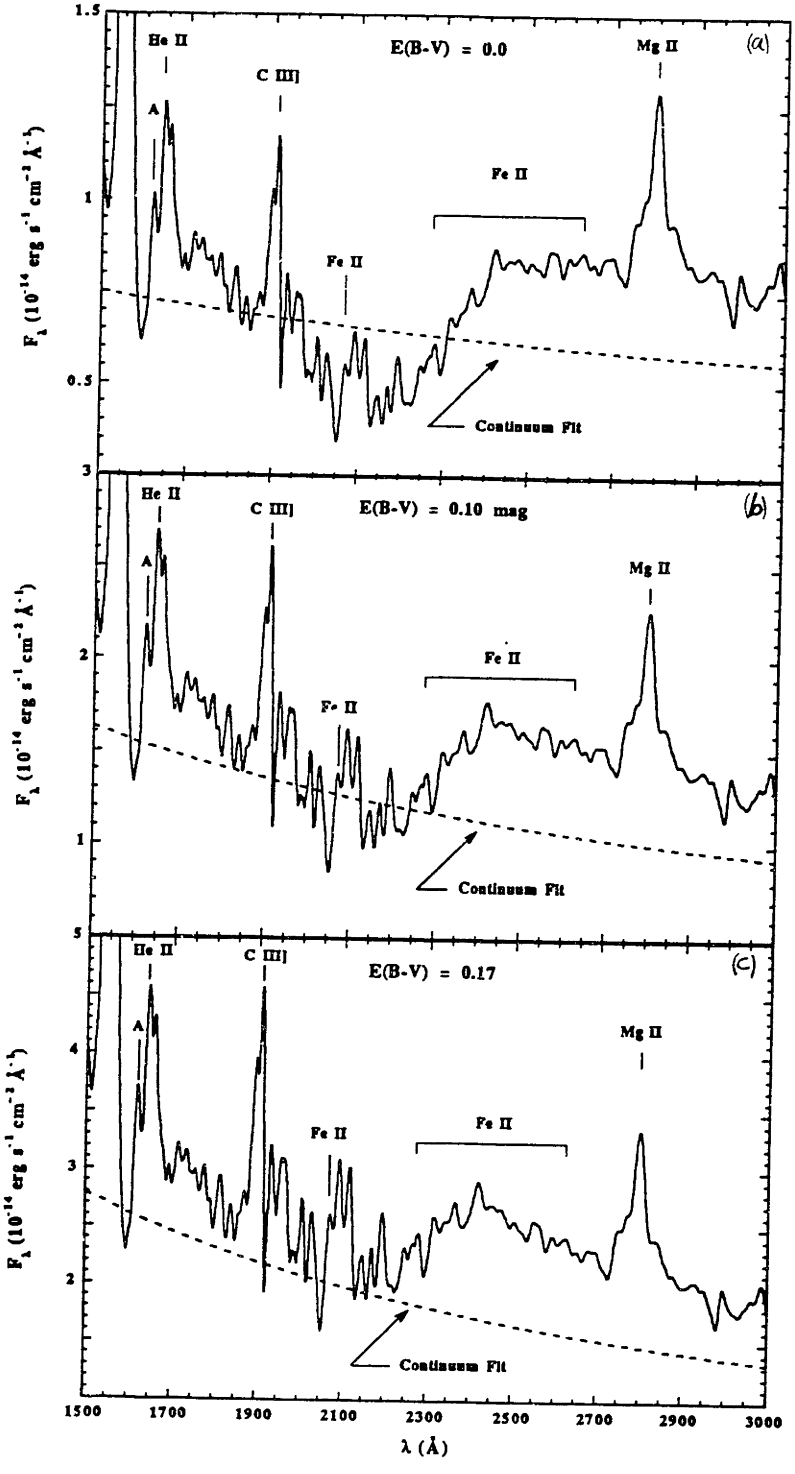
He II
C III]
Fe II
Mg II
E(B-V) = 0.0
(a)
Continuum Fit
E(B-V) = 0.10 mag
(b)
E(B-V) = 0.17
(c)
λ (Å)

Figure 3

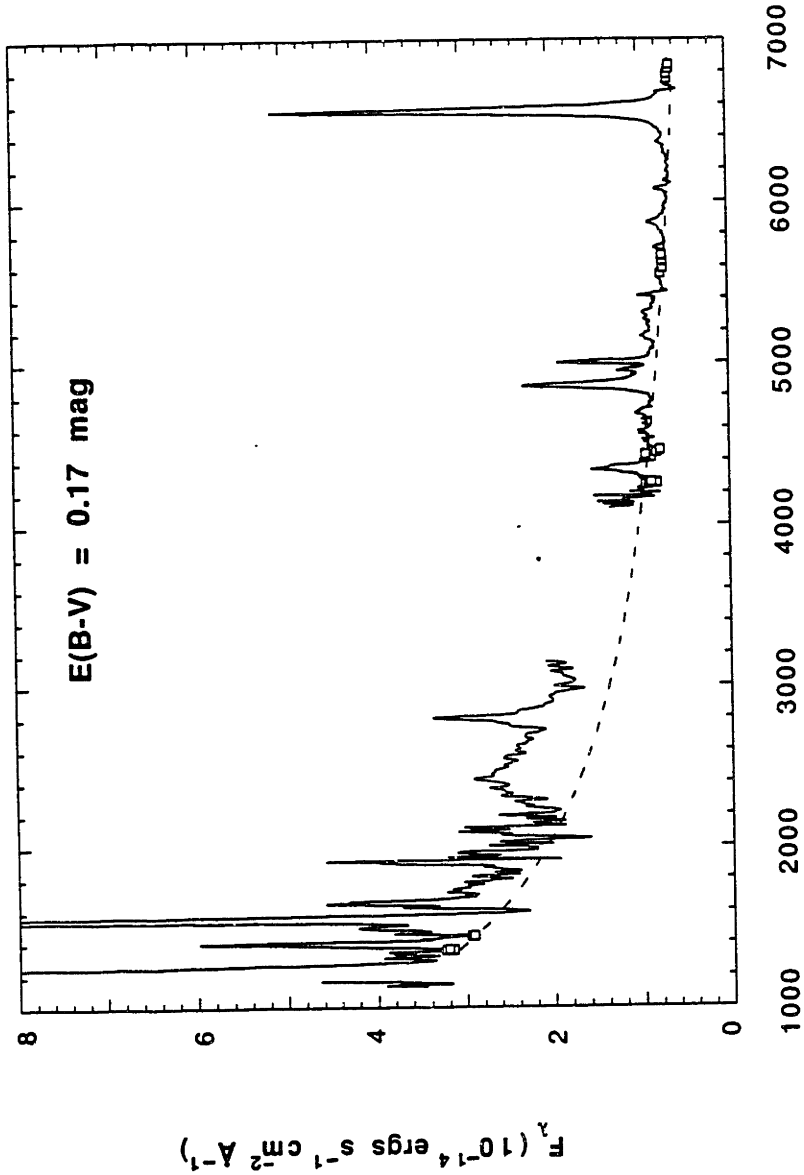
E(B-V) = 0.17 mag
F_λ (10^{-14} ergs s^{-1} cm^{-2} $Å^{-1}$)
λ_{rest} (Å)
0
2
4
6
8
1000
2000
3000
4000
5000
6000
7000

Figure 4

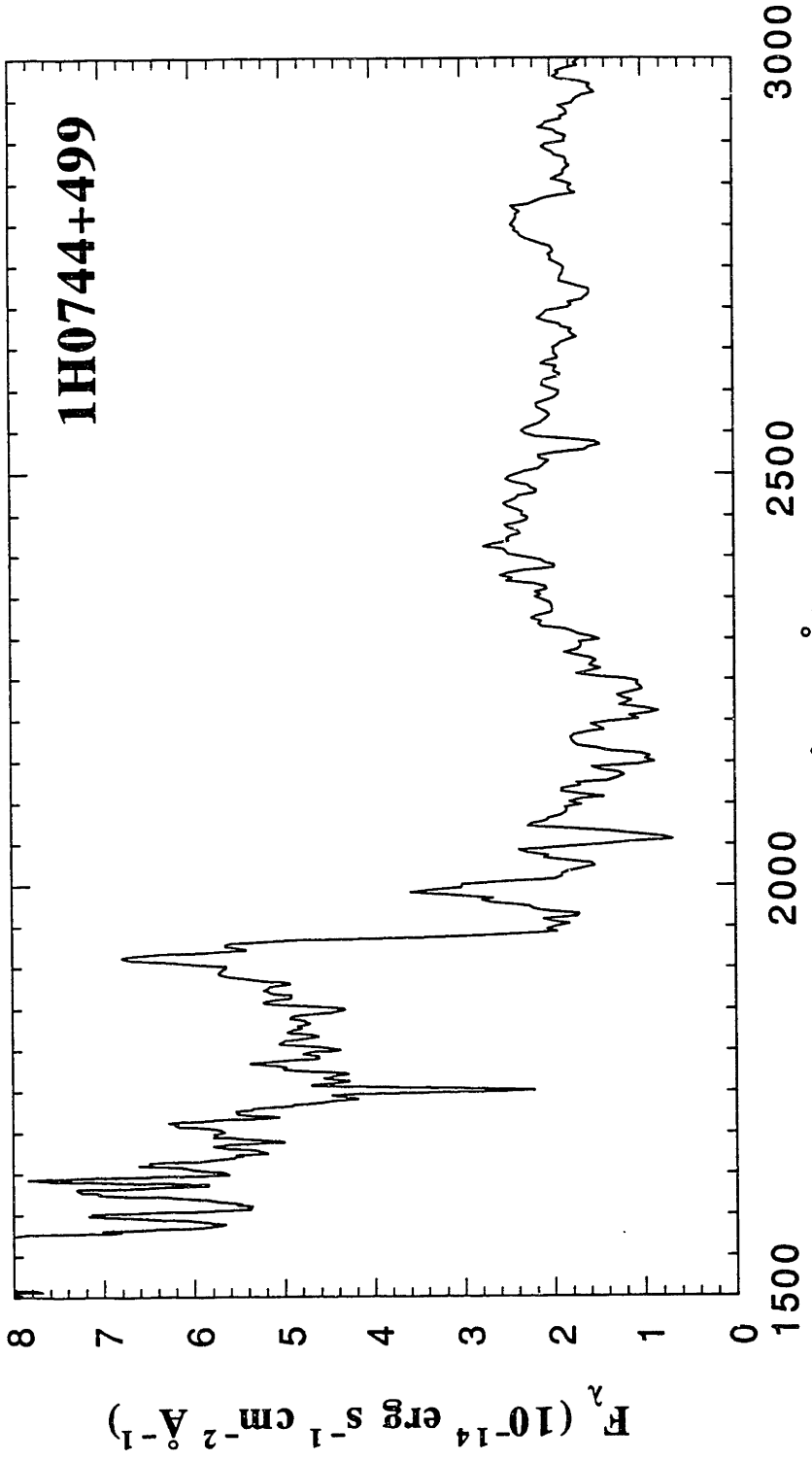
1H0744+499
F_λ (10^{-14} erg s^{-1} cm^{-2} Å^{-1})
λ_{rest} (Å)
0
1
2
3
4
5
6
7
8
1500
2000
2500
3000

Figure 5a

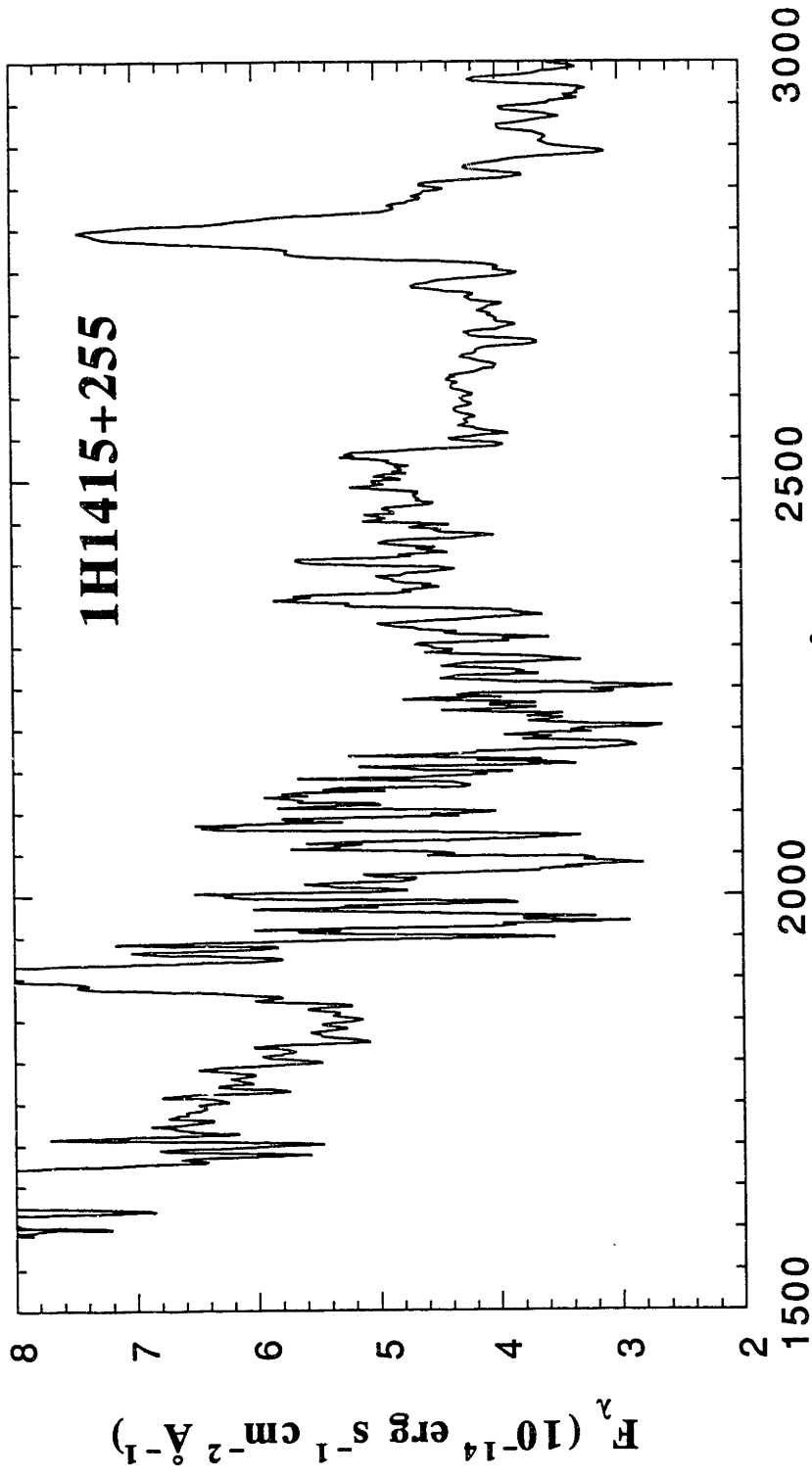
1H1415+255
F_λ (10^{-14} erg s^{-1} cm^{-2} Å^{-1})
λ_{rest} (Å)
1500
2000
2500
3000
2
3
4
5
6
7
8

Figure 5b

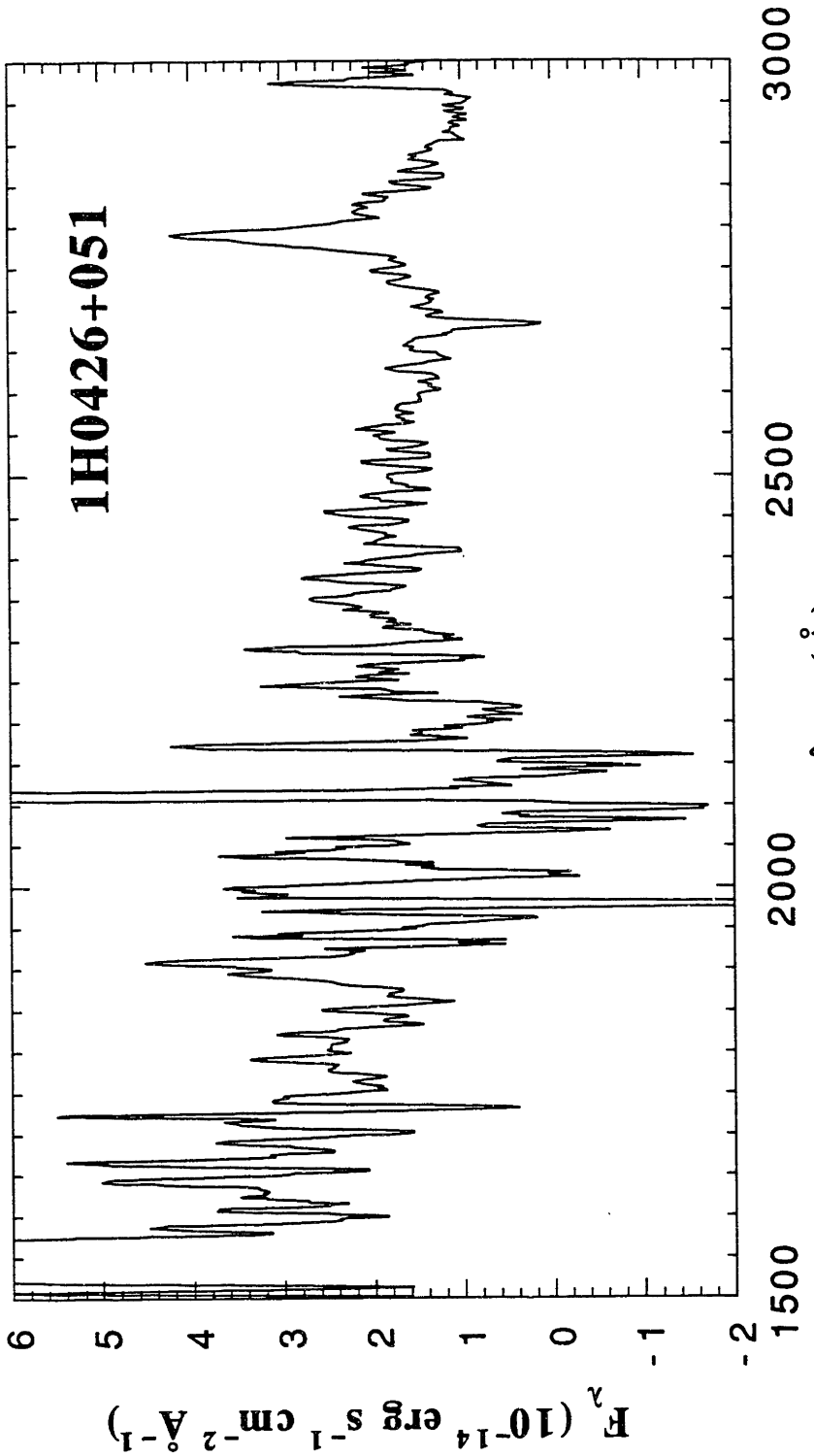
1H0426+051
F_λ (10^{-14} erg s^{-1} cm^{-2} Å^{-1})
λ_{rest} (Å)
6
5
4
3
2
1
0
-1
-2
1500
2000
2500
3000

Figure 5c

CHAPTER 4 :
THE AGN MULTI–FREQUENCY CONTINUUM

The objective of this chapter is to investigate the statistical view of AGN continuum components in the LMA. Correlation tests are made between radio, IR, optical, UV, and X–ray bands to study the relations between various spectral components. The distribution of blue-bump strength is given for a sub–sample of objects observed with the IUE. Optical and UV measures of blue-bump strength are compared. Comparisons are made between broad-line and narrow-line AGN, and between radio-quiet and radio-loud AGN.

1. INTRODUCTION

1.1 Identification of Spectral Components

The roughly flat energy distribution (νF_ν representation) of AGN over so many decades of frequency compels many workers to suggest that a large scale (IR–X) power law–like component underlies this spectrum, with modifications by smaller scale features. The modifications include thermal IR components, a big blue bump, and emission lines. Reddening, discussed in the previous chapter, may also significantly modify the spectrum, especially in the NIR (1–5 μm) to UV bands.

Correlation tests give information about the mix of spectral components and their variations from object to object. Large scale spectral components, if they exist, produce good correlations between fluxes in widely separated bands. Small-scale components which vary from object to object, such as the blue bump in the UV band, or the IR component associated with galaxy disk emission in the 60 μm band, would tend to degrade these correlations. The mix of the small-scale and large-scale spectral components in each band can therefore be inferred by interpreting the quality of correlations between different bands with consideration of small-scale features in each band.

Correlation tests have been used to study the relation of Einstein soft X–ray fluxes and luminosities to near IR or extrapolated 2500 Å fluxes generated from optical data (Zamorani 1981, Kriss & Canizares 1985, Worrall 1987, Kriss 1988, and Mushotzky & Wandell 1989). These tests have also been employed to study the relation of hard X–ray fluxes and luminosities with those in the IR bands (Ward et al. 1987 and Carleton et al. 1987). The results of these studies are discussed throughout this chapter.

In this work, correlation tests are used to investigate the relation of hard X-ray fluxes and luminosities with those of the radio, IRAS, near IR, optical, and UV bands. The hard X-ray band is used as a measure of non-thermal emission closely associated with the putative AGN black hole. A set of criteria are developed to identify objects with strong small-scale components in each band, and to identify those objects which are reddened. The effect of each small-scale component on the large-scale correlations is then determined. A de-convolution of the mix of spectral components is given, using a combination of correlation results and a knowledge of the small-scale components.

1.2 Type 1 and 2 Emission Line Classifications

The relationship of broad- and narrow-lined objects is of special interest, so a clear scheme for classifying them is desirable. As described in the introduction, permitted lines such as Hα and Hβ are observed in the majority of cataloged AGN to have very broad

profiles (5,000 - 20,000 km/s FWHM). Such objects are classified as Seyfert Type 1 objects at low luminosity, and quasars at high luminosity. Objects are classified as Seyfert 2 when all permitted lines are observed with widths similar to narrow (< 500 km s^{-1} FWHM) forbidden lines, such as [OIII], and no broad emission is detected . This can be referred to as the "classical" definition of a Seyfert 2. These classifications can be confused, however, for AGN which have been observed to have a mix of broad and narrow components of permitted lines. When the broad component is very weak, the classification of objects as Seyfert 2 depends on the instrument resolution and the signal to noise ratio of the spectrum. Some objects have even been re–classified when a new and better spectrum has shown a weak broad component (eg. Fillipenko & Sargent 1988).

In this work, a "Type 2" object is defined to be any for which the integrated flux of Hα is greater in the narrow component than in the broad component. All other objects are defined to be Type 1. Note that the Type 2 definition might include objects that are not "classical" Seyfert 2's. Twelve objects in the present sample are of Type 2. The majority of these objects are consistent with conservative Seyfert 2 definitions in the literature (e.g., 8 of the 12 Type 2's in the LMA are also Type 2 in Veron 1989). Results regarding these objects should therefore not be extremely sensitive to differences in the Type 2 definition.

2. THE MULTI–FREQUENCY SPECTRAL ATLAS

The Atlas of LMA Multi–Frequency Spectra appears in Appendix II. Fluxes representing the spectrum in each available band are presented, plotted as Log νF_ν vs Log ν. The 96 spectra are arranged by the RA of their LASS catalogue name (Wood et al. 1984), beginning with Type 1 objects. Type 2 objects are then given separately. Optical data are subject to stellar contamination. These data are therefore shown as a dotted line, representing the upper limit of the nuclear optical emission. The UV and X–ray bands, thought to be purely of nuclear origin, are given a separate symbol from the low frequency data. If possible, extended components were excluded from the IRAS measurements in the

reduction of the co–added fluxes. The reader will find it helpful to refer to the atlas while reading this chapter.

3. CORRELATION TESTS

The Pearson (the usual "linear" correlation coefficient) and Spearman-rank correlation tests compare data sets to determine if their relationship is significantly different than that of data sets chosen at random. In this way, a correlation between data sets may be inferred if the probability that the data sets are randomly related (the "null hypothesis" of the tests) is low.

The Spearman-rank test is a non–parametric test which uses only the rank of each individual value within a data set. The Spearman test is different from the Pearson test in that it assumes nothing about the distributions from which the measurement values were drawn. The Spearman test, however, is insensitive to the form of the relationship of the data sets; for example, it would be insensitive to the index of a power law relating two sets of data. The test is best described as being associated with monotonicity.

When performing a large number of correlation tests, it is expected that some measurements with no actual relationship may show a low probability of the null hypothesis. Therefore, a relationship between two data sets is only robustly inferred if the probability of the null hypothesis is small compared to the inverse of the number of correlations in this work, i.e., if the probability is < 0.01 for the few hundred correlations in this work. The Spearman and Pearson correlation coefficients and probabilities for the tests in this chapter are all given in Table 1.

Some bias might enter the flux correlation tests due to the limited dynamic range of the flux measurements. The X ray fluxes are restricted to a dynamic range of 3.7, and the errors are large, typically 30%. It is possible that a real flux correlation that is present over a large dynamic range would be missed by an analysis of measurements with a small dynamic range compared to the spread in the correlation. Therefore, caution must be

excercised in interpreting the absence of correlations in the flux plane when one or both of the quantities is measured with little dynamic range. On the other hand, luminosity correlations are artificially enhanced by a limited range of flux values. This problem is greatest when the dynamic ranges of the correlated data sets are small, as is the case with X-ray fluxes. Consider the case where the dynamic ranges of a set of measurements in two wavebands are small compared to the mean values, but where the measurements are randomly distributed within their dynamic range. If the objects have a large spread in redshift values, then the luminosity correlation will be very good. This effect occurs because the dynamic range in flux is negligible compared to the dynamic range in the $\sim z^2$ dependence of luminosity. Therefore the need to demonstrate correlations with fluxes in addition to correlations with luminosities is especially inportant when using X-ray data from the LMA sample. It should be noted, however, that most data sets in this work have large dynamic ranges. The dynamic range in the optical, near IR, and IRAS data is $\sim 10^2$, and the radio fluxes have a dynamic range $> 10^4$. These large dynamic ranges tend to reduce the bias problems in the correlations.

To address the bias in the luminosity correlations, all correlations of directly measured quantities were performed with fluxes first. The tests were then repeated with luminosities if the correlations were significant or for special comparisons. In this way, no correlations could have been introduced by the conversion to luminosity alone.
Flux correlations are performed with observed flux density measurements. Luminosity correlations are performed with the luminosities standardized to the measurement frequency *in the emitted frame*. This transformation allows luminosities to be compared at the same frequency for all objects. The following derivation loosely follows Schmidt & Green (1986). A measured frequency ν_1 corresponds to an emitted frequency $\nu_1(1+z)$, due to the redshift effect. Flux, luminosity, and redshift are related by:

(3.0.1) $$4 \pi d_l^2(z) F(\nu_1,\nu_2) = L(\nu_1(1+z),\nu_2(1+z))$$

where $F(\nu_1,\nu_2)$ is the X-ray flux measured in a band from ν_1 to ν_2 (in the observer's frame), d_l is the luminosity distance, defined by this equation, and $L(\nu_1(1+z),\nu_2(1+z))$ is the luminosity in the band from $\nu_1(1+z)$ to $\nu_2(1+z)$ (in the frame of the AGN). The luminosity distance can be obtained from z via the relation (after Weinberg, 1971, equation 15.3.24, assuming a Friedmann universe):

(3.0.2) $$d_l(z) = (2c / H_0)[\,(1+z) - (1+z)^{1/2}\,] \qquad \text{for } q_o = 1/2.$$

To convert to a standard luminosity band from ν_1 to ν_2, it is necessary to express the right hand side of (3.0.1) in terms of $L(\nu_1,\nu_2)$. To do this, the shape of the spectrum must be known or assumed. If a power law spectrum is assumed, i.e., $F_\nu \propto \nu^\alpha$, then

(3.0.4) $$F(\nu_1(1+z),\ \nu_2(1+z)) = F(\nu_1,\nu_2)\,(1+z)^\alpha,$$

where α is the log slope in the frequency range of interest. This leads to the expression for the luminosity in the instrument band from ν_1 to ν_2,

(3.0.5) $$L(\nu_1(1+z),\ \nu_2(1+z)) = L(\nu_1,\nu_2)\,(1+z)^{(\alpha+1)},$$

where the extra factor of (1+z) takes into account the different widths of the two energy bands. Substituting this expression into (2.1.3) yields the desired luminosity in terms of the measured flux:

(3.0.6) $$L(\nu_1,\nu_2) = 4\pi\, d_l^2(z)\ F(\nu_1,\nu_2)\,(1+z)^{-(1+\alpha)}$$

The expression for the monochromatic luminosity, L_ν, the luminosity per unit bandwidth at the emitted frequency ν, in terms of the flux density at the observed frequency ν, F_ν, is nearly identical to (3.0.6):

(3.0.7) $$L_\nu = 4\pi\, d_l^2(z)\ F_\nu(1+z)^{-(1+\alpha)}.$$

For all objects with redshifts of less than 2000 km s^{-1}, $d_l(z)$ was calculated with an effective redshift, which is corrected for local small scale perturbations from the Hubble flow (mostly infall of the local group toward Virgo and rotation of the galaxy; see chapter 7, Table 1 for a list of these values).

4. X-RAY EMISSION

The hard X–rays which the LASS detects are only weakly affected by absorption, and their observed spectral distribution, in the majority of all AGN, is dominated by a single power law component (Mushotzky 1984; Turner & Pounds 1989, hereafter TP) which is believed to arise very close to the putative AGN black hole. Because only one emission component dominates the LASS fluxes, the interpretation of correlations with these fluxes is straightforward. Soft X–rays are quite different; they may be significantly affected by absorption, their spectral slope shows some dependence on radio power, and they may also have an additional component, referred to as a "soft excess". The "soft excess" is often manifested as an unphysical, negative N_H value resulting from a fit of a power law plus HI absorption model to soft X-ray spectra (Wilkes & Elvis 1987). The fit results are consistent with the presence of flux above the extrapolation of the hard (E > 2 keV) X–ray power law (log slope ~ – 0.7) to the lowest energy channels. TP estimates that the "crossover" between the two power laws is at ~ 1 keV. TP and Kruper et al. (1990) both suggest that about 1/2 of all AGN probably have a soft excess.

As mentioned above, the dynamic range of the X-ray fluxes is small, a factor of 3.7 (see Table 1 of Chapter 1), and this can significantly affect correlation results. The limited dynamic range is due to the flux–limit criteria of the LMA sample (i.e. because it was defined with a steep Log N–Log S relation). However, it should be noted that the range of z in the sample is large, (a dynamic range ~10^3), and therefore, the dynamic range of X-ray luminosities is greater than 10^5.

The X-ray flux density used in the correlations below is derived from the lass count rate by the conversion given in Chapter 2, 0.0036 LASS counts s^{-1} cm $^{-2}$ = 0.95 μJy. The integrated flux density required to calculate the luminosity in equation (3.0.6) is derived from the LASS count rates with the conversion 0.002 LASS counts s^{-1} cm $^{-2}$ =

1.0×10^{-11} erg s^{-1} cm^{-2} (2–10 keV); this conversion was determined by the same method used for the conversion above (see Chapter 2).

Beyond this point, the paper is organized into sections covering different regions of the continuum, the radio, IR (which includes some discussion of the optical continuum), and the UV. The relationship of X–ray continuum emission with that from each region of the spectrum is considered in the appropriate section, below.

5. RADIO EMISSION

5.1 Previous Results

Radio loudness can be defined as the ratio of 6 cm VLA flux to optical B band flux, where an object with loudness ≥ 1 is classified as "radio–loud", and all other objects are "radio-quiet". The huge dynamic range in the observed values of this parameter ($\sim 10^5$) is the cause for the historical origin of the radio loud/quiet terminology. A previous generation of radio astronomers with poorer sensitivity instruments dubbed all undetectable sources "radio quiet". The more recent results of Kellermann et al. (1989) suggest that the distribution of relative radio emission strength among optically selected AGN is bi–modal, where most objects are radio quiet (80-85 %), but a secondary, very radio loud population exists mostly at $F_{6cm} / F_B > 10$. In the literature, radio loudness is often still an important, if not primary, basis of classification (e.g., Wilkes and Elvis 1987, the selection for Carleton et al. 1987, and Kriss 1988). Radio loud quasars are brighter in the X–rays (as observed by Einstein) for a given optical luminosity (Zamorani et al., 1981). Wilkes & Elvis (1987) found a correlation of soft X-ray logarithmic slopes with radio loudness. The radio–loud objects they observed with Einstein tended to have a flat ($\alpha \sim -0.5$), power law component in the soft (0.5–4 keV) band, while radio quiet objects tended to be steeper. This finding, together with the Kellermann et al. (1989) results, might suggest two intrinsically different populations of objects, a radio–loud population with flat X–ray spectra, and a radio–quiet population with steep X–ray spectra. Ulvestad and Wilson

(1984) emphasize that there are several established differences between radio–loud and radio quiet AGN, and that these differences are *intrinsic*, that is, they cannot be effects merely due to inclination or obscuration.

5.2 LMA Radio Results

The histogram of "radio loudness" for the LMA appears in Figure 1. Since the sample includes a range of z values, the radio and B fluxes were corrected to their emitted wavelengths by the expression:

(5.2.1) "radio loudness" = $(F_{6cm} / F_B)_{rest} = [F_{6cm} (1+z)^{-\alpha}] / [F_B (1+z)^{-\beta}]$,

which follows from (3.0.4). In this expression, F_{6cm} is the flux density observed in the 6 cm radio band, F_B is the flux density observed in the photometric B band, and $(F_{6cm} / F_B)_{rest}$ is the ratio of the flux density emitted at the rest wavelength of 6 cm to the flux density emitted at the rest wavelngth of B band. The correction assumes a local power-law spectrum for all objects such that $F_\nu \propto \nu^\alpha$ in the radio band and $F_\nu \propto \nu^\beta$ in the optical band. The radio log slope, α, was determined from the 6 cm flux and the first available choice of the following frequencies: 8.4 , 2.7, or 1.4 GHz. If the 6 flux was not available, its value in the emitting frame was interpolated from fluxes at the nearest available frequency. If only one frequency were available, the mean radio slope of the sample (-0.61 ± 0.51) was used. The same procedure also performed for the B band flux, but with the slope calculated from B and V fluxes. In the rare (3 objects) case that B band flux was not available, V band was used. Given the small spread in radio frequencies (factor of 6) relative to the large difference in frequencies between radio and optical bands (factor of $\sim 10^5$), the inaccuracy due to interpolation is unimportant.

Radio fluxes were available for just over half the objects, and the remainder have rather high upper limits (except 4 which limit loudness to <1). The fluxes from the literature do not have a uniform sensitivity limit over the full sky. This is a fundamental problem in the comparison of the LMA radio statistics to other samples, as the detections

are irregularly biased against objects below the flux limits for the various surveys, usually either 250 or 600 mJy. The radio loudness statistics are presented in Table 2a, but these are skewed due to the omission of upper limits. Consideration of only the lower limits of the number of radio loud objects in any category, Table 2b, is more rigorous. At least 35 objects in the LMA have $F_{6cm} / F_B > 1$ (where the parenthesis and the subscript "rest", as given in (5.2.1), have been dropped from here on). There are 12 Type 2's in the LMA, and 8 of these were detected in the radio. At least seven of these have $F_{6cm} / F_B > 1$.

Kellermann et al. (1989), report a bifurcation in the population of their optically selected sample of AGN (for both low-luminosity AGN and quasars, defined to be AGN with M_B<-23). The distribution of radio-loudness for this sample is reproduced in Figure 1b. The histogram of radio loudness for the LMA is significantly different (compare Figs. 1a and 1b). Bifurcation is not evident in the LMA sample. Instead, the LMA distribution appears to have a long tail to high values of radio loudness. Except for upper limit measurements restricting radio loudness to < 1, limits have been excluded from the histogram. Kellermann et al. attribute the bifurcation in their total sample distribution to a deficit of objects with $1 < F_{6cm} / F_B < 10$. (This range corresponds to $0 <$ Log $(F_{6cm} / F_B) < 1$ as plotted in Fig. 1). Greater than 21.4% of the LMA sample have measured values of F_{6cm} / F_B in this interval, 2.0 σ above the 12.3 % of the total Kellermann et al. sample. More comprehensive comparison statistics are given in Table 2c. A large fraction of the LMA Type 2 sample lie in the "deficit" region of Kellermann et al.. This is the primary cause of the different distributions in the two samples; the distribution of Type 1 objects alone is consistent with than given in Kellermann et al. The fraction of Type 2 objects in the deficit region, 42 %, is much greater than Kellermann et al's 12.3%. The fraction of Type 2's in this region is therefore inconsistent with that for optically selected AGN at >95% confidence by Poisson statistics. However, I do not conclude that the distribution of this sample is inconsistent with that of Kellermann et al. (which included virtually no Type

2 objects), but rather, that the radio loudness of hard X-ray selected Type 2 AGN is inconsistent with that of the optically selected Type 1 AGN.

As will be discussed in greater detail below, the B band fluxes which are used in the definition of radio loudness may be composed of several components, some of which may not be due to nuclear emission, and all components in this region may be reddened by material in the AGN or its host. A more physically motivated examination of radio emission is given by the ratio of hard X-ray emission to radio flux. Hard X-ray emission is substantially less vulnerable to reddening than the optical bands, and is dominated by a single non-thermal power-law component. Therefore, the ratio of radio to hard X-ray emission is a "clean" measure of radio power relative to the high-energy continuum associated with the AGN central engine.

The histogram of R/X, the ratio of radio (6 cm) to hard (5 keV) X-ray flux, is given in Figure 2. This distribution is significantly different from the radio loudness histogram. The R/X distribution is broader, and there is less of a "tail" to high values of loudness. Because of the very few objects at high values of R/X, no compelling statistical arguments may be made for a bi–modal distribution in R/X. Table 3 gives a description of the numbers of objects at high values of R/X for various sub-samples. The fractions of Type 2 and Type 1 objects with R/X >1 are consistent within 95% confidence intervals.

No correlation is observed between L_X and radio loudness, F_{6cm} / F_B, represented graphically in Figure 3a. It is quite clear, at the low end of L_X, where the detection statistics are best, that there is no relation between loudness and L_X. No correlation is observed between loudness and F_X either (see Figure 3b). Table 1 shows that the result of Spearman–rank tests on these data confirm the lack of correlation. The limits on the number of very loud objects for various values of L_X are given in Table 2d. The observed fraction of very-loud objects at high luminosities is greater than that at low luminosities, as indicated in the third and fifth columns of the table. However, this result is biased by the detection statistics at high L_X. The detection rate is biased because only the loudest objects

are detected at high L_X, as high L_X objects are necessarily very distant. The distributions of L_X among the radio-loud (RL), radio-quiet (RQ), and upper limit populations are presented separately in Figure 4. The radio-loud and radio quiet distributions are both broad, and roughly consistent. However, inspection of the high L_X region of the figure shows that the population is dominated by upper limits above $L_X = 10^{44}$ erg s^{-1} cm^{-2}, not by radio-loud objects, demonstrating the detection bias.

An unbiased comparison of the distribution of loudness at high and low L_X may be made if one considers instead the lower limit of the fraction of very loud objects at high L_X and compares this to the maximum possible fraction of very loud objects that could be present at low L_X (including all measurements and upper limits). The results of this comparison are given in columns 4 and 6 of Table 2d for a variety of loudness and L_X ranges. The observations are consistent with no increased fraction of loud objects at high values of L_X. This type of analysis shows that there is no evidence, statistically, for a strong and separate RL/RQ–X–ray luminosity relationship. Any relationship between loudness and X–ray luminosity is probably weaker than the intrinsic scatter in these parameters. There appears to be a correlation of L_X and radio loudness for objects with radio loudness > 1 only (see Table 1). However, for other ranges of loudness, including ranges above one, the correlations are not present (see Table 1). Again, this result is subject to the radio detection bias. In summary, for the LMA, no clear monotonic increase in the fraction of radio loud or very radio loud objects with L_X is observed, however, the radio data coverage (the small number of detections at high L_X) is insufficient to disprove a threshold in L_X defining a region of increased radio loudness.

The data were also tested for correlations with the radio spectral slope (described above). AGN radio sources with extended emission have a fairly constant power law energy index of ~ –0.8, and are referred to as "steep", where compact source spectra have a much flatter slope, ~ 0 (Kellermann and Pauliny–Toth, 1981). Radio sources are often divided into steep, with index < –0.5, and flat spectrum sources (>–0.5) which relates to

the relative mix of core and extended emission. For 39 objects in the LMA with sufficient data, a smooth, fairly symmetric distribution of slopes was obtained (Fig. 5), with an average slope of -0.61 ± 0.51, indicating a heterogeneous mix of steep and flat sources. No correlation was found between spectral index and either radio monochromatic luminosity (calculated from (3.0.7)) or X–ray luminosity.

The separation of RL and RQ objects is relevant to some AGN unification models. Barthel (1989) divides all AGN into RL and RQ objects, with relative broad line phenomenon explained by viewing angle dependent obscuration, and radio phenomenon explained by orientation to a relativistic jet. In this model, RL Seyfert 1's and RL quasars are unobscured objects, and RL Seyfert 2s and radio galaxies have broad line emission obscured by a molecular torus. RL quasar radio phenomena are a consequence of looking at a small angle to the jet axis of a RG. RQ Seyfert 1's and quasars, which are unobscured, are unified with Seyfert 2's and highly luminous IR emitting galaxies, respectively, objects which also lack radio and broad-line emission. The paper stresses that the RL/RQ distinction is not only a result of viewing angle. Several other observed phenomenon that are independent of viewing angle (the anti–correlation of BAL absorption troughs with loudness and underlying galaxy differences between RL and RQ objects) are also associated with radio loudness. The data on the LMA do not support the segregation of objects based on their radio loudness, an assumption in the models above.

Some models involving beaming emphasize the difference between lobe–dominated and core–dominated sources (Orr & Browne 1982), where the core–dominated sources, found to have flatter radio spectra, are beamed toward the observer. Few core vs lobe measurements are available for the LMA objects. However, comparisons may be made indirectly through the association of core dominated sources with flat radio spectra. In the LMA, no correlation of X–ray luminosity with radio slope is observed (see Table 1), so, by this measure, there is no evidence for a relationship between core and lobe dominated emission and X–ray luminosity. Note, however, that the X-ray spectral data are not

available to investigate the relationship of radio and hard X-ray slopes for the LMA (but see, for example, Worrall et al. 1987, or Canizares & White 1989 for studies of radio and soft X-ray slopes).

In the larger picture, there are two main conclusions to be drawn from the radio studies of the LMA sample. First, radio emission is unique compared to all other wave bands in that it has no significant relation to the luminosity of the central X–ray source, and no clear relation to the underlying IR–X-ray component (discussed extensively below). Second, no AGN continuum properties investigated here suggest a segregation of AGN based on their relative radio emission, which is commonplace in both theoretical and observational literature.

6. IR EMISSION

6.1 Previous Work

The IR, which I define here as 10–100 μm, is possibly even more insensitive to absorption by dust and gas than X–rays at the longest wavelengths. There is no significant stellar emission in these bands, so the "underlying power law" is generally thought to be easy to detect in these regions. However, thermal components (dust emission) are also present (Carleton et al.). The NIR (1-5 μm) is fairly insensitive to dust absorption compared to the optical and UV, but is subject to some (small) contamination from the blue bump (Mushotzky and Wandel 1989), from starlight, and from emission due to warm dust (Barvanis 1987). Good correlations between NIR and X–ray flux have been reported (e.g. Carleton et al. 1987; Worall 1987) which suggest that the NIR is dominated by non–thermal emission related to that in the X–ray band. Virtually all AGN have a familiar ~1 μm inflection (Neugebauer et al. 1987), and because of this, 1 μm has become the favored wavelength for normalization of AGN spectra.

IRAS sources with large ratios of 25μm to 60 μm flux density (F_{25} / F_{60}) have a high tendency to show Seyfert activity (for example, Hill, Becklin, and Wynn–Williams,

1988). These are known as the IRAS "warm" galaxies. I use the criteria of Hill et al., that the ratio F_{25} / F_{60} > 0.33 defines a warm galaxy. It should be understood that not all Seyferts are "warm", and Hill et al. report that only approximately 1/3 of the optically selected CFA Seyfert galaxy sample are warm. However, given that a galaxy is selected by the warm criteria, it is extremely likely to be a Seyfert. The most interesting property of the warm IRAS galaxy sample is that it contains an unprecedented fraction of Seyfert 2s. DeGrijp et al.(1985) found 16 out of 21 (~70%) warm AGN to be Type 2.

The high F_{25} / F_{60} flux ratio is interpreted as the dominance of an IR power law in this region over the cool host galaxy disk component, which peaks at 60 and 100 μm in spiral galaxies (De Grijp et al. 1985). Kailey & Lebofsky (1988) link the 60 and 100 μm emission to the process of star formation, pointing out that resolvable star forming regions in M31 and M33 have extremely "cool" IRAS colors, the cause being excess emission at wavelengths longer than 25 μm. They also point out some interesting examples of star formation causing cool IRAS colors, the obscured Seyfert 2 Arp 220 and NGC 7469 (a Type 2 object in this sample, 1H2320+086). At 25 μm the power law continuum normally dominates the flux, but the average 25μm luminosities of cool galaxies are lower than those of warm galaxies. Kaily & Lebofsky interpret these observations to mean that the cold nuclei have weaker 25 μm continuum relative to their host galaxies than warm galaxies.

Ward et al. (1987) and Carleton et al. (1987) surveyed IRAS through optical and X–ray data from a hard X–ray selected sample, which included the Piccinotti et al. sample. These works classify all Seyfert I galaxies by their IRAS and optical band characteristics. They discriminate between nuclear-dominated and galaxy-dominated objects on the basis of the 60 μm to 12 μm slope; everything with a log slope significantly steeper than –1 is classified as galaxy-dominated. They used a falling optical spectral shape as a diagnostic of reddening. They found an association of reddening with the galaxy-dominated IRAS spectral type. However, they did not explain the apparent link between the "galaxy–

dominated" IRAS spectrum and the reddened optical spectrum. They explicitly state that the 60 μm emission is associated with the disk of the galaxy, possibly due to a starburst. The association of reddening of the nuclear continuum with the 60 μm disk emission might simply be the result of looking through a dusty galaxy disk, but the reddening could be associated with the nucleus instead.

6.2 Results of IR Analysis

To express IRAS "warmth" in a convenient manner, "warmth" is defined to be $3 \times F_{25\ \mu m} / F_{60\ \mu m}$, so that a galaxy just meeting the warm criterion will have a warmth of 1. Figure 6 gives a histogram of Log_{10}(warmth) in the LMA, which shows that, of 81 objects with 25 and 60 μm detections, 57 are warm. The warmth of each object in the LMA is given in Chapter 2, Table 2. The distribution for the total sample is significantly skewed toward "warm" objects, but Type 2 objects show no preference for being warm. In fact, four of the Type 2 objects are among the coolest objects in the sample. The tendency for hard X–ray selection criteria to yield predominantly Type 1 objects, and the fact that Seyfert 2's do not dominate the warm objects, suggests that hard X-ray selection samples a very different population than the IRAS warmth criterion.

In Figure 7, warmth is plotted against X-ray luminosity, and no correlation is seen. This result shows that the nuclear continuum does not always dominate the host galaxy disk emission in high luminosity objects. Figure 7 indicates that at 60 μm, the nuclear continuum from even the most X-ray luminous objects may have competition from the host galaxy disk emission. Ward et al. (1987) have shown that the 60 μm excess producing a steep 60 – 25 μm slope is usually associated with emission from the host galaxy disk by observing significant aperture-size effects (with measurements from the Kuiper Airborne Observatory), by finding the 60–100 μm luminosities of AGN in the range of normal spirals, and by observing IR spectral features associated with starburst phenomenon. It is not clear whether or not starbursts are related to the nuclear activity, according to Ward et al

(1987). Perhaps the starburst phenomenon explains the high 60 μm galaxy disk luminosity relative to the 25 μm nuclear luminosity in the "cool" high-luminosity objects.

The above result has important implications for detailed spectral modeling. Conventional wisdom states that galactic emission at all bands becomes negligible compared to nuclear emission for high–z objects (for example, Urry 1988). However, imaging studies have shown that quasar host galaxies are much brighter than average galaxies (Smith et al. 1986). The results here suggests that the thermal disk contribution to the IR flux is not constant, and does not have a clear maximum. Therefore, powerful high-redshift quasar nuclei will sometimes have competition from powerful thermal galaxy emission in the IR. Nuclear domination at high redshift may therefore not be a valid assumption in the IRAS bands.

Plots of emission from each IRAS band vs the X-ray band are given in both flux and luminosity in Figures 8 a–h. The results of correlation tests for IRAS bands vs the X-ray band, in both flux and luminosity, are given in Table 1. The IRAS and X-ray uncertainties are the largest of any bands used in this study, so these uncertainties must be considered when comparing correlations. To determine if the correlations were sensitive to these uncertainties, the value of each datum was perturbed at random between +1 σ and –1 σ (i.e. the Gaussian error distribution was approximated by a square function 2 σ in width), and the correlation tests were repeated many times to obtain a distribution of results. The distribution of the resulting flux correlation probabilities is typically broad, but falls off sharply at high null probabilities. The unperturbed Spearman probability was 2.0×10^{-3} for 25 μm flux correlated with X-ray flux. A 1 σ probability upper limit of 4×10^{-3} was measured in 10^3 repeated correlation trials, demonstrating that this correlation is still very likely to exist. A lower limit probability of 6×10^{-5} was measured for the same distribution. The 12 μm results were very similar. The 60 and 100 μm distributions were broader, however. The 60 μm flux with X-ray flux null probability was 4.5×10^{-2} with upper and lower limits of 8×10^{-2} and 5×10^{-3}, respectively. The 12 and 25 μm fluxes

are therefore significantly better correlated with X-ray flux than the 60 and 100 μm fluxes. The distributions of preturbed luminosity correlations were more uniform, and typically restricted to ± 3/4 of a decade. The unperturbed value of the 25 μm vs X-ray luminosity correlation is 7.0×10^{-25}, the 1 σ upper and lower limits are, 4.5×10^{-24} and 1.6×10^{-25}, respectively.

Table 4 gives the results of fits to a power law weighted by the errors in the IRAS measurements. The luminosity correlation slopes become flatter at wavelengths longer than 12 μm.

In all the IRAS vs X plots, only one object at one frequency seems to fall far away from the main body of the correlation (see Figure 8a). The AGN Type 1 1H0140+393 has a 12 μm luminosity about an order of magnitude higher than any other object for its X-ray luminosity, 2.8×10^{44} erg s $^{-1}$ cm^{-2}. The object has a z of 0.08 and peaks at 12 μm in νF_ν. The object appears power-law like from radio through 12 μm, then resumes a normal spectrum at higher frequencies.

To study the steep or "galaxy–dominated" class of sources discussed in Ward et al.(1987), All sources with a 60 to 12 μm log slope less than –1 are shown with a separate symbol. The population of steep sources is significantly above the rest of the sample at 60 μm, but is much closer to the main correlation in the other IRAS bands, confirming that the 60 μm band shows the strongest thermal contribution. The steep objects are also the most IR luminous objects at their value of L_X at 12 and 100 μm, but less so at 25 μm. Table 5a gives a list of steep, or "galaxy dominated" objects with significant 60 μ cool dust emission. Eighteen objects (19% of the LMA) are steep.

There is a population of Type 2 AGN, most of which are steep (or "cold"), which define the upper edge of the IRAS measurements in the IRAS v X planes, in both flux and luminosity (at lower luminosities), at every IRAS frequency. The galaxy disk emission is important in many of the Type 2 objects.

Table 5b gives a list of objects which have a spectrum strongly peaked between 2 and 12 μm, associated with warm dust emission. Twenty objects (~20% of the LMA) have a 12 μm point higher than 25 μm (in νF_ν) but fall toward the NIR, suggesting a peak in the 2 – 12 μm region. Many of the objects with a suggested 2 – 12 μm peak appear to have some characteristics associated with a strong blue bump. This association is addressed again in Section 7.

There is no special behavior in the correlation plots observed among RL objects (not labeled in the figures). They seem spread randomly among all types of objects (Type 1/Type 2 and warm/steep objects) and at all luminosities in all plots, except for the detection bias against quiet objects at high L_X.

In the NIR region, we see that correlations of X–ray measurements with 1.25 μm flux and luminosity are very good, as seen in Figure 9a and b. The quality of the correlations are excellent, as given in Table 1. Another view of the relationship between 1.25 μm and X-ray emission is given by the histogram of log slopes from 1.25 μ to 5 keV,

(6.2.1) $$\alpha_{JX} = \mathrm{Log}\,(L_{5\ keV}/L_{1.25\ \mu m}) \,/\, \mathrm{Log}\,(f_{5\ keV}-f_{1.25\ \mu m}),$$

where $f_{5\ keV}$ and $f_{1.25\ \mu m}$ are the rest frequencies of 5 keV and 1.25 μm respectively. The histogram is presented in Figure 10. All combinations of reddening and stellar contamination diagnostics are indicated by separate symbols on the plot. The distribution is fairly symmetric, but with a small tail to steeper slopes, populated mostly by stellar contaminated objects. Only two objects without evidence of stellar contamination lie in the steep-slope tail of the distribution. The mean value of the distribution, considering only uncontaminated objects, is -1.04 ± 0.05, for the stellar contaminated objects, -1.12 ± 0.10. The typical measurement error is < 0.03. The stellar objects are often steeper because of the elevation of the 1 μm measurement by the starlight contribution to the flux. The uncontaminated objects have a slope close to –1, but with some measurable intrinsic spread.

Several of the Type 2 objects appear to form the upper border of the luminosity correlation, but only for the lower ranges of luminosity where they reside. These objects are also above the main correlation in flux. This is a result of stellar contamination. Significant stellar contamination is easily diagnosed by its bump shape (in νF_ν) from H to V band (1.65 μm –0.44 μm) which is peaked at 1.25 μm. Several Type 2 objects show this contamination in their NIR-opt spectra. (See section 7, below, for more discussion of stellar contamination, and a list of contaminated objects; 12 % of the LMA sample are found to have significant stellar contamination).

6.3 Conclusions of IR Analysis

I find that the IR emission of AGN can be well understood within a framework of an "underlying continuum" plus thermal contributions. Thermal components have been identified centered at 1.25 μm for starlight (observed in 12 % of the LMA), at ~few microns for warm nuclear dust (observed in 20 % of the LMA), and at 60 and 100 μm for host disk emission, cool dust associated with star formation (observed to dominate the IRAS spectrum in 18% of the LMA, including half the Type 2 objects). The excellent correlation of 1 μm and X-ray emission in the LMA is consistent with the small fraction (12%) of stellar contaminated objects identified via their NIR-optical slope (and confirmed with other methods; see UV section). Figures 11a and b show the relative quality of the correlations (measured by the Spearman probability) of X-rays with the flux and luminosity at each measured frequency. The contribution of the thermal components in the IRAS bands can be seen by the lesser quality of the correlations of IRAS vs X-ray bands compared to J and B vs X-ray bands, in both flux and luminosity. The very significant contributions of host disk emission are shown by the departure of the "steep" objects, defined above, from the main body of objects in the IRAS vs X-ray plots. The decreased quality of the luminosity correlations of the 60 and 100 μm bands with the X-ray band

compared to the correlations of the shorter wavelength IRAS bands and the X-ray band is a result of the IR contributions of the host disk emission.

Ward et al.(1987) and Carleton et al.(1987) suggested that the underlying IR-X component is a power law with a –1 log slope, $F_\nu \propto \nu^{-1}$, and that it can be identified by picking the lowest point in the IR spectrum in νF_ν or νL_ν, the "baseline" flux or luminosity. The baseline IR flux correlated with the X-ray flux significantly worse than the 1 μm flux (see Table 1). This implies that there may be some significant variation in the slope of the non–thermal component in the IR, and that the assumption of an underlying $F_\nu \sim \nu^{-1}$ spectrum in the infra–red is only an approximation.

7. OPTICAL EMISSION

Optical bands also show good correlations with X–ray flux and luminosity as given in Figure 12. The optical B monochromatic luminosity was determined by correcting the center frequency of the B and V band fluxes to the rest frame of the AGN, and then interpolating the flux to the rest wavelength center of B band, 4400Å. (In the rare case that B was not available, V was used directly.) Results of the fits are given below in Table 4. (Least square fits were made with L_X as the independent variable, weighting the data one dimensionally by the (dominant) error in L_X.) The dependence of B band luminosity on L_X appears to be slightly flatter than that for the 1.25 μm data. However, fits to the data have high chi–squares (reduced chi–square ~20 for both), so small differences in slope may not be meaningful. Measurements were not made simultaneously, but X–ray variability is typically less than 2 σ (~ 40 %; see Chapter 6), so it is unlikely to be a significant contributor to the poor chi–square. The chi–square is certainly due mostly to the intrinsic spread in the values of all the parameters.

8. UV:THE BIG BLUE BUMP

8.1 Measuring the Blue Bump

The understanding of the global, statistical picture of AGN in the UV is restricted by the relatively small number of observations compared to the number in other bands. While there are several papers in all other bands with large samples of objects, there are few multi–frequency papers with large, well defined samples of AGN observed in the far UV. There are no complete UV surveys with a substantial number of AGN. Before HST (e.g. ApJ Letters 369 No. 2 and ApJ Letters 377 No. 1) and ASTRO I (see Davidsen et al. 1992 for a descripion of the UV instrument), the IUE (see Chapter 2) was the only instrument which could make observations of the UV (Lyα rest to the atmospheric cutoff) of many AGN. This instrument has only a 0.45 m mirror, and most of the hundred or so brightest AGN require eight or more hours of exposure at low dispersion (SW and LW spectra). HST and ASTRO have yet to add significantly to the total number of AGN observations in the UV.

The first AGN observed in the FUV were powerful quasars such as 3C273 (for example, Malkan & Sargent, 1982). These objects had strong big blue bumps that were modeled reasonably well by combinations of thermal emission, and so such was assumed for all AGN. Kriss (1988), in a sample of radic quiet quasars, stated that AGN with low $L_{1\mu m}$ ($< 10^{30}$ erg s^{-1} cm^{-2} Hz^{-1}) have systematically weak blue bumps, however, these results were based on extrapolations of optical, not UV measurements. Recently, however, McDowell et al. (1989) pointed out that several quasars may have weak blue bumps. Unfortunately, as was discussed in the previous chapter, there is significant uncertainty in these measurements due to reddening. More recently, Kinney et al . (1991) published a catalog of quasar observations by the IUE, but without data from other frequencies.

Below, I give the distribution of relative blue-bump strengths for every object in the LMA observed by IUE, applying the diagnostic for UV reddening as described in the previous chapter. The possibility of studying the blue bump using a blue optical band relatively free of emission lines is also investigated. A diagnostic of optical reddening, described below, will be applied where the UV reddening diagnostic is not available.

A convenient measure of blue-bump strength relative to the continuum at 1.25 μm is given by a spectral slope between 1μm and the farthest useful UV continuum flux. To improve S/N, I define an index from the ratio of the log of the 1.25μm (J band) luminosity and the log of three bands in the UV which exclude strong emission lines and are blue enough to avoid FeII emission (Wills, Netzer, and Wills 1985, hereafter WNW). These bands are 1290–1360, 1425–1520 and 1700–1860Å in the AGN rest frame. The index, $\alpha_{J\text{-}UV}$, is defined to be:

$$\alpha_{J\text{-}UV} = \frac{\overline{\text{Log } L_U} - \text{Log } L_J}{\overline{\text{Log } \nu_U} - \text{Log } \nu_J} \tag{8.1.1}$$

where:

$$\overline{\text{Log } L_U} \equiv \frac{1}{3}(\text{Log } L_{U1} + \text{Log } L_{U2} + \text{Log } L_{U3}) \quad \text{and} \tag{8.1.2}$$

$$\overline{\text{Log } f_U} \equiv \frac{1}{3}(\text{Log } \nu_{U1} + \text{Log } \nu_{U2} + \text{Log } \nu_{U3}) \tag{8.1.3}$$

and where L_{Ui} refers to the luminosity in the ith UV band given above, ν_i refers to the center frequency of the band, L_J refers to the luminosity at 1.25μm, the J band, and $\nu_J = c$ / 1.25μm, the center frequency of the J band. The motivation of this bump index is to give a measure of relative strength of the blue bump to that of the non-thermal continuum. The low frequency band in the index was chosen as the 1.25 μm band because the slope from one micron to the UV is an easily understood measure of the large scale shape of the bump, and because the 1.25 μm band is identified with non-thermal emission, as shown by its excellent correlation with the hard X-rays. The bump index will not measure this strength

correctly if the 1.25 μm band has extraneous contributions due to starlight, or if either band is affected by reddening. These effects must therefore be taken into account.

Optical Reddening and Starlight Diagnostics

In the previous chapter, a method was described using observations of the 2175 Å feature as a diagnostic and possible method of correction for reddening. However, this diagnostic tool is not available for many objects in the LMA. Therefore, another method of indicating continuum reddening must be found. Chapter 6 shows that the Balmer decrement is not an accurate indicator of continuum reddening, although it is frequently used in the literature. Ward et al. (1987) promote the idea that a common intrinsically flat (in νF_ν) power law dominates the IR–optical region of AGN, but if dust is present, the UV radiation is redistributed (by reddening) in the IR as thermal radiation, causing the optical continuum to appear steep. They also state that this steepness can be used to diagnose reddening. There are two distinct types of steep optical spectra, a "reddened–type" and another type caused by stellar contamination. In the "reddened–type", the NIR–opt spectrum falls off monotonically in the I-U bands (0.9 - 0.365 μm) from a flat K-J (2.2 - 1.25μm) spectrum (e.g. 1H1308–237, 1H1408–031). The objects identified as reddened in this manner in Ward et al.(1987) are consistent with the predicted effects of reddening on their un-reddened AGN, verifying the validity of this classification. The "reddened–type" spectral shape is therefore a robust diagnostic of significant ($\gtrsim$ 0.5 mag in E(B–V)) optical continuum reddening.

Another type of steep optical spectrum is due to the distinctive shape of starlight, where a bump from ~ 3 – 0.4 μm is clearly traced by a strong upturn in all 4 NIR points, accompanied by a steep drop in the 4 optical bands (e.g., 1H1313+363). Some objects identified as stellar in Ward et al.(1987) with typical aperture size measurements are shown to approach the continuum shape of their uncontaminated objects when smaller apertures are used. Extensive modeling and de-convolution of starlight contributions to AGN spectra

also yields the same distinctive shape given above (Barvanis 1987). This shape is therefore firmly established as a diagnostic of stellar contamination. There is also corroborating evidence for stellar contamination from imaging and spectra in the objects with steep optical spectra (see column 2 of Table 6b). If insufficent photometry data are available to classify an object, observation of significant stellar spectral features or imaging which shows that the galaxy is strong compared the nucleus are also accepted as diagnostics of stellar contamination.

The difficulty with the diagnostics above is that the reddening diagnostic is not robust in a strongly stellar contaminated object. The stellar emission masks the shape of the nuclear optical continuum, so this spectral region may not be used directly to determine the reddening. Because of the negligible contribution of starlight below 3000 Å, reddening measurements using the 2175 Å feature are still valid in even the most extreme cases of extensive stellar contamination. However, IUE spectra are not always available with sufficient signal to noise to determine the depth of the 2175 Å feature. In this case, no accurate reddening determination may be made. Therefore, objects with stellar contamination are noted and studied separately from uncontaminated objects.

To attempt to correct the effect of contaminating stellar flux on $\alpha_{J\text{-}UV}$ for the objects with stellar contamination, the measured 1.25 μm flux was replaced with that predicted by the IR baseline in the calculation of $\alpha_{J\text{-}UV}$. Ward et al.(1987) showed that the infra-red baseline indicates the level of the underlying NIR component, and this was further corroborated for the LMA by the excellent correlation of the baseline and X-ray luminosities (see Table 1). The baseline flux point was usually 2.2 or 3.5 μm. This correction was applied to all those objects which showed a significant systematic rise from 2.2 μm to 1.25 μm, accompanied by a drop of similar or greater magnitude in the optical spectrum (in νF_ν). The average correction to the J band flux was –28%, and increased the typical $\alpha_{J\text{-}UV}$ by ~ 0.15.

Although reddening can be diagnosed in the absence of stellar contamination, it is more difficult to correct than stellar emission, because it affects the UV flux much more strongly than the 1.25 μm flux. Those objects where the IUE spectrum is of insufficient quality to rule out the presence of a 2175 Å feature could be steep due to reddening, and are therefore specially noted. Objects which showed significant 2175 Å features which were for any reason uncorrectable (as discussed in chapter 3) were also put in a separate category. If the optical spectrum of any object showed signs of reddening, it was also treated separately (See Table 6). It should be noted that the latter condition is for objects where the 2175 Å feature strength cannot be determined to be small; no objects showed optical evidence of reddening which was contradicted by clear lack of a 2175 Å feature.

8.2 Results

UV Measurements of Bump Strength

Table 6a–c gives a list of blue bump measures. The best values (those with the smallest errors) are given when repeated UV observations are available. Separate tables are given for stellar contaminated objects and objects with uncorrectable or unknown reddening. Twelve objects were found to have significant stellar contamination, and are listed in Table 6b. Corroborating evidence of stellar contamination from stellar spectral features, from aperture effects, or from a bright extended image, is also given in the table (column 2) for all but one object. Fourteen objects with UV data which cannot be diagnosed as unreddened are given in Table 6c; of these, five show evidence of optical reddening, and two more are observed to have significant 2175 Å features. The object 1H2107-097 had sufficient data available to allow correction for the feature as described in the previous chapter, and so is listed as an uncontaminated object. The relative blue-bump strength parameter, as given by $\alpha_{J\text{-}UV}$, was calculated for eighteen uncontaminated objects, four stellar contaminated objects, and eight objects with either continuum reddening or insufficient data to diagnose reddening.

Figure 13 gives the histogram of relative blue-bump strengths for all the objects in the sample with IUE and JHK data, plotting the best available values for each object. Objects with stellar contamination, with optical reddening, or objects whose reddening is unknown due to poor quality IUE spectra, are all shaded to clearly distinguish them from the objects known to be uncontaminated. The distribution of uncontaminated objects has a median at –0.74. The distribution of the J–UV log slope is asymmetric, considering only uncontaminated objects, with several objects just above –1, but with only one uncontaminated object with $\alpha_{J\text{-}UV}$ below –1. On the strong bump side, there is only one uncontaminated object with $\alpha_{J\text{-}UV}$ greater than 0. This object is 1H1911-589, with an $\alpha_{J\text{-}UV}$ of 0.12± 0.02. This object's IUE flux is highly variable and the average value of the log slope is 0.01 ± 0.11.

A summary of the characteristics of the five strongest and weakest bumps is given below, in Table 7. They all have rising optical spectra that smoothly connect with the IUE data. They all have IRAS spectra which have weak 60 and 100 μm disk emission compared to their non-thermal 25μm emission. Three of the objects peak at 12 μm. Most of the objects that have a peak from 12–2 μm have some association with a strong blue bump, suggesting a possible link between IR emission in this region and blue-bump strength. The strongest bump objects are NOT limited to high–z, or high luminosity (four of the five are below z =0.05, and $L_X = 1.6 \times 10^{44}$ erg s^{-1} cm^{-2}, 2–10 keV). The two objects with repeated observations are UV variable, one by about a factor of five.

The spectral energy distributions of the five weakest bump objects (without contamination) are not as homogeneous as those of the strong bump objects. One of these objects is very unusual in that its spectral energy distribution peaks in the optical. The weak bump objects are mostly low–z objects with very flat (in Fλ) IUE spectra. There is IUE variability among these objects as well, but by smaller factors.

After removal of all objects which may be reddened or stellar contaminated, the weakest bump objects appear to have an $\alpha_{J\text{-}UV}$ lower limit of –1; only a single object

appears to violate this limit (1H2301+086 with a slope of -1.025 ± 0.05), and this object is only 0.5 σ below a –1 log slope. This result strongly supports Ward et al.'s (1987) suggestion that a power law with a –1 log slope underlies the spectrum from the IR all the way to X. If this suggestion is correct, the thermal blue bump component would normally be an addition to the underlying component in the UV region. Objects with an $\alpha_{J\text{-}UV}$ of –1 would then have only a "naked" underlying continuum in the UV region. The observation of a lower limit to the value of $\alpha_{J\text{-}UV}$ of –1 suggests that the underlying power law extends at least from the near IR to the far UV, to ~ 1300 Å.

Several other objects were measured whose *apparent* log slope was much less than –1 (steeper) , but these objects either show evidence in the optical spectrum of reddening or stellar contamination, or their IUE spectra are so poor that the possibility of a 2175 Å feature could not be ruled out. If better stellar removal or reddening detection and correction applied to these objects yields log slopes less than --1, then it would suggest that the underlying power law can be steeper than this value, or that the underlying power law is not present in the UV. The $\alpha_{J\text{-}UV}$ slopes for these objects are given in Table 6.

Optical / Near IR Measures of the Blue Bump

In general, because of the difficulty in obtaining UV data, it would be valuable to be able to measure the blue bump from optical and/or NIR observations. Before such measurements can be made, it must be shown that there is a significant contribution of the blue bump in the optical, and that it is not overwhelmed by other optical emission. To determine this, the bluest region was chosen that is accessible to conventional optical spectrographs, and which represents the continuum, but avoids emission lines including Fe II and the Balmer continuum. The figures in WNW and Netzer et al. (1985) show that Fe II and Balmer continuum contributions are <~ 10% between Hδ and Hε (~4050Å), and between Hδ and Hγ (~4200Å). These regions were therefore chosen for the optical observations.

The correlation of 4200 Å flux with the UV flux used in the definition of $\alpha_{J\text{-}UV}$, given in Table 1, is poor ($P_S > 0.17$). (Far fewer 4050 Å fluxes were available, so this correlation, although similar, was omitted from the table.) Optical data is therefore a poor predictor of UV flux. No significant difference is observed in the correlations between 4050 Å and 4200 Å fluxes and UV flux, as the difference between the two optical fluxes is very small compared to the spread in the correlation. However, the correlation of α_{JO}, the log slope from J–band to 4200 Å, vs $\alpha_{J\text{-}UV}$ is much better ($< 3\times10^{-3}$ with only the objects known to be uncontaminated), and a comparison of the two measures may be seen in Figure 14. This suggests that, statistically, the relative blue bump strength may be investigated using optical and NIR data, within the scatter of the correlation. A fit to the correlation suggests that the two indices are roughly linearly related, $\alpha_{J\text{-}UV} \sim m\,\alpha_{JO} + k$, where $m = 1.58 \pm 0.21$ and $k = 0.54 \pm 0.10$ The residuals of this fit, expressed as a fraction of $\alpha_{J\text{-}UV}$, have an average value of –0.14, $\sigma = 0.37$. The histogram of α_{JO} is given in Figure 15

If the slope from the I band (9000 Å) to 4200 Å were a good indicator of $\alpha_{J\text{-}UV}$, then measurement of the blue bump would be simplified enormously. The strength of the blue bump could be easily measured with just one instrument, and more I band than J band measurements are available in the literature. Unfortunately, the slope from I to 4200Å is not a good indicator of $\alpha_{J\text{-}UV}$. Figure 16 gives a comparison of $\alpha_{J\text{-}UV}$ to α_{IO}. This figure shows more scatter than in the plot of $\alpha_{J\text{-}UV}$ vs α_{JO}. The local optical spectral variations have diluted the blue bump such that there is little correlation on the small scale. Objects with J-UV slopes between –0.5 and –0.1 can not be readily distinguished. The Spearman Rank probability is 0.144 (using only objects known to be uncontaminated) for $\alpha_{J\text{-}UV}$ and α_{IO}, indicating very weak correlation. The I band to 4200 Å slope is therefore not a good tool for studying the blue bump.

Table 6 lists six $\alpha_{J\text{-}UV}$ values and seven α_{JO} values <–1.02 for objects which are not known to be uncontaminated Even though these objects may be contaminated, they

should not be completely ignored. Although it is quite surprising that not a single object known to be un-reddened and uncontaminated by starlight has a slope inconsistent with a lower limit of –1, there is bias in this result. The signal to noise constraint on the UV spectrum required to confirm the lack of substantial reddening introduces a significant bias toward UV bright objects, which are often those with strong blue bumps. To estimate the constraint on the required UV flux, note that the 3 weakest bump objects in the sample, with $\alpha_{J\text{-}UV} < -0.93$, all have a UV spectrum of sufficient quality to diagnose reddening. These objects could still be diagnosed as unreddened if their noise increased between a factor of $\sim 2^{1/2}$ to 2. To estimate the weakest object that could have its 2200Å region diagnosed, the error in the UV flux was assumed to be proportional to (UV flux)$^{1/2}$. The UV flux in the weak bump objects was then reduced until the S/N decreased to the estimated limit. For UV fluxes decreased by a factor of $2^{1/2}$, the $\alpha_{J\text{-}UV}$'s all went down to near –1.3 , and the error in $\alpha_{J\text{-}UV}$ increased to between 0.023 and 0.22. For the a noise increase of a factor of 2, $\alpha_{J\text{-}UV}$ was near –1.6 and the errors ranged from 0.072-0.28. This suggests that significantly weaker bumps might be measured if present. The "–1 uncontaminated bump limit" remains extremely tantalizing, but it would be a stronger conclusion if it were verified in a flux-limited sample with all objects unambiguously diagnosed for reddening by high-quality 2175 Å observations .

Investigation of the strength of blue bumps in Type 2 objects is effectively frustrated by their other characteristics. All of the LMA Type 2 objects are at low red shift, and are of low luminosity. (However, outside this sample such objects do exist at substantial red shifts with large luminosities, e.g. IRAS 1051-273P11, DeGrijp et al. 1985.) This makes them particularly susceptible to stellar contamination. Their *apparent* blue bump measurements all indicate steep log slopes. Only the most distant Type 2 object, 1H2320+084, $z = 0.029$, is apparently free from any stellar contamination or optical reddening (however, its IUE spectrum of insufficient quality to rule out reddening). Its bump measure is $\alpha_{J\text{-}UV} = -0.94 \pm 0.091$. These results are consistent with Type 2 objects

having only weak or absent bumps. Type 2 objects with strong bumps have not been reported in the literature. There is little question that AGN type 2 are *observed* with weaker bumps than type 1's, but their rarity at high luminosity and the tendency for low luminosity Type 2's to be reddened or stellar contaminated make this a biased result. Before the *intrinsic* Type 2 blue bump distribution can be concluded to be significantly weaker than that of Type 1's, the $\alpha_{J\text{-}UV}$'s of more un-reddened, uncontaminated, and high luminosity Type 2's should be measured.

Luminosity Dependence of Blue-bump strength

Figure 17a and b show the comparison of relative blue-bump strength and 1 micron rest frame luminosity, measured by the J–UVslope and the optical–UV slope, respectively. While previous work (Kriss 1988) reports a systematic relative bump weakness for $L_{1\mu m} < 10^{30}$ erg s $^{-1}$ cm^{-2} Hz^{-1}, the plot shows no such threshold. The distribution appears similar for any range of luminosity; even the two highest luminosity objects are of moderate blue-bump strength. On the J–UV slope plot, 1H1226+022 (3C 273) is the most luminous object in the IR band, and has a fairly strong bump, but 1H1911–589, with the strongest bump, has only moderate IR luminosity, 0.46×10^{30} erg s $^{-1}$ cm^{-2} Hz^{-1}. Figure 17a is subject to the same detection biases for $\alpha_{J\text{-}UV}$ as discussed above, but figure 17b is not, as all the objects in the sample observed in good weather in the 4200 Å region yielded spectra of acceptable quality. Note that no stellar objects occur at high luminosities.

Table 8 describes the statistics of the various sub-samples. The mean values of all sub-samples are similar except for that of the low-luminosity total sample, which includes reddened and stellar objects. The mean of this sub-sample is low but with a dispersion so large that it is still consistent with the high luminosity sample. The dispersion is due to the reddened objects, which are in this lower luminosity sample due to the known preference for reddening and obscuration at lower luminosities (Lawrence 1991). The correlation coefficients and probabilities for $L_{1\mu m}$ vs $\alpha_{J\text{-}UV}$ and for $L_{1\mu m}$ vs $\alpha_{J\text{-}O}$ are given in Table 1, with Spearman probabilities of >51% for all measurements, which indicates no correlation.

This result, and the explanation above, leaves no doubt that in the IUE observed sub–sample, there is no correlation of relative blue-bump strength with luminosity, and no threshold effects.

8.3 Discussion

In Kriss (1988), it is argued that the bump strength is dependent on 1 μm luminosity. However, the bump strength in Kriss (1988) was measured using data extrapolated from optical photometry out to at least 2500 Å, not actual data taken in IUE bands. The 2500Å fluxes were probably extrapolated from B band, which, for the quasars in that sample, has significant pollution from the 3000Å bump (WNW). This bump can have a sharp rise in the B band, causing any extrapolation with it to overestimate the flux in UV bands. Finally, stellar contamination and reddening are more common, as shown here and in other works (see Lawrence; TP also finds X-ray obscuration more common in low luminosity AGN, which may be related) at low luminosity. Unless reddening and stellar contamination are identified, any survey of bump strengths will have a luminosity bias. I attempted to remove this bias by noting objects with stellar contamination and UV and optical reddening signatures.

The contribution of the blue bump component in the optical was discussed above, but not the contribution of the blue bump component at frequencies higher than UV. Spectral data are not available in the EUV–X region for the majority of the objects in the sample. However, X-ray observations of one or two of the strong bump objects in this sample show that they might have a soft excess, suggesting that the high energy tail of the thermal bump emission may extend to soft X-ray energies ($E \leq 2$ keV). The object 1H0557-503 (PKS 0558-504) shows an unusually steep power law in its Ginga hard X-ray spectrum (log slope = -1.14 ± 0.06). However, some excess emission below 2 keV appears in the residuals of fits to the Ginga data, suggesting a soft excess (Remillard et al. 1992; see the multi–frequency plot of this object in Appendix II). Lower energy EXOSAT

observations show a slightly steeper component (log slope = $-1.31\ ^{+0.15}_{-0.08}$), but only the lowest few channels appear to depart systematically from the higher energy power law (Remillard 1988,1992). These results suggest a soft excess, but do not clearly establish a spectral "break" between the steep tail of the blue bump and the hard X-ray power law. There is also evidence that 1H1911-589 (ESO141–G55), the strongest measured bump in this sample, has a soft excess (TP). Some additional objects with strong bumps and soft excesses are known outside of this sample as well (e.g. PG1211+143, Bechtold et al. 1987). If many more objects show a significant correlation of soft excess and blue-bump strength, and if high quality observations document spectral "breaks" in these objects, it would suggest that the origin of the soft excess is the blue bump. Given the association of the blue bump with an accretion disk, such results would require accretion disk theories to account for X-ray emission temperatures. The most recent accretion disk theories utilize Compton emission to produce a soft excess (e.g., Cannizzo & Reif 1992).

The possible association of strong variability with the strongest blue bumps, noted above, also has significant implications for AGN accretion disk modeling. An association of disk luminosity and variability is consistent with disk instability models (e.g. White & Lightman 1990).

The association of IRAS spectra peaked near12 μm and a strong blue bump deserves discussion. Barvanis (1987) associates emission in this region with warm nuclear dust. However, one would expect stronger UV radiation to indicate the absence of reddening, limiting the amount of dust along the line of sight. A plausible scenario incorporates non-spherically distributed dust to remove this dust from the line of sight. The observed continuum would then be un-reddened. A cartoon sketch of such a scenario might include a system with dust distributed in a region co–planar with the accretion disk, observed from out of the plane of the disk. The dust could be shielded from the hot, UV-emitting inner disk and the central continuum source if the disk had a relatively cool and optically thick outer region. The shielding is required because nuclear dust sublimates at ~

1500K (Barvanis), much cooler than inner accretion disk temperatures. In this scenario, the dust would be warmed by radiation from the outer edge of the accretion disk.

9. DISCUSSION: REDDENING AND/OR OBSCURATION OF THE TYPE 2 BLR AND CONTINUUM SOURCE

Several authors have proposed that Type 2 objects are Type 1 objects which are viewed at an angle such that a torus of cool material obscures or reddens the broad lines but not the narrow lines (e.g. Lawrence & Elvis 1982). Antonucci & Miller (1985) showed that some narrow line objects have broad lines when viewed in polarized light, supporting the obscuration picture. In these objects, the polarized broad emission is thought to be reflected from material above the torus. In the simplest forms of the obscuration model, the BLR is reddened or obscured such that the broad lines are undetectable, or nearly so. A reddened continuum may be observed, along with scattered broad lines and continuum, unless scattering completely dominates the process by which we observe the continuum. One would therefore expect to see reddening of the continuum that would distinguish the Type 2 objects on correlation plots, particularly in the B band. The Type 2 objects do not distinguish themselves in the continuum correlation analyses in any way that could be directly associated with nuclear emission, except that they are limited to the lowest X-ray luminosity range ($L_X < 5 \times 10^{43}$ erg s^{-1}). Immediately below, I give evidence that not all Type 2's are reddened compared to Type 1s.

The IR spectra of Type 2 objects do not show a stronger tendency than Type 1 objects to have significant nuclear dust emission (a 2-12 μm peak). Such emission might indicate re-radiation by the obscuring material.

To probe the role of reddening in the context of obscuration models, consider a simple model where Type 1 objects are reddened by circumnuclear dust such that they appear to be Type 2 objects. In this model, reddening is expected to significantly lower the

NIR-UV continuum flux of Type 2 reddened objects compared to the Type 1's which are not reddened. Reddening should therefore be obvious in the correlations between X-rays, which are nearly insensitive to reddening, and the NIR-optical bands, which are significantly affected by reddening. In the absence of stellar contamination, one would expect the reddened Type 2 objects to have low J and very low B band fluxes compared to the un-reddened Type 1 objects on the correlation plots. Type 2 objects stay well within the locus of Type 1 objects in the plots of correlations between X-rays and J and B bands, which is not consistent with the heavy reddening required to obscure the BLR. However, stellar emission can add to the continuum in the J and B bands at low luminosities where the Type 2 objects are found. (Note that Type 1 low luminosity objects are also stellar contaminated; ~40% of Type 1 AGN in the same red shift range as Type 2 objects show signs of significant stellar contamination.)

Three of six Type 2's which are not reddened and which have sufficient data for classification show evidence of significant stellar contamination. The observations are consistent with host stellar emission adding enough flux in the NIR-opt region that stellar-contaminated objects do not appear reddened. Given the significant spread in the residuals of the correlation with only un-reddened Type 1 objects (> half an order of magnitude for L_X vs B) this scenario of "masked reddening" via stellar emission is plausible for a wide range of stellar contributions and reddening values. However, Type 2 objects that do not show evidence of stellar contamination but are within the locus of un-reddened Type 1 objects must be unreddened. Three Type 2 objects (1H1308-237, 1H1408-031, 1H2214–313) do show evidence of reddening of the optical continuum, so reddening certainly plays a part in the spectrum of some Type 2s. Two Type 2 objects have insufficient data for classification, but one Type 2 object, 1H2320+084, has a NIR-opt spectrum inconsistent with reddening or stellar contamination.

The object 1H2320+084, z=0.029, the most distant Type 2, is squarely in the middle of the locus defined by Type 1 objects in the plot of L_X vs B. For this object, a

large extinction value, ~ > half an order of magnitude (or E(B-V) ~> 0.30 mag) relative to that in the Type 1 objects can be ruled out by the limits of the spread of the correlations, assuming that the intrinsic NIR–opt spectrum is similar to the other objects in the sample. The assumption of the intrinsic spectrum is required only to rule out pathological intrinsic spectra. One might propose an intrinsically strong blue bump plus reddening to produce a Type 2 with a normal ratio of B to X-ray flux so the object would not appear reddened in the correlations. However, 1H2320+084 has a falling NIR spectrum and a flat optical spectrum. In terms of the models above, if the bump component is strong enough to dominate the optical region, it must also flatten the NIR region. Unfortunately, the 2175 Å region observation was of insufficient quality to yield a useful reddening limit, so the reddening limit above cannot be confirmed independently. In summary, the spectrum of the Type 2 1H2320+084 appears generally similar to other galaxy-dominated Type 1's, and shows no signs of significant reddening. Therefore, models which explain such objects as obscured Type 1's must include a mechanism for much higher efficiency for scattering of the continuum than the broad line radiation.

In an ideal study, the reddening in Type 2 objects could be determined unambiguously from 2175 Å observations, but sufficient quality data are not available here. However, a lower limit to the reddening required in these objects can be obtained if an intrinsic slope is assumed. If one assumes a –1 log slope for Type 2 objects, then the intrinsic continuum would have had to have been reddened by E(B-V) = >~ 0.29 ± .14 mags in 1H0946-144 and by >~ 0.54 ±0.38 mags in 1H2315-423 to obtain their NIR-UV slopes from a –1 spectrum. The object 1H2320+084, discussed above, is above the –1 slope limit and has a lower reddening limit of zero. These reddening values are small compared to E(B-V) > 1 mag (factor of > 10) required to redden broad Hα so that it is undetectable.

In the objects in this sample, the only other evidence for reddening or obscuration of the Type 2 continuum comes from X-ray spectral observations. TP observed many

Type 2 objects in low energy X-rays, including several in this sample, and frequently found them to have large column densities of X-ray absorbing gas. If dust were associated with this gas, this would show that obscuration or reddening is taking place. However, X-ray absorbing columns are NOT direct evidence of dust that could redden or obscure the optical broad lines, i.e. reddening ≠ X-ray obscuration. If the large X–ray absorption ($N_H \sim 10^{23}$ cm^{-2}) were due to extinction by cold material similar to that in the interstellar medium (ISM) of our galaxy, the optical continuum would be extremely heavily absorbed (E(B–V) ~ 300 mag!) if subject to the same extinction. Extinction by such material may be immediately ruled out. If such reddening were really occurring, the optical continuum would be entirely due to stellar emission. Only three Type 2's in the LMA have been observed to have significant stellar spectral features, so this is not the case. X-ray absorbing columns observed for Type 2 objects *cannot* be associated with reddening due to ISM-like material, and are therefore *not* evidence that Type 2 galaxies have reddened BLR or continua. TP also provided observational evidence for this conclusion. They observed AGN, including some in this sample, (1H1210+393 = NGC4151, 1H2251-179 = MR2251, 1H1017+202 = NGC3227, all Type 1, and possibly 1H1832-652 = ESO 103-G35, Type 2) to have absorption which varied on time scales of months or less, suggesting that much of the X-ray gas was close in to the nucleus, closer than the broad line region. Temperatures in this region are probably well above the dust sublimation temperature (see Barvanis 1987), and therefore dust can not exist in the X-ray absorbing material without unusual shielding mechanisms. Since X-ray absorption measurements are not direct indicators of reddening, it still remains for continuum reddening to be demonstrated convincingly in a direct manner in many Type 2 objects (i.e. by the presence of a 2175Å feature or by showing an optical continuum consistent with reddening of a normal AGN continuum without starlight contamination).

To summarize, there is not good evidence that all Type 2 AGN continua are reddened. Scattering could be invoked in such a model to permit unreddened continuum

radiation to reach the observer, so that only minor reddening could be detected. However, the scattering of the broad line radiation must be drastically suppressed compared to the continuum scattering so that the line emission is undetectable by unpolarized measurements. The scattering electrons must then be confined to a region close to the continuum source so that the solid angle for scattering seen by the BLR is small.

SUMMARY

1. My sample shows no bifurcation in radio loudness, F_{6cm} / F_B , as is reported for optically selected samples. Kellermann et al. (1989) do see a bifurcation, and attribute this to a rarity of objects with $1 < F_{6cm} / F_B < 10$. Greater than 14.4% of the LMA lie in this interval at 95% confidence, however, the difference is partly made up of Type 2 objects, where the B band flux may be a poor representation of the nuclear flux. The ratio $F_{6\,cm} / F_X$ gives a much clearer measure of the relation of the underlying nuclear non-thermal component and radio emission, as X-rays are relatively insensitive to reddening and stellar contamination. Such a distribution shows no statistically meaningful indications of a bimodal distribution. In the larger picture, there are two main conclusions of the radio studies:

a. radio emission is different from IR and optical bands in that it has no clearly monotonic relation to the luminosity of the central X–ray source (over the full range of observations), and no significant relation to the underlying I–X component.

b. No continuum properties studied here suggest a segregation of AGN based on their relative radio emission.

2. Hard X–ray selected Type 2 objects show no tendency to satisfy the IRAS warm criteria; four of them are the "coolest" objects in the sample. Hard X-ray selected samples are therefore not biased against host galaxy disk emission in these objects, unlike the "warm" selected Type 2 objects.

3. This work shows that emission is correlated in all bands from 25μm to hard X-rays, except for the UV band. Evidence is given that the lower limit of the NIR-UV slope is –1 (see below), strongly supporting the hypothesis that some underlying component links all these bands. However, the range of 1.25 μm to 5 keV slopes ($\alpha_{JX} = -1.04 \pm .05$ for uncontaminated objects) and the different slopes of the correlations (0.55 at 25μm,

~0.88 at 1.25μm) suggest that the underlying continuum does not have a uniform –1 slope in all bands. It should also be noted that the power law slope in hard X-rays is known to be – 0.7 from about 1 keV to energies of several tens of keV in most measured AGN, so the –1 slope is not observed within the range of X-ray energies.

4. A large intrinsic variation is observed in the shape of the blue bump from object to object. The $\alpha_{J\text{-}UV}$ log slope ranges from –2.7 to + 0.12. However, among objects selected to be free from reddening and stellar contamination, none are observed with an $\alpha_{J\text{-}UV}$ log slope steeper than –1. These results suggest the presence of an "underlying" non-thermal NIR-UV component with an intrinsic slope near –1. In this model, the objects with log slopes near –1 are nearly bumpless (have little or no thermal UV emission), and the UV spectra show the bare underlying AGN non-thermal continuum. Objects with the strongest blue bumps can be extremely variable, up to a factor or ~5, but UV variability is also seen in weak bump objects, albeit at lower levels.

5. I find that optical data, taken in bands near 4050 and 4200 Å (carefully chosen to avoid contamination from Fe II and Balmer continuum emission) allows the computation of a NIR–optical slope which shows some correlation with the NIR–UV slope. This suggests that optical and NIR measurements could be used as an indicator of blue-bump strength.

6. Many objects which have a broad, strong peak between 2–12 μm also have some indication of a strong blue bump. Emission in the 2-12 μm region has been associated with nuclear dust. The association of this emission with blue-bump strength could be related to coplanar distributions of an accretion disk and the dust which emits the 2–12 μm peak. Both the UV emission from the disk and the IR emission from the dust disk would be brightest when viewed face-on.

7. No correlation of the relative blue-bump strength with 1 μm luminosity, or with X–ray luminosity, is present in LMA data. There also appears to be no X-ray luminosity threshold for the existence of weak or strong bumps, as the mean bump strengths (relative to the IR continuum) within various ranges of luminosity are all consistent.

8. It appears that not all Type 2 objects have intrinsic continuum reddening. Three Type 2 objects in the sample (1H1308-237, 1H1408-031, 1H2214-313) show a NIR–opt spectral shape consistent with large intrinsic reddening of the optical continuum. Other objects are inconsistent with significant reddenings, but the stellar contributions in these objects cannot be clearly eliminated, and may be masking the reddening. However, one Type 2 object, 1H2320+084, is not consistent with large ($E(B-V)>\sim0.3$ mag) reddening of the optical continuum, given certain weak assumptions. These results make it clear that optical continuum reddening is common in nearby, low-luminosity Type 2 objects, but they suggest that complete models for Type 2 objects must allow for some fraction of the objects to be un-reddened.

SUGGESTED OBSERVATIONS

1. Two objects in the LMA with blue bumps significantly above the median strength (1H0557–503, $\alpha_{J\text{-}UV} = -0.575 \pm 0.019$, and 1H1911–589, $\alpha_{J\text{-}UV} = +0.119 \pm 0.023$) have been associated with a soft X-ray excess (see Remillard 1988, 1992, and TP, respectively). PG 1211+143 is another example of such an association (Bechtold et al. 1987). In terms of the models above, the thermal bump component in these objects may be present all the way to soft X-ray energies, adding to the underlying I-X component. The strong blue bump objects identified in the LMA seem the most likely and easily observed candidates to display such a phenomenon. I suggest that simultaneous JHK, IUE, and soft X-ray observations be made (and if possible optical spectrophotometry) of the strongest bump objects, to search for additional objects with blue bumps "connecting" in the X-ray band. The connection would be indicated by a discontinuity of spectral slopes at low X-ray energies, caused by the steep bump component "connecting" to the flatter hard X-ray component. The observation of such an excess in several objects, and any correlations with bump strength, would provide more evidence that the soft excess is associated with the bump, not some other component limited to X-ray energies.

2. The clearest possible demonstration of continuum reddening is the presence of a 2175 Å feature. The signal to noise of the IUE spectra of the Type 2 objects studied here was insufficient to determine the 2175 Å feature strength, but the UV signal was usually sufficient for detection. The IUE's low frequency spectrographs' performance in the region near 2175 Å is inherently poor, making such determinations unusually difficult. The FOS instrument on the HST, with no unusual difficulties in the 2175 Å region and more than 5 times the collecting area of the IUE and significantly higher throughput, would easily yield high signal to noise spectra of the objects already observed, and many other Type 2 objects. I suggest that a program to search for 2175 Å features in Type 2 objects,

using the FOS, and with simultaneous JHK and optical spectroscopic observations, should be undertaken. Continuum reddening similar to that from dust in our own galaxy would be clearly demonstrated if present in these objects. I also suggest that both objects that have and have not shown broad lines in polarized light be included in this program, to examine the role of dust in the polarization/reflection mechanism.

REFERENCES

Antonucci , R. R. J., and Miller, J. S., ApJ, 1985, 297,621

Barvanis R., 1987, ApJ, 350, 537,

Bennett, C. L., Lawerence, C. R., Burke, B. F. , Hewitt, J. N., and Mahoney, J., 1986, ApJS, 61, 1

Bechtold et al., 1987, ApJ, 314,669

Canizares, R.C., and White, J. L. 1989, ApJ, 339, 27

Cannizzo, J. K. & Reiff, C. M. 1992, ApJ, 385,87

Carleton, N. P. et al., 1987 ApJ, 318, 595

Davidsen, A. F. et al., 1992 Ap. J., in press

DeGrijp, M. H. K., Miley, G. K., Lub, J., and deJong, T., 1985, Nature, 314, 21

Fillipenko, A. V. & Sargent, W. L. W. 1988, ApJS, 57, 503

Giuricin, F., Mardirossian, F., Mezetti, M., and Bertotti, G., 1990, ApJS, 72, 551

Hill, G. J., Becklin, E. E., Wynn–Williams, C. G., Ap. J. 330:737–742, 1988 July 15

Kellermann, K. I., Sramek, R., Schmidt, MM., Shaffer, D. B., and Green, R. F., 1989, AJ 98, 1195

Kellermann, K. I., Pauliny–Toth, I. I. K., 1981 Ann rev A&A, 19, 373

Kinney, A. L., Bohlin, R.C., Blades, and J.C., York, D. G., 1991, ApJS, 75, 645

Kriss, G. A. 1988, Ap. J., 324, 809

Landolt, A. U., 1973, AJ, 78,959

Lawrence, A., and Elvis, M., 1982 ApJ, 256,410

Lawrence, A., MNRAS 1991, 252,586

Malkan, M. A., Seargent, W. L. W., 1982, ApJ, 254, 22

McDowell et al., 1989 , ApJ, 345, L13–16

Mushotzky, R. F. 1984, Adv. Space Res.,3,10

Mushotzky, R. F., and Wandel, A., 1989, ApJ, 339, 674

Netzer, N., Wamsteker, W., Wills, B., Wills, D., 1985, ApJ, 292, 143

Neugebauer, G., Green, R. F., Matthews, K., Schmidt, M., Soifer, B. T., Bennett, J. 1987, ApJ, 63, 615

Orr. M.J. L., and Browne, I. W. A., 1982 MNRAS, 200, 1067

Piccinotti, G., Mushotzsky, Boldt, E. A., Holt, S.S., Marshall, F.E., Serlemitsos, P.J., Shafer, R. A., 1982 ApJ, 253, 485

Remillard, R., Schwartz, D. A., and Brissenden, R. J. 1988, in *A Decade of UV Astronomy with IUE* (Eur. Space Ag. spec. Pub. 281), p. 273

Remillard, R. A., Brissenden, R. J. V., Grossan, B., Bradt, H. V., Ohashi, T. 1992, (in progress)

Savage, B. & Mathis, J., 1979, ARA&A, 17, 73

Schmidt, M. & Green, R. F., 1986, ApJ, 305, 68

Schueur, P.A.G., and Redhead, A. C. S., 1979, Nature 277, 182

Smith, E.P., Heckman, T. M., Bothun, G. D., Romanishin, W., and Balick, B. 1986, ApJ 306,64

(TP) Turner, T. J., Pounds, K. A., 1989, MNRAS, 240, 833

Ulvestad, J. S., & Wilson, A. S., 1984, ApJ, 285, 439

Van Steenberg, M., and Shull, J., A Decade of UV Astronomy with IUE, Proc. Celebratory Symposium, GSFC, Greenbelt, MD 1988 April 12–15, publ. 1988, ESA SP–281, Vol. 2

Veron–Cetty, M. P., and Veron, P., 1989 March, ESO Scientific Report #7, "A Catalogue of Quasars and Active Galaxies", 4th ed.

Ward et al. , ApJ 1987, 315, 74

Weinberg, S. 1972, Gravitation and Cosmology: Principles and Applications of the General Theory of Relativity, John Wiley and Sons inc., New York.

White, T. R. & Lightman, A. P., ApJ 1990, 352,495

Wilkes, B., Elvis, M., 1987, ApJ, 323, 243

(WNW) Wills, B.J., Netzer, H., and Wills, D., 1985, ApJ , 288, 94

Wood, K., et al., 1984, ApJ Suppl., 56, 507

Worall D. M., Giommi, P., Tananbaum, H., and Zamorani, G. 1987, ApJ, 313, 596

Zamorani, G., et al., 1981, ApJ, 245, 357

TABLE 1

Spearman–Rank Correlation Test Results

X	Y	N	$R_{Spearman}$	$P(>R) / 10^{-3}$	$R_{Pearson}$	$P(>R) / 10^{-3}$
Radio:						
F_X	$F_{6\ cm}$	60	0.015	909	0.280	30
F_X	RL	55	-0.036	794	-0.077	573
$L_{X\ 44}$	RL	55	0.094	497	0.001	992
$L_{X\ 44}$	RL>1 only	34	0.488	3.42	-0.017	924
$L_{X\ 44}$	5> RL >100	14	0.451	106	0.392	166
$L_{X\ 44}$	Top 10 RL	10	0.612	60	0.091	803
α_r	L_X	38	0.007	965	0.063	705
NIR, IR:						
L_X	νL_νI baseln	51	0.759	1.1e–7	0.455	0.796
F_X	νF_νI baseln	51	0.447	1.00	0.428	1.731
Fx	$F_{1\mu m}$	54	0.582	3.9e–3	0.484	0.21
$L_{X\ 44}$	$L_{1\mu m}$	54	0.941	4.5e–23	0.852	3.1e-13
Fx	F_B	75	0.360	1.5	0.526	1.28e-3
L_X	L_B	96	0.900	1.14e-32	0.470	1.33e-3
IR:						
Fx	F12	76	0.331	3.48	0.385	0.596
Fx	F25	79	0.343	1.96	0.405	0.218
Fx	F60	77	0.229	45.4	0.288	11
Fx	F100	65	0.267	31.4	0.295	17
$L_{X\ 44}$	L12	76	0.957	1.2e–38	0.904	4.4e-26
$L_{X\ 44}$	L25	79	0.866	7.0e–22	0.567	4.97e-5
$L_{X\ 44}$	L60	77	0.790	1.3e–14	0.788	1.8e-14
$L_{X\ 44}$	L100	65	0.755	3.7e–10	0.832	9.2e-15
UV:						
<UV>(3 bands)	F_X	31	0.227	220	0.339	62.1
L1μm 30	$\alpha_{J\text{-}UV}$ (Uncontam.)	20	0.107	654	0.043	856
L1μm 30	$\alpha_{J\text{-}UV}$ (all)	31	0.125	622	–0.003	990
<UV>(3 bands)	F_{4200}	47	–0.310	33.7	–0.121	420
$F_{6\ cm}$	$\alpha_{J\text{-}UV}$	29	0.015	937	0.427	20.9
RL	$\alpha_{J\text{-}UV}$	22	–0.320	146	0.060	790
Lx44	$\alpha_{J\text{-}UV}$	20	0.319	171	0.424	62.4
$\alpha_{J\text{-}UV}$	α_{JO} (Uncontam)	16	0.588	16.5	0.625	9.61
$\alpha_{J\text{-}UV}$	α_{IO} (Uncontam.)	15	0.389	152	0.357	191

Table 3 – In this table, the Spearman–Rank test coefficient is given with the more familiar "Pearson" coefficient, along with the probabilities that random distributions would produce an equal or larger coefficient.

Key to Abbreviations:
RL = Radio Loudness, $F_{6\ cm} / F_B$.
<UV>(3 bands) = Average UV flux used to define α_{J-UV}. See text for details.
F_{4200} = Continuum flux at 4200 Å.
(Uncontam.) refers to the sub-sample of all objects determined to be free of reddening and stellar contamination; (all) refers to all objects regardless of stellar contamination or reddening.

TABLE 2

RADIO STATISTICS

2(a) Statistics of Radio Detections

	[1]Type1 Radio Loudness	[1]Type 2 Radio Loudness	[1]Total Radio Loudness
Minimum	0.10	0.302	0.10
Maximum	13792	58.5	13729
Number of Objects	47	8	55
Mean	402	11.7	346
Median	1.57	3.57	1.87
Std Deviation	2029	19.6	1878

[1]Radio loudness is defined as F_B / F_{6cm}, in the rest frame of the AGN.

2(b) Numbers of Radio-Loud vs.Radio-Quiet Objects

Subsample	RL	Max Possible	RQ[1]	Max Possible	RL Lower Limit, 95% confidence[2]
Type 1 (84 total)	28 (33%)	61	23 (4 UL) (27%)	68	19.90 (20.7%)
Type 2 (12 total)	7 (58%)	11	1 (8%)	5	3.3 (27.4%)
Total (55 detections, 4 RQ ULs)	35 (36%)	72	24 (24%)	61	25.87 (26.9%)

[1] Upper Limits which excluded radio loudness (UL) are counted in this column.

[2]Confidence limits were determined from the numbers in the RL column, assuming they are Poisson distributed. Percentage of Type 1 objects, Type 2 objects, or "Total" subsample are given in parenthesis.

2(c) Objects with $1 < F_B / F_{6cm} < 10$

(Sub) Sample	N_{Total}	[1]%($1 < F_B / F_{6cm} < 10$) [Number]	1 sigma interval	Lower Limit, 90% confidence	Lower Limit, 95% confidence
Type 1	86	18.6%[16]	14.0–24.5 %	13.0%	11.7%
Type 2	12	41.7%[5]	23.4–69.8%	20.3%	16.4%
Total Sample	98	21.4%[21]	16.8–27.2%	15.7%	14.4%

(Sub) Sample	N_{Total}	[1]%($1 < F_B / F_{6cm} < 10$) [Number]	1 sigma interval	Upper Limit, 90% confidence	Upper Limit, 95% confidence
[2]BQS	114	12.3%[14]	9.04–16.5%	17.7%	19.2%

[1]Fraction of objects, *detected so far* , which fullfill $1 < F_B / F_{6cm} < 10$, the region where Kellermann et al. (1989) describe a deficit in the number of sources in the BQS. The actual number of objects is given in square brackets.

[2] From Kellermann et al. (1989).

2(d) Loudness and L_X

X-ray Luminosity Subsample erg s^{-1} cm^{-2} (2-10 keV)	Number in Luminosity Subsample described in first col.	RL > 10 % of luminosity subsample [1][# obs, max]	RL > 10, 90% confidence limits [2]% of luminosity subsample (number)	RL > 10^2 % of luminosity subsample [1][# obs, max]	RL > 100, 90 %confidence limits [2]% of luminosity subsample (number)
Low Luminosity $L_X < 10^{45}$	78	≥ 10.3 % [8,31]	max = 51% (39.4)	≥ 2.5% [2,17]	max = 15% (11.8)
High Luminosity $L_X \geq 10^{45}$	19	≥ 31.6% [6,15]	lower = 16.6% (3.15)	≥ 21.1 % [4,10]	lower = 9.2 % (1.75)
Low Luminosity $L_X < 10^{46}$	90	≥13.3 % [12,39]	max= 54 % (48.3)	≥ 4.4 % [4,11]	max= 18.4 % (16.6)
High Luminosity $L_X \geq 10^{46}$	7	≥ 28.6% [2,7]	lower = 7.6 % (0.53)	≥ 28.6% [2,6]	lower = 7.6 % (0.53)

[1]The first entry in each cell, expressed in %, gives the fraction of the luminosity subsample defined in the first column observed with a radio loudness in the range specified at the head of the column.
The numbers in the square brackets give the range of numbers of objects fulfilling the radio loudness criteria at the head of the column within the X-ray luminosity subsample defined in the first column, including all available upper limit information. The first number in brackets is the number of detections fulfilling the criteria, the second number is the maximum possible number of objects that could fulfill the criteria. The maximum number is given by the number in the luminosity subsample minus the number of detections and upper limits which rule out satisfaction of the given criteria.

[2]This column gives the Poissson 90% confidence upper limit ("max") for the number of objects with the radio loudness indicated at the head of the column, if a high luminosity subsample ($L_X \geq$ a given limit) is specified in column 1. The same column also gives the 90% Poisson confidence lower limit ("lower") for the number of objects with the radio loudness indicated at the head of the column, if a low luminosity subsample ($L_X <$ a given limit) is specified in column 1. In this way, a comparison of the numbers of objects above the given radio loudness may be compared above and below the given luminosity without detection bias. See text for full explanation.

TABLE 3

NUMBERS OF OBJECTS WITH R/X GREATER AND LESS THAN 1

Subsample	N(R/X >1)	[1]Max Possible	[2]N(R/X <1)	Max Possible	N(R/X >1) Lower Limit 95% confidence interval[3]
Type 1	34 (41%)	69	16(4 UL) (19%)	51	25.0 (26%)
Type 2	8 (67%)	12	0 (0%)	4	3.98 (33%)
Total (55 detections, 4 RQ ULs)	42 (44%)	81	16 (16%)	55	31.9 (33%)

[1]This column gives the maximum possible number of objects in the subsample (specified in the first column) which could fulfull the criteria given at the head of the preceeding column. This maximum possible number is given by the number of objects in the subsample minus the number of detections and upper limits which rule out satisfaction of the criteria at the head of the previous column.

[2]The number of objects in the subsample indicated in the first column with R/X < 1 are indicated in this column. Upper Limits which exclude radio loudness (UL) are counted in this column.

[3]The Poisson limits on the number of objects with R/X > 1 in the subsample indicated in the first column are given in this column. Confidence limits were determined from the numbers in the N(R/X > 1) column, assuming they are Poisson distributed. The same number, expressed as a percentage, is given in parenthesis.

TABLE 4

CORRELATION SLOPES

Parameter	[1]Log Slope
[2]L_B	1.00 ± 0.03
[2]$L_{1.25\ \mu m}$	0.88 ± 0.03
$L_{12\ \mu m}$	0.71 ± 0.04
$L_{25\ \mu m}$	0.55 ± 0.05
$L_{60\ \mu m}$	0.58 ± 0.1
$L_{100\ \mu m}$	0.68**

[1]This column gives the log slopes of correlations between the X-ray luminosity and some other parameter. For a band p, for the assumption $L_p \propto L_X^{\xi}$, the log slope, ξ, is given.

[2]L_B, $L_{1.25\ \mu m}$ are in units of 10^{30} erg s^{-1} Hz^{-1}, and both are the dependent variable in a fit to L_X in units of 10^{44} erg s^{-1} cm^{-2} integrated from 2–10 keV, weighted by the dominant errors in L_X. (For the IRAS fits, the same units were used, L_X was the independent variable, and the fit was weighted by the dominant errors in the IRAS measurements.)

**Approximate value only; a satisfactory least-squares fit was not obtained with weighted data.

TABLE 5

5(a) List of "Steep" or "Galaxy Dominated" AGN

LASS NAME	Comments
1H0043+294	Weak BB (Blue Bump).
1H0300-482	
1H0445-060	Type 2. 100 μm much weaker than 60 μm.
1H0620-646	
1H1017+202	Weak BB, stellar contaminated. Also has weak 12 μm peak.
1H1238-050	Weak BB.
1H1313+363	Type 2. Also has weak 12 μm peak.
1H1320+066	
1H1350+696	Stellar contamination in optical spectrum.
1H1408-031	Type 2. Stellar contamination in optical spectrum. Entire IRAS spectrum shaped like a bump, where other objects rise monotonically to low frequency.
1H1538-182	
1H1615+655	Strong BB. 100 μm lower than 60 μm.
1H1820+643	
1H1828-593	Type 2. Marginal object, IRAS spectrum close to flat. Weak bump.
1H2018-529	Type 2. Weak UV.
1H2214-313	Type 2. 60, 100 μm very strong compared to 25 and 12 μm.
1H2301+086	Weak bump. Very strong 60 μm.
1H2315-423	Type 2. Weak UV.

5(b) List of AGN with 2-12 μm Peaks, or Significant "Warm Dust" Components

Object	Comments
1H0014+111	Monotonic rise from radio to 12 μm.
1H0106+324	Strong BB.
1H0121–353	Type 2. Weak UV.
1H0140+393	Monotonic rise from radio to 12 μm.
1H0217–639	Strongly rising optical specrum suggests strong BB.
1H0339–822	Strong stellar contamination.
1H0435–274	No NIR, but optical spectrum is well below all IRAS, and IRAS is strongly peaked at 12 μm.
1H0510+031	Strongly rising optical specrum suggests strong BB.
1H0758+762	Prototype object. In this object, a bump rises from 60 μ to 12 μ at low frequencies, and drops from nearly the same level in the NIR at L (3.4 μm) smoothly to V. The spectrum gives the impression that the peak is actually somewhere between 12 and 3 μm. Strong BB.
1H0929+122	No UV coverage below 2000Å, but UV is above X, and optical spectrum rises significantly from I through V, suggesting a moderately strong BB.
1H1017+202	Weak 12 μm peak is superimposed on galaxy dominated IRAS spectrum. Strong stellar contamination evident.
1H1032–142	Sparse data, but strong B,V relative to IRAS and X suggest strong BB possible.
1H1226+022	Low freqeuncy rises smoothly from radio to 12 μm, high frequency drops smoothly from 12 μm through J,H,and K. This famous quasar (3C273) is well–known to have a strong BB.
1H1313+363	Type 2. This object appears to have galaxy emission at 100–60 μm, a 12 μm peak, and strong stellar contamination, as indicated by the NIR–optical spectrum.
1H1429+370	IRAS shows 25 – 12 μm rise; NIR rises smoothly from I through K. Strong BB.
1H1504 +035	IRAS spectrum peaks at 12 μm, but NIR spectrum does not converge toward same peak. Instead, the NIR–optical spectrum is dominated by stellar shape.
1H1530+585	IRAS spectrum rises from 100μm to 12 μm but NIR flat. Strong BB.
1H1911–589	This object, which has the strongest BB in the LMA, has an IRAS spectrum which rises from 100 μm to 12 μm, and a NIR spectrum which shows a drop from Lband (3.4μm) to K band (2.2μm). Although the BB is extremely strong, the 12 – 2 μm peak is not unusually strong.
1H2209–470	This object appears to have galaxy emission at 60 and 100 μm, a peak at 12 μm, and stellar contamination in the NIR-optical region. The BB is weak in this object.
1H2329+294	IRAS rises from 100 – 12 μm. Optical rises swiftly from I – V, consistent with a strong bump.
Additional Comments	
1H0445–060	Type 2. The IRAS spectrum rises from 100 μm to 12 μm, except for the 60 μm point which is the highest in the spectrum. The lack of NIR data and an optical spectrum that is not smooth do not allow this object to be classified as peaked in the 12 μm region. .
1H1540+338	This object has a 12 μm IRAS peak but known variability and lack of a 25 μm detection and NIR data make the identification of a 12 μm peak unclear.

1H2303–089	This is the only object with no IRAS coverage, so it cannot be classified as peaked near 12 μm, however, J through L rise monotonically (in νF_ν) toward 12 μm. The object has a very strong BB.

TABLE 6

BLUE BUMP STRENGTHS

6(a) Objects Uncontaminated by Significant Stellar Emission or Reddening

LASS NAME	$^1\alpha_{J\text{-}UV}$	$\sigma(\alpha_{J\text{-}UV})$	$^1\alpha_{JO}$	$\sigma(\alpha_{JO})$
1H0014+111	–0.930	0.164	–1.15	0.0677
1H0043+294				
1H0048+250			–0.195	0.0467
1H0106+324	–0.355	0.139	–0.751	0.0710
1H0122-590	–0.971	0.015		
1H0227–094				
1H0258–126				
1H0413–116				
1H0435–274				
1H0445–060				
1H0523–118			–0.518	0.0372
1H0555–384			–1.14	0.0754
1H0557–503	–0.575	0.019	–0.960	0.0610
1H0641+741			–0.622	0.0414
1H0659+453	–0.994	0.150	–1.18	0.227
1H0758+762	–0.573	0.0827		
1H0929+122				
1H1032–142				
1H1120+423				
1H1135–372	–0.779	0.130		
1H1210+393	-0.948	0.021	–0.925	0.0415
1H1226+022	–0.584	0.0952	–0.294	0.0220
1H1229+199				
1H1318+560				
1H1420+481				
1H1422+273				
1H1429+370	–0.76	0.152	–0.549	0.046
1H1530+585	–0.621	0.0881	–0.588	0.157
1H1615+655	–0.049	0.272	–0.193	0.162
1H1704+605	–0.768	0.0767	–0.345	0.099
1H1811+670				
1H1820+643				
1H1836–786	–0.935	0.026		
1H1911–589	0.119	0.022	–0.453	0.034
1H2041–108	–0.54	0.069	–0.339	0.045
1H2107–097	–0.787	0.0937	–0.611	0.030
1H2239+294				

1H2251–179	–0.598	0.123	–0.708	0.041
1H2301+086	–1.086	0.0512	–0.953	0.021
1H2303–089	–0.722	0.145	–0.979	0.040
1H2303+039			–0.470	0.053

Notes to table 6a:

[1]See text for definition.

[2]H1210+393 (NGC 4151) is the most UV variable object known. The given value is representative of the medium brightness state (Ulrich et al. 1990). The measured index could vary significantly from this value, however, the *intrinsic* value of the index is not likely to go significantly lower. See Chapter 6, Variability, for more discussion.

6(b) [1]Stellar Contaminated Objects

LASS NAME	[2]Spectral or Imaging Stellar Indications	[3]$\alpha_{J\text{-}UV}$	$\sigma(\alpha_{J\text{-}UV})$	[3]α_{JO}	$\sigma(\alpha_{JO})$
[4](1H0121–353) (Type 2)					
1H0339–822	Obvious disk > 25 " on POSS				
1H0448–041	Stellar Absorption			–0.20	0.16
1H1017+202	Obvious extension on POSS	–2.3	0.301	–0.74	0.16
1H1238–050	Stellar Absorption	–1.17	0.112	–0.85	0.17
1H1313+363 (Type 2)	Stellar Absorption			–0.91	0.043
1H1350+696	>30 " disk on POSS	–1.11	0.12	–0.78	0.16
1H1504+035 (1H1727+308)	[5]Aperture effects				
1H1832–652 (Type 2)	Stellar Absorption			–1.44	0.11
1H2209–470	Stellar Absorption	–1.61	0.033	–1.63	0.037

[1]Objects determined to be significantly reddened as determined by their NIR-optical spectral shape. See text for details.

[2]This column gives corroborating evidence for reddening, in addition to a stellar NIR-optical spectral shape. POSS refers to the Palomar Sky Survey prints.

[3]An estimate of the log slope between the bands indicated is given by replacing the J band (1.25 μm) fluxes with that predicted by the IR baseline flux (see text for more details).

[4] The Type 2 object 1H0121-353 has indications of [5]aperture effects given in Ward et al. (1987), however, no photometry of the NIR region are available and no optical spectra of the Ca H,K region are available to check this report. Ward et al. (1987) showed large aperture optical photometry which was significantly above J band NIR photometry with a small aperture. As no bump measurements are available, the object is only listed parenthetically for completeness.

[5]1H1727+308 has a rapidly rising NIR spectrum and a rapidly falling optical spectrum, as a typical stellar contaminated object would, but the two do not smoothly connect (~ factor of 2 offset). The difference is probably due to aperture effects. The optical spectrum is not of sufficient quality to determine the presence of Ca H,K features, so verification is not available for this diagnosis. Since the diagnosis is not rigorous, the object is listed in this table with parenthesis.

6(c) Reddened or Reddening Undetermined Objects

LASS NAME	Reddening Indication	$\alpha_{J\text{-}UV}$	$\sigma(\alpha_{J\text{-}UV})$	α_{JO}	$\sigma(\alpha_{JO})$
1H0113–148	?			–2.01	0.31
1H0235–525	?	–1.02	0.036	–0.15	0.078
1H0744+499	2175 Å	–0.55	0.074	–0.85	0.065
1H0946–144 (Type 2)	?	–2.08	0.517	–2.28	0.17
1H1308–237 (Type 2)	OPT				
1H1345–300	OPT	–2.54	0.322	–3.44	0.55
1H1408–031 (Type 2)	OPT				
1H1415+255	2175 Å	–0.83	0.073	–1.32	0.049
1H1630+673	OPT				
1H1828–593 (Type 2)	?				
1H1858+797	?	–1.47	0.227	–1.55	0.13
1H2214–313 (Type 2)	OPT			–1.79	0.05
1H2315 –423	?	–2.65	0.246	–2.77	0.17
1H2320+084 (Type 2)	?	–0.94	0.091	–1.83	0.11

[1]A "?" in this column means that the reddening could not be determined by observation of the 2175 Å region because of poor signal quality. "OPT" in this column indicates that the optical continuum fluxes showed evidence of significant continuum reddening, and "2175 Å" indicates that a significant 2175 Å absorption feature was discovered but cannot be corrected.

TABLE 7

WEAK AND STRONG BLUE BUMP OBJECTS

Characteristics of the Five Strongest Blue Bump Objects

LASS NAME	$\alpha_{J\text{-}UV}$	σ_α	Z	Comments
1H0106+324	–0.355	0.222	0.015	Mismatch of LWR(low f) with SWP (high f) spectra indicates variability. Extraordinarily high 12 μm emission. IR disk emission weak.
1H0758+762	–0.573	0.083	0.10	Prototype object with huge 2-12 μm peak which dominates spectrum from IRAS to NIR, and possibly in the optical.
1H1615+655	–0.049	0.272	0.129	IRAS spectrum strongly peaked at 60 μm.
1H1911–589	*0.119	0.022	0.0368	Very powerful, fast–rising UV, variable. Flat IR strongest at 12 μm.
1H2041–108	–0.540	0.069	0.0352	Factor of ~5 variable in UV. IRAS very weak at 60,100 μm.

*N_H not available from 21cm measurements; calculated using csc(b). UV is variable. Max and best signal to noise value given; average is –0.25±0.11.

Characteristics of the Five Weakest Blue Bump Objects

LASS NAME	$\alpha_{J\text{-}UV}$	σ_α	Z	Comments
1H0014+111	–0.93	0.164	0.09	IR peaks at 12 μm, IUE flat (in $F\lambda$).
1H0122–590	–0.971	0.015	0.045	UV Variable. Very weak IRAS emission longward of 12 μm.
1H0659+453	–0.994	0.150	0.056	IUE flat (in $F\lambda$), optical does not connect with IUE or JHK – probably variable.
1H1210+393	–0.948	0.021	0.0033	UV Variable. IRAS strongly peaked at 12-25 μm.
1H2301+086	–1.086	0.051	0.0167	Excellent quality IUE spectra, Variable >~40%. IRAS disk emission dominated.

TABLE 8

LUMINOSITY DEPENDENCE OF BLUE-BUMP STRENGTH

Luminosity Dependence of $\alpha_{J\text{-}UV}$

Uncontaminated Objects (mean $\alpha_{J\text{-}UV}$ σ N)	[1]Total IUE+J Sample (mean $\alpha_{J\text{-}UV}$, σ N)	$L_{1\mu m}$ 30 > 1 (None are contaminated) (mean $\alpha_{J\text{-}UV}$, σ N)	$L_{1\mu m}$ 30 < 1 Uncontaminated (mean $\alpha_{J\text{-}UV}$, σ N)	$L_{1\mu m}$ 30 < 1 All IUE+J objects (mean $\alpha_{J\text{-}UV}$, σ N)
–0.68	–0.94	–0.59	–0.71	–1.14
0.31	0.70	0.31	0.27	0.73
20	30	9	11	21

[1]All objects for which both IUE and J–band observations are available.

Luminosity Dependence of α_{JO}

Uncontaminated Objects (mean α_{JO} σ N)	[1]Total IUE+J Sample (mean α_{JO}, σ N)	$L_{1\mu m}$ 30 > 1 (mean α_{JO}, σ N)	$L_{1\mu m}$ 30 < 1 Uncontaminated (mean $\alpha_{J\text{-}O}$, σ N)	$L_{1\mu m}$ 30 < 1 All IUE+J objects (mean α_{JO}, σ N)
–0.66	–1.05	–0.62	-0.70	–1.21
0.31	0.68	0.40	0.25	0.63
21	39	9	12	30

[1]All objects for which both 4200Å and J–band observations are available.

FIGURE CAPTIONS

Figure 1. Figure (a) gives the histogram of radio loudness, F_{6cm} / F_B, for the LMA, with separate symbols for Type 1 and Type 2 objects. Upper limits which restrict the radio loudness to be < 1 are also given, but higher limits are omitted as they significantly distort the shape of the distribution. Note that instead of bifurcation, a long, smooth tail to high loudness is present. See key for symbols. Figure (b) is the histogram from the sample of Kellermann et al. (1989), reproduced directly from that publication. The top figure is the histogram for all the quasars observed by Kellermann et al. from the BQS survey; the bottom figure gives the distribution for an additional 22 AGN of monochromatic luminosity below $M_B = -23$, the BQS definition of a quasar. The unshaded areas with arrows indicate upper limit measurements. The figures appear significantly different.

Figure 2. A histogram is given of $F_{6\ cm} / F_{5\ keV}$, which is similar to the definition of radio loudness, but which uses 5 keV X-ray flux in the denominator instead of B–band flux to avoid non-nuclear contributions to the ratio. As in the previous figure, only upper limit measurements which restrict the radio loudness to be < 1 are given. No statistically significant deficit regions are evident, and therefore no bifurcation is suggested for this distribution.

Figure 3. Radio loudness vs (a) X–ray Flux and (b) Luminosity. No correlation is evident at low luminosity. At high luminosity, upper limits dominate the sample, suggesting detection bias. See key for symbols.

Figure 4. Histogram of Lx for the separate RL (dark shading), RQ (no shading), and UL (caret pattern) populations. The upper limits dominate the distribution at high luminosities.

Figure 5. Histogram of radio slopes for the LMA. A symmetric distribution with considerable width suggests a large variety of core vs. extended flux within the LMA sample. See text for details.

Figure 6. Histogram of IRAS Warmth for the LMA. Objects with Log_{10} warmth > 0 are defined as "warm" objects. Note that there is a smooth distribution of warmth in the LMA. Note also that Type 2 objects are among some of the least warm objects in the entire sample.

Figure 7. Warmth vs L_X – There is no apparent correlation of warmth with luminosity. This suggests that the relative strength of the host galaxy does not change over the range of luminosities and red shifts within the sample. The same lack of correlation is seen when warmth is plotted against red shift (not shown).

Figure 8. (a)-(h) Correlations in both flux and luminosity for each of the four IRAS bands vs X–rays. Squares denote objects with steep 60 – 12 μm slopes, designated as "galaxy dominated" by Ward et al. (1987). Open triangles denote Type 2 objects. Note how the Type 2 and "steep" objects form the upper border of the correlations at all frequencies.

Figure 9. One micron (a) flux and (b) luminosity vs X–ray flux and luminosity. An excellent correlation is evident.

Figure 10. This histogram gives the distribution for the log slope from 1.25 μ to the 5 keV X-ray band center, along with information regarding stellar contamination and reddening. Note that stellar objects dominate the slope below –1, caused by the increased contribution of starlight the 1.25 μm band. The distribution has a mean near –1. "UV and OPT OK" objects show no evidence of reddening or stellar contamination. "OPT OK" show no evidence of reddening or stellar contamination in the optical band. "Stellar" objects show the NIR-optical bump typical of starlight. Reddened objects showed evidence of continuum reddening either by observations of a 2175 Å feature or they

showed the typical reddened optical continuum shape. "Unclassified" objects are those with insufficient optical data to be classified as reddened or stellar.

Figure 11. The relative quality of the correlations of (a) fluxes, and (b) luminosities, at various frequencies are given in these figures. The Log of the Spearman probability of the null hypothesis, $P_{Spearman}$, is plotted versus the frequency band correlated with X-ray flux. Note that the quality of the correlation is poor for large values of the $P_{Spearman}$ (top of diagram) and good for low values of $P_{Spearman}$ (bottom of diagram). For an explanation of error bars, see text. The radio and UV correlations are not given on the luminosity plot as these correlations may have been induced by the conversion to luminosity.

Figure 12. Luminosity in B band vs X–rays in (a) flux and (b) luminosity also yields a good correlation.

Figure 13. The histogram of $\alpha_{J\text{-}UV}$ (defined in text) is given with different symbols for those objects which have been found to be free from reddening via 2175 Å region observations (the "Uncontaminated" objects), those that show evidence of stellar contamination, and those which have either an uncorrectable 2175 Å feature, signs of optical reddening, or for which the reddening could not be determined, the "2175 Å Undetermined" objects. Note that there is only one "Uncontaminated" object with a slope below –1, but if errors are considered, the value is still consistent with a –1 slope (see text).

Figure 14. This figure shows the correlation of $\alpha_{J\text{-}UV}$ and α_{JO} (defined in text). There is a significant correlation with some spread.

Figure 15. The histogram gives the distribution of α_{JO} (defined in text) for the LMA sample. The following characteristics are associated with the indicated label in the figure : Objects with no signs of optical reddening, labeled "Opt OK"; objects with stellar contamination, labeled "Stellar"; objects which have a 2175 Å feature in their IUE spectra indicating significant reddening, labeled "2175 Å Feature"; objects with IUE spectra too

noisy to detect a 2175 Å feature, labeled "UV Red Unknown"; and objects with optical signs of reddening, labeled " Reddened Opt".

Figure 16. This figure shows $\alpha_{J\text{-}UV}$ plotted against α_{IO} (defined in text). The correlation is poor.

Figure 17. These plots of (a) $\alpha_{J\text{-}UV}$ vs $L_{1\mu m}$, and (b) α_{JO} vs $L_{1\mu m}$, show no relationship between 1μm luminosity and blue-bump strength.

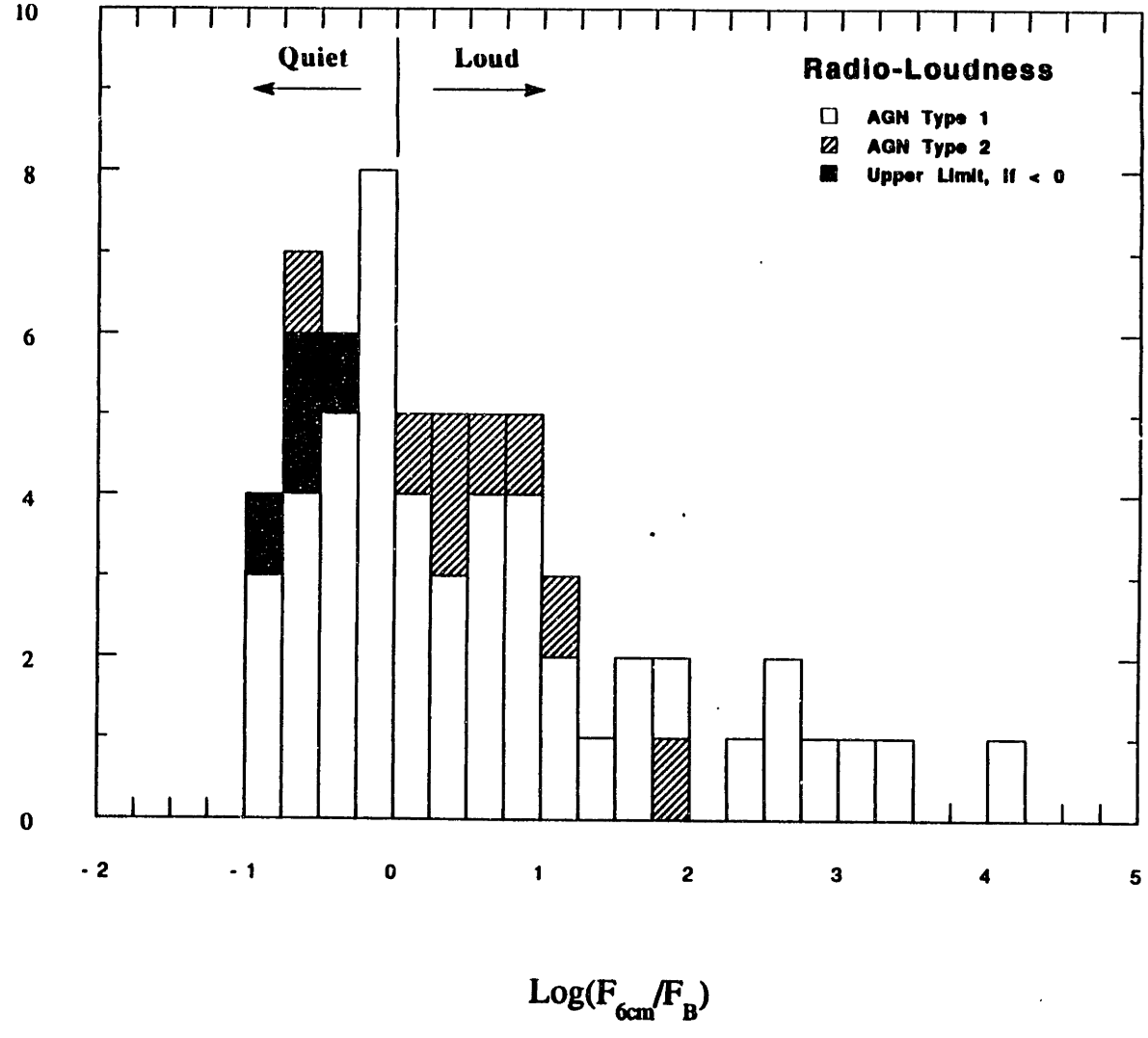
Quiet
Loud
Radio-Loudness
AGN Type 1
AGN Type 2
Upper Limit, if < 0
N
10
8
6
4
2
0
-2
-1
0
1
2
3
4
5
Log(F6cm/FB)

Figure 1a

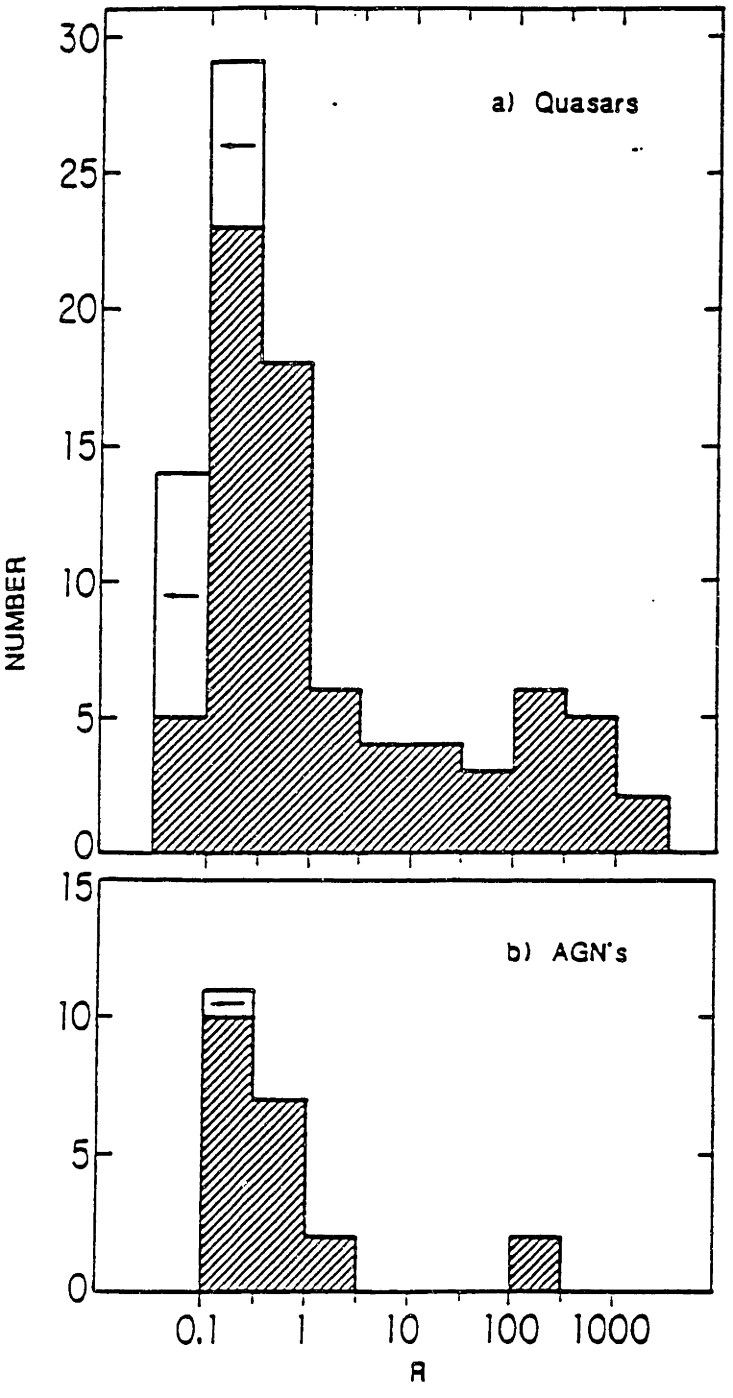

Figure 1b

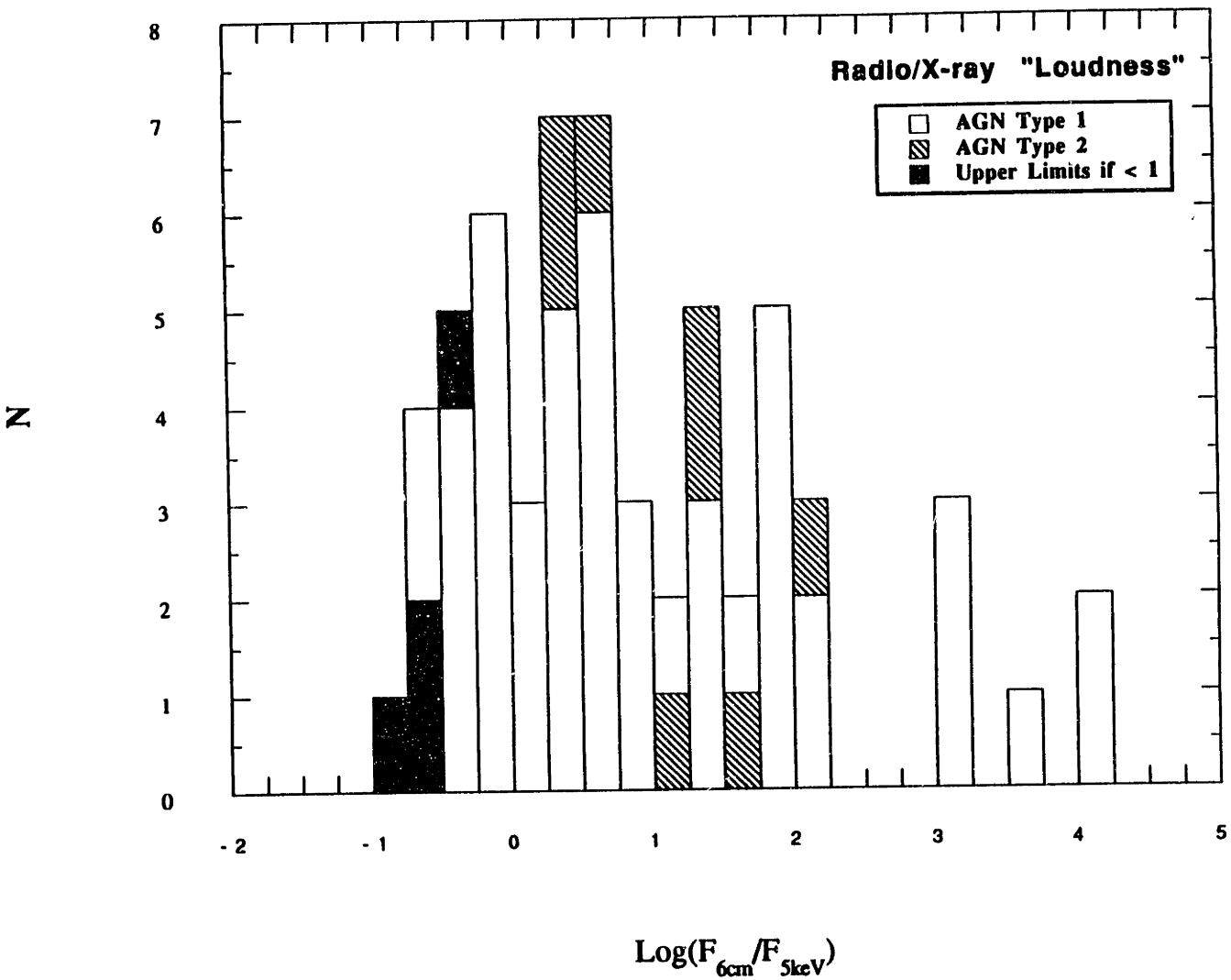
Radio/X-ray "Loudness"
AGN Type 1
AGN Type 2
Upper Limits if < 1
N
0
1
2
3
4
5
6
7
8
-2
-1
0
1
2
3
4
5
Log(F6cm/F5keV)

Figure 2

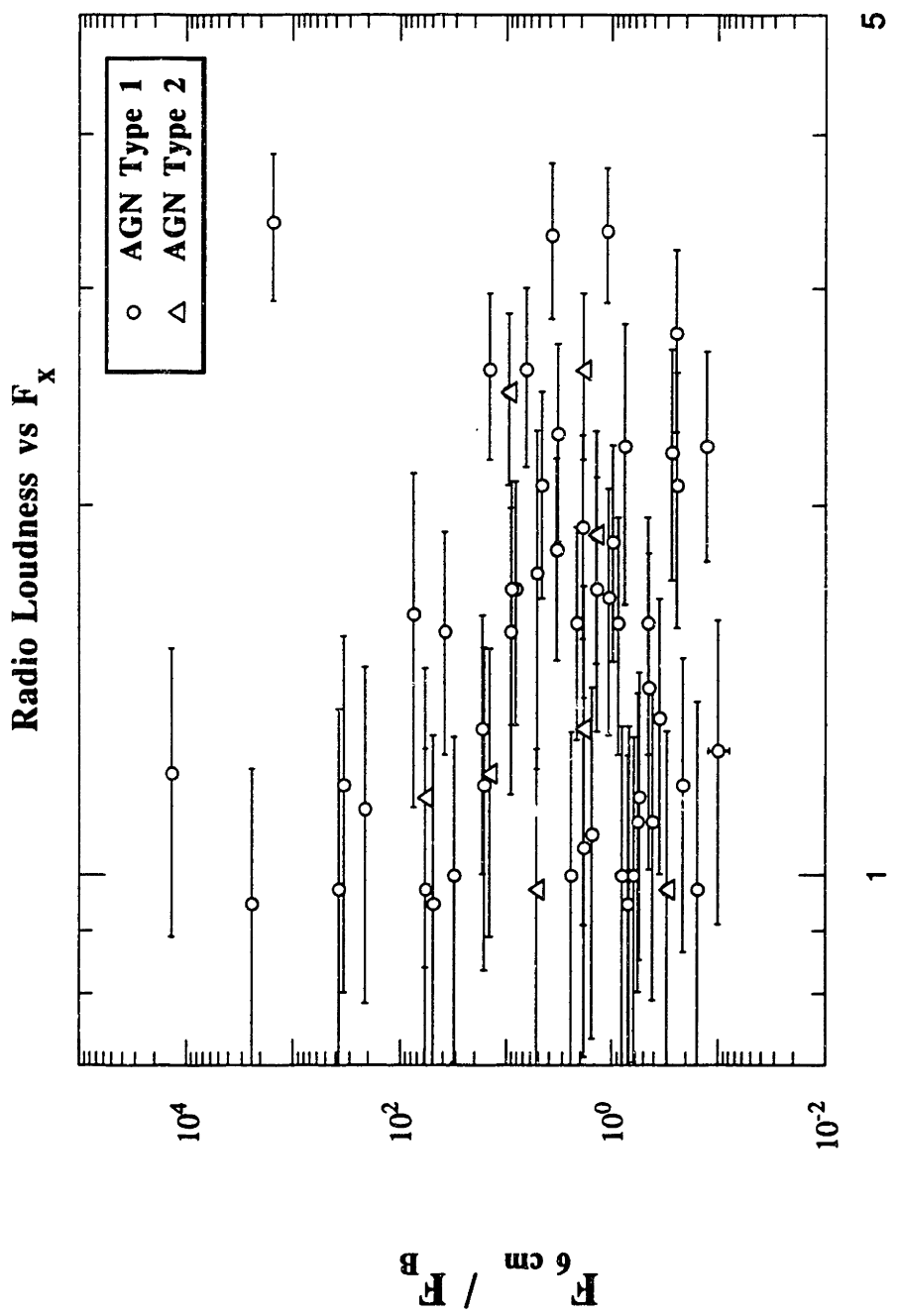
Radio Loudness vs F_x
AGN Type 1
AGN Type 2
$F_{6\ cm} / F_B$
10^4
10^2
10^0
10^{-2}
1
5
$F_x(\mu Jy)$

Figure 3a

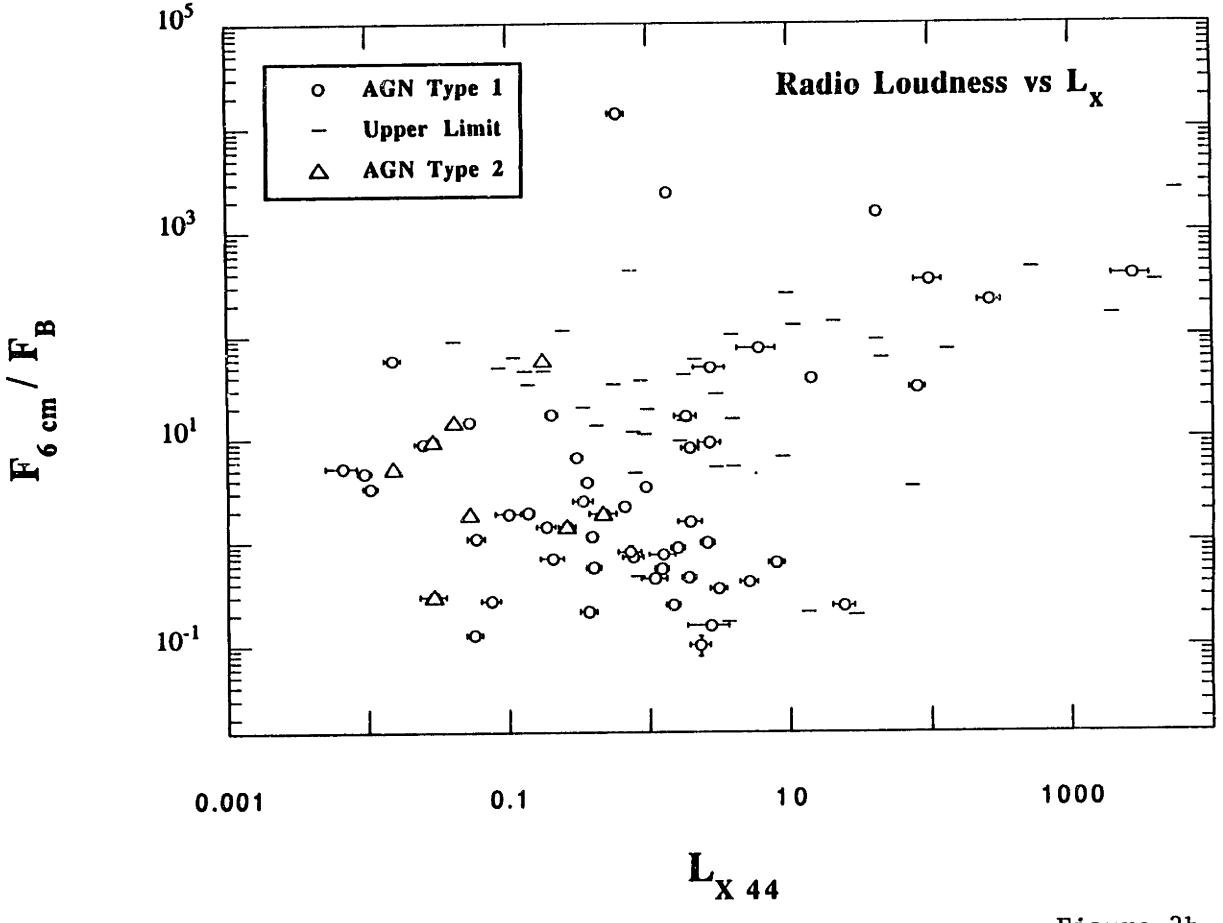
Radio Loudness vs L_X
AGN Type 1
Upper Limit
AGN Type 2
10^5
10^3
10^1
10^{-1}
$F_{6\,cm} / F_B$
0.001
0.1
10
1000
$L_{X\,44}$

Figure 3b

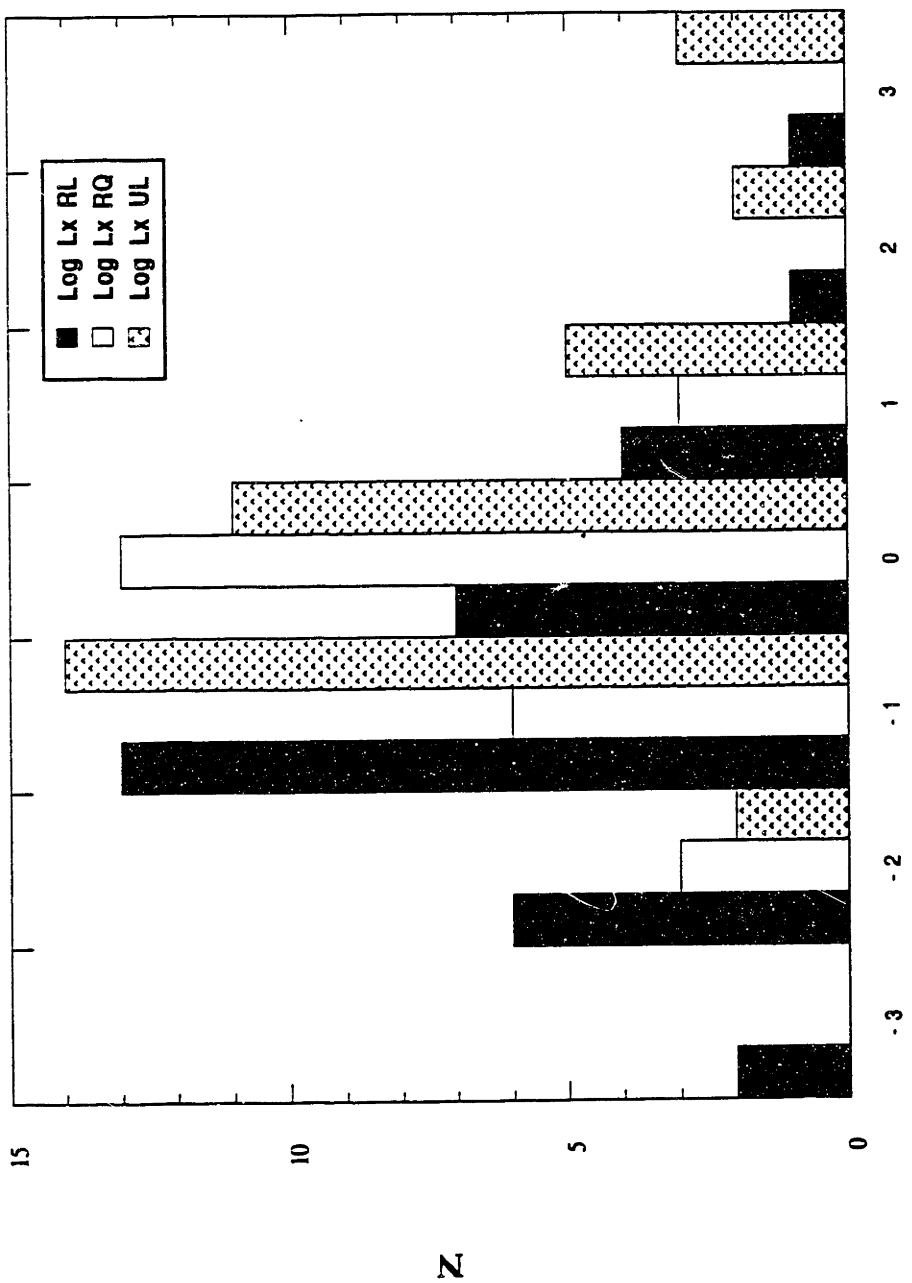

Figure 4

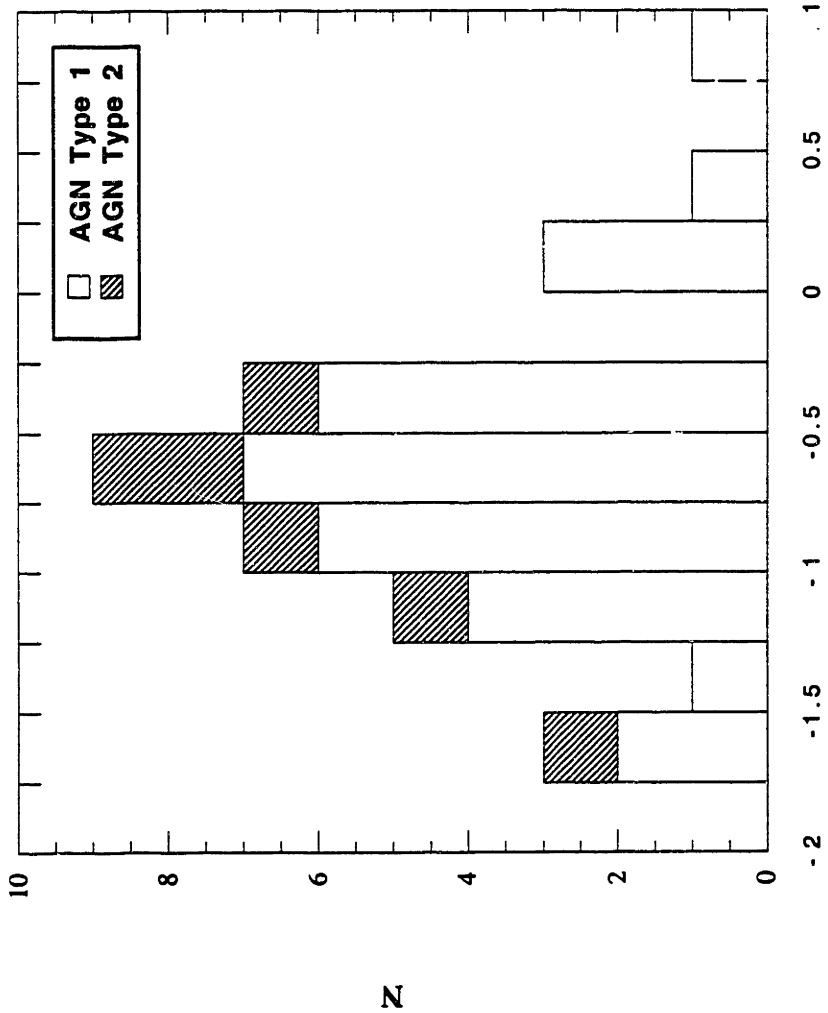

Figure 5

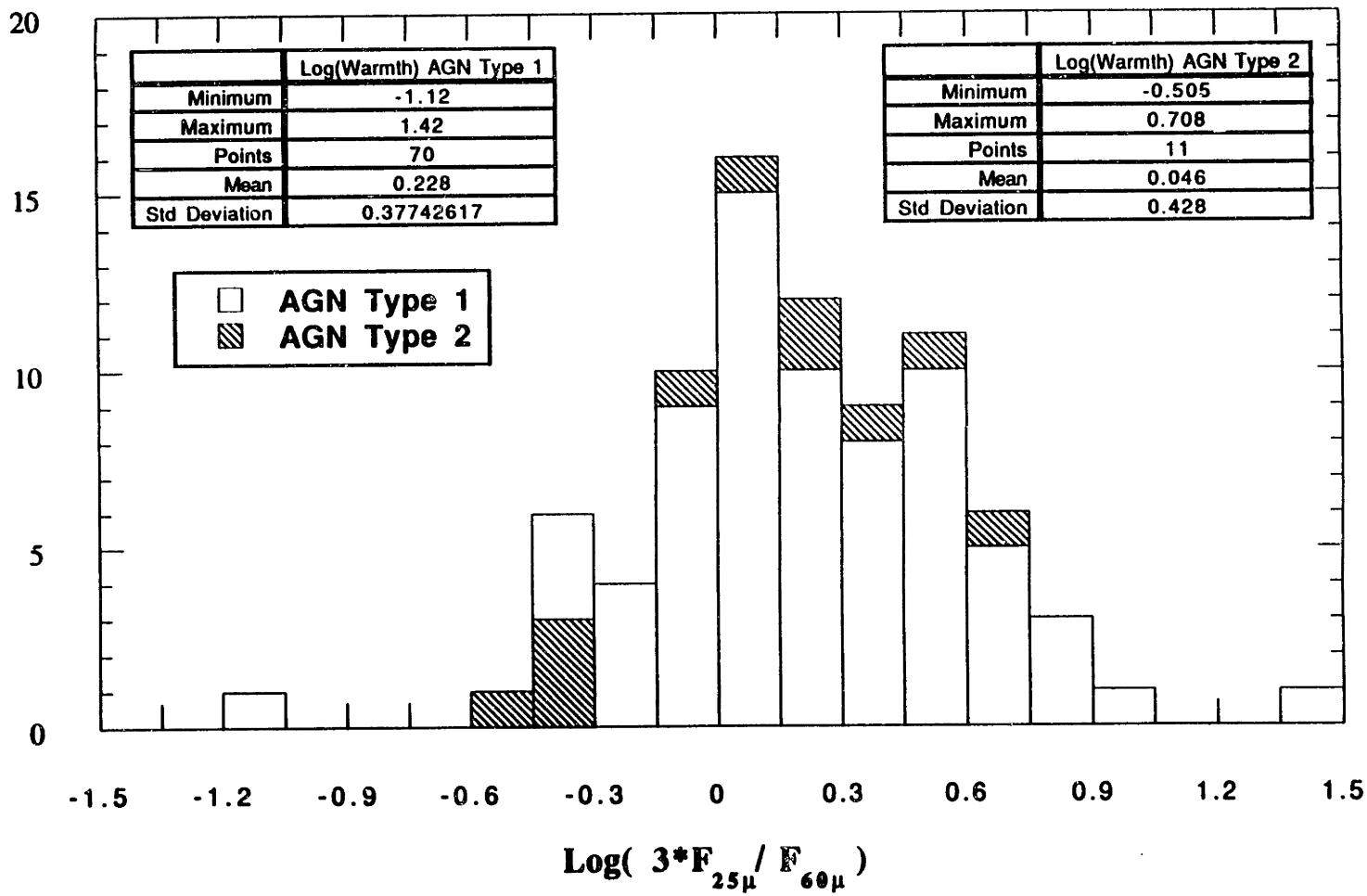
Log(Warmth) AGN Type 1
Minimum -1.12
Maximum 1.42
Points 70
Mean 0.228
Std Deviation 0.37742617
Log(Warmth) AGN Type 2
Minimum -0.505
Maximum 0.708
Points 11
Mean 0.046
Std Deviation 0.428
AGN Type 1
AGN Type 2
20
15
10
5
0
-1.5
-1.2
-0.9
-0.6
-0.3
0
0.3
0.6
0.9
1.2
1.5
Log(3*F25μ / F60μ)

Figure 6

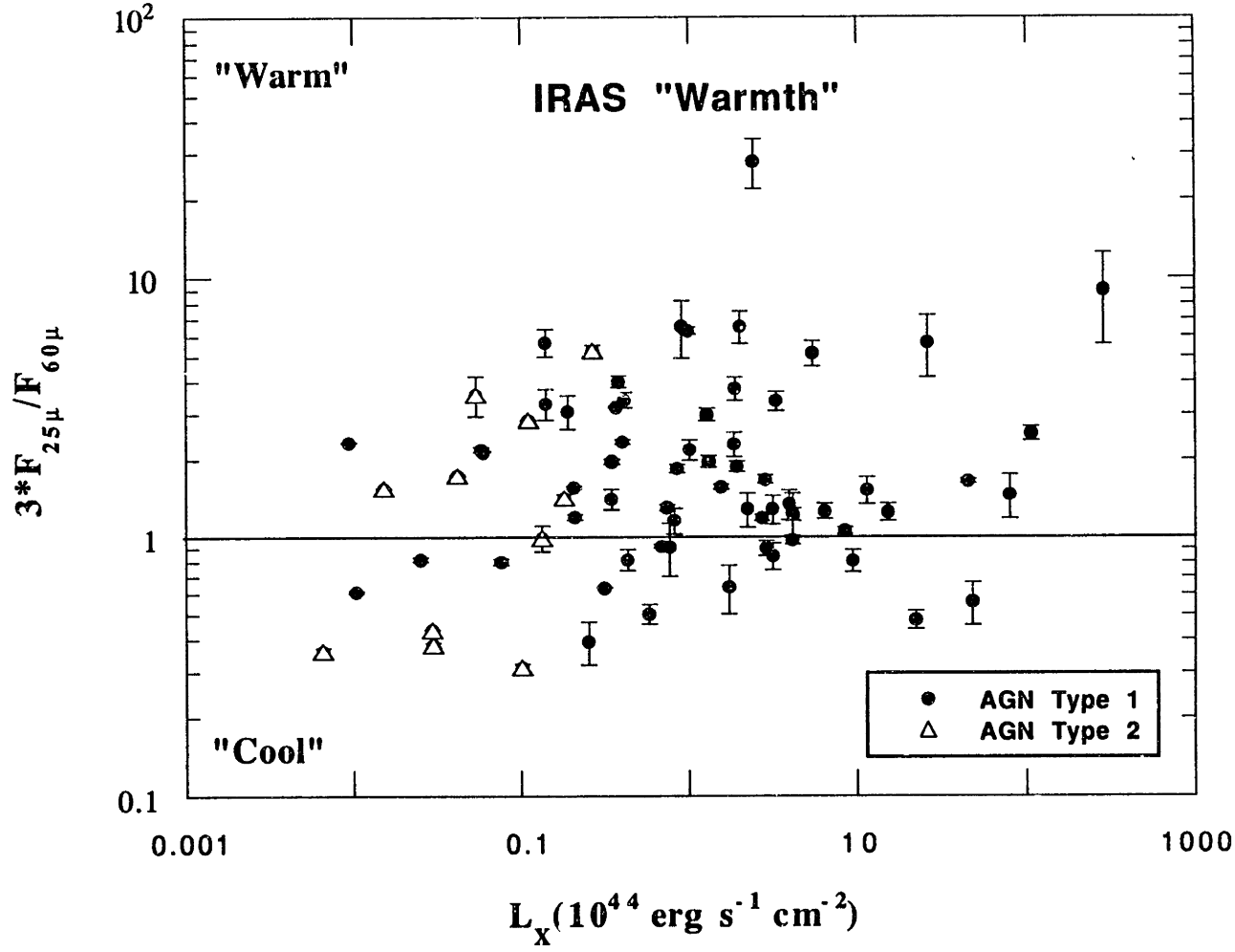
IRAS "Warmth"
"Warm"
"Cool"
AGN Type 1
AGN Type 2
10^2
10
1
0.1
0.001
0.1
10
1000
$3*F_{25\mu}/F_{60\mu}$
$L_X(10^{44}$ erg s^{-1} $cm^{-2})$

Figure 7

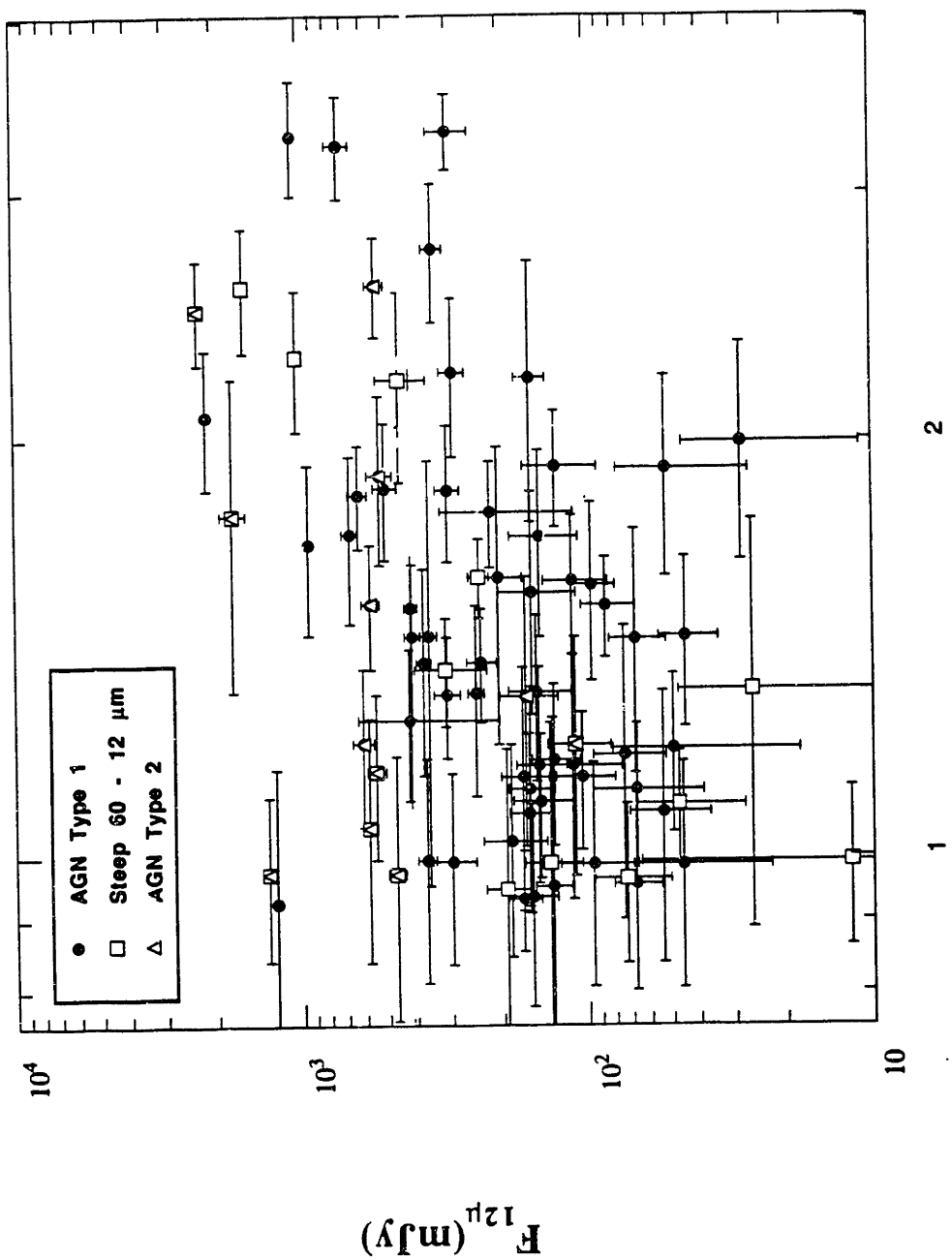
AGN Type 1
Steep 60 - 12 μm
AGN Type 2
10^4
10^3
10^2
10
1
2
$F_{12\mu}$(mJy)
F_X (μJy)

Figure 8a

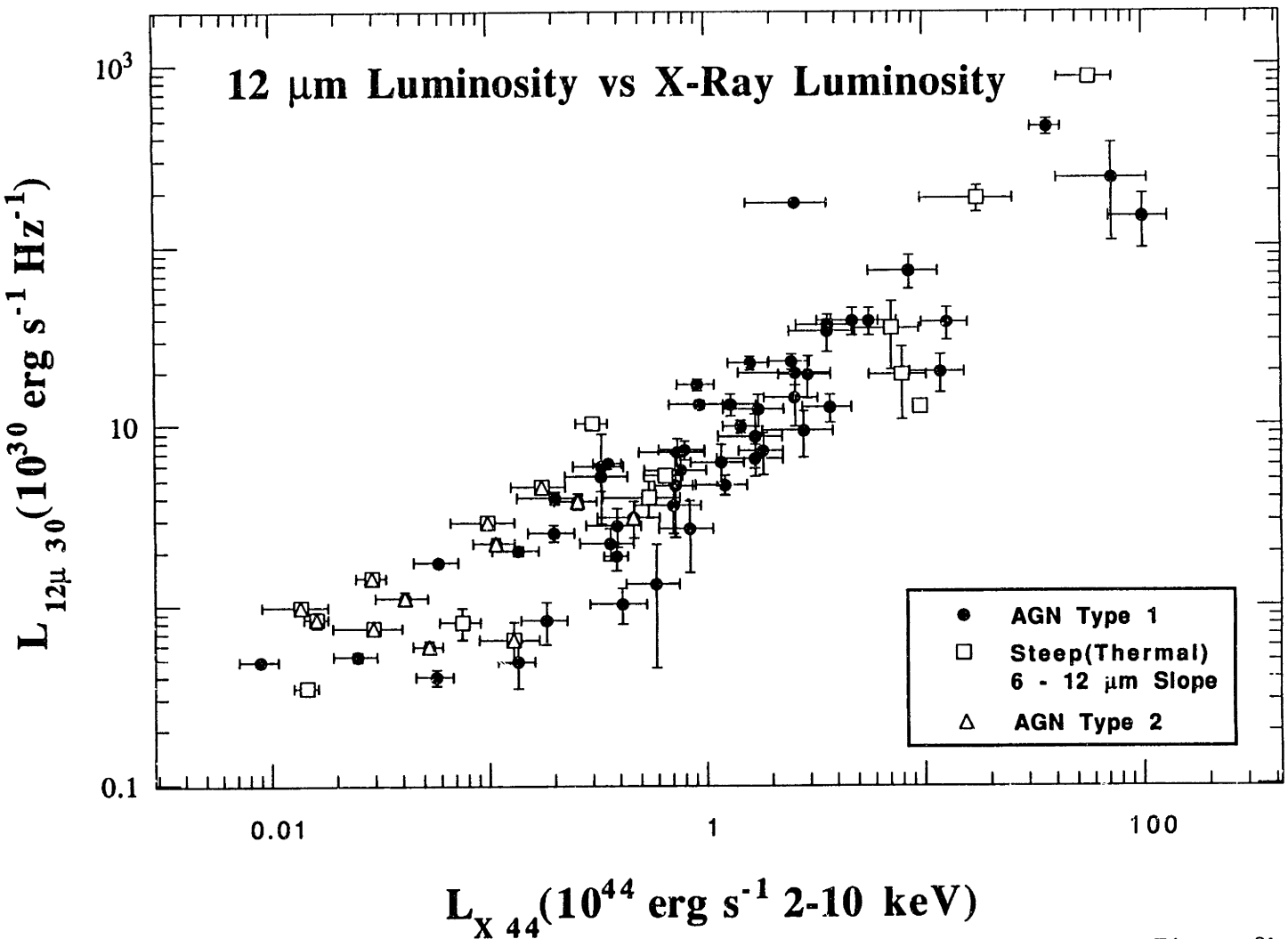
12 μm Luminosity vs X-Ray Luminosity
$L_{12\mu\ 30}(10^{30}$ erg s^{-1} Hz^{-1})
$L_{X\ 44}(10^{44}$ erg s^{-1} 2-10 keV)
10^3
10
0.1
0.01
1
100
AGN Type 1
Steep(Thermal)
6 - 12 μm Slope
AGN Type 2

Figure 8b

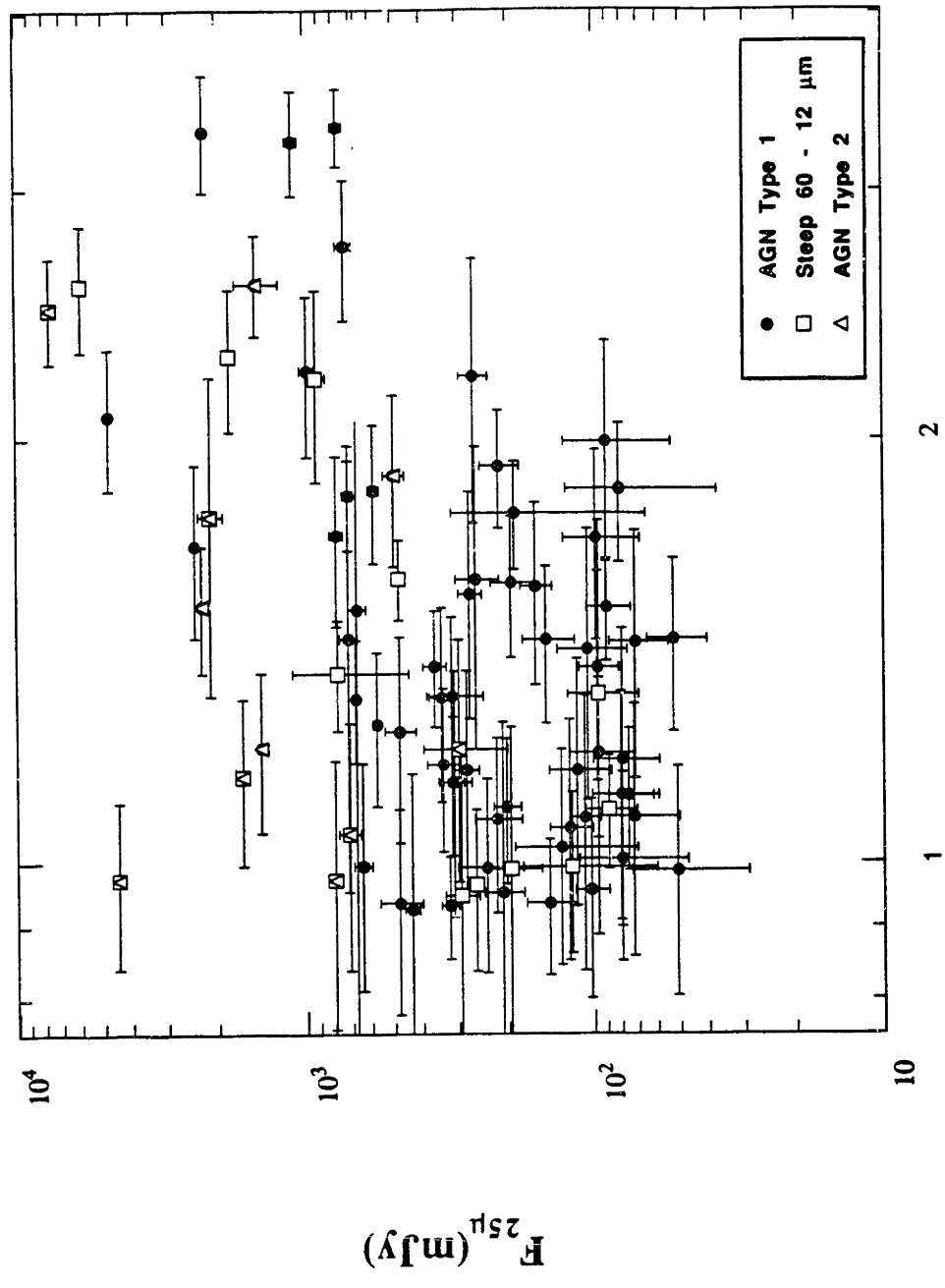
AGN Type 1
Steep 60 - 12 μm
AGN Type 2
$F_{25\mu}$(mJy)
F_x (μJy)
10^4
10^3
10^2
10
1
2

Figure 8c

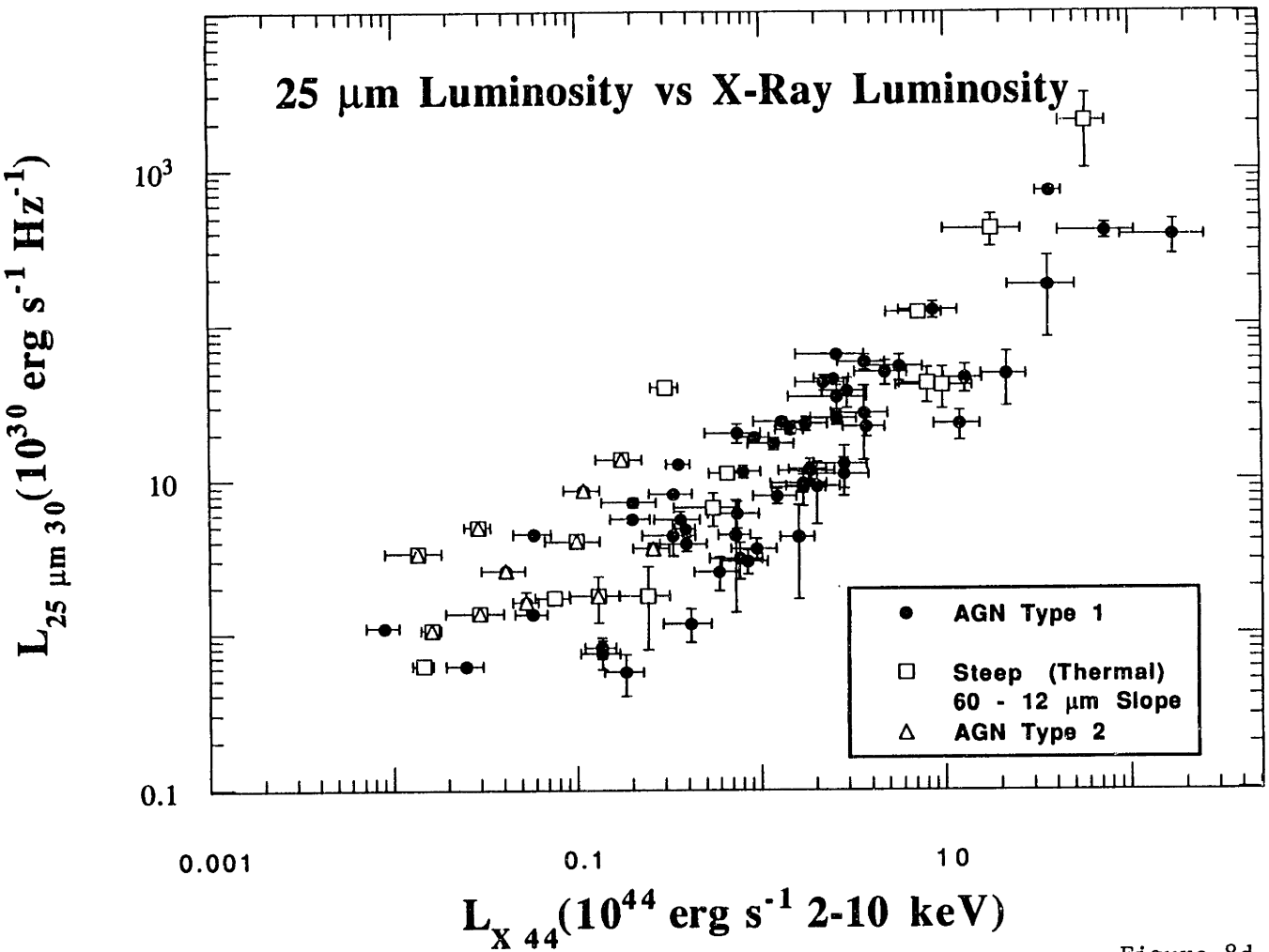
25 μm Luminosity vs X-Ray Luminosity
$L_{25\ \mu m\ 30}(10^{30}$ erg s^{-1} Hz^{-1})
10^3
10
0.1
0.001
0.1
10
$L_{X\ 44}(10^{44}$ erg s^{-1} 2-10 keV)
AGN Type 1
Steep (Thermal)
60 - 12 μm Slope
AGN Type 2

Figure 8d

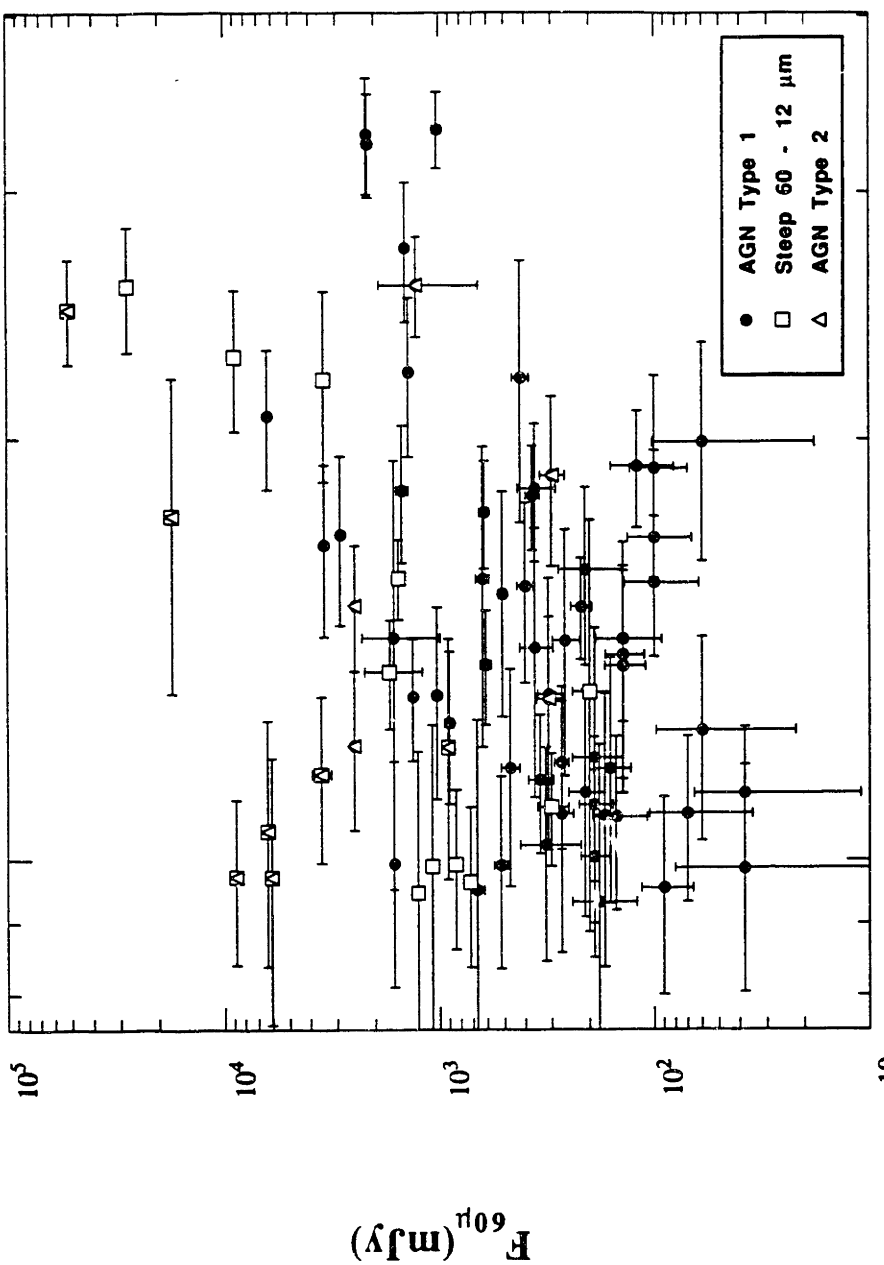
AGN Type 1
Steep 60 - 12 μm
AGN Type 2
10^5
10^4
10^3
10^2
10
1
$F_{60\mu}$(mJy)
F_x (μJy)

Figure 8e

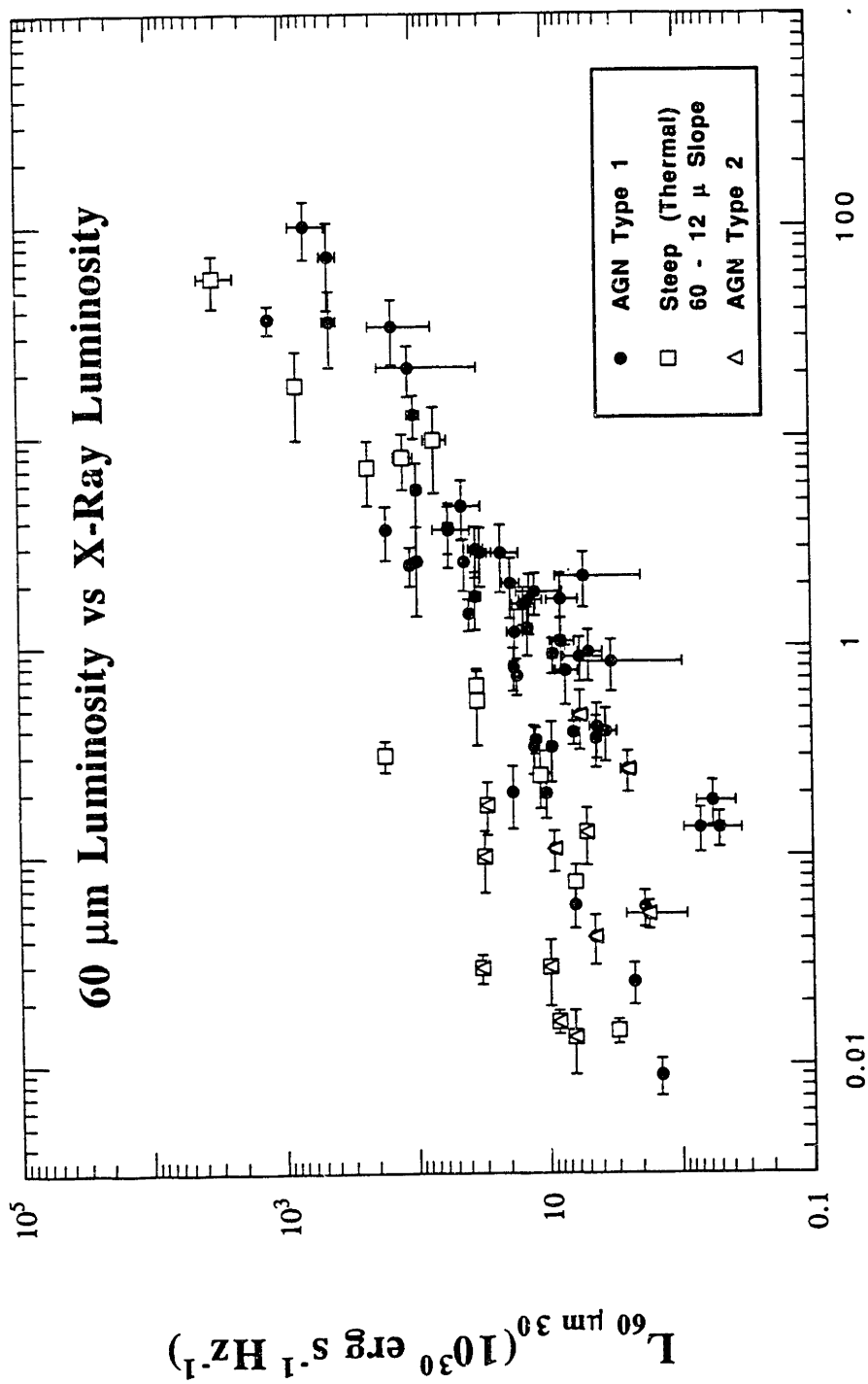
60 μm Luminosity vs X-Ray Luminosity
AGN Type 1
Steep (Thermal)
60 - 12 μ Slope
AGN Type 2
$L_{60\ \mu m}(10^{30}$ erg s^{-1} Hz^{-1})
$L_{X\ 44}(10^{44}$ erg s^{-1} 2-10 keV)
10^5
10^3
10
0.1
0.01
1
100

Figure 8f

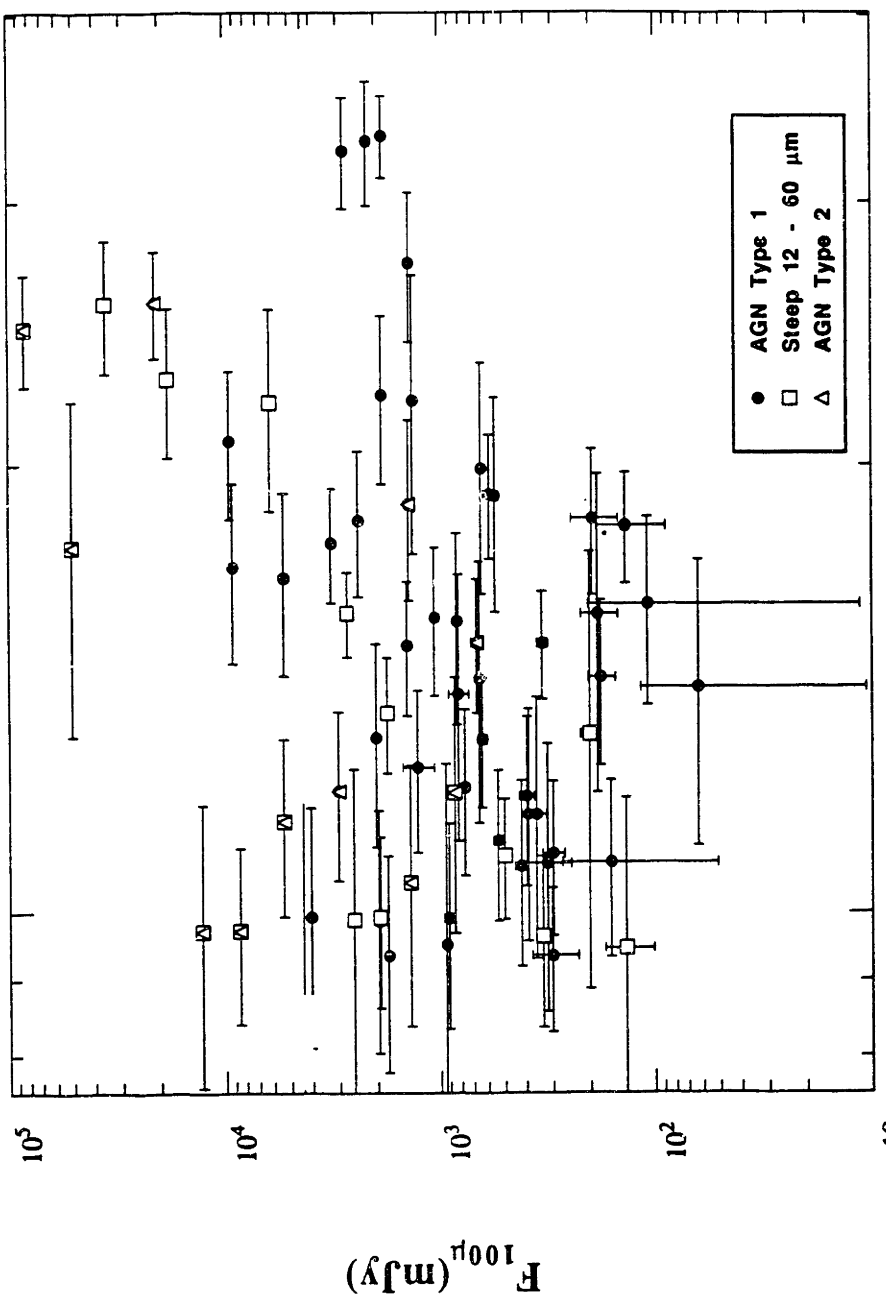
AGN Type 1
Steep 12 - 60 μm
AGN Type 2
10^5
10^4
10^3
10^2
10
1
$F_{100\mu}$(mJy)
F_X (μJy)

Figure 8g

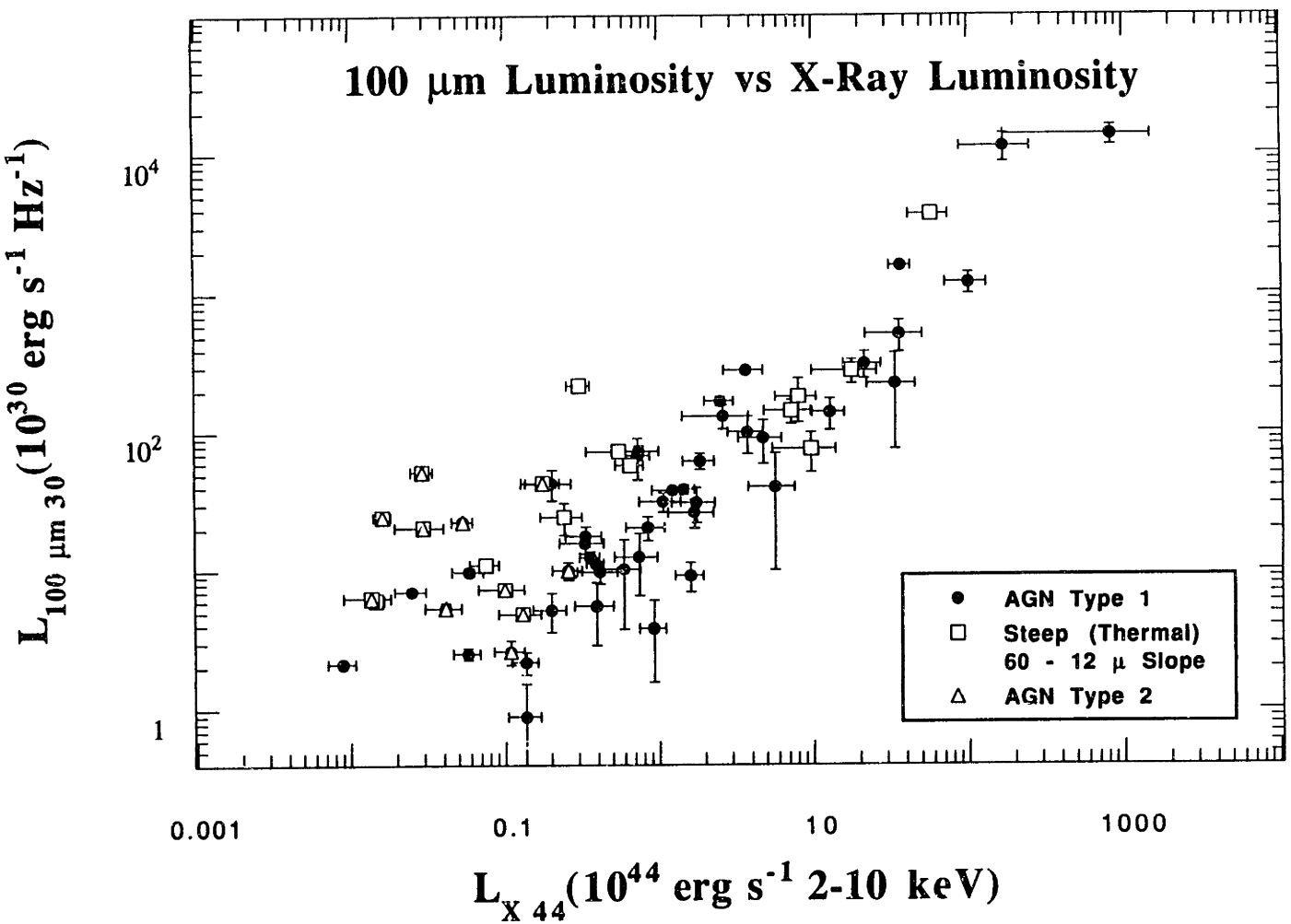
100 μm Luminosity vs X-Ray Luminosity
$L_{100\ \mu m\ 30}(10^{30}$ erg s^{-1} Hz^{-1})
10^4
10^2
1
0.001
0.1
10
1000
$L_{X\ 44}(10^{44}$ erg s^{-1} 2-10 keV)
AGN Type 1
Steep (Thermal)
60 - 12 μ Slope
AGN Type 2

Figure 8h

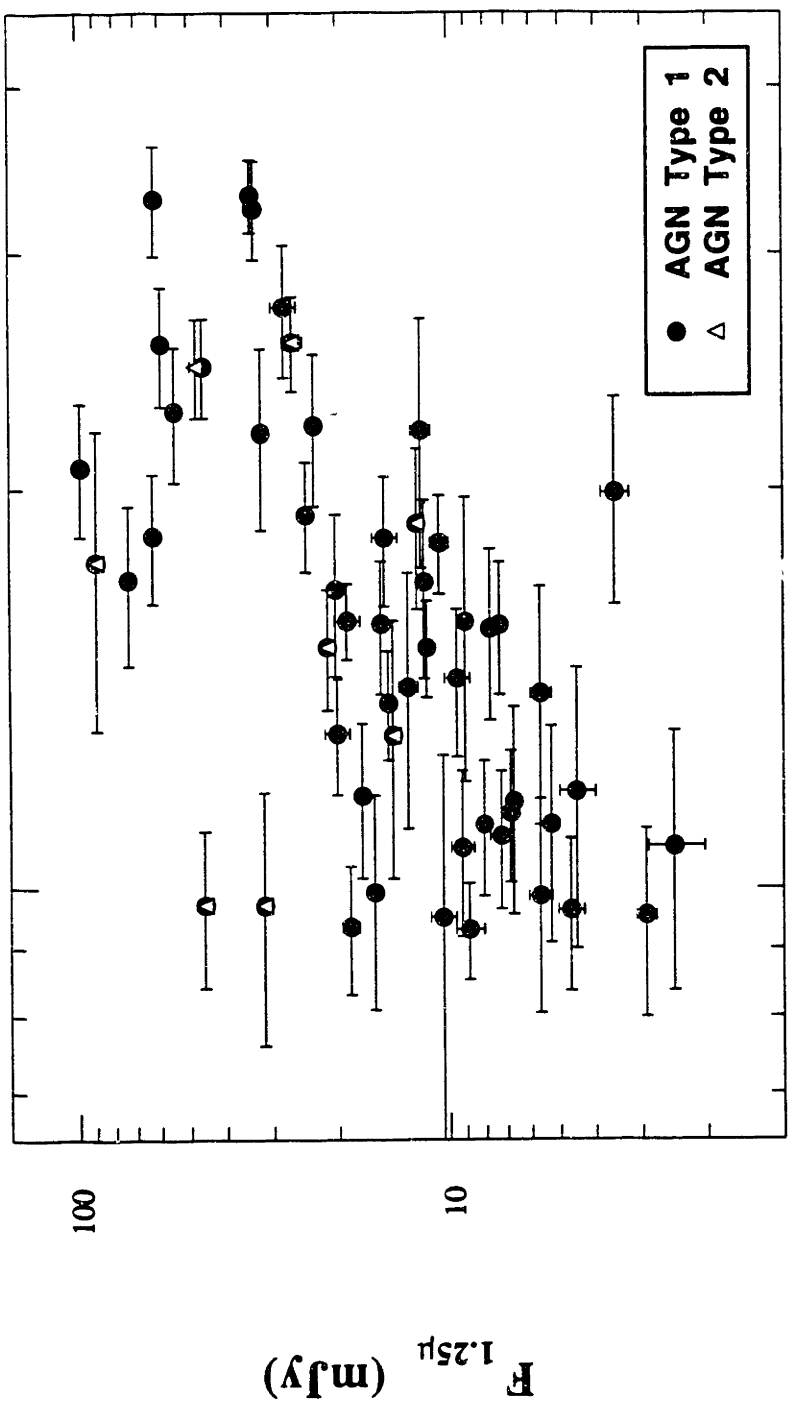

Figure 9a

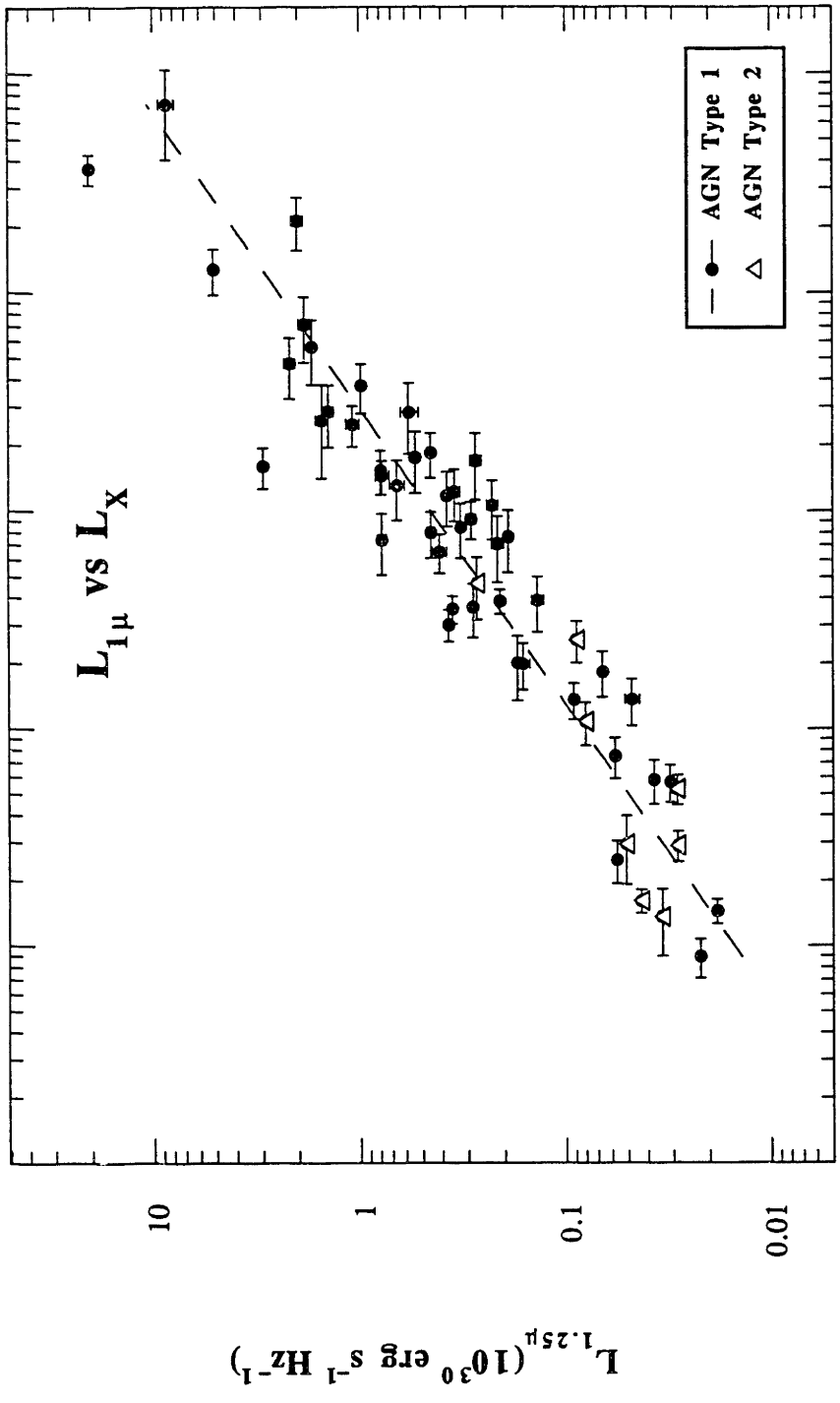
$L_{1\mu}$ vs L_X
AGN Type 1
AGN Type 2
$L_{1.25\mu}(10^{30}$ erg s^{-1} Hz$^{-1})$
$L_X(10^{44}$erg s$^{-1})$
10
1
0.1
0.01
0.001
0.01
0.1
1
10
100

Figure 9b

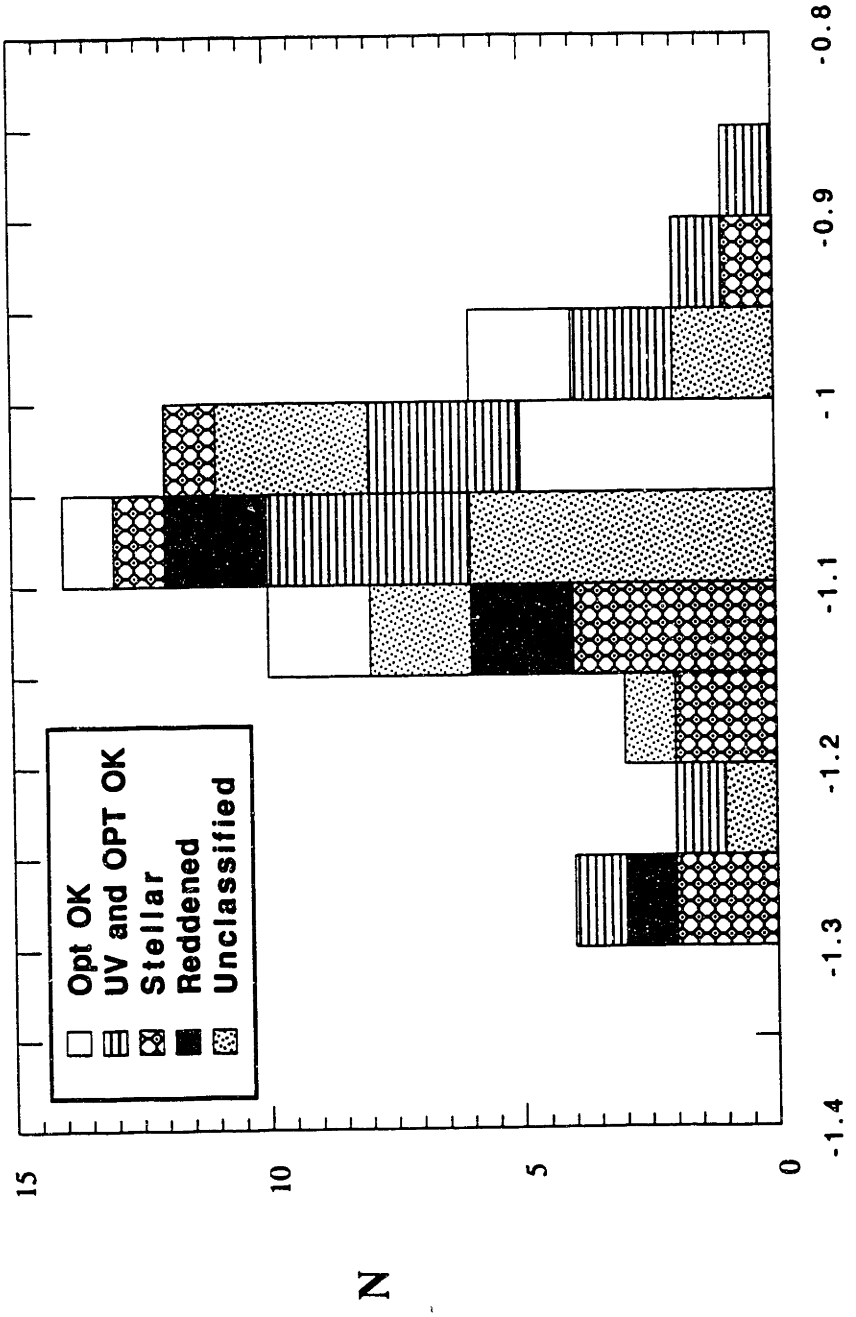
Opt OK
UV and OPT OK
Stellar
Reddened
Unclassified
N
15
10
5
0
-1.4
-1.3
-1.2
-1.1
-1
-0.9
-0.8
$\alpha_{1.25\mu m-X}$

Figure 10

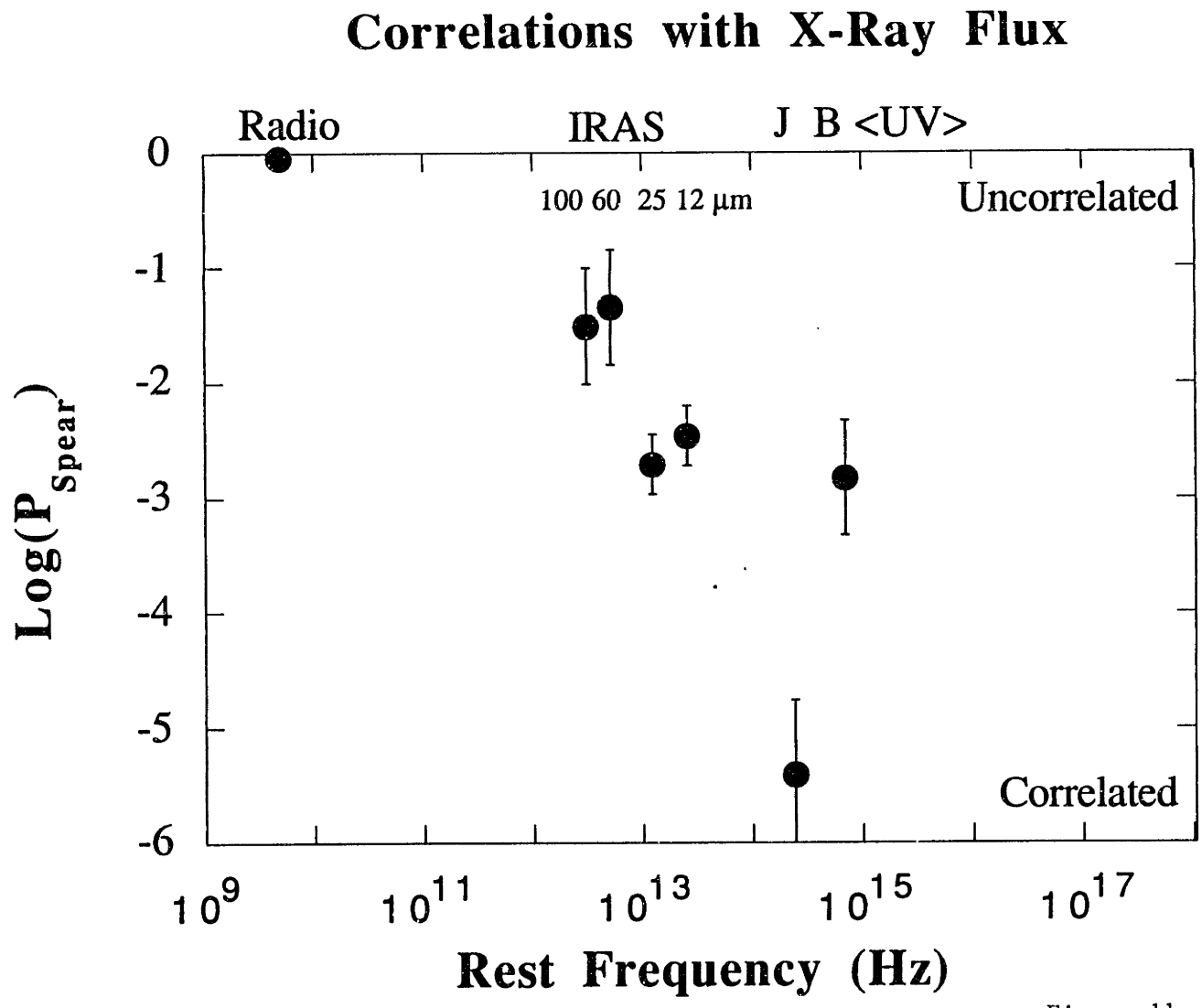
Correlations with X-Ray Flux
Radio
IRAS
J B <UV>
100 60 25 12 μm
Uncorrelated
Correlated
0
-1
-2
-3
-4
-5
-6
Log(P Spear)
10^9
10^11
10^13
10^15
10^17
Rest Frequency (Hz)

Figure 11a

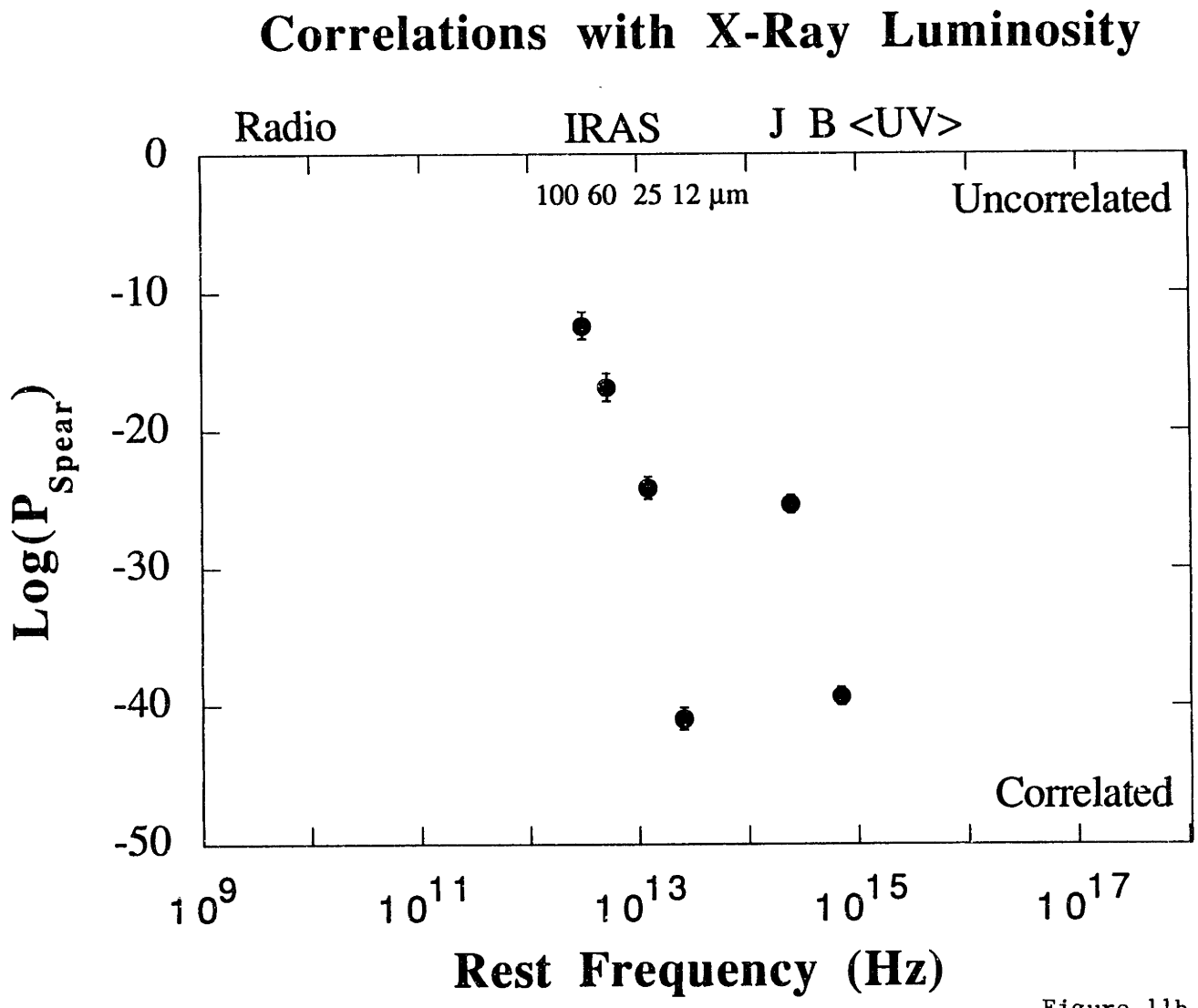
Correlations with X-Ray Luminosity
Radio
IRAS
J B <UV>
100 60 25 12 μm
Uncorrelated
Correlated
0
-10
-20
-30
-40
-50
Log(P Spear)
10^9
10^11
10^13
10^15
10^17
Rest Frequency (Hz)

Figure 11b

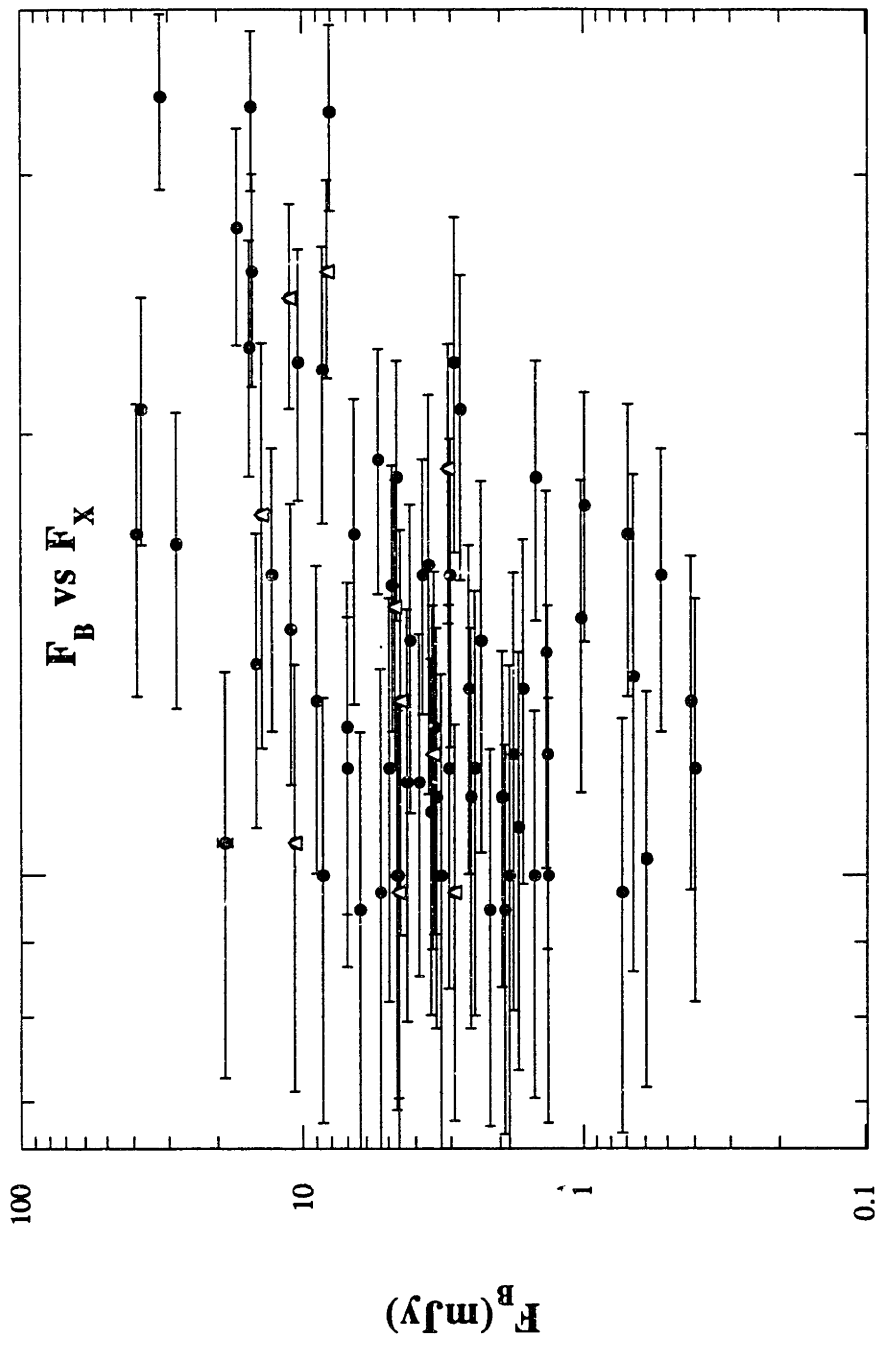

Figure 12a

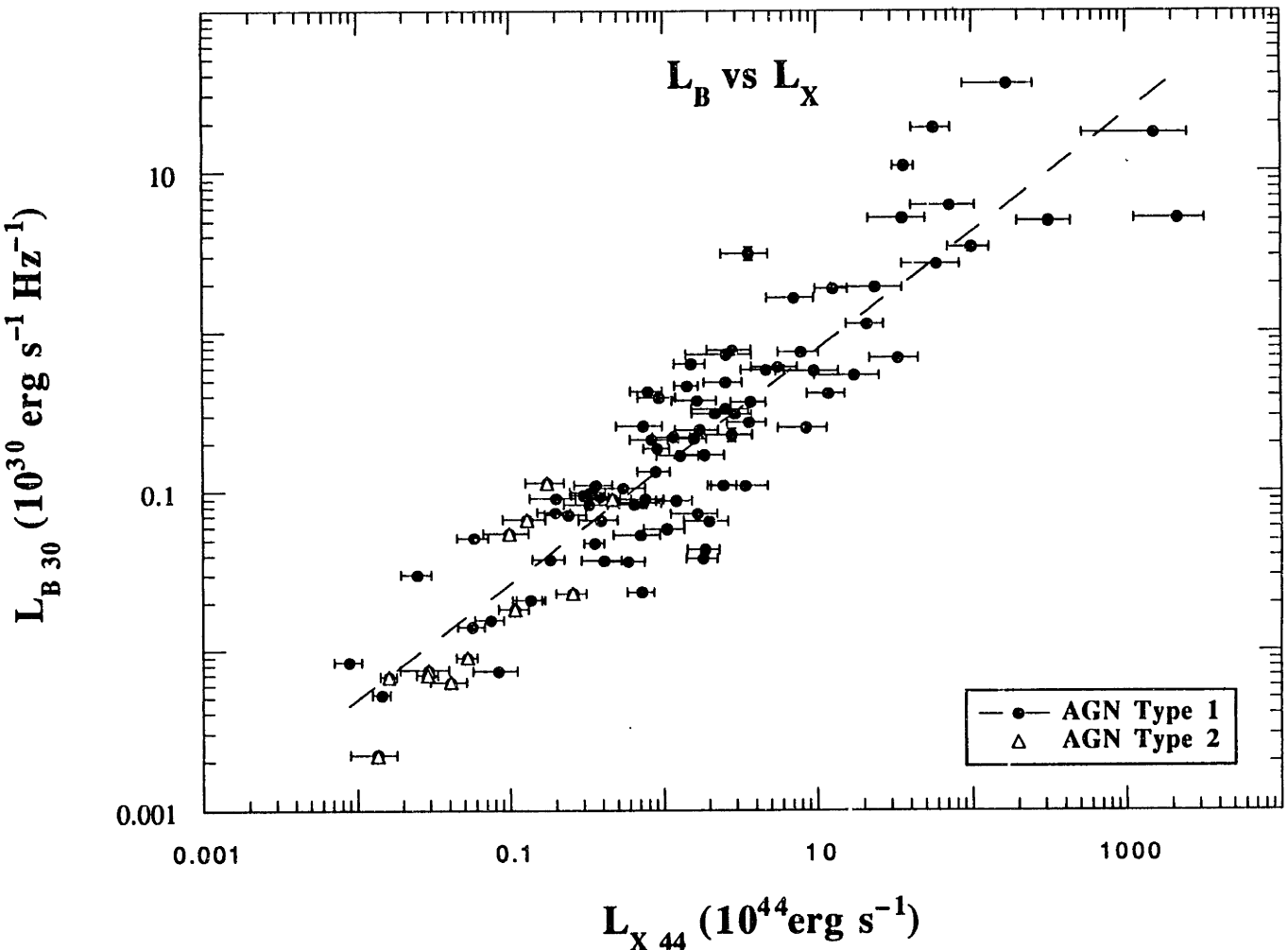
L_B vs L_X
10
0.1
0.001
0.001
0.1
10
1000
$L_{B\ 30}$ (10^{30} erg s^{-1} Hz^{-1})
$L_{X\ 44}$ (10^{44}erg s^{-1})
AGN Type 1
AGN Type 2

Figure 12b

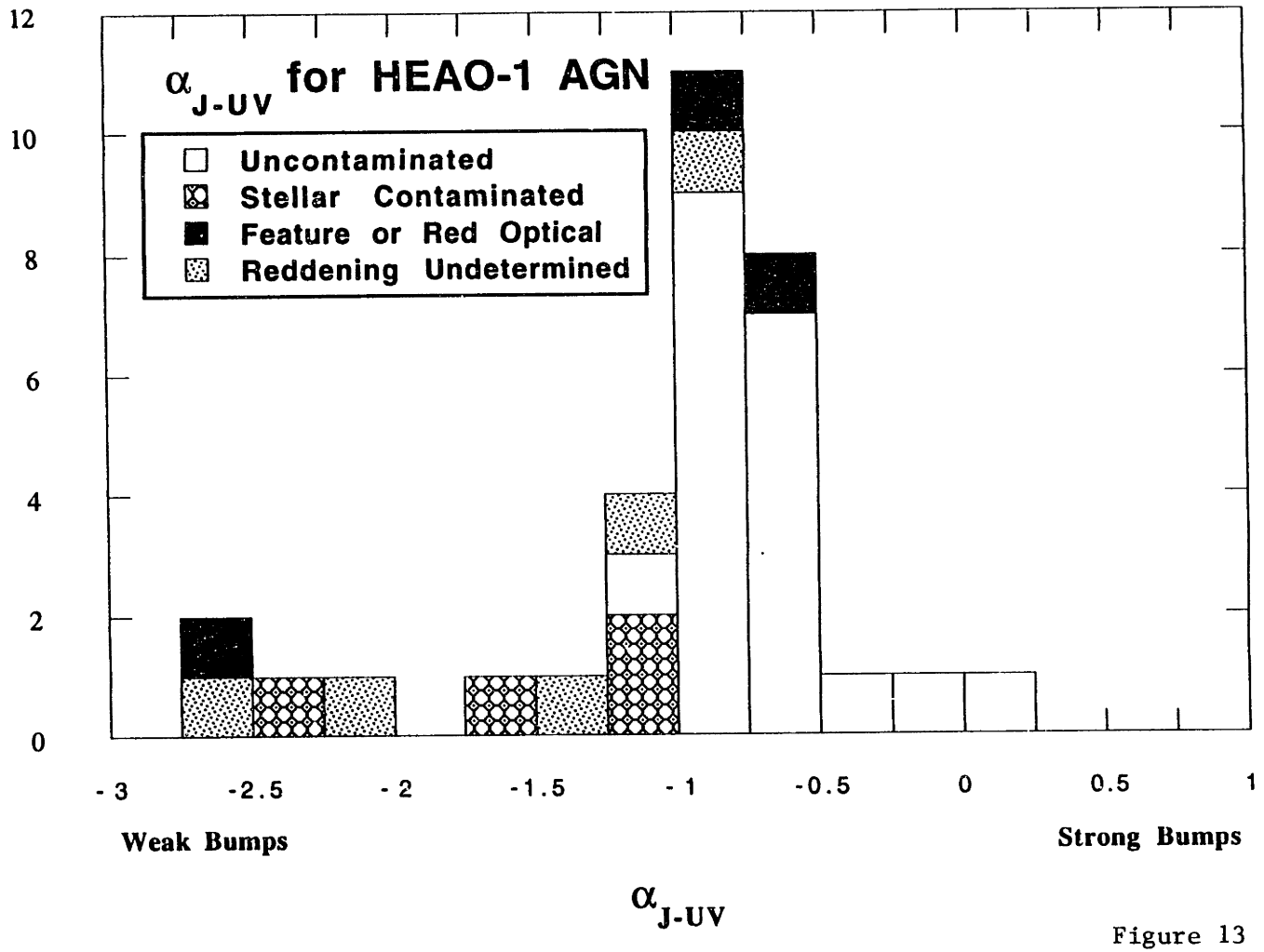
α_{J-UV} for HEAO-1 AGN
Uncontaminated
Stellar Contaminated
Feature or Red Optical
Reddening Undetermined
12
10
8
6
4
2
0
- 3
-2.5
- 2
-1.5
- 1
-0.5
0
0.5
1
Weak Bumps
Strong Bumps
α_{J-UV}

Figure 13

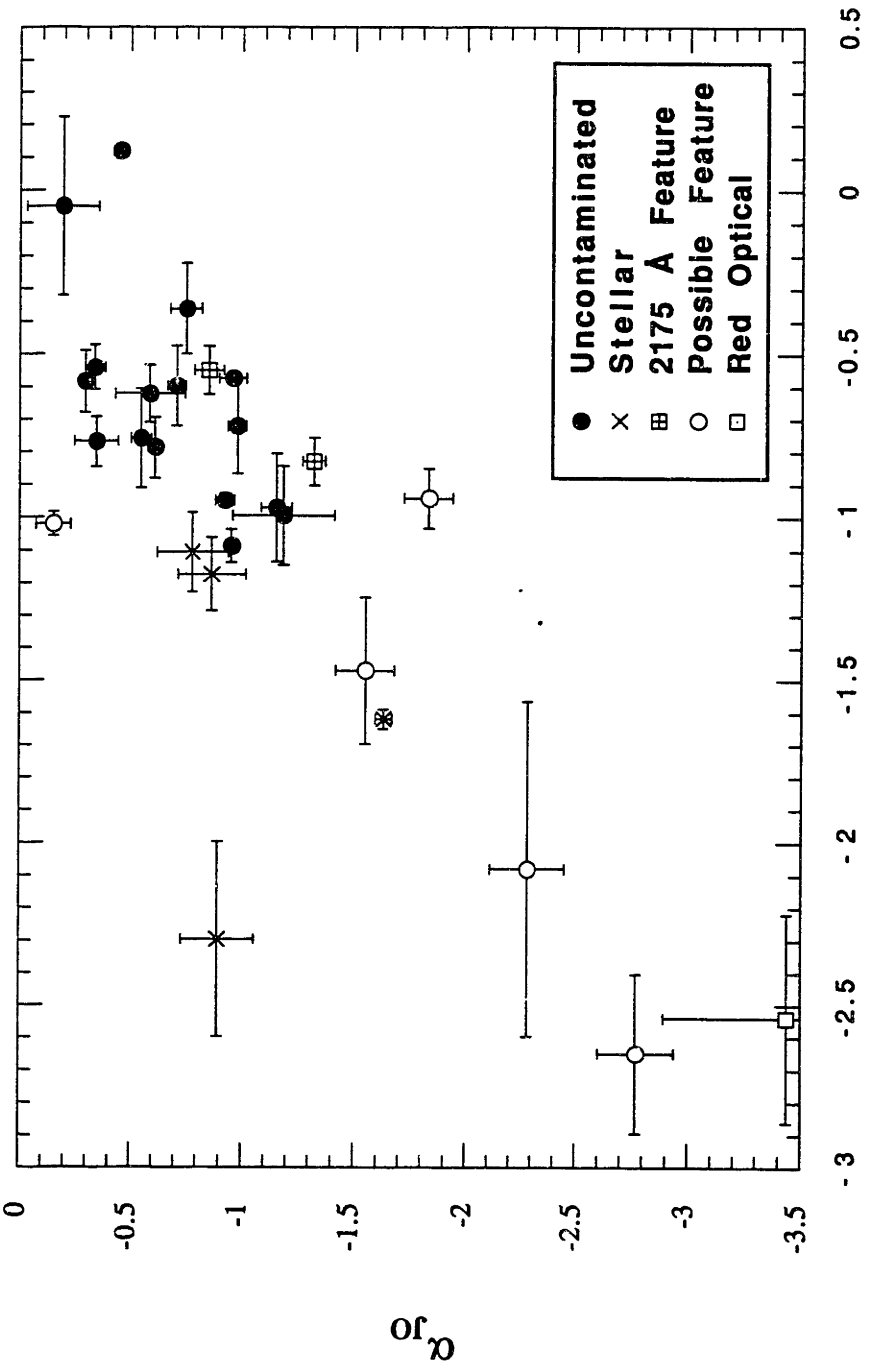
Uncontaminated
Stellar
2175 Å Feature
Possible Feature
Red Optical
0
-0.5
-1
-1.5
-2
-2.5
-3
-3.5
0.5
0
-0.5
-1
-1.5
-2
-2.5
-3
α_{J-UV}
α_{JO}

Figure 14

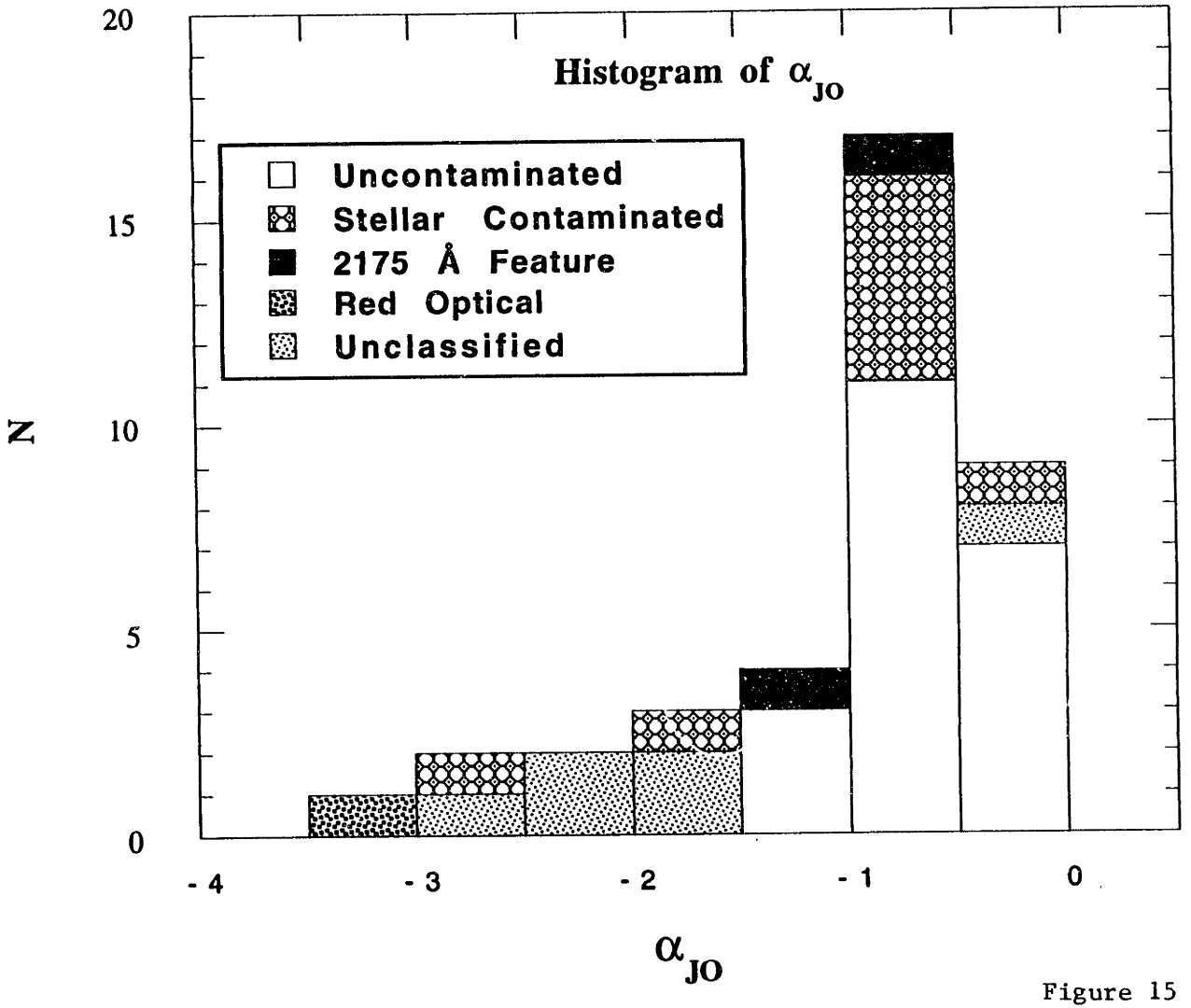
Histogram of α_{JO}
Uncontaminated
Stellar Contaminated
2175 Å Feature
Red Optical
Unclassified
N
20
15
10
5
0
- 4
- 3
- 2
- 1
0
α_{JO}

Figure 15

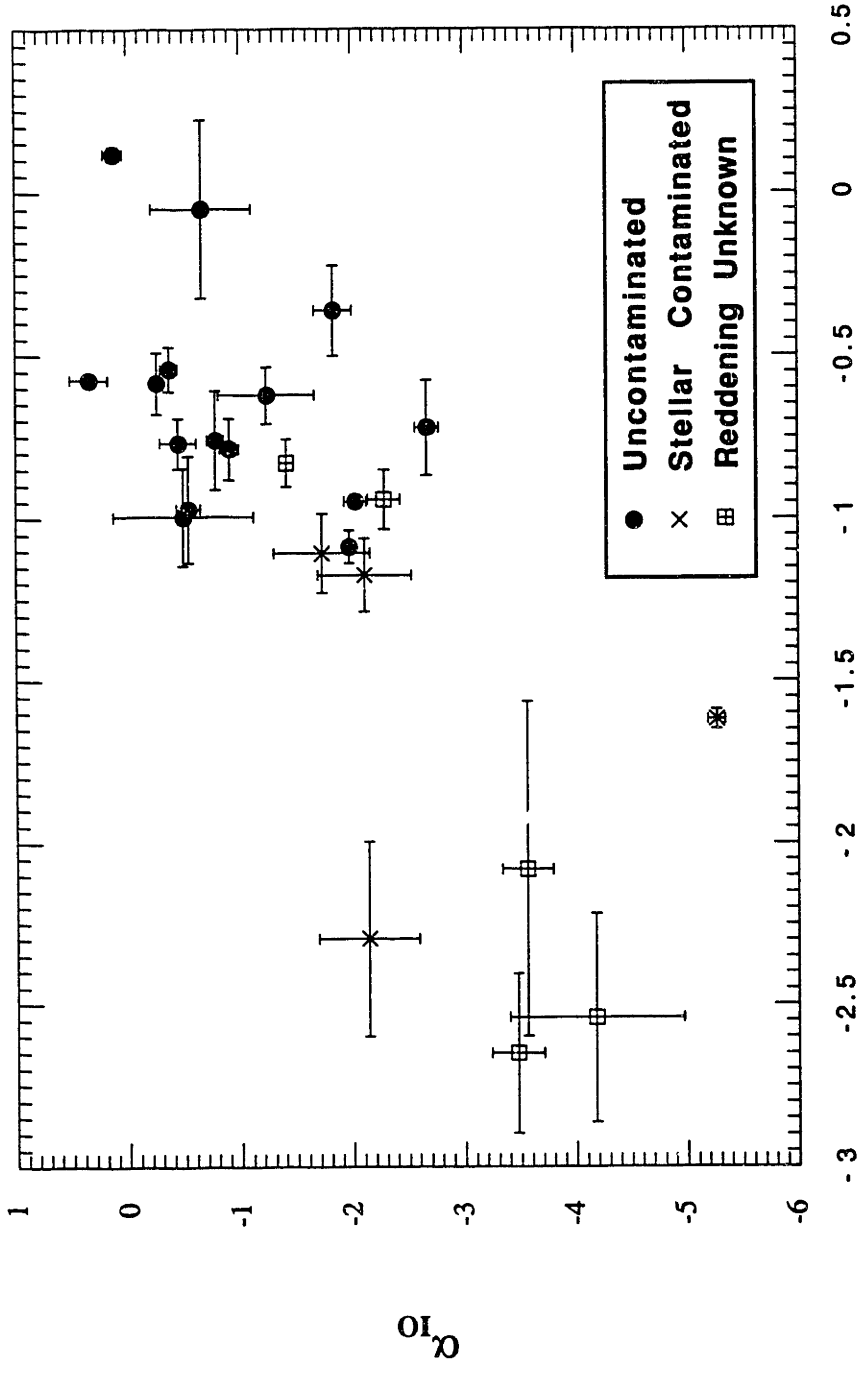
Uncontaminated
Stellar Contaminated
Reddening Unknown
α_{IO}
$\alpha_{J\text{-}UV}$
1
0
-1
-2
-3
-4
-5
-6
0.5
0
-0.5
-1
-1.5
-2
-2.5
-3

Figure 16

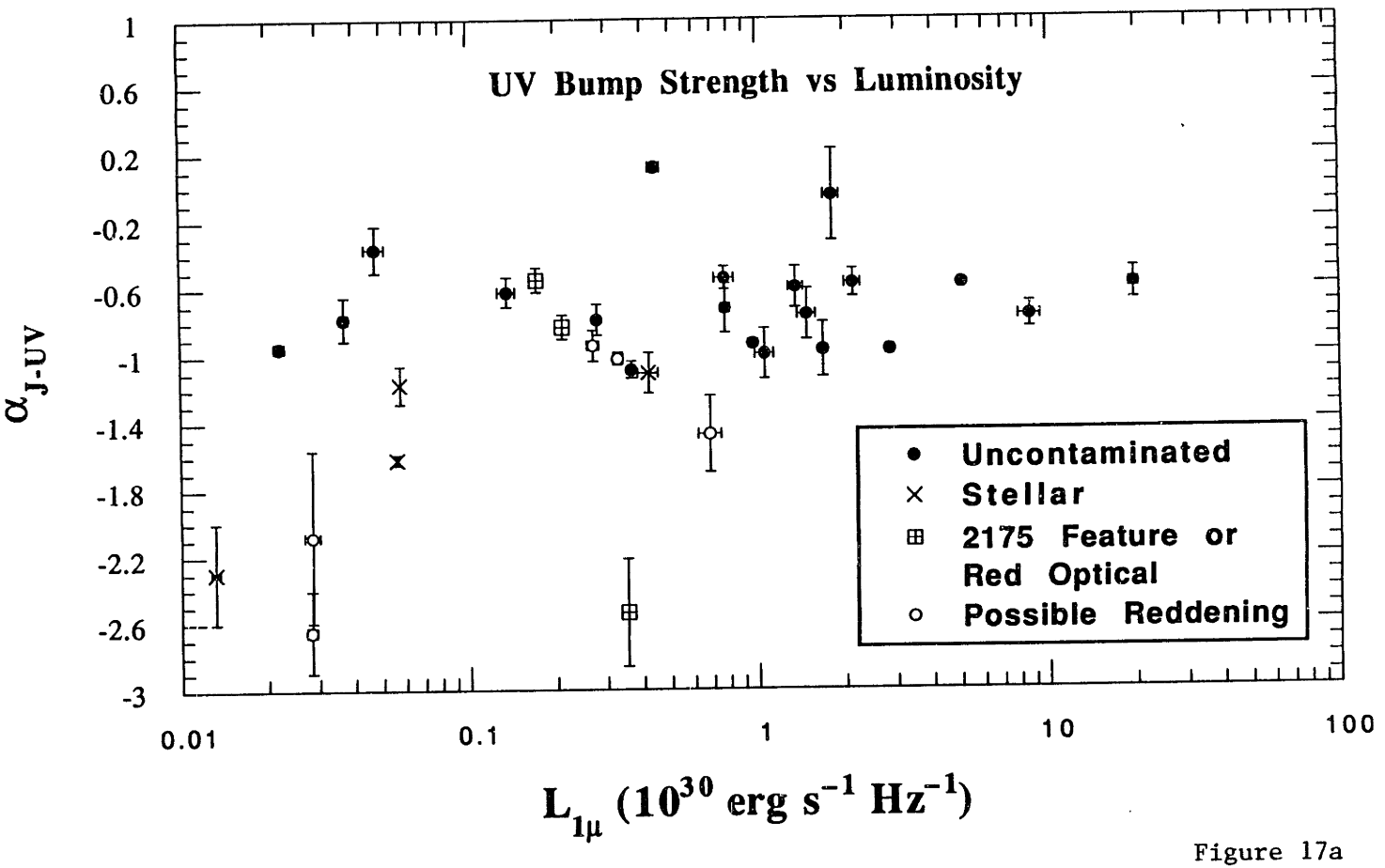
UV Bump Strength vs Luminosity
$\alpha_{\lambda-UV}$
1
0.6
0.2
-0.2
-0.6
-1
-1.4
-1.8
-2.2
-2.6
-3
0.01
0.1
1
10
100
$L_{1\mu}$ (10^{30} erg s^{-1} Hz^{-1})
Uncontaminated
Stellar
2175 Feature or Red Optical
Possible Reddening

Figure 17a

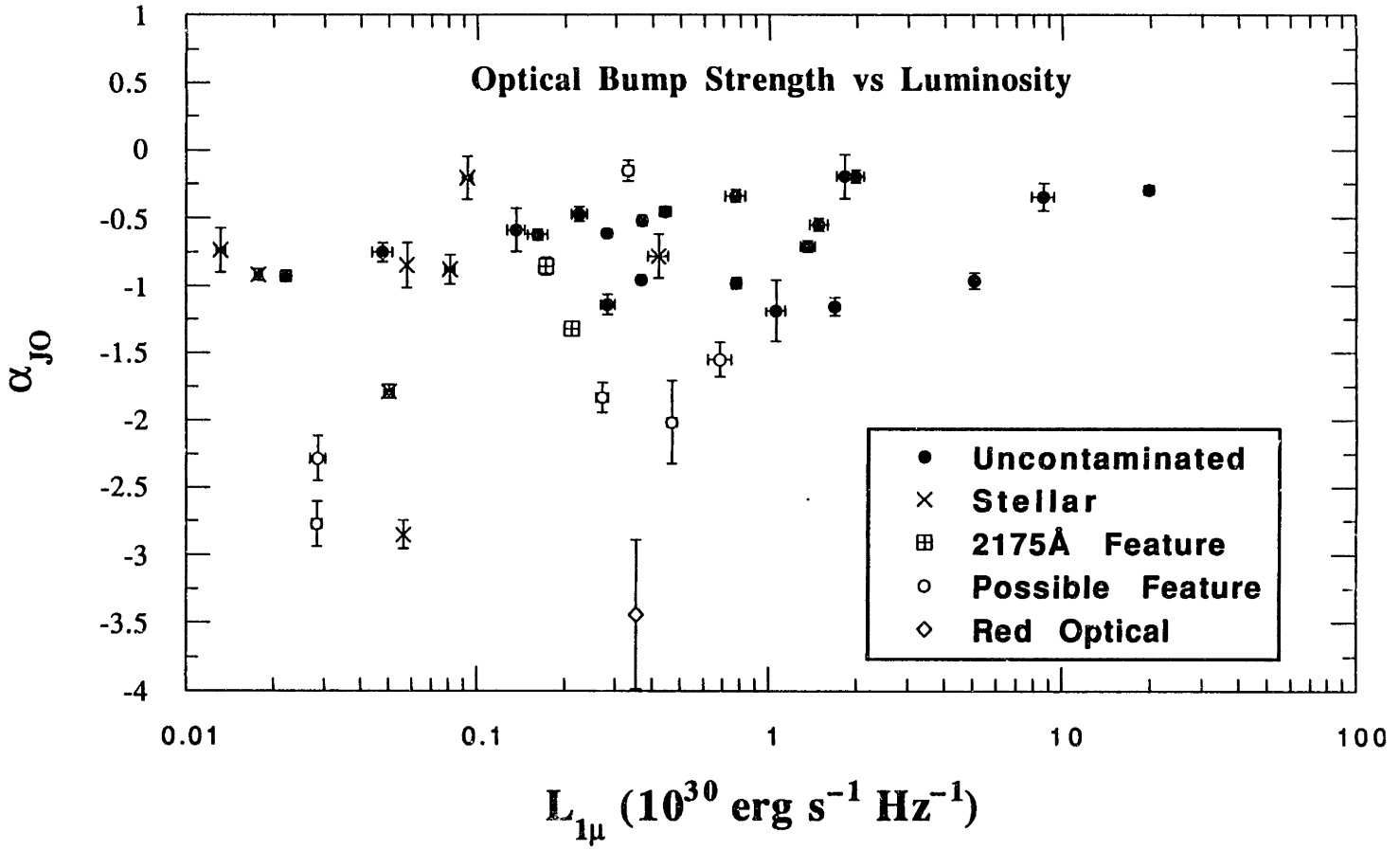
Optical Bump Strength vs Luminosity
α_{OI}
1
0.5
0
-0.5
-1
-1.5
-2
-2.5
-3
-3.5
-4
0.01
0.1
1
10
100
$L_{1\mu}$ (10^{30} erg s^{-1} Hz^{-1})
Uncontaminated
Stellar
2175Å Feature
Possible Feature
Red Optical

Figure 17b

CHAPTER 5: EMISSION LINES AND THE CONTINUUM

The relationship of the X-ray, UV, and radio continuum to the strongest emission lines, including Fe II emission, is investigated in this chapter. The Balmer decrement is studied to determine its value as an indicator of reddening.

1. INTRODUCTION

A great deal of theoretical and observational work has been done on the many aspects of AGN line emission (for a good review, see Osterbrock & Mathews, 1986). The basic picture of AGN line emission, discussed in Chapter 1, included a Broad Line Region (BLR) close to the continuum source with relatively dense clouds emitting permitted lines, and a low density Narrow Line Region (NLR), much further from the continuum source, where forbidden emission occurs. Photoionization by the UV–X continuum is generally accepted as the dominant energy input mechanism for both broad and narrow emission lines (Osterbrock & Mathews). Such a model is motivated by the strong ionizing continuum from AGN, and the clear variations of some emission lines in response to variations in the continuum. The physical conditions inferred from line ratios also support photoionization; e.g. the temperture derived from the CIII977/CIII]1909 ratio is much too cool for collisional excitation, but is typical of the temperatures in photoionized nebulae (Netzer 1990).

In this chapter, I emphasize the relationship of line and continuum emission observations. Such an emphasis is well-suited to explore geometry and other details of photoionization models which might explain the observed emission-line properties of the LMA (LASS/MC identified AGN sample) objects. In the simplest photoionization picture, one would expect that line emission strengths would scale with the strength of the photoionizing continuum. However, in practice, AGN do not produce a single set of emission lines which uniformly scale with the observed continuum. Much of the complexity in the real behavior of emission lines might be explained by photoionization if geometric effects are considered. If the fraction of the photoionizing continuum which reaches the line emission region in each AGN is not proportional to the continuum flux measured by a distant observer, then simple relations between the observed continuum and line emission will not be observed in a large sample of objects. For example, emission from Broad Line Region (BLR) material distributed in a thin disk would result in an angular dependence in broad line flux; the flux would be weak when the disk was oriented nearly edge-on, and strong when the disk was oriented nearly face-on. If the radiation which photoionized this material were isotropic, then a weak or null correlation between the broad lines and the photoionizing continuum would be observed. Because a significant number of sources are observed in this study, the full range of observable viewing angles is sampled, allowing us to probe these geometric effects. High optical depths in the BLR could also modify the continuum reaching the majority of the BLR gas, without blocking a significant fraction of the continuum. Similar effects might be produced by inhomogeneous distributions of obscuring material. Such effects of geometry, obscuration, and optical depths will be considered in the interpretation of the emission-line observations later in this chapter.

In previous work, correlations have been found between total (narrow + broad component) Hβ and optical continuum luminosity, and also between total Hβ and Einstein

soft X-ray luminosities (Blumenthal, Keel, and Miller 1982). The plots of these correlations showed that Seyfert 2's occupied the lowest luminosity regions, progressing smoothly to Seyfert 1's at intermediate luminosities, and to quasars at the highest luminosities. In general, however, only weak correlations were found between other optical spectroscopic properties and the Einstein data. For example, only weak correlations were found between either broad Balmer or FeII equivalent widths and the 2 keV X-ray/optical spectral index. The luminosity of the strongest forbidden emission line, [OIII], did not correlate with X-ray luminosity, but did show some correlation with optical luminosity. This latter result suggests that either the observed soft X-ray continuum does not play a dominant role in photoionizing the NLR, or that significant geometric/obscuration effects, similar to those discussed above, are affecting the correlations.

Fe II emission is of special interest for testing models of the BLR. Fe II emission lines are important indicators of physical conditions in the BLR because Fe II can only be present in high column density ($> 10^{22}$ cm^{-2}; Netzer 1990), optically-thick clouds. Fe II emission (discussed in more detail below) occurs both in the optical and the UV. Optical Fe II emission, which is easily identified in some parts of the spectrum, is not present in all emission-line AGN. However, UV Fe II emission is commonly stronger than all the Balmer emission combined, even when optical Fe II is weak (Wills, Netzer, and Wills 1985, hereafter WNW, and Netzer et al., 1985). Extreme values of one or more of the following physical parameters are required to produce the observed Fe II emission in photoionization models: high densities, high column densities, low ionization parameters, and high relative Fe abundance. In WNW, their best Fe II emision models yielded the following parameter values, where their standard model values (without Fe II emission) are given in parenthesis for comparison: $N_H = 10^{10\text{-}11}$ cm^{-3} ($10^{9.5}$ cm^{-3}), the optical depths at 912Å = 10^7 (10^5), ionization parameter = flux at 912 Å /($h\,N_H$) = $3\times10^{7\text{-}8}$ (1.2×10^8; h is

Planck's constant), and Fe II abundance relative to cosmic = 1-3 (1). These values suggest cool, thick clouds. Mg II is another low-ionization species which requires physical conditions similar to those of Fe II (Netzer 1990). These results suggest that optical depth effects may be important in many AGN.

Emission from Fe II has also been linked to both radio and soft X-ray continuum properties. Wilkes & Elvis (1987) found that optical Fe II equivalent width is correlated with the soft X-ray spectral index. The correlation may be present only for strong Fe emitters (Zheng and O'Brien 1990), and/or it may be stronger for only radio-quiet objects (Wilkes 1990). Joly (1991) found a correlation of optical Fe II strength with the ratio of core to extended radio flux, suggesting that this species may be related to radio jets and shock excitation rather than photoionization.

Numerous papers imply that continuum reddening may be derived from the Balmer decrement, the ratio of the flux in successive lines in the Balmer series. This approach implies an intrinsic Balmer decrement in the absence of reddening, or a Balmer decrement that is somehow predictable for any given object. No models have been published which feature a nearly constant or predictable intrinsic Balmer decrement which is also consistent with observations of other lines. Some recent papers conclude that this parameter is not a straightforward reddening indicator (e.g. Ward et al. 1989, Lawrence 1991). However, Ward et al. suggest that the Balmer decrement may still be investigated statistically, suggesting that objects with heavy reddening may be identified from their extreme decrements ($H\beta/H\alpha <\sim 0.15$)

In this chapter, I use correlation tests to investigate the relationship between the continuum and line emission with the hard X-ray selected LMA objects. Correlations with the hard X-rays will be compared to those studied previously with soft X-rays. Correlations will also be studied with radio fluxes, and with UV data, which is expected to be closely related to the photoionizing continuum. Optical depth effects in the BLR will be

investigated using Fe II strength as an indicator of high optical depths. The Balmer decrement will be investigated as an indicator of continuum reddening by comparing the distribution of decrements in objects determined to be reddened with those determined to be un-reddened by observations of the 2175 Å region.

2. SPECTRAL DATA ANALYSIS

Instrumental details, a journal of observations, and normalization of spectra are described in Chapter 2. In this section, I will describe only specific issues dealing with line-flux measurements. All line flux measurements given are from normalized spectra. In the UV, all line flux measurements for each object are from the same observing epoch. In the optical, non-simultaneous measurements of different lines are given, but line emission ratios are given only for simultaneous data. Line ratios are therefore insensitive to variability unless the line ratios are variable or the variation time scale is shorter than a few days, the typical time between observations at different grism settings.

Optical line flux measurements were made with IRAF software interactively by defining an integration region and subtracting a local continuum from the integral. The integration region limits were chosen to be the two points where the line profile reached the local continuum. These points were determined by eye. The integration regions were typicially 20,000 km/s in width at Hα and 10,000 km/s in width at Hβ. The local continuum was defined by a line between the averages of two small continuum regions on both sides of the integration region. The continuum regions were chosen to sample the continuum without interference from other lines, and were generally 40-80 Å in width. The average continuum region points were entered graphically, via a "mouse" computer interface and a video display. The strong lines and the brightness of the AGN in this sample made the line emission measurements straightforward with a few exceptions described below. The line measurement results are given in Table 1.

The objectivity of line measurements was estimated by repeated measurements of the same line. For strong lines variations in repeated measurements were typically < 15%. In weak lines the variations can be much larger; the scatter is due to the uncertainty in determining the continuum by eye in the presence of significant noise. Measurement errors were therefore given by the range of results from the set of all continuum definitions judged to be reasonable. For blended lines, discussed below, errors include uncertainty due to blending. The estimated uncertainties in the line measurements are given in 1 (See footnotes 1-3).

Broad Hα at 6563Å frequently blends with the much more narrow forbidden lines [NII] 6548, 6584 Å in Type 1 objects. The line fluxes reported for Hα are the result of the integration of the full region containing flux from Hα minus the flux attributed to other lines ([NII] 6548, 6584 Å). [NII] is very close to the center of the Hα profile, but is < 10% of the flux of Hα as reported in papers which carefully de-blend these lines in normal Type 1's. In these objects, subtracting the nearby narrow lines by eye is therefore acceptable within << 10 % error. Significant contributions (>10%) to the flux at Hα could, however, occur in Type 2 objects when Hα is weak compared to [NII]. In these cases, Hα was de-blended by fitting Hα, [NII] 6548, and [NII] 6584 Å each to Gaussian profiles in the IRAF de-blend task. A summary of the fit results is given in Table 2. Most fits clearly separated all lines. If separation of [NII] 6548 was not achieved, then the contribution of [NII] 6548 to Hα was estimated to be 37 % of [NII] 6584, and this quantity was subtracted from the [NII] 6548/Hα blend to estimate Hα. The correction above was derived from the average value of [NII] 6548/[NII] 6584 for all the cases where good separation of [NII] 6548 was achieved, 0.37 ± 0.06 (where the uncertainty is the standard deviation of the measurements).

Fe II measurements cause more difficulties. Fe II emission occurs in broad bands which consist of many transitions of Fe II of nearly identical energies blended together. In

the optical, Fe II is most easily measured in two broad bands, one near 4570Å, which I refer to as "Fe blue" , as it occurrs in the B photometric band, and another set centered at 5190 and 5320Å, "Fe vis", which occurs in the V band. These bands have the appearance of broad bumps usually with much lower peak fluxes than Hβ. The smooth, often weak, blend of lines can be difficult to uniquely separate from the continuum. To further complicate matters, He II at 4686 Å rest often blends into Fe blue. The Fe blue band was typically measured from 4480–4740 Å in the AGN rest frame. (If the Fe II between He II and 4740 Å (dominated by multiplet 43; Phillips 1978) was weak, the region was truncated near 4650 Å.) The Fe vis band was typically measured from 5120–5380 Å in the AGN frame. The typical uncertainty in measuring Fe II was estimated to be < 20%. Because of blending, He II measurements also have relatively larger errors than other broad lines in noisy spectra or where strong blending occurs. The typical uncertainty in He II measurement was estimated to be < 20%.

Measurement of UV Fe II is very difficult. It is most easily visible in a mound from about 2270 Å - 2650 Å in the strongest Fe II emitters, but there is underlying blended emission forming an apparent continuum from perhaps 2000 – 3000 Å. WNW point out that it is extremely difficult to measure this emission without extensive modeling of the optical-UV continuum. The frequent large variability detected in the UV on short time scales (see Chpater 6) suggests that it is dangerous to attempt any such modeling without simultaneous optical and UV data. UV Fe II measurements are therefore not reported here.

The remaining UV lines were significantly more straightforward to measure. First, the reddening due to material in the Milky Way was corrected using a smooth fit to the extinction function given in Savage and Mathis (1979). Next, geocoronal Lyα was removed and replaced by a linear interpolation. (Lyα fluxes from low redshift objects will be affected by this interpolation, but the effect is small). All line fluxes were measured by defining continuum regions on each side of the emission line. These two small regions

were usually 10 channels in width (23 Å in the SW camera, $\lambda < 2000$ Å; 36 Å in the LW camera, $\lambda > 2000$Å). Measurement results are given in Table 3. The line flux errors are those due to the standard deviation in the small regions used to define the continuum flux.

All optical and UV continuum and line fluxes and luminosities in this chapter were de-reddened using the E(B-V) values given in Chapter 3. The extinction function used for the optical data was an empirical power law fit to the data of Savage and Mathis (1979) from 4000 to 9000 Å such that $A_\lambda \propto \lambda^{-1.32}$.

As seen in the previous chapter, the optical continuum may contain several components in addition to the underlying IR-X component (e.g. starlight and the blue bump). While equivalent-width measurements (used in many other studies) of line emission have significant advantages in terms of measurement normalization, they are made up of a line flux divided by a continuum composed of an unknown mix of components. In this study, the absolute integrated line fluxes (or their ratios) are used to isolate the line emission without effects due to an unknown mix of continuum components.

3. THE UV AND OPTICAL SPECTRAL ATLASES

The optical spectra used to determine the line measurements given in this chapter are shown in Appendix III. The Type 1 objects are presented first, ordered by the RA of their HEAO-1 catalog names. The Type 2 objects are shown separately. The log of optical spectral observations is given in Chapter 2, Table 3b. Appendix IV presents the IUE spectra used to derive the line measurements. The objects are presented in the same order as in Appendix III. The observation times are given in Chapter 2, Table 2b.

4. CORRELATION ANALYSES

It is essential that no data reduction procedures or flux corrections which might induce correlations in random data are applied to data used in correlation tests . To assure that no correlations were introduced by the reddening correction, random line fluxes were

generated for each object, corrected by the same procedure as the real data, and then tested for correlations with continuum data. No significant correlations were observed between corrected random line data and X-ray, optical, or UV continuum fluxes (over half the correlations had random probabilities > 50% by both Spearman and Pearson tests).

The results of Spearman-rank and Pearson correlation tests for all correlations in this chapter are given in Table 4. Since, as discussed in chapter 4, the conversion of flux to luminosity may induce correlations in randomly distributed data, all correlations of directly measured quantities were performed with fluxes first, then repeated with luminosities if the correlations were significant or for special comparisons. In this way, no correlations could have been introduced by the conversion to luminosity alone.

As discussed in chapter 4, some bias may enter the correlation tests if the dynamic range of the data is severely limited. Limited dynamic range may therefore cause flux correlations to be degraded or missed; because of this, two pairs of data sets must have very different correlation probabilities if one is to infer reliably that one pair correlates significantly worse than another. The X ray fluxes are restricted to a dynamic range of 3.7, and the errors are large, typically 30%. Therefore, bias could be present in the correlations with X-ray flux. It should be noted, however, that both the possible and observed dynamic ranges of the spectroscopic measurements are very large. The observed dynamic ranges in Hα/F_B (F_B is the B-band flux) and [OIII]$/F_B$ are $>7.3\times10^4$ and >800, respectively. Hα and [OIII] could be detected at <~ 5 % of the observed strength for most objects, so the potential dynamic range is even larger. For weak lines such as Fe II and HeII, however, the detections can be marginal, and the total possible dynamic range of such measurements is smaller. The observed dynamic ranges of Fe II vis (defined below) and He II divided by F_B are about 500 and 100, respectively. Bias effects will be discussed further below, in the discussion section.

4.1 Confirming Previous Results: Correlations Between Optical Continuum and Line Emission

Very good correlations are present between all strong broad and narrow optical lines and the optical continuum (see Table 4) measured contemporaneously. The continuum near 4220 Å (see Chapter 4 for precise definition) and the B band fluxes were used as representative measurements of the optical continuum. The B band and the 4220 Å continua were chosen to minimize the contributions of starlight, which peaks at lower frequencies. The 4220 Å continuum measure was chosen to minimize the contributions of Fe II and Balmer continuum emission as well. The 4220 Å continuum was measured simultaneously with Fe blue, He II, and Hβ for most objects, whereas the B band was measured within a few weeks of the emission lines for ~ 1/2 of the objects. These results are similar to those reported previously. Blumenthal, Keel & Miller (1982) reported similar correlations between emission lines and the continuum near Hβ, although somewhat better correlations between the optical continuum and [OIII] might be present in this sample.

The optical continuum is made up of at least three components, which include starlight, an underlying I-X component, and contributions from the low-frequency side of the blue bump. The interpretation of these correlations is therefore problematic when the relative importance of the I-X continuum and the blue bump is being interpreted. The correlations indicate that the emission lines are closely related to some combination of the I-X underlying component and the blue bump, but the precise mix is often difficult to determine. In contrast, correlations between the hard X-ray continuum and emission lines provide clear information about the relationship between the lines and the I-X underlying component. In a similar manner, correlations between the UV continuum and emission lines provide clear information about the relationship between the lines and the blue bump, since the UV continuum is dominated by the bump (except in objects where it is extremely weak, those with $\alpha_{J\text{-}UV}$ near −1).

4.2 X-Ray and Line Emission

i. Forbidden Line Correlations and Emission from the NLR

Figure 1a shows the correlation of X-ray flux with the flux of [OIII], the strongest forbidden line. The Spearman correlation probability (P_S)is about 10^{-3} (see Table 4), which suggests that a significant correlation is present. The Pearson correlation probability indicates a random relationship is much more likely, however, this appears to be an artifact of only two extreme outlying objects, 1H1210+393 and 1H1540+338. Removal of these two objects from the data set reduces the Pearson probability to about 10^{-5}, but only changes P_S slightly. The high Pearson probability was therefore due to the sensitivity of the Pearson test to outliers. The luminosity correlation, shown in Figure 1b, is very good. The relationship is smooth over the full four orders of magnitude in L_x (X-ray luminosity). Type 2 objects, at the lowest luminosities, blend smoothly into the Type 1 objects at higher luminosities. The slopes of all luminosity correlations are given in Table 5. The dependence of [OIII] luminosity on X-ray luminosity is slightly flatter than unity.

The first of the outlying objects in the [OIII] vs X-ray correlations, 1H1210+393 (NGC 4151), is known for its X-ray emission and absorption variability (Turner & Pounds, 1989, hereafter TP). This object is about a decade too high in [OIII] luminosity compared to the main body of objects in the [OIII] vs X-ray luminosity correlation. The flux of this object has been previously observed to vary from $5.4 - 29.9 \times 10^{-11}$ erg cm^{-2} s^{-1}, 2-10 keV (Yaqoob et al., 1989). The LASS observed the object with a flux of roughly (ignoring spectral slope corrections) 4.8×10^{-11} erg cm^{-2} s^{-1}, 2-10 keV, so the source was X-ray faint at the time of the observation. It is plausible that the X-ray continuum in this object was partially obscured during the X-ray measurement, causing the [OIII] measurement during a later epoch, when the object may have been brighter in X-rays, to appear anomalously large. The other object away from the main correlation is 1H1540+338, one of the most X-ray luminous objects for which [OIII] measurements are

available. It is about a decade below the main body of the correlation in [OIII] luminosity. The object is a quasar with $z = 0.33$, discovered with HEAO–1. The optical spectrum shows that [OIII] emission is very weak compared to Hβ. The object also has an unusually high X-ray flux compared to its IRAS flux, but no other unusual properties obviously related to its [OIII] or X-ray flux.

The good correlation of X-ray and [OIII] luminosity indicates that a simple model where an isotropic continuum photoionizes a spherically symmetric NLR is consistent with observations. The correlation suggests that the hard X-ray luminosity is a good indicator of the photoionizing continuum in the NLR.

No correlations between X-ray flux and permitted or forbidden line fluxes were observed in Type 2 objects (see Table 4). This results suggests that the NLR or the X-ray continuum could be different in Type 1 and Type 2 objects, however, no robust conclusions can be drawn, as the sample size is very small (line measurements were available for only 8 objects).

ii. Permitted Line Correlations and Emission from the BLR

He I and Fe II vis were the only permitted optical emission lines which showed a clearly significant flux correlation with X-rays. The P_S for these correlations were ~ 10^{-3}. These correlations become very significant in luminosity. The correlations are shown in Figures 2(a)-(d), in both flux and luminosity. The log slopes of the luminosity correlations are given in Table 5. Note that the slopes are slightly flatter than unity. Additional X-ray and emission-line correlations are summarized in Table 4.

Some suggestion of a correlation may be present for Hα and Hβ (P_S is about 3.2% for Hα and 4.5% for Hβ) with X-ray flux. However, these fluxes are > 15 times more likely to be randomly correlated with X-ray flux than He I or Fe II vis. Figure 2f shows a plot of Hα vs X-ray flux for comparison.

The permitted line correlation results are surprising. None of the Balmer lines, the strongest lines in the spectrum, showed a strong correlation with X-ray flux. He I, which showed a strong correlation with X-ray flux, is weak compared to the other lines studied, and is often unmeasurable. Fe II emission is very different from the other broad lines, both in its density requirements, discussed above, and in its distribution in strength compared to other lines (see the section on Fe II emission below). In the Type 1 objects, the permitted line fluxes are dominated by the broad component (by definition), and therefore approximate the flux from the BLR alone. Type 2 objects are dominated by NLR emission, but are indicated with separate symbols in the correlation plots in Figures 1 and 2. The Balmer line emission appears to be less correlated with the X-ray flux than narrow line emission, as indicated by the larger P_S for the Balmer line vs X-ray flux correlations compared to that for the strongest narrow line, [OIII], vs X-ray flux correlation. The Balmer line fluxes are more than 23 times more likely to be randomly related to the X-ray flux than the [OIII] flux. Does this result indicate that the relationship between the strongest narrow lines and the X-ray continuum is significantly different from the relationship between the strongest broad lines and the X-ray continuum?

The [OIII] vs X-ray flux and the Hα vs X-ray flux plots are not grossly different. Both show some suggestion that a large fraction of the objects are poorly correlated, but a few measurements at high X-ray and line flux values (i.e. those in the upper right of the plots) are causing the measured correlation. To determine if only a few high X-ray and line flux measurements are dominating the correlations, the flux pairs with the highest X-ray fluxes were removed from the correlations one at a time, and the correlations were re-tested after each pair was removed. After removing only two flux pairs (4% of the data) from the Hα vs X-ray flux correlation, the Spearman probability that the data are no more correlated than random data (hereafter the "random probability") exceeded 10 %. Both the He I and the Fe vis flux correlations were much more robust against the removal of the highest X-

ray flux measurements. When the X-ray brightest objects were excluded from the He I vs X-ray flux correlation, the random probability oscillated between ~2 and 50 times 10^{-3}, and P_S did not stay above the value given by the Hα vs X-ray flux correlation until 12 measurement pairs (35% of the data) were removed The P_S did not exceed 10% until 17 measurements (50% of the data) were removed. The random probability for the Fe II vis vs X-ray flux correlation exceeded the value of P_S for the Hα vs X ray correlation after 3 measurements (10% of the sample) were removed, but the random probability exceeded 10% only after 12 measurements (40% of the data) were removed. The correlation of [OIII] vs X-ray flux is not as robust as the He I and FeII vis correlations, but is more robust than the Hα vs X-ray flux correlation. After removing 4 measurements (7% of the data) P_S for [OIII] vs X-ray flux was no better than that for Hα vs X-ray flux; after removing 6 objects (10% of the data) P_S exceeded 10 %. The luminosity correlations do not offer a strong interpretation of the relative qualities of the Hα vs L_x compared to the [OIII] vs L_x correlation. The luminosity correlation for Hα vs L_x looks slightly, but not grossly, inferior to that for [OIII] vs L_x (see Fig.s 1b and 2g).

Consider the hypothesis that without selection effects or limited measurement dynamic range both Hα and [OIII] correlate with X-ray flux, but with a large spread. The steep Log N vs Log S curve causes few high flux objects to be present in the total LMA sample. As a consequence, the full spread in the correlation is observed at low X-ray flux, but because of the small numbers of objects at high X-ray flux, the spread in the correlation at high flux is determined mostly by Poisson statistics. The data appear to be consistent with this hypothesis. The conclusion that Hα and X-ray flux are much less correlated than [OIII] and X-ray flux is therefore not very robust. The relation of Balmer line emission tc the X-ray continuum therefore may not be extremely different from the relationship of [OIII] and the X-ray continuum.

Fe II Emission

Another surprising aspect of the correlations is the different behavior of the Fe II vis and Fe II blue correlations. A brief discussion of Fe II emission is therefore appropriate. The strength of Fe II emission is unique in that it has no relation to the strength of any other lines. The optical spectra of Type I objects with and without optical Fe II vis and Fe II blue are found to be virtually identical except for the presence of the Fe II emission (e.g. Phillips 1978). The distribution of Fe II/Hβ flux in the LMA, presented in Figure 3, shows a great deal of variation. The object 1H0300–482, a quasar, is very much stronger than all others in both relative Fe II blue and Fe II vis emission (Fe blue/Hβ $\approx$ 1.5), and two more objects, 1H0557-503 (a radio-loud quasar) and 1H1429+370 (a radio quiet quasar), also stand out in relative Fe blue strength (Fe blue/Hβ = 1.1–1.2). It should be noted that weak Fe II emission (Fe blue/Hβ $<\sim$ 5%) may be present but unmeasured in many objects, because of the difficulty in measuring this emission in noisy spectra.

The correlation of Fe vis and X-ray flux is significantly different from the correlation of Fe blue with X-ray flux (see Table 4). Both the Pearson and Spearman probabilities show that Fe vis is very likely to be correlated with X-ray flux, but Fe blue is > 40 times less likely to be correlated with X-ray flux. The two line blends are physically different in that they are blends of different transitions. In Phillips (1978), the strongest multiplets in the Fe blue region were identified as 37, 38, and 43, and the multiplets 42, 48, and 49 were identified with the strongest emission in the Fe vis region. However, significantly different properties between these sets of multiplets are not reported in the literature.

The difference in the correlations of X-rays with Fe vis and Fe blue should not be a measurement artifact. First, there does not appear to be a problem due to blending of He II and Fe II blue emission. In all objects where the He II emission can be clearly de-blended,

it accounts for only a few percent of the total Fe blue flux. Second, there does not appear to be a fixed ratio of FeII blue to Fe II vis, so different relations between the two emission bands and the continuum are plausible. For example, the objects 1H1615+655 and 1H1429+370 both have strong FeII blue, but the former object has extremely weak Fe II vis, while the latter has very strong Fe II vis (see Fig. 4a,b). The histogram of Log (Fe II blue / Fe II vis) is shown in Figure 5, and three objects are more than 3 times the typical measurement error (0.12) from the mean, 0.24. The two objects farthest from the mean were measured with good, low-noise spectra, and the blue and vis regions were recorded only two nights apart, precluding any but the most extreme variability effects. Finally, above it was shown that this correlation is robust to removal of the few highest objects in order of X-ray flux.

Significant variation in Fe blue / Fe vis is not expected in the simplest model. The emission in either band is a function of physical conditions in the emitting material (density, optical depth, ionization parameter, etc.) and the input spectrum. One would expect that since the Fe vis and Fe blue transitions are from the same species, that they would be subject to very similar physical conditions, yielding a constant ratio of Fe blue / Fe vis. However, an example counter to these simple expectations is provided by HI emission. The peak emissivity of Hβ and Hα are located at significantly different radii in the BLR (Gaskell and Sparke, 1986). Therefore, in HI, emission lines significantly separated in energy do not arise from the same material under the same physical conditions The ratio in energy differences between the multiplets near 5320 and 4570 to that between Hα and Hβ is within a factor of 2, suggesting that a similar effect is at least plausible. The analogy to HI should not be taken further, however, as Fe II emission is much more complex. Wavelength coincidences between Fe II lines and the lines of other species ("line fluorescence") are important in radiative excitation of Fe II. (The best known example of such a process is the He II - OIII Bowen Fluorescence; see Netzer, 1990 for more details.)

The physical conditions at the location of some other species which is important in exciting a given Fe II transition may therefore be important in determining the Fe blue/Fe vis. ratio. The variation in the relative strength of the Fe bands could be a result of a dependence of a multiplet(s) in either band on some seemingly unrelated line(s), which could be difficult to identify.

4.3 Radio Emission

In the previous chapter it was determined that no continuum parameters correlated with any parameter of radio emission over the full range of parameter values. Here as well, there appears to be no relation between emission-line fluxes and radio flux, radio loudness, or radio slope (see Table 4).

In previous studies, Fe II emission appeared to be related to the soft X-ray slope, but only in radio-quiet objects (Wilkes 1990). In case some threshold in radio loudness is important in the relation of Fe II and X-ray flux, various sub-samples were defined with different ranges of radio loudness. In the LMA data, no correlations were found in these sub-samples (except for the sample with only three objects; such a result is not significant). The data therefore show no threshold effects of radio loudness in the correlation of Fe II and X-ray flux in the LMA objects.

4.4 UV Continuum

Emission lines respond primarily to continuum radiation of wavelength shorter than the Lyman limit (Gaskell & Sparke, 1986). This wavelength region is unobservable except in the highest z quasars. However, it is probably dominated by the blue bump, which rises sharply in the IUE band from the non-thermal IR–optical continuum, and is thought to fall in the EUV – soft X-ray region to join with the hard X-ray power law. A few objects have both strong blue bumps measured in the UV and soft X-ray excesses (e.g., PG1211+143, Bechtold et al. 1987, 1H0557-503, Remillard et. al. 1992) suggesting that some strong bumps may have already been observed to "connect" with the X-ray

component. A measure of the strength of the blue bump, such as α_{J-UV}, would then be an indicator of the strength of the photoionizing continuum, assuming it is an indicator of blue bump strength at wavelengths shorter than the Lyman limit. In this case, α_{J-UV} should be correlated with line emission strength. However, the blue bump region is thought to be made up of at least two components, the thermal blue bump and an underlying I-X power law. Associations with the underlying I-X power law were already addressed with the X-ray correlations above. To isolate the flux due to the thermal blue bump component, the blue bump strength above the underlying I-X component is used. The excess flux is defined to be the average UV flux, (defined in the previous chapter), minus the underlying I-X flux at the average frequency in the UV continuum bands. The I-X flux was given by the interpolation of a power law between the 1.25 μm and 5.2 keV fluxes redshifted to the frame of the AGN. The average log slope was -1.08 ± 0.09, so if the 1.25 μm flux was not available, a slope of -1.08 was used to predict the I-X flux.

The correlations of optical lines with the average UV continuum flux and the blue bump strength are extremely poor (See Table 4). Even the few optical lines which do correlate with X-ray flux do not correlate with the average or excess UV flux. This is true for both the permitted lines, primarily from the BLR, and narrow [OIII], the strongest line from the NLR.

The relationship of UV lines to the UV continuum is quite different, however. The UV flux correlates extremely well with all the strong high-ionization UV emission lines (see Fig. 6a,d). The only strong UV line that dos not correlate significantly with the UV continuum is MgII, a low-ionization line (See Table 4).

Probably the most important reason for the very different correlations of the UV and optical lines with the UV continuum is that the UV line measurements were measured simultaneously with the UV continuum while the optical line measurements were not. Large amplitude (factors of 2-5) variability on time scales of weeks was reported for 35 %

of a large sample of high luminosity AGN and quasars (Kinney et al.). It is plausible that over the time scales of up to several years between the optical and IUE data, even larger variations may occur. In fact, the UV flux of 1H0122–590 (Fairall 9) changed by a factor of 20 in six years (Koratkar and Gaskell, 1989). Further, low-luminosity AGN have been shown to be even more variable than high luminosity objects (Edelson, Krolik, and Pike, 1990). These observations suggest that the correlations between optical line and UV continuum flux could be significantly affected by UV variability.

Alternatively, the correlation of broad optical line and UV continuum flux may be affected by anisotropic radiation of the UV lines and the blue bump. This could be true even if all broad-line emission material is primarily excited by the blue bump. Anisotropic emission of the UV continuum is expected if the blue bump originates in an accretion disk, because the continuum perceived by a distant observer depends on the orientation of the disk. Therefore, if the UV line emission (particularly Lyα, SiIV, and CIV) were distributed in a co-aligned disk, but the optical emission was distributed differently, for example, spherically, the continuum and the UV emission lines would vary equally due to viewing angle, but the optical lines would not. For a set of objects with different viewing angles, the UV lines would then correlate with the UV continuum, where the optical lines would not, consistent with the observations. The lack of correlation of the low-ionization Mg II emission might also be explained if the continuum and high-ionization lines were distributed in a disk, but the Mg II was distributed spherically, or with otherwise different symmetry.

4.5 The Balmer Decrement and Other Reddening Indicators

If the Balmer decrement of AGN had an intrinsic, universal value, or a narrow intrinsic distribution, then the continuum reddening might be determined by a comparison of the observed and intrinsic Balmer decrements in each AGN. To explore this idea, a comparison can be made of the observed Balmer decrements in objects with and without

continuum reddening. It should be noted, however, that the scheme above assumes that the continuum and the Balmer emission suffer the same extinction.

The distribution of Balmer decrements in the LMA, corrected for extinction within the Milky Way, is given in Figure 7a for the Type 1 objects. Numerical results are summarized in Table 6. The broad- and narrow-lined objects are treated separately because broad and narrow Balmer emission are known to come from very different environments, where different Balmer decrements might occur. The Type 1 objects are divided into three categories, each with a different symbol in the figure. The "un-reddened" objects in the figure are those known to have no significant 2175 Å feature (i.e. no continuum reddening) after application of the correction for extinction by material within our galaxy derived from 21cm observations. These objects were selected to have a signal to noise ratio in the 2175 Å region such that E(B-V) =0.03 could have been easily detected. The maximum reddening in these objects therefore corresponds to a maximum reduction of Hβ/Hα by only about 3 %, which is beyond the typical measurement accuracy (σ(Hβ/Hα) <~ 20 %). The reddened objects are those diagnosed as continuum reddened in Chapter 4 due to the observation of a 2175Å feature in their UV spectrum or the characteristic reddened optical spectral shape. The two objects with 2175Å features have moderate reddening values. The intrinsic extinction in 1H2107-097 corresponds to E(B-V)= 0.07 mag (derived in Chapter 3), and the intrinsic extinction in 1H1415+255 could not be measured accurately, but is probably similar. Such moderate reddening is important, as it changes the flux at Lyα by more than a factor of two, however, its effect is small at optical wavelengths. A value of E(B-V)= 0.07 mag only lowers Hβ/Hα by only about 7%, which is also beyond measurement accuracy. The objects which show the characteristic optically reddened shape, 1H1345-300 and 1H1630+673, are expected to have very large reddening values. For example, 1H1345–300 (IC4329A) is an edge-on spiral with obvious dust lanes. The continuum reddening has been estimated to be roughly E(B–V) ~ 0.8 mag by

means independent of the Balmer decrement (Wilson and Pentson, 1979). 1H1630+673 is expected to have roughly similar reddening. Such large reddening values are expected to lower Hβ/Hα by about 60 %, which is easily measureable. All other objects are in the remaining category, labeled "Reddening Unknown" in Figure 7a.

Note that 1H2107–097 was not listed as a reddened object in Chapter 4, as the data presented for this object were corrected for the measured reddening. The data for 1H2107-097 is used twice in this analysis; it is used once, uncorrected for extinction beyond our galaxy, as a reddened object, and again, corrected for the extinction associated with the AGN and its host, as an un-reddened object.

The average Type 1 un-reddened Balmer decrement is 0.28 ± 0.07 , where the uncertainty is the standard deviation of the distribution. The distribution of the Balmer decrements for the objects whose intrinsic reddening is unknown is extremely broad (Fig. 7a), extending far above and below the locus of the un-reddened objects. The mean of this distribution is 0.29 ± 0.15, where the uncertainty is the standard deviation of the distribution. Some of the objects with unknown reddening appear "less reddened" than the objects known to be unreddened. The two heavily-reddened objects, 1H1345-300 and 1H1630+673, have very low values of Hβ/Hα (< 0.1), as expected. The objects known to be moderately reddened by the presence of 2175 Å features, 1H2107-097 and 1H1415+255, are within one σ of the mean of the unreddened objects.

In the simplest picture, a universal Balmer decrement would occur in all the BLR clouds in all AGN. At the same time, the continuum and the broad line emission would both be subject to the same extinction. If a universal intrinsic Balmer decrement existed, then a significant separation of the heavily reddened and un-reddened distributions of Hβ/Hα would be expected. The unreddened objects would form a tight distribution with Hβ/Hα values clustered at the intrinsic value, varying only by the dominant measurement uncertainty, ~15%. The heavily reddened objects would form a separate distribution at

lower values, near roughly 40% of the intrinsic value of Hβ/Hα, but with a large spread for different reddening values in different objects. This simple picture is clearly not consistent with the data. The Hβ/Hα values for the un-reddened objects range as low as 30% of the maximum un-reddened value. The lowest un-reddened object Hβ/Hα value is about 20% of the very highest Hβ/Hα value in the sample, suggesting an even larger true spread in un-reddened value of Hβ/Hα. The distribution of un-reddened Balmer decrements alone has a spread that corresponds to a very large reddening, E(B-V) ~ 1.1 mag. An intrinsic distribution with this large a spread could not be used to determine any but the most extreme continuum reddening values.

The analysis above used the total narrow and broad components of the Balmer lines, allowing contamination of the actual BLR decrement by the NLR decrement. However, by definition, the broad component dominates in all the Type 1 objects, meaning that it must contribute < 50% of the flux. If the narrow component were 50% of the flux at Hα, and the narrow line decrement were infinite, then the resulting value would be 50% of the true broad line Hβ/Hα. However, this is much smaller than the actual observed spread of the ratios, down to 20 or 30 % of the maximum value, suggesting that such an effect is negligible.

There are two simple interpretations of the large spread in the Type 1 Hβ/Hα values. The simplest interpretation is that the intrinsic spread of broad Balmer decrements is very large, equivalent to the effects of reddening by E(B-V) ~ 1 mag. Such a result is not surprising. Given the enormous variety of lines associated with high and low ionization and high and low density physical conditions observed in AGN, a universal set of BLR physical conditions, leading to a universal Balmer decrement, seems unlikely. Another possible interpretation is that the reddening of the broad lines is greater than that experienced by the continuum, as large as ~1 mag. This interpretation suggests that there is dust local to the BLR, and that both the dust and the Balmer emission are not spherically

distributed. Both conditions could be contributing to the observed Balmer decrement spread.

The distribution of Hβ/Hα for Type 2 objects is given in Figure 7b. The objects known to be reddened by the presence of the characteristic reddened optical spectral shape are shaded in the figure, and these objects are probably very heavily reddened. High-quality observations of the 2175 Å region are not available for any of the Type 2 objects, so significant reddening could be present in all the objects. The objects not known to be reddened do not show the characteristic reddened optical continuum shape , however, so they are probably not severely reddened (E(B-V) <~0.8 mag) . The Type 2 distribution includes only 8 objects, so comparisons between the Type 1 and 2 distributions are difficult. However, a much larger fraction of the Type 2 distribution has values below 0.15 than in the Type 1 distribution, suggesting that Type 2's could have a lower mean Hβ/Hα. The reddened objects are within the spread of the distribution of the objects whose reddenings are unknown. The NLR is significantly spatially separated from the central continuum source, suggesting that a lower extinction could be present in the narrow lines compared to that for the continuum if extinction occurs within the nucleus. This effect is consistent with the presence of heavily reddened objects in the middle of the distribution, however, an intrinsic spread in the NLR Balmer decrement could also explain the distribution.

5. DISCUSSION

5.1 Correlation Results - A Geometric Interpretation

i. The Narrow Line Region - A Simple Geometry

The good correlation of [OIII] flux and luminosity with that in the X-ray band is consistent with a simple picture for the NLR where an isotropic continuum photoionzes the narrow line emission material without significant geometric effects. The [OIII] emission

and X-rays could have the same anisotropic emission, and still produce an observed flux correlation; however, this is unlikely. The [OIII] emitting material is inferred to be roughly-spherically distributed over a large volume, and the NLR apparently "sees" the hard X-ray flux in proportion to the continuum we observe directly. Therefore, the X-ray continuum and [OIII] are most likely to radiate roughly isotropically. Because the X-ray and [OIII] emission is correlated, the X-ray continuum appears to be a good indicator of the photoionizing flux at the narrow-line region. The UV flux, the NIR-UV slope, and the blue bump flux do not show a correlation with the [OIII] flux, suggesting that the blue bump may not be as important in the photoionization of the NLR. This latter suggestion could be significantly affected by variability, however. Simultaneous UV and optical observations would tell us if variability dominated these results or not.

ii. The Broad Line Region - Different Distributions of Line Emission Material ?

The broad line results might suggest a different picture. The He I and Fe vis line fluxes, which are correlated with the X-ray flux, and the Balmer lines, which are less correlated with the X-ray flux, might be responding differently to the I-X continuum, as indicated by the X-ray emission, because the emission material from which these lines arise is distributed differently. The material from the different lines may be distributed with different geometry, at different distances from the continuum source, and possibly with different optical depth and obscuration effects. Note however, that a weak correlation of the Balmer lines with X-ray emission cannot be completely ruled out. Therefore, if selection effects or limited measurement dynamic range are not causing the differences in the correlations, it may be that the Balmer emission has one component with properties similar to those of He I and Fe vis which correlate with X-ray flux, and another component has different properties which do not correlate with X-ray flux.

There is already evidence that broad line emission is not uniformly radially distributed. Gaskell & Sparke (1986), in their early paper on what is now referred to as

"echo mapping", determined that there are at least two significantly separated Broad Line Emission Regions. Echo mapping uses the time delay between continuum and line variations to determine the radial distribution of the line emitting matter. Since the publication of Gaskell & Sparke (1986), more detailed error analysis has revised the interpretation of the resulting size scales (Gaskell and Peterson 1987), however, the stratification of the broad line region has been confirmed using more recent techniques (Peterson et al. 1991). The peak emissivity of "high ionization" lines such as He II, C IV, and Hβ comes from ~20 light-days from the central continuum source in low luminosity AGN (Horne, Welsh, and Peterson 1990, Gaskell and Peterson 1987), whereas "low ionization" lines such as Mg II and Hα, come from ~twice as far away (Gaskell and Sparke, 1986). The peak emissivity of Lyα is only 10 light days in NGC 5548 (Horne, Welsh, and Peterson 1990). The sizes of all these regions can be much larger in high luminosity AGN, however (Koratkar and Gaskell, 1989). The analyses to date have all been one dimensional, i.e. spherical and cylindrical geometry cannot be distinguished. However, two dimensional techniques which can distinguish such structure have been investigated (Welsh and Horne, 1991).

The best correlations of the X-ray continuum with broad lines are from He I and Fe II vis, so it would be interesting to know how these lines relate to the BLR structure found by echo mapping. He I has not yet been investigated directly using echo mapping, but Shuder (1982) argued that He I was located very close to the nucleus, because its width is systematically larger than that for Hα and Hβ. The Hβ width was in the middle of the widths for these three lines. Echo mapping has not been applied to Fe II lines either, probably because of the difficulty of measuring these blended line structures. However, the similar requirement of high optical depths for both Fe II and Mg II suggest that they are both located in the "low-ionization" zone, relatively farther from the nucleus than most other lines. The He I and Fe vis emission therefore do not appear to be at the same radii.

Models where the broad lines originate in the outer regions of large accretion disks have been proposed (e.g. Dumont and Coullin-Souffrain 1990) where back-scattered photons from the disk provide the energy to excite the emission lines. These models locate Fe II in the disk to produce the high densities and optical depths required for emission by this species. However, the correlation between the Fe II vis and X-ray flux, which is inferred to be roughly isotropic, suggests that Fe II vis is roughly sperically distributed. The inclination effects for a disk-distributed emitting material would degrade the correlation with an isotropic continuum. The disk emission model for Fe II is therefore not favored by the correlation results. Other mechanisms do exist for producing optically-thick clouds for Fe II emission outside of disks, however (see, for example, Guilbert, Fabian &McCray, 1983) .

The UV line correlations are consistent with disk distributed UV line emission, if one assumes that the UV continuum originates in an accretion disk. The excellent correlations of Lyα, CIV, and Si IV with the simultaneously measured UV continuum indicate that the high-ionization UV emission lines follow the rapidly varying UV continuum closely and that these lines and the continuum have the same angular dependence. Since the LMA subsample with UV measurements includes several AGN with strong blue bump components, these correlations suggest that the UV lines may be photoionized primarily by the blue bump component. Further, if blue bump arises from an accretion disk, then the UV line emission should be located near the UV continuum source and share the same angular dependence of luminosity and flux as does the UV continuum. If some component of Balmer emission has no intrinsic correlation with X-ray emission, then this emission could also arise from the disk with the UV lines, but this component might not correlate with the observed (non-simultaneous) UV flux due to UV variability.

5.2 Comparisons with Previous Correlation Studies with Soft X-rays

There are two differences in these hard X-ray correlations compared to previous studies with Einstein soft X-ray fluxes which are especially relevant to the current discussion. Correlations were not found between soft X-ray and [OIII] luminosities, but correlations were found between soft X-ray and Hβ luminosity (Blumenthal, Keel & Miller 1982). These results suggest that the soft X-ray emission might be anisotropic, and associated with the same angular distribution of emission as Hβ. For example, the soft X-ray emission in the majority of AGN might be dominated by a soft excess from the inner regions of an accretion disk, as suggested by TP, and as discussed above, Hβ emission might originate in a co-planar disk, but in the cooler, more dense, high-ionization line emission zone. The anisotropic soft X-ray continuum would therefore not be expected to correlate with the spherically distributed [OIII] emission, consistent with observations.

Another difference between this and previous studies deserves mention here. The equivalent width of CIV has been reported to be stronger for weaker blue bumps (Zheng 1991). According to Zheng, CIV is sensitive only to photons of higher energies than any observed bump turnover ($\geq$ 48 eV), and is therefore nearly insensitive to the strength of the blue bump itself. The anti-correlation of the equivalent-width measure was therefore interpreted as a nearly constant flux of CIV coupled with a large range of UV fluxes which depended on the strength of the bump. In Figure 8, the LMA CIV fluxes, normalized to the average UV continuum flux defined in Chapter 4 (similar to the equivalent width measure), are plotted versus $\alpha_{J\text{-}UV}$ (the relative blue bump strength). No correlations are evident in the un-reddened objects. However, for those objects which could be reddened, the data might appear consistent with the relation observed in Zheng (1991) over some observed ranges of bump strength (i.e. from $\alpha_{J\text{-}UV} \sim -1.5$ to ~ -0.5).

5.3 Cloud Depth Effects

Above, the possible differences in correlations between different lines were discussed in terms of the isotropy of the photoionizing radiation and the geometry of the

line-emitting material. Optical depths effects might also affect the correlations of some lines with X-ray flux, independent of geometry. If strong optical Fe II indicates unusually high BLR optical depths, then optical depth effects might be searched for by comparing correlations in Fe II and non-Fe II emitting AGN. Table 4 shows that the sub-samples with and without detected Fe II (typically < 0.05 times the Hβ flux) show similarly poor correlations of Hβ and Hα with X-ray flux. Therefore, either the detection of optical Fe II is not a good indicator of cloud depth effects for the Balmer line emitting regions, or these effects are not the dominant factor underlying the poor correlations between Balmer emission and the hard X-ray flux.

5.4 Balmer Decrement and Reddening

The value of Hβ/Hα expected for Case B emission (emission from an optically thin recombination plasma; e.g. Lang 1974) is 0.36. The average value of Hβ/Hα for the un-reddened LMA objects is 0.28 ± 0.07 (standard deviation of the distribution), so a large number of objects are inconsistent with the Case B value. In fact, more than 10 objects in the LMA have values of Hβ/Hα greater, or less reddened, than this value, showing conclusively that Case B conditions can not dominate the BLR in many AGN.

Above it was shown that moderate continuum reddening values (E(B-V) < 0.5 mag) cannot be inferred from the Balmer decrement. However, the Balmer decrement might still be useful as an indicator of very large reddening. The objects known to be extremely reddened did show very low values of Hβ / Hα. For example, Hβ/Hα = 0.072, (3 σ below the mean of un-reddened objects) for 1H1345–300 (E(B-V ~0.8 mag for the continuum). The Balmer decrement should therefore be useful in identifying candidate very reddened (> ~ 0.5 mag) objects. Further, a useful statistical interpretation of the Balmer decrement could be obtained from a study of the decrement in a large sample of objects with known continuum reddening. The reddening values would have to be determined by means independent of the Balmer decrement, such as with observations of

the 2175 Å feature. Such a study could give, for examle, the 90 % confidence lower limit on E(B-V) for various values of the Balmer decrement. This would be a significant aid in the interpretation of objects suspected to be reddened but which lack other data to corroborate reddening.

6. CONCLUSIONS

1. The hard X-ray continuum correlates well with the strongest narrow line, [OIII]. Since the correlation suggests that the narrow lines are excited by the underlying I–X continuum, and since the NLR is believed to be roughly spherically symmetric, the X-ray continuum must cover a large solid angle to produce the observed correlation.

2. The broad lines of FeII vis and He I correlate significantly with X-ray flux, but the strongest broad lines, Hβ and Hα, demonstrate weak or no correlations with X-ray flux. A weak correlation between Hβ and X-ray flux and Hα and X-ray flux cannot be completely ruled out, however. If the difference in correlations is due to intrinsic properties of the broad-line emitting gas, and not due to selection or related effects, the observations would be consistent with a distribution of the Balmer-line emitting material that is less spherically symmetric (possibly in a disk) than the distributions of He I and Fe vis emitting material.

3. No correlations are observed between any optical emission lines and the UV continuum flux (near ~1450 Å), the NIR-UV slope, or the blue bump flux itself near 1450 Å. No correlation is observed between the flux of UV emission lines and the hard X-ray flux. However, the correlations between the UV continuum flux and the strongest UV emission lines, CIV, SiIV, and Lyα, are all excellent. This behavior is consistent with a model where the high-ionization UV emission lines are photoionized by the blue bump component, and that the UV continuum and the UV line emission have the same angular dependence, which is different from that of the optical lines. For example, the UV lines and continuum might arise from an accretion disk, and the optical lines might be more spherically distributed. Alternatively, the lack of correlation between the UV continuum and the optical lines or between the UV continuum and the X-ray flux could be due to UV variability.

4. There are notable differences between the correlations of Einstein soft X-ray and emission-line fluxes and correlations of LASS hard X-ray fluxes and emission-line fluxes. Einstein fluxes are correlated with Hβ flux, but LASS fluxes demonstrate a weaker correlation; LASS fluxes correlate with [OIII] flux, but Einstein fluxes do not (Blumenthal, Keel & Miller 1982). These results are consistent with a picture where soft X-ray emission is anisotropic, and where some component of broad Hβ emission has the same angular dependence. The soft X-ray flux may be dominated by flux from an accretion disk in the majority of AGN (TP), explaining the anisotropic emission.

5. Fe emission shows no direct relation to radio flux, loudness, or spectral slope. The correlation of optical Fe lines and hard X-ray flux is not affected by radio loudness.

6. The average value of Hβ/Hα for unreddened broad line LMA objects is 0.28, and the standard deviation of the distribution is 0.07. The spread in Hβ/Hα corresponds to very large reddening values, E(B-V) ~ 1.1 mag, but there is no corroboration of reddening of the continuum from the 2175 Å absorption feature in these objects . The spread in the Balmer decrement must therefore likely be intrinsic to the emission in the BLR, unless reddening occurs local to the broad line region that does not affect the continuum. The spread of the Balmer decrement in un-reddened broad-line objects is therefore too great to use the this parameter to determine moderate values of continuum reddening. However, future studies with objects known to be reddened might yield a useful statistical interpretation of the Balmer decrement as an indicator for extremely reddened objects.

REFERENCES

Antonucci , R. R. J., and Miller, J. S., ApJ, 1985, 297,621

Barvanis, Richard, 1990, ApJ, 353, 419

Bechtold et al., 1987, ApJ, 314,669

Blumenthal, G. R., Keel, W. C., and Miller, J. S., 1982, ApJ, 257,499

Boksenberg, A., Shortridge, K., Fosbury, R., Pentson, M., Savage, A., MNRAS, 1985, 172, 289

Coullin-Souffrain, S., Dumont, S., Heidmann, N., Joly, M. 1980, A&A, 83, 190

Edelson, R. A., Krolik, J. H., and Pike, G. F. 1990, ApJ, 359, 86

Gaskell M.C.,and Peterson, B. M., 1987, ApJS, 65, 1

Gaskell, M.C., and Sparke, L. S. 1986, ApJ, 305, 175

Guilbert, P. W., Fabian, A. C., and McCray, R. 1983, APJ, 266, 466

Guilbert P. W. & Rees, M. J. 1988, 233, 475

Horne, K., Welsh, W. F., and Peterson, B. M., 1991, ApJ, 367, L5

Koratkar, P., and Gaskell, M. C., ApJ, 345, 637

Kriss, G. A., Canizares, C. R., and Ricker, G. R., 1980, ApJ, 242, 492

Lang, K. R., Astrphysical Formulae, 1974, Springer-Verlag, New York, p. 112

Lawrence, A., MNRAS 1991, 252,586

Netzer, H. 1990, in Active Galactic Nuclei, ed. Blanford, R. D., Netzer, H., Woltjer, L., Springer-Verlag, New York

Osterbrock, D. E. & Mathews, W. G., 1986, ARA&A, 24,171

Phillips, M. M. 1978, ApJS, 38, 187

Remillard, R. A., Brissenden, R. J. V., Grossan, B., Bradt, H. V., Ohashi, T. 1992, (in progress)

Savage, B. & Mathis, J., 1979, ARA&A, 17, 73

Shuder, J. M. 1982, ApJ, 259,48

(TP) Turner, T. J., Pounds, K. A., 1989, MNRAS, 240, 833

Trinchieri , G., Fabbiano, G., & Elvis, M.1990, ApJ, 356, 430

Ward, M. J., Done, C., Fabian, A. C., Tennant, A. F., Shafer, R. A. 1988, ApJ, 324,767

Welsh, W. F., and Horne, K., 1991, ApJ, 379, 586

Wilkes, B., Elvis, M. 1987*a*, ApJ, 323, 243

Wilkes, B. J., Elvis, M., and McHardy, I. 1987*b*, ApJ, 321, L23

Wills, B.J., Netzer, H., and Wills, D. 1985, ApJ , 288, 94, (WNW)

Wilson, A. S., and Pentson, M. V., 1979, ApJ, 232, 389

Yaqoob, T., Warwick, R. S., & Pounds, K. A. 1989, MNRAS, 236, 153

Yee, H. K. C. 1980, ApJ, 241,45

Zheng, W., and O'Brien, P.T. 1990, ApJ, 353, 433

TABLE 1

INTEGRATED FLUXES OF OPTICAL EMISSION LINES CORRECTED FOR EXTINCTION DUE TO MATERIAL WITHIN THE MILKY WAY

LASS NAME	[1]Hα	[1]HeI	[2]HeII	[1]Hβ	[3][OIII]	[2]FeII vis	[2]FeII blue	[2]Hγ	[4]Hβ / Hα	Hγ/Hα
1H0014+111	13.050	0.724	0.081			0.599	0.639	2.212		0.169
1H0016–257	14.430			0.240	0.079			0.117	0.017	0.008
1H0043+294	5.674			2.249	0.836	0.736			0.396	
1H0048+250	9.818::	0.363:	0.242:	3.142::	1.273:		0.675:::	1.124::	0.320	0.114
1H0106+324				2.446	0.638		0.579	0.787		
1H0113–148										
1H0121–353	0.358			0.095	1.103				r0.265	
1H0122–590			0.183	5.198	1.089	1.385	2.396	0.892		
1H0140+393										
1H0150–537										
1H0217–639	15.250	1.108								
1H0227–094			0.173:	2.912:			0.462:	1.147		
1H0235–525	18.310	1.528		6.310	0.660			2.569	0.345	0.140
1H0239–585										
1H0258–126				0.066::	0.199					
1H0300–482	1.461		0.022	0.318	0.115	0.333	0.462	0.301	0.218	0.206
1H0311–348	4.603	0.237		0.824	0.186	0.228	0.227	0.335	0.179	0.073
1H0339–822										
1H0347–413	10.720	0.817	0.231	3.880	0.863	1.188	0.815	1.618	0.362	0.151
1H0355–116										
1H0413–116				2.470	0.510	0.325	0.270	0.903		
1H0435–531	4.747	0.390	0.532	2.695	0.669	1.288	1.963	1.391	0.568	0.293
1H0435–274	10.220	0.370	0.185	1.684	1.789	0.409	0.140	0.576	0.165	0.056
1H0445–060					0.707:					
1H0448–041	5.646			0.377:	0.672:	0.311: ::	1.269:::	0.387:::	0.067	0.068
1H0507–459	4.879			1.222	1.506			0.608	0.250	0.125
1H0510+031										
1H0523–118			0.152	4.468	2.515		0.860	0.915		
1H0555–384	14.550	0.396		2.977	1.370			0.568	0.205	0.039
1H0557–503	5.436			2.837			3.274	1.656	0.522	0.396
1H0620–646										
1H0641+741			0.148	6.376	9.240			3.099		
1H0659+453										
1H0707+443	10.310	0.666	0.786	3.208	2.570	0.743	1.758	1.577	0.311	0.153
1H0744+499			0.667	7.420	3.68:		1.812	5.059		
1H0753+456										
1H0758+762	21.980	1.048								
1H0929+122			0.456	2.586			1.454	1.477		
1H0932+107	0.824	0.035		0.16::	0.587				NS	
1H0946–144	3.32:			0.489	3.200				0.147:	
1H1003+428	0.916			0.301		0.168	0.170			

1H1017+202			0.244	8.572	9.225			2.464		
1H1032-142	35.670	1.572		14.662	1.516	1.335	3.203	4.466	0.411	0.125
1H1039–073										
1H1120+423	4.983	0.130								
1H1135–372										
1H1210+393	172	7.475	3.281	42.49	107.5		4.723	19.310	0.272	0.112
1H1226+022		0.899		20.960	3.710	6.793	5.060	7.583		
1H1229+199	8.593	0.334	0.325	2.834	0.693	0.782	1.411	1.654	0.330	0.192
1H1238–050	14.970		0.255	5.000	2.313		3.058	1.849	0.334	0.123
1H1308–237	1.22	0.243		0.220	2.914				0.256	
1H1313+363									0.053	
1H1318+560	2.890	0.332		1.067	0.976				0.369	
1H1320+066	0.400	0.010		0.077	0.145	0.040	0.040	0.062	0.193	0.154
1H1321+692	1.32	0.097	0.12::	0.25:::	0.23:	0.076	0.095:::		0.191	
1H1325–246										
1H1334–340	8.383			0.627	0.919				0.075	
1H1341+402									0.311	0.265
1H1345–300	127.8			9.167	4.698	6.106			0.072	
1H1350+696	16.080		0.246	5.890	1.703	0.905	2.256	1.445	0.366	0.090
1H1408–031										
1H1415+255	43.520	2.539	1.053	10.100	5.972	1.457	0.906	5.150	0.232	0.118
1H1420+481	8.047	0.314	0.132	3.190	1.162	0.186	0.312	0.796	0.396	0.099
1H1422+273				0.700	0.366			0.196		
1H1429+370	13.100	0.283		3.612	1.184	1.621	4.045	1.721	0.276	0.131
1H1448+415										
1H1504+035									0.309	0.292
1H1530+585	8.706	0.163	0.267	1.970	2.095	0.187	0.315	1.065	0.226	0.122
1H1538–182	0.206									
1H1540+338	0.207	0.034	0.017	0.077	0.025		0.045	0.052	S0.374	
1H1615+655	15.210	0.050	0.082	2.685	0.841	0.069	1.254	0.874	0.177	0.057
1H1630+673	0.430::			0.030:::	0.302				0.070::	
1H1703–013										
1H1704+605	2.240::	0.035		0.234	0.529				S0.126	
1H1727+308	5.014	0.058	0.364	1.251	1.205	0.064	0.580	0.789	0.250	0.157
1H1811+670	6.359			1.923	0.540			1.441	0.302	0.227
1H1820+643	28.40		0.088	8.540	2.491	0.761	1.006	2.729	NS	NS
1H1828–593	8.57			1.510	5.936			1.837	0.337	0.410
1H1832–652	1.59:			0.11::	2.322				0.13	
1H1836–786										
1H1858+797										
1H1911–589	15.68	4.268	1.980	8.782	2.289	2.753	4.296	5.959	0.560	0.290
1H1927–516									[r]0.448	[r]0.225
1H2018–529										
1H2041–108	57.200	2.751	2.786	15.400	9.363	1.320	1.060	10.700	0.269	0.187
[5]1H2107–097	19.960	1.715	0.757	5.934	2.151	1.986	1.692	2.639	0.297	0.132
1H2129–624										
1H2209–470	7.213			0.564	0.693			0.657	0.078	0.091
1H2214–313	0.053			0.022	0.221				0.147	
1H2239+294			1.029	3.190	[c]2.745:		2.230	1.031		
1H2251–179	26.620	0.534		5.588	4.434			2.771	0.210	0.104
1H2301+086			0.600	4.025	8.013		1.809			
1H2303–089			0.167	[c]2.824:			0.412	1.371		
				:						
1H2303+039				[c]2.834:			0.364	1.447		
1H2315–423	3.35			0.785	1.721				0.305	
1H2320+084			0.383	0.881				0.856		

The table above gives fluxes of the lines indicated in units of 10^{-13} erg cm^{-2} s^{-1}.

[1]For these lines, the uncertainties are given by the following symbols:

No symbol	< 15%
":"	15-30%
":."	30-45%
":.:"	>45%

[2]For these lines, the uncertainties are given by the following symbols:

No symbol	< 20%
":"	20-35%
":."	35-50%
":.:"	>50%

[3]For [OIII], the uncertainties are given by the following symbols:

No symbol	< 10%
":"	10-30%
":.:"	>30%

[4]The ratios of line fluxes are given only for simultaneous measurements. The symbol "NS" in this column indicates that the Hα and Hβ measurements were not taken from observations in the same observing epoch. "S" indicates that the line fluxes given were not simultaneous, but another set of fluxes which were simultaneous were used instead.

[5]The object 1H2107-097 was corrected for intrinsic redddening and Milky way reddening, as described in Chapter 3.

[r]Only relative line ratios are reported for these objects, as absolute fluxes are not reliable due to weather conditions.

[c]These lines have been cut off by the end of the spectrograph. The fluxes were determined by fitting the available portion of the spectrum to a symmetric Gaussian. The error was determined by estimating the amount of the line that is absent.

TABLE 2

Hα DE-BLENDING RESULTS FOR TYPE 2 OBJECTS

LASS NAME	AGN NAME	[1,2]Hα	[NII] 6548	[NII] 6584	Comments
1H0121–353	NGC 526A	0.33rel	0.08rel	0.29rel	good de-blend
1H0445–060	NGC 1667	NA			
1H0946–144	NGC 2992	3.32:	?	1.53	[NII]6548 not de-blended
1H1308–237	NGC 4968	0.86	0.37	1.03	Good de-blend
1H1313+363	NGC 5033	0.77rel	0.83rel	1.85rel	OK
1H1408–031	NGC 5506	NA			
1H1828–593	Fairall 49	4.48	?	1.19	[NII]6548 not de-blended
1H1832–652	ESO 103–G35	0.87:	?	0.62	[NII]6548 not de-blended
1H2018–529	Fairall 341	NA			
1H2214–313	NGC 7172	0.049:	0.048	0.118	Good de-blend, but noise in continuum adds uncertainty.
1H2315–423	NGC 7582	2.57	0.611	1.81	Excellent de-blend
1H2320+084	NGC 7674	NA			

[1]Flux of indicated line in units of 10^{-13} erg cm^{-2} s^{-1}; **These fluxes are not corrected for extinction.**

[2]The symbol ":" indicates that the estimated total error is 15-25%; all other errors are estimated to be <15%. "rel" indicates that the result is not properly flux calibrated, and may be used only in a ratio to another line flux from a spectum scaled to match the same continuum level. "NA" indicates that spectral observations are not available.

TABLE 3

INTEGRATED FLUXES OF UV EMISSION LINES CORRECTED FOR EXTINCTION DUE TO MATERIAL WITHIN THE MILKY WAY

LASS NAME	^{1}Lyα	σ	SiIV	σ	C IV	σ	Mg II	σ
1H0014+111	2.16E-12	3.23E-13			1.03E-12	1.07E-13	2.98E-13	2.03E-13
1H0016–257								
1H0043+294								
1H0048+250	5.04E-12	5.49E-13	5.99E-13	5.99E-14	2.09E-12	2.46E-13		
1H0106+324	1.34E-11	3.60E-12	1.88E-12	6.70E-13	6.61E-12	4.82E-13	2.12E-13	9.27E-14
1H0113–148								
1H0121–353							1.29E-13	8.33E-14
1H0122–590	3.17E-11	1.03E-12	2.52E-12	8.58E-13	9.84E-12	6.19E-13	1.89E-12	3.30E-13
1H0140+393								
1H0150–537								
1H0217–639								
1H0227–094	8.22E-12	9.73E-13	7.37E-13	8.43E-14	6.49E-12	7.10E-13		
1H0235–525	1.57E-12	1.31E-12	4.03E-13	7.18E-13	2.26E-12	5.09E-13		
1H0239–585								
1H0258–126								
1H0300–482								
1H0311–348								
1H0339–822								
1H0347–413								
1H0355–116								
1H0413–116	1.04E-12	7.71E-13	3.33E-13	5.06E-13	4.59E-13	2.31E-13		
1H0435–531								
1H0435–274								
1H0445–060								
1H0448–041								
1H0507–459								
1H0510+031								
1H0523–118								
1H0555–384								
1H0557–503								
1H0620–646								
1H0641+741								
1H0659+453	5.21E-13	1.05E-12	1.43E-12	3.00E-13	1.55E-13	2.30E-13	4.72E-13	9.68E-14
1H0707+443								
1H0744+499	1.27E-11	2.92E-12			3.51E-12	4.52E-13	2.96E-13	5.31E-14
1H0753+456								
1H0758+762	6.88E-12	3.86E-13	8.43E-13	3.17E-13	2.07E-12	1.78E-13	4.73E-13	1.10E-13
1H0929+122	2.39E-12	1.58E-12	6.54E-13	3.68E-13	2.59E-12	4.90E-13		
1H0932+107								
1H0946–144								
1H1003+428								
1H1017+202							2.44E-13	3.28E-14

1H1032–142								
1H1039–073								
1H1120+423								
1H1135–372	2.15E-11	1.82E-12	1.56E-12	6.96E-13	1.16E-11	7.23E-13	2.25E-12	2.47E-13
1H1210+393								
1H1226+022	1.42E-11	1.06E-12	1.68E-12	4.91E-13	3.49E-12	4.86E-13	7.97E-15	5.58E-13
1H1229+199	9.01E-12	6.89E-13	1.52E-12	4.75E-13	2.64E-12	3.09E-13	3.47E-13	5.51E-14
1H1238–050	3.66E-12	7.08E-13	7.45E-14	2.32E-13	1.92E-12	6.01E-13	4.15E-13	5.59E-14
1H1308–237								
1H1313+363								
1H1318+560								
1H1320+066								
1H1321+692								
1H1325–246								
1H1334–340								
1H1341+402								
1H1345–300								
1H1350+696	3.36E-12	3.11E-13	2.53E-13	5.06E-14	2.72E-12	2.90E-13	2.94E-13	6.28E-14
1H1408–031								
1H1415+255	1.45E-11	1.94E-12	6.85E-13	2.34E-13	7.05E-12	3.19E-13	1.14E-12	9.91E-14
1H1420+481	9.23E-13	3.28E-13			3.47E-13	1.85E-13	1.51E-13	8.91E-14
1H1422+273								
1H1429+370	3.62E-12	1.15E-12	9.11E-13	4.61E-13	7.43E-13	3.26E-13	5.41E-13	2.82E-13
1H1448+415								
1H1504+035								
1H1530+585	5.02E-12	1.63E-12	3.66E-13	1.83E-13	2.35E-12	2.21E-13	2.65E-13	6.64E-14
1H1538–182								
1H1540+338								
1H1615+655	1.30E-11	2.65E-12	8.90E-13	1.18E-12	4.30E-12	1.08E-12		
1H1630+673								
1H1703–013								
1H1704+605								
1H1727+308								
1H1811+670			4.30E-14	1.75E-13				
1H1820+643	5.35E-12	5.49E-13	3.80E-13	1.55E-13	1.65E-12	8.16E-13		
1H1828–593								
1H1832–652								
1H1836–786	1.50E-12	7.54E-13	5.30E-13	3.46E-13	5.30E-13	3.40E-13	3.70E-13	1.02E-13
1H1858+797	2.25E-12	3.00E-13	8.81E-14	1.50E-13	1.15E-12	1.06E-13	2.55E-13	3.74E-14
1H1911–589	3.15E-11	2.87E-12	3.15E-12	6.61E-13	1.15E-11	6.27E-13	2.05E-12	1.99E-13
1H1927–516								
1H2018–529								
1H2041–108	8.60E-12	3.52E-12			3.50E-12	1.80E-12	1.40E-12	3.31E-13
[2]1H2107–097	8.36E-12	4.49E-13	8.64E-13	1.73E-13	2.72E-12	3.61E-13	3.81E-13	9.22E-14
1H2129–624								
1H2209–470	3.50E-11	3.37E-12	1.60E-12	1.93E-13	5.60E-12	3.08E-13	3.30E-12	1.07E-13
1H2214–313								
1H2239+294								
1H2251–179	1.50E-11	8.94E-13	1.20E-12	1.09E-12	3.60E-12	6.12E-13	5.40E-13	1.13E-13
1H2301+086	6.50E-12	1.48E-12	9.20E-13	5.22E-13	3.50E-12	4.26E-13	7.10E-13	1.10E-13
1H2303–089	8.60E-12	5.18E-13	8.30E-13	8.17E-13	3.60E-12	4.97E-13	7.00E-13	3.01E-13
1H2303+039								
1H2315–423								
1H2320+084								

[1]This column reports the flux of the Lyαλλ1216Å+ NVλλ1239Å blend.

This table gives integrated line fluxes as described in the data reduction section. Units are erg $cm^{-2}s^{-1}$.

[2]The objects 1H2107-097 was corrected for intrinsic extinction in addition to extinction for material within the Milky Way, as described in Chapter 3.

Table 4

SPEARMAN-RANK CORRELATION TEST RESULTS

X	Y	$R_{Spearman}$	$P(>R)\ 10^{-3}$	$R_{Pearson}$	$P(>R)\ 10^{-3}$	N
	Continuum vs Optical Emission Lines (Flux)					
F_B	Hα	0.470	2.55	0.652	0.00683	39
F_B	He I	0.574	3.36	0.779	0.0073	24
F_B	Fe_{vis}	0.751	0.0364	0.610	2.01	23
F_B	Fe_{blue}	0.666	0.0174	0.644	0.0398	34
F_B	Hβ	0.589	0.00273	0.772	8.5e-09	54
F_B	He II	0.532	3.57	0.804	0.00026	28
F_B	Hγ	0.615	0.0243	0.752	2.15e-05	40
F_B	OIII	0.527	0.101	0.568	0.0211	49
F_{4220}	Hα	0.850	1.39e-06	0.670	0.0377	31
F_{4220}	He I	0.819	0.000571	0.720	0.0494	25
F_{4220}	Fe_{vis}	0.781	0.0299	0.785	0.0254	21
F_{4220}	Fe_{blue}	0.819	9.81e-06	0.774	1.99e-4	32
F_{4220}	Hβ	0.908	1.12e-13	0.790	4.87e-07	42
F_{4220}	He II	0.571	3.54	0.884	1.01e-05	24
F_{4220}	Hγ	0.874	3.34e-09	0.797	6.17e-06	36
F_{4220}	OIII	0.787	7.44e-06	0.424	8.91	37
α_r	Fe_{blue} / x	0.040	897	-0.264	383	13
$F_{6\ cm}$	Hα	-0.158	433	-0.099	625	27
$F_{6\ cm}$	Hβ/ Hα	0.139	621	0.520	46.8	15
$F_{6\ cm}$	He I	0.252	328	-0.043	869	17
$F_{6\ cm}$	He II	0.167	459	0.286	197	22
$F_{6\ cm}$	N II	0.346	247	-0.159	604	13
$F_{6\ cm}$	OIII	0.181	305	-0.034	849	34
F_X	Hα	0.294	32.6	0.488	0.213	53
F_X	He I	0.514	1.86	0.398	19.7	34
F_X	Fe_{vis}	0.524	2.96	0.733	0.00408	30
F_X	Fe_{blue}	0.272	81.0	0.335	30	42
F_X	Hβ	0.243	49.1	0.396	1.01	66
F_X	He II	0.144	423	0.412	17.2	33
F_X	Hγ	0.213	137	0.458	0.817	50
F_X	OIII	0.403	1.39	0.192	141	60
F_X	OIII	0.425	0.890	0.527	0.0212	58
1H1210+393 and 1H1540+338 removed	1H1210+393 and 1H1540+338 removed					
RL	Fe_{blue}	0.115	575	0.419	33	26
RL	Fe_{vis}	-0.044	871	0.636	8.04	16

RL	Hα	-0.220	244	-0.088	643	30
RL	Hβ	-0.050	755	-0.046	771	42
RL	Hβ / Hα	-0.172	354	-0.014	942	31
RL	OIII	0.167	323	-0.041	808	37
F_{UV}	Hα	0.495	19.1	0.078	730	22
F_{UV}	He I	0.473	88	0.736	2.71	14
F_{UV}	Fe_{vis}	0.407	105	0.301	240	17
F_{UV}	Fe_{blue}	0.270	213	0.414	49.3	23
F_{UV}	Hβ	0.370	40.4	0.477	6.72	31
F_{UV}	He II	0.386	93.1	0.542	13.7	20
F_{UV}	Hβ / Hα	-0.102	679	0.341	153	19
F_{UV}	OIII	0.151	442	0.215	271	28
		Excess Bump Flux = F_{Bump}				
F_{Bump}	Hα	0.187	523	-0.025	932	14
F_{Bump}	Hβ	0.466	38.3	0.129	588	20
F_{Bump}	He I	0.462	131	0.424	169	12
F_{Bump}	Fe_{blue}	0.379	110	0.434	63.1	19
F_{Bump}	Fe_{vis}	0.445	170	0.257	445	11
F_{Bump}	[OIII]	0.335	204	-0.001	997	16
		Narrow Line Objects Only				
F_X	Hα	0.429	397	0.157	766	6
F_X	Hβ	0.095	823	-0.002	997	8
F_X	OIII	0.429	289	0.043	919	8
		Radio-Loudness Sub-Samples				
RL<1 : F_X	Fe_{blue}	-0.085	753	-0.050	853	16
1<RL<10: F_X	Fe_{blue}	-0.048	911	-0.030	943	8
RL>10: F_X	Fe_{blue}	0.800	200	0.859	141	4
RL<1 : F_X	Fe_{vis}	0.283	460	0.084	829	9
1<RL<10: F_X	Fe_{vis}	0.600	285	0.688	199	5
RL>10: F_X	Fe_{vis}	1.000	0	0.961	178	3
		Continuum vs Optical Emission Lines (Luminosity)				
L_X	He I	0.689	0.00946	0.370	34.3	33
L_X	Fe_{vis}	0.767	0.00125	0.721	0.0102	29
L_X	[OIII]	0.840	4.71e-14	0.744	9.89e-09	60
		Emission Lines vs. Emission Lines(Flux)				
F_{blue}	Hβ	0.704	9.66e-05	0.641	0.00274	44
F_{blue}	Hβ/Hα	0.379	32.4	0.296	99.7	32
F_{blue}	[OIII]	0.567	0.208	0.425	7.77	38
Hβ/Hα	Hγ/Hα	0.578	0.146	0.228	168	38
FHeII	Hα	0.476	21.6	0.832	0.000839	23
FHeII	Hβ	0.498	3.2	0.835	1.49e-06	33
		Continuum vs UV Emission Lines (flux)				
$F_{6\ cm}$	Lyα	0.022	910	0.127	502	30
$F_{6\ cm}$	Si IV	-0.026	897	0.339	84	27
$F_{6\ cm}$	C IV	-0.017	930	0.009	961	30
$F_{6\ cm}$	Mg II	-0.115	560	-0.159	420	28
F_X	Lyα	0.159	334	0.139	399	39
F_X	Si IV	0.130	442	0.144	394	37
F_X	C IV	0.115	493	0.138	408	38
F_X	Mg II	0.082	634	0.107	536	36
RL	Lyα	-0.185	327	-0.070	712	30
RL	Si IV	-0.176	380	-0.051	802	27

RL	C IV	-0.199	291	-0.101	596	30
RL	Mg II	-0.277	154	-0.136	489	28
UV	Lyα	0.798	0.000131	0.622	0.24	30
UV	Si IV	0.738	0.00727	0.695	0.0406	28
UV	C IV	0.791	0.000199	0.662	0.0686	30
UV	Mg II	0.503	10.4	0.374	65.8	25
		Continuum vs UV Lines (Luminosity)				
L_{UV}	Lyα	0.866	6.04e-14	0.389	4.02	53
L_{UV}	Si IV	0.674	0.0172	0.287	105	33
L_{UV}	C IV	0.840	1.18e-15	0.704	4.29e-08	66
L_{UV}	Mg II	0.757	0.00204	0.612	0.42	29
		Reddening Measures				
Hβ / Hα	N_H	-0.078	622	-0.013	937	42
Hγ / Hα	N_H	0.137	433	-0.031	861	35
Hγ / Hβ	N_H	-0.300	45.4	-0.247	102	45
Hα / Hβ	Lx/Hβ	0.514	0.0696	0.460	0.46	54
F6 / Hβ	Lx/Hβ	0.290	243	-0.061	811	18
		Fe II Sub-Samples				
			N0 Fe II			
Hα	F_X	0.334	70.9	0.431	17.4	30
			Fe II			
Hα	F_X	0.138	552	-0.088	704	21
			N0 Fe II			
Hβ	F_X	0.393	11.1	0.456	2.75	41
			Fe II			
Hβ	F_X	0.199	374	0.193	389	22

TABLE 5

CORRELATION SLOPES

X	Y	Log Slope	σ
L_X	HeI	0.70	0.11
L_X	Fe vis.	0.88	0.12
L_X	[OIII]	0.77	0.06
$L_{<UV>}$	CIV	0.81	0.03
$L_{<UV>}$	Lyα	0.84	0.06

The table gives best fit power law slopes for the correlations indicated.

TABLE 6

BALMER DECREMENTS

Sample	Hβ / Hα	N	Hγ / Hα	N
Type 1 un-reddened	0.28 ± 0.07	14	0.13 ± 0.05	14
Type 1 unknown	0.29 ± 0.15	25	0.17 ± 0.10	20
Type 2 unknown	0.20 ± 0.11	6	0.37	1
Type 1 reddened	0.16 ± 0.11	4	0.11	1
Type 2 reddened	0.20 ± 0.08	2	...	...

FIGURE CAPTIONS

Figure 1. The correlation of X-ray flux and the narrow [OIII] flux is presented in Figure 1a. Figure 1b shows the correlation of X-ray and [OIII] luminosity. The best fit log slope of the luminosity correlation is 0.77 ± 0.06. Note outlying objects 1H1210+393, about an order of magnitude high in [OIII] luminosity at the very lowest end in luminosity, and 1H1540+338, about a decade low in [OIII] luminosity near the highest end of the X-ray luminosity scale.

Figure 2. Figures 2a-e show plots of the permitted lines which correlate significantly with X-ray flux. Figures 2a and 2b give the correlation of He I and X-ray continuum emission in flux and luminosity. The best fit slope to the luminosity relation is 0.70 ± 0.11. Figures 2c and 2d give the same for FeII vis (blended Fe II emission manifested as large mounds centered near 5190 and 5320Å) and X-rays. The best fit slope for the luminosity relation is 0.88 ± 0.12. A plot of FeII blue (the mound centered near 4570Å) vs X-ray flux is also given for comparison in Figure 2e. Note that the correlation in flux is significantly poorer for FeII blue. The strongest permitted lines, the Balmer lines, did not show significant correlations with X-ray flux. The correlation of the strongest Balmer line, Hα, with X-ray flux is shown in Figure 2f, and the luminosity correlation is shown in Figure 2g.

Figure 3. Figures 3a and 3b give the distribution of Fe II blue flux divided by Hβ flux, and Fe II vis flux divided by Hβ flux, respectively, in the LMA sample. Fe II blue is defined to be the Fe II emission present in a mound near 4570 Å. Fe II vis. is defined to be the Fe II emission in mounds near 5190 and 5320Å. Note that a large range in the strength of Fe II emission occurs in AGN.

Figure 4. The optical spectrum of 1H1429+370, Figure 4a, shows typical strong Fe II emission, with strong lines clearly present on both sides of the Hβ/[OIII] structure. Figure 4b shows the optical spectrum of 1H1615+655, which shows strong Fe II blue emission near 4570 Å, but only very weak Fe II vis emission near 5190 and 5320 Å.

Figure 5. The histogram of Log(Fe II blue/FeII vis) is presented in this figure. The two highest values of Fe II blue/FeII vis are more than 3 times the measurement uncertainty from the mean. These values were derived from high signal-to-noise, contemporaneous measurements. This suggests that significant intrinsic variation in the ratio of Fe II blue/FeII vis actually occurs, and is not an artifact of measurement errors.

Figure 6. The two best correlations of UV emission lines with the average UV continuum, labeled "<UV>" in the figures, are shown in both flux and luminosity. The average UV spectral luminosity, labeled "$I_{<UV>}$", is the continuum luminosity from 1290–1860 Å, averaged in log space, as defined in Chapter 4. Figures 6a and 6b show Lyα vs <UV> in flux and luminosity. The best-fit power law to the luminosity correlation has a log slope of 0.84 ± 0.06, and is shown in figure 6b. Figures 6c and 6d show the correlation of CIV and the UV continuum, in both flux and luminosity. The best-fit power law to the luminosity relation has a slope of 0.81 ± 0.03, and is shown in figure 6d. Note that the correlations of these UV emission lines with the UV spectral luminosity are excellent.

Figure 7. Figure 7a shows the distribution of Type 1 Balmer decrements in the LMA. Objects known to be un-reddened by 2175 Å region observations, objects known to be reddened by either 2175 Å features or a characteristic optical spectral slope, and objects whose reddening is unknown are all shown with different symbols. See figure for key. Note the large spread in the distribution of un-reddened objects.

Figure 7b shows the distribution for Type 2 objects. Objects known to be reddened are shown with a solid symbol.

Figure 8. This figure shows CIV flux, normalized to the average UV continuum flux (defined in Chapter 4), plotted against the strength of the blue bump, as measured by the log slope from 1.25 μm to the UV, $\alpha_{J\text{-}UV}$. Objects known to be un-reddened, objects knows to be reddened, and objects with unknown reddening are all given separate symbols. There is no correlation within the un-reddened objects.

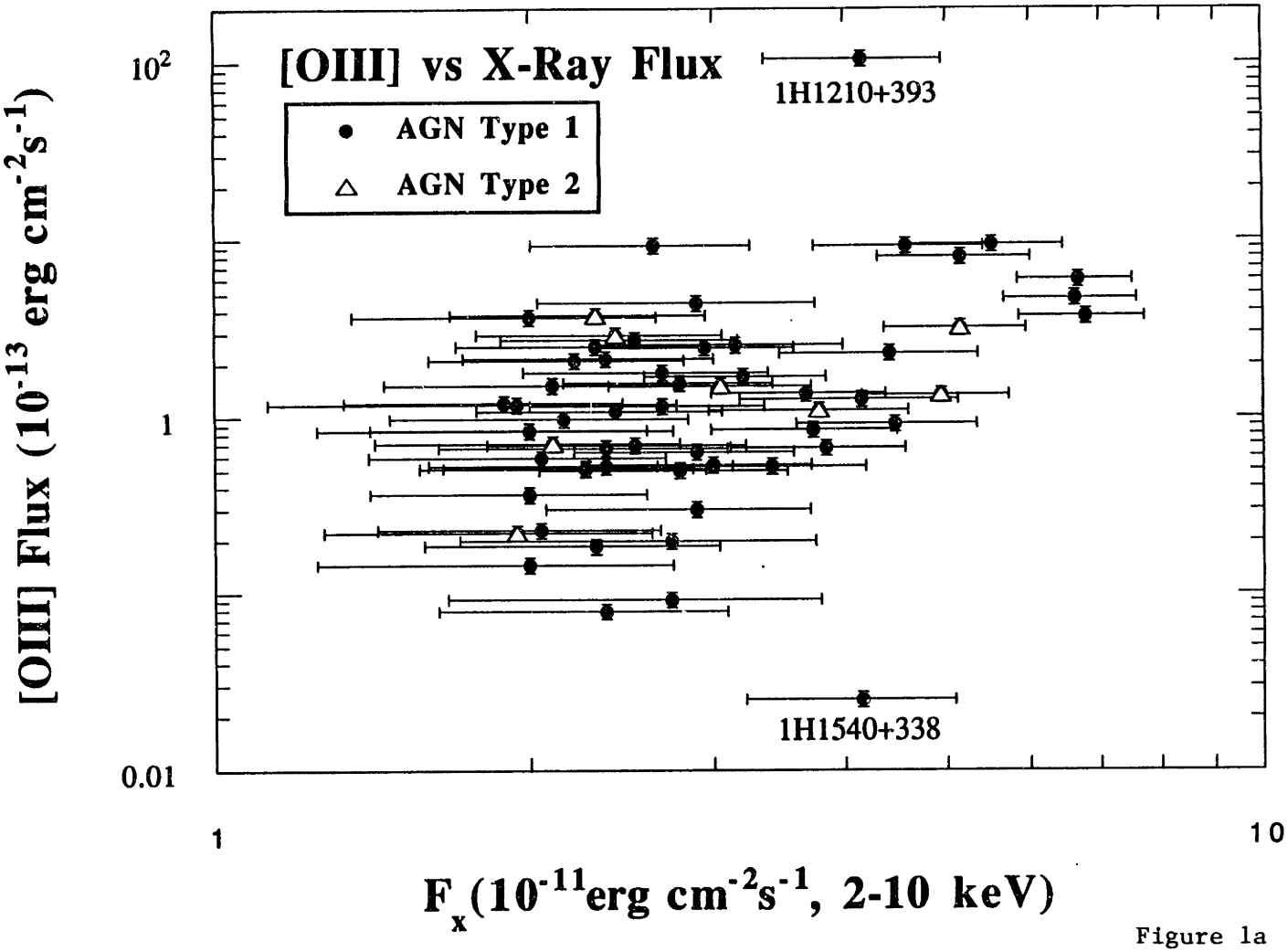
[OIII] vs X-Ray Flux
AGN Type 1
AGN Type 2
1H1210+393
1H1540+338
[OIII] Flux (10^{-13} erg cm^{-2}s^{-1})
10^2
1
0.01
1
10
F_x(10^{-11}erg cm^{-2}s^{-1}, 2-10 keV)

Figure 1a

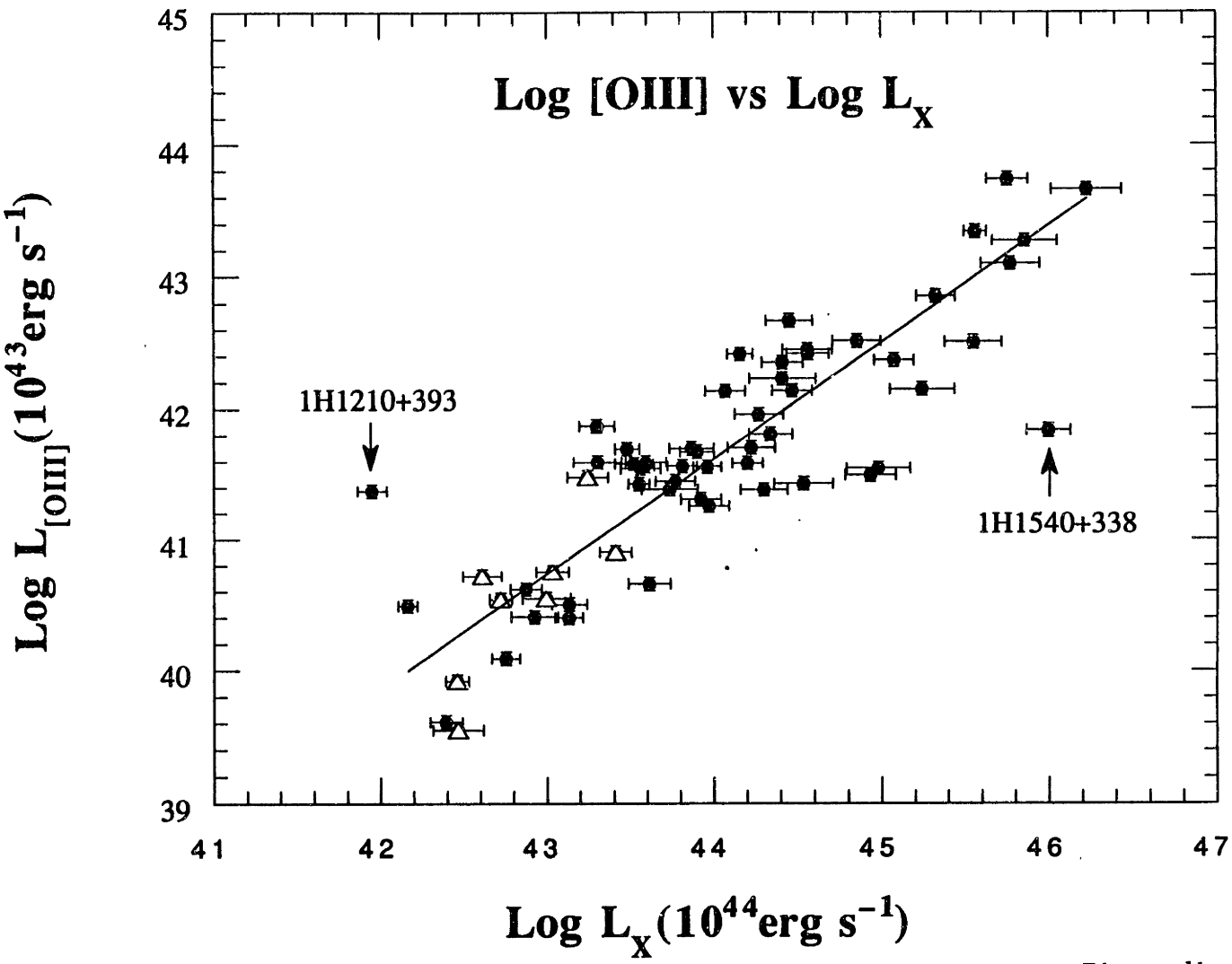
Log [OIII] vs Log L_X
1H1210+393
1H1540+338
Log $L_{[OIII]}(10^{43}erg\ s^{-1})$
Log $L_X(10^{44}erg\ s^{-1})$
45
44
43
42
41
40
39
41
42
43
44
45
46
47

Figure 1b

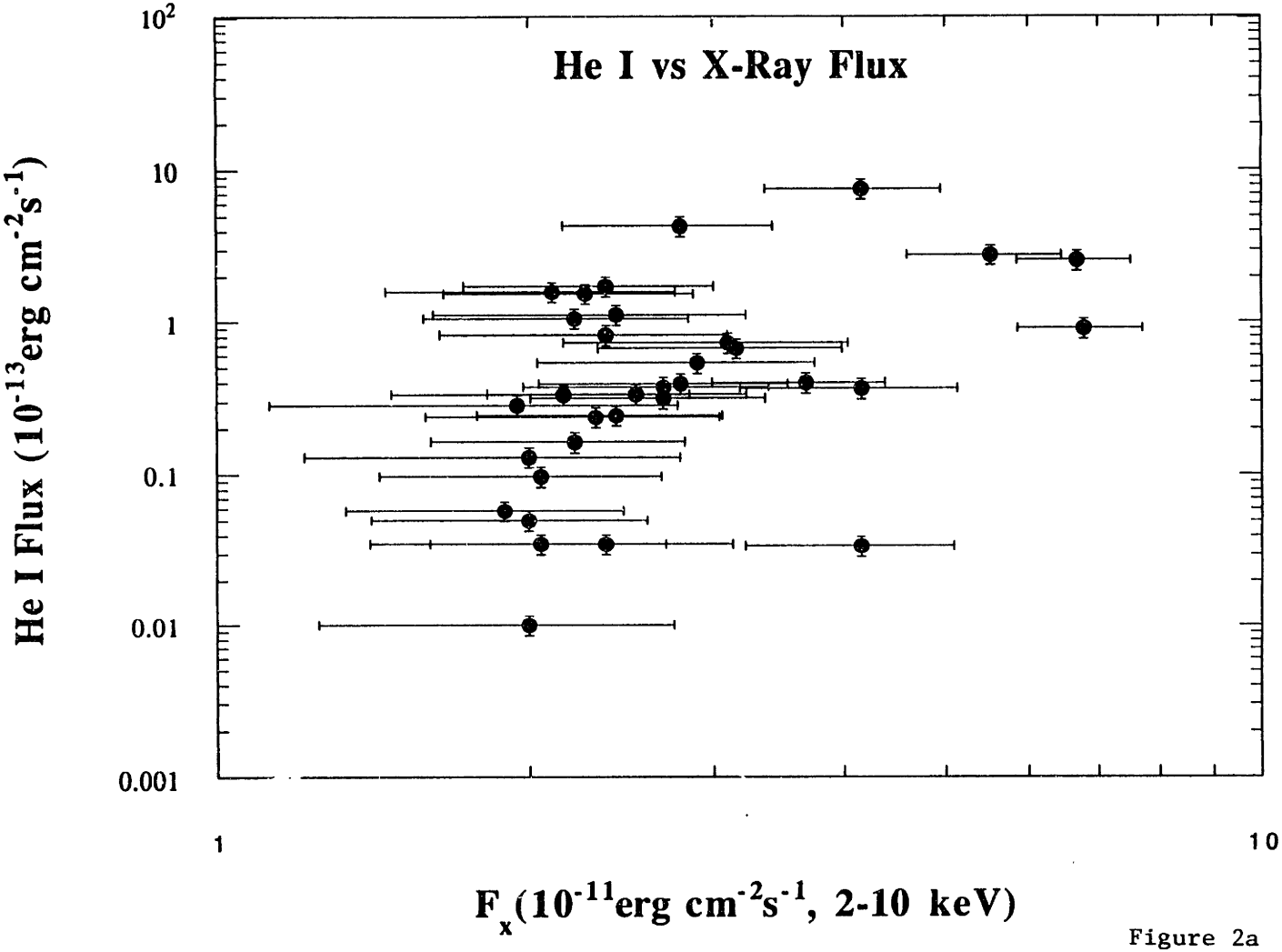
He I vs X-Ray Flux
He I Flux (10^{-13}erg cm^{-2}s^{-1})
10^2
10
1
0.1
0.01
0.001
1
10
F_x(10^{-11}erg cm^{-2}s^{-1}, 2-10 keV)

Figure 2a

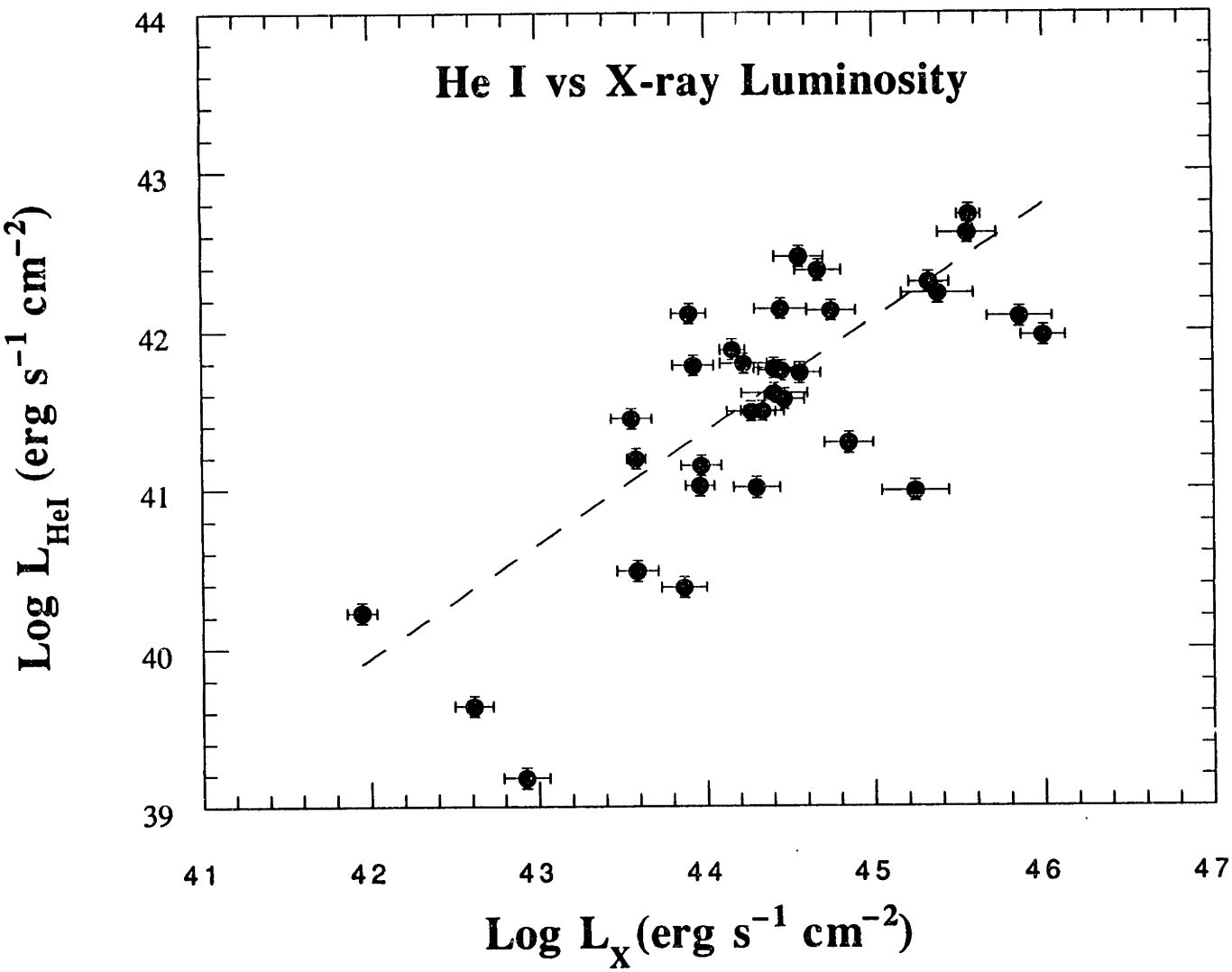
He I vs X-ray Luminosity
Log L_{HeI} (erg s^{-1} cm^{-2})
Log L_X(erg s^{-1} cm^{-2})
44
43
42
41
40
39
41
42
43
44
45
46
47

Figure 2b

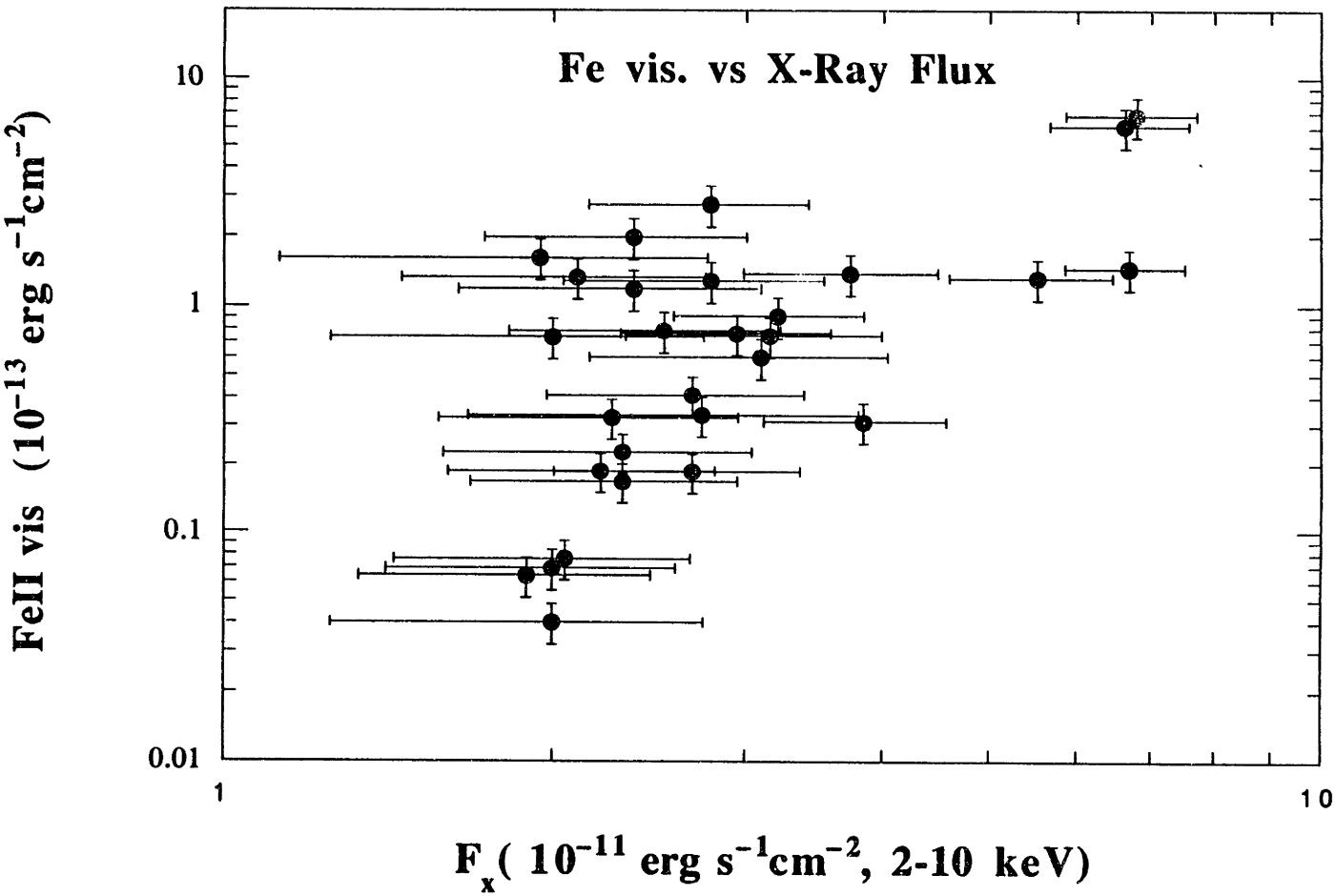
Fe vis. vs X-Ray Flux
FeII vis (10^-13 erg s^-1cm^-2)
10
1
0.1
0.01
1
10
F_x(10^-11 erg s^-1cm^-2, 2-10 keV)

Figure 2c

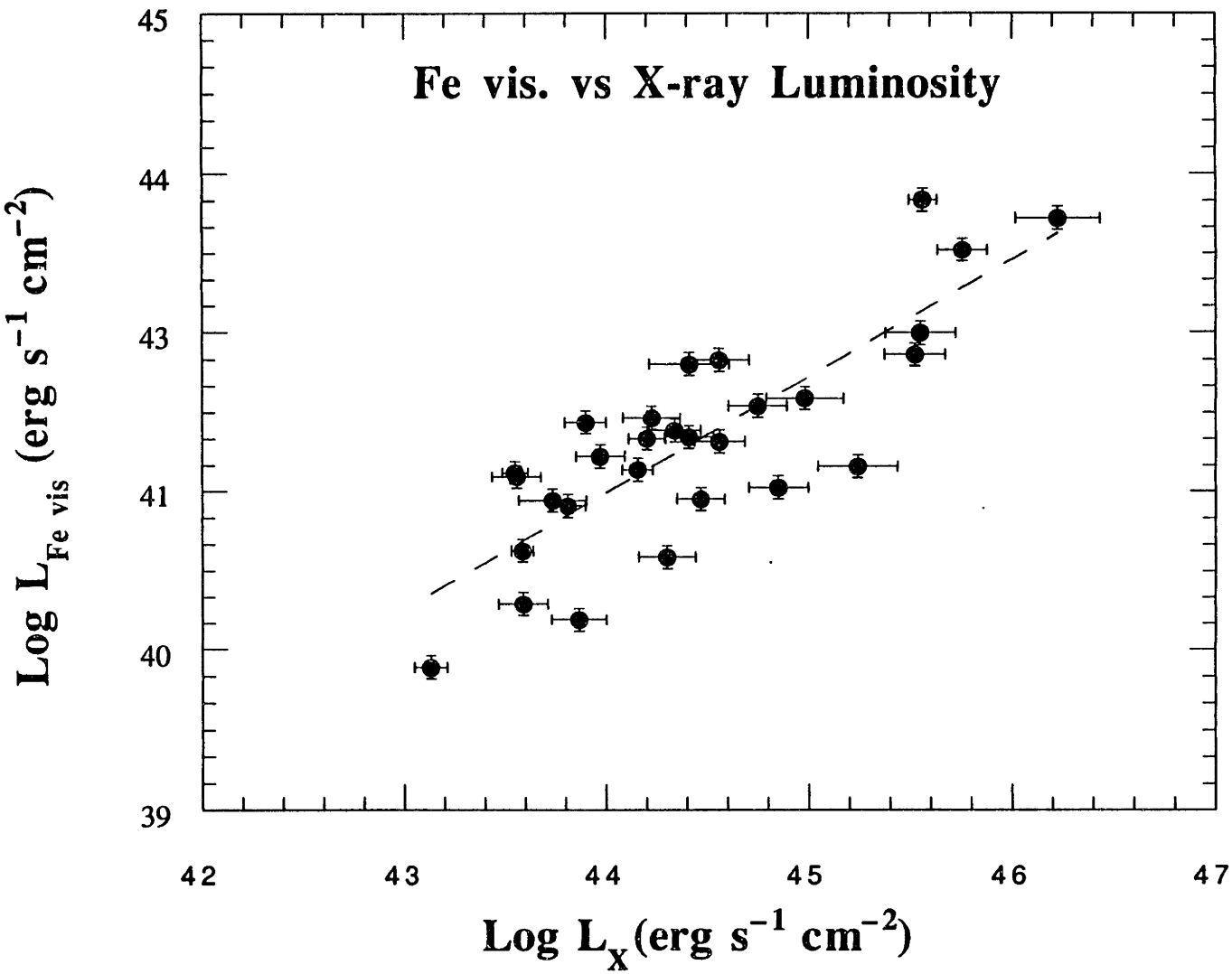
Fe vis. vs X-ray Luminosity
Log $L_{Fe\ vis}$ (erg s^{-1} cm^{-2})
Log L_X(erg s^{-1} cm^{-2})
45
44
43
41
40
39
42
43
44
45
46
47

Figure 2d

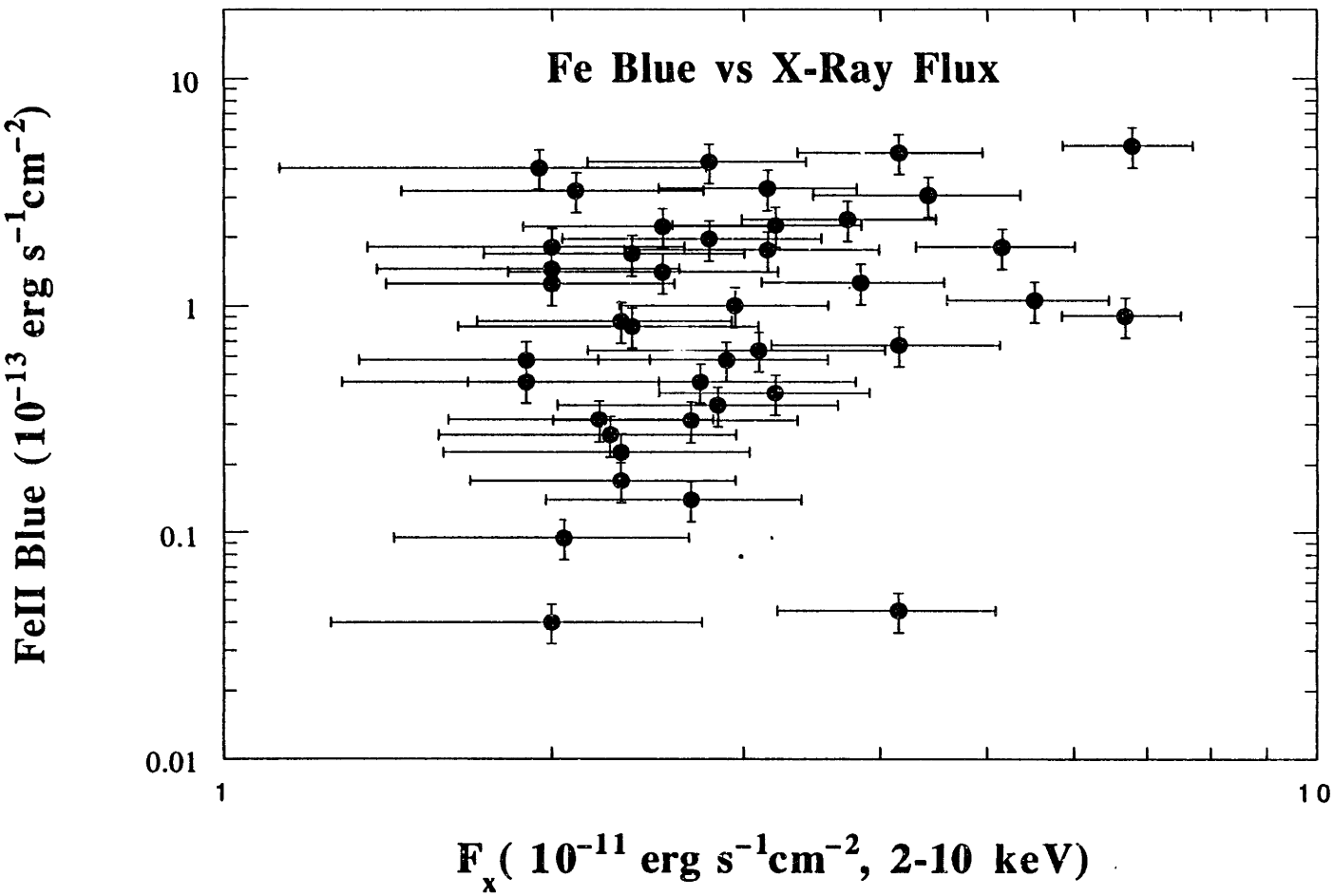
Fe Blue vs X-Ray Flux
FeII Blue (10^{-13} erg s^{-1}cm^{-2})
10
1
0.1
0.01
1
10
F_x(10^{-11} erg s^{-1}cm^{-2}, 2-10 keV)

Figure 2e

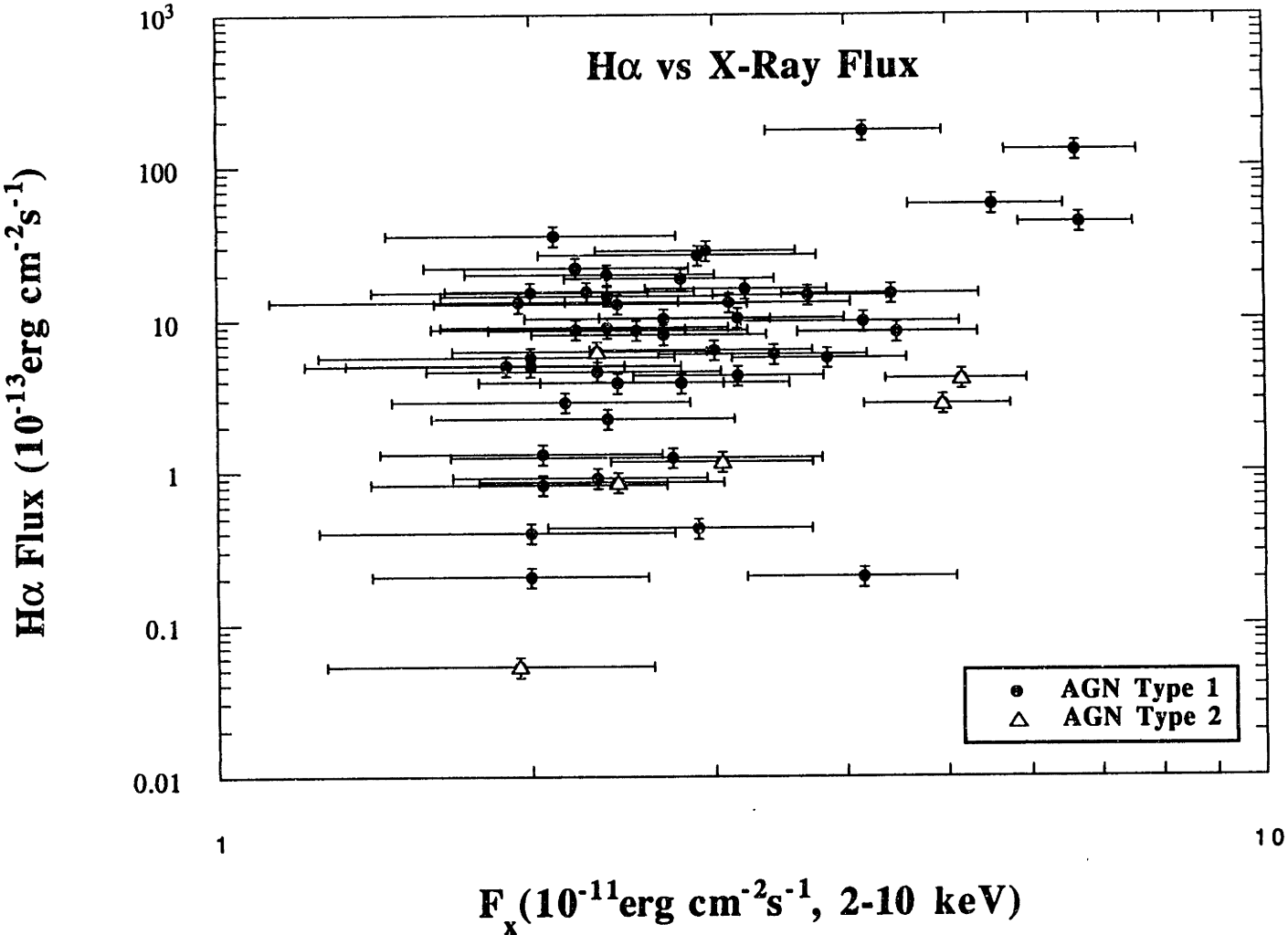
Hα vs X-Ray Flux
Hα Flux (10^{-13}erg cm^{-2}s^{-1})
F_x(10^{-11}erg cm^{-2}s^{-1}, 2-10 keV)
10^3
100
10
1
0.1
0.01
1
10
AGN Type 1
AGN Type 2

Figure 2f

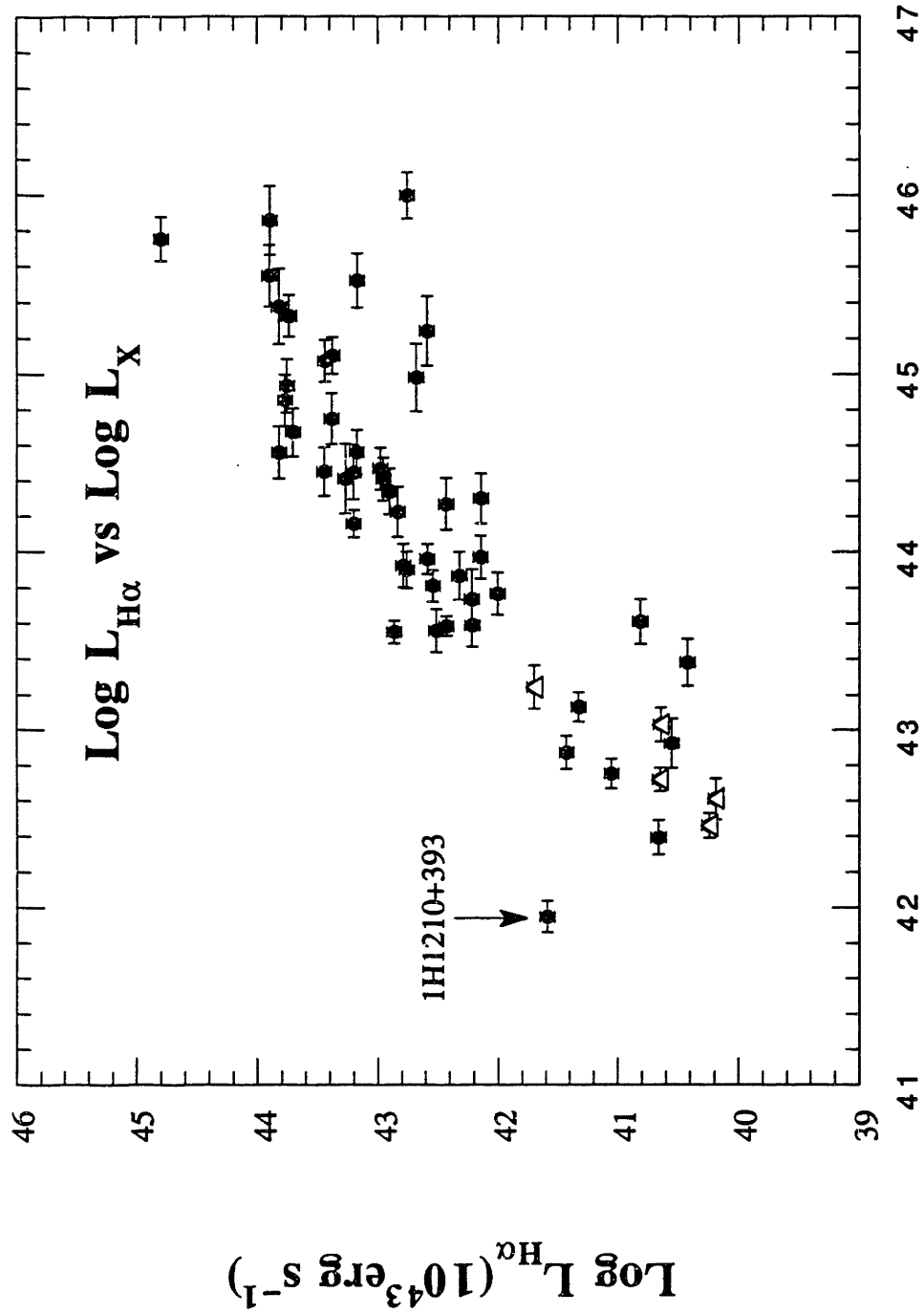
Log $L_{H\alpha}$ vs Log L_X
1H1210+393
Log $L_{H\alpha}(10^{43}$erg s$^{-1})$
Log $L_X(10^{44}$erg s$^{-1})$
46
45
44
43
42
41
40
39
41
42
43
44
45
46
47

Figure 2g

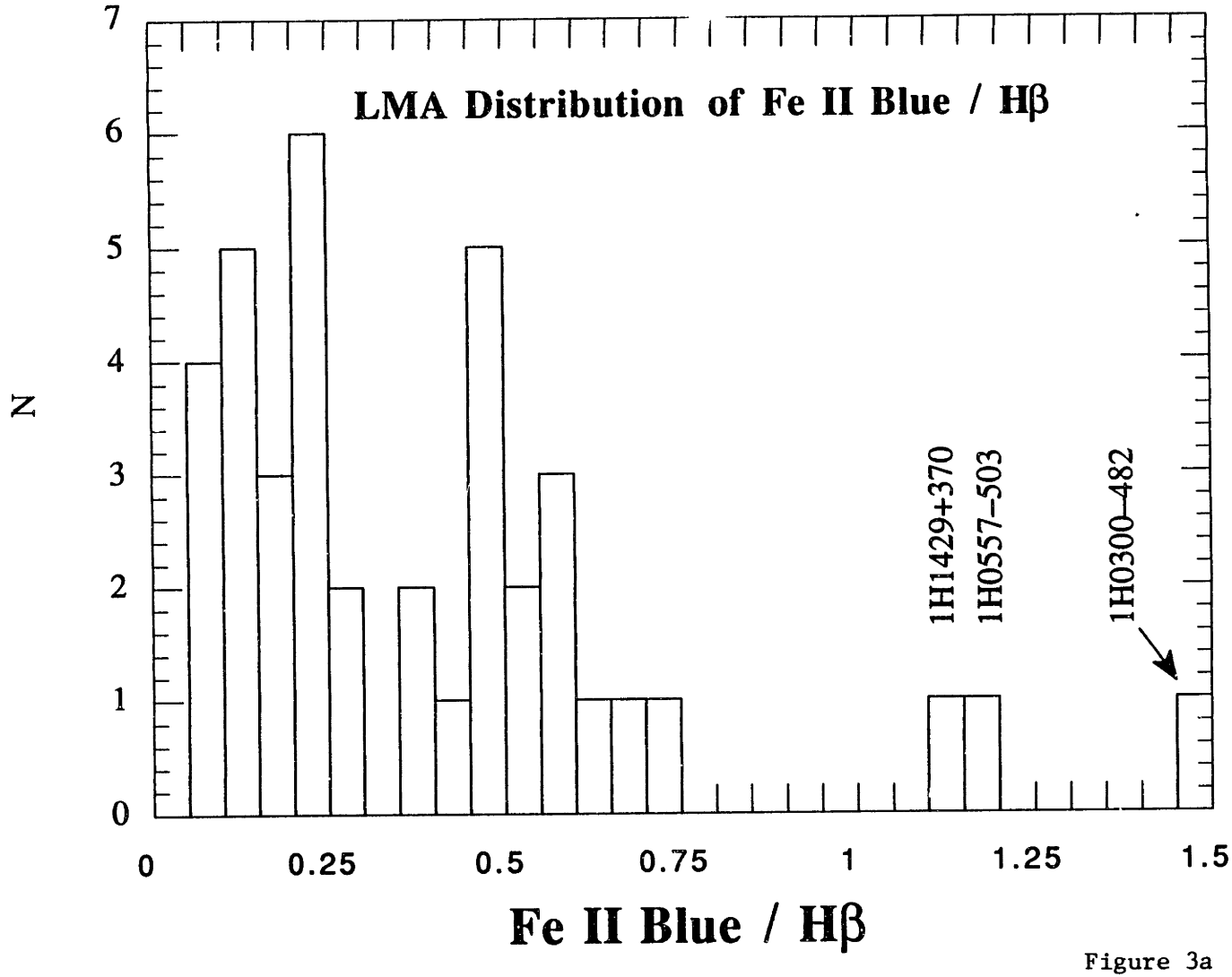
LMA Distribution of Fe II Blue / Hβ
N
0
1
2
3
4
5
6
7
0
0.25
0.5
0.75
1
1.25
1.5
Fe II Blue / Hβ
1H1429+370
1H0557–503
1H0300–482

Figure 3a

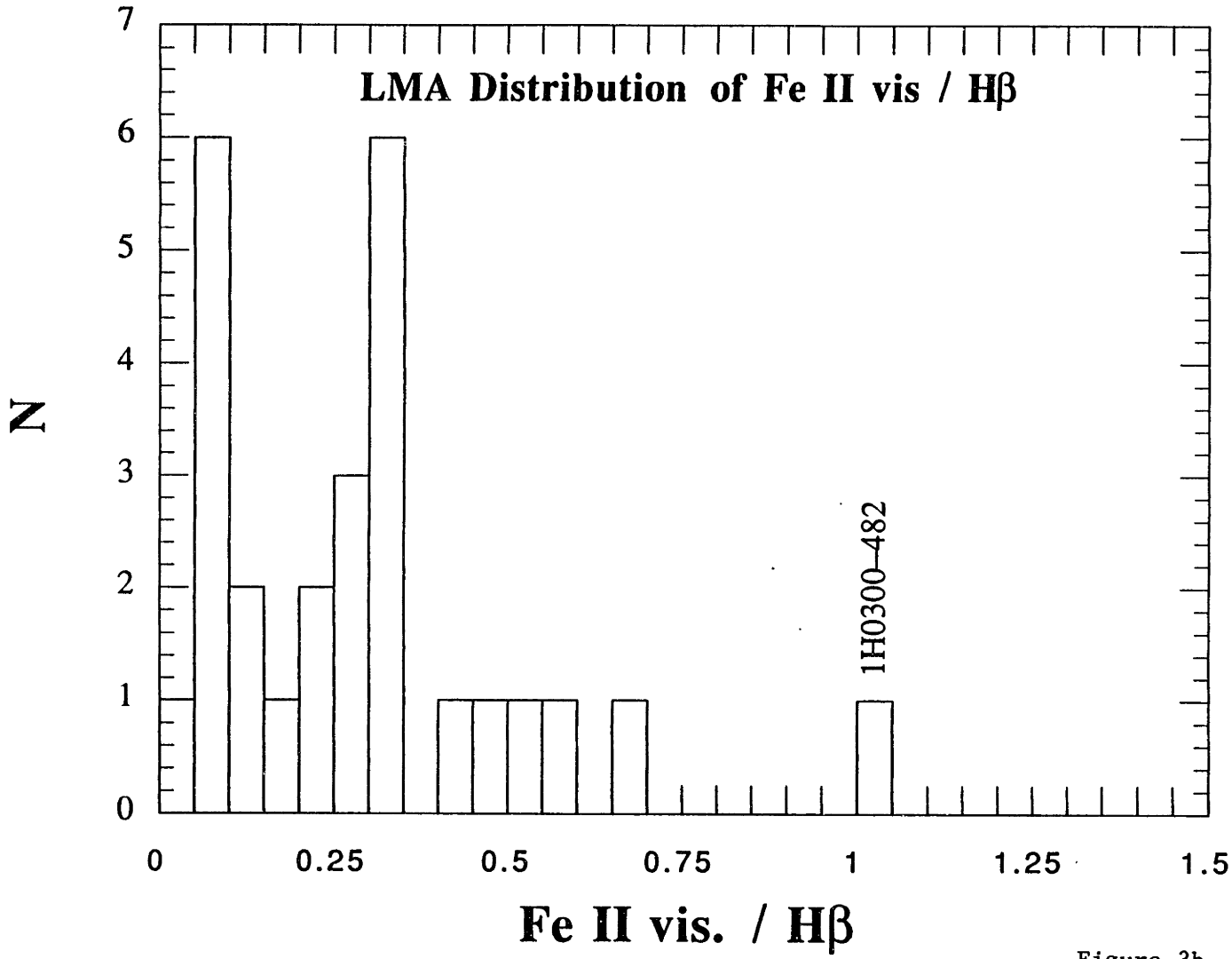
LMA Distribution of Fe II vis / Hβ
N
0
1
2
3
4
5
6
7
0
0.25
0.5
0.75
1
1.25
1.5
1H0300–482
Fe II vis. / Hβ

Figure 3b

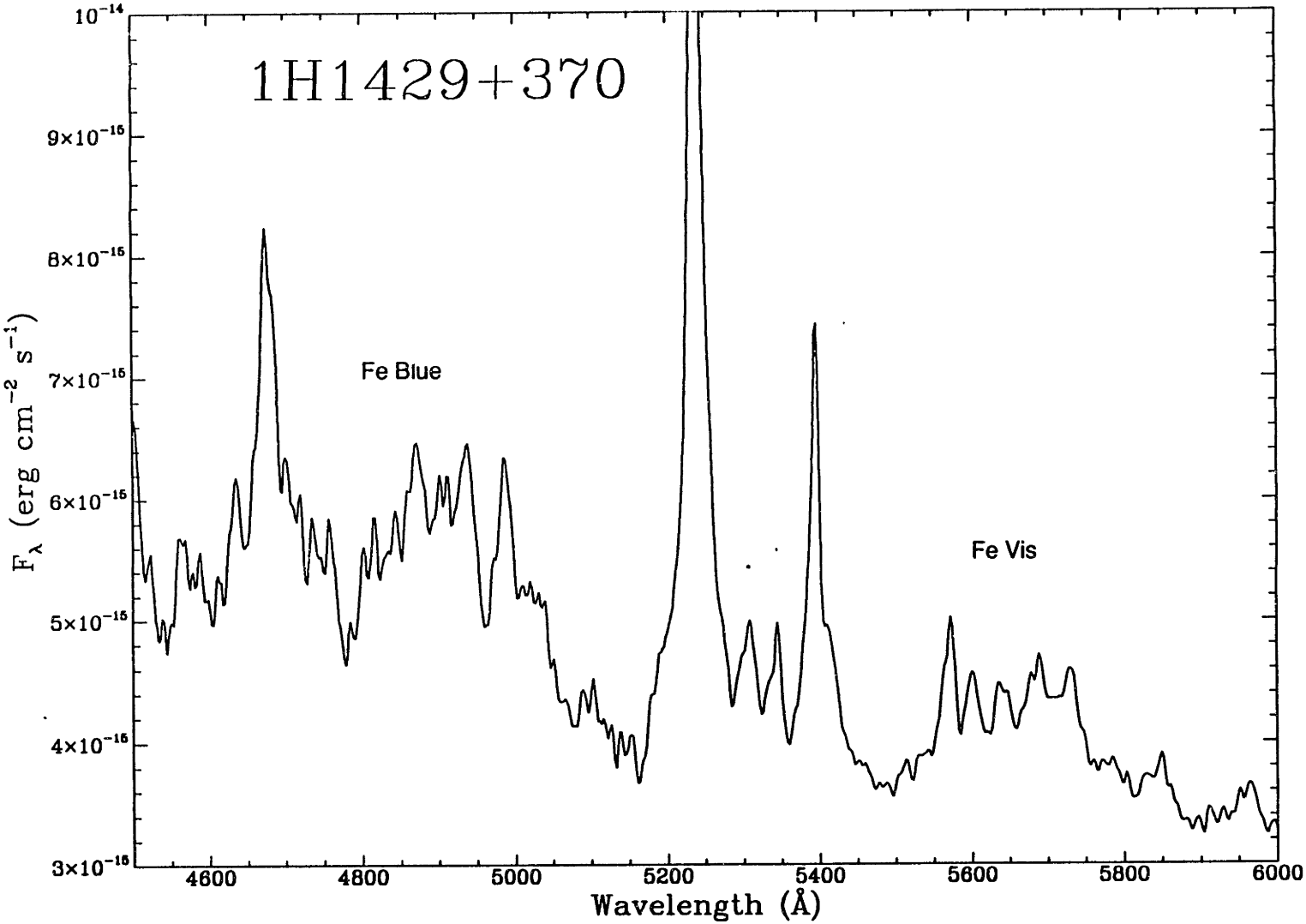
1H1429+370
Fe Blue
Fe Vis
F_λ (erg cm^{-2} s^{-1})
Wavelength (Å)
10^{-14}
9×10^{-15}
8×10^{-15}
7×10^{-15}
6×10^{-15}
5×10^{-15}
4×10^{-15}
3×10^{-15}
4600
4800
5000
5200
5400
5600
5800
6000

Figure 4a

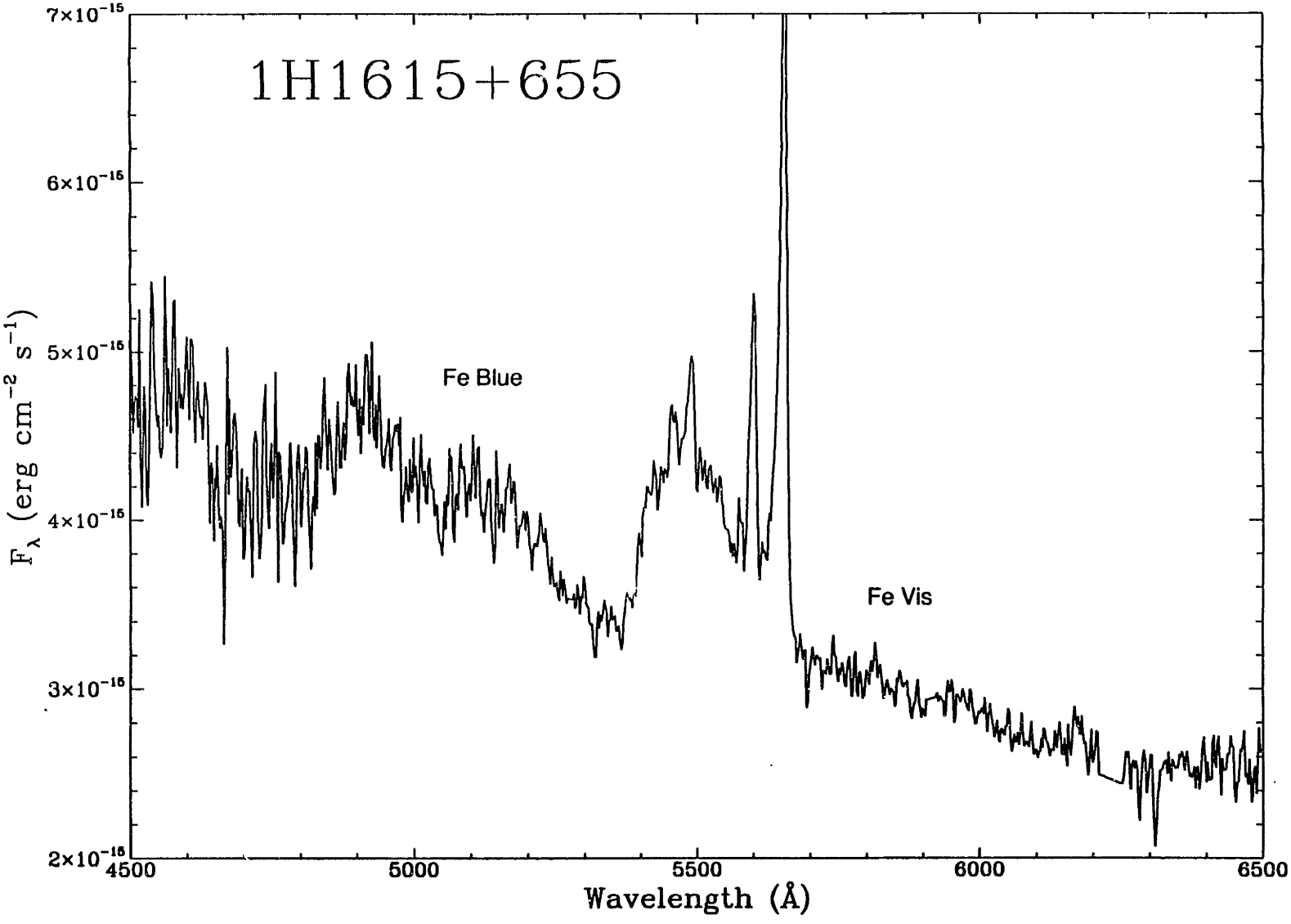
1H1615+655
Fe Blue
Fe Vis
F_λ (erg cm^{-2} s^{-1})
Wavelength (Å)
7×10^{-15}
6×10^{-15}
5×10^{-15}
4×10^{-15}
3×10^{-15}
2×10^{-15}
4500
5000
5500
6000
6500

Figure 4b

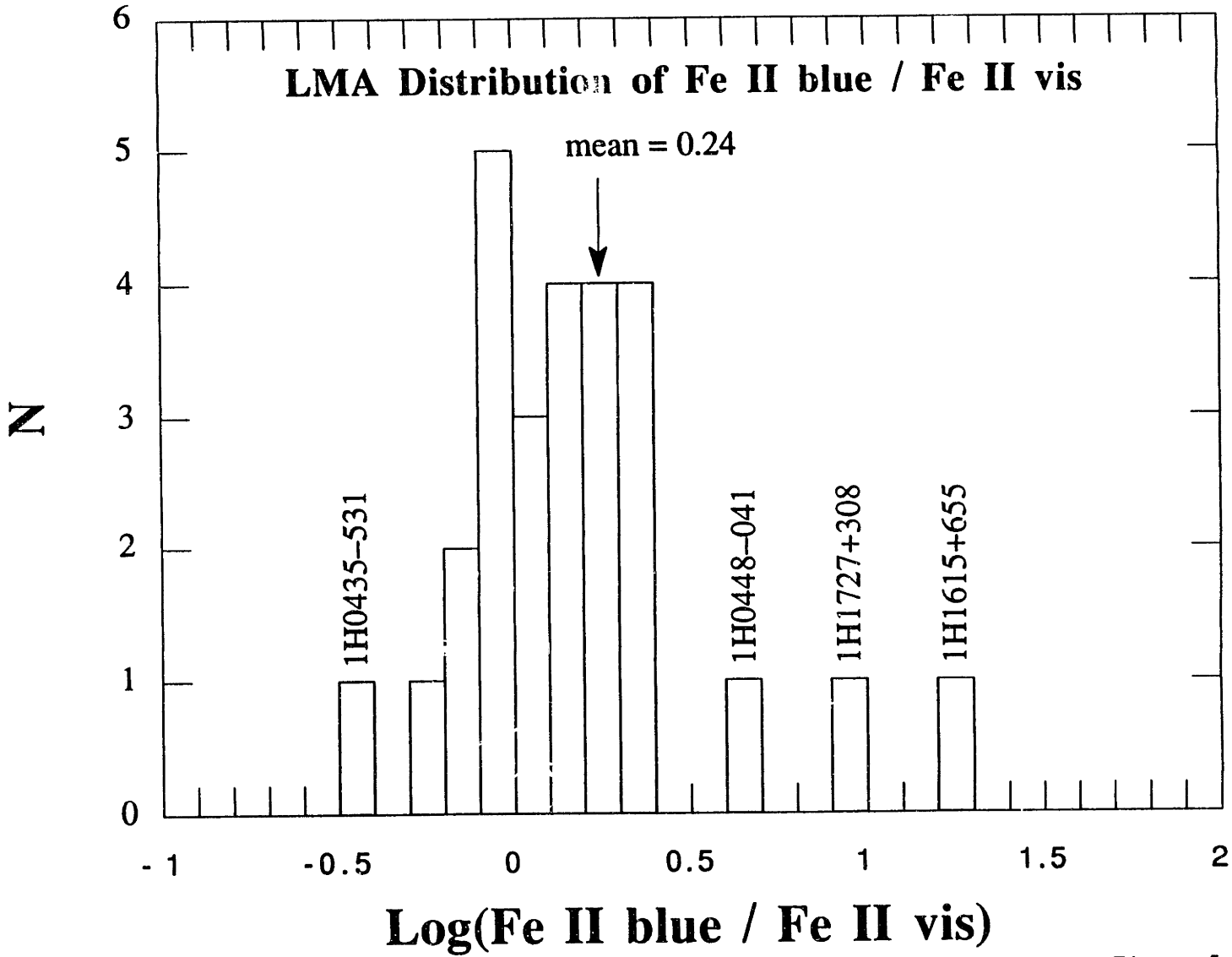
LMA Distribution of Fe II blue / Fe II vis
mean = 0.24
N
1H0435-531
1H0448-041
1H1727+308
1H1615+655
0
1
2
3
4
5
6
-1
-0.5
0
0.5
1
1.5
2
Log(Fe II blue / Fe II vis)

Figure 5

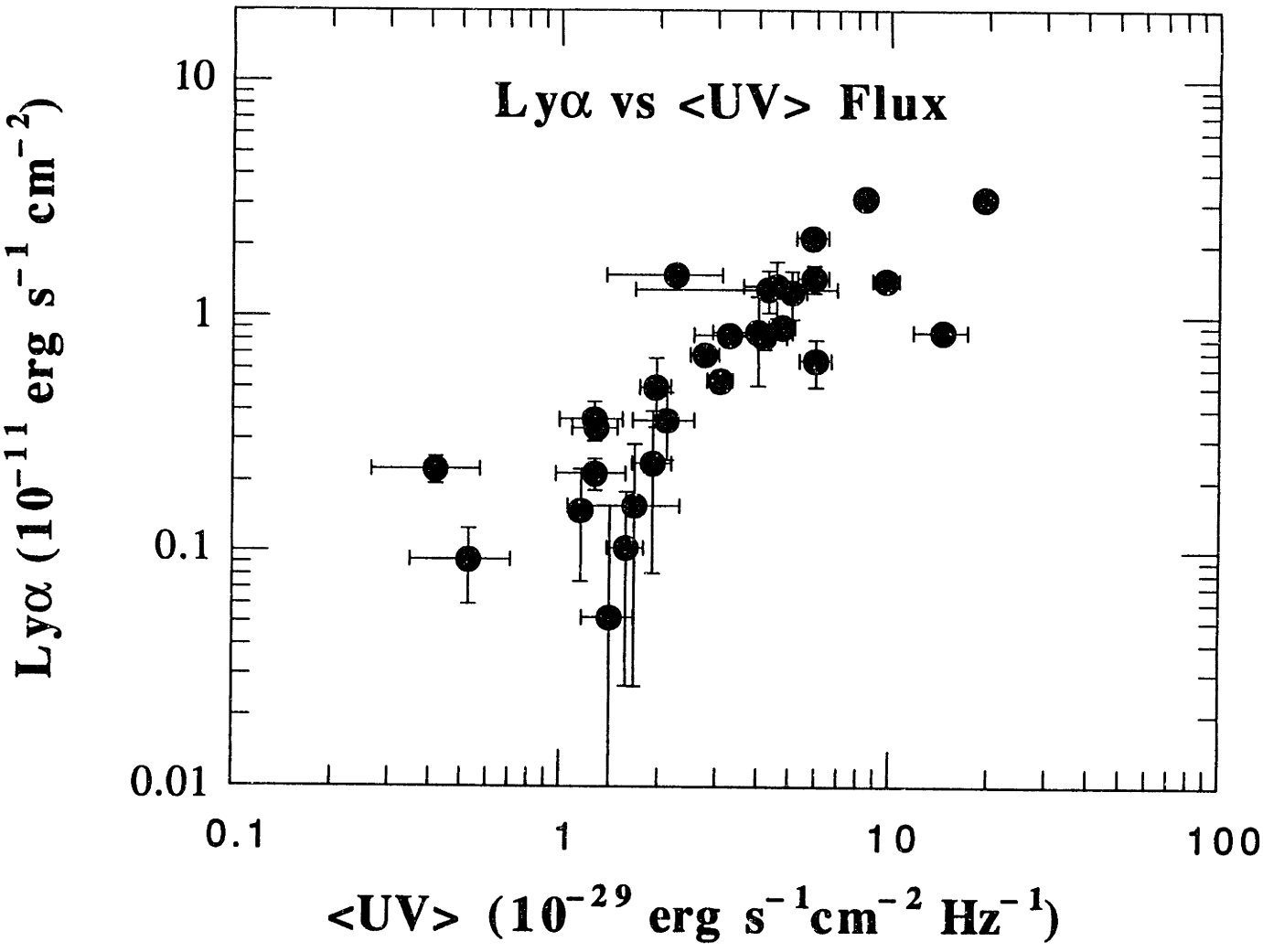
Lyα vs <UV> Flux
Lyα (10^{-11} erg s^{-1} cm^{-2})
<UV> (10^{-29} erg $s^{-1}cm^{-2}$ Hz^{-1})
10
1
0.1
0.01
0.1
1
10
100

Figure 6a

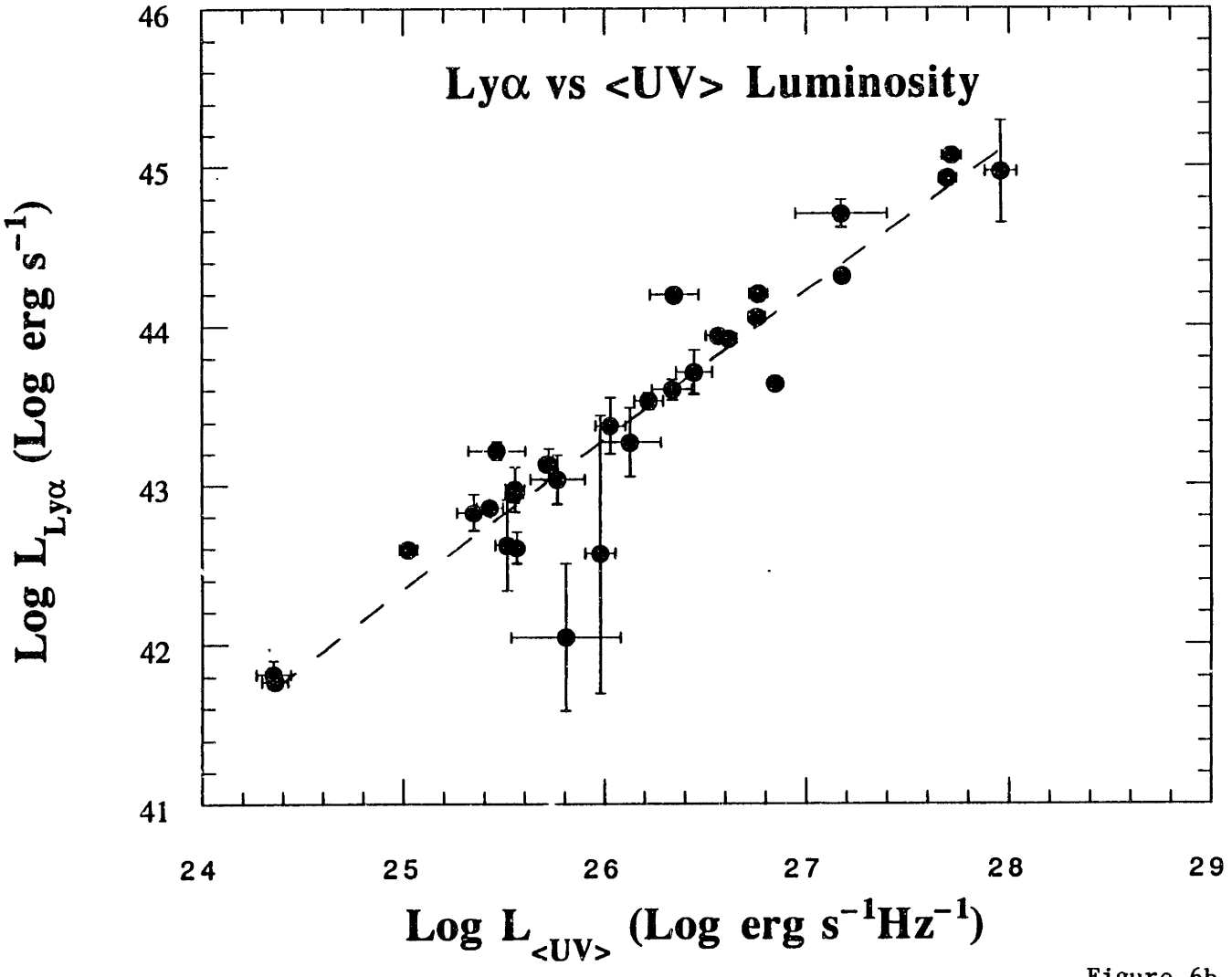
Lyα vs <UV> Luminosity
Log $L_{Ly\alpha}$ (Log erg s^{-1})
Log $L_{<UV>}$ (Log erg $s^{-1}Hz^{-1}$)
46
45
44
43
42
41
24
25
26
27
28
29

Figure 6b

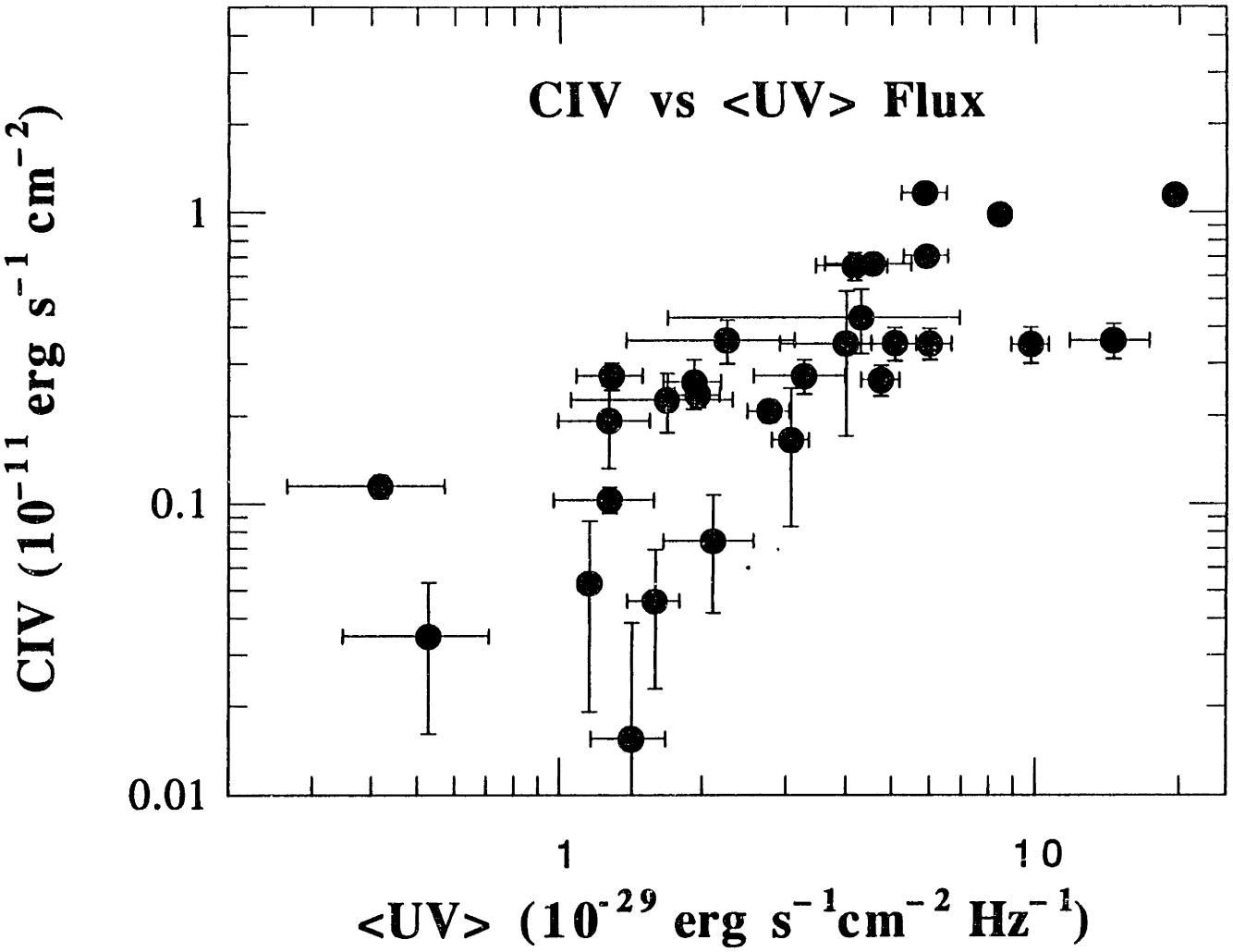
CIV vs <UV> Flux
CIV (10^{-11} erg s^{-1} cm^{-2})
1
0.1
0.01
1
10
<UV> (10^{-29} erg $s^{-1}cm^{-2}$ Hz^{-1})

Figure 6c

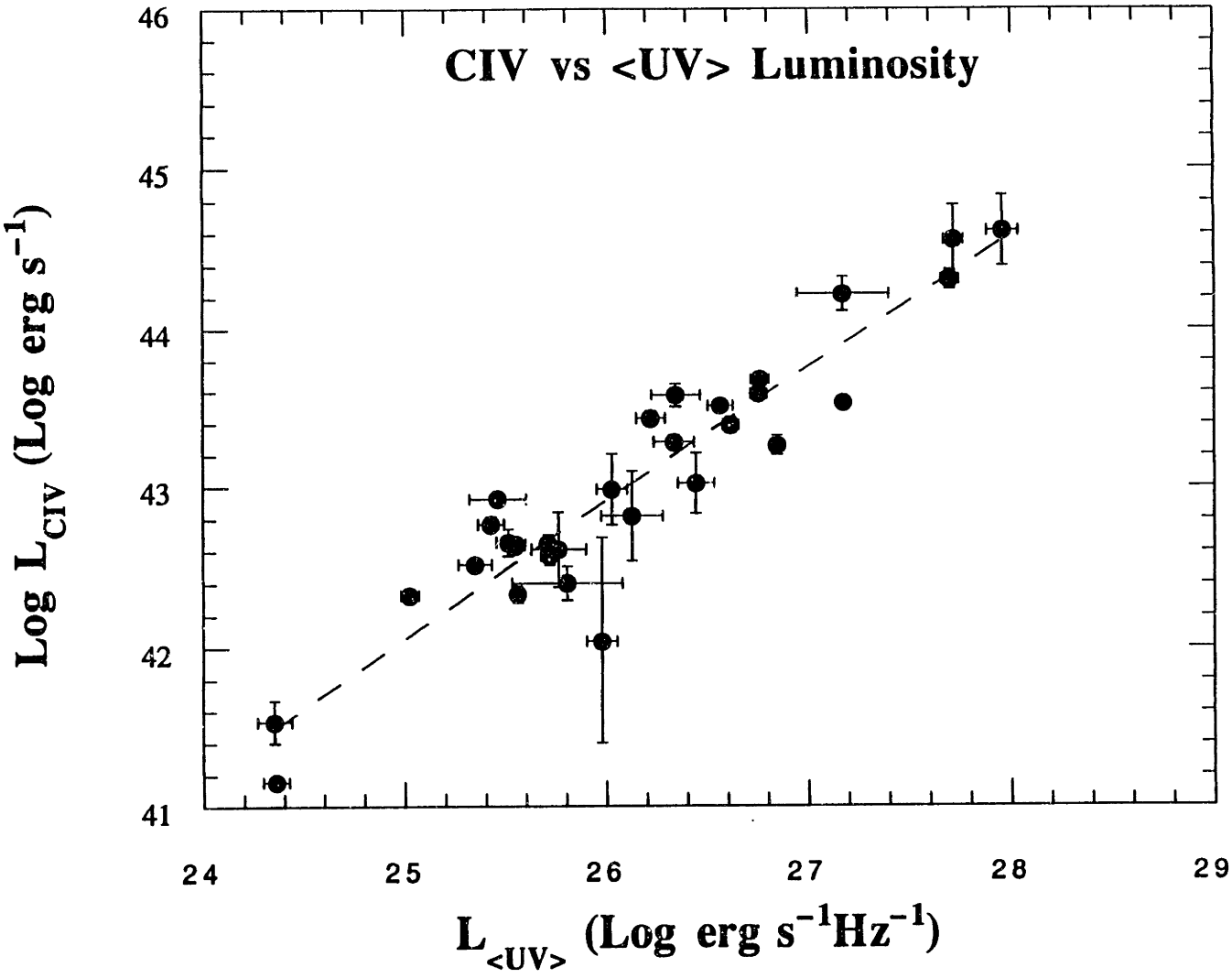
CIV vs <UV> Luminosity
Log L_{CIV} (Log erg s^{-1})
$L_{<UV>}$ (Log erg $s^{-1}Hz^{-1}$)
46
45
44
43
42
41
24
25
26
27
28
29

Figure 6d

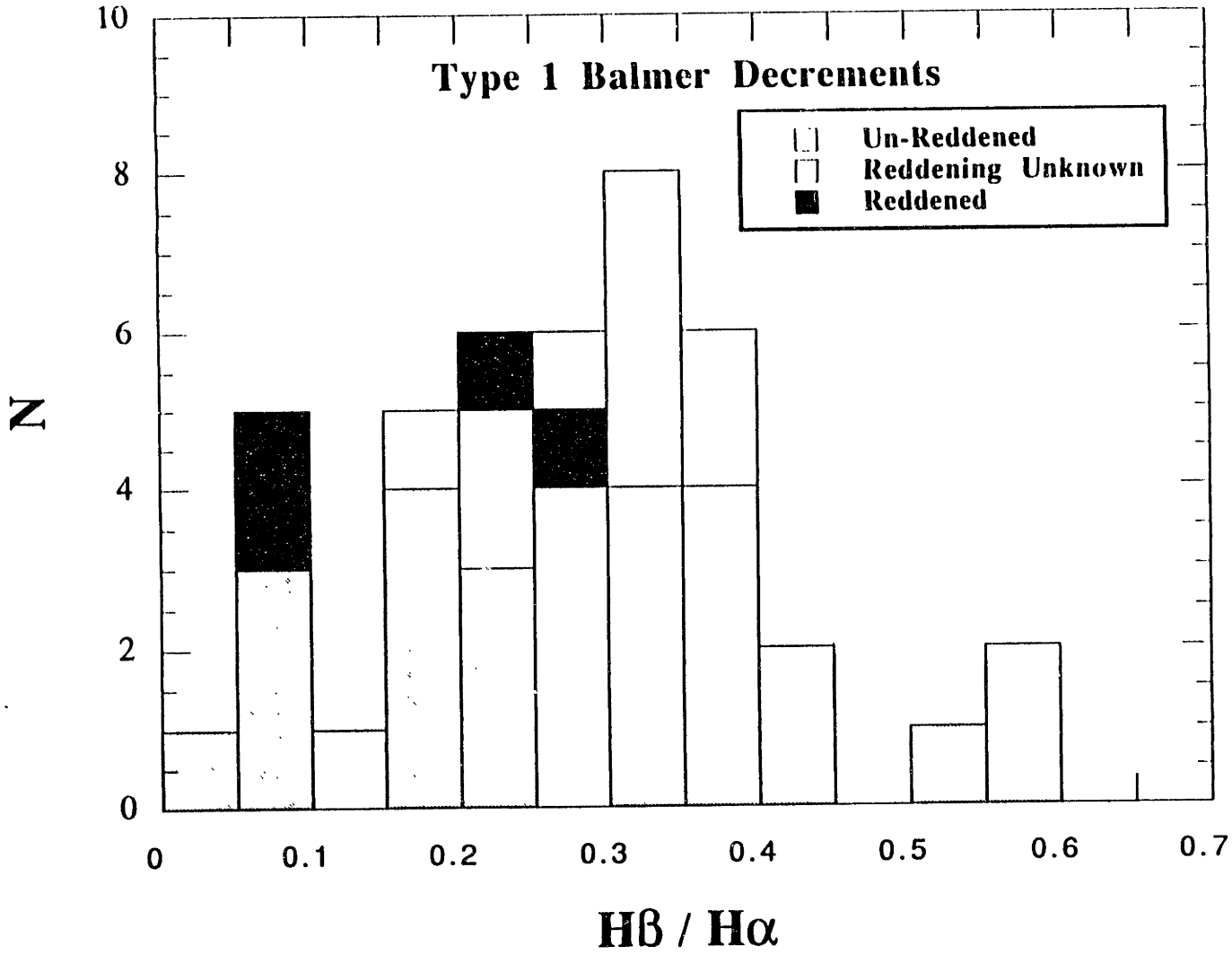
Type 1 Balmer Decrements
Un-Reddened
Reddening Unknown
Reddened
N
Hβ / Hα
0
2
4
6
8
10
0
0.1
0.2
0.3
0.4
0.5
0.6
0.7

Figure 7a

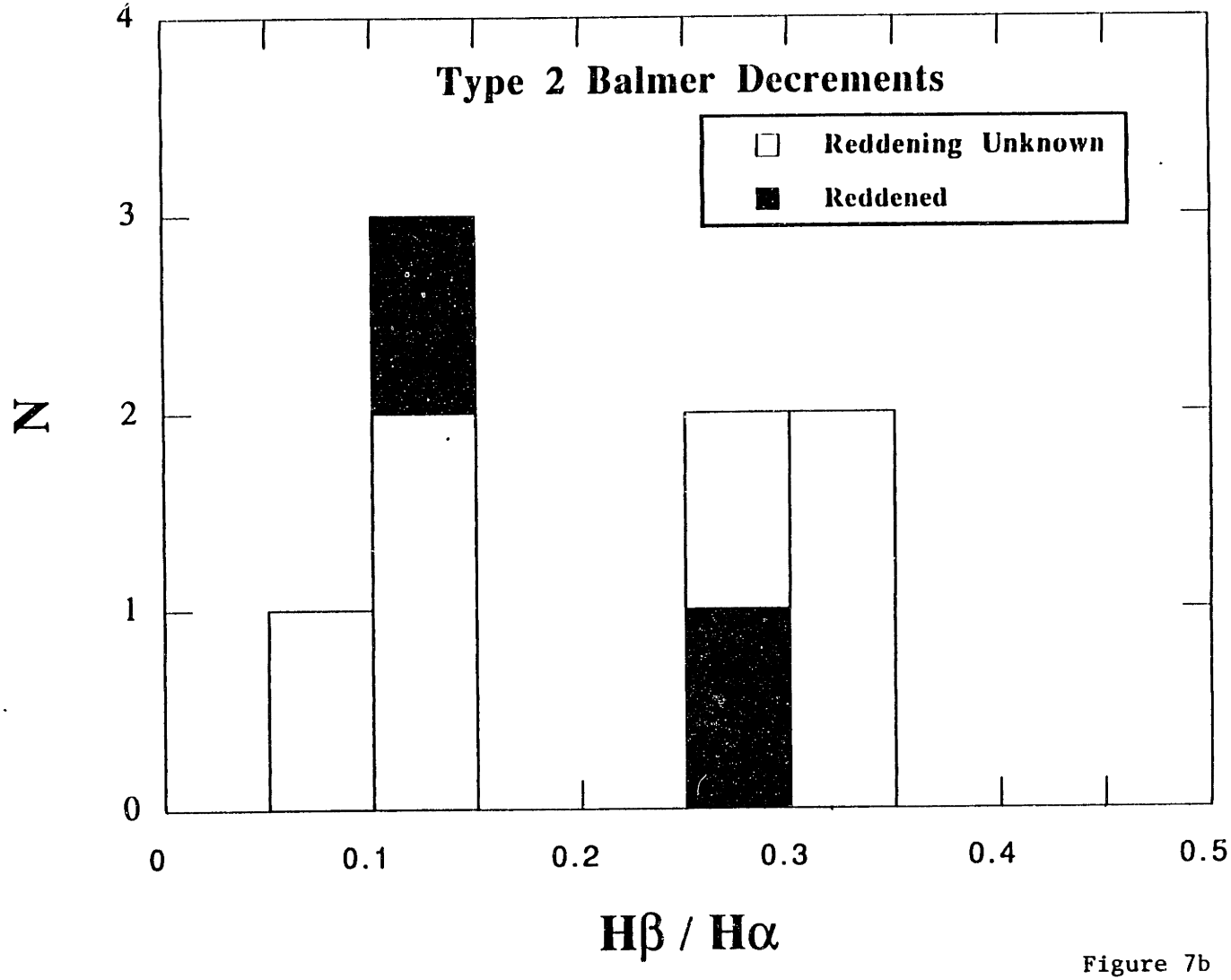
Type 2 Balmer Decrements
Reddening Unknown
Reddened
N
0
1
2
3
4
0
0.1
0.2
0.3
0.4
0.5
Hβ / Hα

Figure 7b

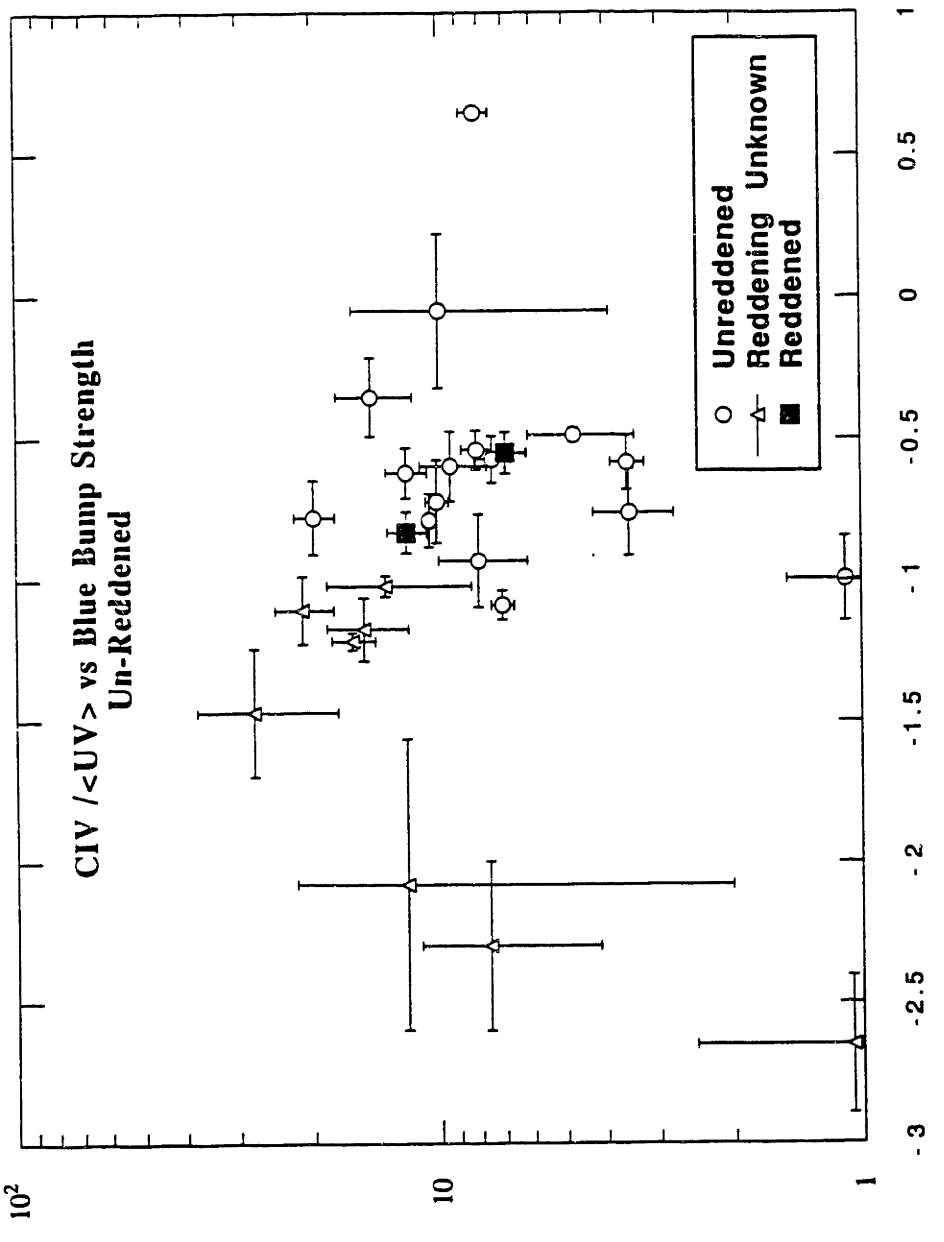
CIV /<UV> vs Blue Bump Strength
Un-Reddened
Unreddened
Reddening Unknown
Reddened
CIV / <UV>
α_{J-UV}
10^2
10
1
1
0.5
0
-0.5
-1
-1.5
-2
-2.5
-3

Figure 8

CHAPTER 6: AGN VARIABILITY

In this chapter, reports of variability are reviewed, and the use of variability to determine emission region sizes is discussed. A limited sample of repeated measurements in the Near IR, Optical, UV and X-Ray are presented, including original X-ray observations using the Ginga LAC instrument, in order to characterize the variability of the sample. Finally, the impact of variability on the remainder of this work is assessed.

(Note that the values $H_0 = 70$ km s^{-1} Mpc, $q_0 = 0.5$ are used throughout this work.)

1. INTRODUCTION

Observations of variability can give information about the emission processes and the spatial dimensions of AGN. Emission components at different frequencies may be associated if their variability is in concert. Spatial relationships between emission regions may be inferred by time lags between the components. Accretion disk instabilities are thought to have signatures detectable as time variability (White and Lightman, 1990). Variability may therefore contain information about accretion disk structure. Variability is often used to infer emission region size scales, but caution must be exercised in making and interpreting such measurements, as discussed below. Extremely rapid variations in luminosity can show that relativistic motion of emitting material occurs in the AGN.

While observations of variability can give useful information on a variety of AGN topics, it can also cause problems for the interpretation of multi-frequency spectra and

correlations. If the data for these spectra and correlations are not obtained simultaneously, as is the case for most of the objects in this sample, large relative variability could distort the shape of the spectra or degrade correlations that are present with simultaneous data. In this chapter, variability is investigated using a sample of repeated optical and UV measurements, some repeated X-ray measurements, and reports of variability from the literature. The observed and reported variability measurements are used to assess the impact of variability on the remainder of this work, and to investigate several of the topics given above.

1.1 Size Scale "Measurements" From Variation Time Scales

Under normal conditions, the size limit of an emission region may be derived from the variation time scale. Consider a spherical ball of radiating plasma. If the plasma suddenly changes in luminosity, the observed time for the variation is limited by the light travel time across it. For a radiating sphere of diameter l, $\Delta t \geq l/c$, where l is the diameter of the plasma, and the size limit is therefore:

(1.1.1) $$l \leq c\,\Delta t\,.$$

This relation suggests that the shortest time scale for any luminosity variation gives the size of the emission region, with some variation for non-spherical geometry.

There are some conditions where the limit given in (1.1.1) does not apply. If the emission is not uniform, for example, if only a small part of the emission region changes in luminosity, then the variation time scale will give the size limit appropriate for only a small part of the emission region. However, for reasonable physical conditions (including Eddington-limited accretion for significant fractions of the total emitting area), it can be argued that emission is *roughly* uniform throughout the emitting volume. Given this assumption, large amplitude variations would generally involve large fractions of the emitting region. For these reasons, emission-region size estimates should only be derived from large amplitude ($\gtrsim$ 100%) variations in flux.

If the emitting material is traveling at relativistic velocities, the emission will be relativistically beamed; this process causes difficulty in the estimating the emission region size from the variation time scale. Relativistic motion compresses the variation time scale, and if beaming is accompanied by changes in the direction of motion of the emitting material, apparent luminosity changes can be observed when no variation actually occurs. The measured time scales for beamed emission depend strongly on the velocity of the emitting material and the viewing angle; they are weakly or not at all dependent on the emission region size. (See Urry 1988 for a more detailed discussion of beaming.) Evidence will be presented below that beamed X-ray emission has been observed in a "normal" AGN. If beamed X-ray emission is common in "normal" AGN, then emission region size estimates based on X-ray variation time scales may not be correct.

A technique now referred to as "echo mapping" uses variability to measure size scales in a more sophisticated way than using the variability time scale directly. In this technique, cross correlations are used to determine a time lag between variations in the continuum flux (assumed to originate at small radii) and those of a re-processed signal, such as the flux from an emission line. The time lag is associated with the radius at which the line emission originates. Using this technique, Gaskell & Sparke (1986) determined that there are at least two significantly separated broad line emission regions. (See Chapter 5 for more discussion of these findings.) The echo mapping technique has not yet been applied to continuum emission regions.

1.2 Characterizing Variability

Studies of X-ray light curves from long, uninterrupted observations, show that their power density spectra (PDS) are similar to that of noise with amplitude $\propto \nu^{-\alpha}$, where ν is the frequency, and α is frequently near -1 (Urry 1991). Two well-studied examples are NGC 4051(Lawrence *et al.* 1987) and 1H1408–031 (NGC 5506; McHardy and Czerny 1987). Such light curves, often characterized as "flicker noise", will not have a well

defined mean. Further, the longer such a source is observed, the larger the maximum amplitude of variability that will be observed. At frequencies corresponding to the shortest time scales the power approaches zero. The frequency where the spectrum turns over and approaches zero roughly corresponds to the emission region size, if beaming is not important. A turnover in the power density must also occur at the low frequencies, so that the power does not diverge. AGN monitored for ≥ 10 years do not show tendencies for the X-ray and optical variability amplitudes to continue growing with additional observations, suggesting that the low-frequency cutoff has already been observed (Urry 1991).

In other wave bands, fewer PDS have been reported, but a very extensive observing campaign of 1H1415+255 (NGC5548; Malkan, 1991) shows that the UV and optical PDS are proportional to $\nu^{-\alpha}$ with $\alpha \leq -2$, and the most complete samples of optical data shows the basic characteristics of flicker data very clearly (e.g. Smith *et al.* 1991). Power-law PDS could be common in all wave bands. Obviously, an object with this type of spectrum is poorly described by only one or two observations, or by an rms variability of samples of objects. Observations with sufficient signal to noise, long baseline, and regular sampling that are optimal for PDS are available for only a few AGN, however. Therefore, a few repeated observations of one or a sample of sources should not be ignored, however, the limitations of such observations must be kept in mind when they are interpreted. In particular, the time between repeated observations (i.e.what Fourier component is being sampled) and the statistical interpretation of these observations must be considered. To this end, when available, the time scale and the number of observations used will be emphasized in variability reports, and at the very least, long and short time-scale variability will be discussed separately.

1.3 Previous Observations of AGN Variability

The longest wavelengths have generally been characterized to have the weakest variability for AGN (Urry 1988). Radio variability is observed most often in compact cores of radio-loud sources. The most radio-variable extragalactic objects are "pure blazars", defined here to be objects with compact radio cores, significantly polarized radio and optical emission, and relatively smooth, concave-upwards spectra from radio through at least the NIR bands (Urry 1988). Blazars are a poorly defined class of variable extragalactic objects which includes BL Lacs and Optically Violently Variable quasars (OVV's). A "non-blazar" is defined to be an object that lacks significant polarization, that does not have the spectral shape above, and that does not regularly vary at large amplitude. Some objects, including 1H1226+022 (3C273), may show some weak blazar-like tendencies. This object shows more variability than most AGN, and the variability is correlated over several decades in frequency, as occurs in blazars, but the spectrum is clearly non-blazar. It is possible that such objects may have a mix of pure-blazar and non-blazar components (Urry 1988). (Generally there is an absence of optical polarization in the LMA objects; Brissenden 1989.) The models for the pure-blazar multi-frequency continuum differ from those of non-blazar AGN in that pure-blazar spectra are smooth and can be modeled by synchrotron related processes (Urry 1988), while AGN spectra require a mix of thermal and non-thermal components.

Non-blazar AGN do not produce the variability seen in blazars at radio frequencies, and so they may be said to generally vary less than factors of two over time scales a few years (Kellermann & Pauliny-Toth 1981). Significant variability has not been observed in radio-quiet sources, but this may be a consequence of measurement difficulties. Few long wavelength IR repeated observations have been made, but variability is not expected at $\geq$ 60 μm since this emission is associated with cool galaxy dust distributed over galaxy-sized distances (See Chapter 4).

With UBVRIJHK photometry, Cutri *et al.* (1985) found that for most quasars, the amplitude of variability increased with frequency, and was negligible at 2.2 μm. In general, the Near IR was found to remain constant, while the optical frequencies varied. (1H1226+022, 3C273, showed variability from K through U in concert, but this AGN is atypical, showing some blazar-like characteristics. Note, however, that Courvoisier *et al.* 1987 found the variability in this object for wavelengths longer than 5 μm to be uncorrelated to that at shorter wavelengths, and of smaller amplitude.) A four year monitoring program of optically selected PG quasars showed that only 10% vary more than a factor of 30% in the optical (Keel 1990). Other studies of optically selected AGN confirm this result (see Huang, Mitchell and Usher 1990 for a study of quasars, Hamuy and Maza 1987 for a study which includes Seyferts and quasars). Lyutyi (1977) suggests that short time scale (~ 10 days) variability (<~ 0.12 mag) may be different in quasars and Seyferts, and that variation characteristics may be related to luminosity. In the optical, the average range of variability of a large sample of quasars has been reported to increase with observing time from ~0.8 mag after two years of monitoring to ~1.5 mag after 10 years; the range of variability levels off after 10 years (Smith *et al.*1991).

An excellent, brief review of IUE variability is given in the introduction of Kinney (1991). All studies find UV variability ubiquitous. Kinney (1991) found that 35% of all quasars and high luminosity AGN observed by IUE varied by a factor of 2 or more. The variability of the CfA sample of six Seyferts observed repeatedly by IUE was analyzed by Edelson, Krolik, and Pike (1990). A fractional rms variation of 20–80% with a median of 22% was reported . The interval between observations for these results was irregular, and varied from a few days to over two years; the total length of the light curves was 5-12 years. Spectacular behavior has been reported in the literature for several individual objects; probably the largest of these reported a change of a factor of 20 in the UV continuum flux of 1H0122–590 (Fairall 9) in six years (Koratkar and Gaskell, 1989).

Large amplitude (~factor of two increase from the long term average flux value) variability is present in several AGN on time scales ≥ 6 months in hard X-rays (Tennant and Mushotzky 1983). In a survey of 48 AGN including both hard and soft X-ray measurements (Turner & Pounds 1989), approximately seven objects were reported to have hard X-ray variability greater than a factor of two. Variability of factors of 3 up to a maximum of a factor of 4 was reported in only four objects in the hard X-rays. In general, large amplitude variability was reported in the soft bands below 2 keV, without accompanying hard X-ray variations, and was associated with variable absorption. In a wider literature survey, reports of variability of factors of 3 or greater in the hard X-rays are very rare.

Large amplitude (>~ factors of 2), rapid variability (time scales $\leq 10^4$ s) events, which are of interest for emission region size estimates, have been reported, but are statistically rare in AGN (Trinchieri 1990). The shortest time for a hard X-ray variation of greater than a factor of two in a non-blazar AGN, less than 100 s, was reported for NGC 6814 (Tennant, 1991).

A significant relation between the minimum observed variation time scale and the quiescent luminosity has been reported (Barr & Mushotzky 1986) in AGN (defined here to be non-blazar emission line AGN). The lowest luminosity objects tend to have the shortest minimum time scales. The measurements in this report are mostly >~ factors of 2 variations observed in the hard X-ray band (a few are extrapolated from soft X-rays). This relationship contrasts with that for BL Lac objects, which show no relation of variation time scale and luminosity. The models of optically thick, pair-dominated plasmas given in Barr & Mushotzky (1986) yield a minimum variation time scale $\propto L^{-1}$, where L is the X-ray luminosity. However, the rapid variability of BL Lacs is not consistent with optically thick emission, and the steep X-ray slopes, if extrapolated to higher energies, are not

consistent with pair-dominated plasmas; therefore, these objects do not yield the relation of L and time scale observed for "normal" AGN.

2. VARIABILITY OF THE LMA SAMPLE

2.1 Characterizing the X-ray Variability of the Sample

The long term variablity of the LMA sample can be characterized by a comparison of the LMA 2-10 keV fluxes with those objects also observed by EXOSAT (reported in TP). A comparison of 27 objects observed by both the LASS and EXOSAT experiments shows that the average fractional rms deviation is 39 %, over a time scale of 6-9 years. The maximum rms deviation was 85% for 1H1210+393.

2.2 Post-HEAO X-ray Observations

1H2107–097

Two objects in the LMA (LASS/MC identified AGN sample) were observed in hard X-rays (in addition to their LASS measurement) as part of this investigation. The first object, 1H2107-097, is a low luminosity (3.65×10^{43} erg s^{-1}, 2–10 keV) Type 1 AGN that was identified as part of the LASS/MC identification program (H2106-099, Remillard *et al.* 1986). The object has an optical spectrum which shows moderate optical Fe II and high excitation emission lines including [FeVII] and [Fe X] (see optical spectra given in the appendix of chapter 5). The LASS instrument recorded a flux of $2.25 \pm 0.39 \times 10^{-11}$ erg $s^{-1}cm^{-2}$ (2-10 keV) during 1977 November 5-11, and a flux of $0.75 \pm 0.47 \times 10^{-11}$ erg s^{-1} cm^{-2} (2-10 keV) during 1978 May 3-9 (Wood *et al.* 1984, Remillard *et al.* 1986), for a decrease in flux of $1.5 \pm 0.61 \times 10^{-11}$ erg s^{-1} cm^{-2}. The object is one of the approximately 50 AGN discovered by the LASS as a bright X-ray source. A search of the HEAO-1 database showed that this object demonstrated one of the most significant suggestions of X-ray variability among these new sources. Our interest in X-ray variability on and AGN multi frequency spectra prompted Ron Remillard, Roger Brissenden, Hale

Bradt, and myself to undertake comprehensive, nearly-simultaneous spectral observations of the object.

X-ray measurements were taken of 1H2107-097 with the Ginga LAC instrument on 1988 May 18 and again during 1988 May 22–23. These observations were performed during a high background epoch, and were therefore not sensitive to small amplitude variations. Large amplitude variations (flare-like behaviors defined as those satisfying the following criteria: >1 consecutive point, >50% of the mean flux and > 2 sigma above the mean) on time scales from 128 seconds to one day are ruled out by our data. The Ginga fluxes are given in Table 1a. The results from May 18 and May 22/23 are each derived from approximately one day of satellite observations. Comparison of the two days of Ginga observations showed a change in flux of only $(-0.30 \pm 0.25) \times 10^{-11}$ erg s^{-1} cm^{-2} (weighted mean=1.50×10^{-11} erg s^{-1} cm^{-2}). The log slope (see Table 1b) changed from -0.80 ± 0.021 to -1.02 ± 0.096, only about 1.9 σ. The Ginga fluxes fall roughly in between the two HEAO fluxes (see Fig. 1a). The weighted mean Ginga measurement is within 2.5 sigma of either HEAO measurement, so large amplitude ($\gtrsim$ factor of two) variability between HEAO and Ginga measurements was not demonstrated.

This object displays little long-term variability in the UV ($\leq$ 10% over ~1 yr.) but more in the optical (31% over ~ 5 yr.) (See Fig. 1b. The data appear in Tables 3 and 5, discussed in the next section). No significant variations were observed in the Near IR in two repeated measurements. These observations are roughly consistent with typical AGN behavior, although the optical variability is greater than that observed in most AGN (in the upper ~10% of variability in optically selected AGN, according to Keel 1990).

1H0557-503

i. Observations

Another newly identified AGN, 1H0557–503 (PKS 0558–504, Remillard *et al.* 1986), was also observed with Ginga. The object is a radio-loud quasar with strong

optical Fe II emission. It shows negligible polarization (Brissenden 1989) and no significant optical variability (Remillard et al. 1992), and therefore cannot be considered a blazar or OVV quasar. A very steep (log slope = –1.31) soft X-ray spectrum had been found in previous EXOSAT observations, and IUE observations showed a very strong blue bump (Remillard *et al.* 1988). These results suggested that higher energy X-ray observations might show a spectral break between the steep low energy and the presumably flatter (log slope ≈–0.7) high energy X-ray components. If such a break were observed, the steep low-energy component could be attributed to the strong blue bump, but the break energy might be higher than could be explained by accretion disk models. Ron Remillard, Roger Brissenden, Hale Bradt, and I undertook a multi-frequency, nearly-simultaneous observing campaign during 1989 November to attempt to observe this break simultaneously with a strong blue bump.

The object was observed with the Ginga LAC instrument during November 13–14 1989 (UT) (These observations are also reported in Remillard *et al.* 1991, 1992b). The data were reduced by me at the Institute for Space and Astronautical Science, Japan. The reduction of the data is discussed in chapter 2, Observations and Data Reduction. Optical and UV observations of the object were also made during part of the X-ray observation period.

A comparison of the Ginga and EXOSAT fluxes shows that 1H0557–503 demonstrates long term X-ray variability of a factor of 2.06 in observations ~ 5 years apart. The 2–10 keV integrated flux changed from $(2.62 \pm 0.15) \times 10^{-11}$ erg s^{-1} cm^{-2} on 1984 Oct. 17-18 to $(1.27 \pm 0.1) \times 10^{-11}$ erg s^{-1} cm^{-2} (approximate 1 σ equivalent error given) on 1989 Nov. 13-14, 2–10 keV. Optical monitoring showed variations of < 8 % of the mean flux in V band during the entire 5 year period. Equally small changes in the IUE flux were detected in observations ~2 years apart (see discussion and tables in UV section for more details).

A spectacular, rapid X-ray flare was also observed during the Ginga observation. Figure 2a shows the light curve for part of these observations at 128-s time resolution. The gaps in the data are due to normal interruptions of observations, including, but not limited to, passage through high–background regions of the orbit, such as the SAA. The flare is shown in an expanded scale, at 64-s resolution in Figure 2b. From Nov. 13 23:00 to Nov. 14 02:30 UT, "Level A", the average count rate was 6.83 ± 0.11 cts/s (counts per second), excluding the flare. The object then produced a rapid flare beginning at 01:09 with a roughly triangular profile, peaking at 12.90 ± 0.78 cts/s at 01:12 (a rise time of <~ 200 s). After the peak, the flux descended somewhat more slowly until a pre-scheduled interruption of observations (reduction of the detector high voltages during the readout of the spacecraft's star tracking cameras) at 01:18. The decay of the flare is roughly consistent with the rise, however, the full decay is not seen due to the data interruption (see Fig. 2b). The significance of the peak bin is 7.8 σ above the Level A average count rate. To conservatively judge the change of amplitude and time scale, however, the flare peak can be compared with the immediate pre-flare flux, 7.73 ± 0.30 cts s^{-1} (the average of seven 64 s points just before the flare). The flare peak is 6.2 σ above the pre-flare rate; the integrated flare (01:09–01:18, eight 64 s points) is more than 8 σ above this level. These observations suggest that the luminosity of the object changed at a rate of about $3.2 \pm 0.5 \times 10^{42}$ erg s^{-2} during the flare. This flare is therefore unusual in an observation of a non-blazar object because of its rapid time scale, large amplitude (an increase of 68% from the region just before the flare to the peak), and the large inferred value of the rate of change of luminosity.

Because of the rarity of such an event, alternative sources of the flare must be addressed in detail. A similar discussion is given in our paper Remillard *et al.* (1991). The flare was detected in each of the 8 detector modules of the LAC separately, which argues against failure or anomalies in one or a few modules. Further, X-rays below 10 keV are

expected to be absorbed in the top layer of each detector, and only a small fraction should pass through to the middle layer. At the time of the flare, a modest increase in the middle layer count rate was recorded (4.1 σ), consistent with that for an X-ray source with the quiescent spectral shape measured for the target quasar.

Both the particle rejection design of the LAC detectors and the lack of unusual particle activity levels during the flare further assure that the flare signal was due to X-rays, not particle events. The LAC detectors are gas filled proportional counters, and so can detect particle events. Charged particles with high energies are effectively dealt with by use of an anti-coincidence detector layer. Most such particles will penetrate all layers of the detector, while X-rays will interact in only a single layer. The anti-coincidence electronics thus eliminate most particle events by rejecting all events which occur nearly simultaneously in the anti-coincidence layer. The Particle Intensity Monitor (PIM), the count rate of four shielded wires in each detector (used in anti-coincidence), showed no anomalous activity (Fig. 2a). If the flare were associated with a non-X-ray event, an increase in the PIM count rate of ~ 1 count/s compared to the pre-flare rate would be expected. The All Sky Monitor X-ray detector and the Gamma Ray Burst Detector on board the Ginga spacecraft both have much larger fields of view than the LAC instrument. These detectors both showed no abnormal variations during the flare.

The SUD background monitor showed no unusual activity during the flare (see Fig. 2a). The SUD count rate is that in the highest energy channels (> 37 keV) and has been shown to be a good indicator of the background counting rates at all LAC energies (Hayashida *et al.*). If the flare were associated with a background event, a SUD increase of ~ 6 counts/s would be expected. No such increase in the count rate is observed. Further, in 210 LAC observations of source-free fields, with identical background subtraction techniques, no events that resembled the intensity and short time scale of the flare were found.

Low energy electrons within the earth's magnetosphere can cause spurious X-ray events. The LAC field of view (1° × 2° FWHM) was ~ 155° from the local magnetic field direction, while electron trajectories are expected to be close to 90° from the magnetic field. This situation effectively excludes the possibility of electrons entering the detectors and mimicking X-rays (Hayashida *et al.* 1989). A check of available monitors of particle and geomagnetic activity in the earth's neighborhood was made to determine if any unusual activity occurred at the time of the flare. The IMP-8 satellite recorded an increase in the density of the solar wind at a distance of 30 Earth radii just before the flare, but other monitors within the Earth's magnetosphere, where the Ginga satellite operates, showed no unusual activity at the time of the flare (Coffey 1989, 1990).

Finally, consider local sources of X-rays. Solar X-rays could not have been the source of the flare, as the LAC detectors were shielded from the sun by the earth at the time of the flare, and because the quasar was more than 30° from the earth's limb. In addition, the LAC field of view did not include any auroral zones (including the SAA) during the flare, which can be sources of X-rays. Taken together, all the observations presented above strongly suggest that the flare is a genuine celestial X-ray event.

Could the event have come from an unknown source, not 1H0557–503? Consider other celestial objects known for rapid variability. Stars with active coronae have been observed to flare in X-rays with time scales of minutes (but with 10 – 30 % amplitude) to hours for dMe stars (Ambruster, Sciortino, and Glub 1987), and from hours to days for RS CVn stars (Schwartz *et al.* 1981). However, previous observation by the EXOSAT LE imaging instrument yielded no other detections (in the 0.2–2 keV band) within ~ 1° of the target quasar (Remillard, Schwartz, and Brissenden 1988). Further, the spectral characteristics of the flare are quasar-like, not star-like (See Table 2). Figure 2c shows the total spectrum in an interval of 360 s surrounding the flare. The net flare spectrum (Flare minus Level A) is similar to the quasar's quiescent spectrum, but with poorer statistics

(shown in Fig. 2d). A fit to the net flare spectrum (see Table 2), however, still requires T > 6.3 keV at 90 % confidence for a fit to a thermal bremsstrahlung spectrum, much hotter than that expected for dMe stars (Schwartz, 1981, Haisch, 1983). One flare has been observed from a dMe star (H0449–55) at a higher temperature (10–17 keV), but the time scale for this flare was three hours, and strong soft X-ray emission from the object is detected in quiescence by the EXOSAT LE (Griffiths 1979). A power law fit to the net flare spectrum yields a log slope consistent with that for the quiescent spectrum, –0.75 with 90% confidence errors of +0.27 and –0.31 . This log slope also confirms the X-ray origin of the flare, as particle events (entering through the front window) typically have a log slope ≥ 0. The quasar is therefore very likely to be the true source of the flare.

ii. Implications

The large amplitude of the flare suggests that it could be used to determine the size of the X-ray emission region. If the flare were not due to beamed emission, the emission region radius would be estimated to be $r \leq c\,\Delta t / 2 \approx$ 100 light –seconds, or 3×10^{12} cm. Now, however, compare this to the size of the emission region derived by assuming isotropic accretion and radiation. If the average luminosity is within the Eddington limit, that is, if radiation pressure does not make accretion impossible, then the quasar would have a black hole mass given by:

(2.2.1) $$M_{BH} \geq L_{ave}\,\sigma_T / (4\pi G\, m_p\, c)$$

where M_{BH} is the mass of the (putative) black hole, σ_T is the cross section for Thomson scattering, G is the Gravitational constant, m_p is the mass of the proton, c is the velocity of light, and L_{ave} is the average bolometric luminosity of the quasar. However, the Schwarzschild radius, R_S, of a black hole of this mass is

(2.2.2) $$R_S = 2\,G\,M_{BH} / c^2 \gtrsim 2.4 \times 10^{13}\ \text{cm}$$

assuming L_{ave} is $\gtrsim 20\ L_X$, which was estimated from the observed multi-frequency spectrum from radio to ~ 25keV. This is a factor of 8 larger than the maximum size of the

emission region inferred above. As light cannot escape from within R_S, a logical paradox ensues.

A more detailed treatment of this problem incorporates the time scale for photon diffusion out of a blob of accreting matter (Fabian 1986). In this description of the problem, fewer geometric constraints are required, but a similar paradox occurs. Let R be the radius of a roughly spherical blob of accreting gas. Assume the blob produces a rapid, energetic flare by converting gravitational energy into radiation. Assume Thomson scattering dominates all scattering processes. The optical depth for scattering is then $\tau = R\ \sigma_T\ n$, where n is the electron density. $M \approx m\ n\ (4/3)\ \pi R^3$ is the mass of the blob, where m = the average mass per electron, approximately the mass of a proton for cosmic-abundance material. The time for the photons to diffuse out of the gas depends on the optical depth of the gas as given below:

First consider the case for optically thin emission, $\tau << 1$. In this case, scattering has a negligible effect, and photons escape at the speed of light. The time for the typical photon to escape, Δt, is given by:

$$\Delta t \approx R/c \approx 1/c \left(\frac{M}{m\ n \frac{4\pi}{3}}\right)^{1/3} . \qquad (2.2.3)$$

The conversion of gravitational potential energy to luminosity can be parameterized in terms of the fraction of the particle rest mass energy converted to luminosity, η. In this case, $\Delta L = \eta\ M\ c^2 / \Delta t$. The rate of change of luminosity is then given by:

$$\frac{\Delta L}{\Delta t} = \frac{\eta\ M\ c^2}{(\Delta t)^2} \propto \eta\ M^{1/3}\ n^{2/3} \qquad \tau<<1 \qquad (2.2.4)$$

Next consider the case where the emission is optically thick, $\tau >> 1$. The mean free path is then given by $1 / (\sigma_T n)$. The photons will then "random walk" out of the blob between scatterings. The number of scatterings, N, experienced by the average photon is

then given by the relation $R \approx N^{1/2}/(\sigma_T\ n)$. The average distance traveled by the photon is then $N/(\sigma_T\ n)$, and the time for the photons to diffuse out of the blob is given by:

(2.2.5) $$\Delta t \approx N/(c\ \sigma_T\ n).$$

Eliminating N gives:

(2.2.6) $$\Delta t \approx \frac{\sigma_T\ n\ R^2}{c} = \frac{\sigma_T\ n}{c}\left(\frac{M}{m\ n\ \frac{4\pi}{3}}\right)^{2/3}.$$

The rate of change of luminosity is therefore given by:

(2.2.7) $$\frac{\Delta L}{\Delta t} \approx \frac{\eta\ M\ c^2}{(\Delta t)^2} \propto \eta\ M^{-1/3} n^{-2/3} \qquad \tau >> 1$$

For the optically thin case, equation (2.1.4), $\Delta L/\Delta t$ increases with mass or density. For the optically thick case, equation (2.1.6), $\Delta L/\Delta t$ decreases with mass or density. The maximum of $\Delta L/\Delta t$ will therefore occur at $\tau \approx 1$. In this case, $R = 1/(\sigma_T\ n)$ and $M \approx 4/3\ \pi\ m\ \sigma_T^{-3}\ n^{-2}$. The expression for $(\Delta L/\Delta t)_{max}$ is then given by:

(2.2.8) $$(\Delta L/\Delta t)_{max} = \eta\ m\ c^2/\Delta t^2 = 4/3\ \pi\ \eta\ m\ c^4/\sigma_T \approx \eta\ 2 \times 10^{42}\ \mathrm{erg/s^2},$$

where the proton mass was used for the average mass per electron. For most models, η cannot be larger than a few tenths (Fabian 1986). For the 1H0557–503 flare, η would be ~2, which is impossible.

The paradoxes above do not apply if the apparent change in luminosity is due to relativistically beamed emission. This mechanism can large distortions of apparent luminosity changes compared to those actually occuring at the source. Similar arguments to those in the preceeding paragraphs have been used to suggest beaming of X-rays from BL Lac nuclei and Optically Violently Variable (OVV) quasars. It should be noted that observations of superluminal motion in the cores of AGN radio sources (Barthel 1989) imply that relativistic motion has been observed in a more direct manner in the radio bands.

This flare is one of the most dramatic examples of rapid variability observed in AGN's. Pure blazars are the most variable class of extragalactic objects. This class,

defined in the introduction, include BL Lacs and some OVV quasars. BL Lacs are distinguished by their featureless continuum which lacks emission lines. One BL Lac object, H0323+022, has shown a 30 s "dip" in X-rays which yields $\Delta L / \Delta t =\sim 5 \times 10^{43}$ erg s^{-2} (Feigelson *et al.* 1986). Some OVV quasars are pure blazars, but this classification requires only that the objects demonstrate unusual variability. The OVV quasar 3C 279 demonstrates a classic "pure-blazar" continuum (Makino *et al.* 1989, 1991), and superluminal motion (Unwin 1989), another trait associated with many pure blazars, but significant polarization has not been reported. Previously 3C279 (Makino *et al.* 1989) was the only non-BL Lac object believed to demonstrate beamed X-ray emission (with the possible exception of LB9743, Matilsky, Shrader, & Tananbaum 1982). The flux of 3C279 was observed to increase by 20 % in 45 minutes (Makino *et al.* 1989) giving $\Delta L / \Delta t \geq 2.9 \times 10^{42}$ erg s^{-2}. The flare in 1H0557–503, with a dL / dt value of approximately 3.2×10^{42} erg s^{-2}, is therefore most surprising because such behavior is normally restricted to pure blazars, and if 3C279 is not a pure blazar, then to BL Lacs and OVV quasars. The 1H0557–503 flare is the largest (inferred) value of dL / dt yet observed in a non-blazar AGN, and the shortest time scale, large-amplitude event ever observed in any quasar.

2.3 UV Sample

To investigate the UV variability of the LMA, the IUE public archives were searched for repeated measurements of LMA objects. Only measurements with a reasonable signal to noise ratio (average UV continuum flux / noise > 2.5) were accepted. The UV continuum measure used to investigate variability is the same as that used previously for correlations and J–UV slopes, the average of three bands, 1290–1360, 1425–1520 and 1700–1860Å in the AGN rest frame. The bands were chosen to avoid contamination by emission lines including Fe II and Balmer continuum emission. The UV continuum measurements for the 19 LMA objects with acceptable sectra are given in Table

3, along with the observation dates. To characterize variability, the weighted mean flux change between consecutive measurements is given, expressed as a fraction of the weighted mean of all measurements. The maximum change between observations (also as a ratio to the weighted mean flux) is also given for objects with three or more observations. The time scale given is the time in years between measurements. The time scales between measurements varied from 0.1 to 4 years, but the majority of the measurements were separated by 1 to 3 years. Note that weighted mean changes are, numerically, conservative, as they will give much lower numbers than are commonly reported in the literature. For example, when "factor of 2" variability is reported in the literature, this usually means that a source was observed to double in flux, usually in only two measurements. The average flux change between consecutive measurements normalized by the weighted mean flux would be 0.67 in this case, assuming equal errors for the two measurements.

The distribution of UV flux change normalized by the mean flux is given in Figure 3, and shows significant UV variability in the LMA sample. The median fractional change is 0.29. The distribution falls off from a maximum at zero, and half of the objects change by $\geq \sim 0.35$ times the weighted mean flux. More than a quarter of the objects with repeated observations have an average variation above 0.5. The maximum fractional variation of 1H2303–089, 6.3, is much larger than the maximum variation of other objects, and is of high signficance (4.5 σ). The maximum UV variations are all of the same order as the average variations (see Table 3). This behavior suggests that the majority of variable objects probably vary often on time scales of ~ few years, rather than being inactive between large, but rare, flares.

Although significant large amplitude variability is evident in these measurements, the times between these measurements are too long to yield interesting emission region size estimates. The characteristic radius of UV emission from a hypothetical accretion disk is ~

3–30 times the Schwarzschild radius, or 10^{14}–10^{15} cm (~$3 \times 10^{4-5}$ light s.) for large black holes (Urry 1988). The minimum time interval between observations in this sample is $\gtrsim$ 10^{-1} yrs. or $\gtrsim$ 10^{6} s.

The correlation plot of UV variability vs L_X, Figure 4, shows no correlation. The correlation probabilities, given in Table 4, verify the lack of correlation of both the average and maximum UV variations with L_X.

No significant relation of UV variability with radio loudness is observed (see Table 4). The Spearman and Pearson probabilities show no evidence for a correlation between mean variation and radio loudness .

2.4 Optical Sample

The repeated optical measurements are given in Table 5, with the average and maximum deviations defined as above for the UV data. The intervals between optical measurements are fairly short, with most in the range of 0.35 to 1.25 years. The median fractional deviation is 0.11. The histogram of optical data, Figure 5, does show substantial variability, although it is clear that the UV data are more variable. The distribution also appears to be of a different character from the UV data. Where the UV variability distribution seemed to fall off smoothly with amplitude, the distribution of optical variations is flatter, with a peak at ~0.07. Because of the small number of objects in the distribution, however, the peak variability is not well constrained.

The correlation plot of V band variability vs L_X, Figure 6, shows no obvious correlation. The Spearman probability (Table 4) also indicates no correlation. No indications of a correlation of radio-loudness and optical variability are evident, and this is confirmed by the correlation probabilities given in Table 4.

There may be some increased tendency for optical variability in the LMA compared to optically selected samples, since 40% of the objects in the repeated observation sample are observed to have > 30 % measurement to measurement variation. The typical

measurement error is ≤ 4 %, much smaller than this variation. This incidence of > 30 % variation is more common than indicated in the study by Keel (1990). A simple picture where X-ray selected objects are uniformly highly variable across the spectrum is not appropriate, however. For example, 1H0557–503, an X-ray variable object, has been observed optically many times with only minimal variability (<0.07 times the mean flux). These time scales are of little interest in terms of emission region size estimates, as the observations are separated by a minimum of ≥ one month, corresponding to a size scale much larger than that normally attributed to continuum emission.

3. DISCUSSION

3.1 Does Variability Affect the Conclusions in Other Chapters?

Because non-simultaneous data are used in this study, significant variability could change the shape of the multi–frequency spectra presented in Chapter 4. Further, the lack of correlations between different frequency bands discussed in Chapters 4 and 5 might be misleading if variability significantly affected the correlations. The correlations would be affected if the sources varied more between observations at the different frequencies than the correlation spread.

The typical value of the fractional variability was ~40 % in the X-rays in 6-9 years, ~ 30% in the UV over 1-3 years, and ~10 % in the optical over ~ 1 year. These values are much smaller than the typical spreads of 1/2 to 1 decade observed in the luminosity correlations in the previous chapters. If one may assume that the typical changes reported here are similar to those between the LASS and other observations (i.e. that variation amplitude is not a very strong function of the time between observations in the range of 1-12 years), this suggests that most of the spread in the correlations is intrinsic, not due to variability, and that variability is not a significant problem in interpreting the correlations in previous chapters. Even variations much larger than typical are not a problem for the interpretations given in previous chapters. The literature reviewed above, the X-ray

comparisons, and the optical observations of the LMA showed that changes from observation to observation by a factor of 2 (or ~ 0.7 in the ratio to the mean) are rare in all bands except in the IUE band. Even variations of factors of two are still small compared to the 1/2 to 1 decade spreads in the correlations, so the correlations are very robust against variability. Such variations would not cause major difficulties in the interpretation of the multi-frequency spectra of individual objects either. The reddening and starlight diagnostics used in Chapter 4 depended on the shape of the NIR and optical bands, and are not sensitive to their relative normalizations. The interpretation of the multi–frequency spectra also generally emphasized shapes in each region (e.g. 60–100 μm slope, falling or rising optical or IUE shape), rather than relative strengths of widely separated frequency bands. Further, the few measures that addressed relative strength between bands (e.g. radio / optical "loudness" and radio / X-ray "loudness") were also not sensitive to factor of two variations, as the dynamic range of these measurements were factors of 10^4 or more. The notable exception of a comparison between bands which is sensitive to variability is the J–UV log slope, α_{J_UV}, because of the large amplitude of the observed UV variations compared to those in the J band.

3.2 Different Variability In Different Frequency Bands

The object 1H1210+393 shows variability (Ulrich *et al.* 1991) that suggests that its α_{J_UV} value during weak states might be less than –1. Observations in the NIR for this object demonstrate minimal NIR variability, even between epochs of significant UV variability (Bassani *et al.* 1986). The NIR flux may therefore be assumed to be constant. If the UV flux (defined in Chapter 4) of 1H1210+393 decreased by a factor of 2 in its low state, as suggested by the measurements in Ulrich *et al.* (1991), compared to the 1982.3 value used in Chapter 4, the α_{J_UV} would then decrease from -0.90 ± 0.02 to $\sim -1.28 \pm 0.05$. This rough calculation suggests that 1H1210+393 might, at some epochs, exceed the apparent limit to the intrinsic IR-UV slope derived in chapter 4, $\alpha_{J\_UV} > -1$. However,

TP and Perola *et al.* (1986) have determined that the reported UV variation is due to variable absorption. The absorption is not an intrinsic property of the emission mechanism, and so the intrinsic α_{J_UV} may not be below the –1 limit.

The de-coupled variability documented in this object suggests that the NIR emission region is significantly separated from the UV and X-ray continuum regions. Perola *et al.* showed that nearly simultaneous observations in the X-ray and UV are well correlated, suggesting that both the UV and X-ray emission are simultaneously absorbed. The NIR emission must come from a different region than the UV and X-ray emission, as it is not occulted / absorbed by the material affecting the UV and X-ray emission. The NIR radiation might be reprocessed with a much longer time scale for variation than the UV radiation, or it might come from a different region entirely. A bump between ~ 2–12 μm would indicate thermal re-processing in a warm nuclear dust region, but none is observed in this object. There is therefore no evidence that thermal reprocessing from dust is de-coupling the variation of the NIR and that of the UV and X-ray components. In Chapter 4 it was argued that the NIR flux was mostly non-thermal in origin, and should come from a similar region to that of the non-thermal I–X underlying (~–1 log slope) component. The very different response of the X-rays and UV compared to that of the NIR in 1H1210+393 suggests a problem with this picture.

X-ray and optical time scales in 1H0557-503 are de-coupled in a similar manner to that in 1H1210+393. While X-ray observations show long term variations greater than a factor of 2, optical V band monitoring of the object over the same period yielded less than 10 % variability. In 1H0557-503, however, different optical and X-ray emission regions suggest themselves naturally within "standard" models. As usual, the variable X-ray emission is thought to come from a very small region close to the black hole. The optical emission is associated with the blue bump in this object, not the non-thermal continuum, as the bump dominates the optical through UV bands. The two IUE observations have shown

this blue bump to be remarkably steady (< 10% variation over approximately 2 years). The majority of the optical emission therefore probably arises from an unusually stable accretion disk, with a separate, and very long time scale for variation.

3.3 What are the Implications of Beaming ?

The evidence for X-ray beaming in a "normal" non-blazar AGN opens a Pandora's box of implications in all emission line AGN if quiescent emission can be beamed. How can the true (unbeamed) X-ray luminosity be measured? Are bands other than X-rays and radio beamed? What fraction of quiescent AGN emission in any given band is beamed? Is the relativistic Doppler factor, and therefore the angular anisotropy, similar in all AGN, or does it have a luminosity dependence? Models for the relative shapes and amplitudes of the multi-frequency AGN spectrum would also be affected by beaming of a significant fraction of the non-thermal continuum.

AGN density and luminosity functions could be significantly affected by beaming. If many AGN have beamed and un-beamed components, then flux-limited samples used to determine the luminosity function would be strongly biased toward beamed objects. The fraction of beamed objects oriented along the line of sight could be detected at much larger distances than those objects without beamed components. Alternatively, if beamed objects have little or no unbeamed (isotropic) emission, then only the objects oriented close to the line of sight could be detected. The magnitude of such a bias would depend on the angular size of the beam.

It should be noted that there is significant evidence that X-rays are normally not beamed. As discussed above, the IR and NIR X-ray variability is generally not correlated. However, the IR and NIR bands were shown in Chapter 4 to be correlated with X-ray luminosity. The good correlations obtained between X-rays and OIII luminosity in Chapter 5 also suggest that the X-ray continuum illuminates a farily large solid angle and that the observer sees a proportional level of flux as well.

In radio studies, beaming can be inferred by jet-like morphologies, by polarization, and by observation of superluminal motion. In other bands, beaming can only be inferred by observations of flares similar to that in 1H0557-503. The development of additional diagnostics for beaming at greater than radio frequencies would help elucidate the importance of beaming in the spectra of normal, quiescent AGN. Additional clues to X-ray beaming may lie in the steep X-ray spectrum of 1H0557–503 (an average log slope of –1.1 from 2-10 keV), which is rare among emission line AGN. Steep X-ray spectra (log slopes steeper than –1.0) are also characteristic of BL Lacs, many or which are believed to be beamed. Note, however, that 3C279, another object thought to demonstrate beamed emission (but not an LMA AGN), does not have a steep X-ray spectrum (Makino *et al.* 1989).

4.CONCLUSIONS

1. The quasar 1H0557-503 was observed to increase in X-ray flux by 67 % in about 200 s. This rapid X-ray flare yields an apparent value of dL / dt of 3.2×10^{42} erg s^{-2} ($H_0 = 70$ km s^{-1} Mpc^{-1}, $q_0 = 0.5$) which violates the efficiency limit for the conversion of gravitational potential energy to luminosity for unbeamed emission. Therefore, the flare is very likely to have originated from relativistically beamed emission, and demonstrates that beaming can occur, at least in the X-rays, in non-blazar AGN.

2. A significant implication of the beamed emission in 1H0557-503 is that an unknown fraction of the steady non-thermal flux from AGN could be beamed. Such a possibility would make the interpretation of luminosity measurements problematic. However, in Chapters 4 and 5 good correlations of X-rays and IR, NIR and [OIII] luminosity were presented, none of which generally vary together with X-rays. These results suggest that the effect of beaming on X-ray emission is limited to the scatter observed in these correlations, ~1/2 decade in luminosity.

3. A comparison of the LASS and EXOSAT (from TP) fluxes for LMA objects observed by both instruments yields an average fractional rms deviation of 39 % over a time scale of 6-9 years. The maximum rms deviation from this comparison was 85% for 1H1210+393. A wider search of the literature has shown that variations of factors of three or greater in non-blazar AGN in the hard X-rays are statistically rare.

4. A selection of repeated observations of LMA objects by the IUE satellite were used to investigate UV variability in the LMA. The typical time between measurements was 1-3 years. The UV distribution of changes in consecutive measurements relative to the weighted mean is broad, with a well defined peak at zero, tailing off smoothly to a maximum at 1.56. The median value is 0.29. The distribution of relative amplitude of UV

variability shows that large amplitude variability is common, consistent with previous studies.

5. A small number of repeated V band photometric measurements were used to characterize the optical variability of the LMA sample. The intervals between optical measurements are typically 0.35 to 1.25 years. The distribution of changes in consecutive measurements relative to the weighted mean is rather flat, but a peak is present below 10% of the weighted mean flux. The median value is 0.11. Forty percent of the sub–sample with repeated optical measurements vary more than 0.3 times the weighted mean flux; the maximum is 0.56 times the mean flux. If this small sub-sample of repeated optical measurements is representative of the total sample, it would suggest that X–ray selected objects are more optically variable than optically selected objects.

6. No obvious relationship of either UV or optical variability with either X-ray luminosity or radio loudness is observed. The UV and optical variability characteristics on time scales of six months to a few years are therefore similar for quasars and Seyferts, and for radio-loud and radio-quiet AGN.

7. Despite the fact that variability is commonly observed in AGN, there are only rare instances of variations that are greater than a factor of 0.7 relative to the mean (approximately a factor of two change between two measurements) in all bands except the IUE band. The typical variations are much smaller. The correlations in previous chapters, which cover several decades in luminosity and have spreads of 1/2 to 1 decade, would be unaffected by such small variability. Therefore, the observed levels of variability would have no effect on the majority of the conclusions in the previous chapters.

REFERENCES

Ambruster, C. W., Sciortino, S., and Glub, L. 1987, ApJS, 65,273

Barr, P., and Mushotzsky, R. F. 1986, Nature, 320, 421

Barthel, P. D. 1989, ApJ, 336, 606

Bassani, L., *et al.* 1986, ApJ, 311, 623

Bregman *et al.* 1986, ApJ, 301, 708

Brissenden, R., 1989, Unpublished Thesis, Mt. Stromlo Observatory, ANU.

Courvoisier T. J.-L., *et al.* 1987, A&A, 176, 197

Coffey, H. E.1989, ed., NOAA Solar-geophys. Data Prompt Reports, 544, 10

Coffey, H. E.1990, ed., NOAA Solar-geophys. Data Prompt Reports, 545, 138

Cutri, R. M., *et al.* 1981, ApJ, 245, 818

Edelson, R. A., Krolik, J. H., and Pike, G. F. 1990, ApJ, 359, 86

Feigelson, E., *et al.* 1986, ApJ, 302, 337

Griffiths, T. E. *et al.* in X-ray Astronomy (COSPAR), (eds Baity W. and Petersen, L.) p. 93, (Pergammon, New York, 1979).

Guilbert P. W. & Rees, M. J. 1988, 233, 475

Haisch, B. H. *et al.* 1983, ApJ, 267, 280

Hayashida, K., *et al.* 1989, Publ. Astr. Soc. Japan, 41, 373

Kellermann, K. I., and Pauliny-Toth, I. I. K. 1981, Ann. Rev. AA , 19, 373.

Keel, W.C., 1990, in Conference proceedings on Quasar and Blazar Variability, ed.s P. J. Wiita, H.R. Miller (Atlanta, Ga.)

Kinney, A. L., Bohlin, R.C., Blades, and J.C., York, D. G., 1991, ApJS, 75, 645

Koratkar, P., and Gaskell, M. C., ApJ, 345, 637

Kunieda, H., Turner, T. J., Awaki, H., Koyama, K., Mushotzsky, R., Tsusuka, Y. 1990, Nature, 345, 786

Lawrence, A., Watson, M. G., Pounds, K. A., and Elvis, M. 1987, Nature, 325, 694

Lyutyi, V.M. 1977 , Sov. Astron. 21(6), Nov-Dec

Malkan, M. A. 1991, in *Variability of Active Galsctic Nuclei* (Proceedings of the Georgia State Conference on AGN), ed.s Miller, H. R., Wiita, P. J., Cambridge, N.Y., N Y.

Makino, F. *et al.* 1991, in *Variability of Active Galsctic Nuclei* (Proceedings of the Georgia State Conference on AGN), ed.s Miller, H. R., Wiita, P. J., Cambridge, N.Y., N Y.

Makino, F. *et al.* 1989, ApJ, 347, L9

Matilsky, T., Shrader, C. and Tananbaum, H. 1982, 258, L1

McHardy, I., and Czerny, B., 1987, Nature, 325, 696

Netzer, H. 1990, in Active Galactic Nuclei, ed. Blanford, R. D., Netzer, H., Woltjer, L., Springer-Verlag, New York

Obrien, P. T., Gondhalekar, P. M., and Wilson, R., 1988, MNRAS, 233,801

Obrien, P. T., Gondhalekar, P. M., and Wilson, R., 1988, MNRAS, 233,845

Pounds, K. A., and Turner, T. J. 1986, in *Variability of Galactic and Extragalactic X-Ray Sources*, ed. A. Treves, (Milan: Assoc. Advanc. Astron.), p. 1

Remillard et. al., 1986, ApJ, 301, 742

Remillard, R., Schwartz, D. A., and Brissenden, R. J. 1988, in *A Decade of UV Astronomy with IUE* (Eur. Space Ag. spec. Pub. 281), p. 273

Remillard, R. A., Grossan, B., Bradt, H. V., Ohashi, T. , Hayashida, K., Makino, F., &Tanaka, Y. 1991, Nature, 350, 589

Remillard, R. A., Brissenden, R. J. V., Grossan, B., Bradt, H. V., Ohashi, T. 1992, (in progress)

Sadun, A., 1992, J. Roy. Astr. Soc. Can., 86,15

Schwartz, D. A. *et al.*, 1981, MNRAS, 219, 225

Smith, A. G., Nair, A. D., Clements, S. D. 1991, in *Variability of Active Galsctic Nuclei* (Proceedings of the Georgia State Conference on AGN), ed.s Miller, H. R., Wiita, P. J., Cambridge, N.Y., N Y.

Tennant, A. F., Mushotzsky, R. F, Boldt, E. A.,and Swank, J. H.1981, 251,15

Tennant, A. F., & Mushotzsky, R. F. 1983 ApJ, 264, 92

(TP) Turner, T. J., Pounds, K. A., 1989, MNRAS, 240, 833

Ulrich, M. -H., *et al.* 1984, MNRAS, 206, 221

Ulrich, M. -H., Boksenberg, A., Bromage, G. E., Clavel, J., Elvius, A., Pentson, M. V., Perola, G. C., and Sniders, M. A. J. 1991, ApJ382, 483

Unwin, S. C. *et al.* 1989, ApJ, 340, 117

Urry, C. M., 1991, in *Variability of Active Galsctic Nuclei* (Proceedings of the Georgia State Conference on AGN), ed.s Miller, H. R., Wiita, P. J., Cambridge, N.Y., N Y.

Urry, C.M., Kruper, J.S., Canizares, C.R., Rohan, M.L., and Oberhardt, M.R. 1986, in *Proceedings of the Conference on Variability in Galactic and Extragalactic X-Ray Sources*, (Held in Como, Italy, October 1986), ed. A. Treves, p. 15.

Urry, C.M., in Multiwavelength Astrophysics, Ed. France Cordova , (Cambridge Univ. Press), p. 279 (1988)

White, T. R. & Lightman, A. P., ApJ 1990, 352,495

Wood, K., *et al.*, 1984, ApJ Suppl., 56, 507

Zheng Ap. J., 324, 801, 1988.

Table 1a

1H2107–097 X-Ray Flux

Date	Instrument	F_X @ 5 keV (μJy)	2-10 keV Flux (10^{-11} erg s^{-1} cm^{-2})
1977 November 5–11	HEAO LASS scan 1	1.2 ± 0.2	2.3 ± 0.38
1978 May 3–9	HEAO LASS scan 2	0.39 ± 0.2	0.74 ± 0.38
1988 May 18.03 — 18.64 UT	Ginga LAC	0.77 ± 0.03	1.52 ± 0.059
1988 May 22.93 — 23.47 UT	Ginga LAC	0.60 ± 0.12	1.22 ± 0.24

Table 1b

X-Ray Spectra Fit Parameters

Parameter	1977 – HEAO	1978 – HEAO	1988 May 18 - Ginga	1988 May 22/23 - Ginga[a]
Coefficient 'A' (keV/keV-4000 cm^2-s)	...	...	16.5 ± 0.56	18.1 ± 2.93
α[b]	...	...	−0.80 ± 0.021	−1.02 ± 0.096
Fe Emission Center Energy(keV)	...	...	6.03 ± 0.27	6.33 ± 0.26
Equivalent Width (Å)	...	...	0.115 ± 0.049	0.133 ± 0.057
Log_{10} N_H(cm^{-2})	...	...	$<10^{21}$[c]	$<10^{21.9}$[c]
χ^2_ν[d]			1.04	1.19
Flux (μJy) at ~5 keV	1.2 ± 0.2	0.39 ± 0.2	0.77 ± 0.03	0.60 ± 0.12

Note: The symbol "±" refers to 90% one dimensional confidence limits.

[a]The observations on this day are considered to be of inferior quality due to poor background subtraction due to high background activity, and are included only for completeness. Note larger errors in power law slope and normalization compared to the May 18 spectrum.

[b]The X-ray energy exponent is defined by $F_\nu \propto E^\alpha$.

[c]Reduced χ^2 for 17 d.o.f.

[d]The Ginga fit values for N_H are unreliable, so only an upper limit may be given for the column density. This is due to two factors. First, the Ginga LAC is not sensitive to any column densities but those above 10^{21} cm^{-2} due to the poor low energy response of the detectors. Second, the Ginga analysis software does not allow asymmetric errors which are required by our data.

Table 2

1H0557–503 Spectral Fits

	[1]Log Slope	Normalization (counts cm^{-2} s^{-1} keV^{-1})	χ^2_ν	X-Ray Flux (erg cm^{-2} s^{-1}, 2–10 keV)
Level A (excluding Flare)	1.01 ± 0.07	6.2 ± 0.6	1.73	1.57×10^{-11}
[2]Flare Interval	0.92 ± 0.12	9.0 ± 1.5	1.25	2.64×10^{-11}
Level B	1.24 ± 0.08	6.2 ± 0.6	1.97	1.11×10^{-11}
[3]Net Flare (Power Law fit)	0.75 (+0.31, –0.27)	2.9 ± 1.3	0.93	
Net Flare (Thermal bremsstrahlung fit)	KT = 10.8 (+9.3 –4.5)	2.1 ± 0.42	0.90	

[1]All error bars are 90 % confidence intervals, varying one parameter at a time, with 29 degrees of freedom for the first three fits and 14 for the net flare spectrum. The χ^2_ν values for level A and B are inflated by the soft X-ray excess at $E \leq 2$ keV.

[2]The Flare interval consists of 360 s of data centered on the peak flux.

[3]Flare minus level A.

Table 3
Repeated UV Observations

Name	[1]<Change>	σ	[2]Δt (Max Change yrs.)	[3]Max Change	σ	[4]Time (yrs)	<[5]UV> (mJy)	σUV	[4]Time (yrs.)	[5]<UV> (mJy)	σUV
1H0122–590	0.33	0.16	4.01			82.13	15.42	1.68	86.14	11.23	1.16
1H0557–503	0.18	0.04	2.15			89.88	8.95	0.11	87.73	10.57	0.33
1H1135–372	0.38	0.34	5.00			78.34	3.92	1.22	83.34	5.80	1.09
[6]1H1210+393	0.23	0.61	3.83			78.11	14.62	3.01	82.31	13.49	0.19
1H1226+022	0.29	0.01	2.98	0.73	0.01	79.13	9.29	2.06	82.11	20.16	0.16
						85.14	15.86	0.11	87.01	15.86	0.15
						89.15	11.33	0.11			
1H1238–050	0.36	0.19	1.88			80.15	1.24	0.41	84.03	1.71	0.02
						87.35	2.58	0.55			
1H1350+696	0.53	0.08	2.92			78.34	1.27	0.35	84.12	5.67	0.10
						87.04	1.03	0.57			
1H1415+255	0.17	0.02	0.84	0.33	0.02	80.11	6.03	0.13	83.14	5.48	0.07
						85.13	3.98	0.06	86.20	3.98	0.06
						89.12	0.05	0.93			
1H1429+370	0.18	0.89	1.96			82.16	2.09	0.77	84.12	1.73	1.63
1H1530+585	0.13	0.27	0.90			84.12	1.95	0.37	85.02	2.22	0.42
1H1820+643	0.053	0.17	1.83			87.21	3.02	0.32	89.04	2.86	0.37
1H1858+797	1.10	0.21	3.82			80.34	0.57	0.05	84.16	0.25	0.02
1H1911–589	0.55	0.03	2.94			79.17	57.59	0.86	82.11	35.02	0.51
1H2041–108	0.48	0.02	3.93	0.81	0.04	78.16	4.00	1.09	79.15	10.55	0.16
						80.16	7.47	0.25	84.09	16.25	0.27
						89.13	8.88	1.17			
1H2107–097	0.076	0.32	0.95			88.45	3.27	0.71	87.50	3.03	0.72
1H2209–470	0.077	0.05	0.12			80.15	3.00	0.10	80.27	2.78	0.09
1H2251–179	0.25	0.27	2.75	0.45	0.41	78.36	2.25	0.87	79.36	2.53	0.05
						82.11	3.66	1.05			

1H2301+086	0.11	0.09	2.07	0.26	0.13	78.16 83.22	6.00 7.65	0.66 0.81	81.15	6.05	0.06
1H2303–089	1.56	0.55	1.01	6.31	1.39	79.35 83.36	14.53 3.33	2.75 1.18	80.36	1.98	0.05

[1]<Change> refers to the average change in flux between consecutive measurements divided by the weighted mean of all measurements.

[2]Δt_{max} refers to the time between observations, in years, where the maximum change was observed.

[3]Max Change refers to the maximum of all consecutive changes observed, divided by the weighted mean of all observations.

[4]Time gives the approximate time of the measurement following, in years of the 20th century.

[5]V gives the V band flux in mJy observed in the epoch given in the previous column. Where more than two observations were available for the same object, they continue in the next row.

[6]The data for 1H1210+393 (NGC 4151) shown here represent only a limited search of the publicly available IUE database as of approximately 1991, eliminating all low-quality data. Much more extensive multiple observations of the object exist, e.g. Ulrich *et al.* 1991. Variability as large as factors of ~7 over years and factors of 2 variation in days have been reported (Ulrich *et al.* 1991).

Table 4

Correlation Tests of Variability

X	Y	N	$R_{Spearman}$	$P(>R)\ 10^{-3}$	$R_{Pearson}$	$P(>R)\ 10^{-3}$
[1]Opt Variation	L_X	10	0.241	503	0.503	138
[2]Opt Variation, max	L_X	4	...	...	–0.272	728
[3]UV Variation	L_X	23	–0.149	497	–0.142	518
[4]UV Variation, max	L_X	8	–0.048	911	–0.217	605

[1]Opt Variation refers to the average change in V band flux between consecutive measurements divided by the weighted mean of all measurements.

[2]Opt Variation, max - the maximum variation between two consecutive measurements of the V band flux divided by the weighted mean flux.

[3]UV Variation refers to the average change between consecutive measurements of the average of three UV continuum bands centered at ~ 1300Å, divided by the weighted mean of all measurements. (See text for more specific definitions of bands.)

[4]UV Variation, max - as above, the maximum consecutive variation divided by the weighted mean flux.

TABLE 5

Repeated Optical Observations

Name	[1]<Change>	σ	[2]Δt_{max} (yrs.)	[3]Max Change	σ	[4]Time (years)	[5]V (mJy)	σV	[4]Time	[5]V (mJy)	σV
h0510+031	0.0646	0.026	0.82			86.08	4.23	0.079	86.9	4.51	0.084
h0523–118	0.138	0.016	0.8	0.243	0.028	84.75	3.78	0.07	86.1	4.39	0.082
						86.9	3.48	0.06	89.1	3.45	0.06
h0557–504	0.0489	0.017	0.38	0.064	0.026	86.92	3.52	0.065	87.3	3.30	0.061
						87.9	3.45	0.06	89.1	3.58	0.1
h1325–246	0.557	0.039	1.23			86.17	2.64	0.049	87.4	1.41	0.067
h1504+035	0.451	0.028	1.23			86.17	5.13	0.095	87.4	3.48	0.032
h1615+655	0.341	0.022	0.35			89.4	7.67	0.064	89.75	5.19	0.15
h1630+673	0.0652	0.014	0.02			89.42	3.77	0.03	89.4	3.53	0.04
h1703–013	0.080	0.039	0.37			89.67	1.63	0.09	89.3	1.50	0.04
h1811+670	0.073	0.062	0.34			89.36	1.89	0.043	89.7	[6]2.05	0.11
h2107–097	0.174	0.013	0.9	0.307	0.020	82.75	6.95	0.097	87.4	5.08	0.081
						87.5	5.52	0.08	88.4	5.04	0.07
						89.0	6.40	0.10	90.0	7.60	0.1

[1]<Change> refers to the average change in flux between consecutive measurements divided by the weighted mean of all measurements.

[2]Δt_{max} refers to the time between observations, in years, where the maximum change was observed.

[3]Max Change refers to the maximum of all consecutive changes observed, divided by the weighted mean of all observations.

[4]Time gives the approximate time of the measurement following, in years of the 20th century.

[5]V gives the V band flux in mJy observed in the epoch given in the previous column. Where more than two observations were available for the same object, they continue in the next row.

[6]These measurements were derived from measurements relative to a reference star in the object's field. No absolute measurements are available on this date.

FIGURE CAPTIONS

Figure 1. The optical V band and X-ray fluxes for 1H2107-097 are plotted as a function of time. The X axis units are the year of observation minus 1900. The X-ray fluxes from Ginga and HEAO-1 are consistent with negligible or no variability. The optical V band data shows substantial variation.

Figure 2. (a) The LAC top-layer background-subtracted count rate (1–11 keV), the SUD background count rate, and the Particle Intensity Monitor (PIM) count rate are plotted for 1H0557–503 as a function of hours UT on 13–14 November 1989. The data are presented in 128 s time bins. (b) The LAC count rate only is shown at 64 s resolution. (c) The Ginga 2–17 keV X-ray background-subtracted spectra for the Flare and Level A intervals are shown separately (see text for definition of intervals). (d) The net flare spectrum, the spectrum during the flare interval minus level A spectrum is shown. A power law fit to the net flare spectrum (see Table 2) shows that it is consistent with that for the quiescent spectrum of the object, suggesting that the flare originates from the quasar.

Figure 3. (a) This histogram of relative UV variation, the weighted mean change between consecutive observations divided by the weighted mean of observations, is given. Different symbols are used for different ranges of significance, the ratio of the variation to its error. A key to the symbols is given on the figure.

Figure 4. The average UV variation is plotted vs X-ray luminosity. No correlation is evident.

Figure 5. This figure gives the histogram of average optical V band variation, the weighted mean change between measurements divided by the weighted mean flux. All measurements are of high significance (<5% error).

Figure 6. The average optical V band variation is plotted vs X-ray luminosity. No correlation is evident.

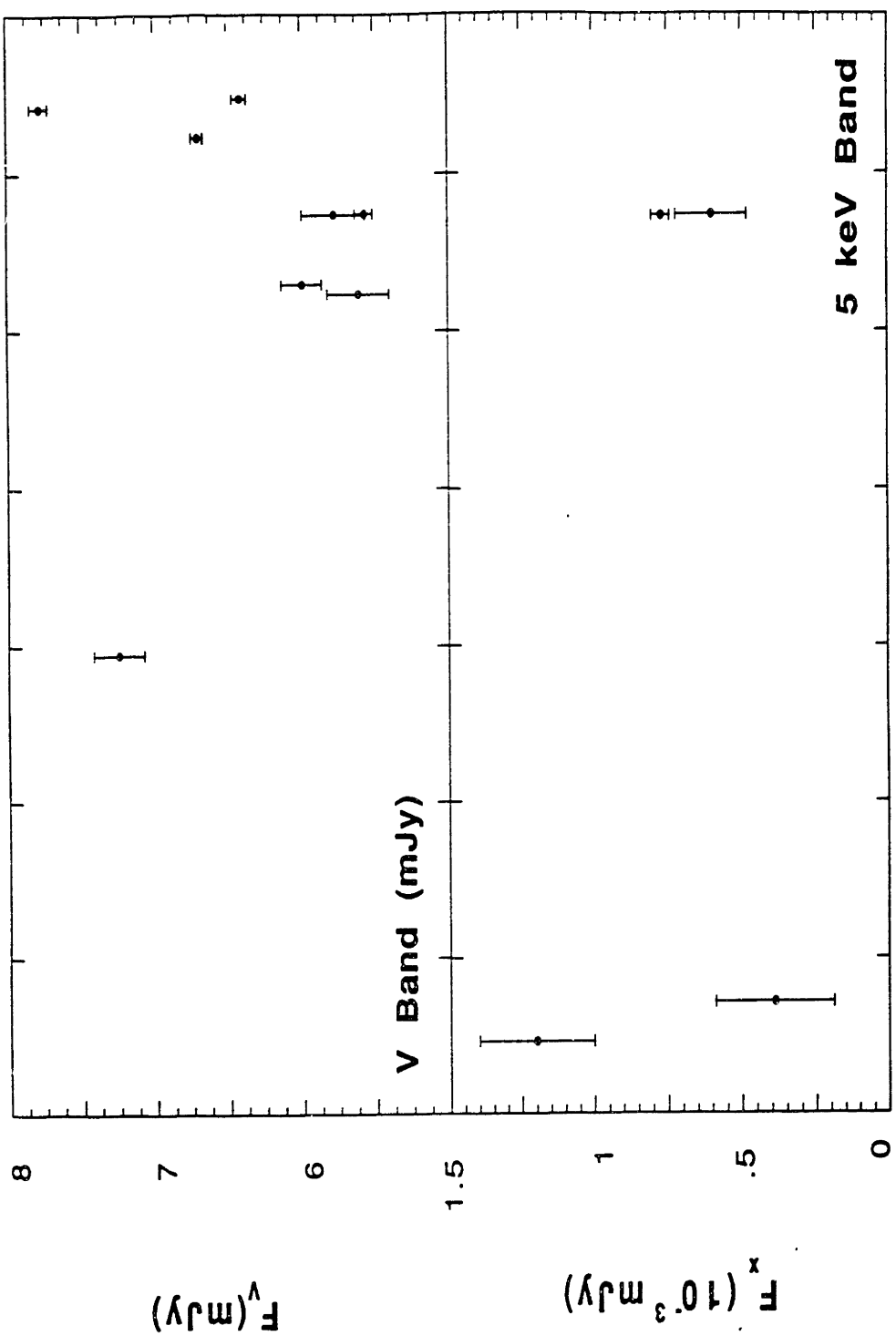

Figure 1

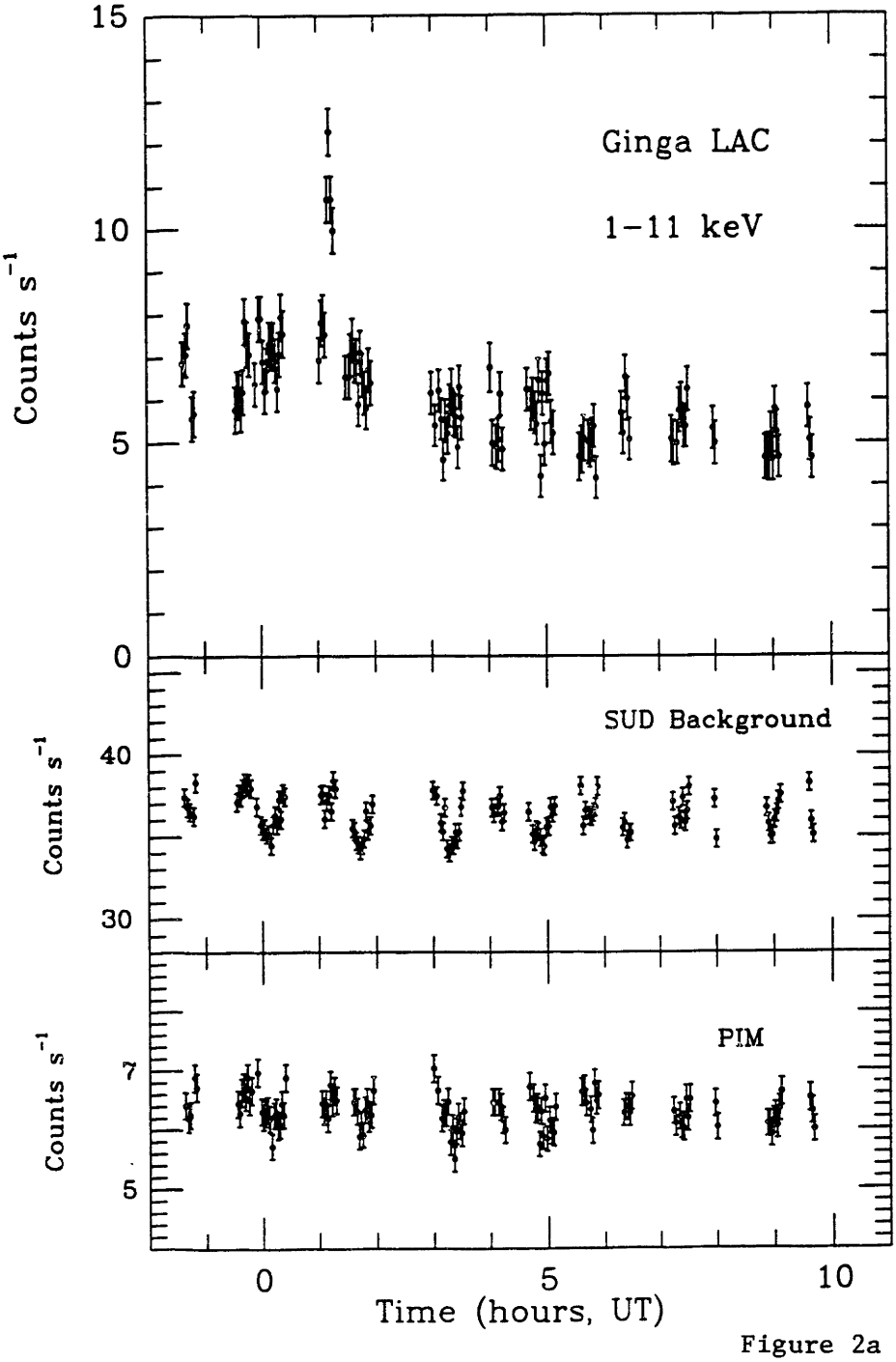

Figure 2a

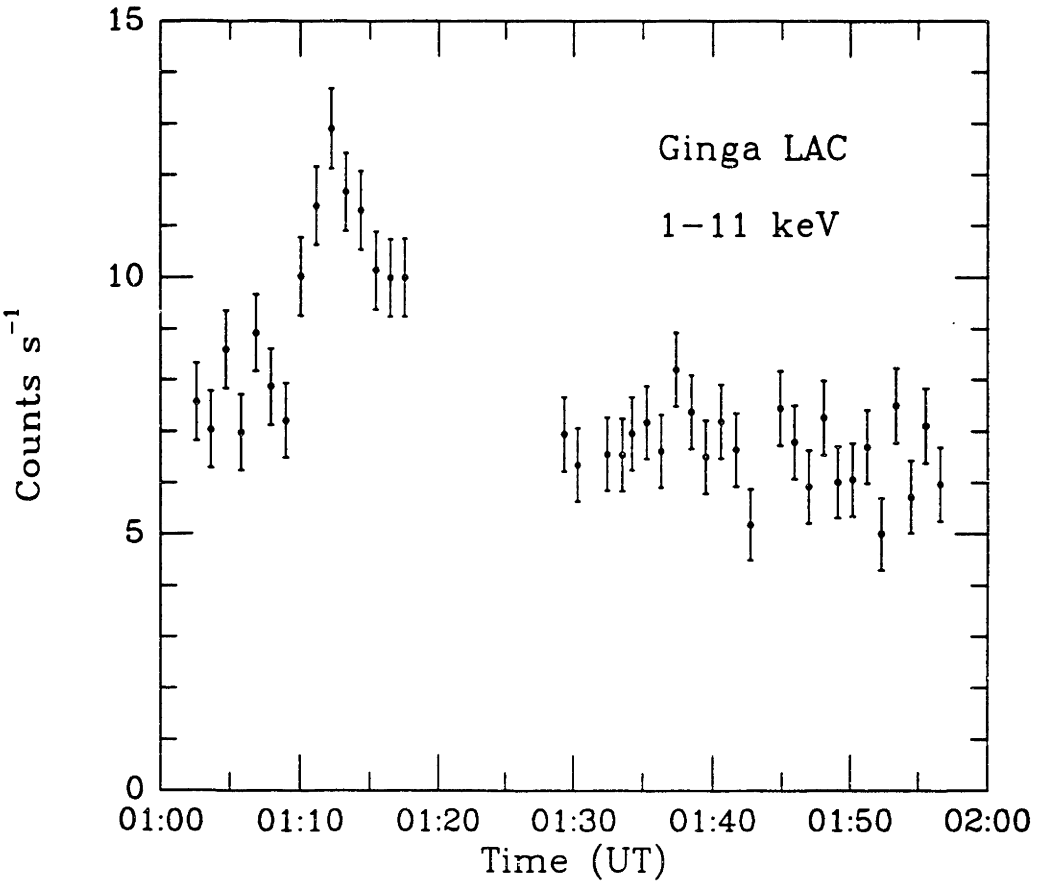
Ginga LAC
1−11 keV
Counts s^{-1}
Time (UT)
0
5
10
15
01:00
01:10
01:20
01:30
01:40
01:50
02:00

Figure 2b

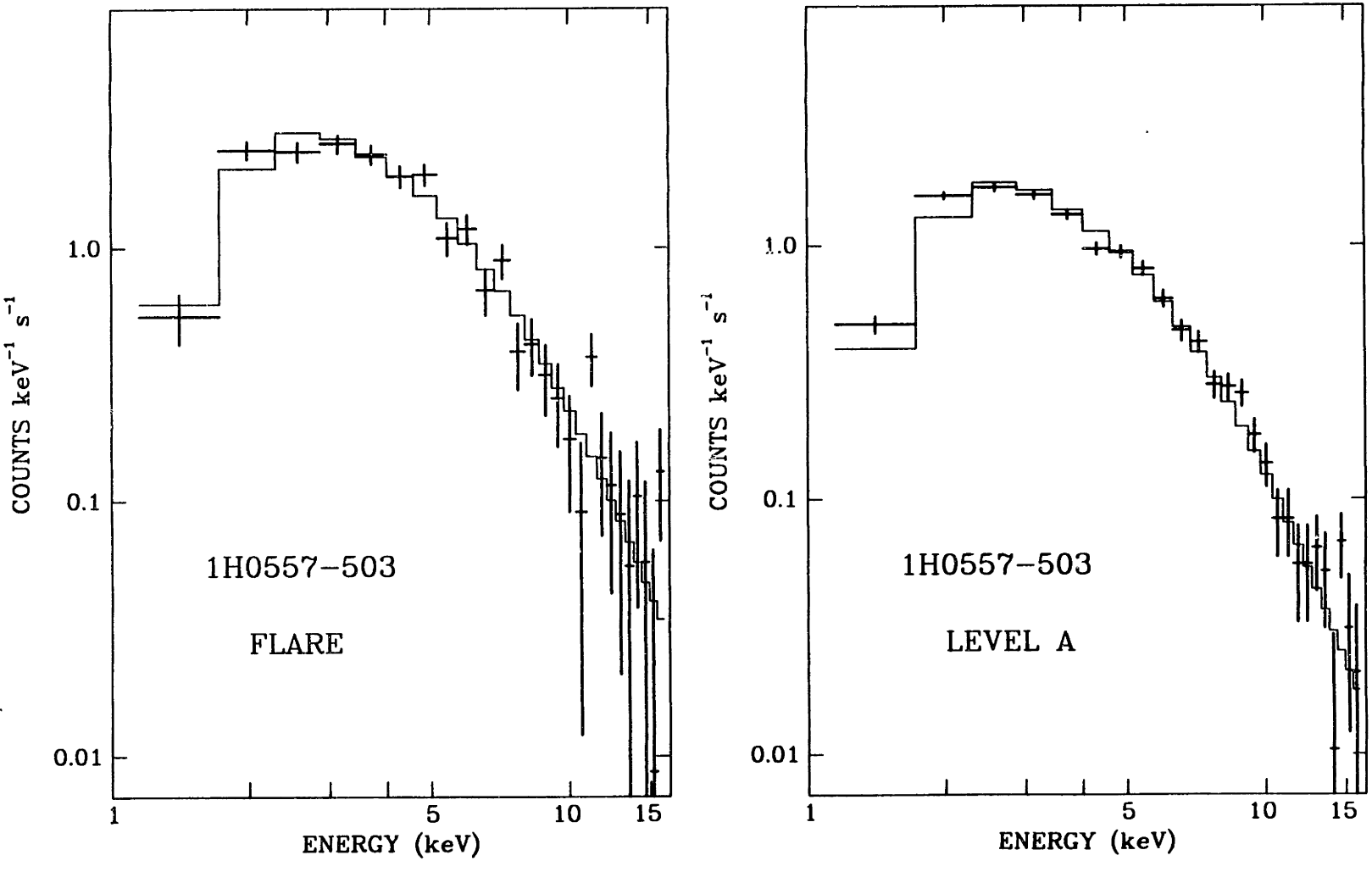
COUNTS keV^{-1} s^{-1}
1.0
0.1
0.01
1H0557−503
FLARE
1
5
10
15
ENERGY (keV)
COUNTS keV^{-1} s^{-1}
1.0
0.1
0.01
1H0557−503
LEVEL A
1
5
10
15
ENERGY (keV)

Figure 2c

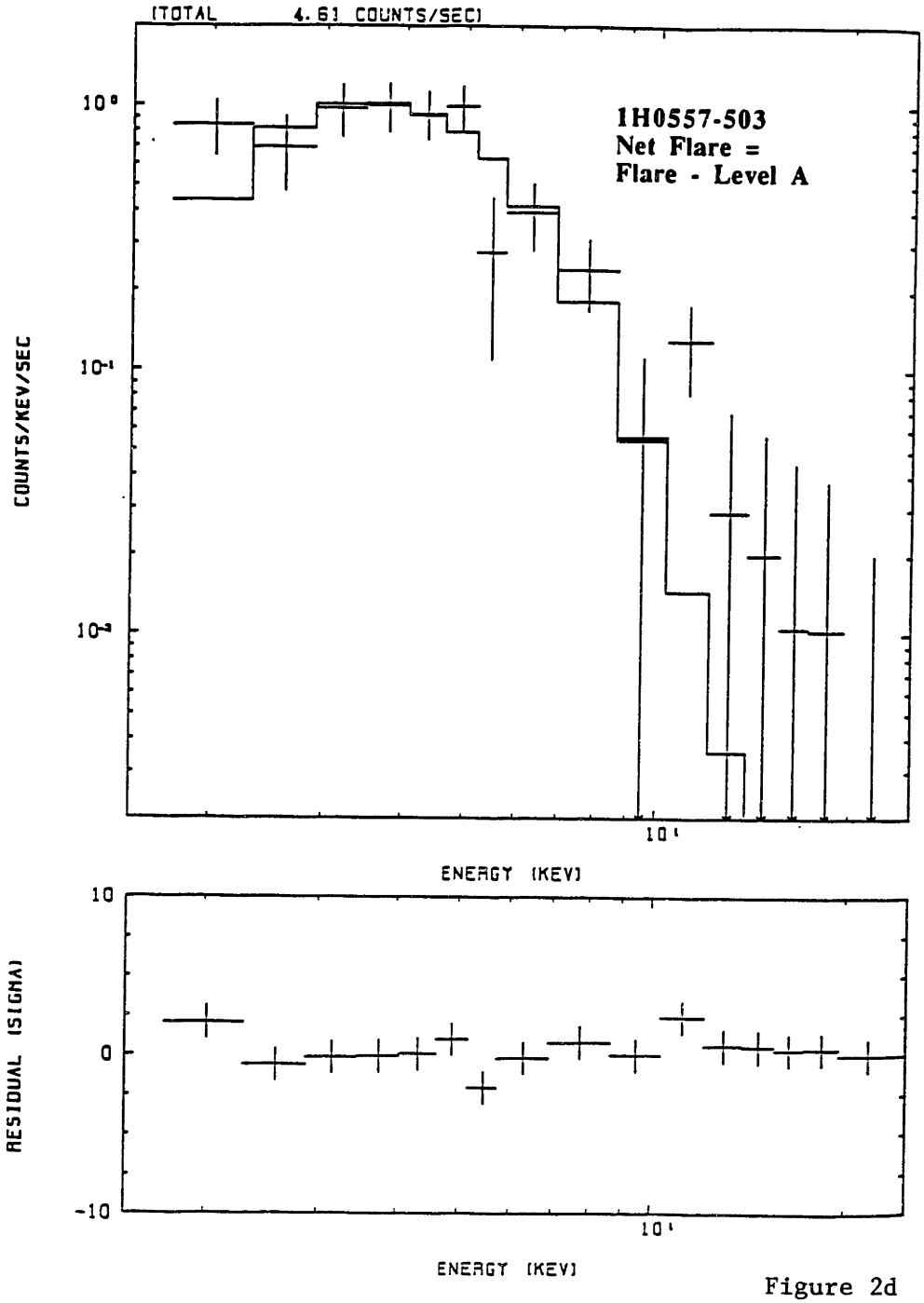
(TOTAL 4.61 COUNTS/SEC)
1H0557-503
Net Flare =
Flare - Level A
COUNTS/KEV/SEC
ENERGY (KEV)
RESIDUAL (SIGMA)
ENERGY (KEV)

Figure 2d

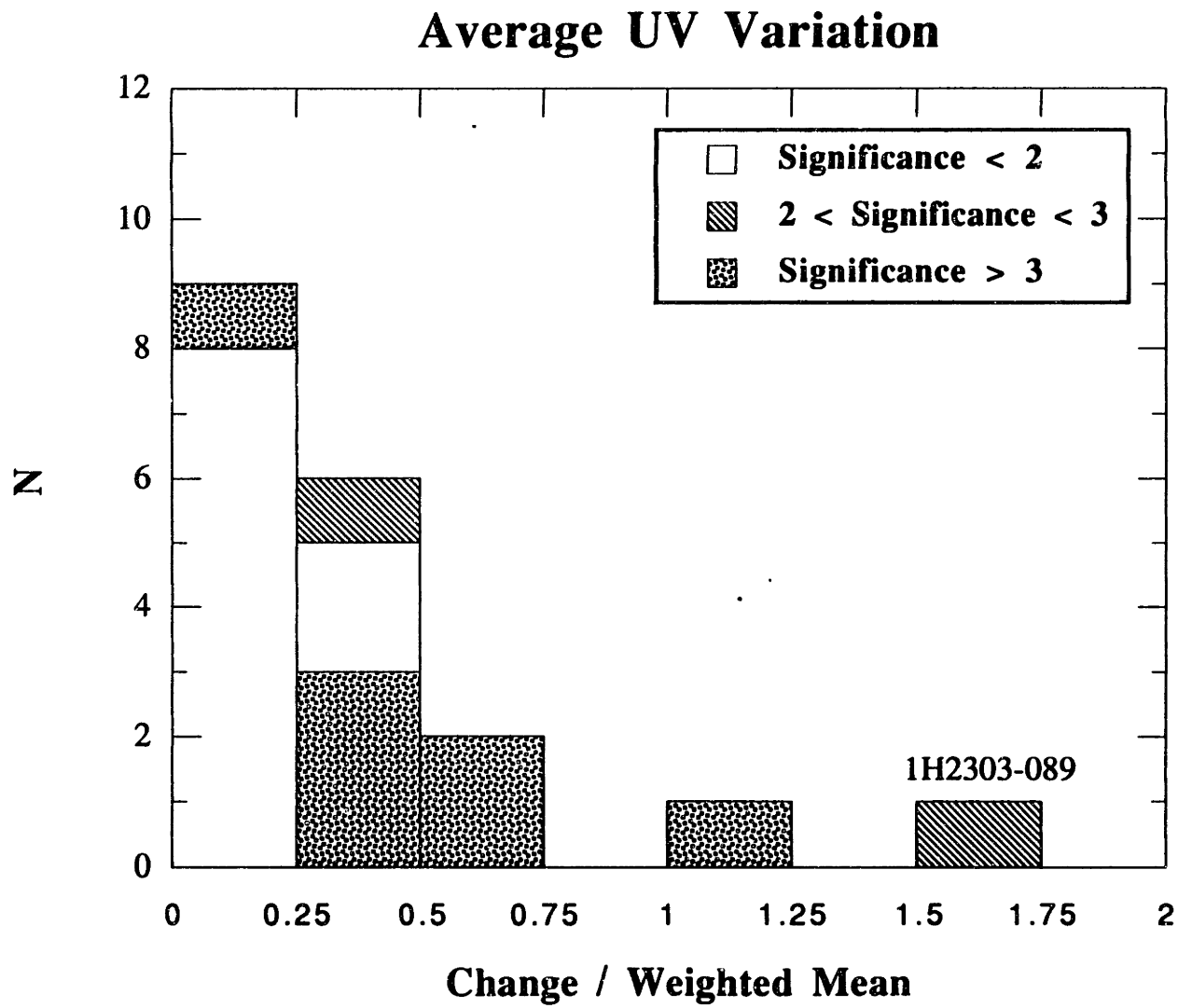
Average UV Variation
Significance < 2
2 < Significance < 3
Significance > 3
1H2303-089
N
Change / Weighted Mean
0
2
4
6
8
10
12
0
0.25
0.5
0.75
1
1.25
1.5
1.75
2

Figure 3

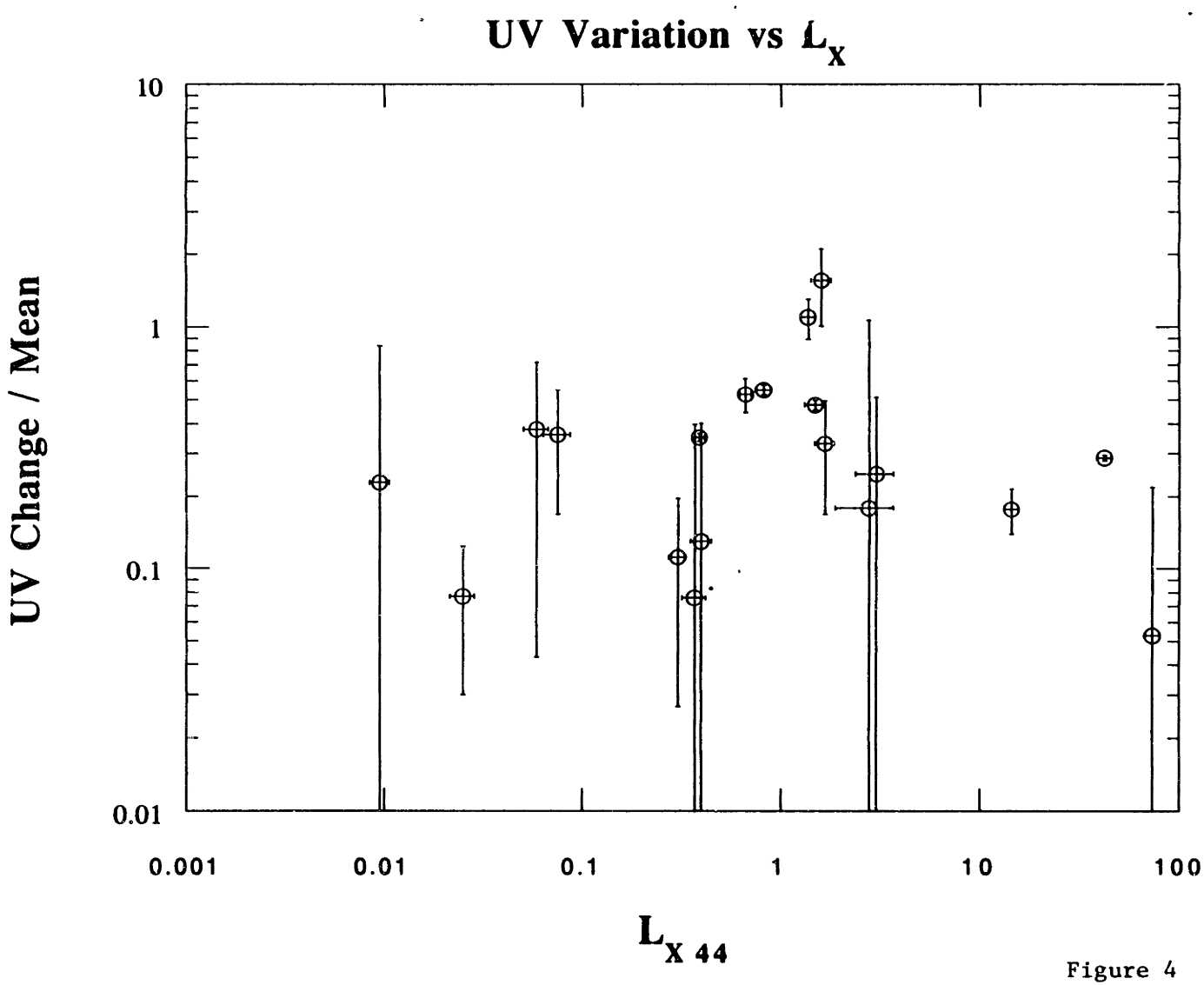
UV Variation vs L_X
UV Change / Mean
10
1
0.1
0.01
0.001
0.01
0.1
1
10
100
$L_{X\ 44}$

Figure 4

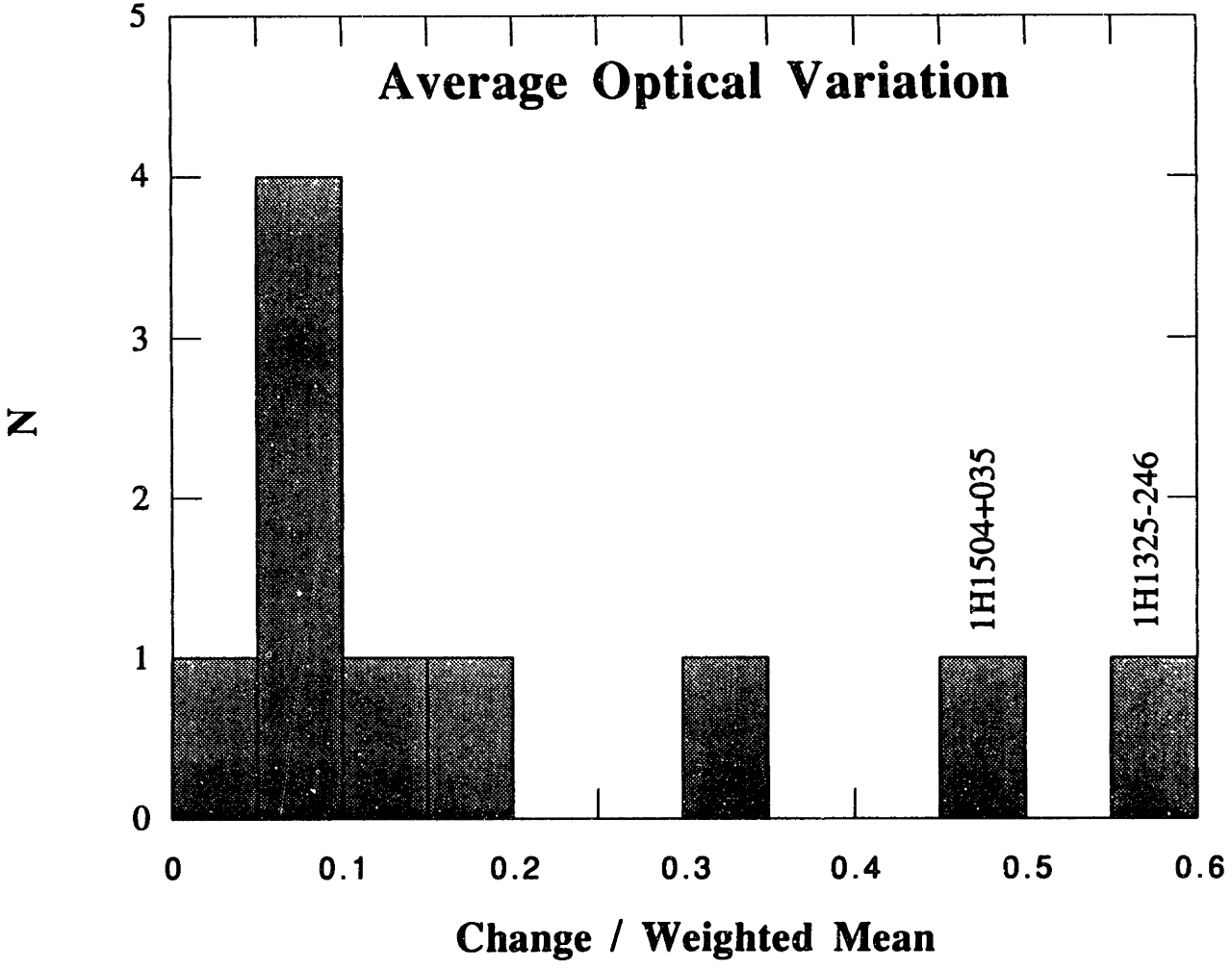
Average Optical Variation
N
Change / Weighted Mean
0
1
2
3
4
5
0
0.1
0.2
0.3
0.4
0.5
0.6
1H1504+035
1H1325-246

Figure 5

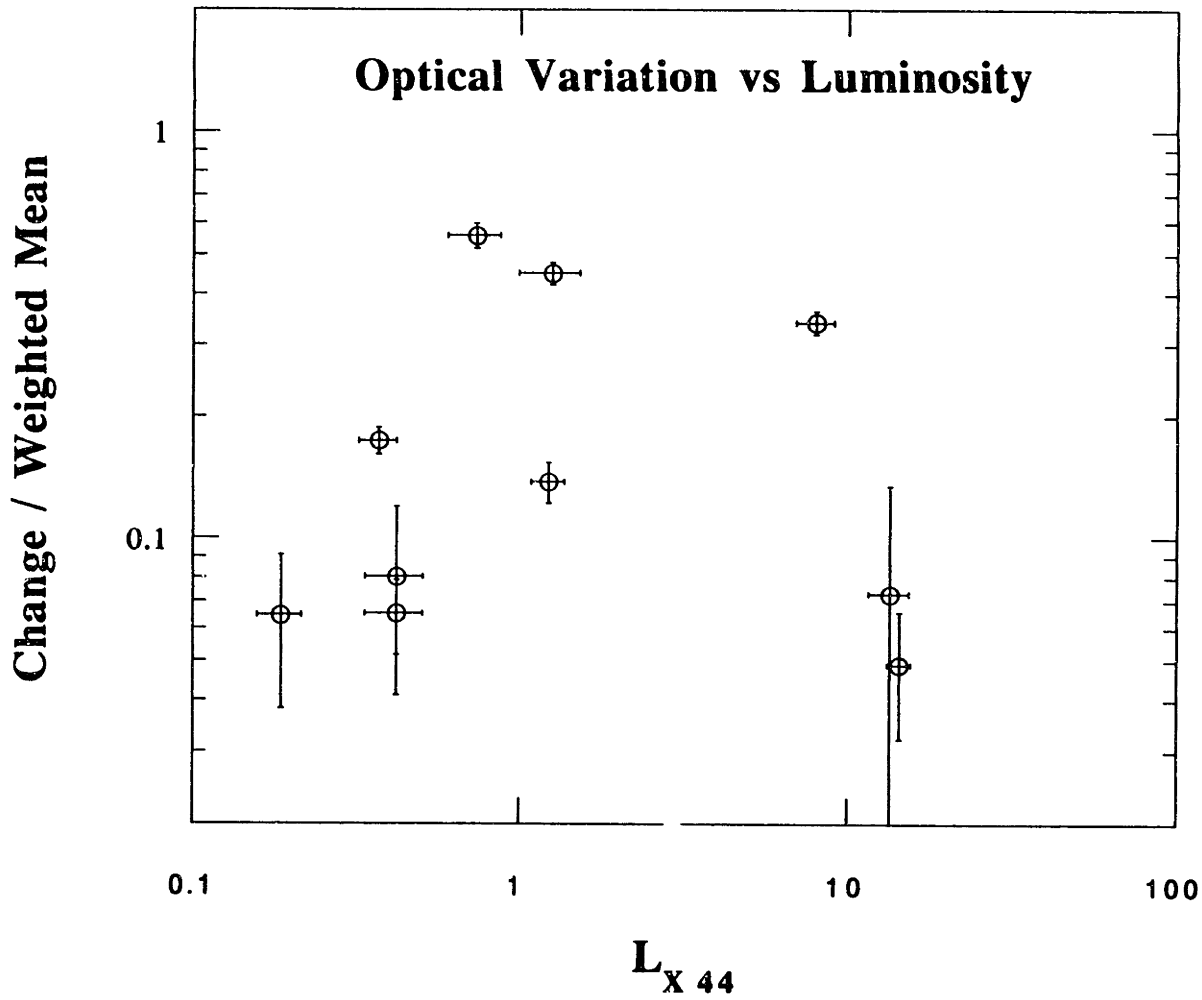
Optical Variation vs Luminosity
Change / Weighted Mean
1
0.1
0.1
1
10
100
$L_{X\ 44}$

Figure 6

CHAPTER 7:
THE X-RAY LUMINOSITY DISTRIBUTION OF AGN

In this chapter, I give the X-ray luminosity distribution of AGN derived from the LMA sample. The distribution of Type 2 objects is given separately. An estimate of the contribution of AGN to the 2–10 keV diffuse X-ray background is also given.

(All calculations in this chapter were performed for a Freidmann universe with the following parameter values: $H_O = 70$ km s^{-1} Mpc^{-1}, and $q_O = 0.5$, where H_O is Hubble's constant and q_O is the deceleration parameter.)

1. INTRODUCTION

The luminosity function, a description of the distribution of objects in space density and luminosity, is given by:

$$\Phi(L) = \frac{dN}{dV\,dL}; \tag{1.0.1}$$

where dN is the number of objects of luminosity in the interval (L, L+dL) in the differential volume dV.

Luminosity functions are useful for investigating the cosmological origins of AGN and for comparing the properties of different classes of objects related to their observed

density and luminosity. For example, obscuration models (discussed in previous chapters) have been suggested where narrow line objects are broad-lined objects viewed such that their Broad Line Regions (BLR) are obscured. Significant differences in the X-ray luminosity functions (XLF) of the Type 1 and 2 objects might be caused by X-ray absorption related to the BLR obscuring material. This work includes the first luminosity function for Type 2 objects derived from an all-sky hard X-ray sample. A discussion of the role of X-ray absorption in these objects is also given, based on a comparison of the Type 1 and 2 XLF's derived from the LMA (LASS/MC identified AGN sample).

Luminosity functions are also useful for determining the class contributions to the diffuse background in the band in which the function is measured. In this chapter, the contribution of AGN to the Diffuse X-ray Background (DXRB) radiation will be estimated using the XLF. The DXRB is very different from the well-known Cosmic Microwave Background, which is made up of thermal radiation from optically thick material resulting from conditions in the universe at a time corresponding to $z > \sim 1000$. The DXRB also appears to be isotropic, but has little else in common with the microwave background. The DXRB is a high-energy phenomenon with a spectrum that can be fit by an isothermal bremsstrahlung model corresponding to optically thin material at a temperature of ~40 keV (Marshall et al. 1980) in the range of 3-50 keV. Some fraction of the DXRB is thought to originate from the ensemble of discreet extragalactic sources, the largest part of which is from AGN (Marshall et al. 1980, Piccinotti et al. 1982). This fraction of the DXRB would then originate from a later cosmological epoch than the microwave background. The estimated fraction of the DXRB due to AGN is a topic of continuing controversy.

1.1 Previous Work

The best known previous hard X-Ray AGN luminosity function was given in Piccinotti et al. (1982). The Piccinotti et al. sample consists of all the HEAO-1 A-2 sources down to a flux of 4.0×10^{-11} ergs s^{-1} cm^{-2} in the 2-10 keV band at high galactic latitudes

($|b| > 20°$). Out of the 60 sources in the sample, 30 were clusters of galaxies, making this the most common type of source, and 25 were AGN, the second most prevalent type of source. The remaining sources were made up of four BL Lac objects, and one "normal" galaxy. The resulting XLF for AGN, which excludes one quasar, is: $dN / (dL_{44}\ dV) \approx 2.7 \times 10^{-7}\ L_{44}^{-2.75}$ $(10^{44}$ ergs $s^{-1})^{-1}$ Mpc^{-3}, where $H_O = 50$ km s^{-1} Mpc^{-1} and L_{44} is the 2–10 keV X-ray luminosity in units of 10^{44} erg s^{-1}. This result is similar to previous work (Pye and Warwick 1979). Integration of the XLF over the ~ $10^{42.5}$ – 10^{45} erg s^{-1} range allowed an estimation of the contribution of AGN to the 2–10 keV DXRB of ~20% (but greater than 40% was possible).

The Einstein Medium Sensitivity Survey (MSS; Maccacaro et al. 1982) was performed in the soft X-ray band with an imaging instrument which covered only a small fraction of the sky. The limiting flux, however, was roughly equivalent to a decade lower than that of Piccinotti et al. ($\leq 5\times10^{-12}$ ergs s^{-1} cm^{-2} in the 0.3–3.5 keV band). This survey detected a much larger proportion of emission line AGN than Piccinotti et al. Their explanation was that the relative contributions of the different classes are a function of the survey flux limit; the number of AGN grows relative to the number of clusters as the limiting flux decreases.

The Extended Medium Sensitivity Survey (EMSS; Gioia et al. 1990) consisted of a sample from the re-analysis of data from the same instrument, with a significantly lower flux limit ($\leq 3\times10^{-12}$ ergs s^{-1} cm^{-2} in the 0.3–3.5 keV band), yielding over 400 emission line AGN. Their "local" XLF ($z \leq 0.1$) is consistent with the power law found by Piccinotti et al. for $L_X > 2\times10^{43}$ erg s^{-1}, where L_X is the luminosity in the 2-10 keV band, but below this the EMSS turns over to a flatter function. This was interpreted to be a result of intrinsic absorption in low-luminosity objects. The EMSS had sufficient numbers of objects to calculate separate luminosity functions in shells of different redshift intervals. This analysis demonstrated significant evolution of the XLF at $z \geq 0.4$.

1.2. The LMA X-ray Luminosity Distribution

The essential features of the XLF for the LMA sample, compared to that of Piccinotti et al., are a larger number of objects, 96, an increase in the range of luminosity of about three orders of magnitude, and a greater variety of objects. For comparison, one quasar (3C 273) was in the source list of the Piccinotti et al. sample, but it was removed because it was the only one. In the LMA sample, the smooth transition of low luminosity, nearby objects to high luminosity objects at cosmological distances allows us to determine if there is any significant discontinuity in luminosity density between the Seyfert and quasar classifications. The small subsample of Type 2 objects allows us to construct an XLF for these objects separately, and to investigate possible differences between the XLFs of the two types of emission-line classifications.

2. THE VOLUME DISTRIBUTION OF THE LMA SAMPLE

In Chapter 2, the LMA sample was demonstrated to be complete in terms of the X-ray detections and optical identifications. The completeness of the optical identifications is estimated to be > 86 % at the flux limit of the sample and virtually complete for the sample of AGN. Below, I discuss the volume distribution of the sample to show that it is suitable for use in determining the luminosity distribution.

To first order we expect that any extragalactic population of sources must be uniformly distributed, and in the Euclidian approximation this can be demonstrated by a Log dN/dS – Log dS curve with a slope of –5/2. This was demonstrated in Chapter 2 for all sources in the LASS survey not associated with anisotropic local structure for fluxes ≥ 0.0036 counts s^{-1} cm^{-2} in the LASS instrument. Therefore, the LASS sources form an isotropic population that is complete to the flux limit of the survey, approximately 0.95 μJy at 5 keV for the typical AGN spectrum.

2.1 The V/V_{max} Test

2.1 (i) Calculation of V/V_{max}

Another method of addressing the volume distribution of sources is to consider the $\langle V/V_{max} \rangle$ statistic, the average ratio of the volume enclosed by the distance to each source to the volume enclosed by the maximum distance at which each source could have been detected. Any uniform distribution of sources would yield $\langle V/V_{max} \rangle = 1/2$. This simple argument is the basis of demonstrations of cosmological evolution in samples of distant quasars (e.g. Schmidt 1968). In a sample of objects at great distance, deviations of $\langle V/V_{max} \rangle$ from a value of 1/2 are interpreted as an indication of cosmological evolution in density (where the objects are not uniformly distributed in volume) and / or luminosity (where the value of $\langle V/V_{max} \rangle$ is a consequence of biased detection due to a spatially non-uniform luminosity distribution).

At low redshift, for a sample with a uniform limiting sensitivity, V/V_{max} depends only on the limiting sensitivity and the measured flux of each object. For small redshifts, $4 \pi d^2 F = L$, where d is the distance to an object, F is the meaured flux of the object, and L is the luminosity of the object in the measurement band. The volume of space enclosed by the distance to the object is therefore related to the flux by $V \propto F^{-3/2}$. The quantity V_{max} is the volume of space enclosing the greatest distance at which the object could be detected, therefore $V_{max} \propto F_{min}^{-3/2}$, where F_{min} is the limiting flux of the sample. This yields the familiar formula,

$$V/V_{max} = (F/F_{min})^{-3/2} \qquad \text{for } z << 1. \tag{2.1.1}$$

Twenty-three objects in the LMA have significant redshifts, $z > 0.1$, so it was necessary to perform all calculations accounting for non-Euclidian space. The calculation of V/V_{max} described here is similar to that given in Schmidt (1968). In an expanding, non-Euclidian universe, V is not simply proprtional to some power of F. The volume V in

this case is parameterized as a function of z, so $V=V(z)$. The co-moving volume is used so that $\langle V/V_{max} \rangle = 1/2$, independent of z, and is given by:

$$V(z) = \int_0^Z \frac{\frac{c}{H_o}}{(1+z)^3} \frac{d_l^2(z)}{(1+z)^{1/2}} \Delta\Omega \, dz \qquad (2.1.2)$$

(after Avni 1978). The volume for each object can be calculated directly from its redshift z, using $V=V(z)$, but $V_{max}=V(z_{max})$, so z_{max} must be found separately. From chapter 4, equations (3.0.1) to (3.0.4), the luminosity in the instrument band from E_1 to E_2 is given by:

$$4\pi d_l^2(z) \; F(E_1,E_2) \; (1+z)^{-(1+\alpha)} = L(E_1,E_2) \qquad (2.1.3)$$

where $F(E_1,E_2)$ is the X-ray flux measured in a band from E_1 to E_2 (in the observer's frame), $d_l(z)$ is the luminosity distance, and $L(E_1,E_2)$ is the luminosity in the band from E_1 to E_2 (in the frame of the AGN). To use this formula, the shape of the spectrum must be known. AGN are known to have power-law spectra with a log slope near –0.7 at hard X-ray energies and above. A log slope of $\alpha = -0.7$ was therefore assumed in the calculation of all X-ray luminosities. The standard deviation in the 2–10 keV spectral index of a large sample of AGN is only 0.12 (Turner & Pounds 1989; hereafter TP), therefore this assumption is well-justified. One determines z_{max} by the substitution of F_{min} and the luminosity calculated from the observed flux in (2.1.3) to get:

$$4\pi d_l^2(z_{max}) \; F_{min} \; (1+z)^{-(1+\alpha)} = L \qquad (2.1.4)$$

where the energy intervals have been dropped, and are understood from now on to be over the standard 2-10 keV band. V/V_{max} is then calculated from $V=V(z)$ and $V_{max} = V(z_{max})$.

To determine V/V_{max} for each object, first, (2.1.4) was solved for z_{max} numerically to an accuracy of better than 10^{-4} in the log of z, using the 2-10 keV fluxes measured by the LASS instrument. Next, the co-moving volumes $V(z)$ and $V_{max}(z_{max})$ of each object were calculated by numerically integrating the expression for $V(z)$, (2.1.2).

The solid angle used in the calculation of volumes was $\Delta\Omega = 8.2$ str due to elimination of the galactic plane and the Magellanic Clouds in the LMA sample. The volume calculated by this method is shown in Figure 1, along with the volume given by a linear distance vs z relation and a Euclidian volume versus distance relation, $V = (c\ z\ /\ H_O\ )^3$, for comparison. The non-Euclidian expression falls off from the Euclidian volume significantly at $z \geq 0.1$.

The function V/V_{max} depends on the observables z and F, and the quantity F_{min}, so it may therefore be paramterized as $V/V_{max}\,(z,F/F_{min})$. In order to illustrate the variation of V/V_{max} with z, Figure 2 shows $V/V_{max}\,(z,F/F_{min})$ plotted against $F/F_{\min}$ for various values of z. The Euclidian expression, $V/V_{max} = (F/F_{min})^{-3/2}$, is also plotted for comparison. The Euclidian and non-Euclidian functions are nearly indistinguishable on the plot for $z \leq 0.01$, but significant differences are manifested at $z \geq 0.1$. For all objects with redshifts of less than 2000 km/s, all calculations in this chapter were performed with an effective redshift, z_{eff}, which is corrected for local small scale perturbations from the Hubble flow (mostly infall of the local group toward Virgo and rotation of the galaxy). References and values are given in Table 1.

2.1 (ii) V/V_{max} Results

The distribution of V/V_{max} for the LMA sample is shown in Figure 3a. In the figure, the error bars show the Poisson 90% confidence interval for the number of objects in each bin. The value of $\langle V/V_{max} \rangle$ is 0.63 ± 0.02 for the LMA sample, where the uncertainty was derived by propagating the measurement errors. The distribution is not perfectly uniform as predicted by a uniform spatial distribution of objects. The lowest V/V_{max} bin, 0–0.2, is much lower than predicted. The K-S probability that deviations as large as those observed would occur is extremely small, 1.1×10^{-4}, indicating that the distribution is not consistent with a uniform one. Figures 3b and 3c plot V/V_{max} against z and luminosity, respectively. As both luminosity and z increase, V/V_{max} increases. Deviations above $V/V_{max} = 0.5$ greater than 3 σ are observed starting with the third bin, z

$\geq 10^{-1.5}$. The results were not sensitive to the choice of binning of V/V_{max} as a function of either luminosity or z.

2.2 Testing the Volume Distribution as a Function of Flux: The V'/V'_{max} *Test*

The most significant concern with the $<V/V_{max}>$ value is that a non-uniformity in the volume distribution might be due to an inherent bias in the selection of the LMA sample. The faintest X-ray sources have, in general, the largest error boxes, and therefore the highest probability of spurious identifications. Confusion and flux measurement errors are most significant at low flux levels as well, leading to the highest probability of spurious X-ray detections at low flux. Further, faint, distant objects are the most numerous of optical candidates for X-ray sources, and are therefore the most likely candidates for spurious optical identifications. However, this line of reasoning discounts the extensive efforts to prevent such spurious identifications. The following analysis shows independently that the $<V/V_{max}>$ value does not indicate a significant number of spurious detections at low fluxes, because at the lowest fluxes, V/V_{max} is consistent with that for a uniform distribution of sources.

A modified V/V_{max} test can be applied to investigate the volume distribution within limited regions associated with two flux boundaries, F_{up} and F_{low}. A uniform distribution of sources will still yield a uniform distribution of V/V_{max} between the flux boundaries if V and V_{max} are modified to take into account the limited detection volumes associated with F_{up} and F_{low}. Consider separating the sample into two subsamples, one above and one below a flux F_{sep}. Each of these subsamples must be considered separately. In the subsample above F_{sep}, the limiting fluxes are given by F_{up} = infinity and $F_{low} = F_{sep}$. The modified volume fraction, V'/V'_{max}, is therefore:

(2.2.1) $$V'/V'_{max} = V(z)/V_{max}(F_{sep}) \qquad F > F_{sep}$$

where $V(z)$ is the volume enclosed at the distance to the object, and $V_{max}(F_{sep})$ is the volume associated with the distance at which the source will be detected at a flux of F_{sep}.

To simplify the remainder of this explanation, I will introduce the notation that $V(d/F)$ is used to mean "the volume associated with the distance such that the source would be detected at the flux F". For the low flux subsample, the volume associated with the flux of each AGN, V', is that volume *outside* the region where each source would be detected with a flux F_{sep} ($V(d/F_{sep})$), but within the region associated with the distance to each object, $V(z)$. The volume $V(d/F_{sep})$ must therefore be subtracted from $V(z)$. The maximum volume, V'_{max}, is that associated with the maximum volume for the source to be detected, $V(d/F_{min})$, outside the inner volume $V(d/F_{sep})$. V'/V'_{max} is therefore given by:

$$V'/V'_{max} = (V(z) - V(d/F_{sep})) / (V_{max}(F_{min}) - V(d/F_{sep})). \qquad F \leq F_{sep} \tag{2.2.2}$$

Table 2 gives $\langle V'/V'_{max} \rangle$ for a variety of separating fluxes, F_{sep}. The results show that there is no effect of high V'/V'_{max} for faint sources; just the opposite, the few brightest sources are significantly above the value of 0.5 expected for a uniform distribution. This result provides solid evidence that there is no bias in V/V_{max} introduced by the identifications at the lowest fluxes.

2.3 Flux Bias Effects

Consider a flux-limited sample where the fractional flux uncertainty is relatively large. Significant numbers of objects with a true flux below a given flux limit will be measured above the limit due to Gaussian fluctuations in the measured flux. This effect is asymmetric, with more objects scattering into the sample than out of it, because more objects are present on the low side of the flux limit than on the high side due to the steepness of the Log N - Log S distribution. The result is that the distribution of true fluxes for a given measured flux is not centered at the measured flux, but at a lower flux. For a flux limited sample, this effect might cause an anomalous elevation in the $\langle V/V'_{max} \rangle$ value because the objects that scatter into the sample will be distributed mostly near the flux limit (i.e. $F/F_{min} \sim 1$), a "Malmquist effect".

To determine if this effect is important in the LMA, the flux of each object was decreased by a constant fraction of the measurement uncertainty, i.e. F_x was replaced by $F_x - k\,\sigma$, and $\langle V/V_{max} \rangle$ was then re-evaluated for a variety of values of k. Objects with values of F_x that were reduced below the flux limit were removed from the sample. If a systematic overestimation of the measured fluxes was present, then for some value of k, the V/V_{max} distribution should become consistent with that for a uniform distribution. The fluxes of the LMA objects were decreased by factors of $k\,\sigma$, for k in the range of 0 to 3.0, and the results are shown in Table 3. For any decrease in flux between 0 and 3 σ, no significant decrease in V/V_{max} occurred. This result suggests that the anomalous value of V/V_{max} is not due to a systematic overpopulation of AGN near the flux limit. It is the concentration of high values of V/V_{max} in the high flux objects, as shown in the previous section, that causes the high value of $\langle V/V_{max} \rangle$.

Any systematic flux error which increases or decreases all of the fluxes in the sample would affect the value of $\langle V/V_{max} \rangle$. To consider this type of error in a general way, consider an unknown source of error which changes the flux of each object by some fixed fraction of the flux uncertainty. To determine if such an effect might be relevant to the V/V_{max} results, the F_x of all objects was changed by a fixed fraction of the measurement uncertainty such that the average of V/V_{max} becomes 0.50. If the LMA sample is kept intact, a flux increase of 0.66 σ is required to make $\langle V/V_{max} \rangle = 0.50$. The net effect of this shift in flux, however, is to merely shift the V/V_{max} distributions downward, as shown in Figure 4. The same systematic increase of V/V_{max} with z and luminosity is still present (compare Fig. 4 to Fig. 3c). Therefore, in general, a flux bias problem which causes an effective underestimation of the fluxes cannot be relevant to the anomalous V/V_{max} distribution.

2.4 Cosmological Evolution

Non-uniformities in V/V_{max} have been associated with cosmological evolution in samples at large z. The distribution of z in the LMA is given in Figure 5. Optical samples of quasars (e.g. Hartwick and Schade, 1990) have shown increased concentrations of quasars near $z = 2$, with some evolution observed at $z = 0.4$; the results of the EMSS also show evolution at redshifts as low as $z = 0.4$ in the soft X-ray band. As can be seen from the figure, however, the LMA does not include many high - z objects. There are only 9 objects, or less than 10% of the sample, at distances $\gtrsim 0.4$. Significant departure from $V/V_{max} = 0.5$ is observed in Figure 3b at $z \approx 0.03$, not at very high redshifts, as is observed in other samples.

To determine if cosmological evolution is the cause of the anomalous V/V_{max}, the pure density evolution model of Schmidt (1968) was applied to the sample. The choice of model was motivated by the relative simplicity of the calculations used in this model and the availability of comparison samples investigated with this model. To account for density evolution, a weighted volume element is used such that

(2.4.1) $$V'(z) = V(z)\ (1+d_l(z))^n$$

where n is the evolution parameter. A value of $n = 32$ is required to give $\langle V/V_{max} \rangle = 0.50$ for the LMA sample. For $n > 17$, $\langle V/V_{max} \rangle \leq 0.5 + 1.0\ \sigma$. These values of the evolution parameter are unreasonably high. Schmidt (1968), with a sample of high-redshift quasars which displayed obvious evolution, determined that $n \approx 5 \pm 1$. Cosmological evolution is therefore weaker than the effect(s) that are causing the non-uniform V/V_{max} distribution in the LMA. However, observable evolutionary effects are not expected for the LMA.

2.5 Discussion and Summary of V/V_{max}

It should be noted that the deficit of low V/V_{max} objects is also observed, but to a lesser extent, in the Piccinotti et al. sample. The distribution of V/V_{max} for the Piccinotti et

al. sample (calculated here from the data given in Piccinotti et al.) has a mean of 0.553 ± 0.060 (Piccinotti et al. report 0.523 ± 0.059). This value is consistent with that for LMA sample. The distribution of V/V_{max} for the Piccinotti et al. sample shows that the bins from 0 to 0.2 have considerably fewer objects than the rest. When values of V/V_{max} from 0 to 0.2 are excluded from a K-S test of the LMA V/V_{max} distribution, the probability of deviations from uniformity as large as those observed climbs from 0.01% for the full sample to 22%, which does not indicate a large departure from uniformity. These results might suggest that AGN are locally under-dense, i.e., on a scale smaller than that attributed to cosmological evolution. The effect might be only marginally present in the Piccinotti sample because of the smaller sample size and the resulting larger uncertainties.

In summary, the departure of $<V/V_{max}>$ from 1/2 for the LMA objects does seem to indicate a distribution with more objects at large distances than expected, but the fluxes for these AGN are not clustered near the flux limit. However, such a result is unlikely to be caused by cosmological evolution or a systematic flux error. The cause of the $<V/V_{max}>$ value therefore remains unclear, and it is possible that there is a real deficiency of nearby AGN. The lack of concentration of high V/V_{max} values at low flux assures that confusion and erroneous identifications are not the dominant cause of the high $<V/V_{max}>$ value. A value of $V/V_{max} = 0.46 \pm 0.03$ was obtained for clusters of galaxies in the LASS flux-limited sample (Ho, 1992), so instrumental problems appear to be unrelated to the anomalous value of $<V/V_{max}>$ for the LMA. These factors together suggest that no major systematic errors are present in the data; therefore, the LMA data will be used for the determination of the AGN X-ray luminosity function.

3. DETERMINING THE HARD X-RAY LUMINOSITY FUNCTION

3.1. Calculation of the Luminosity Function

The 2–10 keV luminosity of each object is given by:

(3.1.1) $$L_x = 4\,\pi\, d_l^2(z_{eff})\, F(2,10\ \text{keV})\, (1+z)^{-(1+\alpha)}$$

where $F(2,10\ \text{keV})$ is the 2–10 keV flux, and α is the 2–10 keV log slope, assumed to be –0.7 for all objects. For this value of the spectral slope, $F(2,10\ \text{keV})$ is derived from the LASS measurements using the conversion given in Chapter 2, 1 LASS count s^{-1} cm^{-2} = 1.90×10^{-8} erg s^{-1} cm^{-2} (2–10 keV).

The simplest way to represent the luminosity function is to determine the space density of objects in various luminosity bins. The binned function has the advantage of allowing the data to be easily plotted, however, it has the disadvantage that the results are dependent on the choice of bin sizes and limits. Alternatively, the cumulative distribution of luminosity values in a sample may be used directly, without binning, to test a trial luminosity function model until an acceptable model is found. This procedure is described in the next section. Both representations of the luminosity function will be presented here. The binned luminosity function is constructed as follows:

Felten (1976) shows that Schmidt's (1968) estimator of the density function, in the case of uniform flux limit, is given by:

(3.1.2) $$\phi = \Sigma\ 1/V_{mi}$$

summed over all solid angle elements surveyed, and that it is unbiased in the general case. V_{mi} is the maximum volume out to which the ith source can be detected at or above the flux limit of the sample, as described above. The binned representation of the differential luminosity function, $\Phi(L)$, in an interval of ΔL about L, is given by the density function divided by the luminosity interval:

(3.1.3) $$\Phi(L) \approx \phi(L) / \Delta L$$

where ΔL is the luminosity interval from which $\phi(L)$ was derived, and the sum defining $\phi(L)$ is restricted to the luminosity values within a band of ΔL. The uncertainty of this value due to experimental errors is then:

(3.1.4) $$\sigma^2_{\Phi(L)} = \sigma^2_{\phi(L)} / \Delta L^2 + \sigma^2_{\Delta L} (\phi(L)/\Delta L^2)^2$$

however, the Poisson uncertainty in the number of objects in a luminosity interval generally dominates these experimental uncertainties.

3.2. Analysis of the Luminosity Function

The next step in the analysis of this function is to see if a smooth function fits the data. Approximate fits to the binned function were obtained using the method of least squares. The Gaussian one sigma error normally used to weight the data in least-squares fits was approximated by half the size of the Poisson uncertainty interval which contains the same integrated probability as the Gaussian distribution from $-1\ \sigma$ to $+1\ \sigma$.

As discussed previously, the method above yields a model function that depends on the choice of binning and the choice of bin centers. This problem can be avoided by using the Kolmogorov-Smirnov test to choose the values of the model luminosity function parameters which are most likely to represent the distribution of the luminosity data, for the given survey properties. Specifically, the K-S test compares normalized probability distributions of luminosity data and models. The normalized "cumulative" (or integral) distribution of luminosity values is given in terms of the luminosity function by:

(3.2.1) $$\frac{N(\leq L)}{N} = \frac{\int_{L_{min}}^{L} \Phi(L)\, V_{max}(L)\, dL}{\int_{L_{min}}^{L_{max}} \Phi(L)\, V_{max}(L)\, dL}$$

where $N(\leq L)$ is the number of objects with luminosity $\leq L$, and N is number of objects in the full sample. One may adopt a power law model luminosity function, $\Phi = A\,L^{\gamma}$, for a trial model. The normalized cumulative distribution then becomes,

$$\frac{N(\leq L)}{N} = \frac{\int_{L_{min}}^{L} A\,L^{\gamma}V(L)\,dL}{\int_{L_{min}}^{L_{max}} A\,L^{\gamma}V(L)\,dL} \quad , \tag{3.2.3}$$

and this distribution may be compared to the normalized cumulative distribution of the observed objects. The K-S test yields a probability of observing the given deviations of the data from the model. The luminosity function parameters may therefore be "fit" by choosing those parameters which give a maximum K-S probability. Note, however, that the normalization constant, A, drops out of this expression, and therefore this constant must be fit separately. The constant A was determined by a least squares fit to the un-normalized cumulative distribution in luminosity,

$$N(\leq L) = \int_{L_{min}}^{L} A\,L^{\gamma}V(L)\,dL \quad . \tag{3.2.4}$$

To simplify the computation of the integrals, the volume term, $V(L)$, was approximated by:

$$V(L) = \begin{cases} \frac{4}{3}\pi\left(\frac{L_x}{4\pi F_x}\right)^{3/2}\Delta\Omega & L_x \leq 3\times10^{44}\ \text{erg s}^{-1} \\ 1.37\times10^{8}\,L^{0.925} & L_x > 3\times10^{44}\ \text{erg s}^{-1} \end{cases} \tag{3.2.5}$$

where $\Delta\Omega$ is 8.2 str / 4π str, the fractional solid angle of the sample. The high luminosity expression was derived from a fit of the volumes of the LMA objecs from 3×10^{44} to 2.2×10^{47} erg s^{-1}. Within the finite range of the fit, the maximum deviation from the true volumes was <15 %, and the average deviation was less than a few %.

4. LUMINOSITY FUNCTION RESULTS

4.1. Ensemble Function

The binned XLF for the total LMA sample was constructed by choosing bins of one decade of luminosity, from 10^{41} to 10^{48} ergs s^{-1}. The function is presented in Figure 6. Each bin is plotted at the mean luminosity of the objects in the bin. The error bars shown indicate the probability intervals corresponding to Gaussian one sigma errors. The function appears to be power-law like for most of the range in luminosity, but flattens significantly at low luminosity. Most bins contain more than 10 objects, but the lowest and highest luminosity bins contain only one and two objects, respectively. This luminosity function does not demonstrate a rapid decrease at high luminosities such as that seen for normal galaxies (Kirshner, Oemler, & Schechter 1979).

A single power law was used as an XLF model for a fit to the cumulative luminosity distribution with the lowest luminosity object excluded. The K-S test (for slope) and least squares method (for normalization) were used to determine the paramters of this fit. The best-fit model luminosity function is shown as a solid line in Figure 6, and has a log slope of -2.49 ± 0.019. The parameter values of all cumulative distribution fits are given in Table 4a. The probability that the model and the observed distributions are consistent (the peak "K-S probability") is 13.5 %. This result suggests that the fit is acceptable as an approximation to the luminosity function, but other functions could fit significantly better. This and all other K-S "fits" of the log slope given in this chapter yielded symmetric, sharply peaked distributions of K-S probability as a function of log slope. The given uncertainty corresponds to the values where the K-S probability dropped to 1/e of its peak value. The best fit slope for a least-squares fit of the binned function over the same range gives a log slope of -2.50 ± 0.07. The slopes for this and all other cumulative distribution fits are very similar to the best-fit slopes of the binned luminosity

function over the same luminosity ranges. A variety of fits to the binned luminosity function are given in Table 4b for comparison to the cumulative distribution fits. The normalizations from the two fits generally differ, however, and the normalizations from the binned fits tend to overestimate the number of objects observed. This is an artifact of the large luminosity bins.

Fits to the luminosity function over various ranges in luminosity indicate that an improved representation of the luminosity function might be given by a combination of different power laws in high and low luminosity regions. A variety of fits in different luminosity ranges are summarized in Table 4a and b. The low luminosity region is flatter than at high luminosity. A power law fit to the first three bins of the binned function yields a log slope of -1.50 ± 0.46 from $10^{41} - 10^{44}$ erg s^{-1}. This low-luminosity fit has a high χ^2 value, however, and inspection of Figure 6 suggests that a more curved function is required to fit this region. The curvature is primarily due to the very lowest luminosity bin, $10^{41} - 10^{42}$ erg s^{-1}. To emphasize this point, the line representing the best fit to the cumulative distribution has been extended as a dotted line in Figure 6; the lowest luminosity bin is far below it. The predicted number of objects from $10^{41} - 10^{42}$ erg s^{-1}, given a continuation of the –2.49 log slope power law, is 21.9. Only one object is observed, so continuation of the power law to 10^{41} erg s^{-1} is therefore ruled out by Poisson Statistics at >99.95 % confidence. Such a flattening of the XLF at low luminosities is expected so that the total number of AGN does not diverge at low luminosities. A minimum AGN luminosity of $\sim 3 \times 10^{41}$ erg s^{-1} has been estimated by requiring that AGN X-ray production does not exceed the X-ray background (De Zotti 1980). This minimum luminosity is roughly consistent with the steep drop in the number of objects in the LMA XLF observed below 10^{42} erg s^{-1}.

The sum result of fitting power laws to the binned data for various ranges of luminosity is that the function gets steeper as luminosity increases (see Table 4). A fit of a

power-law to the cumulative luminosity distribution from $10^{44} - 10^{47.5}$ erg s^{-1} (the latter value is roughly the highest luminosity observed) yields a log slope of -2.73 ± 0.11 with a K-S probability of 41%. If a power law with the –2.49 log slope obtained for nearly the full range of luminosity is fit only at high luminosity, $10^{44} - 10^{47.5}$ erg s^{-1}, the maximum K-S probability is only 7×10^{-3}. A single power law fit is therefore unacceptable over the full range of luminosity. The number of objects expected from the –2.49 slope power law in this range is greater than 70, but only 48 are observed. The function therefore steepens at high luminosities.

4.2. Type 2 Objects

The luminosity distribution for the Type 2 objects alone appears in Figure 7. The 12 Type 2 objects in the sample were grouped into bins of 1/2 decade in luminosity starting at 10^{42} erg s^{-1} for the binned representation shown in the figure. The Type 2 XLF is roughly power-law like to ~ $10^{43.5}$ erg s^{-1}. However, the bin from $10^{43.5}$ to 10^{44} erg s^{-1} appears to be below the power law defined by the objects at lower luminosity, and no objects are observed above 10^{44} erg s^{-1}. A power law fit to the cumulative luminosity distribution of Type 2 objects from 10^{42} to $10^{43.5}$ erg s^{-1} yields a log slope of -2.45 ± 0.45 (see Table 4a), and is shown as a solid line in Figure 7.

The lack of Type 2 AGN detected at high luminosities suggests that the Type 2 XLF steepens or is truncated in this region. In the following luminosity intervals, $10^{42\text{-}42.5}$, $10^{42.5\text{-}43}$, $10^{43\text{-}43.5}$ erg s^{-1}, 4,3, and 4 objects were detected, respectively. However, only one object was detected from $10^{43.5}$ to 10^{44} erg s^{-1}, and zero were detected above this range. The most luminous Type 2 detected has a 2–10 keV luminosity of 4.64×10^{43} erg s^{-1}. The lack of Type 2 objects at high luminosity is not a detection bias. The statistic $< V/V_{max} > = 0.60 \pm 0.06$ for the Type 2 objects alone shows that a nearly uniform distribution of Type 2 objects has been detected. Extending the –2.45 log slope power law from 10^{44} to $10^{47.5}$ erg s^{-1} (roughly the highest observed luminosity) yields approximately

40 expected objects, and is inconsistent with the zero observed objects at >99.95% confidence. Even if the log slope of the Type 2 XLF is chosen to be –3.20 (the steepest slope within the 90% confidence limit), 5.7 Type 2 objects are expected above 10^{44} erg s^{-1}. This is again inconsistent with the LMA distribution at > 99.5% confidence. The Type 2 XLF must therefore be truncated or steepen at $L_x \geq 10^{44}$ erg s^{-1}.

The extension of the –2.45 log slope power law is shown as a dotted line in the Figure 7. For comparison, a crude 90% upper limit to the XLF is shown in Figure 7 for a bin between 10^{44} and $10^{47.5}$ erg s^{-1}. This limit was derived from the 90% confidence upper limit on observing zero objects with the luminosity at the center of the bin, $10^{45.75}$ erg s^{-1}, at the flux limit of the sample. This limit is only a rough approximation because of the large size of the bin. The figure shows, however, that power law is far above the upper limit.

4.3. An Estimate of the Contribution of AGN to the Diffuse X-Ray Background

Integration of the luminosity function allows an estimate of the contribution of AGN to the 2–10 keV DXRB volume emissivity, the amount of energy in the DXRB per unit volume in this band. Following Piccinotti et al., I compare the volume emissivity of AGN to that of the total volume emissivity of the 2–10 keV DXRB given in Schwartz and Gursky (1974) as 2.2×10^{39} erg s^{-1} Mpc^{-1} for a very similar choice of cosmological parameters. The volume emissivity of AGN in the LASS band, B_{AGN}(2–10 keV), is given by:

$$B_{AGN}(2\text{–}10\ \text{keV}) = \int_{L_{min}}^{L_{max}} \Phi(L)\, L\, dL \qquad (4.3.1)$$

Because of the steepness of the XLF at high L_X, this integral is not sensitive to the value of L_{max} (the integrand $\sim L^{-1.7}$ in this region); because of the flattening at low luminosities, it is also not very sensitive to the choice of L_{min} (the integrand is flatter than $\sim f(L)^{-0.5}$ at the lowest luminosities). The shape of the observed luminosity function

therefore gives a good justification for integrating over the limits of observed luminosities in the sample. The XLF was represented by three seperate power laws. A fit of the cumulative luminosity distribution from $10^{41.5}$ to $10^{42.5}$ erg s^{-1} yields a log slope of –1.24. This function was chosen to represent the XLF only from the lowest luminosity observed, 8.9×10^{41} erg s^{-1}, to $10^{42.5}$ erg s^{-1} (the middle of the second bin shown in Fig. 6). A power law with a log slope of –2.04 was used from $10^{42.5}$–10^{44} erg s^{-1}, and finally, the –2.73 slope power law was used for the high luminosity region, from 10^{44} – 2.17×10^{47} erg s^{-1}. The resulting 2–10 keV emissivity is $(5.7\ ^{+1.8}_{-2.4}) \times 10^{38}$ erg s^{-1} Mpc^{-3}. The AGN contribution to the DXRB is therefore 26^{+8}_{-11}%. The large uncertainty comes from the poorly constrained fit at low luminosities.

5. COMPARISONS TO OTHER SAMPLES

5.1. Log N - *Log* S

A comparison of the normalizations of the Log N - Log S curves of a few X-ray samples is given in Table 5. When considering these comparisons, several differences in the samples must be kept in mind. Some of the other samples do not include high z objects (e.g. Piccinotti et al.), and other samples are sensitive to a different energy range and do not include any bright objects (e.g., the EMSS). Because of these factors and evidence that the relative mix of AGN, clusters, BL Lacs, and galactic sources changes with flux (Maccacaro et al. 1982), neither the normalization of the Log N - Log S curves nor the numbers of any specific class of source will precisely match those predicted by other surveys. The critera that went into constructing the Log N - Log S curves can also yield different normalizations of the curve. For example, Piccinotti et al. did not define their sample in the Log dN - Log dS plane. Instead, they defined their sample by setting the flux limit to be that for which all sources would be detected at $> 5\ \sigma$ significance (using

σ predicted from exposure considerations). These authors then fit all the sources meeting this criterion with a power law function to show that this subsample of the detected sources is consistent with a –5/2 slope. Piccinotti et al. do not give the distribution of detection significance from which only the 5 σ objects were taken; it is possible that such a cut reduced the normalization constant of their Log N - Log S curve.

The LMA sample Log N - Log S curve has a markedly different normalization from the other samples discussed above. However, the curves may not be inconsistent because of the dependence of the relative mix of X-ray classes on mininum sensitivity, because of the different spectral response of each instrument, and finally, because the curves were defined in different ways with different significance criteria. Maccacaro et al. (1982) also found significant differences between their normalization and that of Piccinotti et al., suggesting that the flux dependence of the mix of sources was the most important factor. In the comparison of LASS and Piccinotti et al. samples it should be noted that the LASS sensitivity is much higher in the ~2-4 keV range, admitting many more detections of "soft" X-ray types, such as stars with active coronae.

5.2. *Luminosity Functions*

A comparison of the parameters describing X-ray luminosity functions from different survey instruments is given in Table 4c. As expected from the disparate Log N – Log S normalization results, none of the XLF normalizations in the table agree well. However, the XLF shapes show better agreement. A comparison of the LMA sample to that of the Piccinotti et al. sample is of particular interest since both samples were selected by hard X-ray flux. For comparison purposes, I formed a binned luminosity function from the Piccinotti et al. data, using the same techniques as that for the LMA data, and the flux conversion for the average slope given in Piccinotti et al. This function is shown in Figure 8. The Piccinotti et al. data were binned in the same 1 bin per decade grouping as for the LMA. The sample includes only 23 sources spanning $10^{42} - 10^{45}$ erg s^{-1}. No objects

were detected in the Piccinotti et al. sample from $10^{41} - 10^{42}$ erg s^{-1}. Note that the lowest luminosity object in the LASS sample, 1H1210+393, was also detected in the Piccinotti et al. sample, but at more than three times the flux detected by the LASS. (The object is known for its extreme variability). This object therefore appears in next higher luminosity bin in the Piccinotti et al. sample. The Piccinotti 90% upper limit for the detection of zero objects at the limiting flux, with the luminosity at the center of the first bin, $10^{41.5}$ erg s^{-1}, is shown in the figure. This upper limit shows that the limiting sensitivity of the Piccinotti et al. sample was insufficient to discover the flattening of the XLF below 10^{42} erg s^{-1} evident in the LMA sample. The Piccinotti et al. XLF is lower than that of the LMA by about a factor of two, but the slopes of the two functions are very similar. The greatest difference in the XLF is in the bin from $10^{43} - 10^{44}$ erg s^{-1}, where the LMA is a factor of four higher than the Piccinotti et al. sample, with a difference that is significance at the level of 4.5 σ. Piccinotti et al. report that the luminosity function is well represented by a power law with a slope of -2.75 ± 0.15 (confirmed in the re-analysis of their XLF shown in Fig.8) . The result for the LMA, fit in the range of $10^{42} - 10^{45}$ erg s^{-1}, shows that the K-S probability peaks at a flatter log slope, -2.40 ± 0.05 (see Table 4), a disagreement of ~ 2.3 σ. In summary, the two functions approximately agree in slope, but the normalizations disagree significantly, and the Piccinotti et al. sample does not detect an XLF flattening at low luminosities.

The EMSS sample originated from an instrument sensitive to 0.3–3.5 keV X-rays. For a log slope of –0.7, the luminosity in this band is within ~1% of that in the 2–10 keV band reported for the LMA and Piccinotti samples. While significant dispersion about a log slope of –0.7 occurs in the low energy band, the average slope is within a few tenths of –0.7. Below, I treat the integrated luminosities in the soft EMSS band and the 2–10 keV bands as approximately equal for a given object.

The very deep EMSS sample showed significant curvature of the luminosity function. The basic features of the EMSS local luminosity function (fit only to objects with $z < 0.1$) are in good agreement with those of the LMA. The fit parameters of this function were not given in Maccacaro et al. (1991) because the function deviated significantly from a power law due to its curvature. The low luminosity end shows significant flattening (as does the LMA function). The EMSS de-evolved luminosity function was obtained from high-z sources, but the luminosities of these sources were corrected to $z = 0$ in Maccacaro et al. (1991) by the best-fit evolution models. The fit parameters for this function are given in Table 4. The low luminosity index of the EMSS de-evolved function is much flatter than the lowest luminosity LMA fit. However, the EMSS fit was made over a significantly lower range in luminosity, so a direct comparison cannot be made. At higher luminosities, the LMA and EMSS log slopes agree within a few sigma.

In summary, the shape of the LMA XLF is in good agreement with that given by the EMSS, showing a similar curvature. The lack of curvature in the Piccinotti et al. XLF is a consequence of the smaller range of luminosity in that sample, the statistical limitations of their small sample size.

5.3. The AGN Contribution to the Diffuse X-Ray Background

Piccinotti et al. calculated the 2–10 keV DXRB volume emissivity due to AGN assuming their high-energy power law extrapolated to low luminosities, and then imposing a minimum-luminosity cutoff. This approach was necessary, because the A-2 sensitivity was not sufficient to determine a flattening at low luminosity (note the upper limit at lower luminosities in Figure 8). For any parameter values remotely near their best fits, the emissivity is more sensitive to the choice of low luminosity cutoff than to the particulars of the function being integrated. Piccinotti et al. show that for a steep function at low luminosities, L_{min} must be chosen such that the integrated Log N-Log S curve does not give a number of sources exceeding the number actually observed. The "best value" of

their sample's contribution to the DXRB is ~20%, using L_{min} of $\geq 4 \times 10^{42}$ erg s^{-1}. (In the LMA, the integration was carried out down to 8.9×10^{41} erg s^{-1}.) However, for other possible choices of L_{min} they estimated a contribution of ~ 40%. The value derived with the LMA sample is 26^{+8}_{-11} %. The observation of the turnover in the luminosity function has improved the certainty of the estimate of the contribution of AGN to the DXRB.

The contribution of AGN to the DXRB was determined to be ~40% near 2 keV from the XLF of the EMSS sample (Maccacaro et al. 1991). Direct comparisons of this result with that for 2-10 keV contribution is not meaningful because the spectra of AGN and the DXRB are significantly different.

6. DISCUSSION

6.1. The Low-Luminosity Flattening of the Luminosity Function

Maccacaro et al. (1991) suggested that the flattening of their XLF at low luminosities compared to that of the higher X-ray energy observations of Piccinotti et al. might be due to low-energy absorption occurring in the low-luminosity objects. If the absorption proposed by Maccacaro et al. (1991) had a characteristic column ~10^{23} cm^{-2} necessary to cause the flattening of the LMA hard X-ray luminosity function, and if the column tended to decrease with luminosity, as suggested by Maccacaro et al.(1991), then the flattening of the EMSS would occur at a much higher luminosity than in the LMA. This is a consequence of the steep energy dependence of X-ray absorption. The LMA flattens significantly below 10^{42} erg s^{-1}. Smaller bins show that flattening in the range of 10^{42} – 10^{43} erg s^{-1} is also consistent within errors. The EMSS sample is reported to flatten at $\leq 5 \times 10^{42}$ erg s^{-1} (Maccacaro et al. 1991), consistent with the results for the LMA . This result suggests that the low luminosity flattening in the EMSS XLF is intrinsic, not due to absorption.

It is difficult to compare the EMSS and LMA sample shapes at low luminosity more quantitatively, because the few LMA objects below 10^{42} erg s^{-1} do not constrain the fits well in this region. A deeper survey in the hard X-rays would yield more low-luminosity objects. In the future, the AXAF or ASTRO-D instruments could be used for deep surveys of limited regions of the sky at energies up to ~10 keV. To address the absorption question in more detail, low-energy spectroscopic observations could be made of a selection of objects from the low luminosity EMSS sample, to determine if their absorption columns are $\gtrsim 10^{23}$ cm^{-2}, large enough to affect hard X-ray selection. TP have shown that very few objects in their sample have $N_H \gtrsim 10^{23}$ cm^{-2}, however, the TP sample is not defined by any meaningful criteria, and the result may be biased. The ROSAT instrument has sufficient sensitivity to observe a number of these objects, as will the ASTRO-D instruments.

6.2. *The Luminosity Function of Type 2 Objects*

The luminosity function of Type 2 objects derived from a flux-limited, hard X-ray, sample is of special interest, as none have been reported previously. The Type 2 function is different from the the Type 1 function in that it shows a more severe steepening at high L_X than the Type 1 function. The luminosity functions presented by Edelson, Malkan, and Reike (1987) from 60 μm data show a somewhat faster fall off of the Type 2 compared to the Type 1 luminosity function, which might be an effect similar to the steepening or truncation in the XLF, but not nearly as severe. However, the optical magnitude limited CfA Redshift survey sample shows no evidence for a steepening of the Type 2 luminosity function (Huchra & Burg 1992).

The IRAS warm selection criterion (defined in Chapter 4 as $F_{25\,\mu m} / F_{60\,\mu m} > 0.33$) is of special interest in the study of Type 2 objects because it selects predominantly these objects from IRAS AGN samples. However, of the 59 warm objects in the LMA, only 7 are Type 2. Also, these Type 2's are among the "coolest" objects (i.e., they have the

lowest values of $F_{25\ \mu m}$ / $F_{60\ \mu m}$) in the sample. Since both the IRAS and LASS instruments are both relatively insensitive to obscuring material, and both detect many AGN, why are their AGN populations so different? Why does the LASS fail to see either predominantly Type 2 warm objects, or just a large fraction of Type 2 objects, as in the IRAS sample of AGN (e.g. DeGrijp et al., 1985, Lawrence, 1991)? In fact, *unbiased* optical samples, i.e., those that do not select by UV excess, also yield a majority of Type 2 objects. These samples select on total galaxy magnitude. The fraction of Type 2's in unbiased optical samples is 0.6–0.8. Unbiased radio samples yield a fraction of 0.71, and IR samples which select on total galaxy luminosity (Lawrence 1991) yield a similar value. The low fraction of Type 2 objects in the LMA suggests that many Type 2 objects are missing. The true parent population of AGN may therefore be much larger than the parent population of the LMA.

The low LMA Type 2 fraction is related to the steepening of the Type 2 XLF. Figure 9 shows the cumulative fraction of Type 2 objects in the LMA sample as a function of luminosity. The fraction is consistent with the range of 0.6–0.8 seen in other samples, up to $L_X = 10^{43.5}$ erg s^{-1}. Above this region, where the XLF steepens or is truncated, the Type 2 fraction is always well below that of other unbiased samples. Therefore, if the unbiased samples above did not include objects with luminosities in their respecitve bands which corresponded to $L_X \geq 10^{43.5}$ erg s^{-1}, then the Type 2 fractions of all the samples might be consistent. The same luminosity dependence of the Type 2 fraction seen in the X rays might also be present in samples defined in other bands if these samples were expanded to include higher luminosity objects. Huchra and Burg (1992) report no steepening of the optical Seyfert 2 luminosity function, and these authors also report that the optical Type 2 fraction does not vary with optical luminosity. The sample these authors used, however, covers only optical luminosities significantly below about $M_B = -23$, which is commonly considered the minimum optical luminosity criterion for the quasar

classification. The LMA sample includes a significant number of high luminosity objects classified as quasars, with $L_x > 5 \times 10^{44}$ erg s^{-1}. Many of the objects at high L_x would then be outside of the optical luminosity range of the Huchra and Burg sample because they are quasars, while the CfA sample primarily consists of nearby bright galaxies. It is therefore possible that if optical surveys sampled objects with M_B <–23, they would detect the drop in the Seyfert 2 fraction at high luminosity.

Many models of Type 2 objects suggest that these objects are obscured. The energy dependence of obscuration, together with the luminosity functions and Type 2 fractions observed at different frequencies, puts definite constraints on the geometries and the type of the material that may be used in obscuration models. Photons in the IRAS and LASS bands are relatively insensitive to obscuration by inter-stellar material, however, the LASS band photons are more sensitive to intervening gas and less sensitive to the fraction of matter contained in dust particles. The fact that the LASS could not detect as large a fraction of Type 2 objects as IRAS could be explained if the *majority* of the parent population of Type 2 AGN are obscured by nearly dustless gas with extremely high columns, $N_H \gtrsim 10^{24}$ cm^{-2}. From this parent population, the LASS instrument would select only the merely moderately obscured (N_H <~10^{24} cm^{-2}) AGN, while the optical and IR samples could be largely unaffected by the obscuration because of the absence of dust. In this case, between 126 and 336 Type 2's would be counted in the LMA if no obscuration were present, in order to make the total Type 2 fraction 0.6–0.8. The actual number of Type 2's (12) would then suggest that ~90–95 % of all Type 2 AGN are being missed by hard X-ray selection. Alternatively, re-processed emission in the optical/IR bands due to the obscuring material itself could account for the higher detection rate of the Type 2 AGN in flux-limited optical or IR samples. Note, however, that both of the conjectures above explain the differences in the Type 2 fractions among the different wavebands, but they do not explain the XLF cutoff.

TP studied a few "Narrow Lined X–ray Galaxies" and Seyfert 2's with very weak broad lines and higher absorbing columns than Seyfert 1's, N_H ~10^{22} –10^{23} cm^{-2} (including 5 LMA objects). These objects were not unusually optically weak, and showed no correlation between Balmer decrement and absorbing column. TP concluded that higher X-ray absorbing columns are associated with the narrow line phenomenon. Further, TP suggested that the proposed obscuring material is close to the central source, where high temperatures would vaporize any dust. All these observations are consistent with dustless obscuration in Type 2's. It should be noted, however, that these gas columns are quite modest and the possibility of a high N_H subset of the Type 2 AGN's is not based on empirical results.

If obscuration is causing the steepening or truncation of the Type 2 XLF, it must be luminosity dependent. The *highest* luminosity Type 2's must be either completely smothered, or very rare, in order to form the observed XLF truncation or steepening. An X-ray absorbing column which increases with L_X cannot be invoked to solve the problem, however. Lawrence (1990) shows that the X-ray absorbing column decreases with L_X. Some other mechanism must be invoked to make the Type 2 classification rare in X-ray samples in some other way. If the optical and IR Type 2 luminosity functions were found to steepen at high luminosity, the following scenario would give a self-consistent explanation for the observed Type 2 fractions and luminosity functions: Assume that obscuring material cannot exist in high-luminosity AGN. In this case, no material would be present to obscure high luminosity BLRs to optical observations. Therefore, none of the high-luminosity objects would be classified as Type 2, producing a truncation of the Type 2 luminosity function *in all bands*. A maximum AGN luminosity where obscuring dust could occur might be provided naturally by the luminosity required to evaporate most of the dust in the nucleus.

7. CONCLUSIONS

1. The LMA X-ray luminosity function (XLF) can be represented from 10^{42} to 10^{48} erg s^{-1} (2–10 keV) by a power law with a log slope of -2.49 ± 0.019. The K-S probability that a power law with this slope is consistent with the data is 13.5 %. There is evidence for curvature in the XLF at both high and low luminosities, however. At the lowest luminosities, below 10^{42} erg s^{-1}, the –2.49 slope power law predicts far more objects than are observed. This suggests significant flattening, and possibly a cutoff of the XLF below 10^{42} erg s^{-1}. The XLF also steepens at the highest luminosities. A power law fit in the range $10^{44} - 10^{48}$ erg s^{-1} yields a log slope of -2.73 ± 0.11 with a K-S significance of 41 %. A power law with a log slope of –2.49 fit only in this region has a K-S probability of 0.5 %.

2. The low-luminosity cutoff of the XLF occurs at comparable luminosities in the LMA hard and EMSS soft X-ray samples. If the flattening in the LMA hard XLF were due to absorption, very large N_H columns ($\geq 10^{24}$ cm^{-2}) would be required. In the luminosity dependent absorption model suggested in Maccacaro et al. (1991), the low-luminosity XLF cutoff must occur at much higher luminosity in the EMSS soft XLF than in the LMA hard XLF, because of the steep energy dependence of the X-ray absorption. Since no evidence is found for a difference in the cutoff luminosity, the data do not require a luminosity dependent absorption. The XLF cutoff may therefore be intrinsic to the AGN's.

3. The contribution of AGN to the 2–10 keV diffuse X-ray background is estimated to be 26^{+8}_{-11} %. The relatively flat shape (log slope ~ –1) of the luminosity function at low luminosities and the steep shape (log slope ~–3) at high luminosities make this number relatively insensitive to the choice of high and low cutoff luminosities used in the calculations.

4. The LMA yields more objects above a given (approximate) limiting flux than other samples. This could be attributed to a combination of different instrument band passes, an evolution in the relative numbers of different types of sources with luminosity, and differences in sample definitions. The same effect is seen in a comparison of the deeper EMSS sample to that of Piccinotti et al.

5. The Type 2 XLF is roughly power-law like at low luminosities. No objects are observed at greater than ~10^{44} erg s^{-1} in the LMA sample, suggesting that the function steepens or is truncated above this energy. A power law fit from 10^{42} – $10^{43.5}$ erg s^{-1} yields a log slope of –2.45 ± 0.45, and is a good representation of the low-luminosity distribution of the Type 2 objects. An extension of the –2.45 slope power law to $10^{47.5}$ erg s^{-1} is inconsistent with the observed number of objects at >99% confidence. The Type 2 XLF must therefore steepen or truncate above 10^{44} erg s^{-1}.

6. The total fraction of Type 2 objects is much lower in the LMA sample than in unbiased, flux-limited samples defined at other wavelengths. However, at $L_x \leq 10^{43.5}$ erg s^{-1}, the Type 2 X-ray fraction is consistent with the fractions observed in samples at other wavelengths. Therefore, if the intrinsic Type 2 luminosity function in other bands showed the same steepening observed in the LMA above a luminosity corresponding to $L_x = 10^{43.5}$ erg s^{-1}, the Type 2 fraction in the LMA would be consistent with that in other bands. Optical Seyfert 2 / Seyfert 1 fractions reported so far show no dependence on luminosity (Huchra and Burg 1992). However, the fractions reported so far are from samples limited to low luminosity objects. It is possible that the luminosity dependence of the Type 2 fraction would be observed if the coverage of optical samples were extended to higher luminosities.

REFERENCES

Avni , Y. 1978, A&A, 63, L13.

DeGrijp, M. H. K., Miley, G. K., Lub, J., and deJong, T., 1985, Nature, 314, 21

Felten, J. E., Ap. J., 207:700, 1976 August 1

Gehrels, N., 1986, ApJ, 303,336

Gioia, I. M., Maccacaro T., Schild, R. E., Wolter, A., Stocke, J.T., Morris, S. L., & Cleary, J. P. 1990, ApJS, 72, 567

Hartwick, F. D. A., & Schade, D. 1990, Ann Rev A&A, 28, 437

Ho, Erling, Unpublished Bachelor's Degree Thesis, 1992, Massachusetts Institute of Technology.

Huchra, J., & Burg, R. 1982, ApJ, 393, 90

Kruper, J. S., Urry, C. M., Canizares, C. R., 1990, ApJS, 343,66

Kirshner, R. P., Oemler, A., & Schecter, P.L.1979, AJ, 84, 951

Lawrence, A., MNRAS 1991, 252,586

Maccacaro et al., 1982, Ap. J., 253, 504

Maccacaro, T. Della Cecca, R., Gioia, I. M., Morris, S. L., Stocke, J. T., Wolter, A. 1991, ApJ, 374, 117

Marshall, F. E., et al., 1980, ApJ, 235, 4

Piccinotti, G., Mushotzky, R.F., Boldt, E. A. , Holt, S. S., Marshall, F. E., Serlemitsos, P.J., Schafer, R. A., 1982, Ap. J., 253:485

Press, W. H., Flannery, B. P., Teukolsky, S. A., Vetterling, W. T., 1988, Numerical Recipes in C, Cambridge University Press.

Pye, J. P., and Warwick, R. S., 1979, MNRAS, 247, L1

Schmidt, M. 1968, ApJ, 151, 393

(TP) Turner, T. J., Pounds, K. A., 1989, MNRAS, 240, 833

Tully, R. B. 1988, Nearby Galaxies Catalog , Cambridge University Press.

Veron-Cetty, M. P.& Veron, P., A Catalogue of Quasars and Active Nuclei, 4th ed., ESO Scientific Report No.7, European Southern Observatory, 1989

Weinberg, S. 1972, Gravitation and Cosmology: Principles and Applications of the General Theory of Relativity, John Wiley and Sons inc., New York.

Wood, K., et al., 1984, ApJS, 56, 507

Zombeck, M. V. 1990, Handbook of Space Astronomy and Astrophysics, 2nd ed., Cambridge University Press, Cambridge

Table 1

Effective Redshifts for Objects with v < 2000 km/s

Object	[1]z_{eff}
[a]1H1017+202	0.0039
[a]1H1210+393	0.00323
[b]1H1313+363	0.00468
[a]1H1408–031	0.00578
[a]1H2209–470	0.00590
[a]1H2315–423	0.00525

[1]The perturbations of the local velocity field can introduce significant errors in the calculations of luminosities, distances, and volumes used in this chapter if an uncorrected redshift measurement is used for nearby (v < 2000 km/s) objects. Instead, all distance related calculations used an effective redshift, z_{eff}, derived from a velocity corrected for local perturbations.

[a]Calculated from velocities given in Kruper, Canizares, and Urry (1990)

[b]Calculated from the distance given in Tully (1988). The distance value was derived from a similar velocity model used in (a) above.

Table 2

Results of the "V'/V'_{max}" Test of the Uniformity of the Sample

Separating Flux (μJy)	[1]$\langle V'/V'_{max} \rangle$ [2]Upper Flux Sub-sample	N [2]Upper Flux Sub-sample	[1]$\langle V'/V'_{max} \rangle$ [3]Lower Flux Sub-sample	N [3]Lower Flux Sub-sample
2.75	0.814 ± 0.079	4.	0.547 ± 0.026	92.
2.50	0.792 ± 0.069	6.	0.540 ± 0.028	90.
2.25	0.740 ± 0.060	8.	0.525 ± 0.030	88.
2.00	0.742 ± 0.051	14.	0.524 ± 0.034	82.
1.75	0.726 ± 0.042	22.	0.521 ± 0.041	74.
1.50	0.706 ± 0.034	36.	0.540 ± 0.056	60.
1.25	0.654 ± 0.029	53.	0.550 ± 0.076	43.
1.10	0.648 ± 0.026	72.	0.671 ± 0.102	24.
1.00	0.592 ± 0.025	77.	0.401 ± 0.115	19.
0.975	0.613 ± 0.024	86.	0.541 ± 0.158	10.
0.947	0.631 ± 0.021	96.	...	...

[1]For an explanation of V'/V'_{max}, see section 2.1 (ii). For a uniform distribution, $\langle V'/V'_{max} \rangle = 0.5$

[2]Each row in the table corresponds to a sample divided into an "upper flux" and a "lower flux" subsample at the Separating Flux, given in column 1. The "Upper Flux Subsample" columns give the average value of V'/V'_{max} and N, the number of objects, in the upper flux subsample. The error given is the error in the mean of the sample indicated. The error for $V'/V'_{max} = | V'/V'_{max}(F+\sigma_F) - V'/V'_{max}(F-\sigma_F) | / 2$. This error is very asymmetric due to the truncation of V'/V'_{max} at 0 and 1. These errors should therefore not be approximated as Gaussian.

[3]Same as above, but for the lower flux subsample.

Table 3.

[1]Average V/V_{max} for Fluxes Reduced by kσ

[1]Flux Reduction Factor, k [σ]	$<V/V_{max}>$	Uncertainty	[2]Number Remaining in Sample
0.0	0.630	0.02	96
0.2	0.593	0.023	77.
0.4	0.614	0.025	72.
0.6	0.639	0.027	67.
0.8	0.609	0.030	54.
1.0	0.613	0.033	48.
1.2	0.608	0.036	41.
1.4	0.644	0.038	39.
1.6	0.652	0.041	34.
1.8	0.657	0.046	29.
2.0	0.622	0.052	22.
2.2	0.667	0.057	21
2.4	0.682	0.058	18
2.6	0.629	0.068	13.
2.8	0.584	0.078	10
3.0	0.543	0.083	8

[1]To produce this table, all fluxes in the sample were reduced by k σ, where k is given in column 1. If the flux of an object was reduced below the flux limit, the object was removed from the sample. After removal of the objects below the flux limit, $<V/V_{max}>$ was evaluated. The resulting $<V/V_{max}>$ is given in the second column.

[2]This column gives the number of objects remaining in the sample after removal of objects with reduced fluxes below the flux limit.

Table 4

A. Results of Cumultaive Luminosity Distribution Fits[1]

[2]Fit Comments	Normalization (10^{-8} Mpc^{-3} [10^{44} erg s^{-1}]$^{-1-\alpha}$) $\pm\sigma$	χ^2_ν	γ=Log Slope $\pm\sigma$	K-S Probability
AGN Type 1's and 2's				
10^{42} – 10^{48} erg s^{-1} (Lowest L_X Object Excluded)	35.8 ± 5.3	2.64	–2.49 ± 0.019	13.5 %
$10^{41.5}$ – $10^{42.5}$ erg s^{-1} (Low L_X only)	260 ± 140	0.07	–1.24 ± 0.85	98 %
$10^{42.5}$ – 10^{44} erg s^{-1} (Medium L_X)	87 ± 20	0.06	–2.04 ± 0.27	99 %
10^{44}– 10^{48} erg s^{-1} [High Luminosity Fit]	65 ±13.5	0.30	–2.73 ±0.11	41 %
FORCED FIT FOR K-S PROBABILITY 10^{44}– 10^{48} erg s^{-1}	...	...	–2.49, FROM ABOVE	0.50 %
10^{42} - 10^{45} erg s^{-1} (For Comparison with Piccinotti)	42.5 ± 0.7	0.98	–2.40 ± 0.05	29 %
AGN Type 2 Only				
10^{42} – 10^{44} erg s^{-1}	7.48 ± 3.0	0.044	–2.65 ± 0.30	97 %
10^{42} – $10^{43.5}$ erg s^{-1} (Highest L_X object excluded)	14.8 ± 6.4	0.043	–2.45 ± 0.45	99 %

[1]This table gives results of K-S fits (for slope) and least squares fits (for normalization) of power-law X-ray luminosity functions to the cumulative luminosity distribution. See text for an explanation of the fitting procedure.

[2]The luminosity range given is the range of luminosities used in the fit and the range of luminosities used to normalize the cumulative luminosity distribution in the K-S fits.

Table 4

B. Results of Binned Luminosity Function Fits

[1]Fit Comments	Normalization (10^{-8} Mpc^{-3} [10^{44} erg s^{-1}]$^{-1-\gamma}$) $\pm\sigma$	γ=Log Slope $\pm\sigma$	χ^2 χ^2_ν	N_{bins}
All bins 10^{41} – 10^{48} erg s^{-1}	0.67 ± 0.61	–2.17 ± 0.17	67.6 13.5	7
10^{42} – 10^{48} erg s^{-1} (Lowest L_X bin excluded)	43.6 ± 9.7	–2.50 ± 0.07	14.2 3.54	6
	Low-Luminosity Fits			
10^{41} – 10^{44} erg s^{-1} (low luminosity; Poor fit indicates that more curvature than power law is required)	170 ± 132	–1.50 ± 0.46	7.0 7.0	3
	Increasing Luminosity			
10^{42} – 10^{45} erg s^{-1} (lowest L_X bin excluded)	68.4 ± 0.68	–2.26 ± 0.01	0.01 0.01	3
10^{42} – 10^{46} erg s^{-1} (Lowest L_X bin excluded.)	48.2 ± 12.6	–2.45 ± 0.10	9.98 9.98	3
10^{42} – 10^{47} erg s^{-1} (Highest and lowest L_X bins excluded)	43.5 ± 11.0	–2.50 ± 0.08	13.8 4.60	5
	Fits to High Luminosity Only			
10^{43} – 10^{48} erg s^{-1}	54.8 ± 11.5	–2.58 ± 0.08	7.13 2.38	5
10^{44} – 10^{48} erg s^{-1}	128 ± 25.4	–2.82 ± 0.08	0.94 0.47	4
10^{45} – 10^{48} erg s^{-1}	69.4 ± 73.0	–2.68 ±0.25	0.73 0.73	3
	Type 2 objects Only			
1/2 decade bins, full sample 10^{42} – 10^{44} erg s^{-1}	5.01 ± 2.71	–2.72 ± 0.18	0.28 0.14	4
1/2 decade bins,low-luminosity only 10^{42} – $10^{43.5}$ erg s^{-1}	19.8 ±11.8	-2.32 ±0.19	0.06 0.06	3

[1]The luminosity range given is from the lowest to the highest luminosity borders of the bins used in the fits.

Table 4

C. Comparison Samples

[1]Fit Comments	Normalization (10^{-8} Mpc^{-3} [10^{44} erg s^{-1}]$^{-1-\gamma}$) $\pm \sigma$	γ=Log Slope $\pm \sigma$	χ^2 χ^2_ν	N_{bins}
A-2 **(Piccinotti et al.)** $10^{42} - 10^{45}$ erg s^{-1}	[2]22.8 $\pm$1.27	2.75 $\pm$ 0.15	...	...
EMSS **(Maccacaro et al.)** 0.25 decade bins				
*0.16 – 2.5 × 10^{43} erg s^{-1}	*325	*–1.35 $\pm$ 0.13		6
*2.5 × 10^{43} – 10^{47} erg s^{-1}	*9.7	*–3.05 $\pm$0.05		11

[1]The luminosity range given is from the lowest to the highest luminosity borders of the bins used in the fits.

[2]Piccinotti et al. reported a normalization of 27 $\pm$ 0.15, however, they used $H_0 = 50$ km s^{-1} Mpc^{-1} in the derivation of this value. For a fair comparison, the numbers given in the table were corrected to $H_0 =$ 70 km s^{-1}Mpc^{-1}, using:
Normalization ~ $H_0^{5+2\gamma}$
where γ is the log slope of the fit. The Piccinotti fit values were derived using an un-binned technique, so the number of bins is not given.

*The results given by Maccacaro et al. were corrected from $H_0 = 50$ km/s/Mpc using the same conversion given above. The results are for faint sources only, de-evolved using their best fit evolution models. For this table, the luminosity in the 0.3–3.5 keV band used in Maccacaro et al. was assumed to be equivalent to that in the 2–10 keV band reported for the LMA. This approximation is equivalent to assuming all AGN have a log slope of –0.7 in both bands.

Table 5

Numbers of Objects in Different Samples Compared

	$^1N_{AGN}(\geq F_{Picci})$	$^2N_{exGal}$ $(\geq F_{Picci})$	$^1N_{AGN}$ $(\geq F_{LMA})$	$^2N_{exGal}$ $(\geq F_{LMA})$	$^3N_{HL}$	$N_{Clusters}$
LMA (>3σ)	34	126	96	~203	313	91
Schrader et. al. (>5σ)	^{4}NA	^{4}NA	^{4}NA	^{4}NA	[241]	^{4}NA
Piccinotti et al. (>5σ)	24	51	[42]	[155]	^{5}85	30
MSS (>5σ)	21.2	NA	46.5	NA	NA	NA

Please note: All "expected" numbers, i.e. those extrapolated from Log-*N* – Log-*S*, not from data, are given in brackets.

[1]Number of AGN greater than the equivalent Piccinotti or LMA flux limits, $|b| > 20°$. Equivalent 2–10 keV flux is calculated assuming $\alpha = -0.65$ or -0.7 power law spectrum.

$F_{Picci} = 3.6 \times 10^{-11}$ erg s^{-1} cm^{-2}, $F_{LMA} = 1.8 \times 10^{-11}$ erg s^{-1} cm^{-2}.

[2]Total number of $|b| > 20°$ sources identified with objects outside the galaxy, such as AGN, BL Lacs, and clusters.

[3]Total number of sources with $|b| > 20°$, not associated with galactic binaries. Schrader et. al. do not have enough identifications to consider the extragalactic only numbers. Since the distribution of galactic objects not associated with X-ray binaries appears to be isoptropic, the LASS Log *N*-Log-*S* curve includes all high–latitude, non-X-ray binary objects. The number for the LMA in this column represents the number of sources used to define the LMA flux limit.

[4]Schrader et. al., using exclusively LASS fine collimator data near the north ecliptic pole, had only 21 total objects, and only 2 AGN within the flux limit of A-1, so a statistically meaningful answer could not be obtained.

[5]This number does not include objects near the LMC or SMC.

FIGURE CAPTIONS

Figure 1. The non-Euclidian volume, calculated by the expression given in the text, is given along with the the volume given by a linear distance - z relation, $V = (c\,z\,/\,H_O)^3$, for comparison. The solid angle is assumed to be $4\,\pi$ sr for this figure.

Figure 2. The quantity V/V_{max} is shown as a function of the ratio of observed and minimum fluxes, F/F_{min}. The Euclidian expression for V/V_{max}, $(F/F_{min})^{-3/2}$, is compared to the values obtained by the calculations described in the text, for various values of z. (A spectrum with a log slope of -1 was assumed to simplify the calculations for the figure). The z value label nearest the end of each line segment indicates the value of z at which the V/V_{max} function represented by that line segment was calculated. The Euclidian and non-Euclidian functions are nearly indistinguishable on the plot for $z \leq 0.01$, but significant differences are manifested at $z \geq 0.1$.

Figure 3. (a) The distribution of V/V_{max} for the LMA is given, in bins of 0.2. The indicated errors are the 90% confidence intervals due to the poisson fluctuations of the number of sources detected in each bin. The small number of sources in the first bin occurs in other surveys as well. See text for details. (b) This figure gives V/V_{max} as a function of Log z; V/V_{max} increases with z. Figure (c) gives V/V_{max} as a function of 2–10 keV X-ray Luminosity. V/V_{max} also increases with luminosity.

Figure 4. This figure shows V/V_{max} as a function of 2–10 keV X-ray Luminosity if the fluxes of all objects are increased by 0.66 σ. The average of V/V_{max} is now 0.5, but note that the distribution of V/V_{max} still shows an obvious systematic trend to high V/V_{max} with luminosity (compare to Fig. 3(c) above).

Figure 5. This histogram shows the distribution of redshifts in the LMA. Note that there are very few objects at $z \geq 0.4$ where evolution has been seen in previous studies.

Figure 6. The binned representation of the X-ray luminosity function, calculated as described in the text, is shown for bins spanning one decade. Each value of the function is plotted at the mean luminosity of the objects in the bin. The points are plotted with Poisson errors corresponding to one sigma Gaussian confidence intervals. The solid line indicates the best fit, from $10^{42} - 10^{48}$ erg s^{-1}, of a power law model to the un-binned data. The lowest luminosity object was omitted from this fit. The fit is extended as a dotted line below 10^{42} erg s^{-1} to emphasize that the luminosity function flattens or cuts off below 10^{42} erg s^{-1}. The power law shown has a slope of -2.49 ± 0.19.

Figure 7. The luminosity function of the Type 2 objects in the LMA is shown with the objects grouped into bins of 1/2 decade in luminosity from $10^{42} - 10^{44}$ erg s^{-1}. Note that no objects are observed past 10^{44} erg s^{-1}, and that the function appears to truncate or steepen above $10^{43.5}$ erg s^{-1}. The best fit of the un-binned data to a power law, shown as a solid line in the figure, yields a log slope of -2.45 ± 0.45 from $10^{42} - 10^{43.5}$ erg s^{-1}. A rough 90% confidence upper limit of the XLF at high luminosity, derived from observing zero objects in a bin from 10^{44}–$10^{47.5}$ erg s^{-1}, is shown at $10^{47.25}$ erg s^{-1}, the center of the bin. Note that the extrapolation of the low-luminosity power law (shown as a dotted line) is far above this point, confirming that the XLF must steepen at high luminosities.

Figure 8. The LMA and the Piccinotti et al. luminosity functions are shown together for comparison. The LMA is binned the same as in previous figures. The Piccinotti sample is also grouped in bins covering one decade in luminosity. Note that the functions are different by ~ factor of two (this is not obvious on the large scale of the figure), but that the functions have similar slopes. Note also that the upper limit derived from the minimum flux of the Piccinotti et al. sample is insufficient to detect the turnover in the XLF evident in the LMA data.

Figure 9. The cumulative fraction of Type 2 objects vs luminosity is presented in this figure, in bins of 1/2 decade. Above $10^{43.5}$ erg s^{-1}, the fraction is significantly below

the values of 0.6-0.8 reported for unbiased samples selected in other wavebands. The fraction closely parallels the shape of the Type 2 XLF (See Fig. 7), indicating that the steepening or truncation of the XLF is probably related to the low fraction of Type 2's in the LMA. The error bars indicate the 1 σ Poisson errors on the number of objects in each bin.

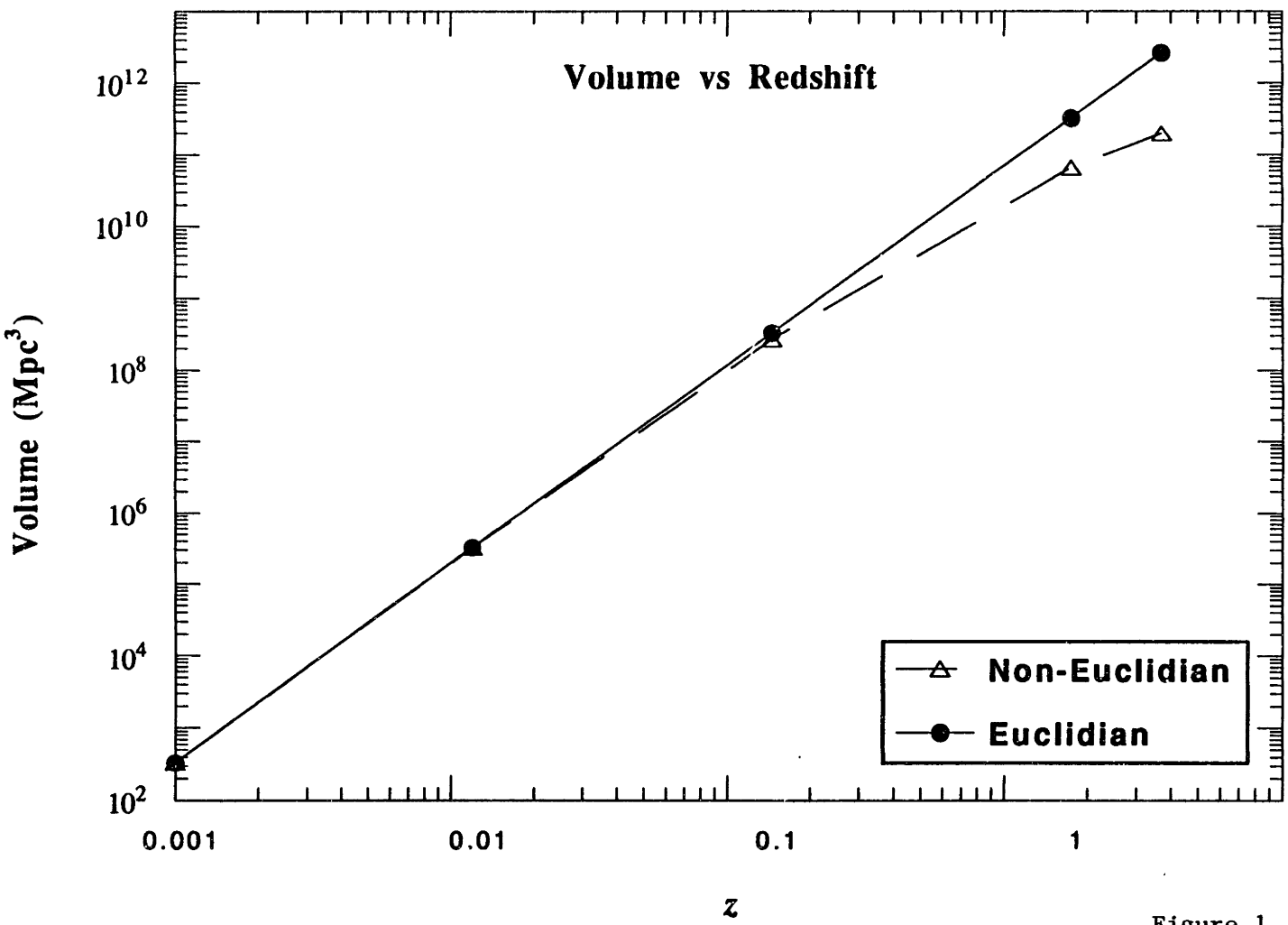
Volume vs Redshift
Volume (Mpc^3)
10^{12}
10^{10}
10^8
10^6
10^4
10^2
0.001
0.01
0.1
1
z
Non-Euclidian
Euclidian

Figure 1

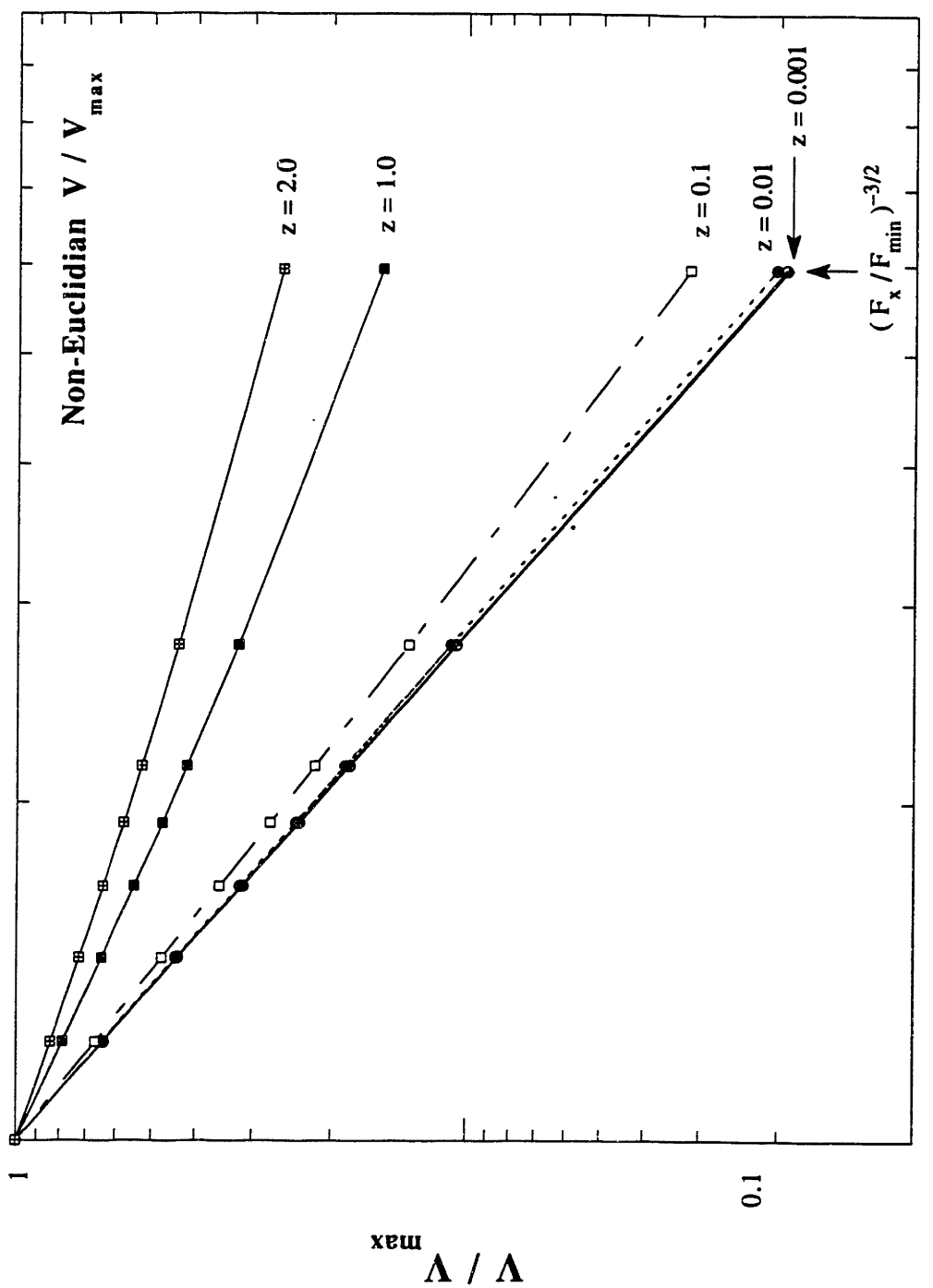
Non-Euclidian V / V max
z = 2.0
z = 1.0
z = 0.1
z = 0.01
z = 0.001
(F x / F min)-3/2
1
0.1
1
V / V max
F x / F min

Figure 2

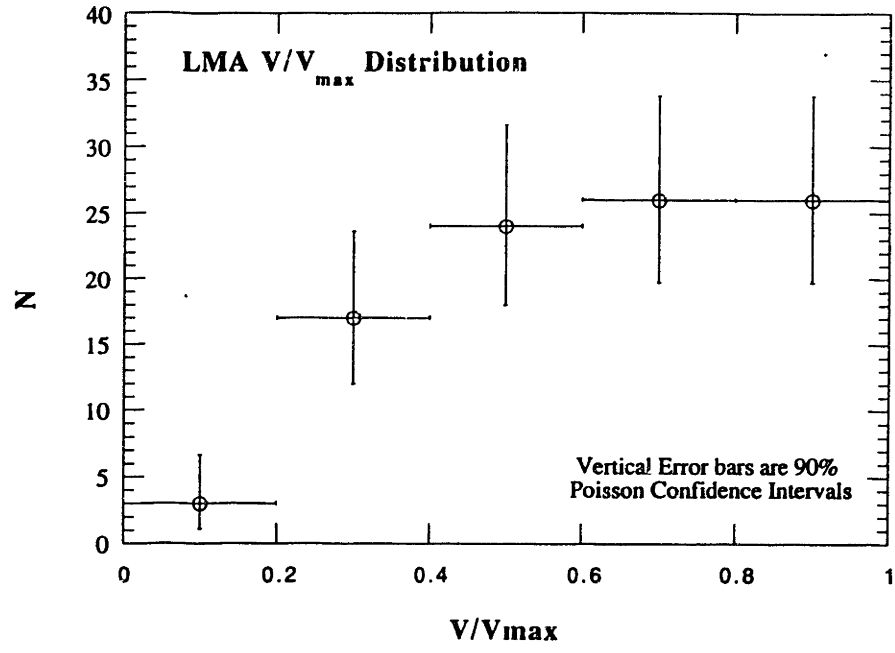

Figure 3a

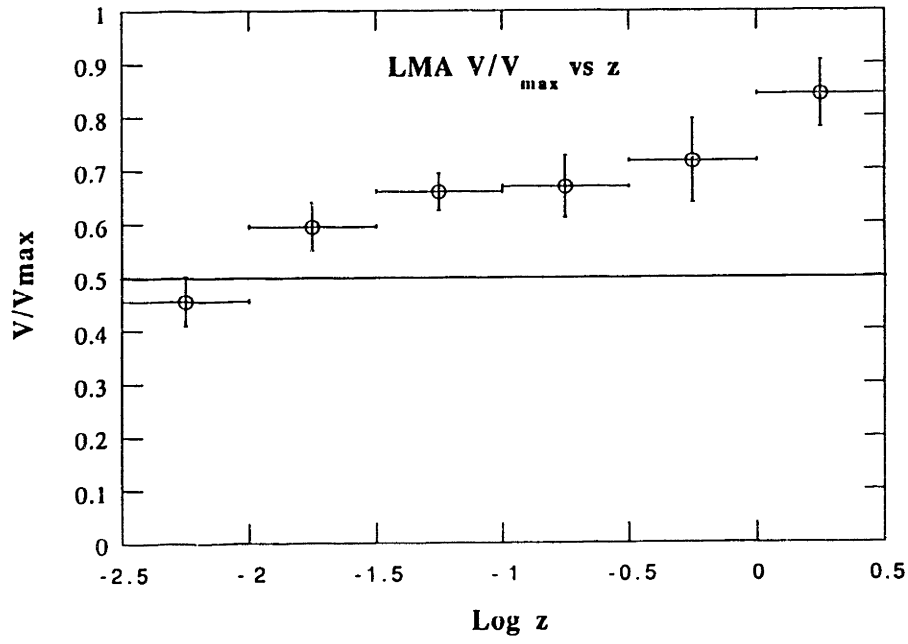

Figure 3b

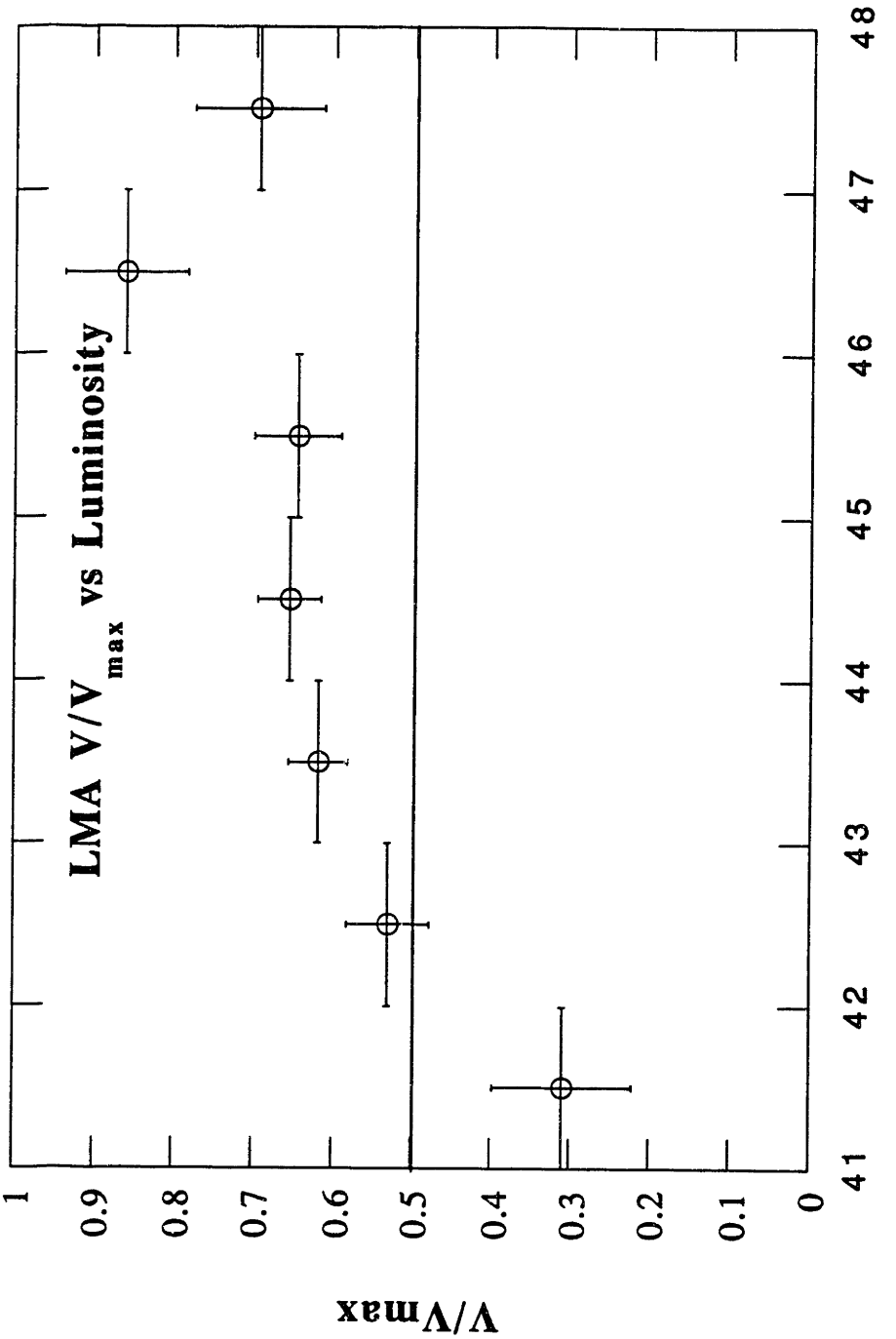
LMA V/V max vs Luminosity
V/Vmax
L X 4 4
0
0.1
0.2
0.3
0.4
0.5
0.6
0.7
0.8
0.9
1
41
42
43
44
45
46
47
48

Figure 3c

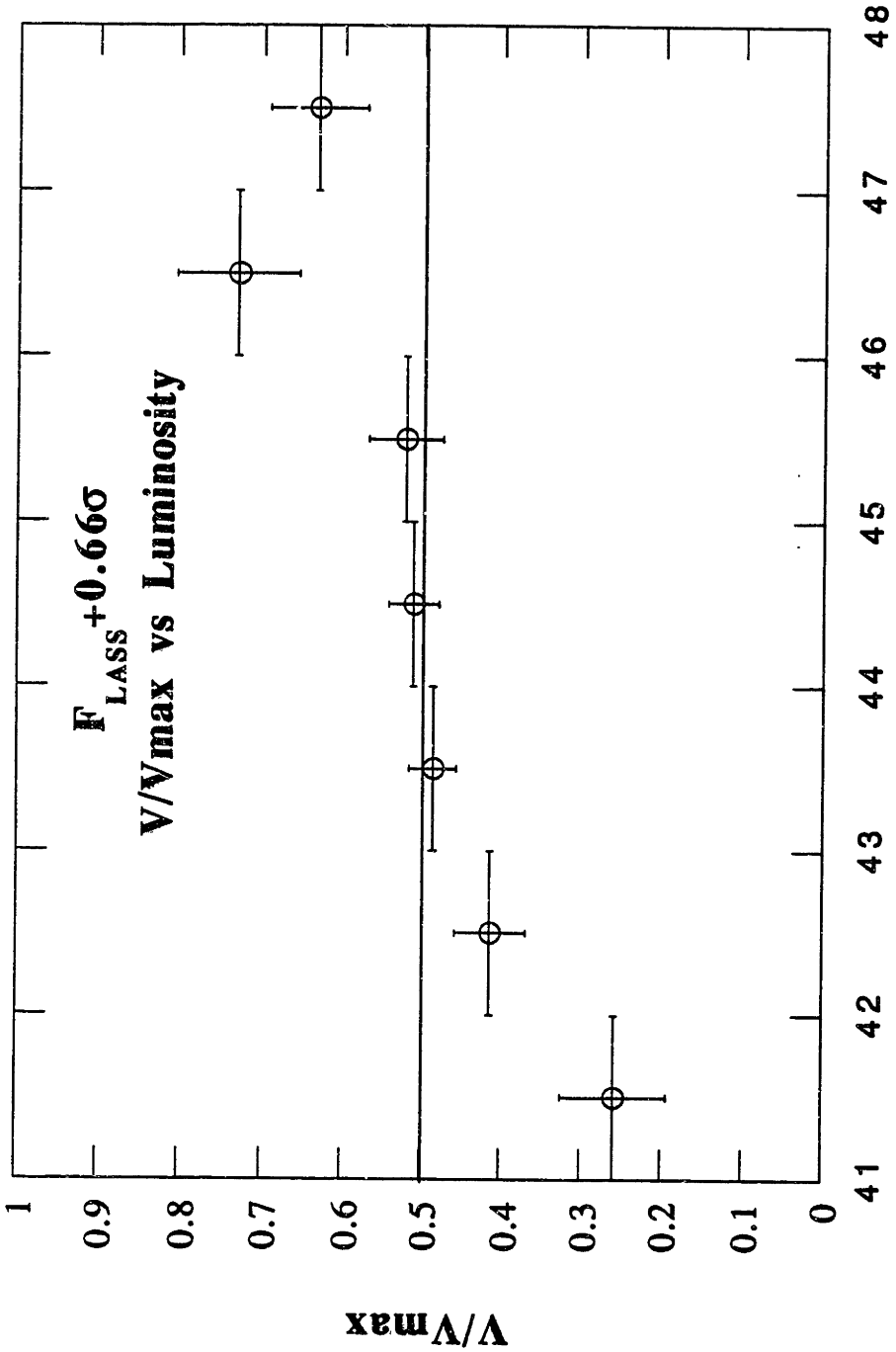
F_{LASS}+0.66σ
V/Vmax vs Luminosity
V/Vmax
L_{X44}
0
0.1
0.2
0.3
0.4
0.5
0.6
0.7
0.8
0.9
1
41
42
43
44
45
46
47
48

Figure 4

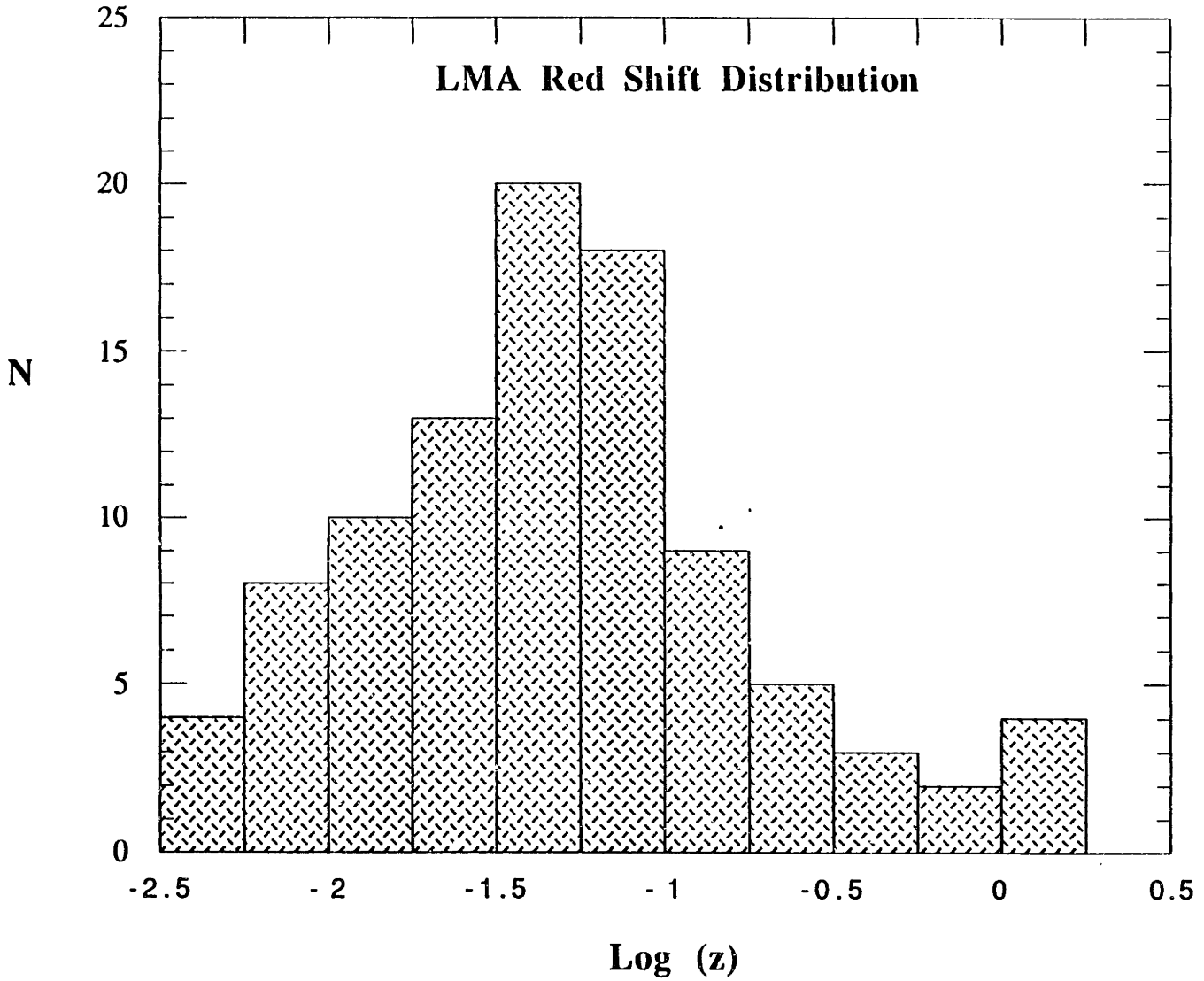

Figure 5

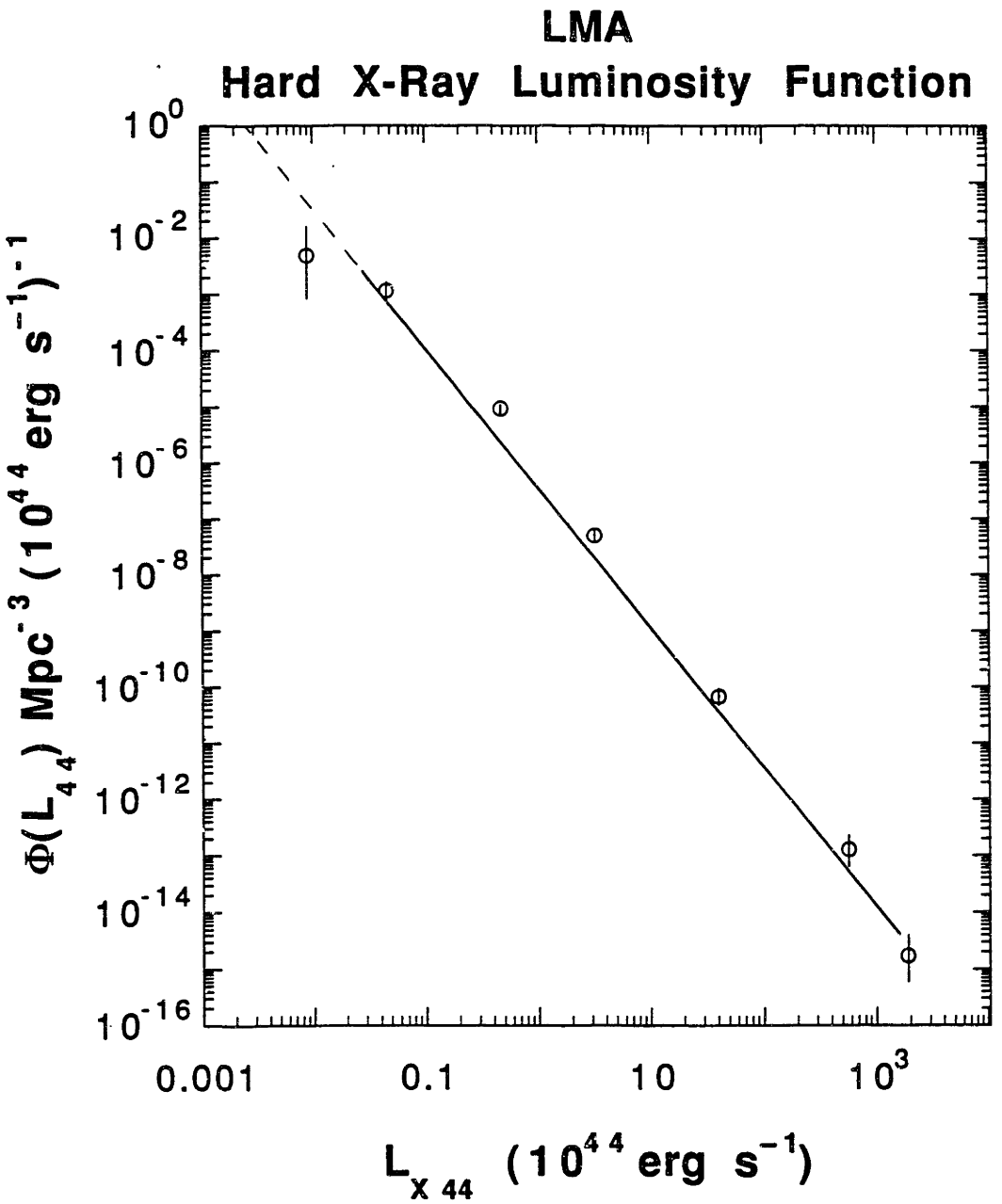
LMA
Hard X-Ray Luminosity Function
10^0
10^{-2}
10^{-4}
10^{-6}
10^{-8}
10^{-10}
10^{-12}
10^{-14}
10^{-16}
$\Phi(L_{44})$ Mpc^{-3} (10^{44} erg s^{-1})$^{-1}$
0.001
0.1
10
10^3
$L_{X\,44}$ (10^{44} erg s^{-1})

Figure 6

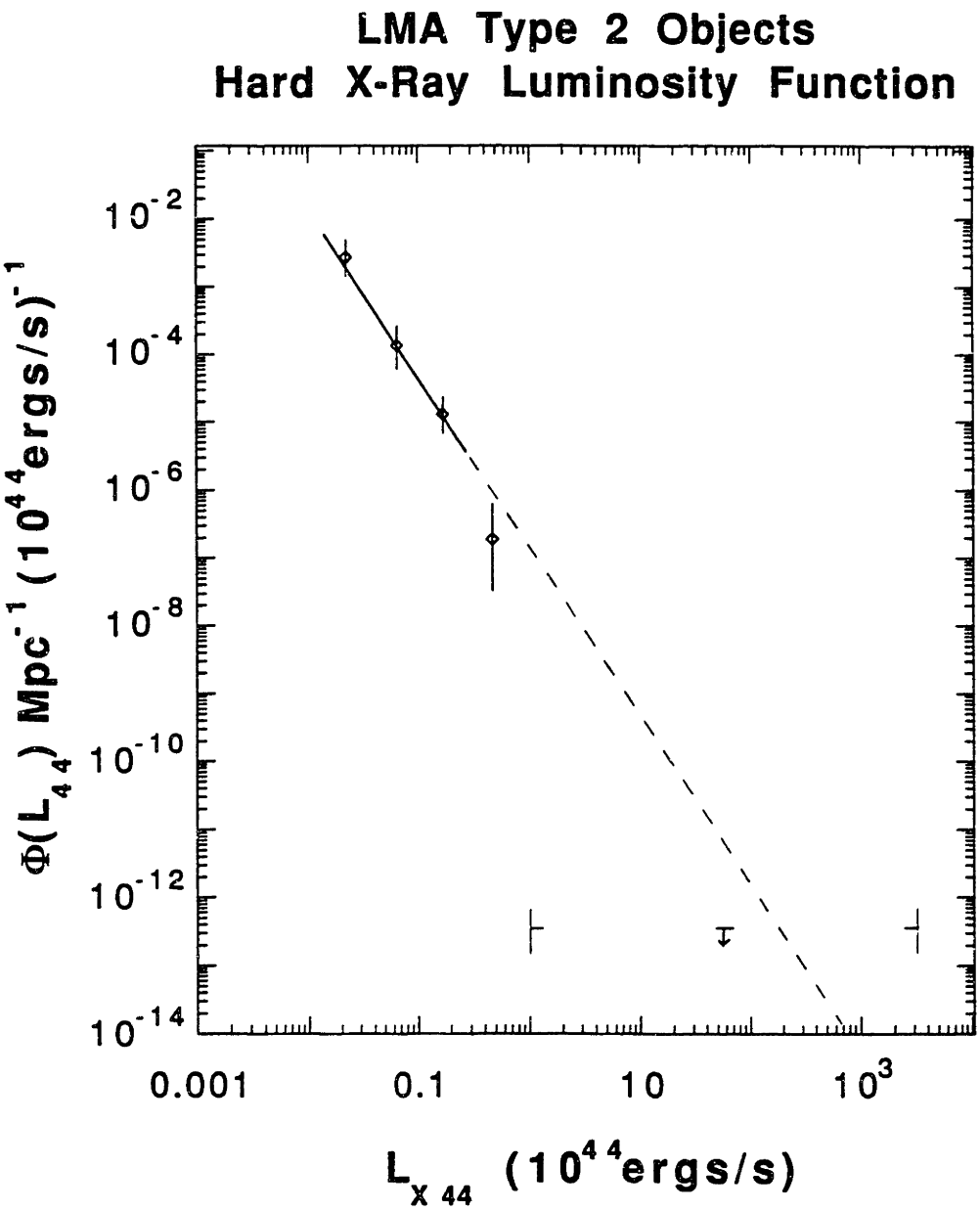
LMA Type 2 Objects
Hard X-Ray Luminosity Function
10^{-2}
10^{-4}
10^{-6}
10^{-8}
10^{-10}
10^{-12}
10^{-14}
$\Phi(L_{44})$ Mpc^{-1} (10^{44}ergs/s)$^{-1}$
0.001
0.1
10
10^{3}
$L_{X\,44}$ (10^{44}ergs/s)

Figure 7

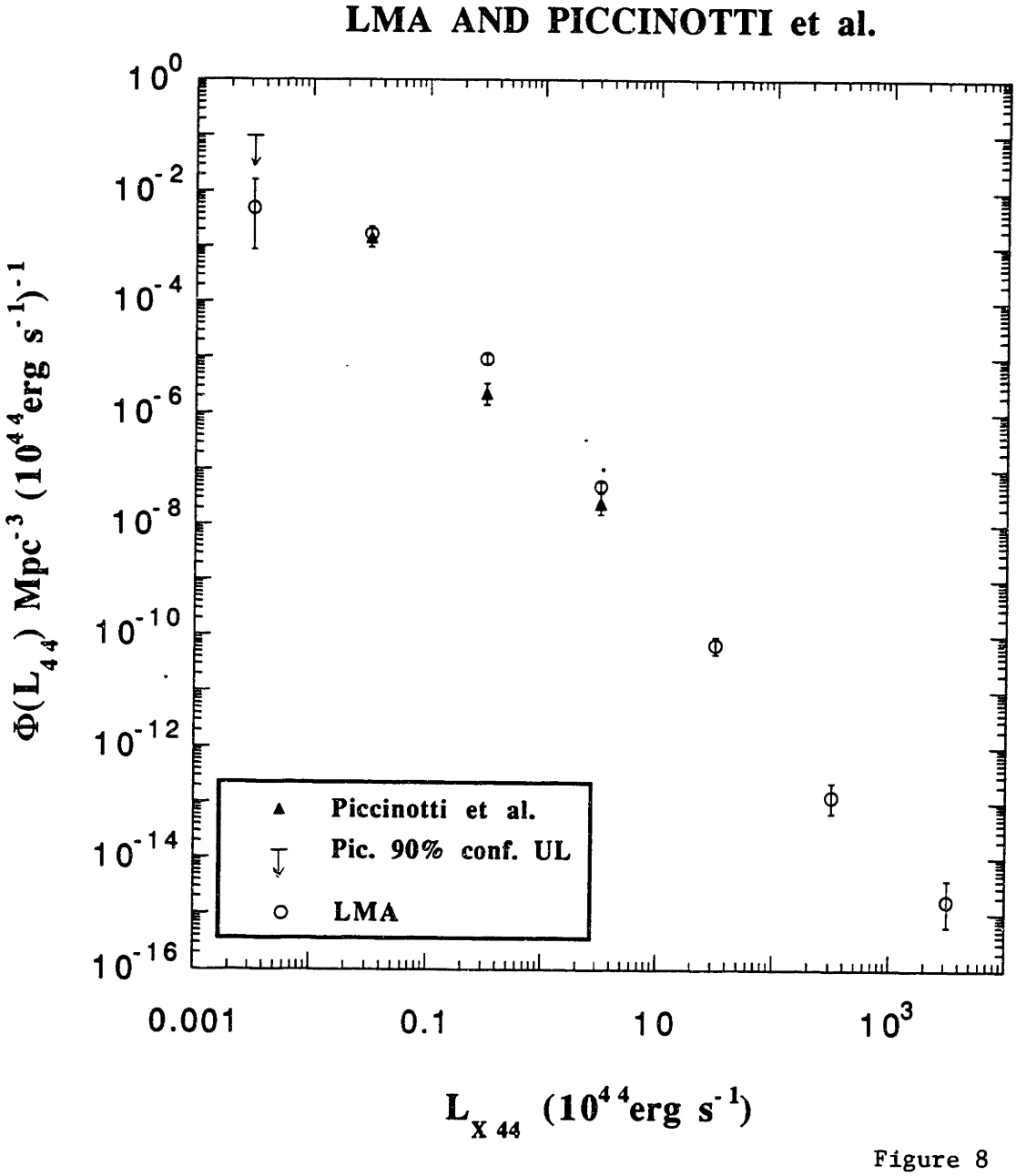
LMA AND PICCINOTTI et al.
10^0
10^{-2}
10^{-4}
10^{-6}
10^{-8}
10^{-10}
10^{-12}
10^{-14}
10^{-16}
$\Phi(L_{44})$ Mpc^{-3} (10^{44}erg s^{-1})$^{-1}$
Piccinotti et al.
Pic. 90% conf. UL
LMA
0.001
0.1
10
10^3
$L_{X\,44}$ (10^{44}erg s^{-1})

Figure 8

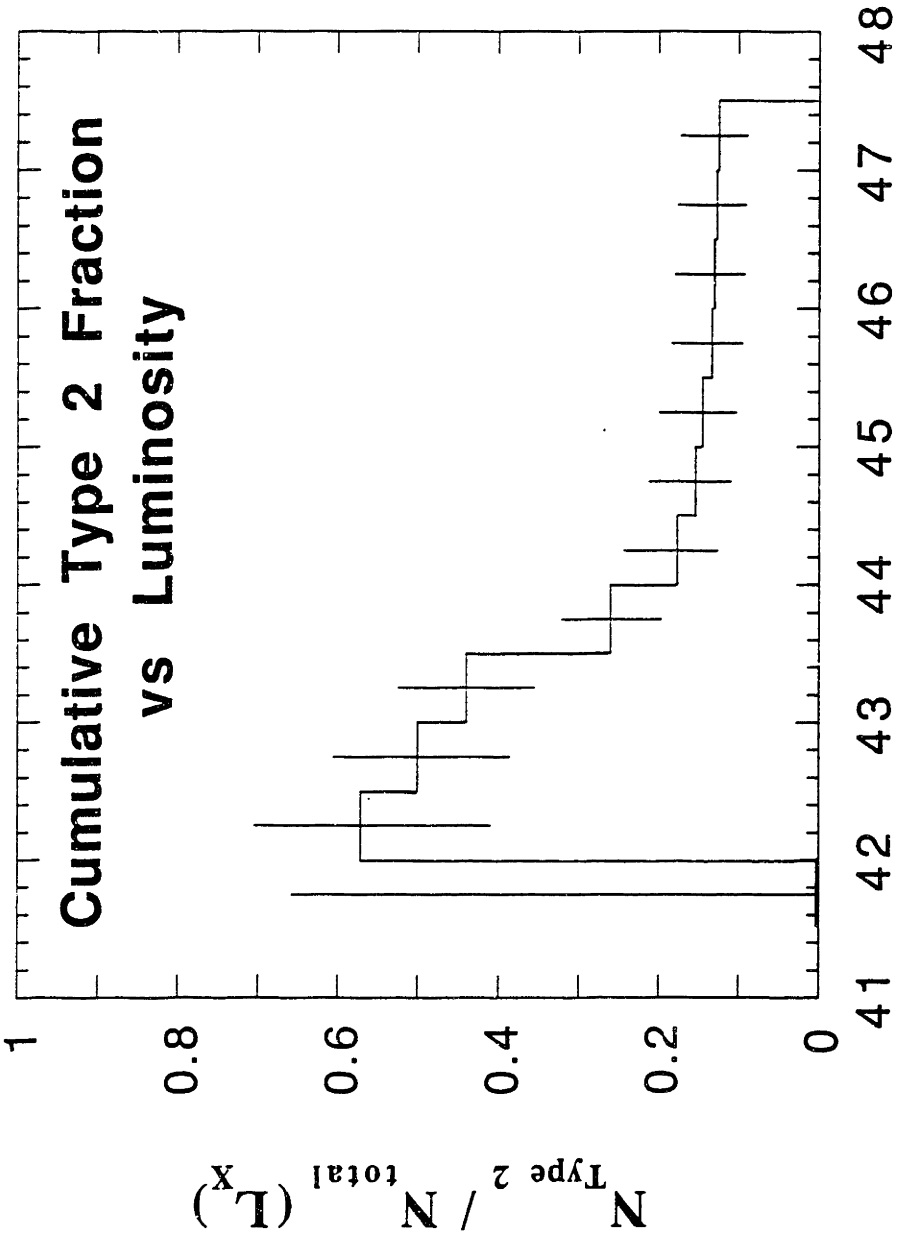
Cumulative Type 2 Fraction
vs Luminosity
$N_{Type\ 2} / N_{total} (L_X)$
0
0.2
0.4
0.6
0.8
1
41
42
43
44
45
46
47
48
Log (L_X) (Log erg s^{-1})

Figure 9

APPENDIX I

CONFUSION NOISE AND IDENTIFICATION CONFUSION RATE ESTIMATES

1. CONFUSION NOISE ESTIMATE

Confusion noise is the flux contribution of fluctuations in the ensemble of unresolved sources within the field of view, or "beam" of an instrument. In the LASS instrument, a background is fit to a large area nearby detected sources. The noise in this background fit includes many contributions, including that of confusion noise, but the noise is measured in an area that is large compared to the detector beam. Therefore, although the reported errors include noise in the background, they do not give a correct estimate of the confusion noise in the LASS beam.

The contribution of confusion noise for point-like sources can be estimated by extrapolating the Log N – Log S curve below the flux limit of the sample to predict the behavior of unresolved sources. The derivation below follows Rohlfs (Rohlfs, K. 1986, New York, Springer-Verlag).

Let $p(s)$ be the probability density of detecting a source with a flux between S and S+dS d, per steradian, over a beam of solid angle Ω. The average number of sources detected is then:

$$\overline{\nu} = \Omega\, p(s)\, \mathrm{d}s$$

If the sources are randomly distributed, ν will be Poisson distributed:

$$f(\nu) = \frac{\overline{\nu}^{\nu}}{\nu!} e^{-\overline{\nu}}$$

and so

$$\sigma_{\overline{v}}^2 = \overline{v}$$

The average output due to sources between S and $S + dS$ is given by:

$$\overline{S} = S\ \overline{v}$$

It can be shown that the variance of this output is therefore:

$$\sigma_{\overline{S}}^2 = S^{\,2}\overline{v}$$

If the signal is caused by sources with different fluxes, their variances add quadratically. Therefore, the variance due to fluxes between the survey flux limit S_{lim} and zero is given by:

$$\sigma_{S_{lim}}^2 = \Omega \int_0^{S_{lim}} S^2 p(s)\, ds$$

In Chapter 2 it was shown that $dN \sim S^{-5/2}\, dS$, so $N(s) = N_{lim}\ (S / S_{lim})^{-3/2}$, and therefore $p(s) = 3/2\ N_{lim}\ S^{-5/2}\ S^{3/2}{}_{lim}$, where N_{lim} gives the number of sources per steradian at the limiting flux S_{lim}. Evaluating the integral gives:

$$\sigma_{S_{lim}}^2 = \frac{1}{3\ N_{lim}\ \Omega} S_{lim}^2 \qquad (*)$$

where $N_{lim}\ \Omega$ is the average number of sources per beam at the limiting flux S_{lim}.

In the LASS bandpass, there are 313 sources in the sky with $S/\sigma > 3$ and $|b| > 20°$ detected by the LASS above 0.95 μJy. As was shown in chapter 2, only a negligible number of sources (2) are removed by applying the significance criterion, so the final answer will not be affected by imposing this criterion.

For the scan collimator, the number of independent beam areas on the sky is approximately 6750, so $N_{lim}\ \Omega = 0.046$, and the signal to confusion noise ratio for the scan collimators at the flux limit is

$$(S / \sigma)_{\mathrm{lim,scan}} = 2.68.$$

Finally, to complete the calculation, the noise from the scan collimator modules (1° × 4° FWHM, total 6600 cm^2) is combined with the noise from the fine collimator modules

(1 / 2° × 1° FWHM, total 2700 cm^2). As can be seen from the expression for σ^2 above, $\sigma \sim \Omega^{-1/2}$, where Ω is the beam area, and the signal to noise for the fine collimator module is therefore $8^{1/2}$ times that for the scan collimator module, 7.58. Confusion noise from multiple detectors viewing the same sky adds linearly, unlike Gaussian noise, which adds quadratically. This is because Gaussian noise is dependent on the the total number of photons; confusion noise is independent of the number of photons, and constant in time as long as all sources are constant in time. The confusion noise from the two types of detectors is therefore estimated by:

$$\left(\frac{S}{\sigma}\right)_{lim,total} = \frac{A_{scan}S_{scan} + A_{fine}S_{fine}}{A_{scan}\sigma_{scan} + A_{fine}\sigma_{fine}}$$

where A_{fine} is the effective area of the fine collimator module, and A_{scan} is the effective area of the scan collimator. The resulting signal to noise at the flux limit (the worst case) due to confusion in the LASS is therefore:

$$(S / \sigma)_{\mathrm{lim,total}} \leq 3.62 \ .$$

where I have used the symbol ≤ to emphasize that this calculation completely omits the restrictions on the confusion noise given by the confirming fluxes of the MC, the fine collimator modules alone, other imaging X-ray detectors, and optical candidate searches described in Chapter 2.

Since $(S / \sigma)_{\mathrm{lim,total}} \sim (N\Omega)^{-1/2}$ and since $N\Omega \sim S^{-3/2}$, the general expression for signal to noise is given by:

$$(S / \sigma)_{\mathrm{confusion}} \leq 3.62\ (S/S_{lim})^{3/4} \ .$$

2. IDENTIFICATION CONFUSION RATE ESTIMATE

Below I estimate the number of spurious X-ray detections due to the chance addition of multiple unresolved sources within a single instrument beam.

The probability that the fluctuations in the population of unresolved sources will add up to a flux between S' and $S' + dS$ is:

$$p(S_{ur} = S')\, dS = G(S', \sigma^2_S(S'))\, dS$$

where $G(S', \sigma^2_S(S'))$ is a Gaussian function with mean S', and $\sigma_S(S')$, the deviation of the contribution of sources of flux up to S', calculated above. The probability per beam of unresolved sources of flux less than S_{max} adding up to S' is then

$$\int_0^{S_{max}} G[S', \sigma^2_{ur}(S')]\, dS' = \frac{\overline{N}_{fake}}{N_{beam}} = \frac{1}{\sqrt{2\pi}} \int_0^{S_{max}} \frac{1}{\sigma_{ur}(S')}\, exp\left[\frac{1}{2}\left(\frac{S'}{\sigma_{ur}(S')}\right)^2\right] dS' \quad (1)$$

where N_{fake} is the number of "fake" sources, those due to additions of unresolved sources, and N_{beam} = the number of beam areas on the sky. from above,

$$\sigma^2_{ur}(S') = 3\ \Omega\ N\ S^{3/2}_{min}\ S^{1/2} \quad (2)$$

The number of independent source identification positions on the sky is that for the scan collimator alone for many faint sources, due to the source acceptance algorithm used by Wood et al. (1984). Therefore, I use the appropriate parameters for the scan collimator field of view alone to derive an upper limit estimate to the number of confused sources. Substituting expression (2) above into expression (1) and integrating from a flux of zero to the maximum observed flux (3.39 μJy) yields:

$$\langle N_{fake} \rangle = 37.4$$

APPENDIX II: AN ATLAS OF MULTI-FREQUENCY SPECTRA OF THE LMA SAMPLE.

The Multi-Frequency spectra of the 96 objects of the LMA are presented in this appendix, ordered by the R. A. of their LASS catalogue names, Type 1 objects first, then Type 2 objects.

Key

Open Circles – UV and X–ray data, thought to represent pure nuclear continuum.

Dotted Lines – BVRI Optical photometry, thought to be an upper limit, due to the possiblity of stellar contamination.

Filled diamonds – Photometry taken from Veron-Cetty & Veron (1989).

Filled Squares – Infra-red photometry with $\lambda > 1$ μm.

Filled Symbols in Optical Bands – Spectrophotometry, each symbol for a different observing epoch. See Table 3 of Chapter 2 for details of observations.

TYPE 1 OBJECTS

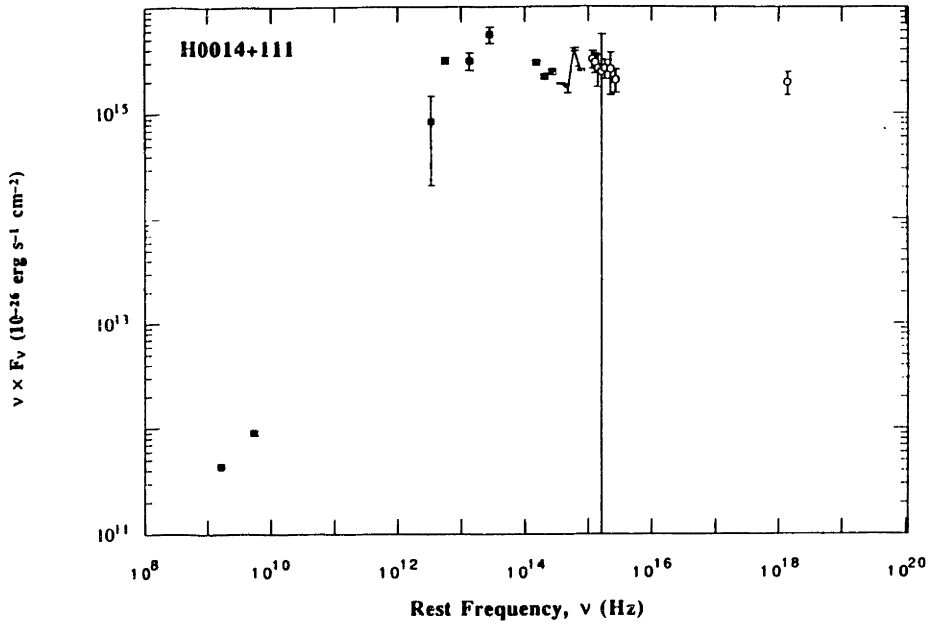
H0014+111
10^{15}
10^{13}
10^{11}
10^{8}
10^{10}
10^{12}
10^{14}
10^{16}
10^{18}
10^{20}
Rest Frequency, ν (Hz)
ν × Fν (10⁻²⁶ erg s⁻¹ cm⁻²)

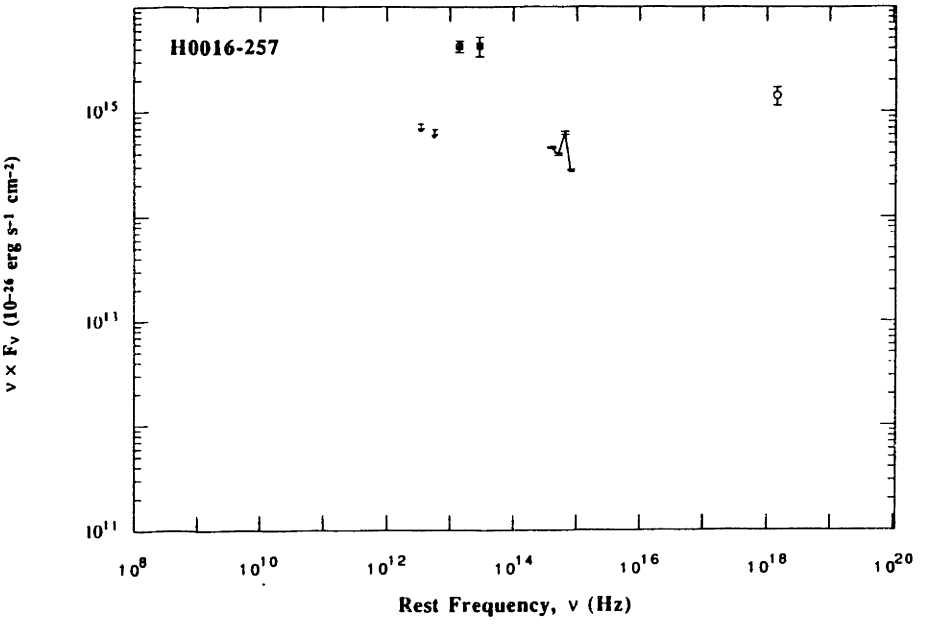
H0016-257
10^{15}
10^{13}
10^{11}
10^{8}
10^{10}
10^{12}
10^{14}
10^{16}
10^{18}
10^{20}
Rest Frequency, ν (Hz)
ν × Fν (10⁻²⁶ erg s⁻¹ cm⁻²)

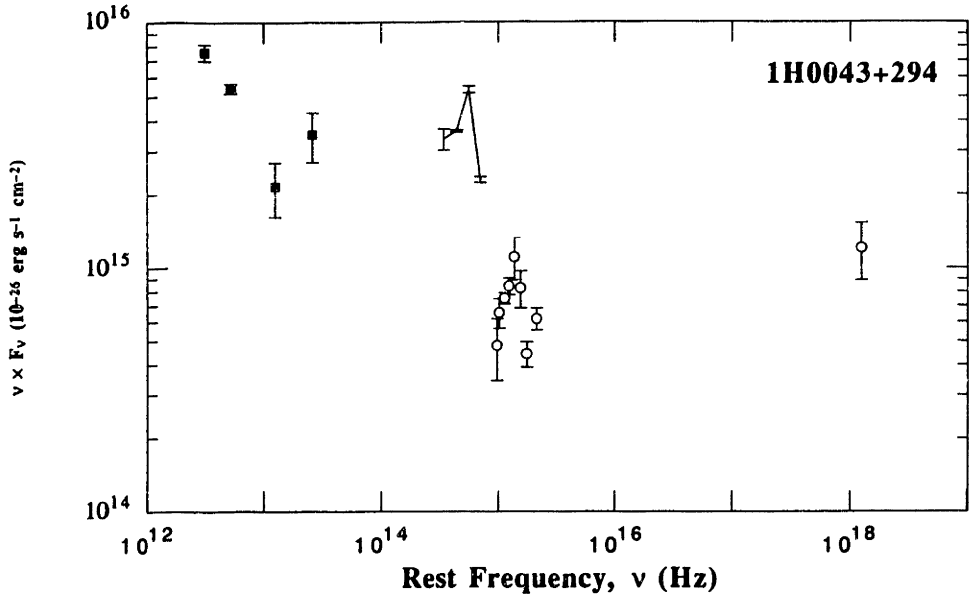
1H0043+294
10^{16}
10^{15}
10^{14}
10^{12}
10^{14}
10^{16}
10^{18}
$\nu \times F_\nu$ (10^{-26} erg s^{-1} cm^{-2})
Rest Frequency, ν (Hz)

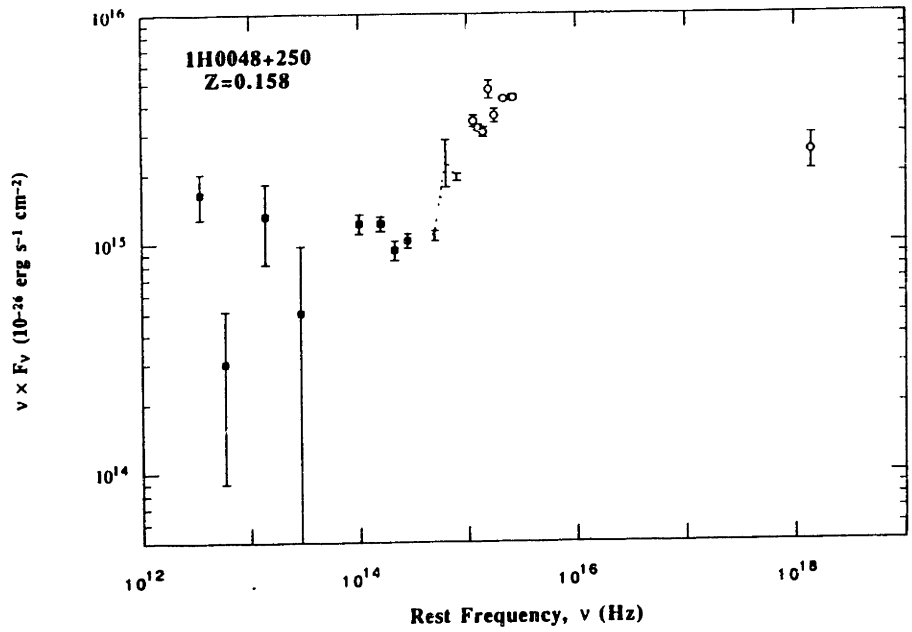
1H0048+250
Z=0.158
10^{16}
10^{15}
10^{14}
10^{12}
10^{14}
10^{16}
10^{18}
$\nu \times F_\nu$ (10^{-26} erg s^{-1} cm^{-2})
Rest Frequency, ν (Hz)

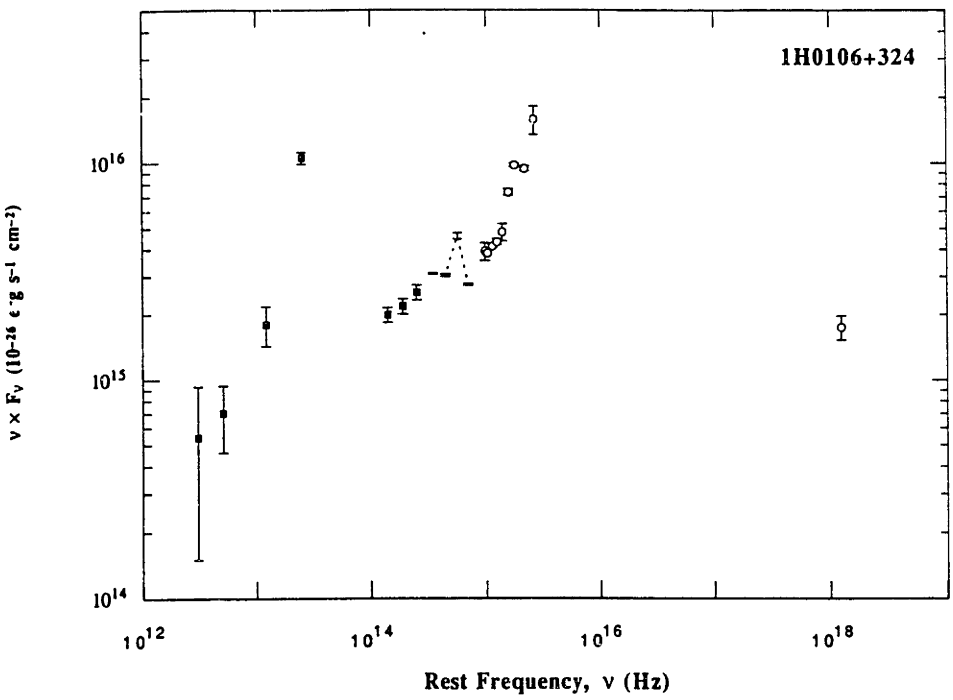
1H0106+324
10^{16}
10^{15}
10^{14}
10^{12}
10^{14}
10^{16}
10^{18}
$\nu \times F_\nu$ (10^{-26} e$^-$g s^{-1} cm^{-2})
Rest Frequency, ν (Hz)

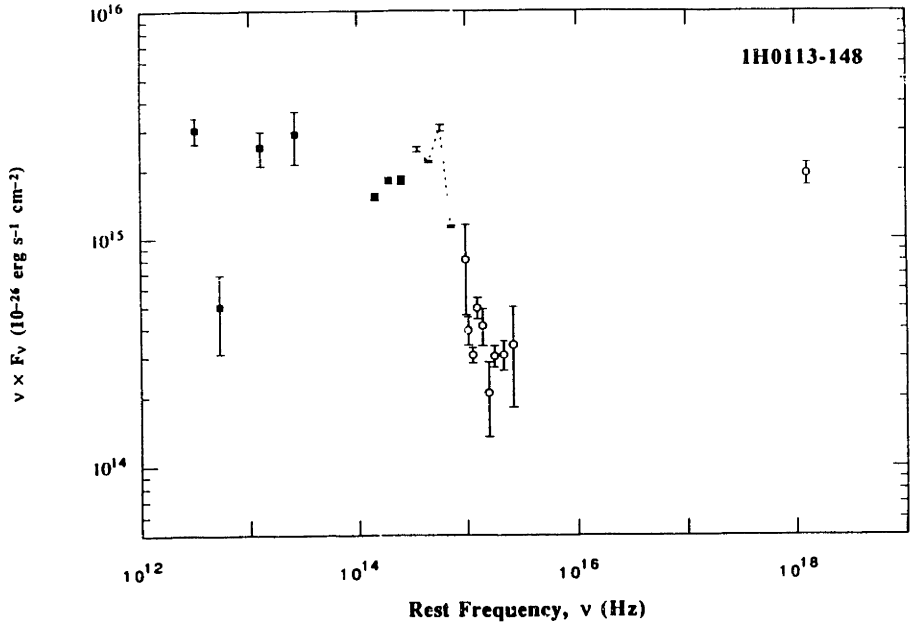
1H0113-148
10^{16}
10^{15}
10^{14}
10^{12}
10^{14}
10^{16}
10^{18}
$\nu \times F_\nu$ (10^{-26} erg s^{-1} cm^{-2})
Rest Frequency, ν (Hz)

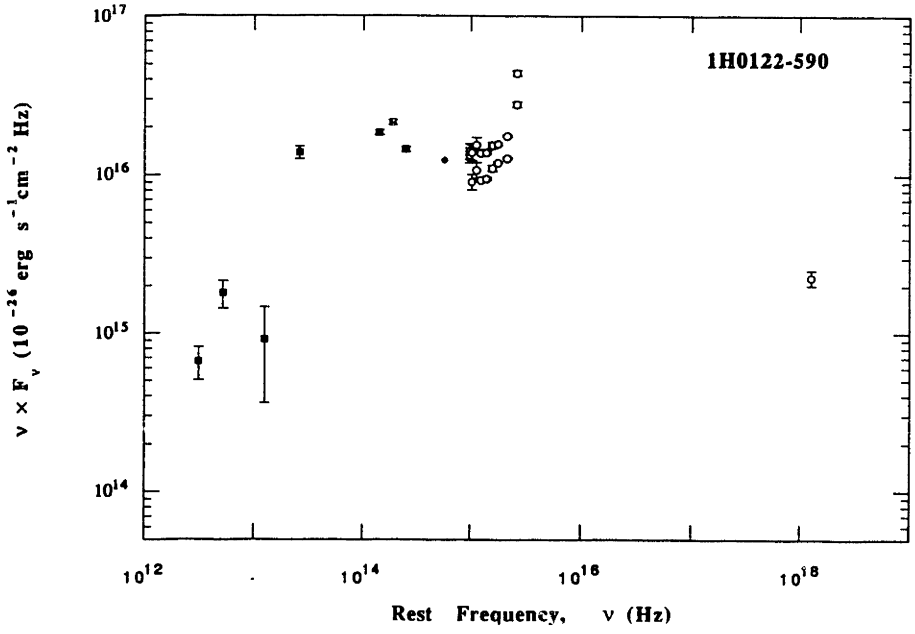
1H0122-590
10^{17}
10^{16}
10^{15}
10^{14}
10^{12}
10^{14}
10^{16}
10^{18}
$\nu \times F_\nu$ (10^{-26} erg s^{-1}cm^{-2} Hz)
Rest Frequency, ν (Hz)

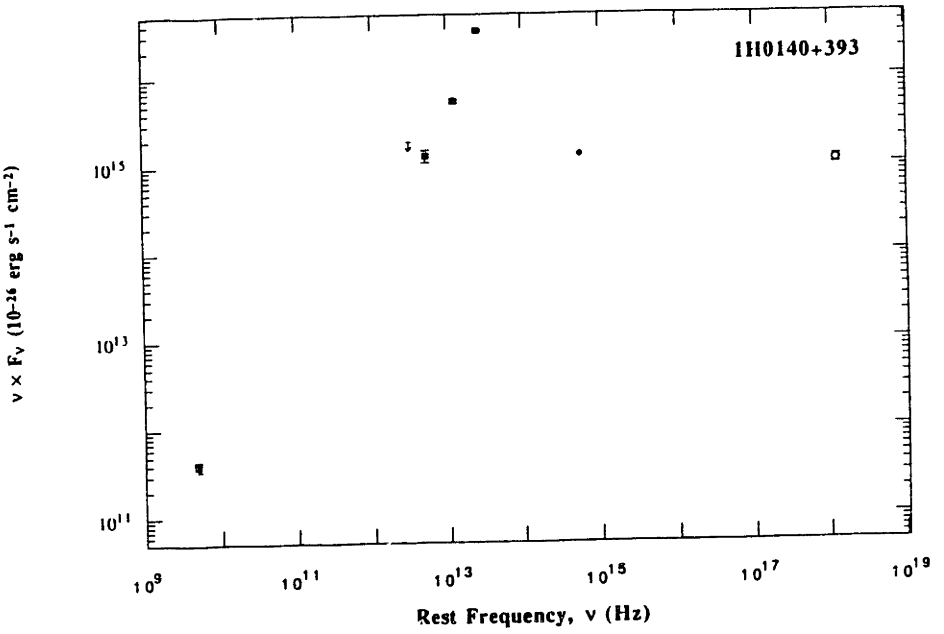
1H0140+393
10^{15}
10^{13}
10^{11}
10^{9}
10^{11}
10^{13}
10^{15}
10^{17}
10^{19}
$\nu \times F_\nu$ (10^{-26} erg s^{-1} cm^{-2})
Rest Frequency, ν (Hz)

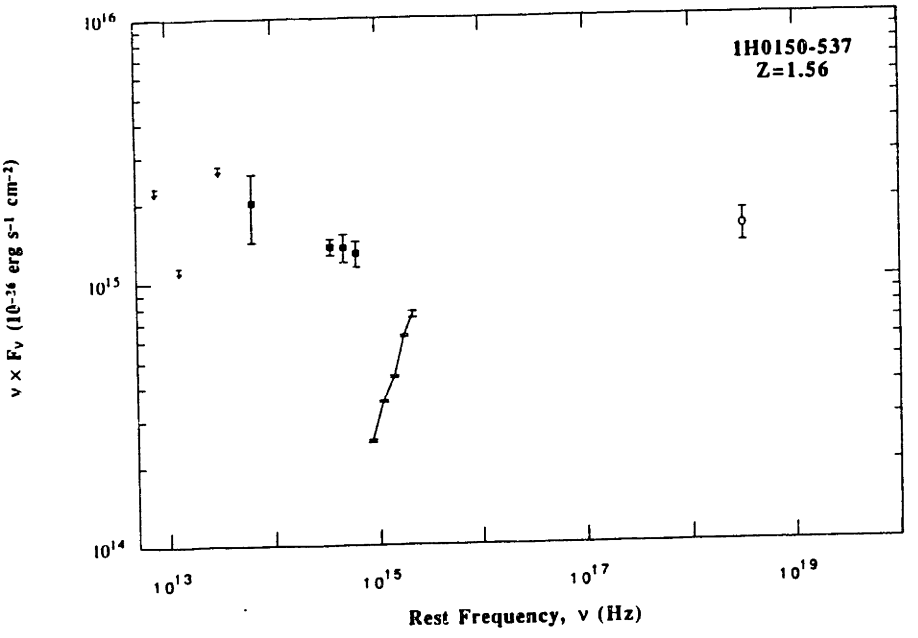
1H0150-537
Z=1.56
10^{16}
10^{15}
10^{14}
10^{13}
10^{15}
10^{17}
10^{19}
$\nu \times F_\nu$ (10^{-26} erg s^{-1} cm^{-2})
Rest Frequency, ν (Hz)

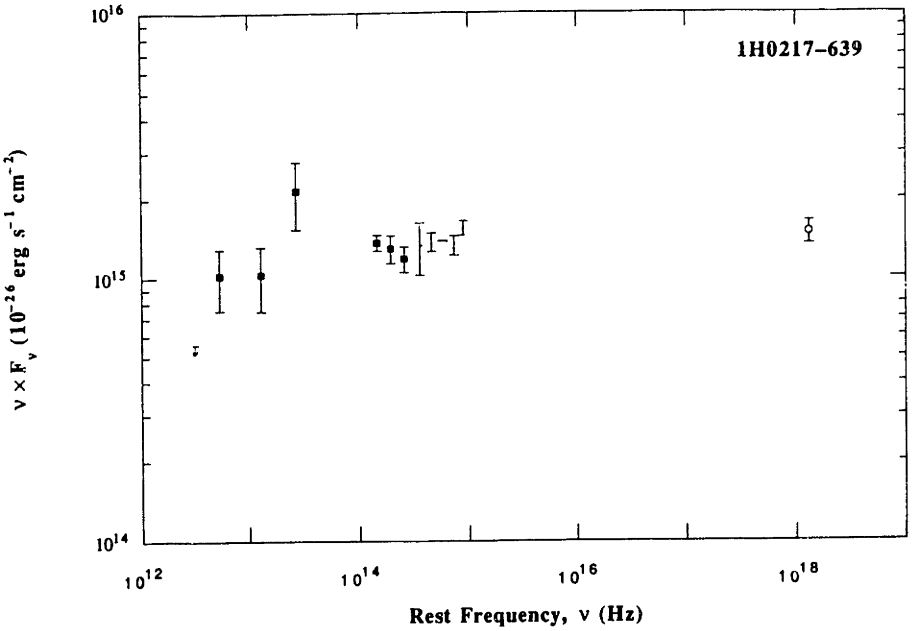
1H0217-639
10^{16}
10^{15}
10^{14}
10^{12}
10^{14}
10^{16}
10^{18}
$\nu \times F_\nu$ (10^{-26} erg s^{-1} cm^{-2})
Rest Frequency, ν (Hz)

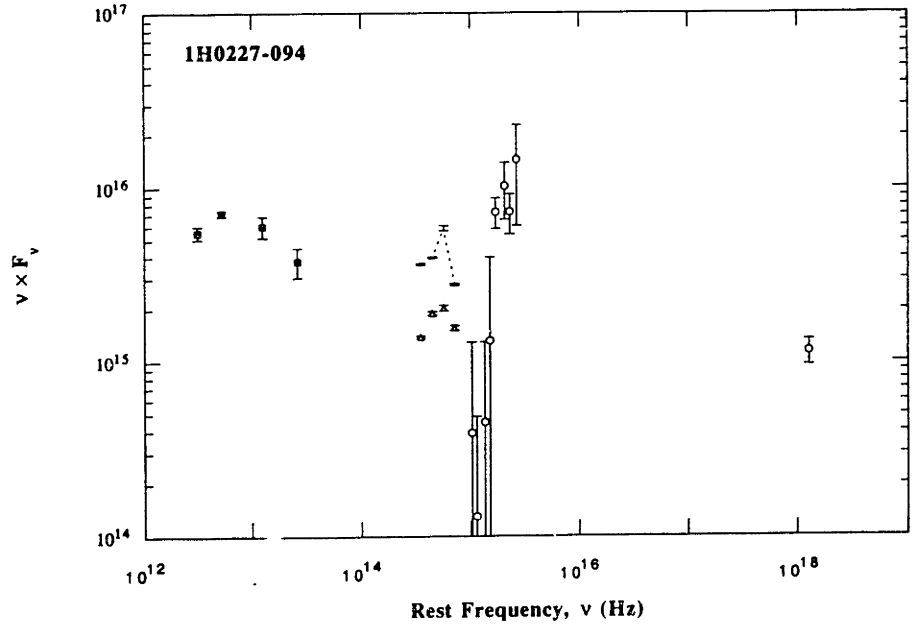
1H0227-094
10^{17}
10^{16}
10^{15}
10^{14}
10^{12}
10^{14}
10^{16}
10^{18}
$\nu \times F_\nu$
Rest Frequency, ν (Hz)

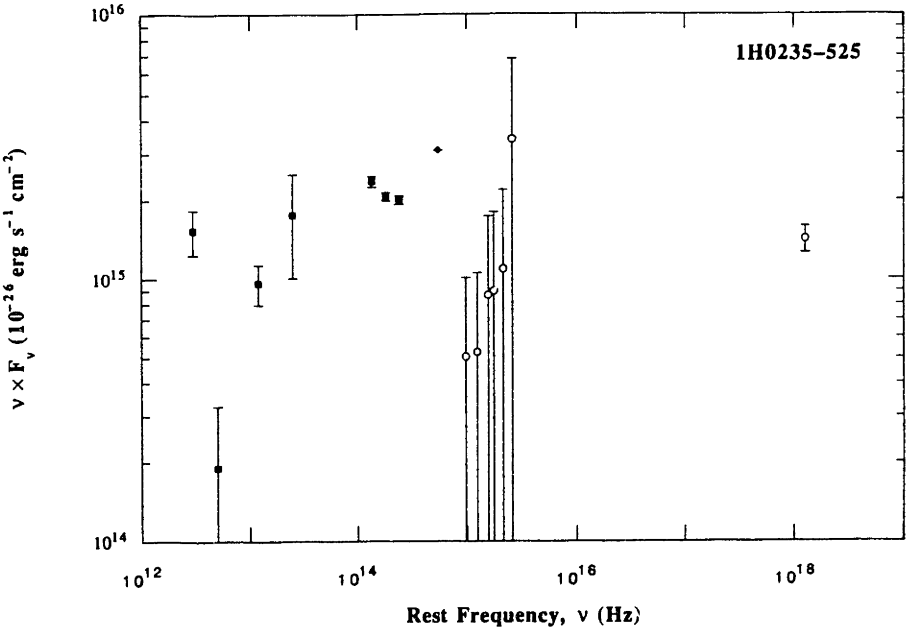
1H0235-525
10^{16}
10^{15}
10^{14}
10^{12}
10^{14}
10^{16}
10^{18}
$\nu \times F_\nu$ (10^{-26} erg s^{-1} cm^{-2})
Rest Frequency, ν (Hz)

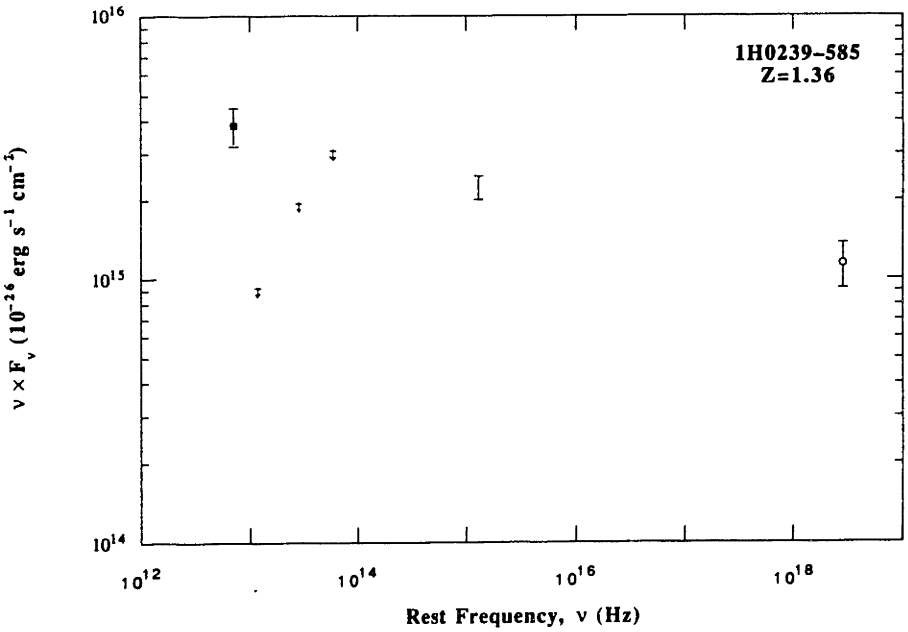
1H0239-585
Z=1.36
10^{16}
10^{15}
10^{14}
10^{12}
10^{14}
10^{16}
10^{18}
$\nu \times F_\nu$ (10^{-26} erg s^{-1} cm^{-2})
Rest Frequency, ν (Hz)

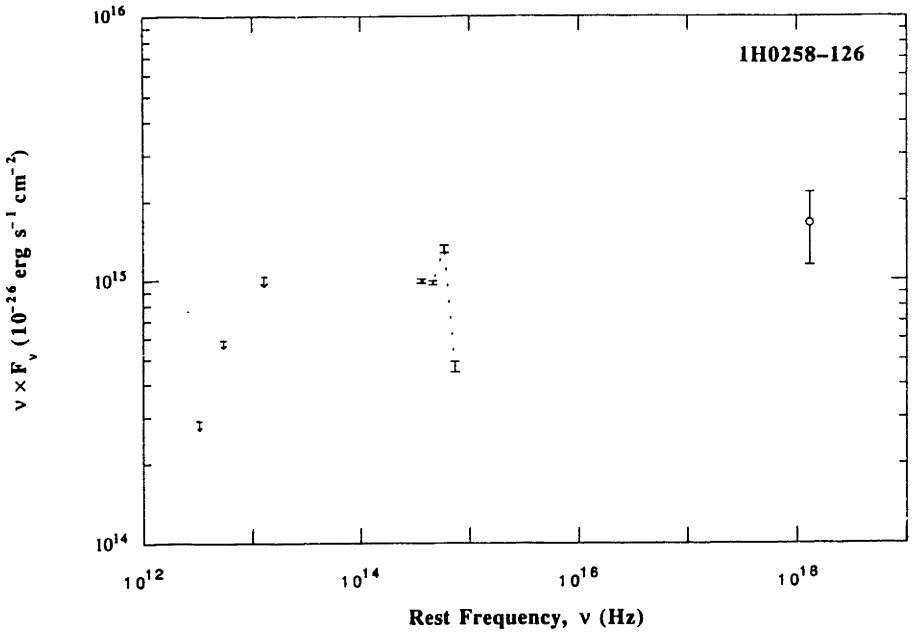
1H0258–126
10^{16}
10^{15}
10^{14}
10^{12}
10^{14}
10^{16}
10^{18}
$\nu \times F_\nu$ (10^{-26} erg s^{-1} cm^{-2})
Rest Frequency, ν (Hz)

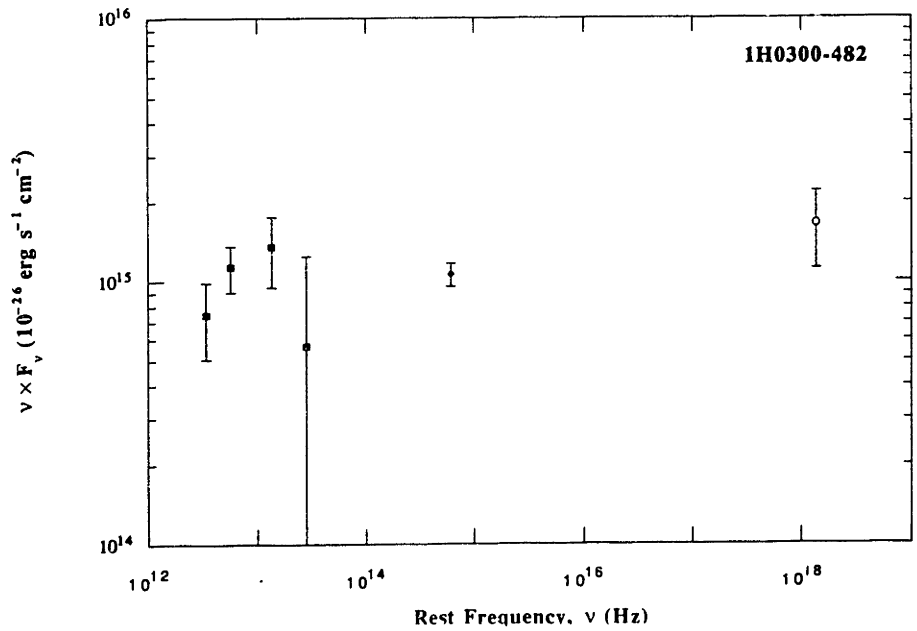
1H0300-482
10^{16}
10^{15}
10^{14}
10^{12}
10^{14}
10^{16}
10^{18}
$\nu \times F_\nu$ (10^{-26} erg s^{-1} cm^{-2})
Rest Frequency, ν (Hz)

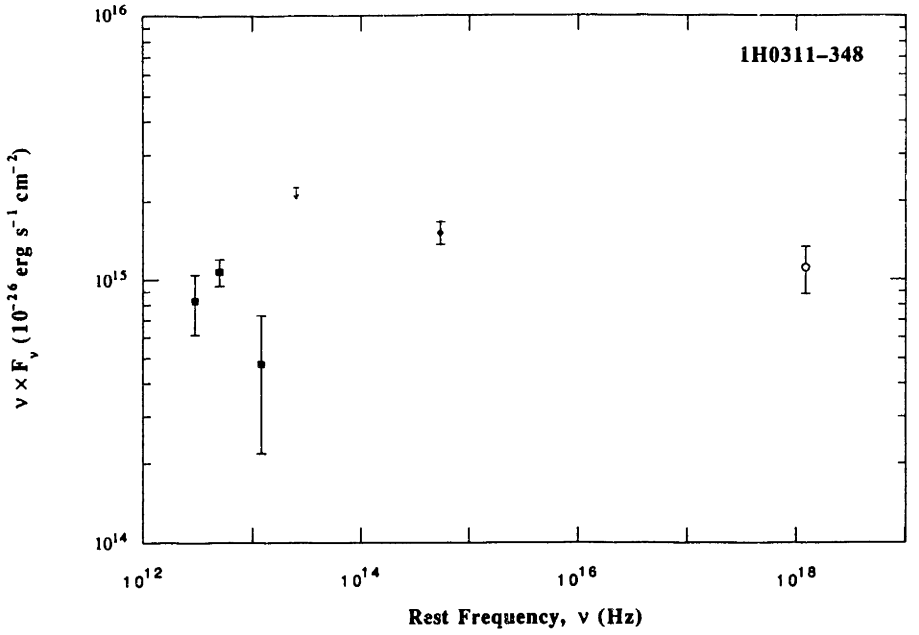
1H0311-348
10^{16}
10^{15}
10^{14}
10^{12}
10^{14}
10^{16}
10^{18}
$\nu \times F_\nu$ (10^{-26} erg s^{-1} cm^{-2})
Rest Frequency, ν (Hz)

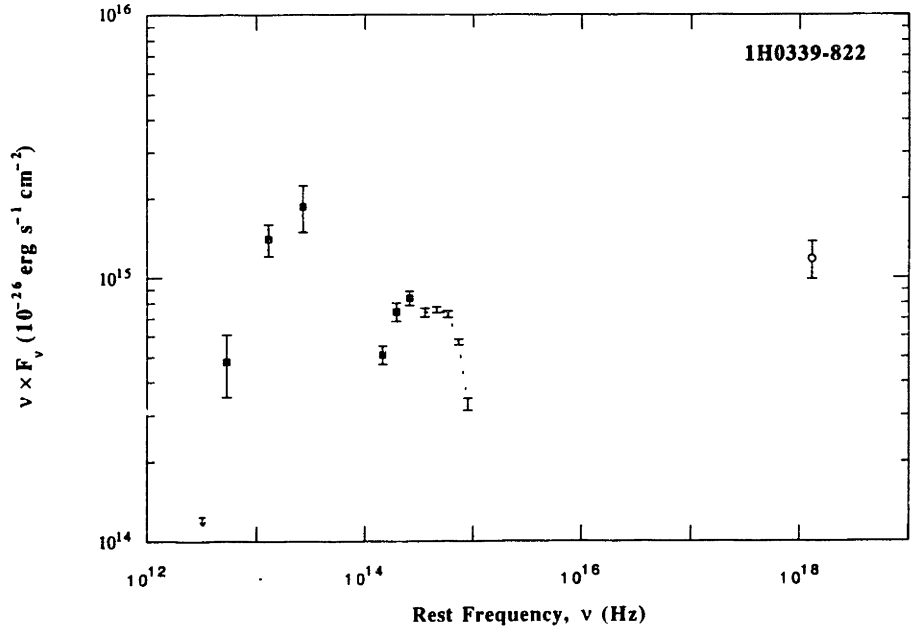
1H0339-822
10^{16}
10^{15}
10^{14}
10^{12}
10^{14}
10^{16}
10^{18}
$\nu \times F_\nu$ (10^{-26} erg s^{-1} cm^{-2})
Rest Frequency, ν (Hz)

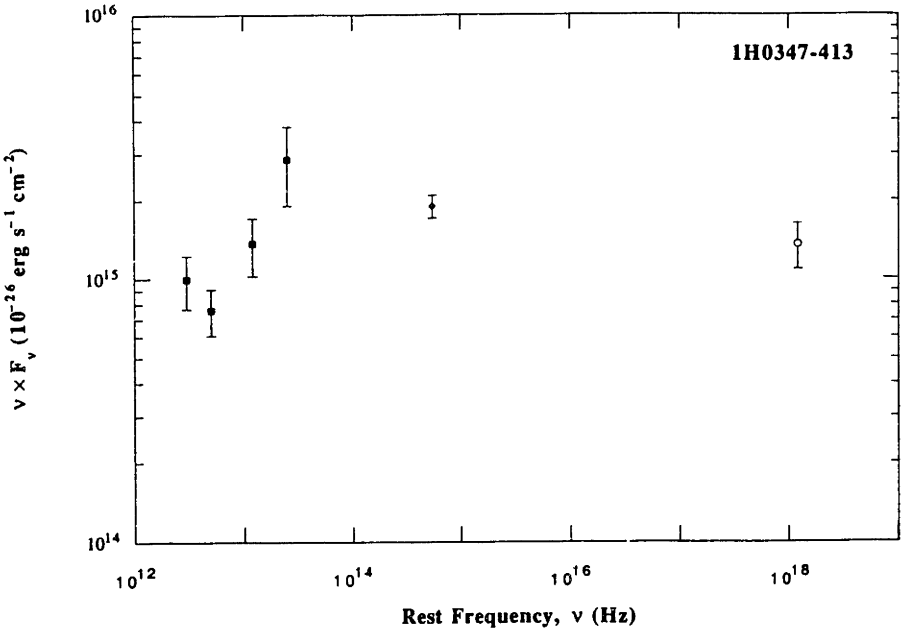
1H0347-413
10^{16}
10^{15}
10^{14}
10^{12}
10^{14}
10^{16}
10^{18}
$\nu \times F_\nu$ (10^{-26} erg s^{-1} cm^{-2})
Rest Frequency, ν (Hz)

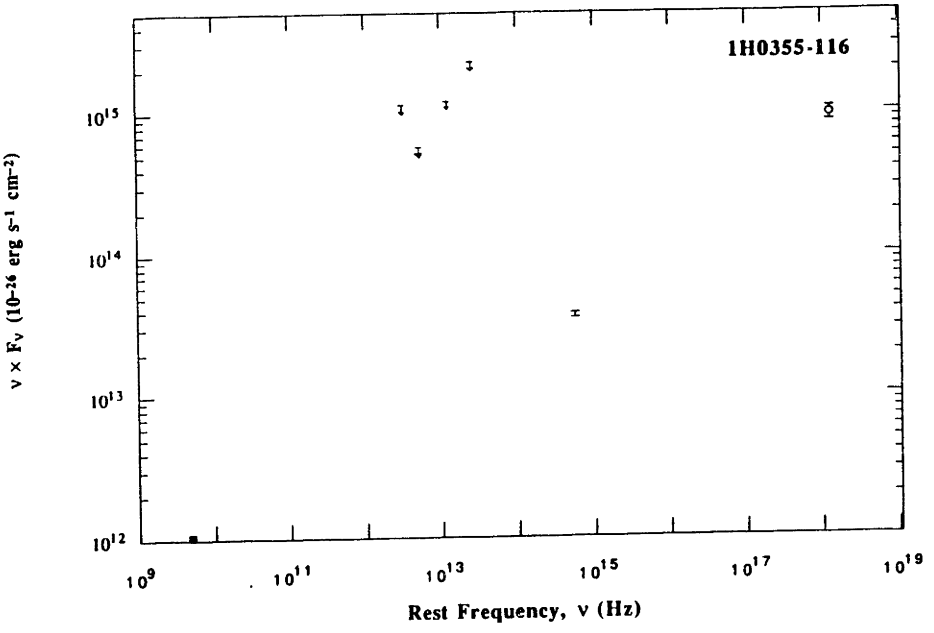
1H0355-116
10^{15}
10^{14}
10^{13}
10^{12}
10^{9}
10^{11}
10^{13}
10^{15}
10^{17}
10^{19}
$\nu \times F_\nu$ (10^{-26} erg s^{-1} cm^{-2})
Rest Frequency, ν (Hz)

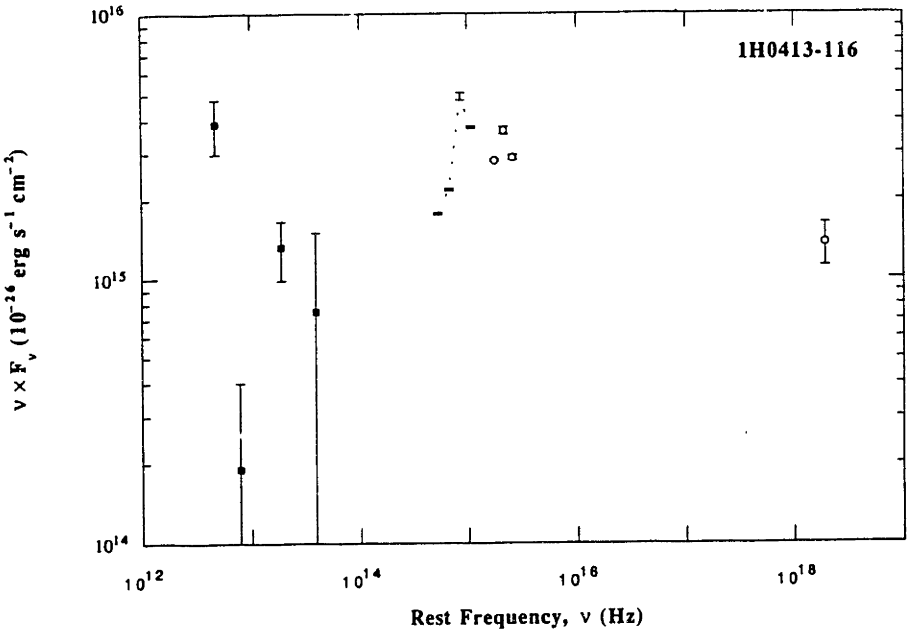
1H0413-116
10^{16}
10^{15}
10^{14}
10^{12}
10^{14}
10^{16}
10^{18}
$\nu \times F_\nu$ (10^{-26} erg s^{-1} cm^{-2})
Rest Frequency, ν (Hz)

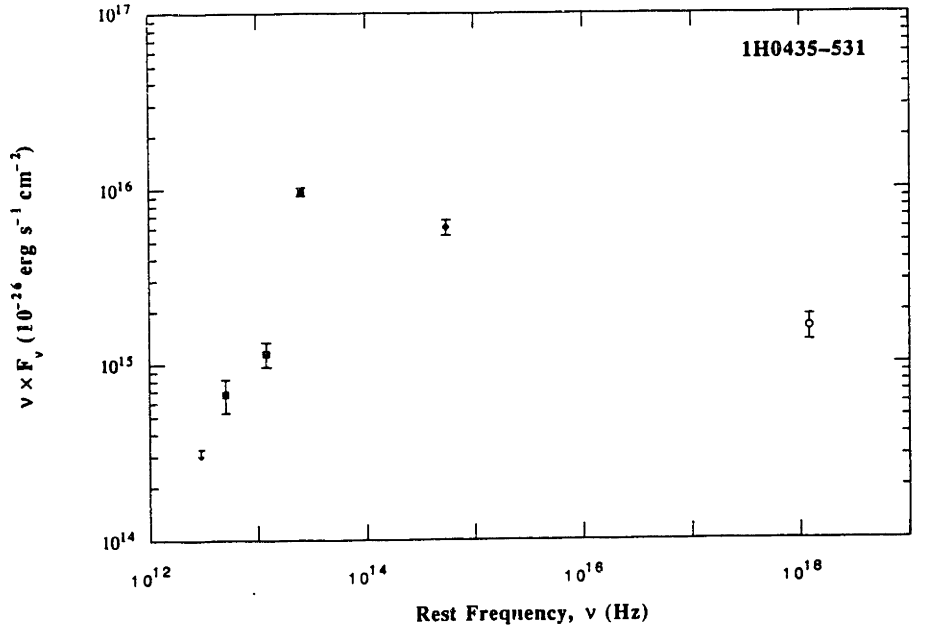
1H0435-531
10^{17}
10^{16}
10^{15}
10^{14}
10^{12}
10^{14}
10^{16}
10^{18}
$\nu \times F_\nu$ (10^{-26} erg s^{-1} cm^{-2})
Rest Frequency, ν (Hz)

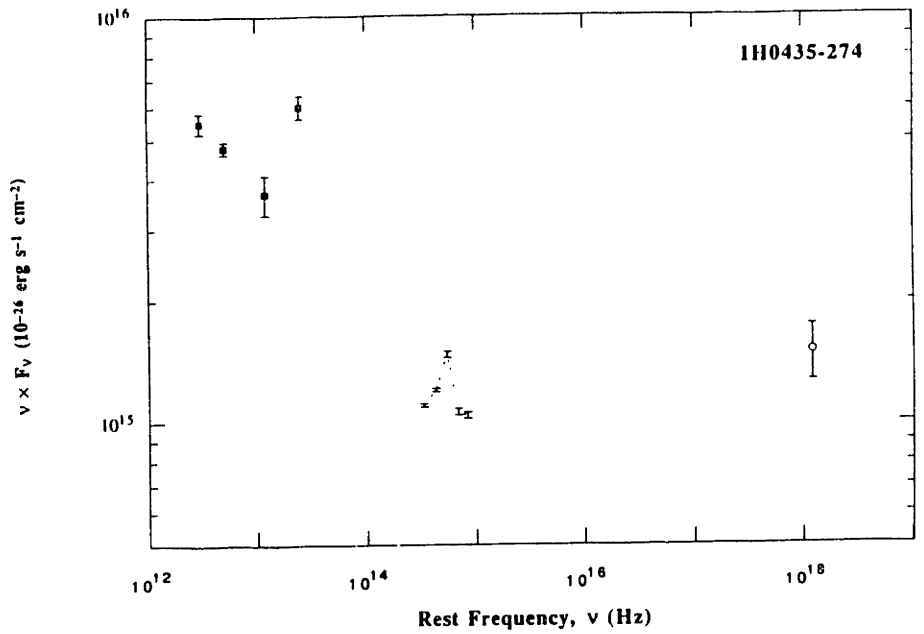
1H0435-274
10^{16}
10^{15}
10^{12}
10^{14}
10^{16}
10^{18}
$\nu \times F_\nu$ (10^{-26} erg s^{-1} cm^{-2})
Rest Frequency, ν (Hz)

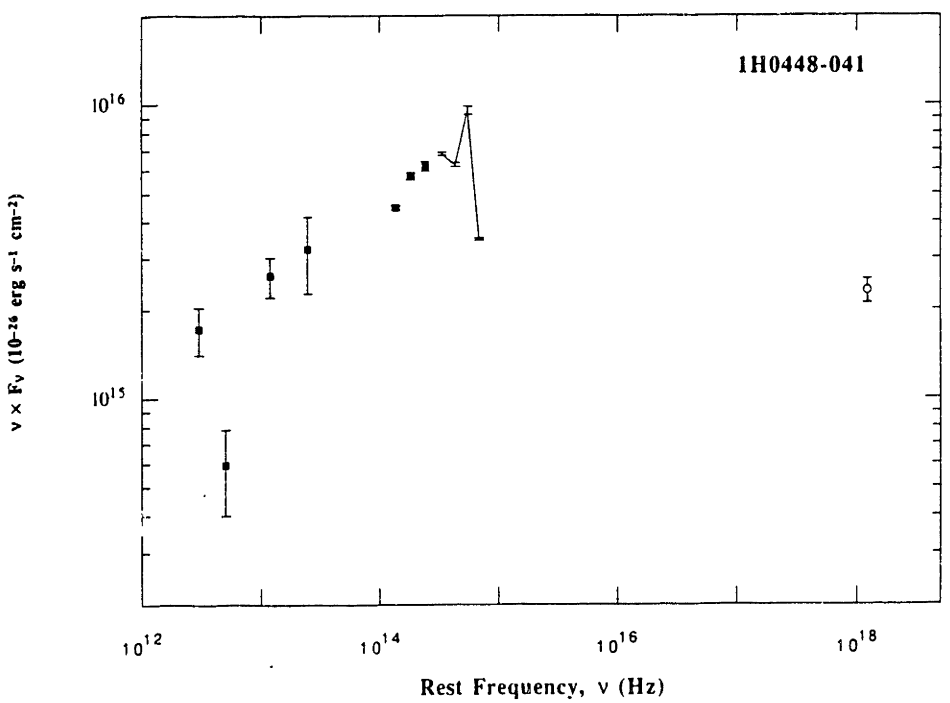
1H0448-041
10^{16}
10^{15}
10^{12}
10^{14}
10^{16}
10^{18}
$\nu \times F_\nu$ (10^{-26} erg s^{-1} cm^{-2})
Rest Frequency, ν (Hz)

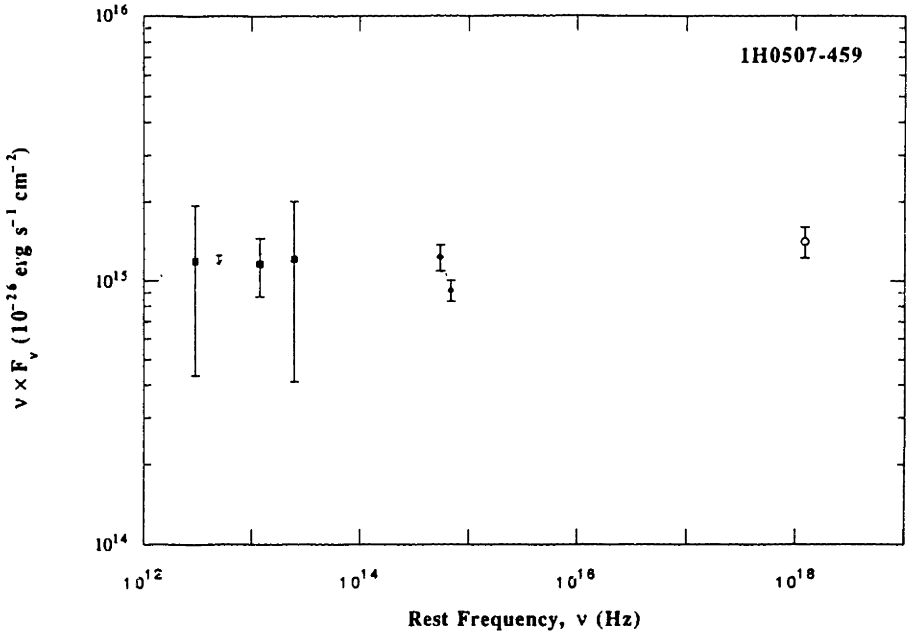
1H0507-459
10^{16}
10^{15}
10^{14}
10^{12}
10^{14}
10^{16}
10^{18}
$\nu \times F_\nu$ (10^{-26} erg s^{-1} cm^{-2})
Rest Frequency, ν (Hz)

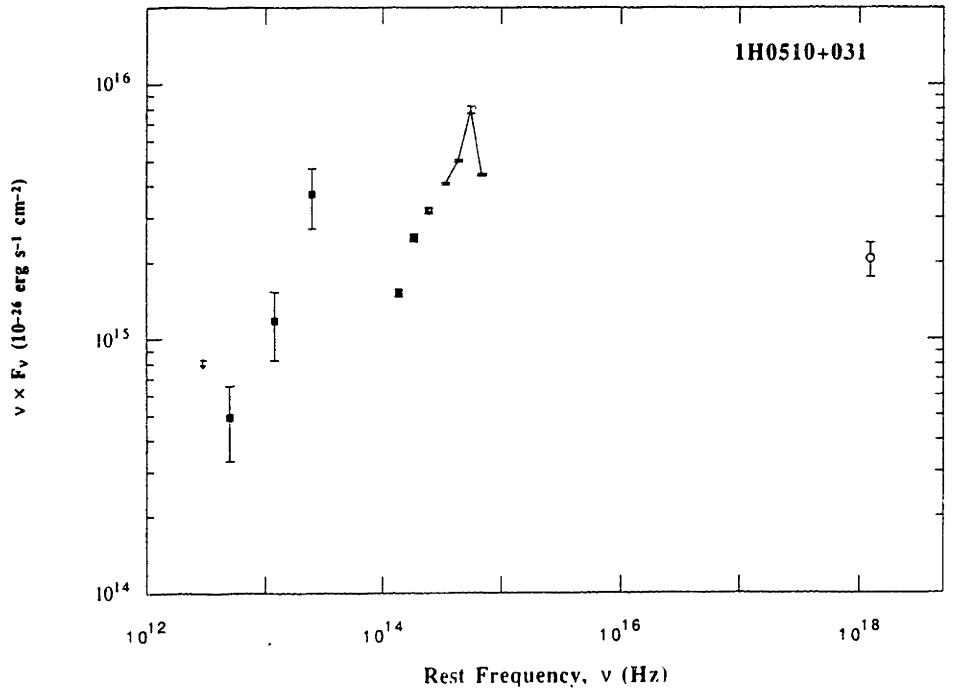
1H0510+031
10^{16}
10^{15}
10^{14}
10^{12}
10^{14}
10^{16}
10^{18}
$\nu \times F_\nu$ (10^{-26} erg s^{-1} cm^{-2})
Rest Frequency, ν (Hz)

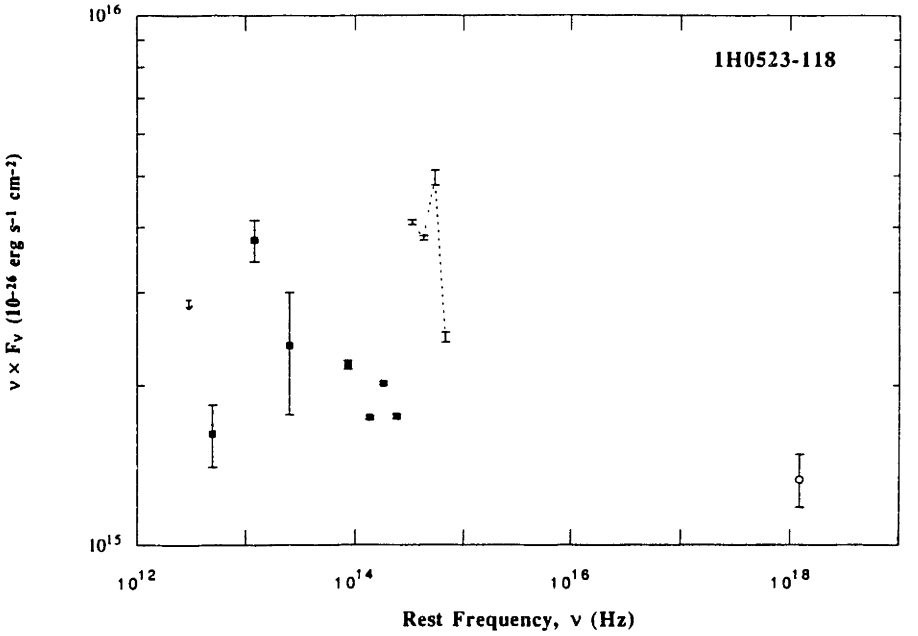
1H0523-118
10^{16}
10^{15}
10^{12}
10^{14}
10^{16}
10^{18}
$\nu \times F_\nu$ (10^{-26} erg s^{-1} cm^{-2})
Rest Frequency, ν (Hz)

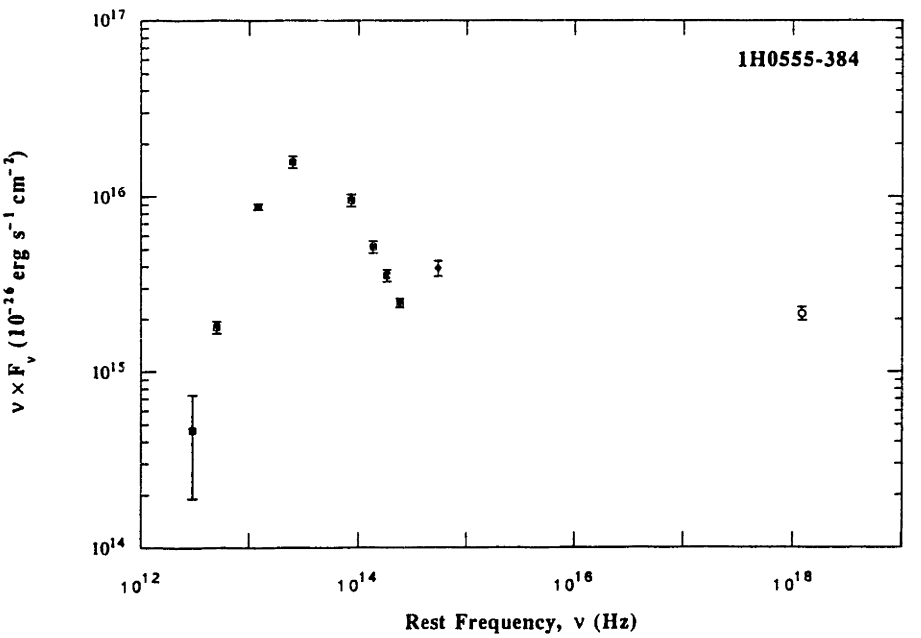
1H0555-384
10^{17}
10^{16}
10^{15}
10^{14}
10^{12}
10^{14}
10^{16}
10^{18}
$\nu \times F_\nu$ (10^{-26} erg s^{-1} cm^{-2})
Rest Frequency, ν (Hz)

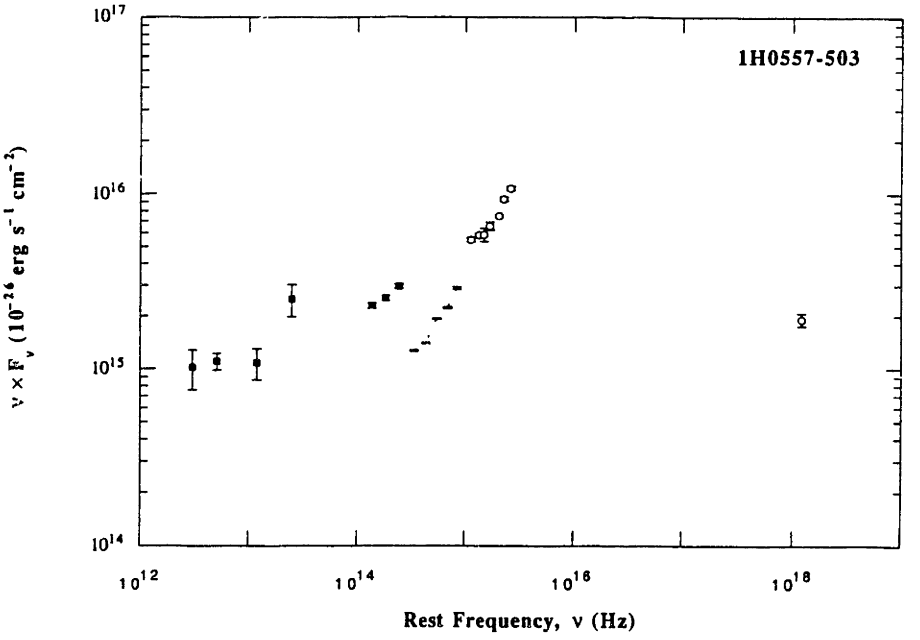
1H0557-503
10^{17}
10^{16}
10^{15}
10^{14}
10^{12}
10^{14}
10^{16}
10^{18}
$\nu \times F_\nu$ (10^{-26} erg s^{-1} cm^{-2})
Rest Frequency, ν (Hz)

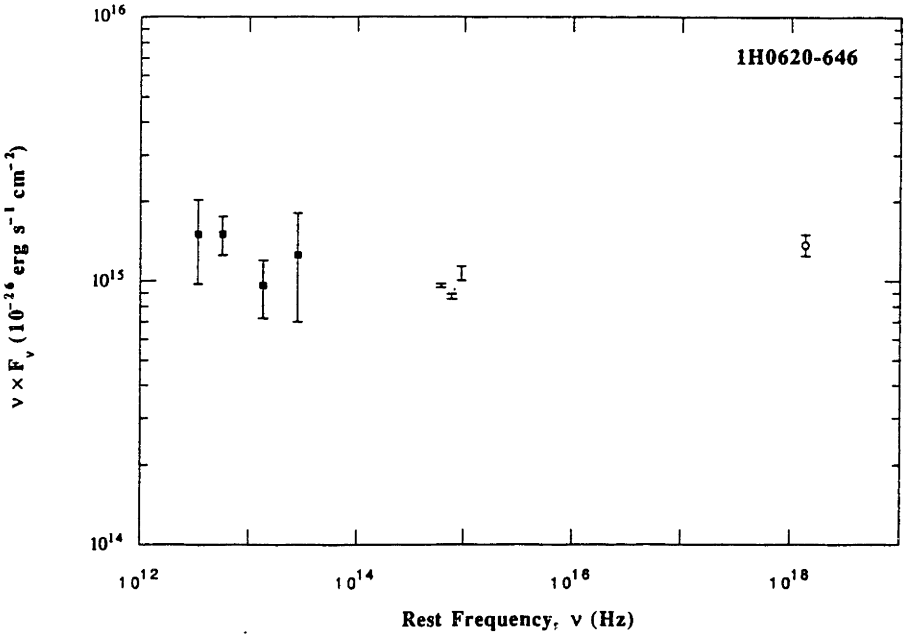
1H0620-646
10^{16}
10^{15}
10^{14}
10^{12}
10^{14}
10^{16}
10^{18}
$\nu \times F_\nu$ (10^{-26} erg s^{-1} cm^{-2})
Rest Frequency, ν (Hz)

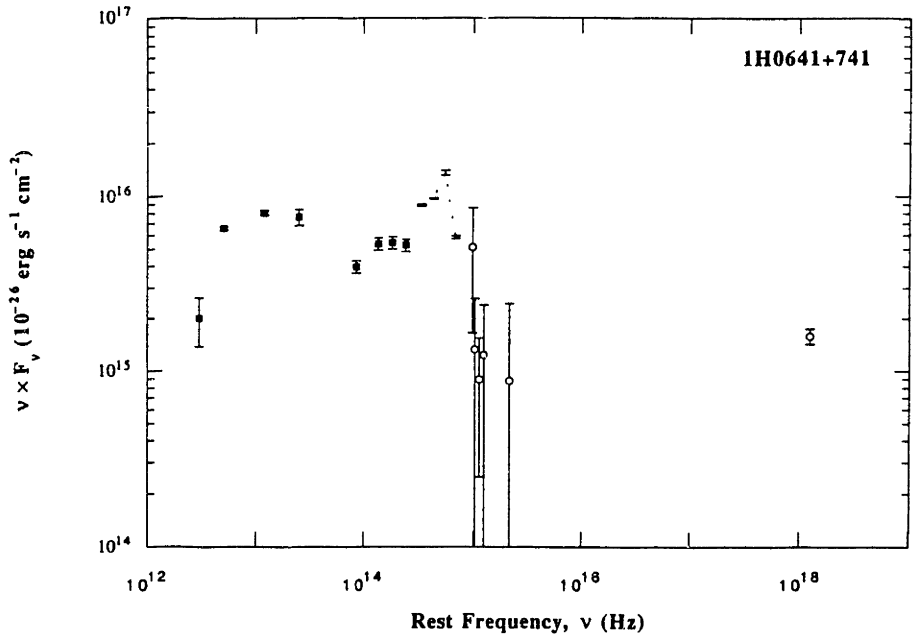
1H0641+741
10^{17}
10^{16}
10^{15}
10^{14}
$\nu \times F_\nu$ (10^{-26} erg s^{-1} cm^{-2})
10^{12}
10^{14}
10^{16}
10^{18}
Rest Frequency, ν (Hz)

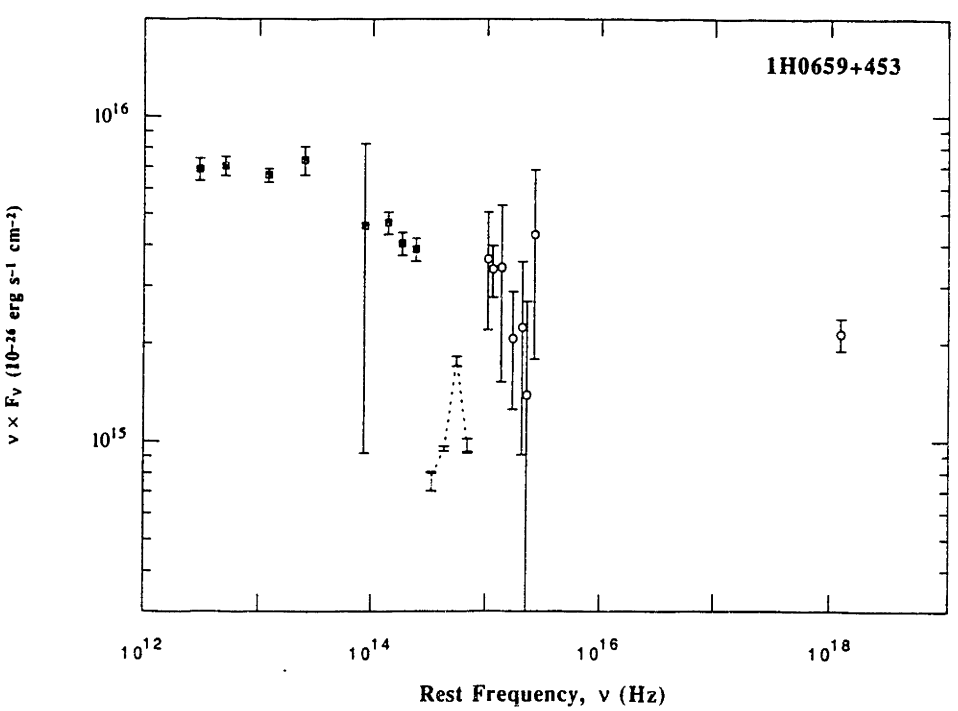
1H0659+453
10^{16}
10^{15}
$\nu \times F_\nu$ (10^{-26} erg s^{-1} cm^{-2})
10^{12}
10^{14}
10^{16}
10^{18}
Rest Frequency, ν (Hz)

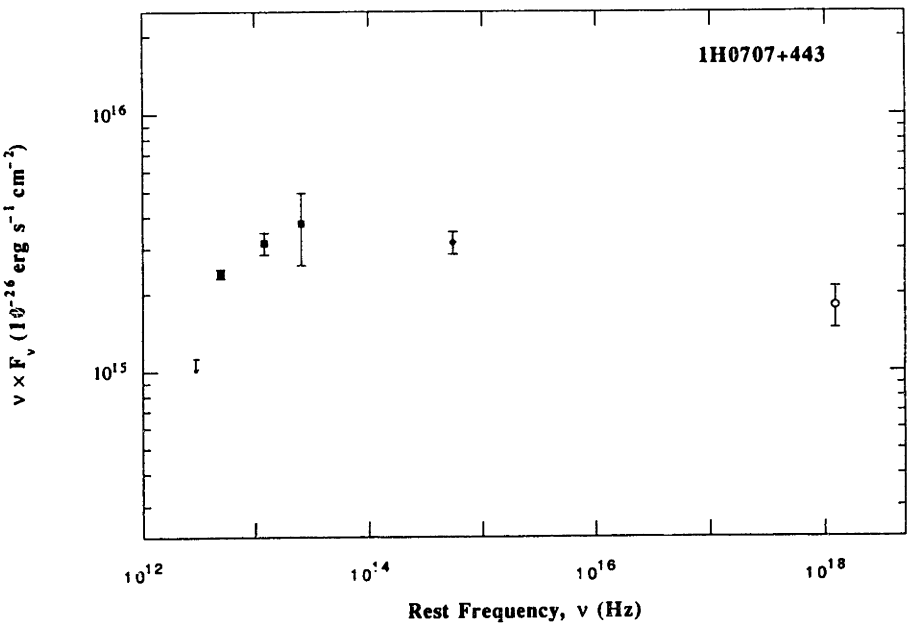
1H0707+443
10^{16}
10^{15}
$\nu \times F_\nu$ (10^{-26} erg s^{-1} cm^{-2})
10^{12}
10^{14}
10^{16}
10^{18}
Rest Frequency, ν (Hz)

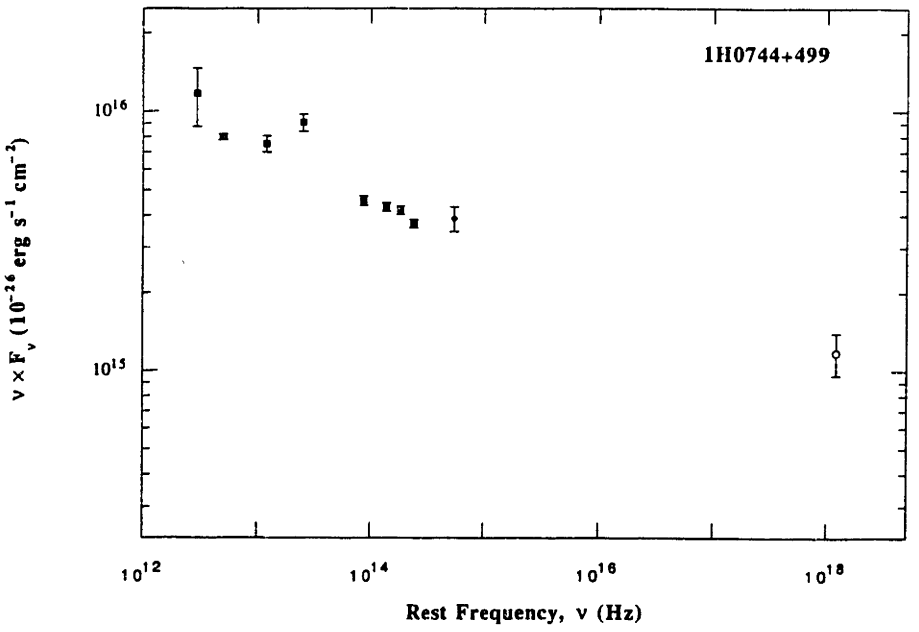
1H0744+499
10^{16}
10^{15}
10^{12}
10^{14}
10^{16}
10^{18}
$\nu \times F_\nu$ (10^{-26} erg s^{-1} cm^{-2})
Rest Frequency, ν (Hz)

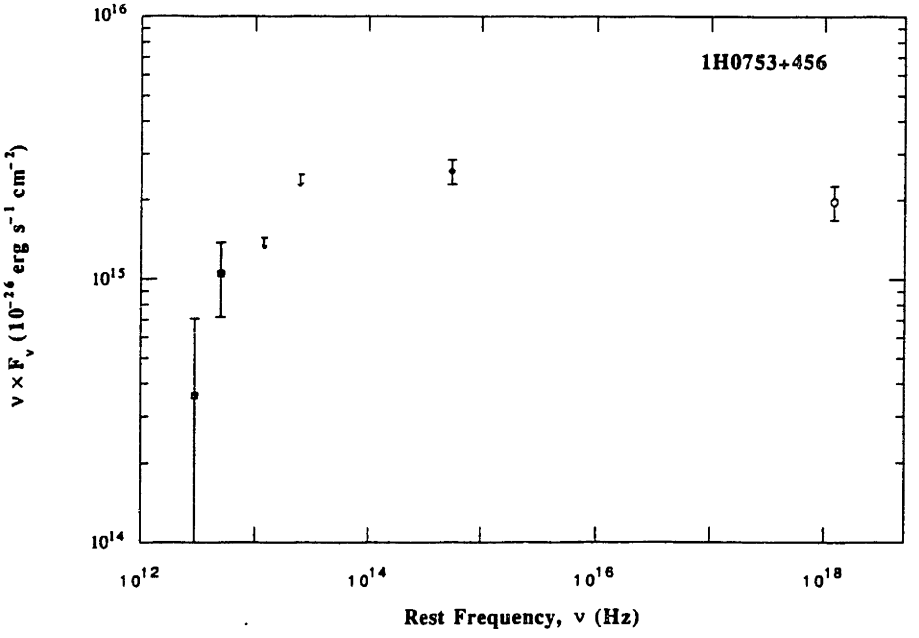
1H0753+456
10^{16}
10^{15}
10^{14}
10^{12}
10^{14}
10^{16}
10^{18}
$\nu \times F_\nu$ (10^{-26} erg s^{-1} cm^{-2})
Rest Frequency, ν (Hz)

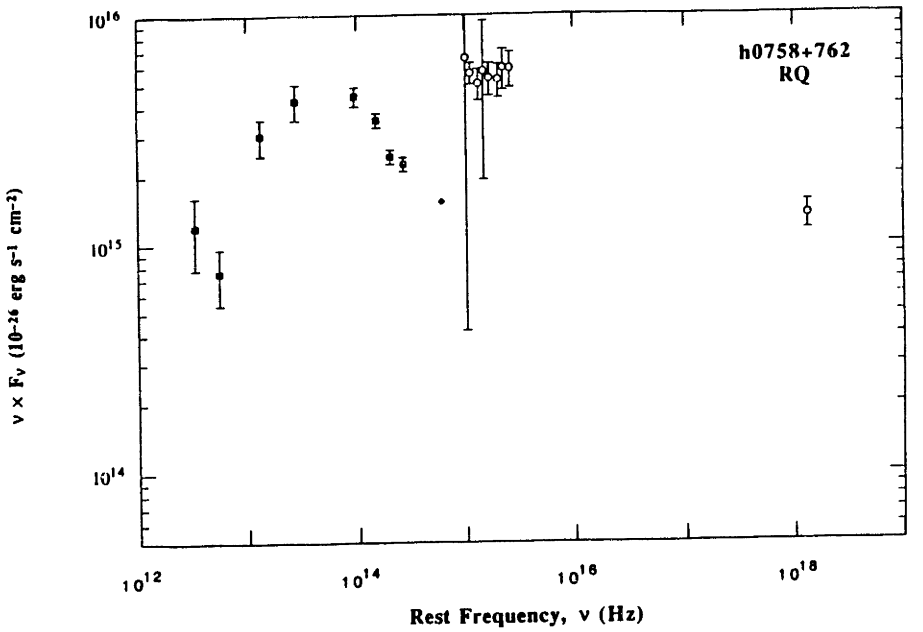
h0758+762
RQ
10^{16}
10^{15}
10^{14}
10^{12}
10^{14}
10^{16}
10^{18}
$\nu \times F_\nu$ (10^{-26} erg s^{-1} cm^{-2})
Rest Frequency, ν (Hz)

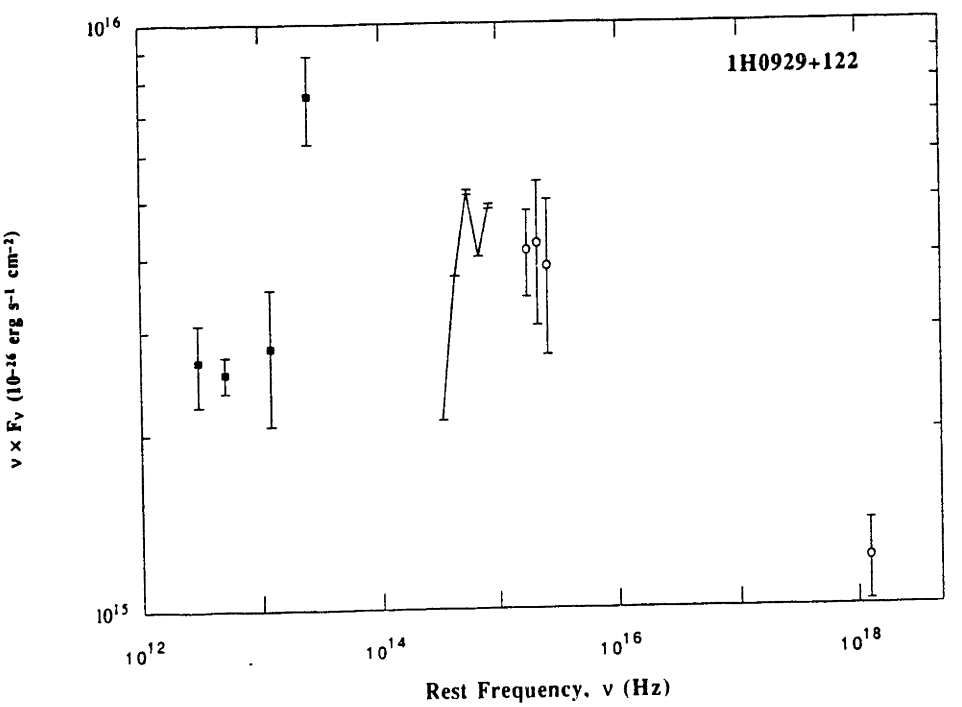
1H0929+122
10^{16}
10^{15}
10^{12}
10^{14}
10^{16}
10^{18}
$\nu \times F_\nu$ (10^{-26} erg s^{-1} cm^{-2})
Rest Frequency, ν (Hz)

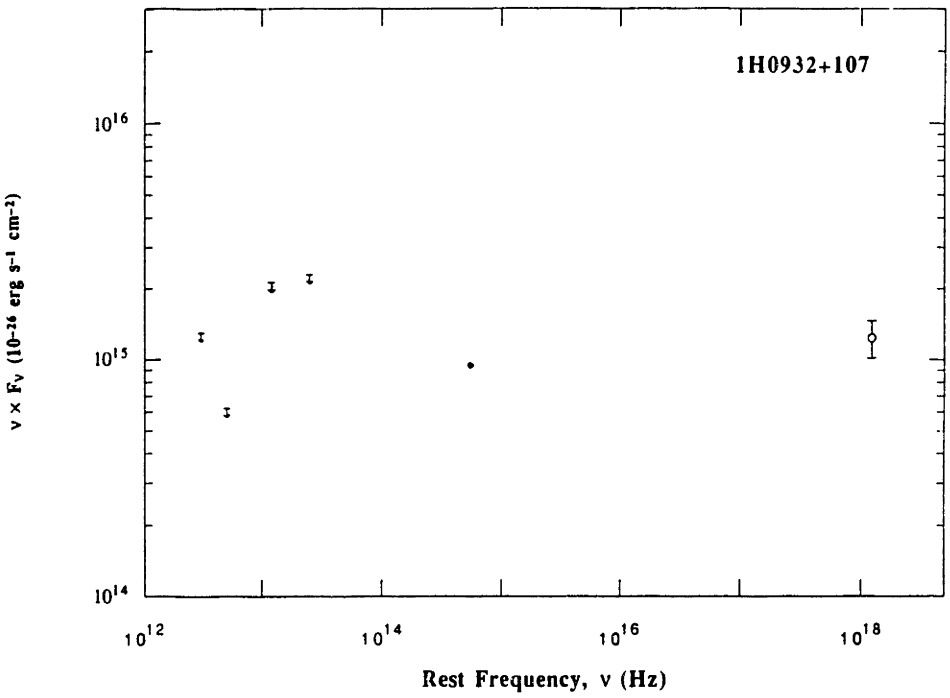
1H0932+107
10^{16}
10^{15}
10^{14}
10^{12}
10^{14}
10^{16}
10^{18}
$\nu \times F_\nu$ (10^{-26} erg s^{-1} cm^{-2})
Rest Frequency, ν (Hz)

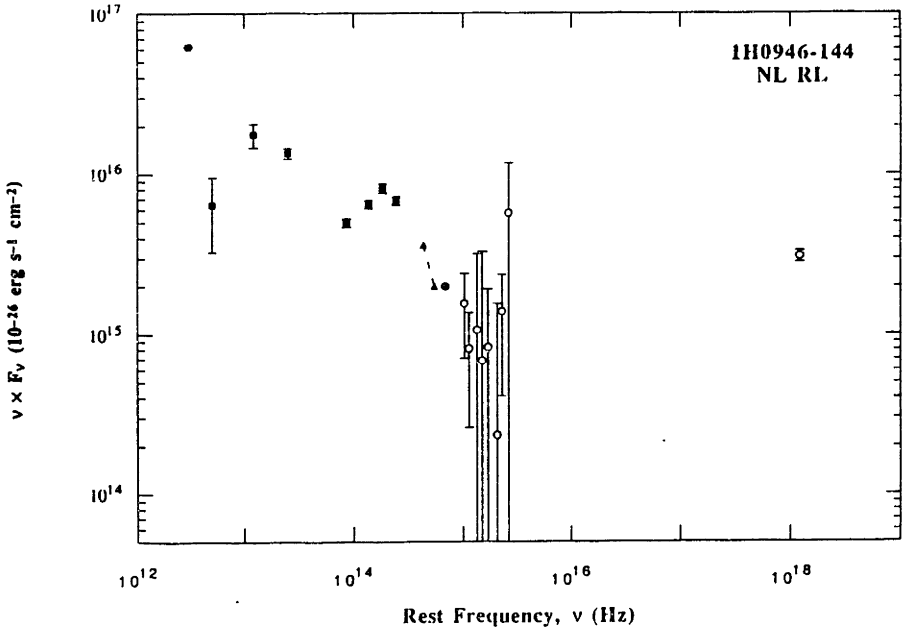
1H0946-144
NL RL
10^{17}
10^{16}
10^{15}
10^{14}
10^{12}
10^{14}
10^{16}
10^{18}
$\nu \times F_\nu$ (10^{-26} erg s^{-1} cm^{-2})
Rest Frequency, ν (Hz)

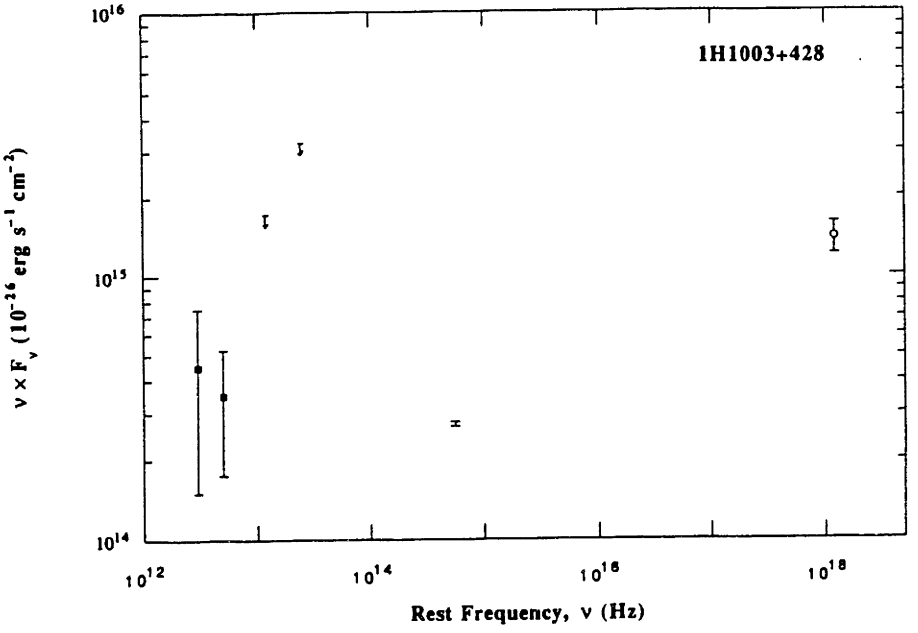
1H1003+428
10^{16}
10^{15}
10^{14}
10^{12}
10^{14}
10^{16}
10^{18}
$\nu \times F_\nu$ (10^{-26} erg s^{-1} cm^{-2})
Rest Frequency, ν (Hz)

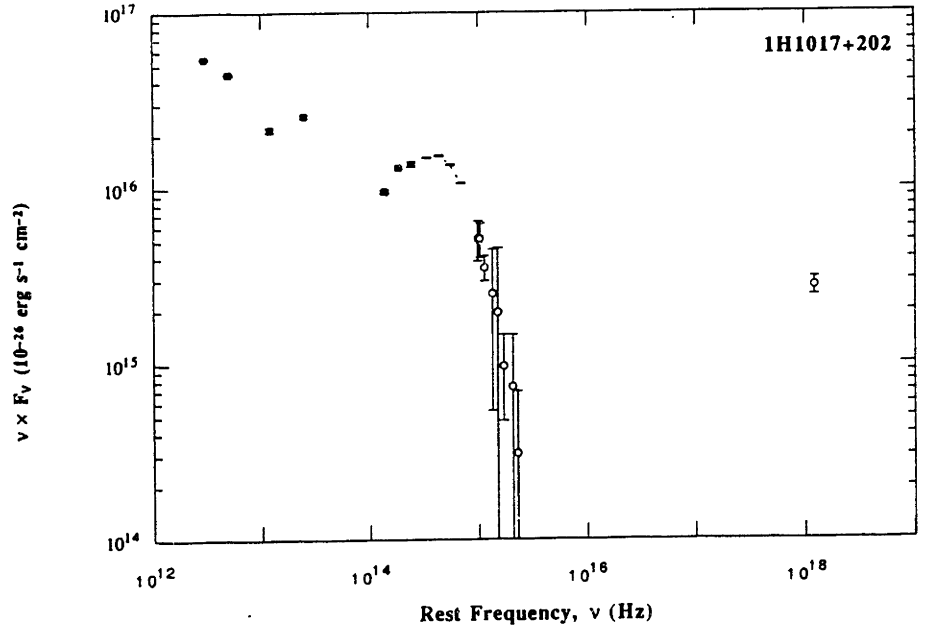
1H1017+202
10^{17}
10^{16}
10^{15}
10^{14}
10^{12}
10^{14}
10^{16}
10^{18}
$\nu \times F_\nu$ (10^{-26} erg s^{-1} cm^{-2})
Rest Frequency, ν (Hz)

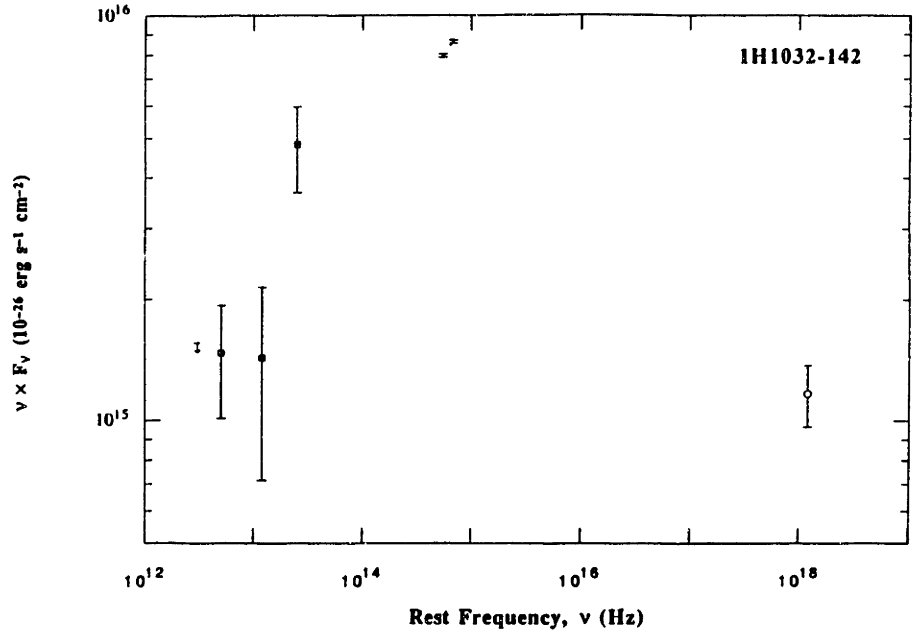
1H1032-142
10^{16}
10^{15}
10^{12}
10^{14}
10^{16}
10^{18}
$\nu \times F_\nu$ (10^{-26} erg s^{-1} cm^{-2})
Rest Frequency, ν (Hz)

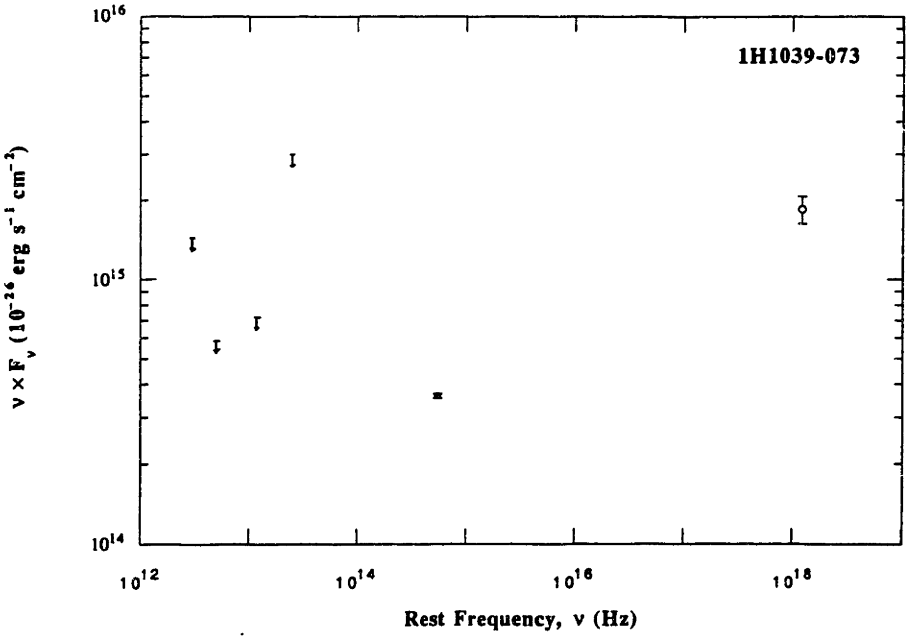
1H1039-073
10^{16}
10^{15}
10^{14}
10^{12}
10^{14}
10^{16}
10^{18}
$\nu \times F_\nu$ (10^{-26} erg s^{-1} cm^{-2})
Rest Frequency, ν (Hz)

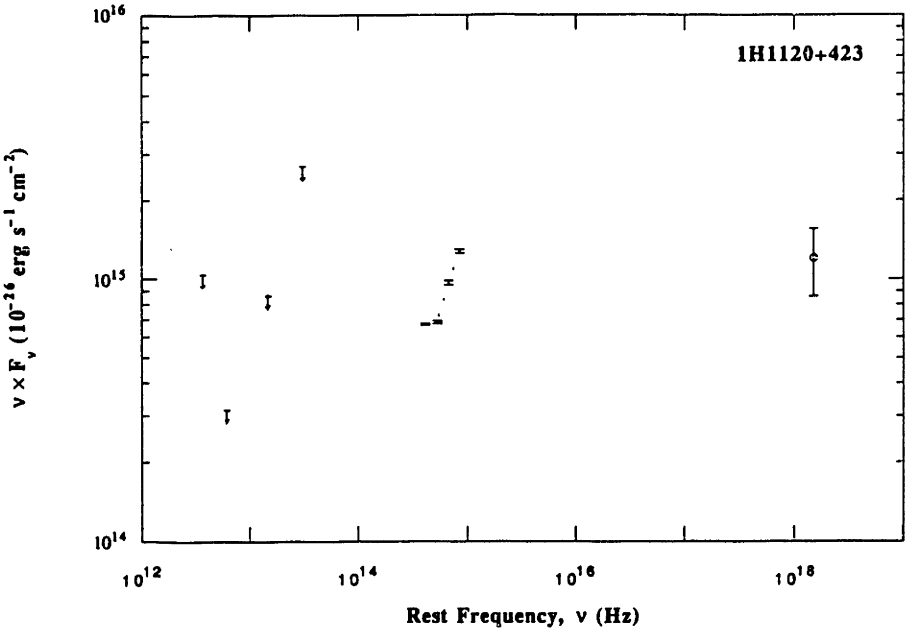
1H1120+423
10^{16}
10^{15}
10^{14}
10^{12}
10^{14}
10^{16}
10^{18}
$\nu \times F_\nu$ (10^{-26} erg s^{-1} cm^{-2})
Rest Frequency, ν (Hz)

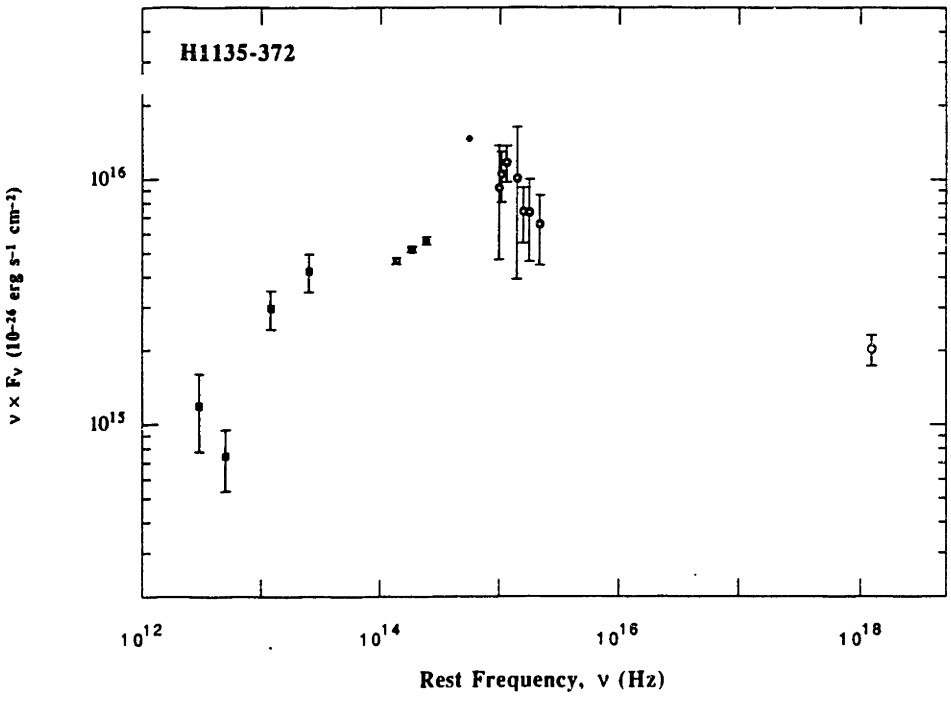
H1135-372
10^{16}
10^{15}
10^{12}
10^{14}
10^{16}
10^{18}
$\nu \times F_\nu$ (10^{-26} erg s^{-1} cm^{-2})
Rest Frequency, ν (Hz)

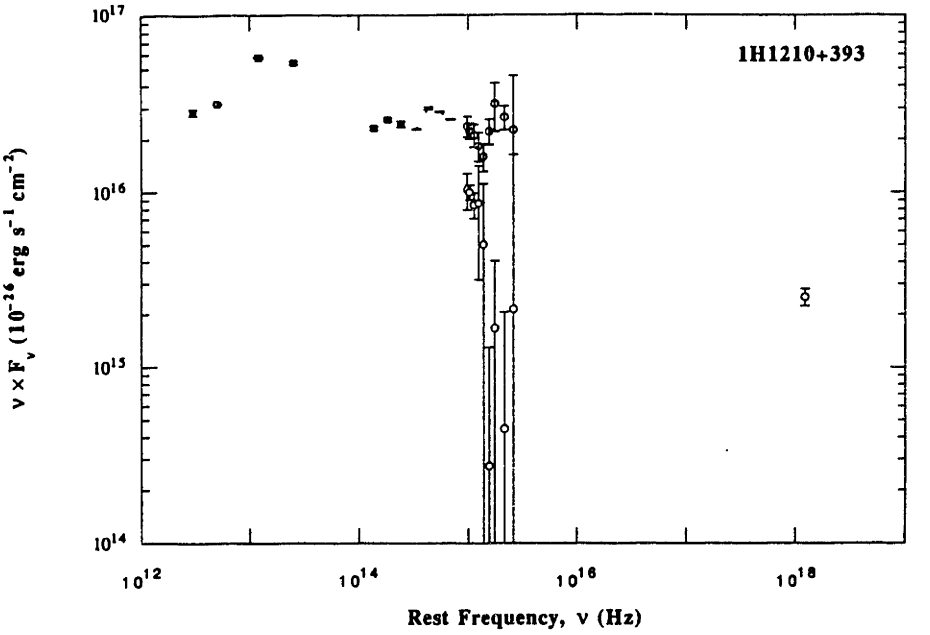
1H1210+393
10^{17}
10^{16}
10^{15}
10^{14}
10^{12}
10^{14}
10^{16}
10^{18}
$\nu \times F_\nu$ (10^{-16} erg s^{-1} cm^{-2})
Rest Frequency, ν (Hz)

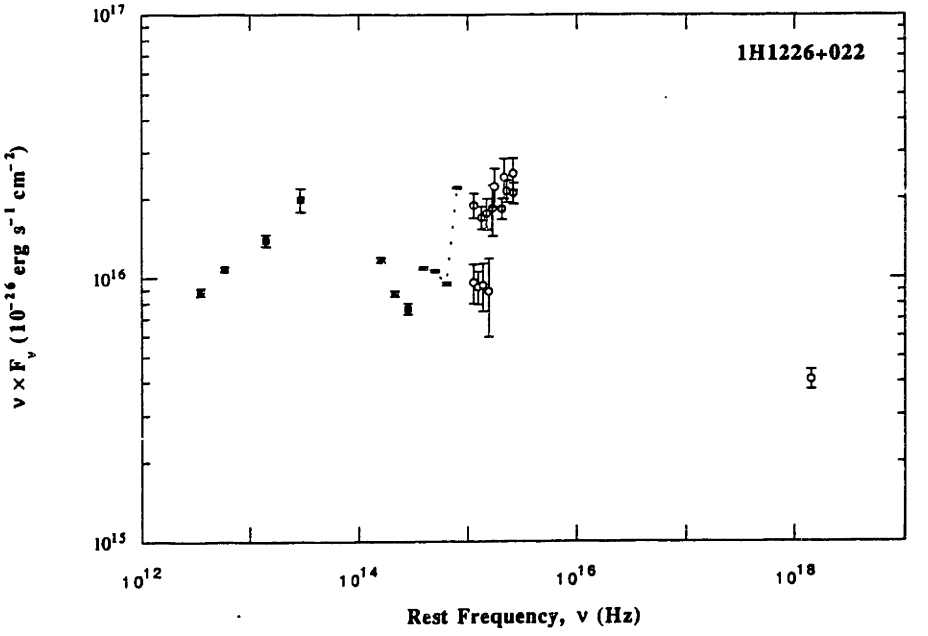
1H1226+022
10^{17}
10^{16}
10^{15}
10^{12}
10^{14}
10^{16}
10^{18}
$\nu \times F_\nu$ (10^{-16} erg s^{-1} cm^{-2})
Rest Frequency, ν (Hz)

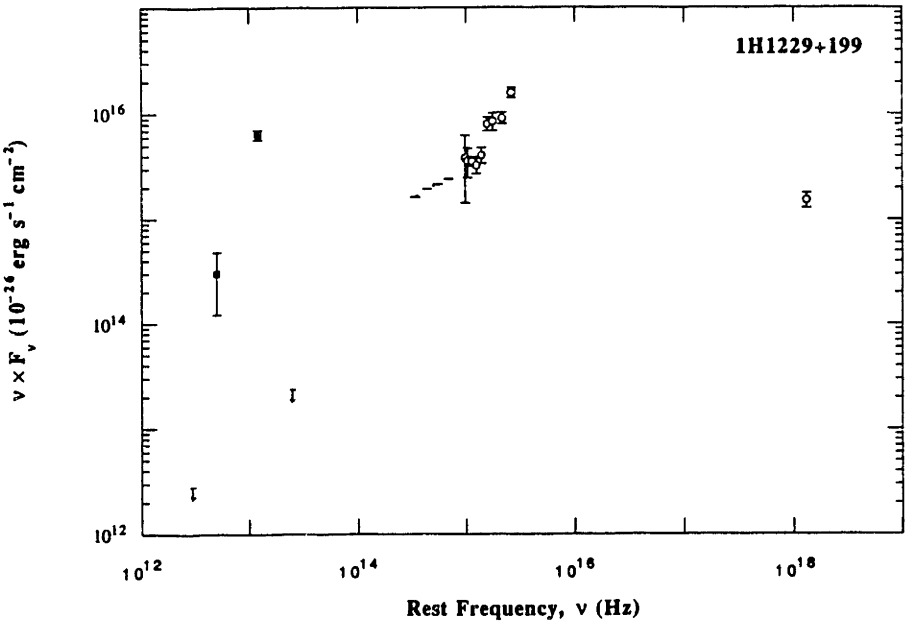
1H1229+199
$\nu \times F_\nu$ (10^{-26} erg s^{-1} cm^{-2})
10^{16}
10^{14}
10^{12}
10^{12}
10^{14}
10^{16}
10^{18}
Rest Frequency, ν (Hz)

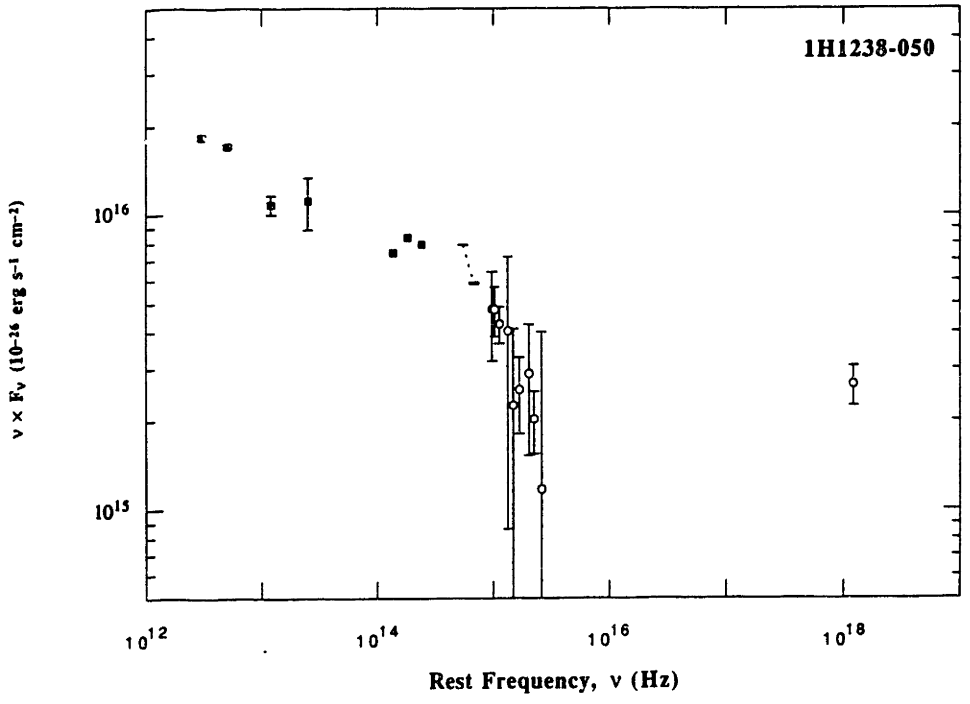
1H1238-050
$\nu \times F_\nu$ (10^{-26} erg s^{-1} cm^{-2})
10^{16}
10^{15}
10^{12}
10^{14}
10^{16}
10^{18}
Rest Frequency, ν (Hz)

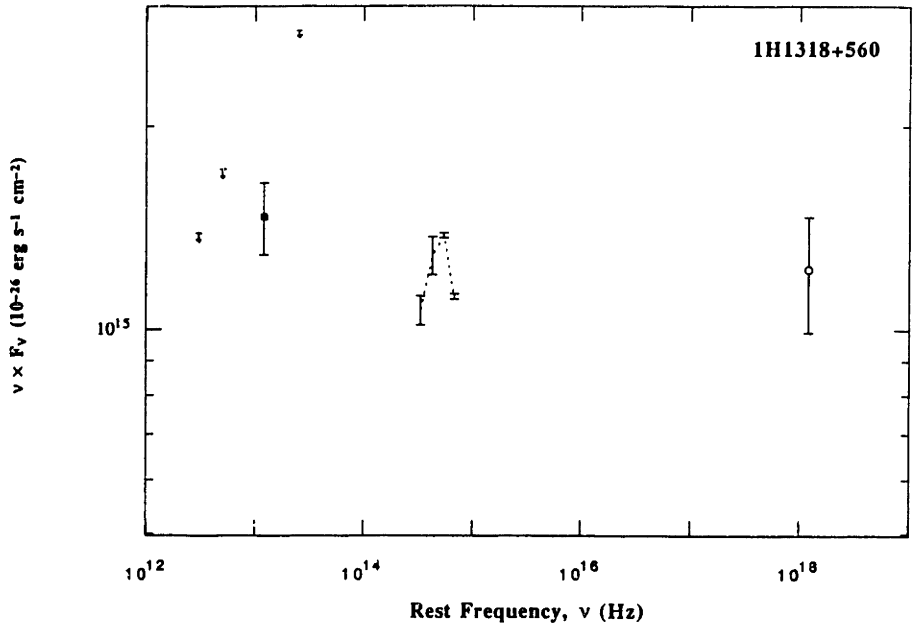
1H1318+560
$\nu \times F_\nu$ (10^{-26} erg s^{-1} cm^{-2})
10^{15}
10^{12}
10^{14}
10^{16}
10^{18}
Rest Frequency, ν (Hz)

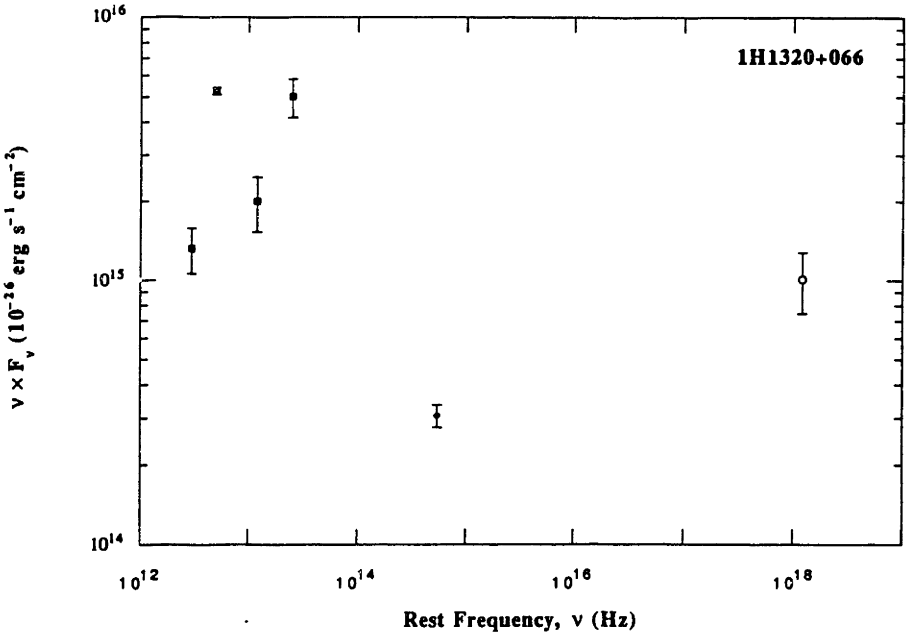
1H1320+066
$\nu \times F_\nu$ (10^{-26} erg s^{-1} cm^{-2})
10^{16}
10^{15}
10^{14}
10^{12}
10^{14}
10^{16}
10^{18}
Rest Frequency, ν (Hz)

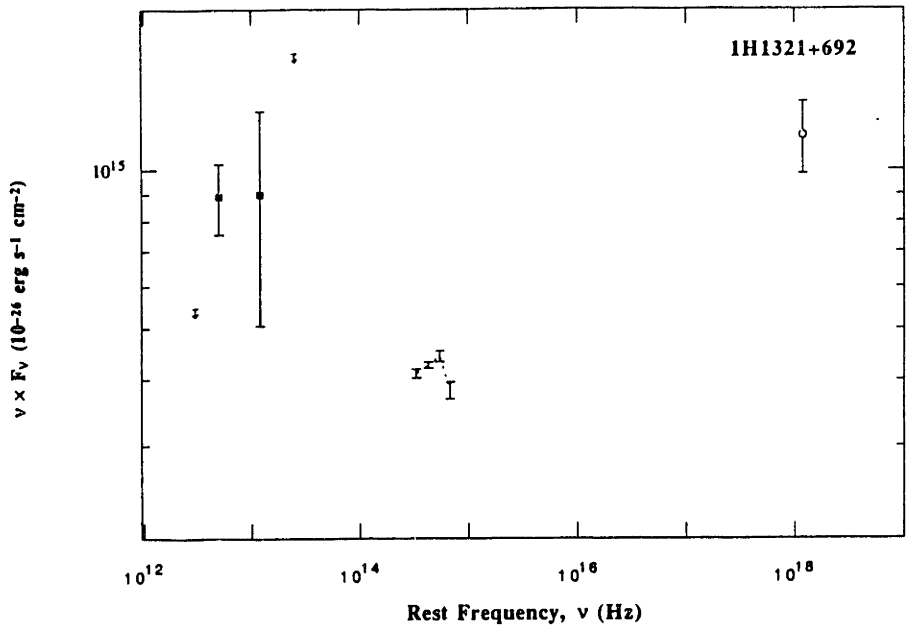
1H1321+692
10^{15}
10^{12}
10^{14}
10^{16}
10^{18}
$\nu \times F_\nu$ (10^{-26} erg s^{-1} cm^{-2})
Rest Frequency, ν (Hz)

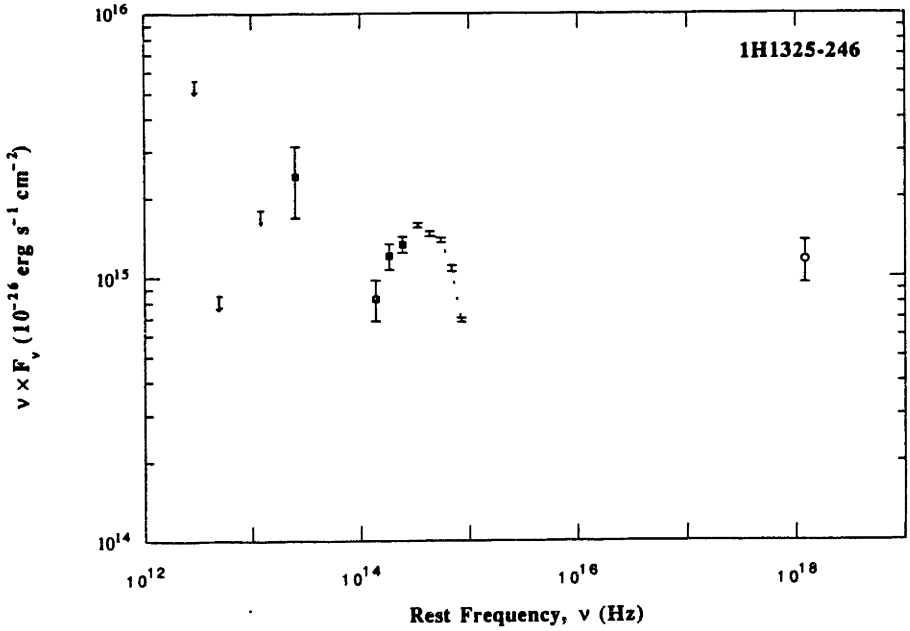
1H1325-246
10^{16}
10^{15}
10^{14}
10^{12}
10^{14}
10^{16}
10^{18}
$\nu \times F_\nu$ (10^{-26} erg s^{-1} cm^{-2})
Rest Frequency, ν (Hz)

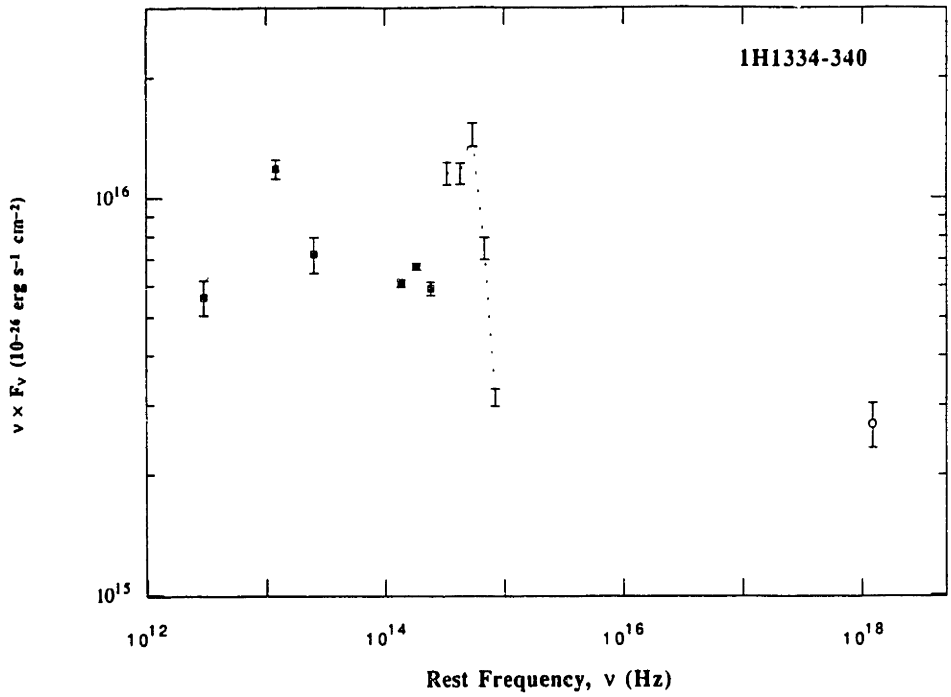
1H1334-340
10^{16}
10^{15}
10^{12}
10^{14}
10^{16}
10^{18}
$\nu \times F_\nu$ (10^{-26} erg s^{-1} cm^{-2})
Rest Frequency, ν (Hz)

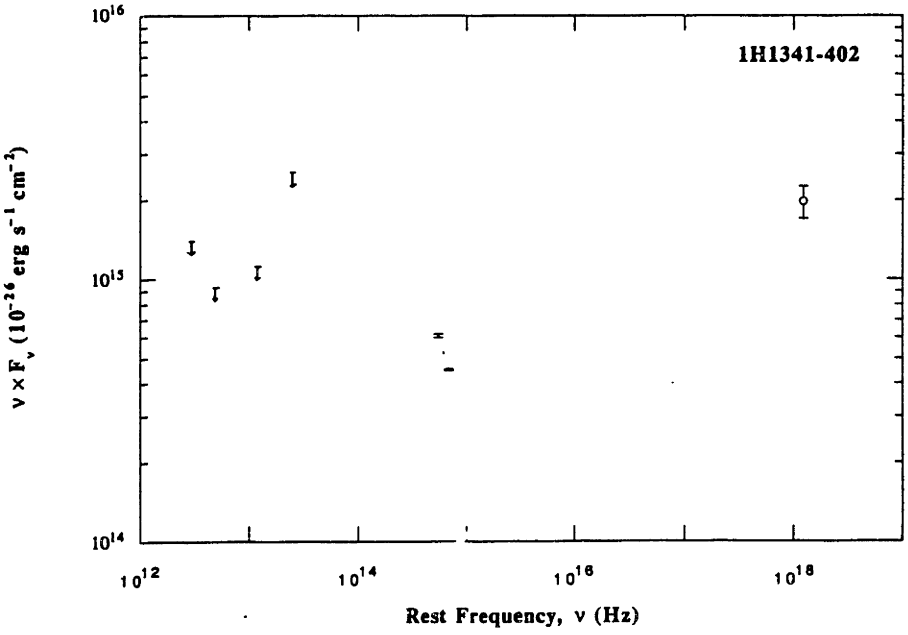
1H1341-402
10^{16}
10^{15}
10^{14}
10^{12}
10^{14}
10^{16}
10^{18}
$\nu \times F_\nu$ (10^{-26} erg s^{-1} cm^{-2})
Rest Frequency, ν (Hz)

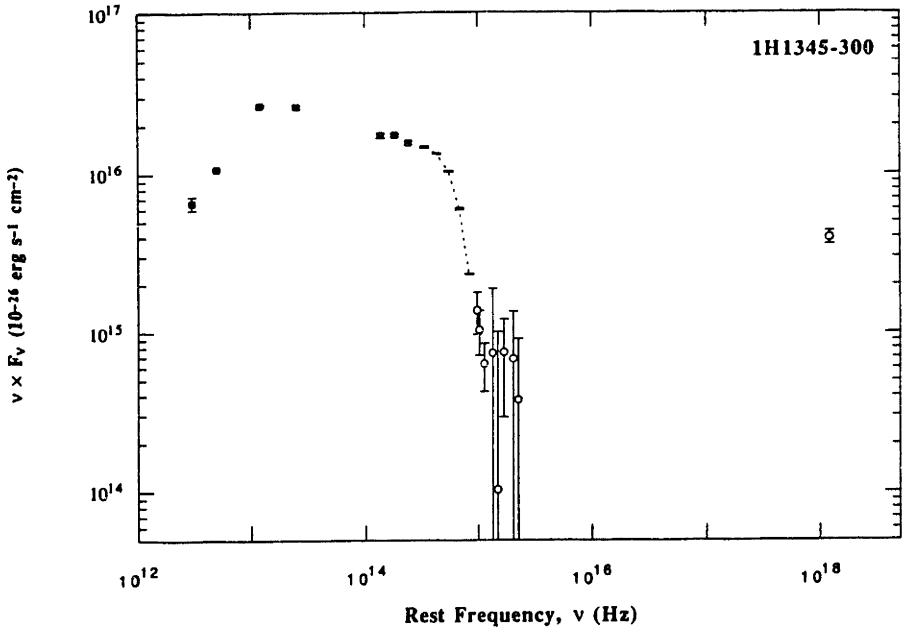
1H1345-300
10^{17}
10^{16}
10^{15}
10^{14}
$\nu \times F_\nu$ (10^{-26} erg s^{-1} cm^{-2})
10^{12}
10^{14}
10^{16}
10^{18}
Rest Frequency, ν (Hz)

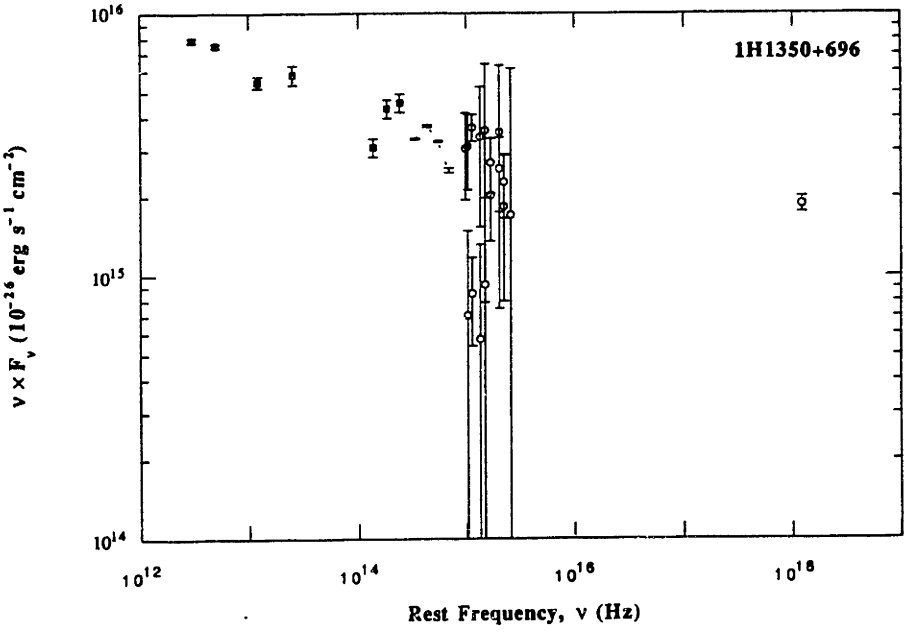
1H1350+696
10^{16}
10^{15}
10^{14}
$\nu \times F_\nu$ (10^{-26} erg s^{-1} cm^{-2})
10^{12}
10^{14}
10^{16}
10^{18}
Rest Frequency, ν (Hz)

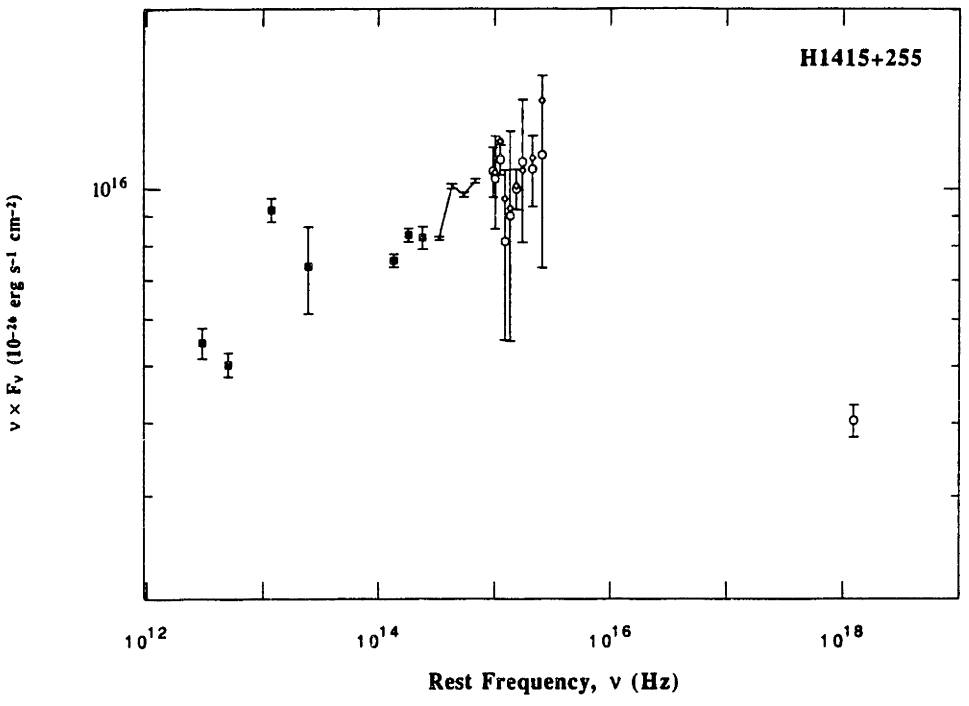
H1415+255
10^{16}
$\nu \times F_\nu$ (10^{-16} erg s^{-1} cm^{-2})
10^{12}
10^{14}
10^{16}
10^{18}
Rest Frequency, ν (Hz)

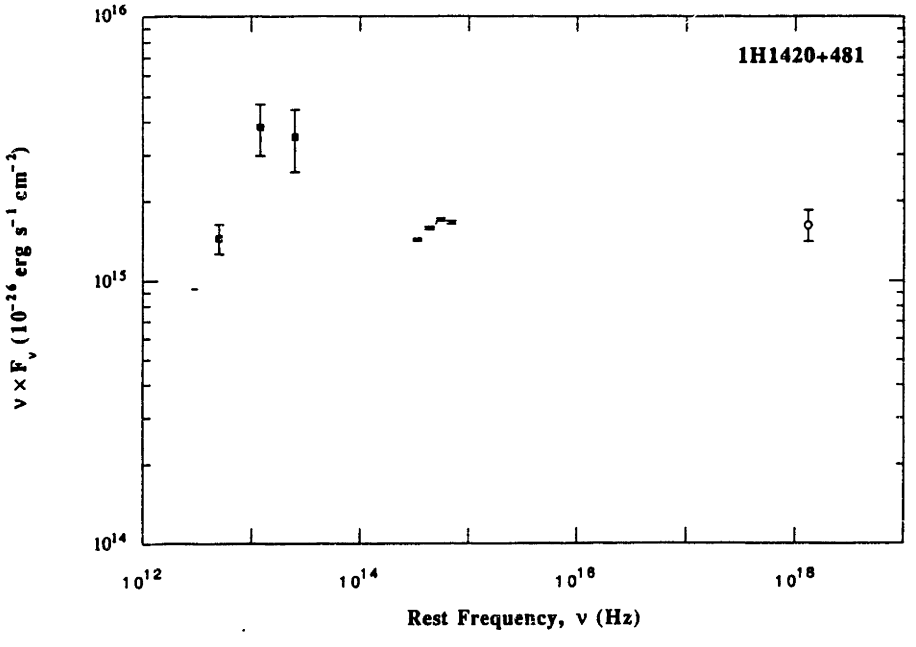
1H1420+481
10^{16}
10^{15}
10^{14}
$\nu \times F_\nu$ (10^{-16} erg s^{-1} cm^{-2})
10^{12}
10^{14}
10^{16}
10^{18}
Rest Frequency, ν (Hz)

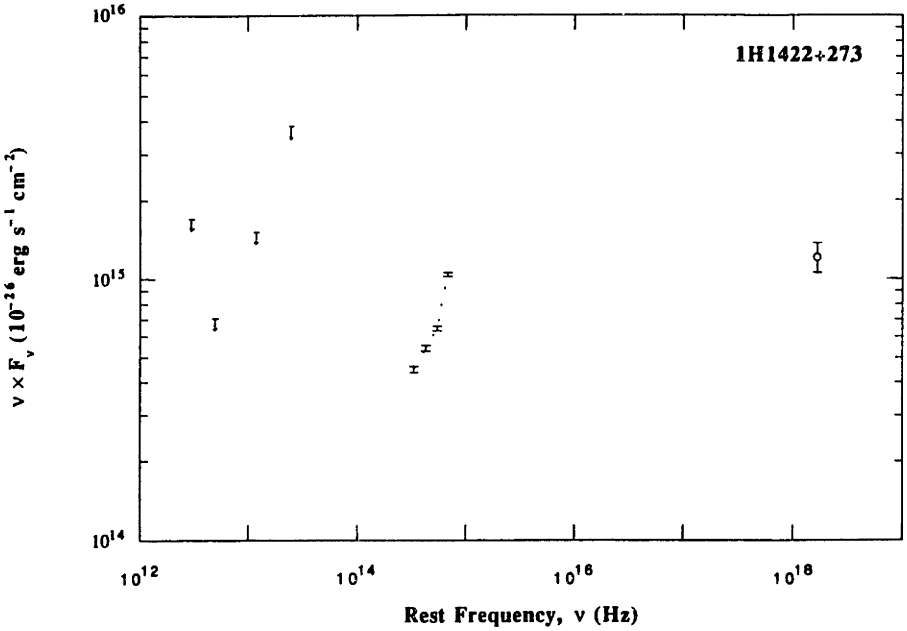
1H1422+273
10^{16}
10^{15}
10^{14}
10^{12}
10^{14}
10^{16}
10^{18}
$\nu \times F_\nu$ (10^{-26} erg s^{-1} cm^{-2})
Rest Frequency, ν (Hz)

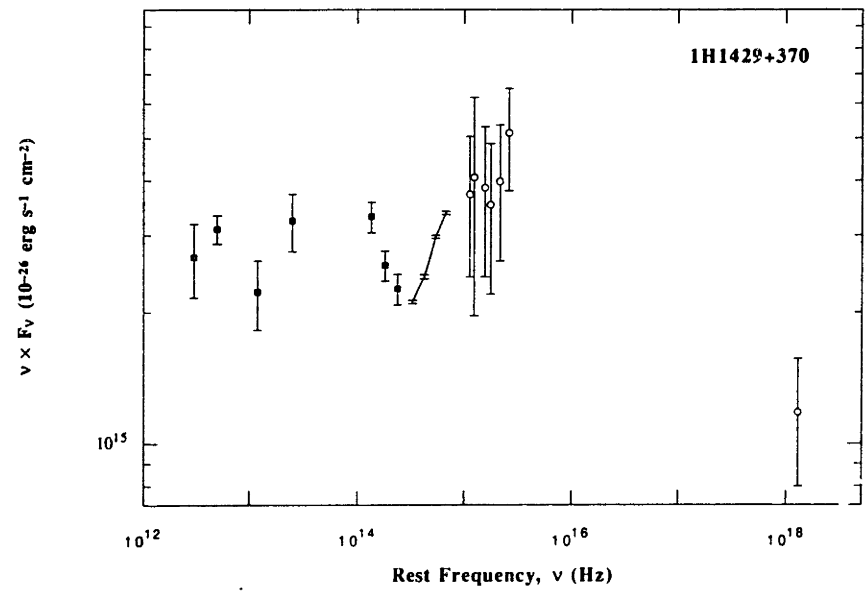
1H1429+370
10^{15}
10^{12}
10^{14}
10^{16}
10^{18}
$\nu \times F_\nu$ (10^{-26} erg s^{-1} cm^{-2})
Rest Frequency, ν (Hz)

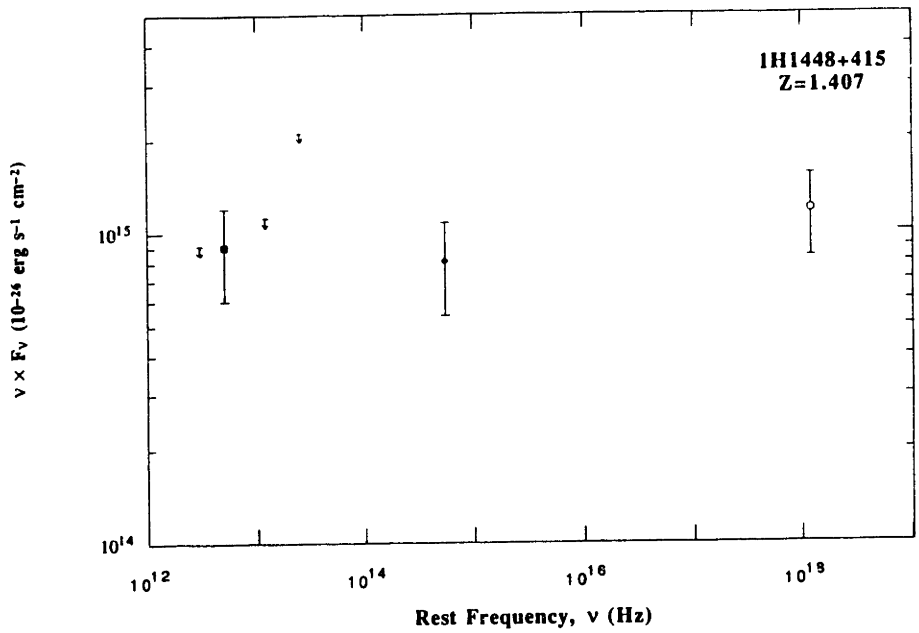
1H1448+415
Z=1.407
10^{15}
10^{14}
10^{12}
10^{14}
10^{16}
10^{18}
$\nu \times F_\nu$ (10^{-26} erg s^{-1} cm^{-2})
Rest Frequency, ν (Hz)

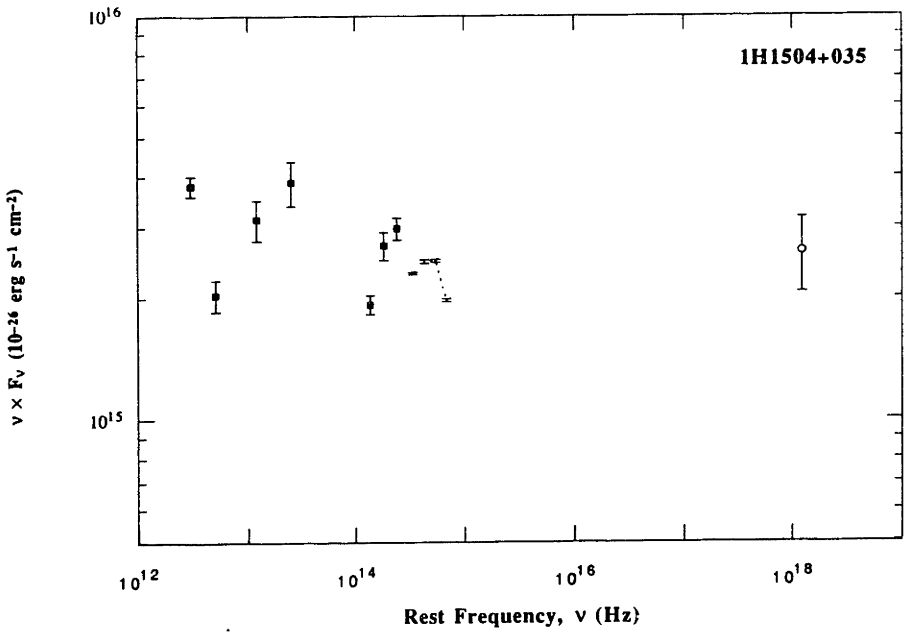
1H1504+035
10^{16}
10^{15}
10^{12}
10^{14}
10^{16}
10^{18}
$\nu \times F_\nu$ (10^{-26} erg s^{-1} cm^{-2})
Rest Frequency, ν (Hz)

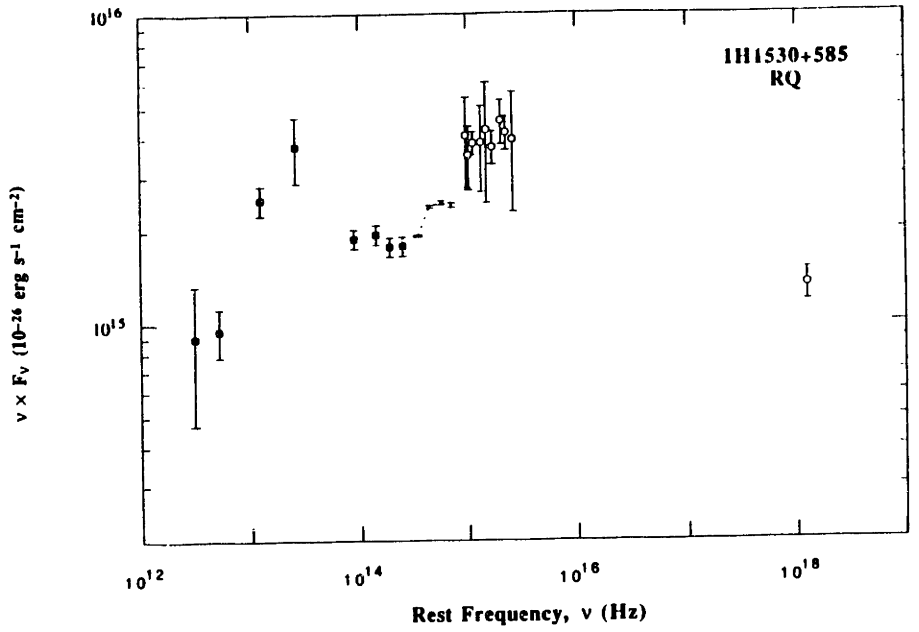
1H1530+585
RQ
10^{16}
10^{15}
10^{12}
10^{14}
10^{16}
10^{18}
$\nu \times F_\nu$ (10^{-26} erg s^{-1} cm^{-2})
Rest Frequency, ν (Hz)

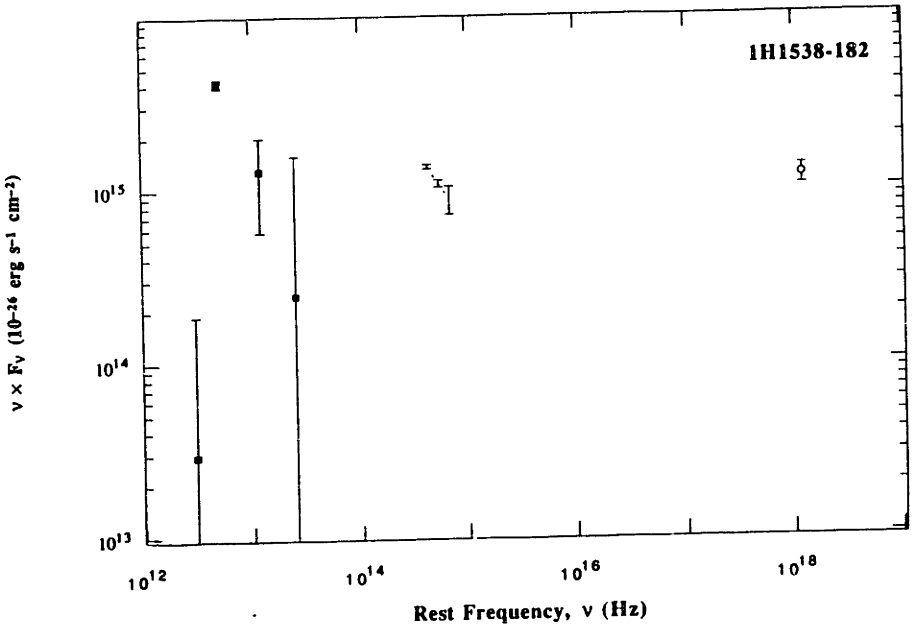
1H1538-182
10^{15}
10^{14}
10^{13}
10^{12}
10^{14}
10^{16}
10^{18}
$\nu \times F_\nu$ (10^{-26} erg s^{-1} cm^{-2})
Rest Frequency, ν (Hz)

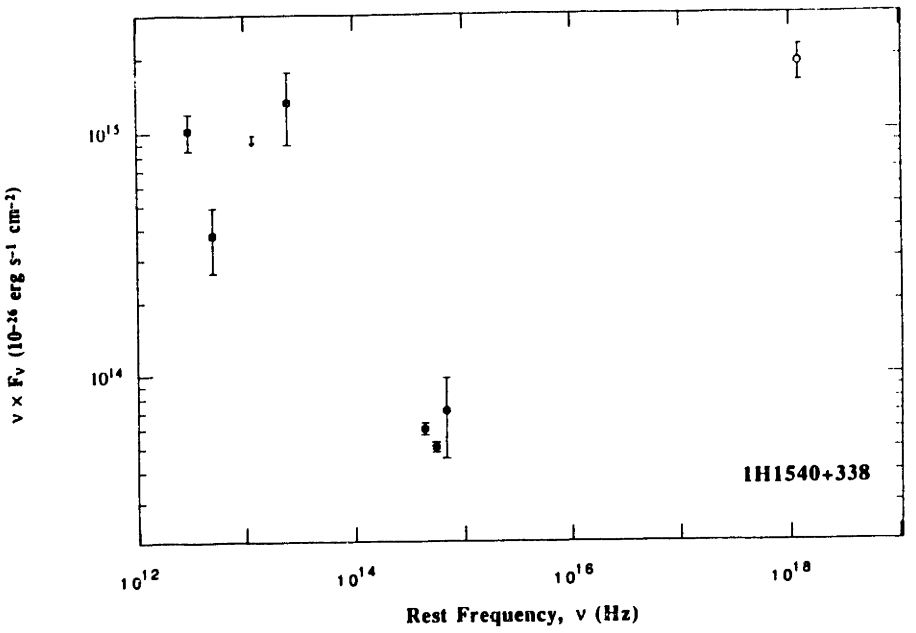
1H1540+338
10^{15}
10^{14}
10^{12}
10^{14}
10^{16}
10^{18}
$\nu \times F_\nu$ (10^{-26} erg s^{-1} cm^{-2})
Rest Frequency, ν (Hz)

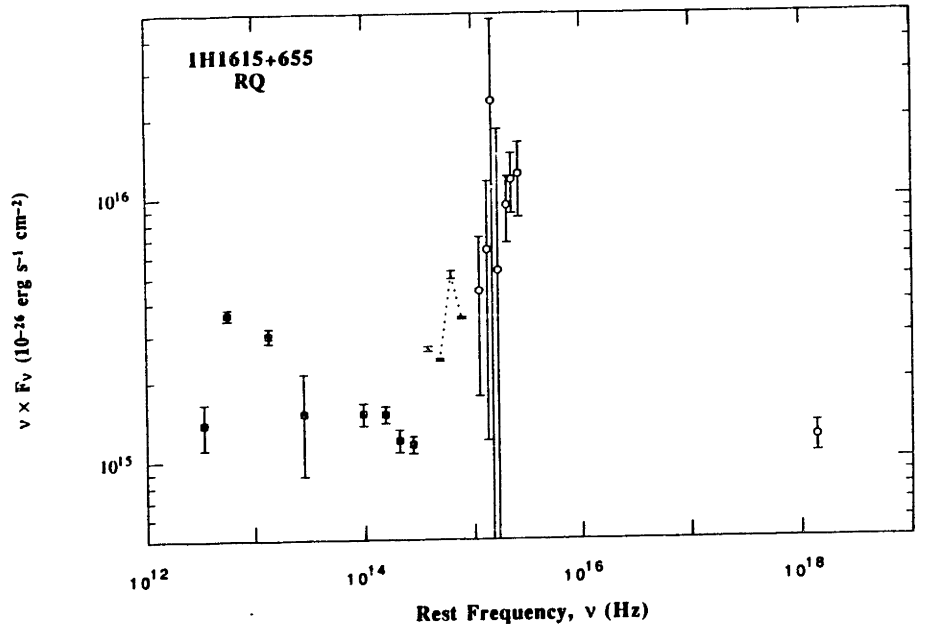
1H1615+655
RQ
10^{16}
10^{15}
10^{12}
10^{14}
10^{16}
10^{18}
$\nu \times F_\nu$ (10^{-26} erg s^{-1} cm^{-2})
Rest Frequency, ν (Hz)

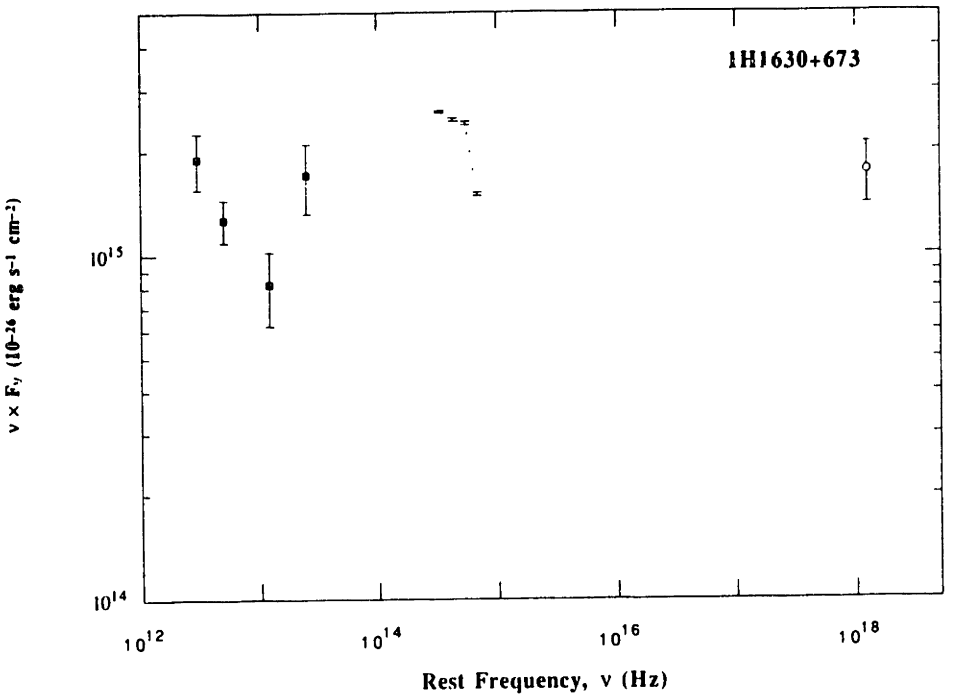
1H1630+673
$\nu \times F_\nu$ (10^{-26} erg s^{-1} cm^{-2})
10^{15}
10^{14}
10^{12}
10^{14}
10^{16}
10^{18}
Rest Frequency, ν (Hz)

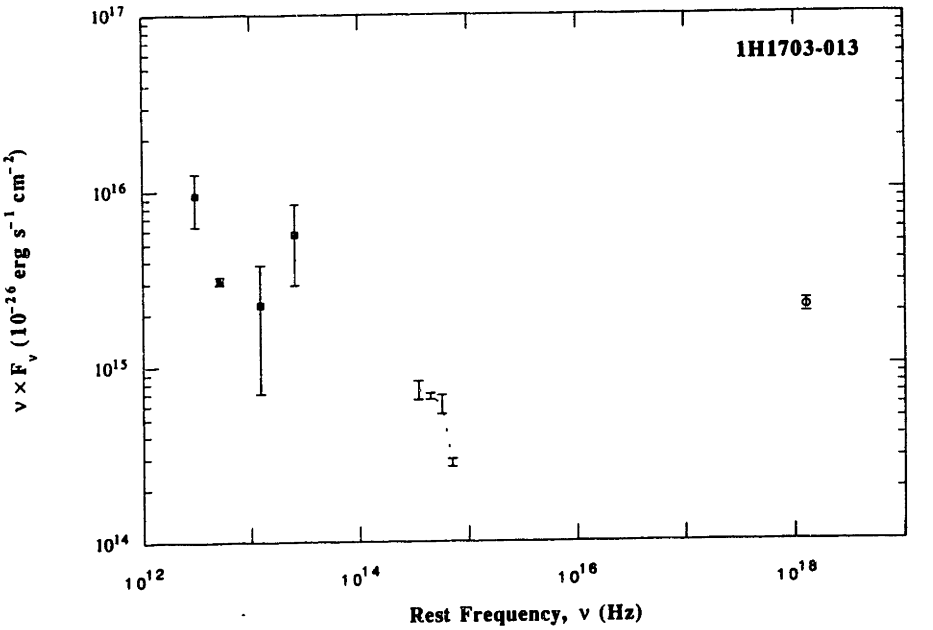
1H1703-013
$\nu \times F_\nu$ (10^{-26} erg s^{-1} cm^{-2})
10^{17}
10^{16}
10^{15}
10^{14}
10^{12}
10^{14}
10^{16}
10^{18}
Rest Frequency, ν (Hz)

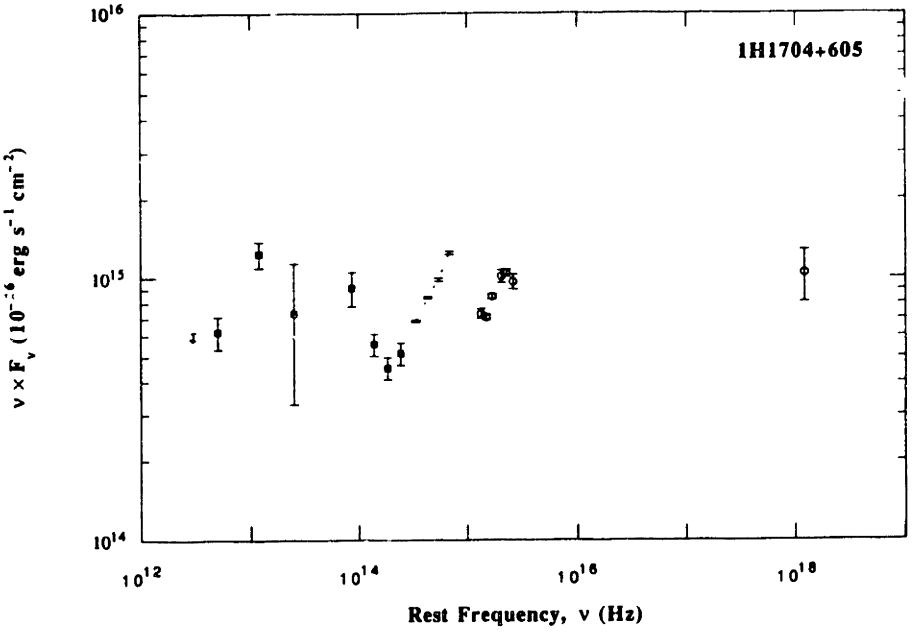
1H1704+605
10^{16}
10^{15}
10^{14}
10^{12}
10^{14}
10^{16}
10^{18}
$\nu \times F_\nu$ (10^{-16} erg s^{-1} cm^{-2})
Rest Frequency, ν (Hz)

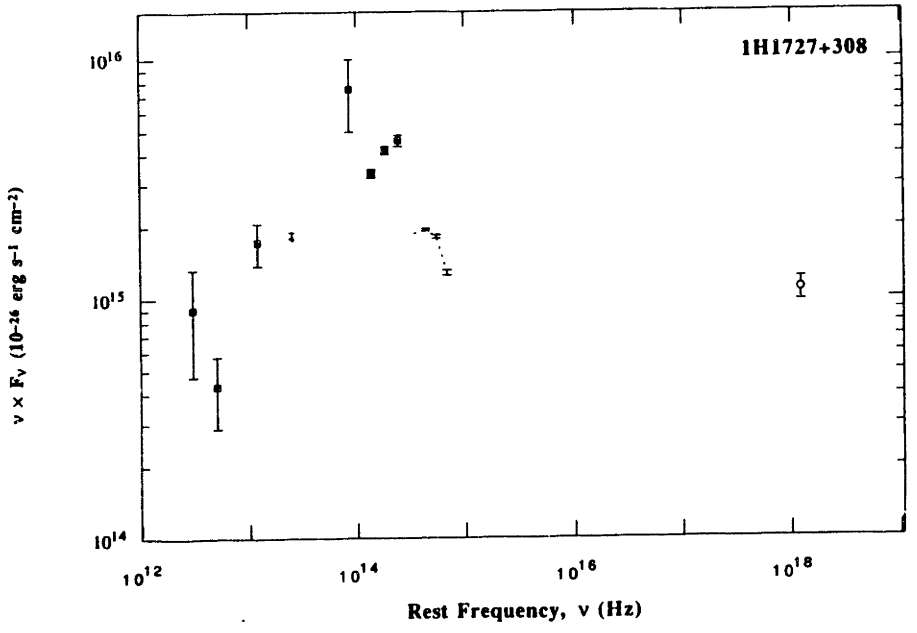
1H1727+308
10^{16}
10^{15}
10^{14}
10^{12}
10^{14}
10^{16}
10^{18}
$\nu \times F_\nu$ (10^{-16} erg s^{-1} cm^{-2})
Rest Frequency, ν (Hz)

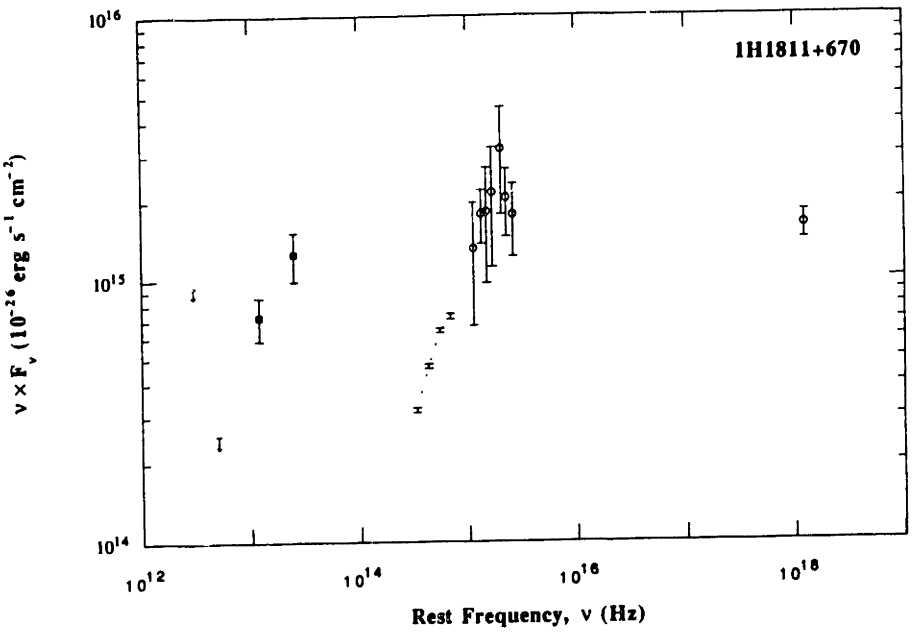
1H1811+670
10^{16}
10^{15}
10^{14}
10^{12}
10^{14}
10^{16}
10^{18}
$\nu \times F_\nu$ (10^{-26} erg s^{-1} cm^{-2})
Rest Frequency, ν (Hz)

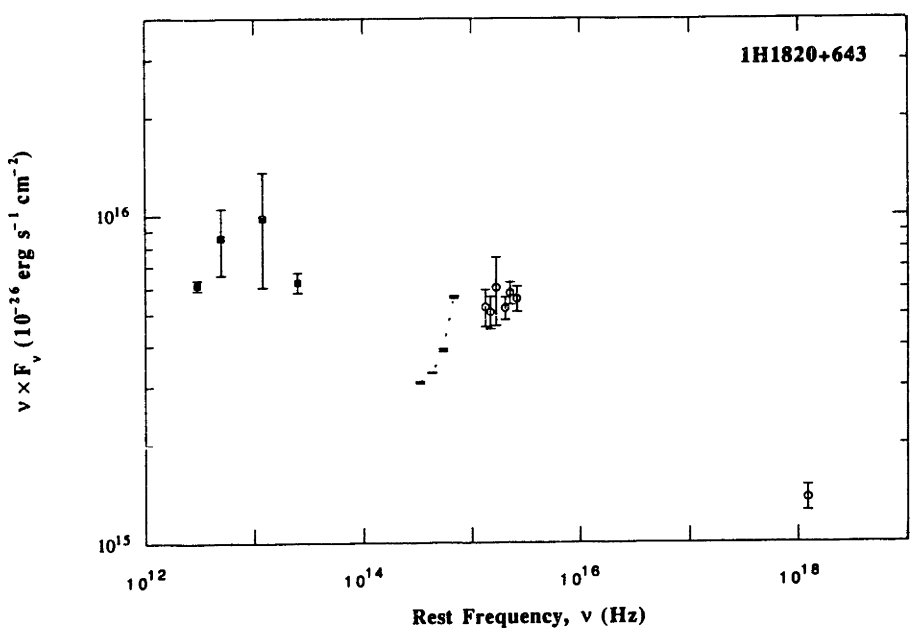
1H1820+643
10^{16}
10^{15}
10^{12}
10^{14}
10^{16}
10^{18}
$\nu \times F_\nu$ (10^{-26} erg s^{-1} cm^{-2})
Rest Frequency, ν (Hz)

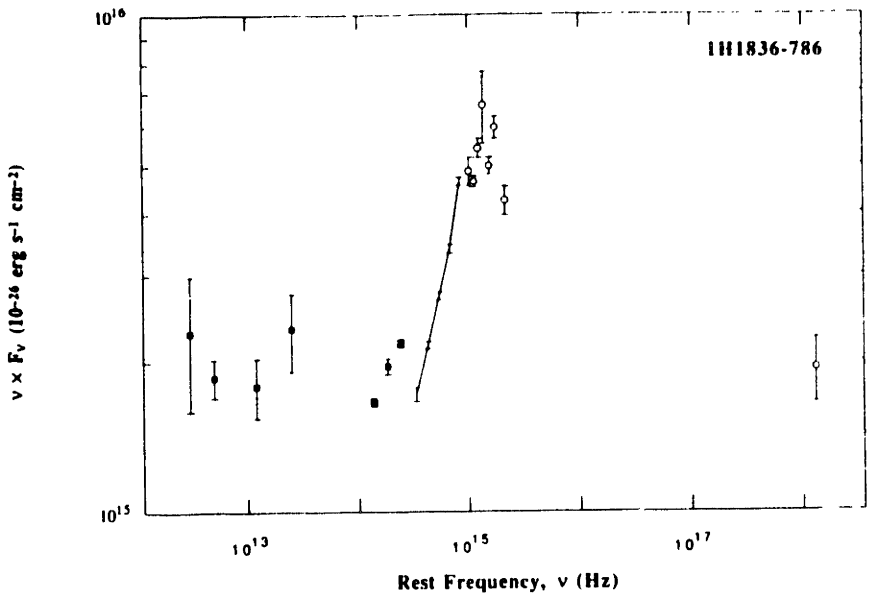
1H1836-786
10^{16}
10^{15}
10^{13}
10^{15}
10^{17}
$\nu \times F_\nu$ (10^{-26} erg s^{-1} cm^{-2})
Rest Frequency, ν (Hz)

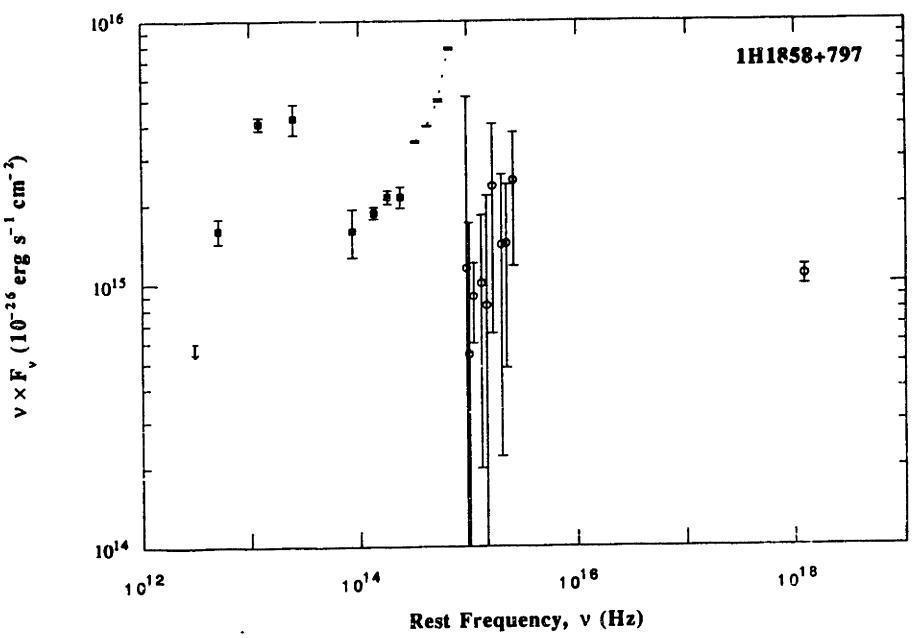
1H1858+797
10^{16}
10^{15}
10^{14}
10^{12}
10^{14}
10^{16}
10^{18}
$\nu \times F_\nu$ (10^{-26} erg s^{-1} cm^{-2})
Rest Frequency, ν (Hz)

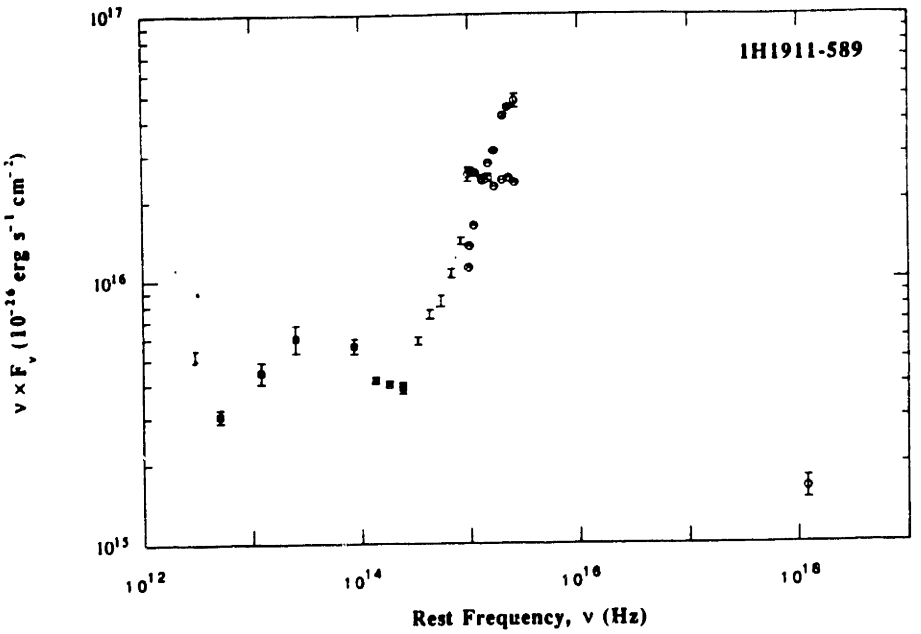
1H1911-589
10^{17}
10^{16}
10^{15}
10^{12}
10^{14}
10^{16}
10^{18}
$\nu \times F_\nu$ (10^{-16} erg s^{-1} cm^{-2})
Rest Frequency, ν (Hz)

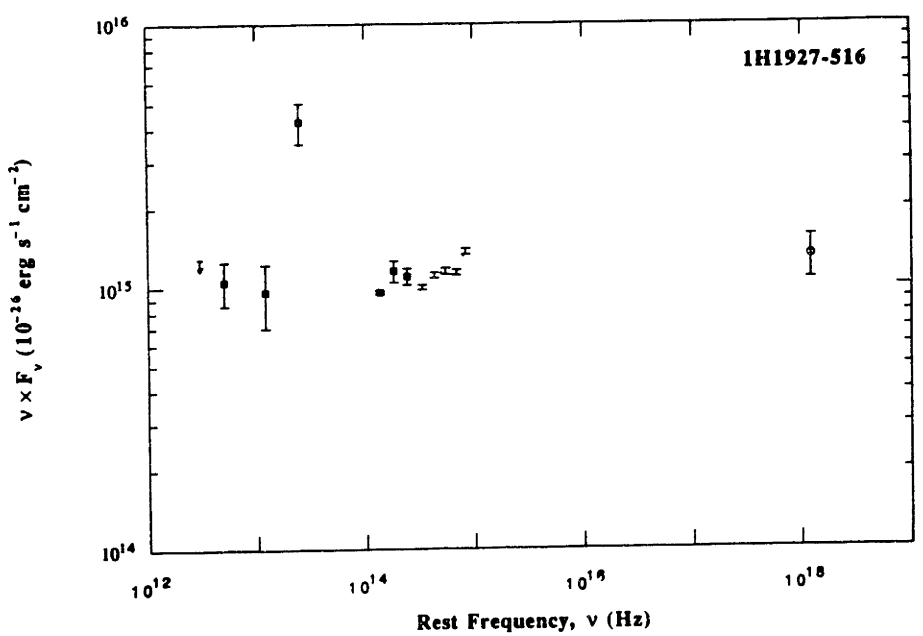
1H1927-516
10^{16}
10^{15}
10^{14}
10^{12}
10^{14}
10^{16}
10^{18}
$\nu \times F_\nu$ (10^{-16} erg s^{-1} cm^{-2})
Rest Frequency, ν (Hz)

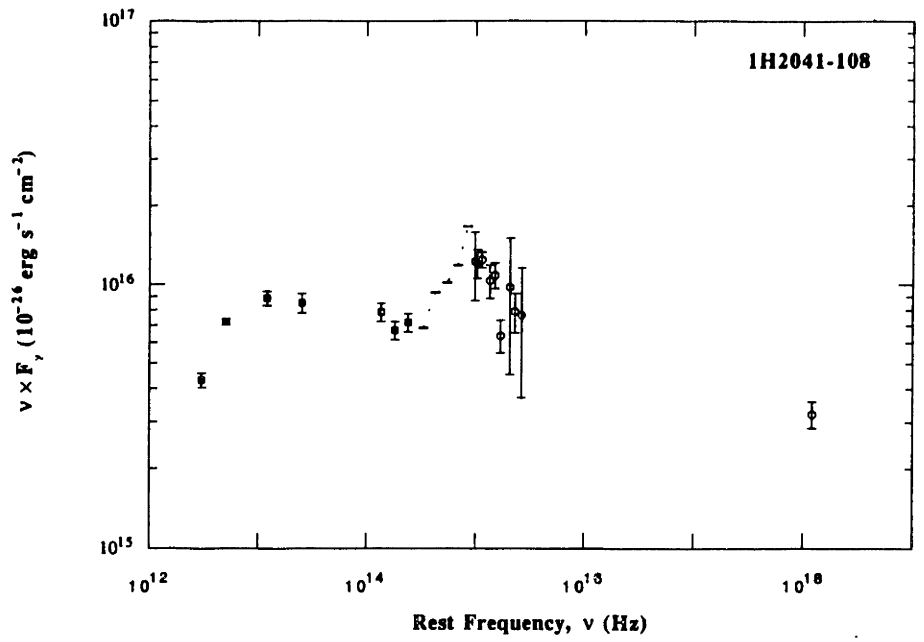
1H2041-108
10^{17}
10^{16}
10^{15}
10^{12}
10^{14}
10^{15}
10^{18}
$\nu \times F_\nu$ (10^{-26} erg s^{-1} cm^{-2})
Rest Frequency, ν (Hz)

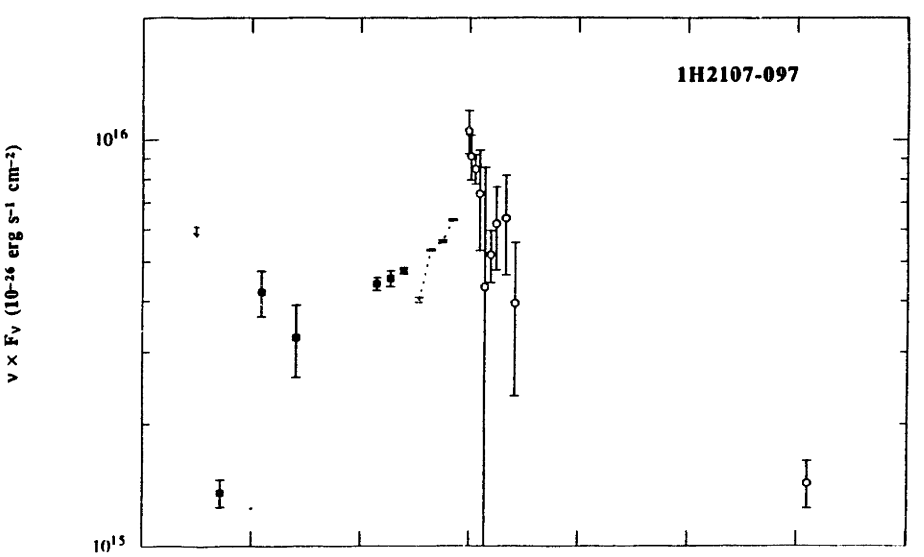
1H2107-097
10^{16}
10^{15}
$\nu \times F_\nu$ (10^{-26} erg s^{-1} cm^{-2})

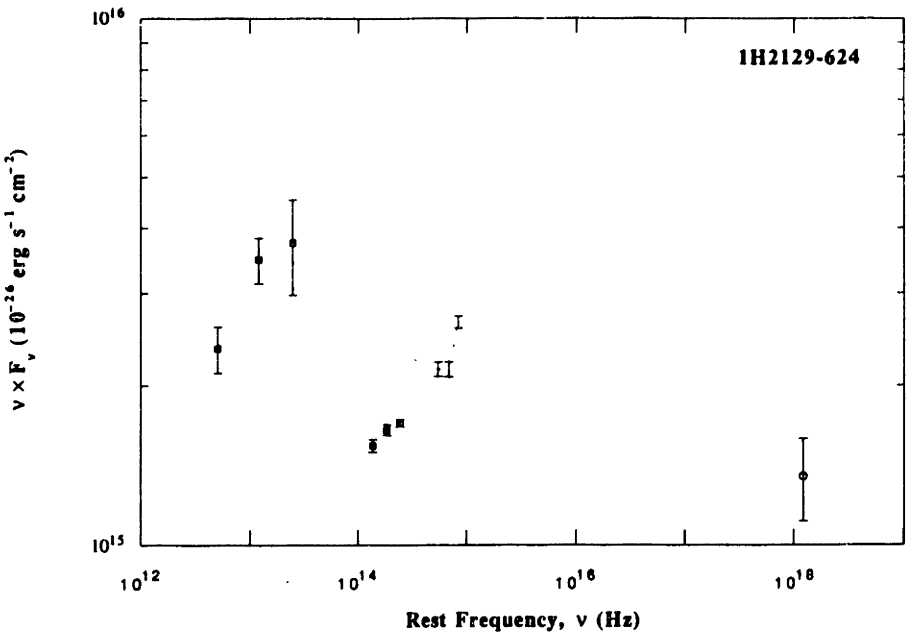
1H2129-624
10^{16}
10^{15}
10^{12}
10^{14}
10^{16}
10^{18}
$\nu \times F_\nu$ (10^{-26} erg s^{-1} cm^{-2})
Rest Frequency, ν (Hz)

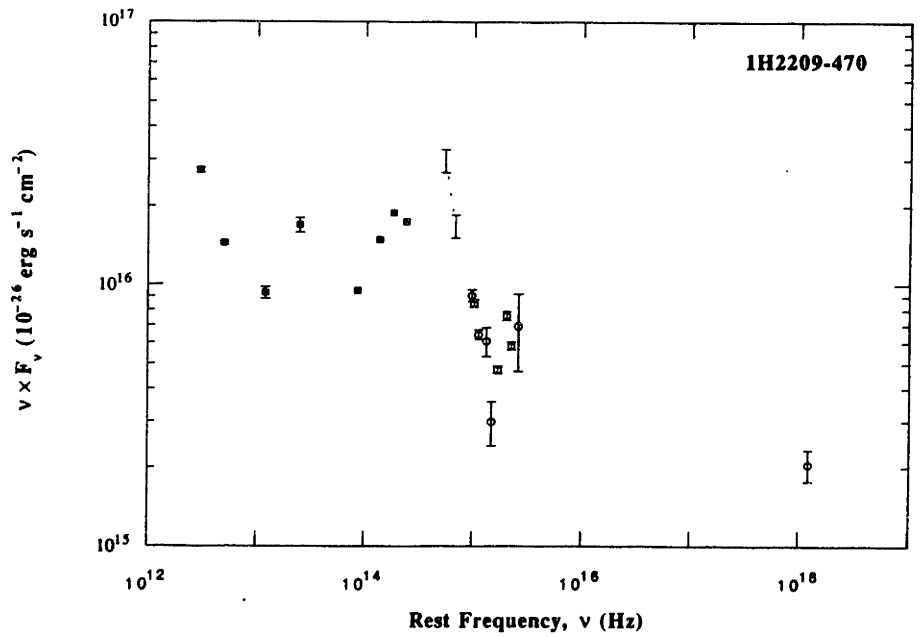
1H2209-470
10^{17}
10^{16}
10^{15}
10^{12}
10^{14}
10^{16}
10^{18}
$\nu \times F_\nu$ (10^{-26} erg s^{-1} cm^{-2})
Rest Frequency, ν (Hz)

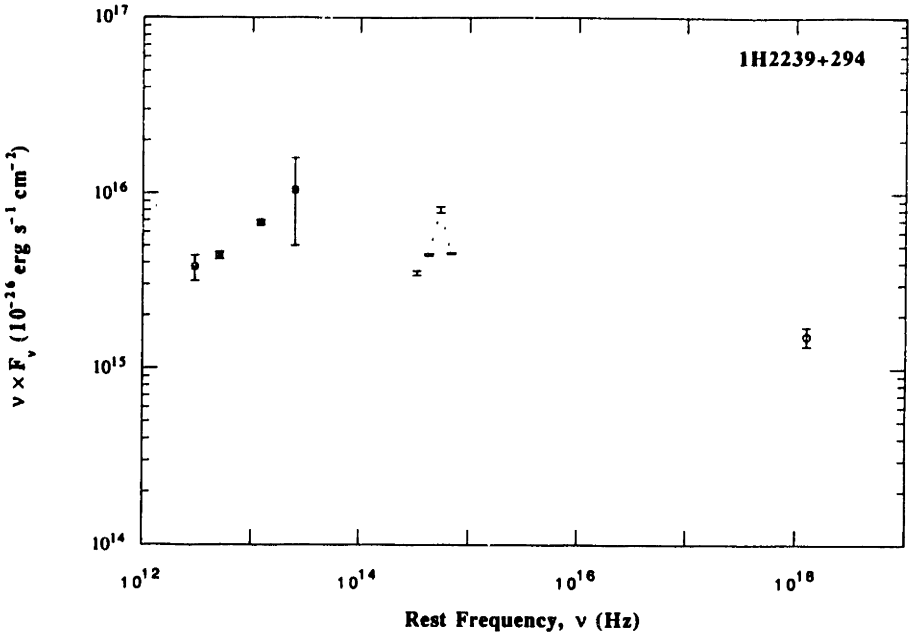
1H2239+294
10^{17}
10^{16}
10^{15}
10^{14}
10^{12}
10^{14}
10^{16}
10^{18}
$\nu \times F_\nu$ (10^{-26} erg s^{-1} cm^{-2})
Rest Frequency, ν (Hz)

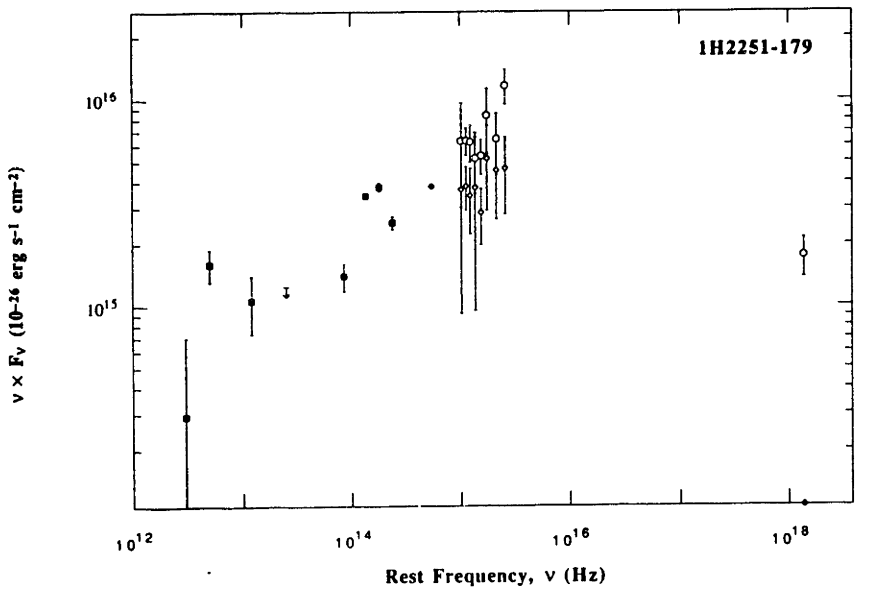
1H2251-179
10^{16}
10^{15}
10^{12}
10^{14}
10^{16}
10^{18}
$\nu \times F_\nu$ (10^{-26} erg s^{-1} cm^{-2})
Rest Frequency, ν (Hz)

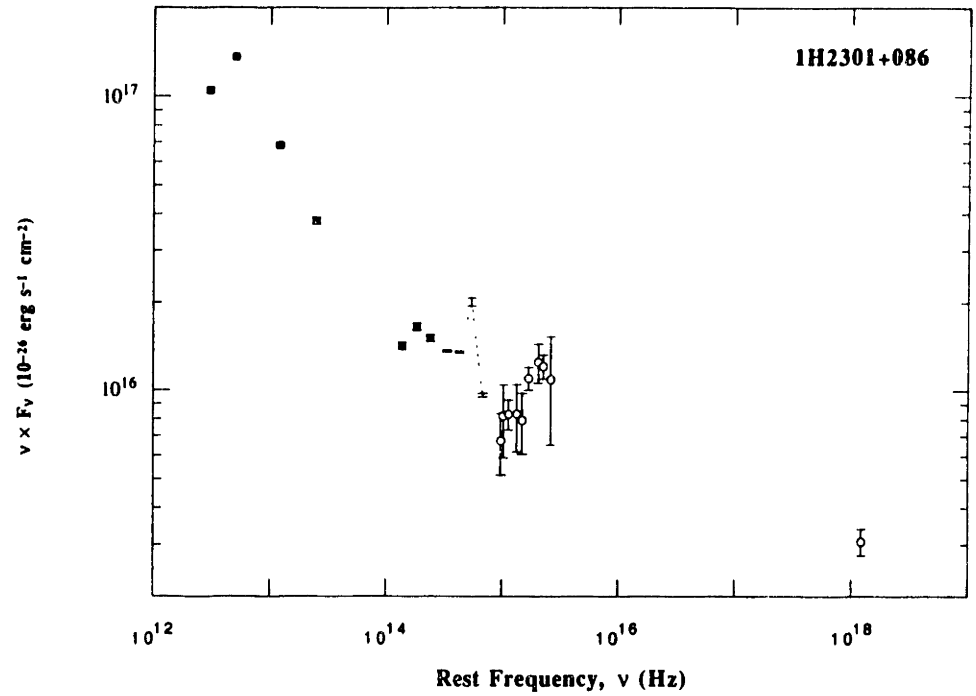
1H2301+086
10^{17}
10^{16}
10^{12}
10^{14}
10^{16}
10^{18}
$\nu \times F_\nu$ (10^{-26} erg s^{-1} cm^{-2})
Rest Frequency, ν (Hz)

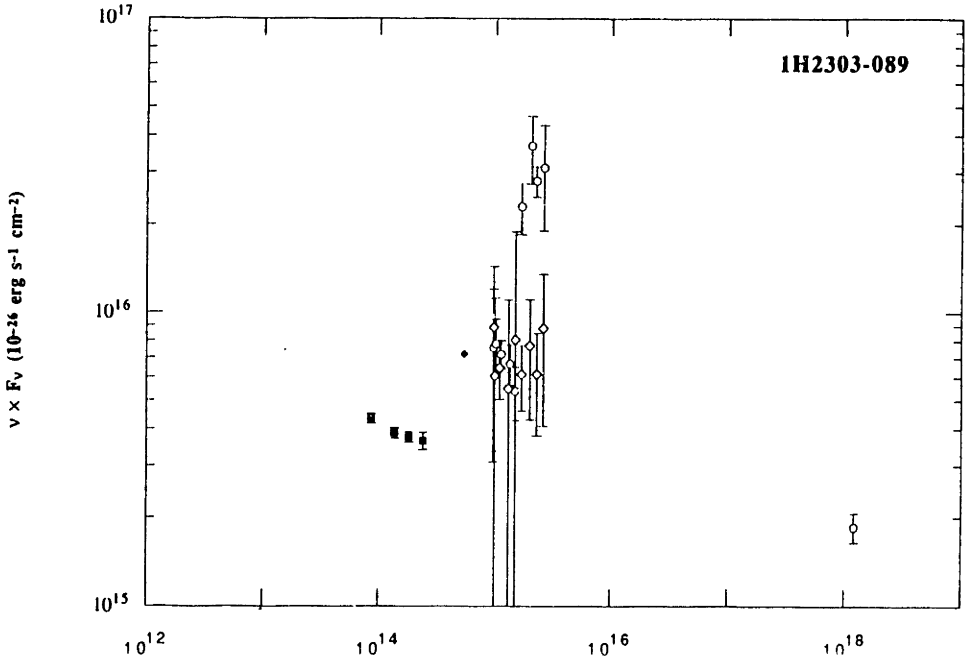
1H2303-089
10^{17}
10^{16}
10^{15}
10^{12}
10^{14}
10^{16}
10^{18}
$\nu \times F_\nu$ (10^{-26} erg s^{-1} cm^{-2})

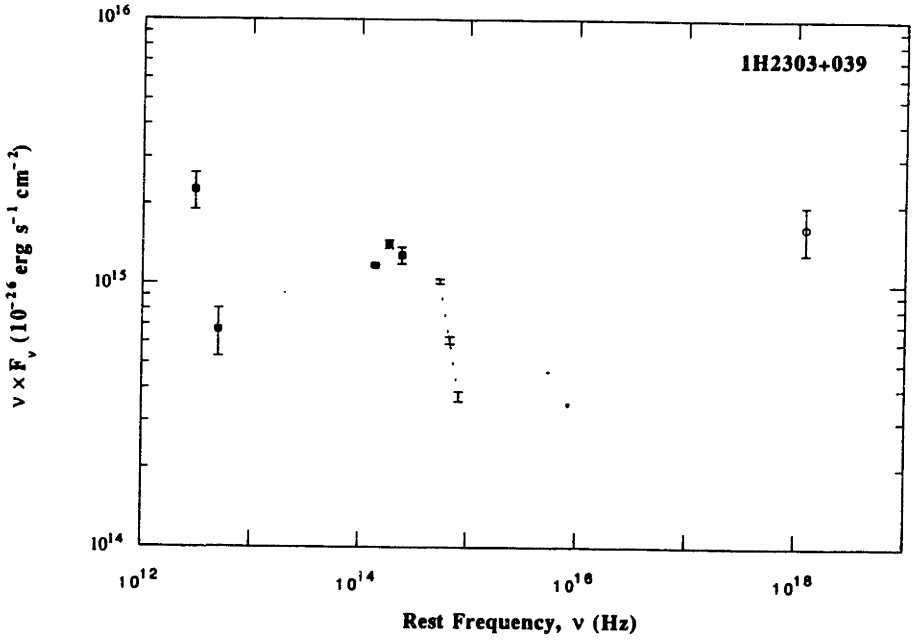
1H2303+039
10^{16}
10^{15}
10^{14}
10^{12}
10^{14}
10^{16}
10^{18}
$\nu \times F_\nu$ (10^{-26} erg s^{-1} cm^{-2})
Rest Frequency, ν (Hz)

TYPE 2 OBJECTS

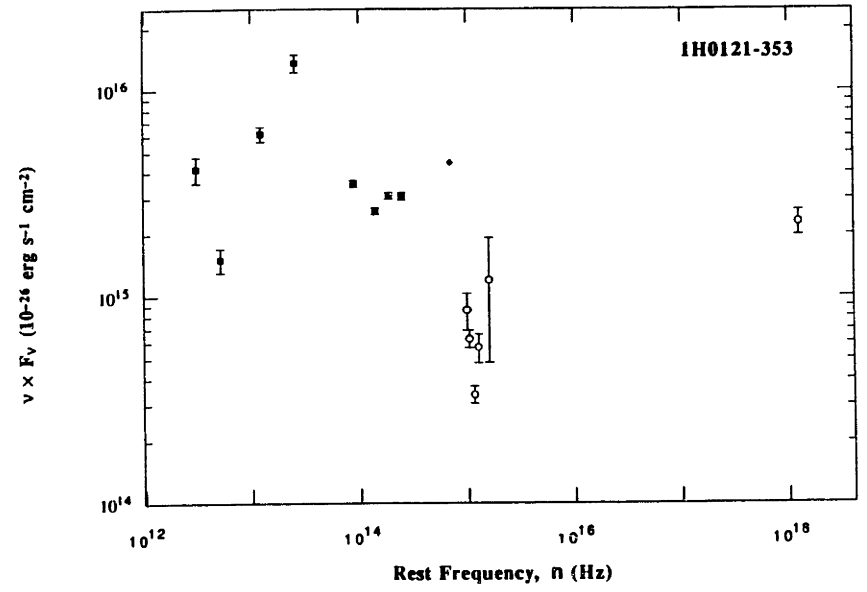

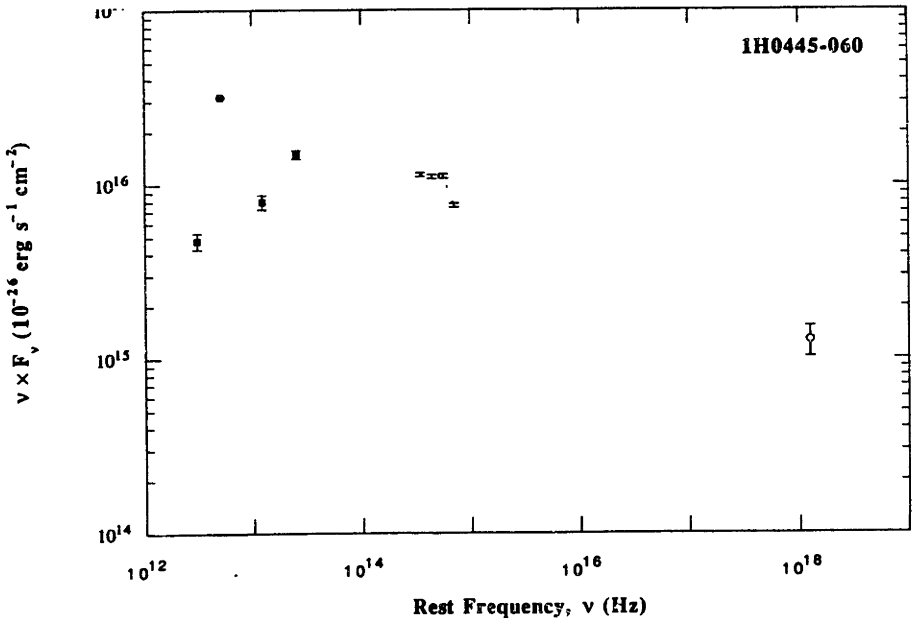

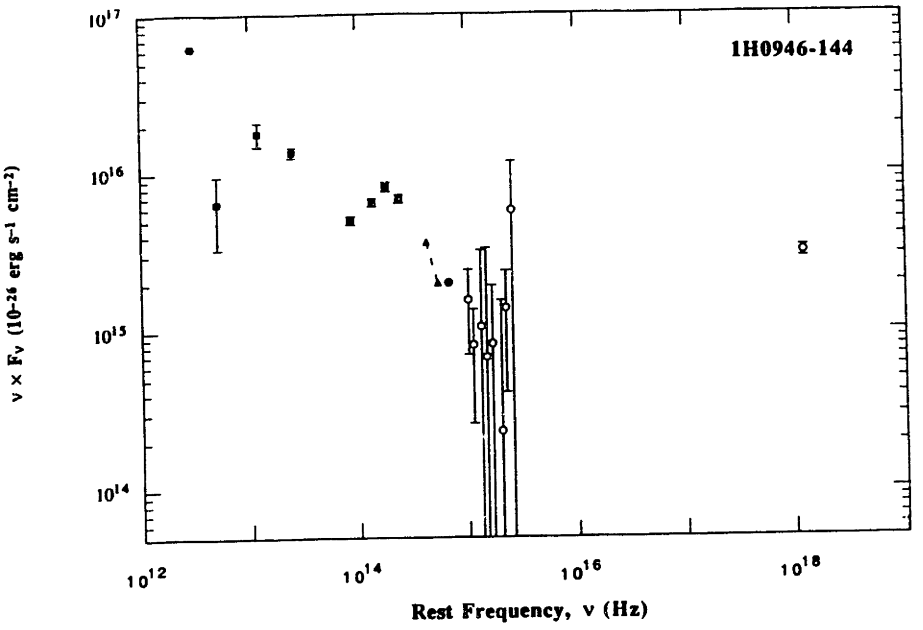
1H0946-144
10^{17}
10^{16}
10^{15}
10^{14}
10^{12}
10^{14}
10^{16}
10^{18}
$\nu \times F_\nu$ (10^{-26} erg s^{-1} cm^{-2})
Rest Frequency, ν (Hz)

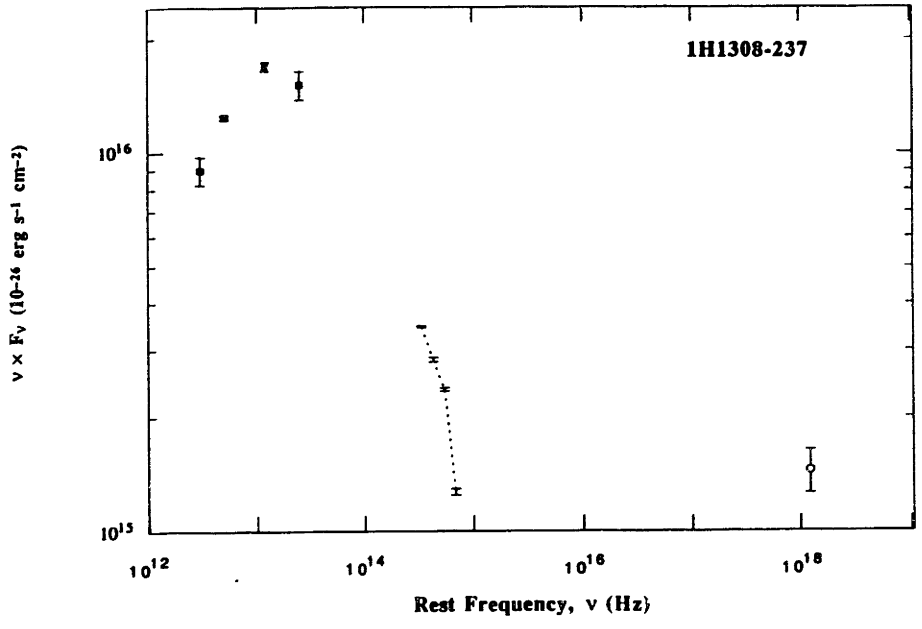
1H1308-237
10^{16}
10^{15}
10^{12}
10^{14}
10^{16}
10^{18}
$\nu \times F_\nu$ (10^{-26} erg s^{-1} cm^{-2})
Rest Frequency, ν (Hz)

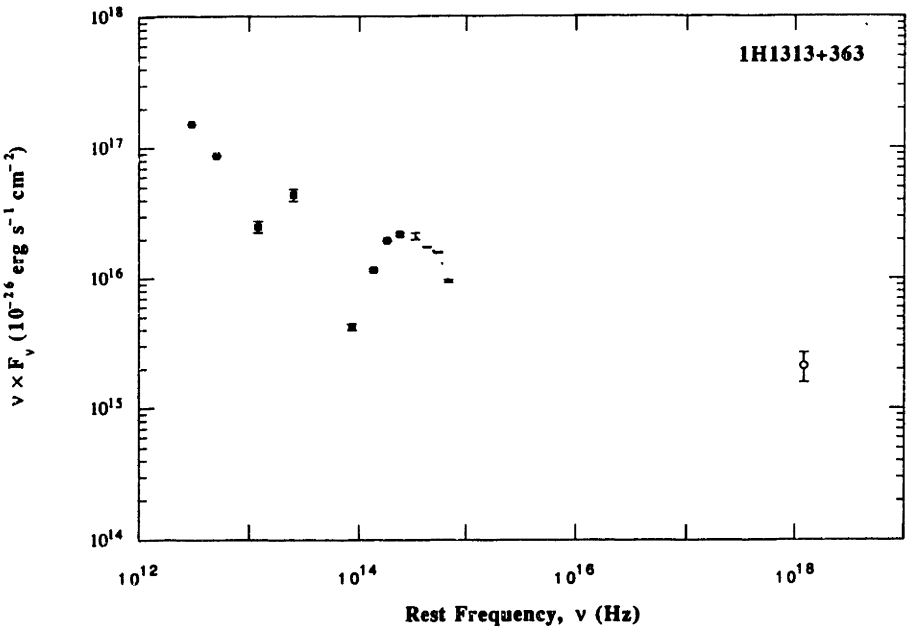
1H1313+363
10^{18}
10^{17}
10^{16}
10^{15}
10^{14}
10^{12}
10^{14}
10^{16}
10^{18}
$\nu \times F_\nu$ (10^{-26} erg s^{-1} cm^{-2})
Rest Frequency, ν (Hz)

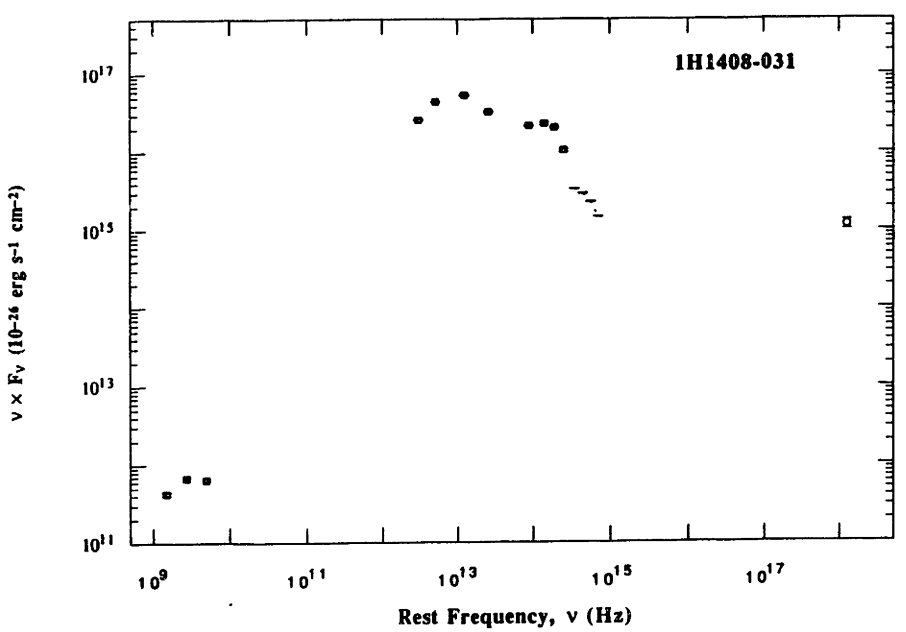
1H1408-031
10^{17}
10^{15}
10^{13}
10^{11}
10^{9}
10^{11}
10^{13}
10^{15}
10^{17}
$\nu \times F_\nu$ (10^{-26} erg s^{-1} cm^{-2})
Rest Frequency, ν (Hz)

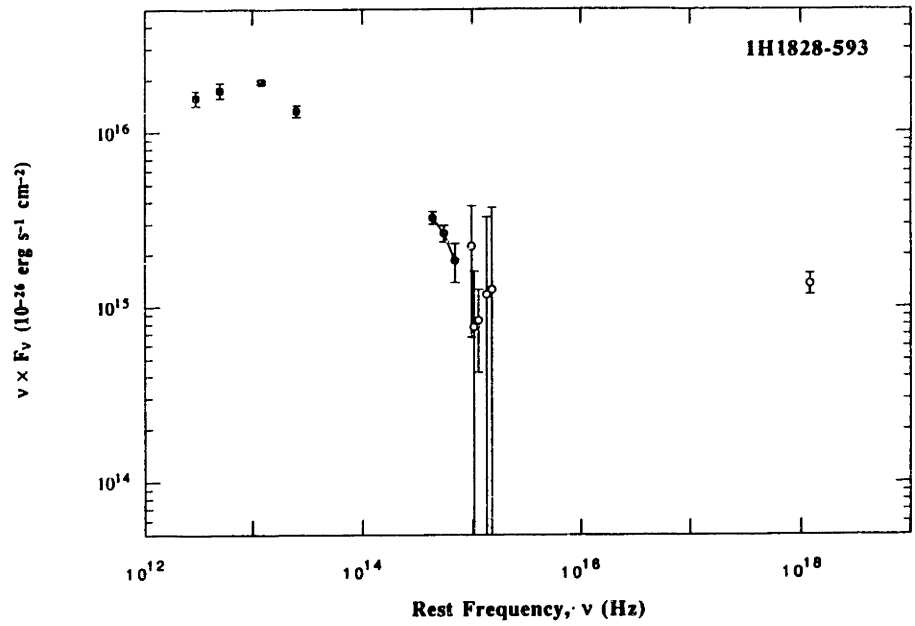
1H1828-593
10^{16}
10^{15}
10^{14}
10^{12}
10^{14}
10^{16}
10^{18}
$\nu \times F_\nu$ (10^{-26} erg s^{-1} cm^{-2})
Rest Frequency, ν (Hz)

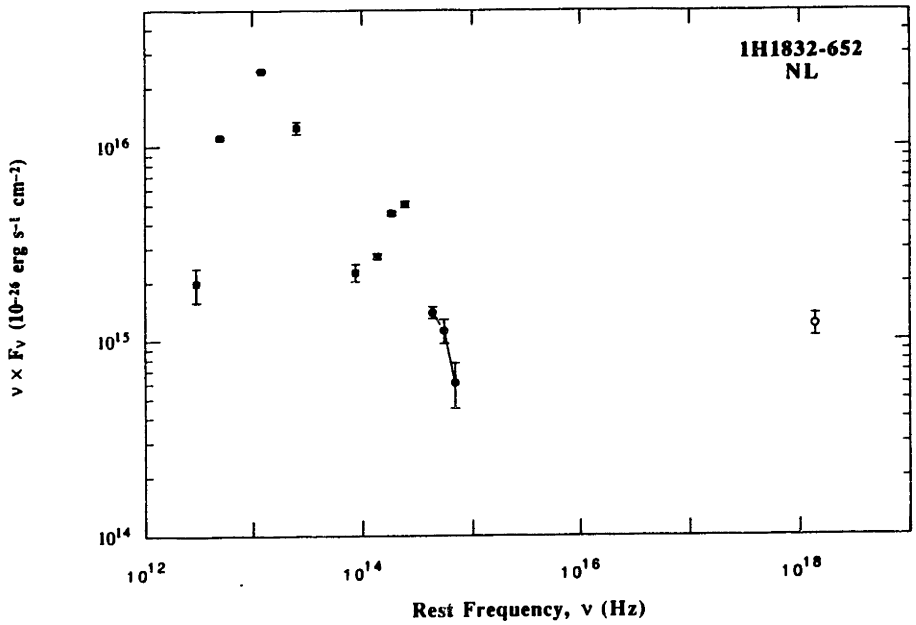
1H1832-652
NL
10^{16}
10^{15}
10^{14}
10^{12}
10^{14}
10^{16}
10^{18}
$\nu \times F_\nu$ (10^{-26} erg s^{-1} cm^{-2})
Rest Frequency, ν (Hz)

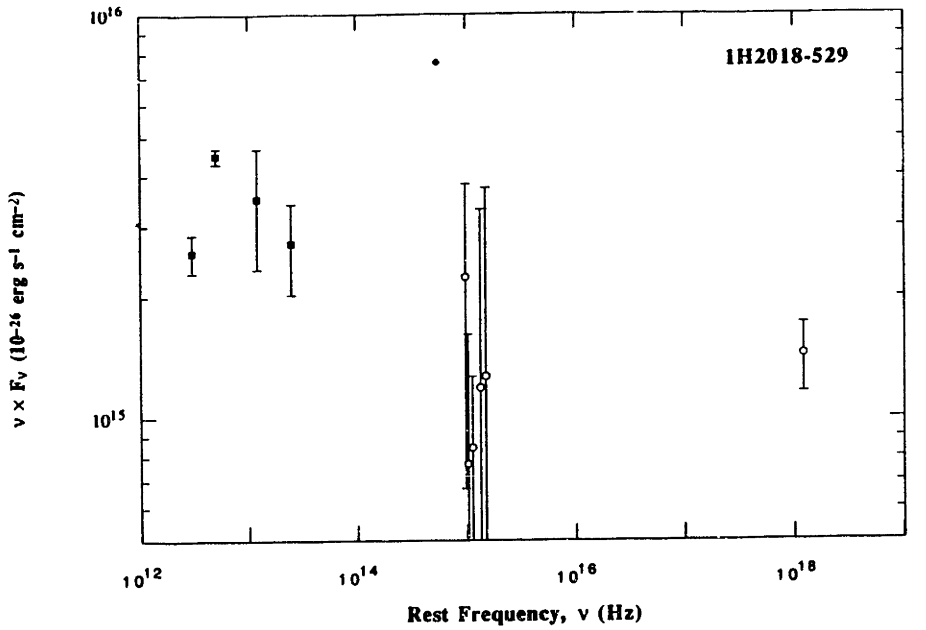
1H2018-529
10^{16}
10^{15}
10^{12}
10^{14}
10^{16}
10^{18}
$\nu \times F_\nu$ (10^{-26} erg s^{-1} cm^{-2})
Rest Frequency, ν (Hz)

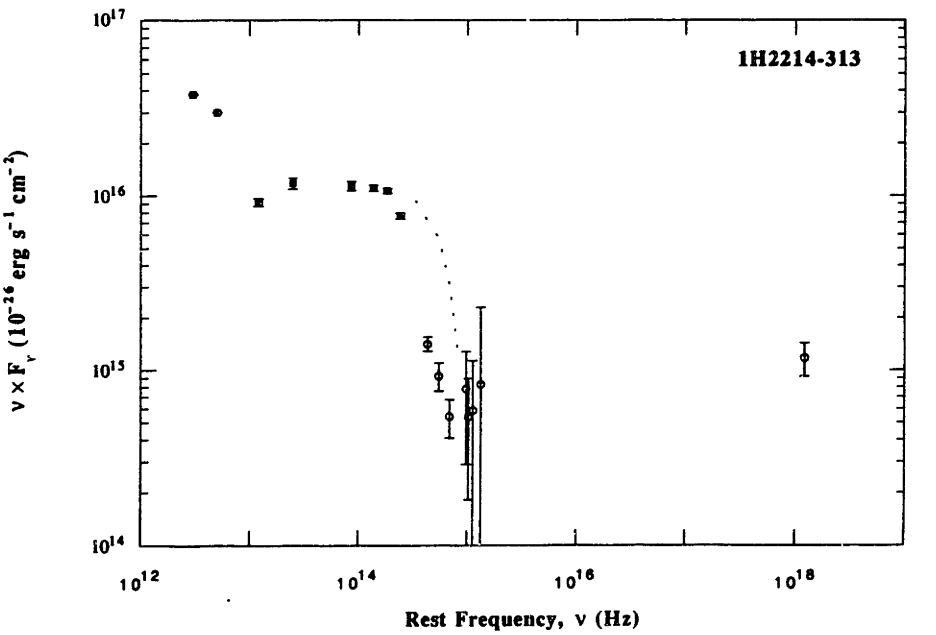
1H2214-313
10^{17}
10^{16}
10^{15}
10^{14}
10^{12}
10^{14}
10^{16}
10^{18}
$\nu \times F_\nu$ (10^{-26} erg s^{-1} cm^{-2})
Rest Frequency, ν (Hz)

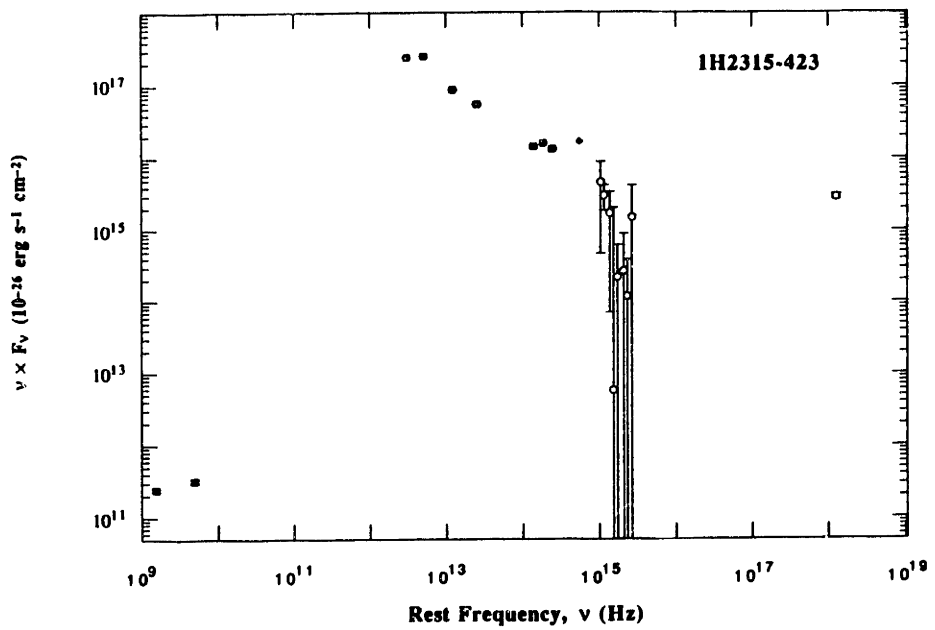
1H2315-423
10^{17}
10^{15}
10^{13}
10^{11}
10^{9}
10^{11}
10^{13}
10^{15}
10^{17}
10^{19}
$\nu \times F_\nu$ (10^{-26} erg s^{-1} cm^{-2})
Rest Frequency, ν (Hz)

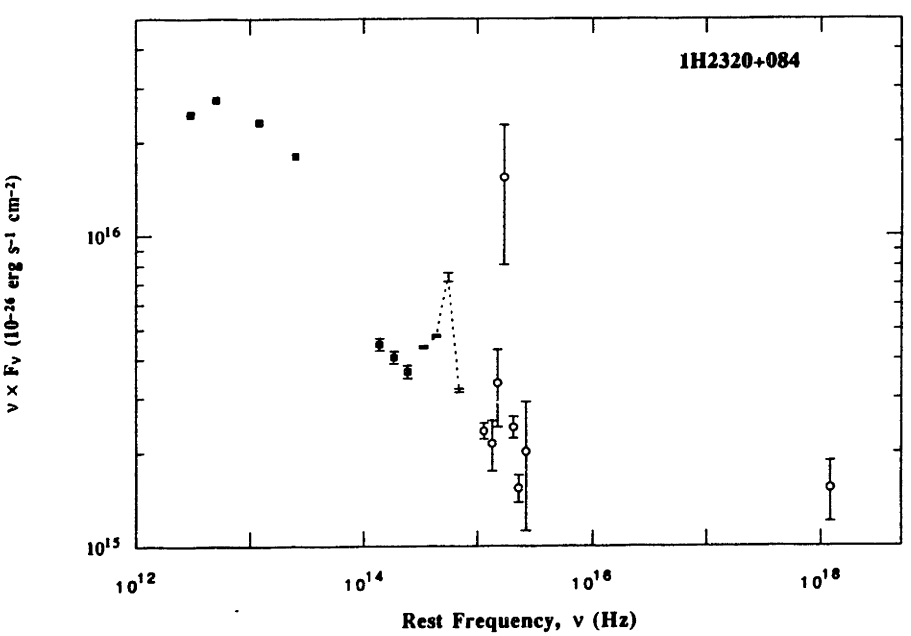
1H2320+084
10^{16}
10^{15}
10^{12}
10^{14}
10^{16}
10^{18}
$\nu \times F_\nu$ (10^{-26} erg s^{-1} cm^{-2})
Rest Frequency, ν (Hz)

APPENDIX III
UV SPECTRAL ATLAS

This appendix gives 40 IUE spectra of LMA objects. The reduction of these spectra is described in Chapter 2, Section 2.

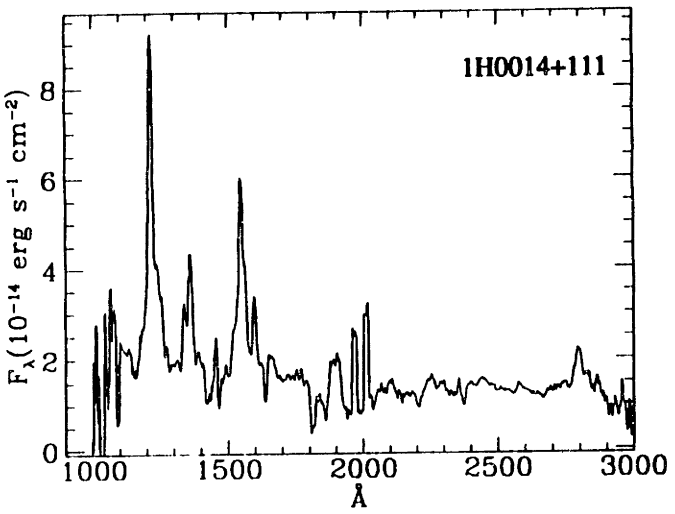
1H0014+111
$F_\lambda(10^{-14}$ erg s^{-1} cm^{-2})
0
2
4
6
8
1000
1500
2000
2500
3000
Å

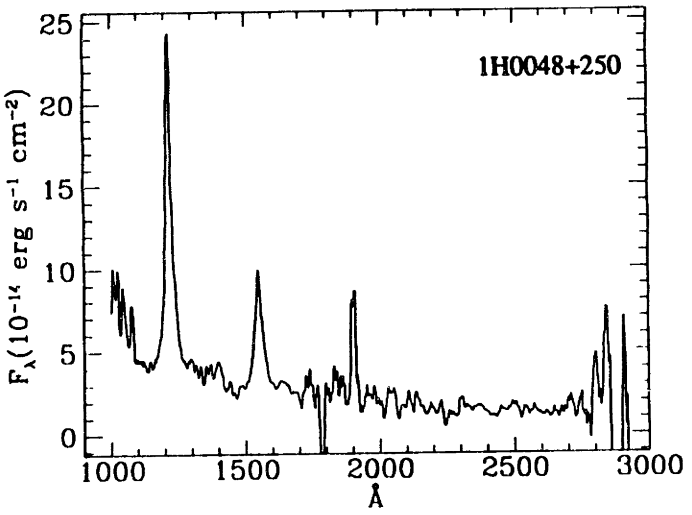
1H0048+250
$F_\lambda(10^{-14}$ erg s^{-1} cm^{-2})
0
5
10
15
20
25
1000
1500
2000
2500
3000
Å

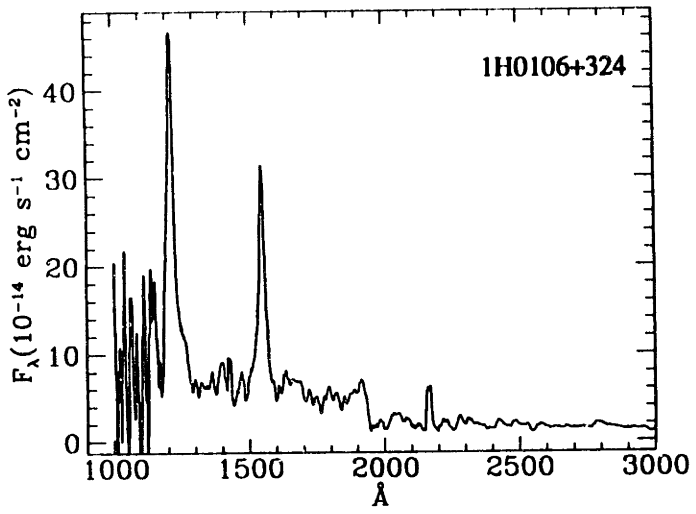
1H0106+324
$F_\lambda(10^{-14}$ erg s^{-1} cm^{-2})
0
10
20
30
40
1000
1500
2000
2500
3000
Å

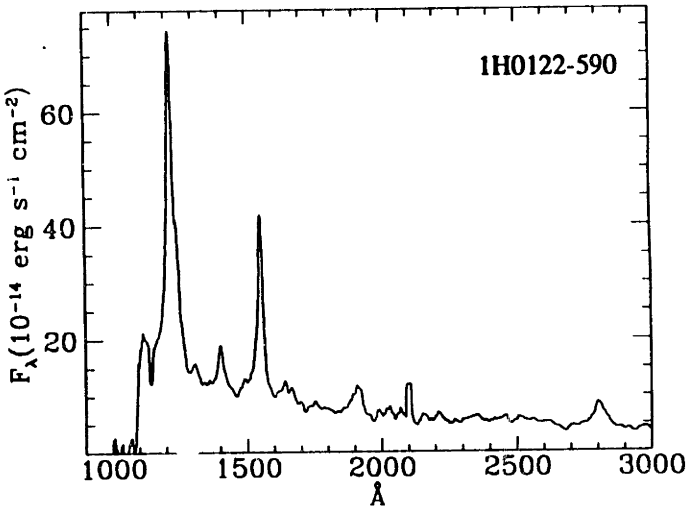
1H0122-590
$F_\lambda(10^{-14}$ erg s^{-1} cm^{-2})
20
40
60
1000
1500
2000
2500
3000
Å

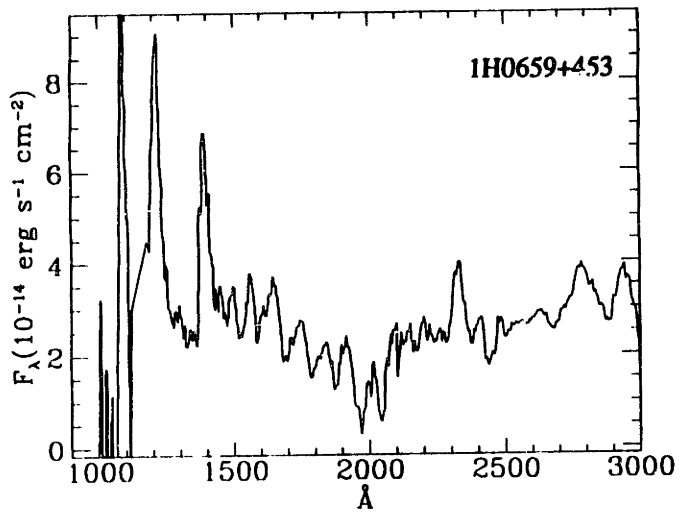
1H0659+453
$F_\lambda(10^{-14}$ erg s^{-1} cm^{-2})
0
2
4
6
8
1000
1500
2000
2500
3000
Å

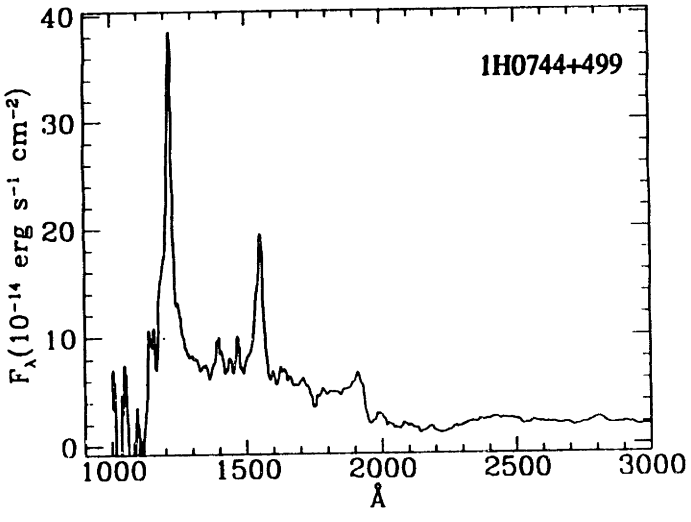
1H0744+499
$F_\lambda(10^{-14}$ erg s^{-1} cm^{-2})
0
10
20
30
40
1000
1500
2000
2500
3000
Å

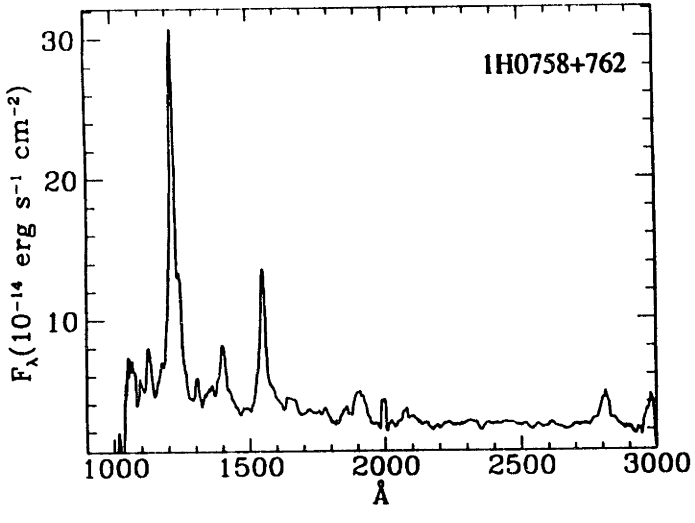
1H0758+762
$F_\lambda(10^{-14}$ erg s^{-1} cm^{-2})
10
20
30
1000
1500
2000
2500
3000
Å

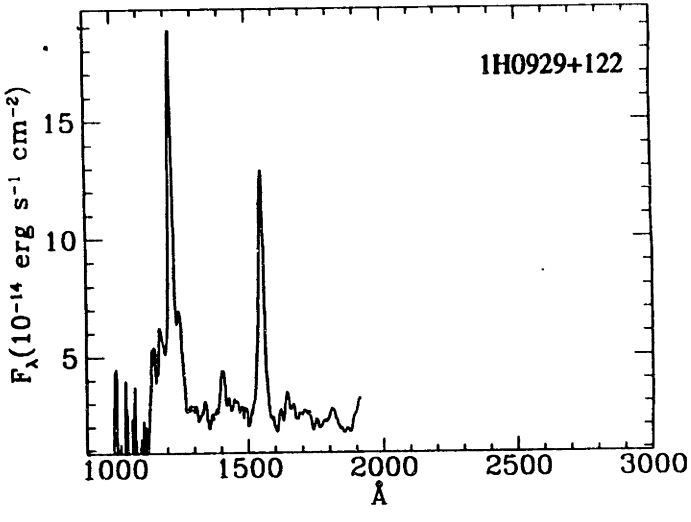
1H0929+122
$F_\lambda(10^{-14}$ erg s^{-1} cm^{-2})
5
10
15
1000
1500
2000
2500
3000
Å

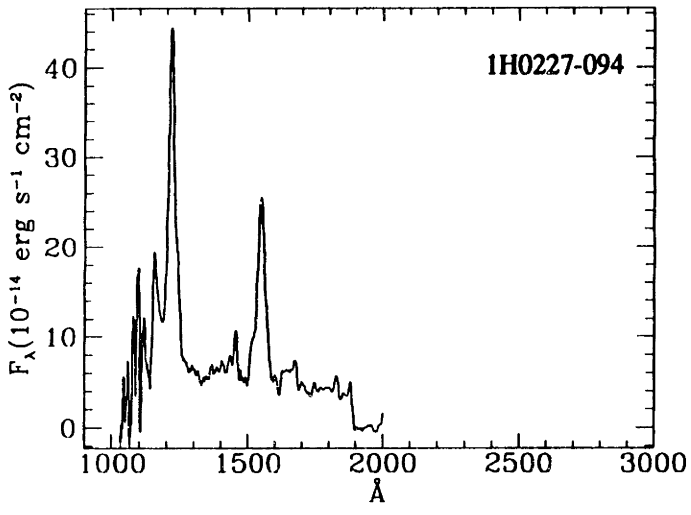
1H0227-094
$F_\lambda(10^{-14}$ erg s^{-1} cm^{-2})
0
10
20
30
40
1000
1500
2000
2500
3000
Å

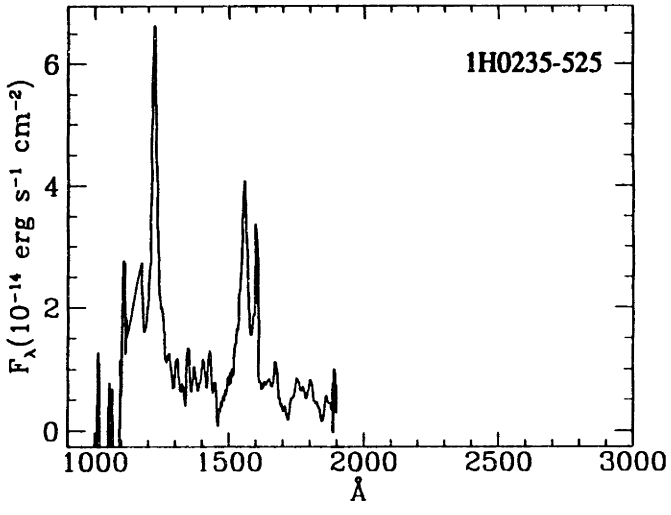
1H0235-525
$F_\lambda(10^{-14}$ erg s^{-1} cm^{-2})
0
2
4
6
1000
1500
2000
2500
3000
Å

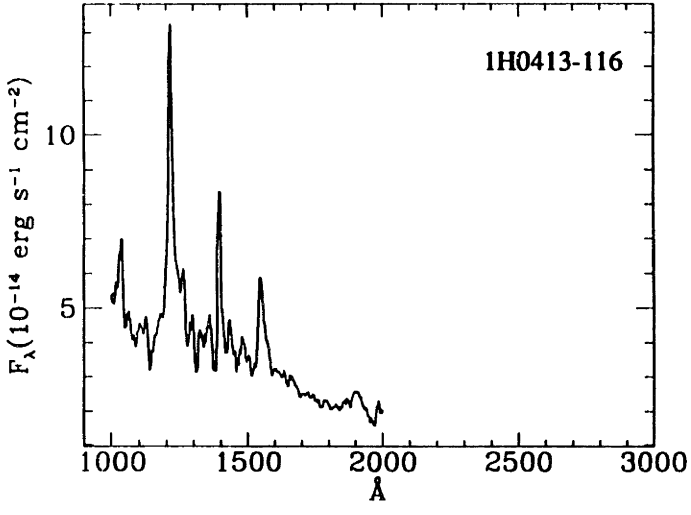
1H0413-116
$F_\lambda(10^{-14}$ erg s^{-1} cm^{-2})
5
10
1000
1500
2000
2500
3000
Å

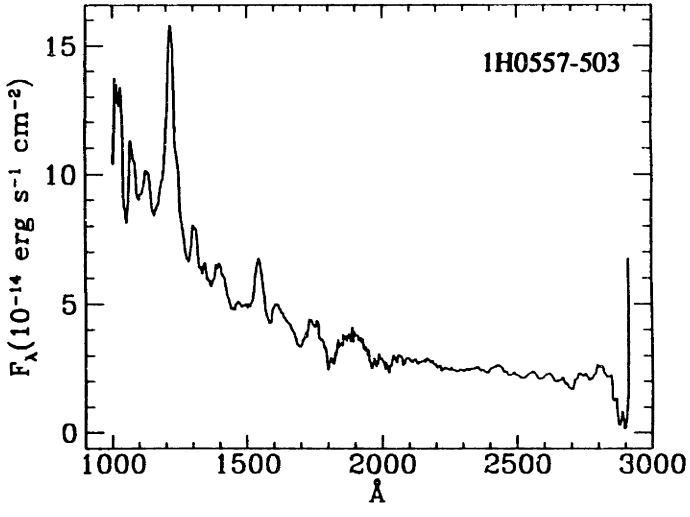
1H0557-503
$F_\lambda(10^{-14}$ erg s^{-1} cm^{-2})
0
5
10
15
1000
1500
2000
2500
3000
Å

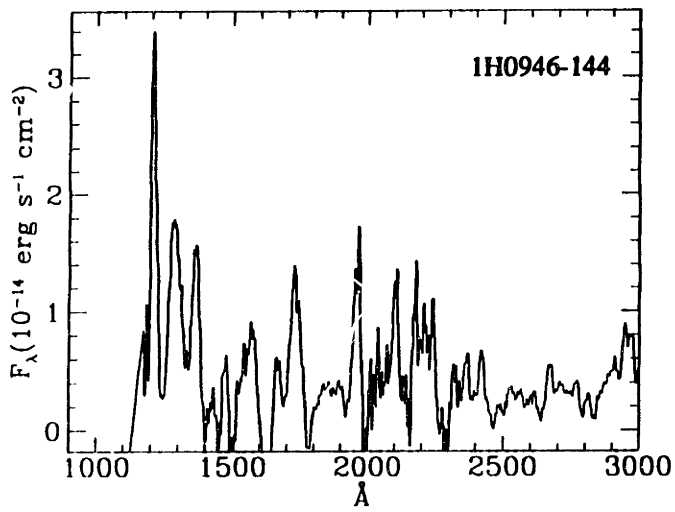
1H0946-144
$F_\lambda(10^{-14}$ erg s^{-1} cm^{-2})
0
1
2
3
1000
1500
2000
2500
3000
Å

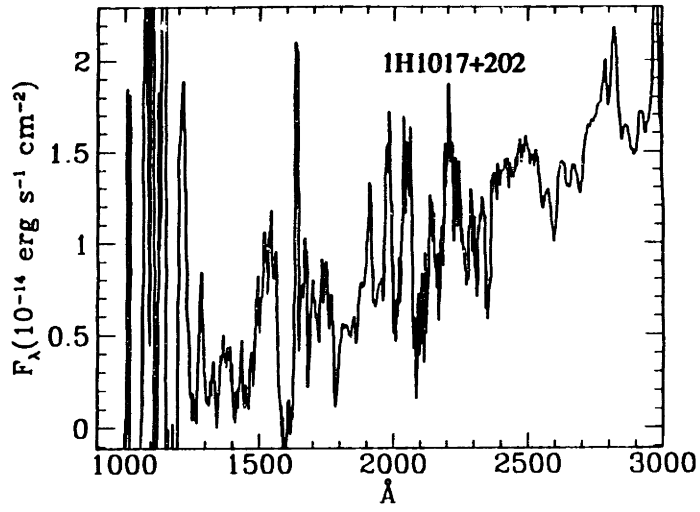
1H1017+202
$F_\lambda(10^{-14}$ erg s^{-1} cm^{-2})
0
0.5
1
1.5
2
1000
1500
2000
2500
3000
Å

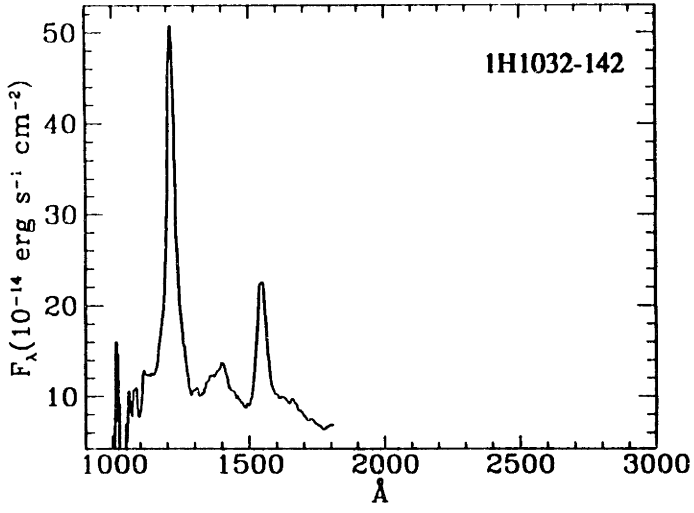
1H1032-142
$F_\lambda(10^{-14}$ erg s^{-1} cm^{-2})
10
20
30
40
50
1000
1500
2000
2500
3000
Å

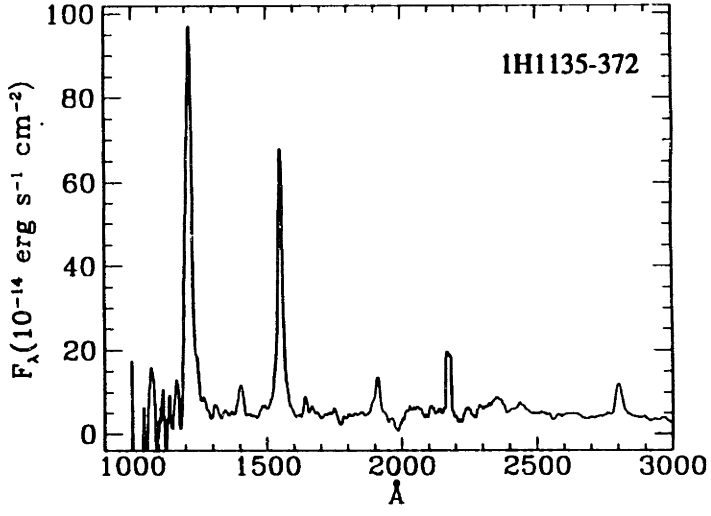
1H1135-372
$F_\lambda(10^{-14}$ erg s^{-1} cm^{-2})
0
20
40
60
80
100
1000
1500
2000
2500
3000
Å

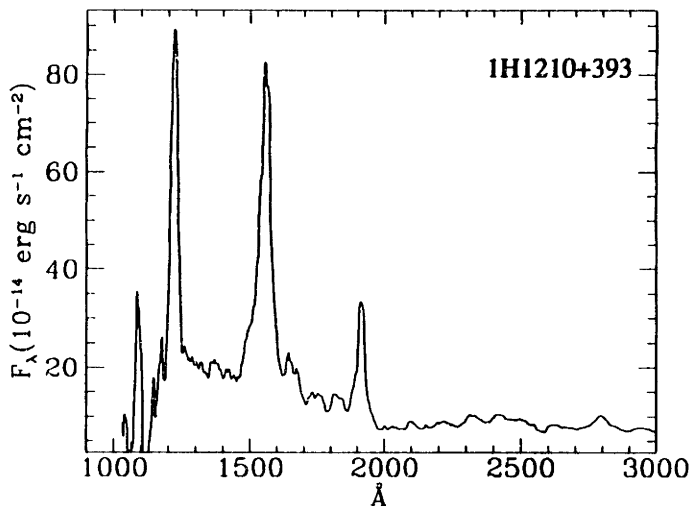
1H1210+393
$F_\lambda(10^{-14}$ erg s^{-1} cm^{-2})
Å

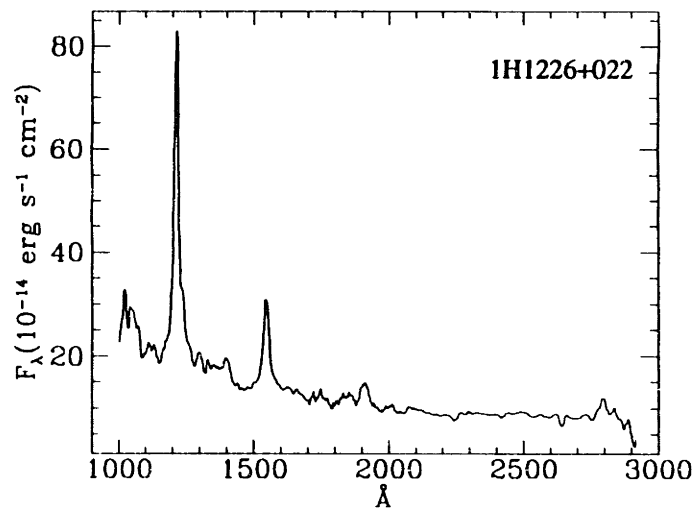
1H1226+022
$F_\lambda(10^{-14}$ erg s^{-1} cm^{-2})
Å

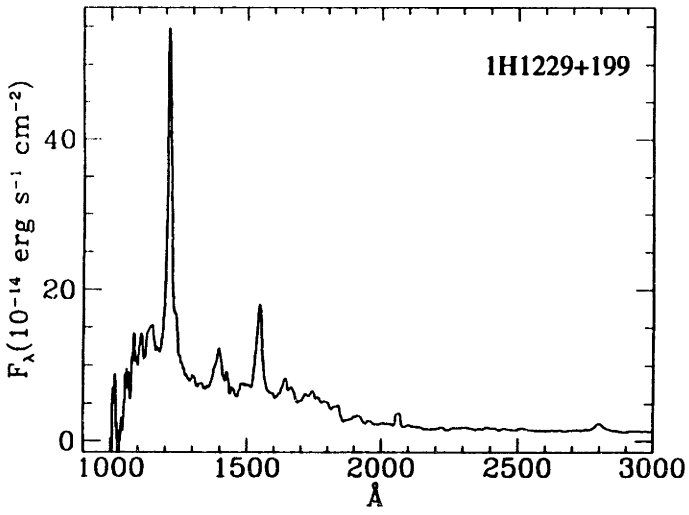
1H1229+199
$F_\lambda(10^{-14}$ erg s^{-1} cm^{-2})
Å

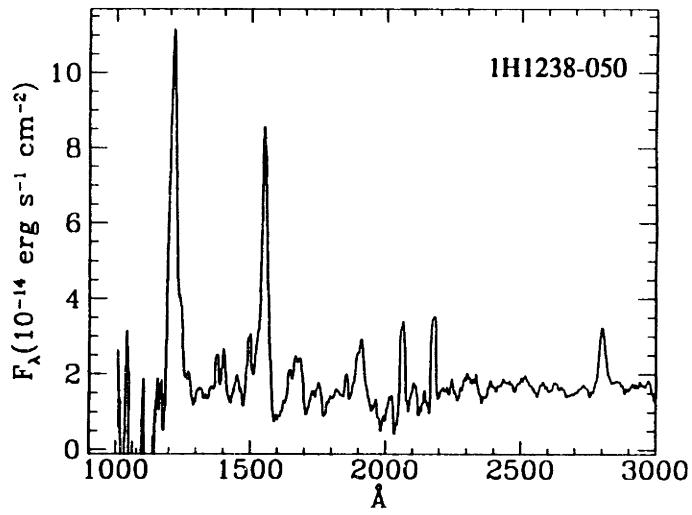
1H1238-050
$F_\lambda(10^{-14}$ erg s^{-1} cm^{-2})
Å

1H1350+696
1H1415+255
1H1420+481
1H1429+370
$F_\lambda(10^{-14}$ erg s^{-1} cm^{-2})
Å
1000
1500
2000
2500
3000

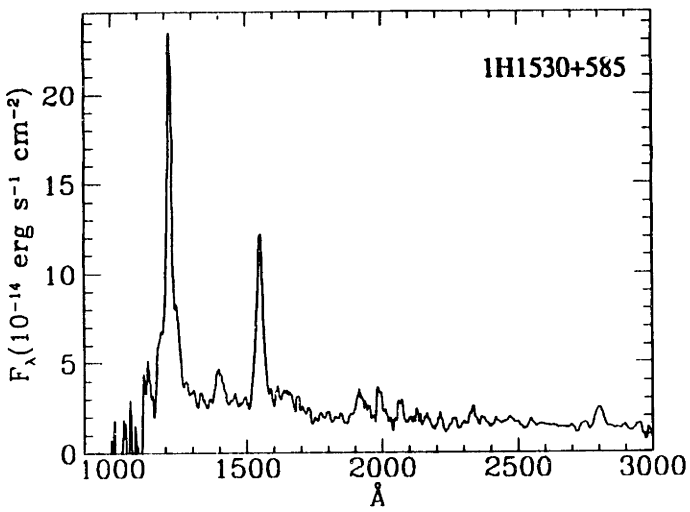
1H1530+585
$F_\lambda(10^{-14}$ erg s^{-1} cm^{-2})
0
5
10
15
20
1000
1500
2000
2500
3000
Å

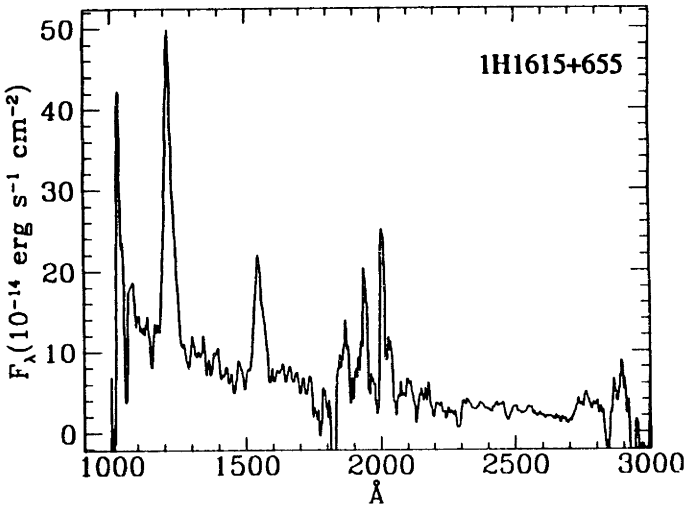
1H1615+655
$F_\lambda(10^{-14}$ erg s^{-1} cm^{-2})
0
10
20
30
40
50
1000
1500
2000
2500
3000
Å

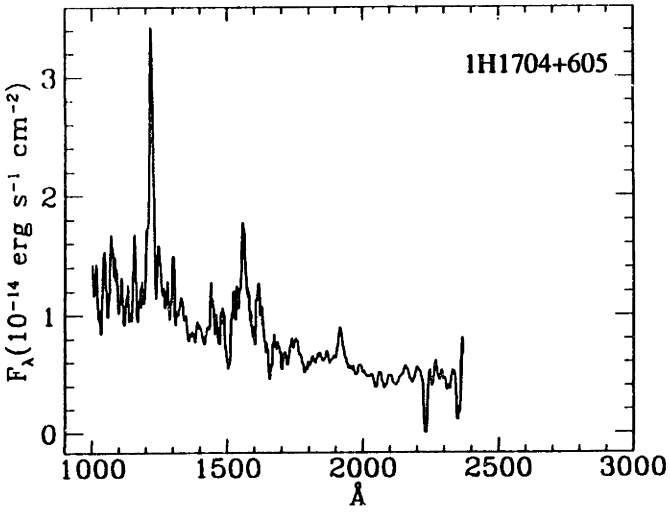
1H1704+605
$F_\lambda(10^{-14}$ erg s^{-1} cm^{-2})
0
1
2
3
1000
1500
2000
2500
3000
Å

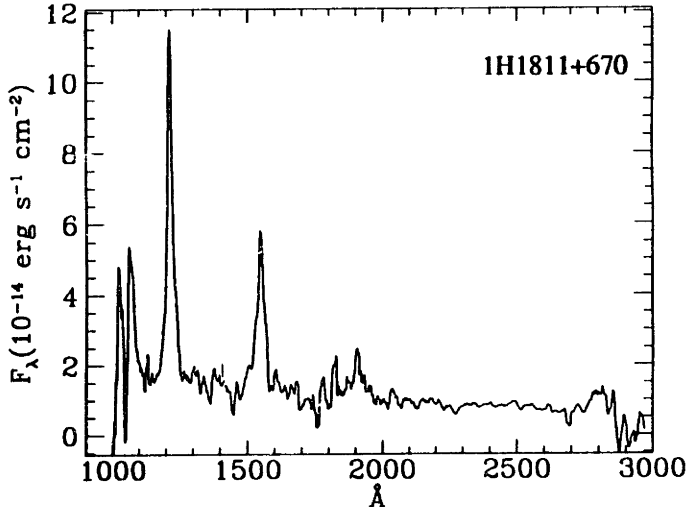
1H1811+670
$F_\lambda(10^{-14}$ erg s^{-1} cm^{-2})
0
2
4
6
8
10
12
1000
1500
2000
2500
3000
Å

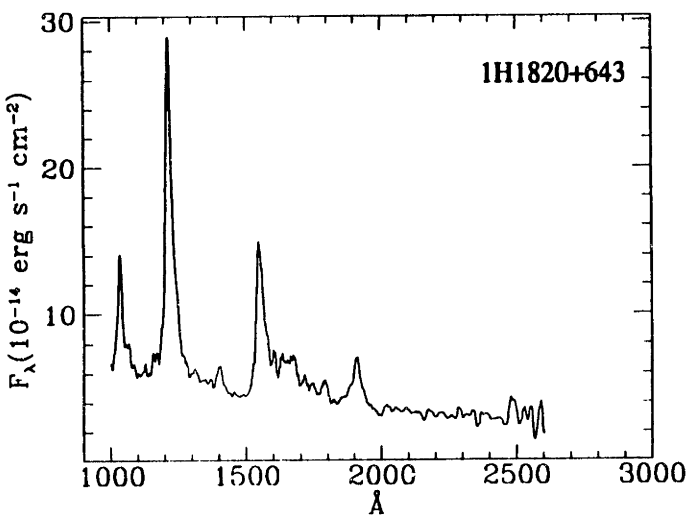
1H1820+643
$F_\lambda(10^{-14}$ erg s^{-1} cm^{-2})
Å

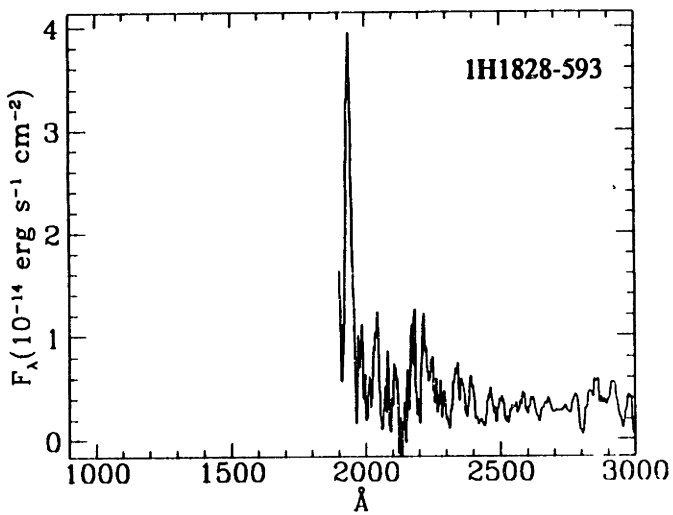
1H1828-593
$F_\lambda(10^{-14}$ erg s^{-1} cm^{-2})
Å

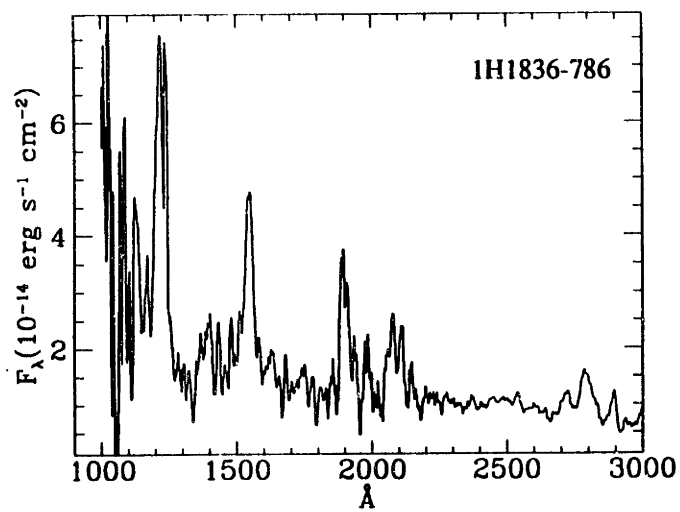
1H1836-786
$F_\lambda(10^{-14}$ erg s^{-1} cm^{-2})
Å

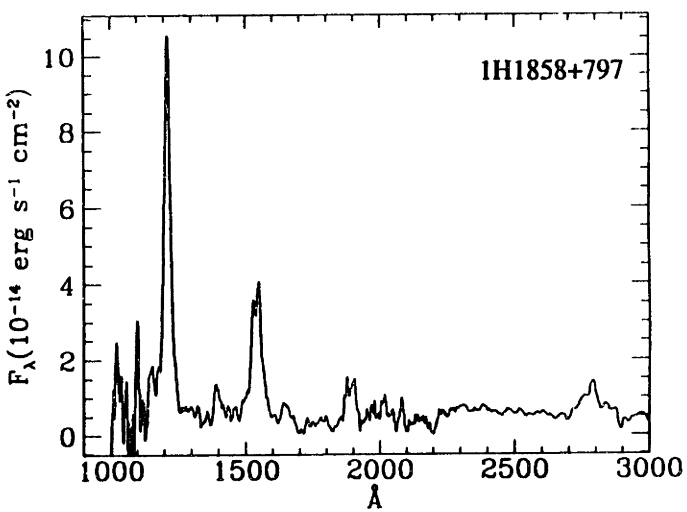
1H1858+797
$F_\lambda(10^{-14}$ erg s^{-1} cm^{-2})
Å

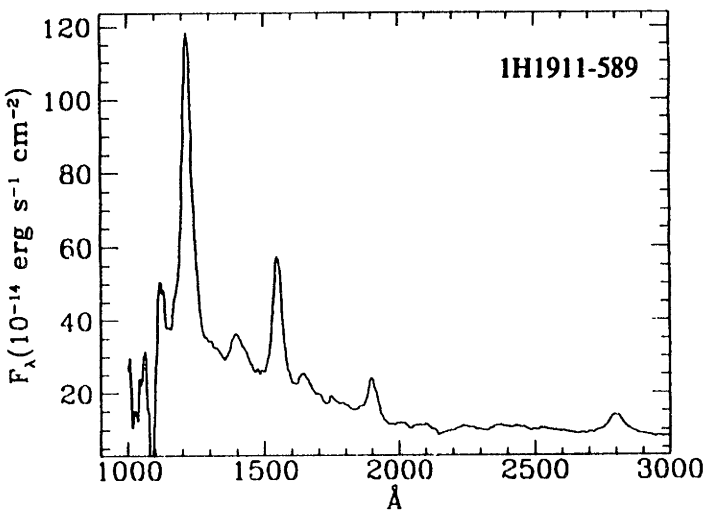
1H1911-589
$F_\lambda(10^{-14}$ erg s^{-1} cm^{-2})
Å

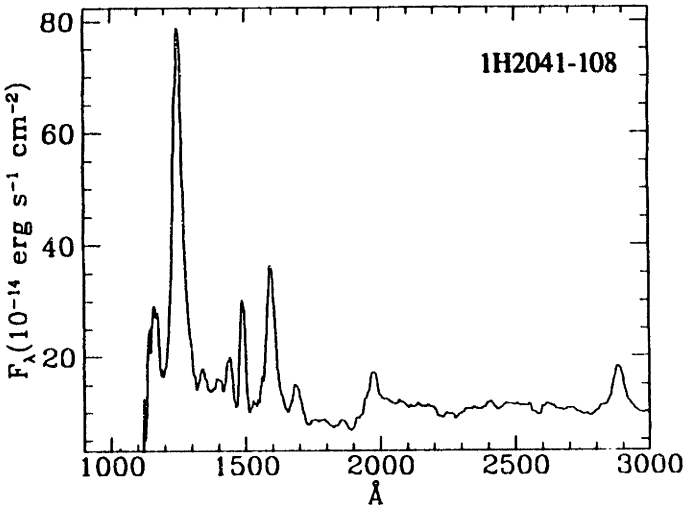
1H2041-108
$F_\lambda(10^{-14}$ erg s^{-1} cm^{-2})
Å

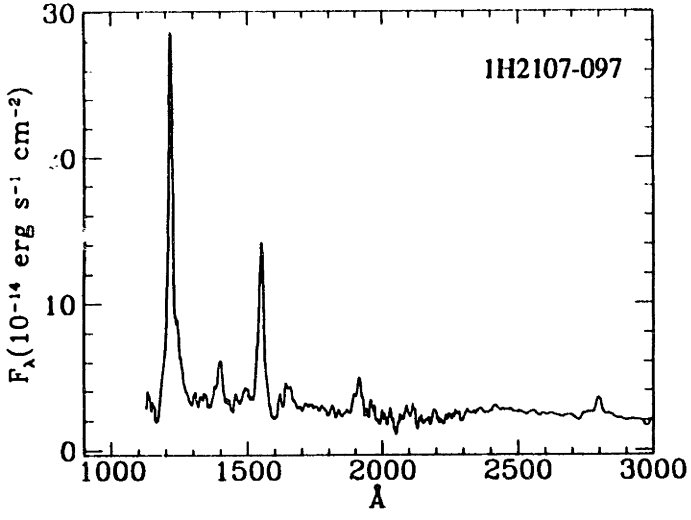
1H2107-097
$F_\lambda(10^{-14}$ erg s^{-1} cm^{-2})
Å

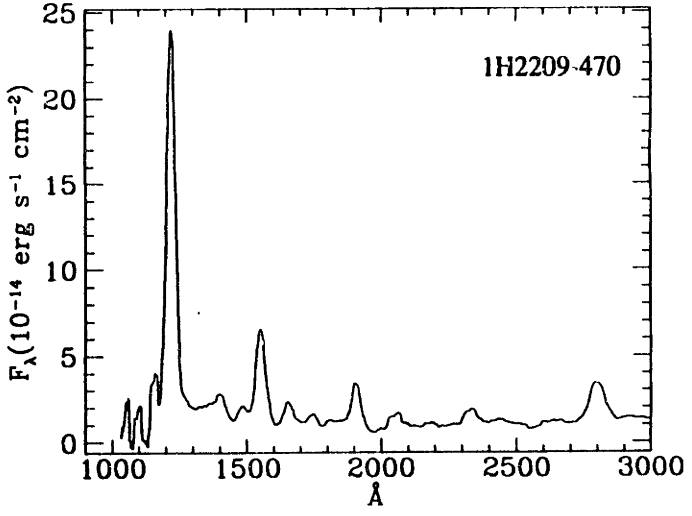
1H2209-470
$F_\lambda(10^{-14}$ erg s^{-1} cm^{-2})
Å

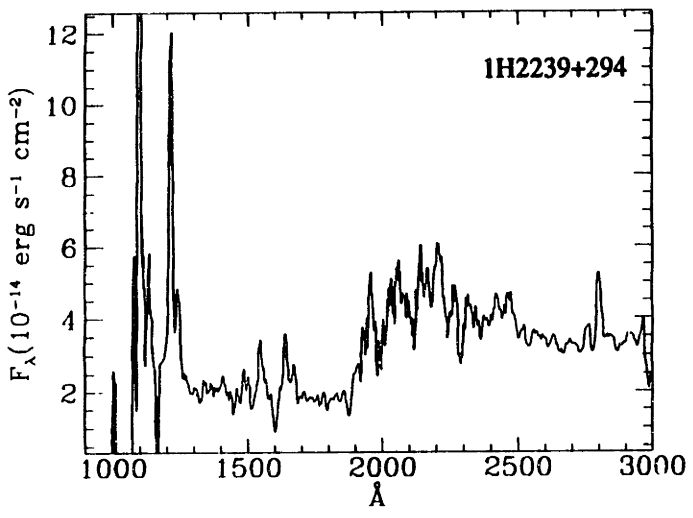
1H2239+294
$F_\lambda(10^{-14}$ erg s^{-1} cm^{-2})
Å

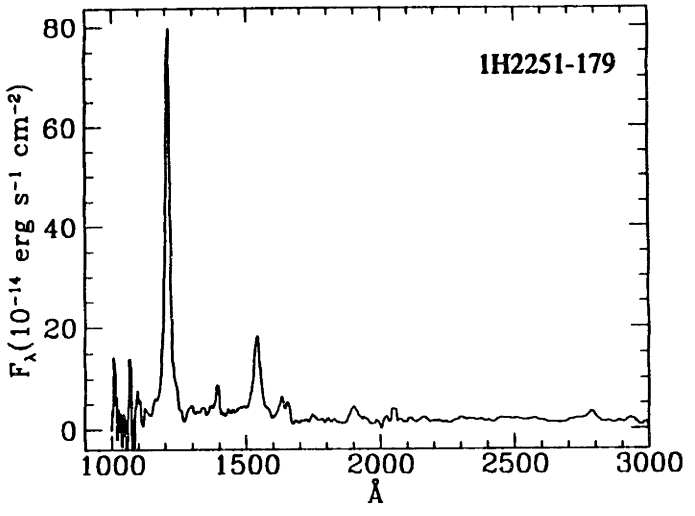
1H2251-179
$F_\lambda(10^{-14}$ erg s^{-1} cm^{-2})
Å

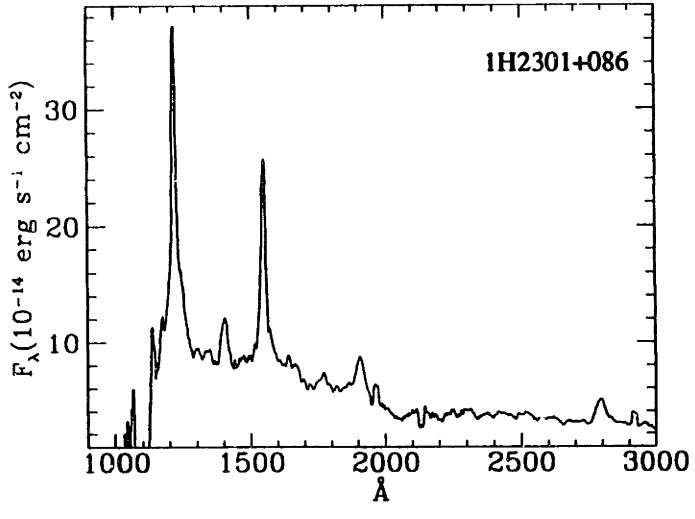
1H2301+086
$F_\lambda(10^{-14}$ erg s^{-1} cm^{-2})
Å

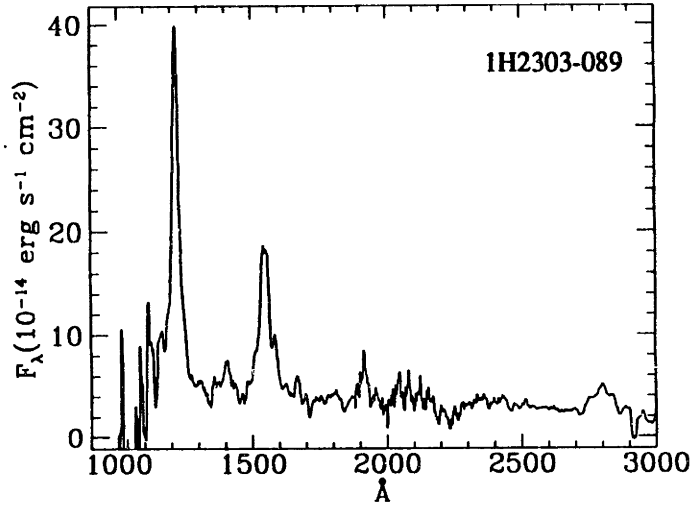
1H2303-089
$F_\lambda(10^{-14}$ erg s^{-1} cm^{-2})
Å

APPENDIX IV
OPTICAL SPECTRAL ATLAS

This appendix contains selected optical spectra of 87 LMA objects. More than one spectrum is given per object when the spectra are not simultaneous and cover different wavelength intervals. Each spectrum is labeled with the LASS name of the target object, followed by the observing run code in parenthesis. For an explanation of the observing run codes, see the key given in Chapter 2 at the end of Table 3. For those spectra where the flux unit is given as "relative units", the flux calibration is only approximate due to poor observing conditions. The relative shape of the spectrum is still accurate, however. The reduction of these spectra is described in Chapter 2, Section 3.

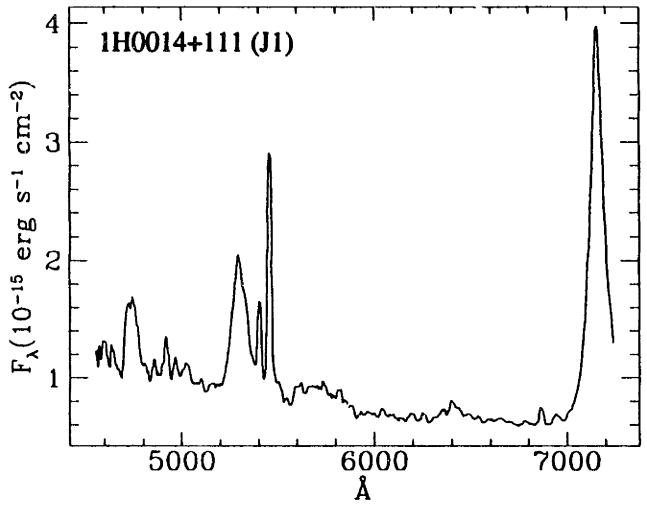
1H0014+111 (J1)
$F_\lambda(10^{-15}$ erg s^{-1} cm^{-2})
Å

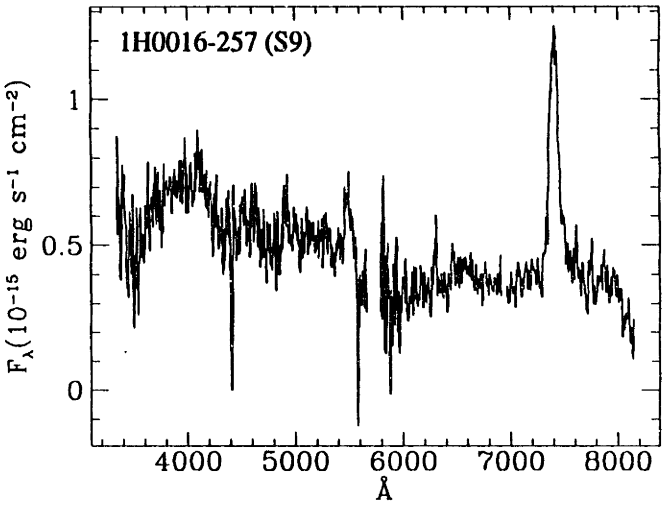
1H0016-257 (S9)
$F_\lambda(10^{-15}$ erg s^{-1} cm^{-2})
Å

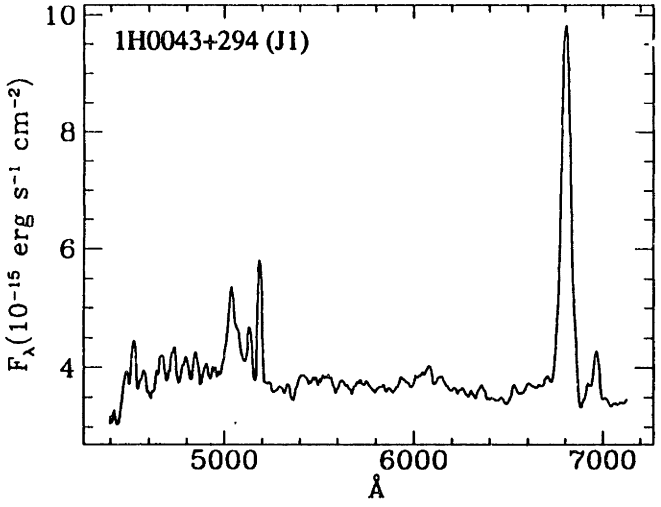
1H0043+294 (J1)
$F_\lambda(10^{-15}$ erg s^{-1} cm^{-2})
Å

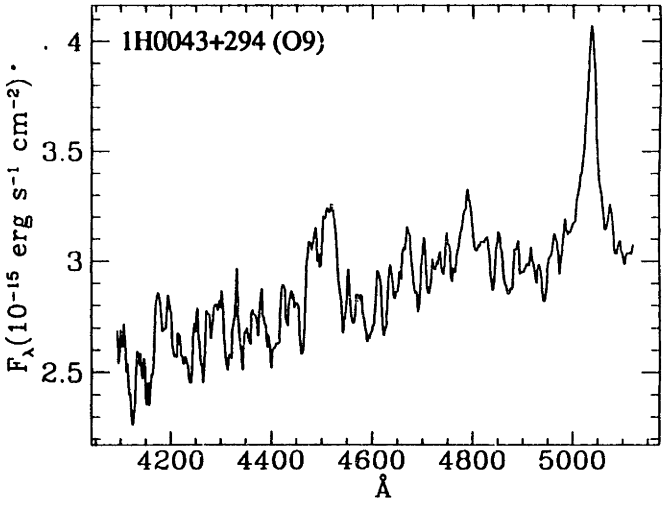
1H0043+294 (O9)
$F_\lambda(10^{-15}$ erg s^{-1} cm^{-2})
Å

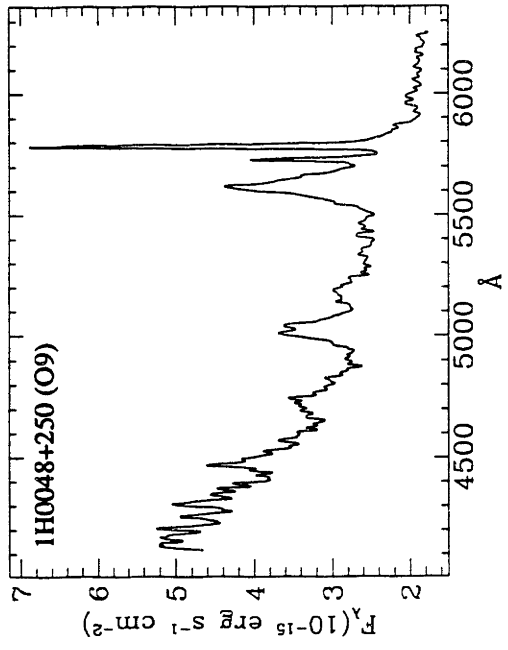
1H0048+250 (O9)
$F_\lambda(10^{-15}$ erg s^{-1} cm^{-2})
Å

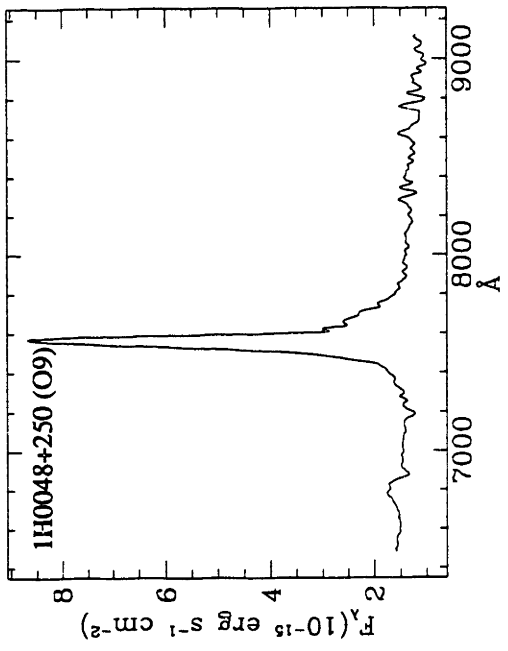
1H0048+250 (O9)
$F_\lambda(10^{-15}$ erg s^{-1} cm^{-2})
Å

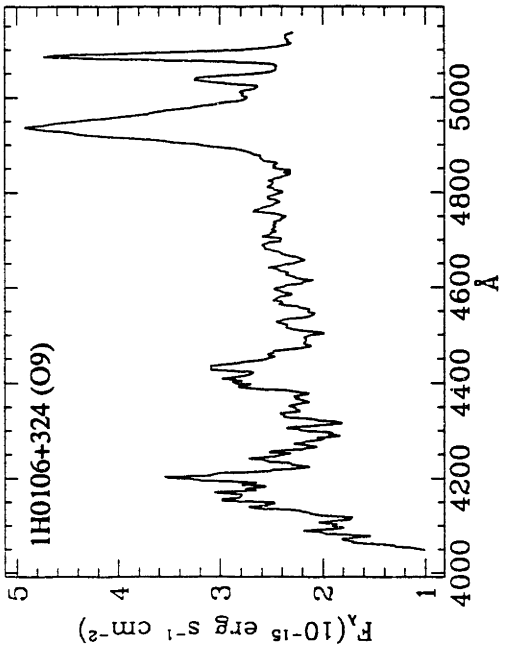
1H0106+324 (O9)
$F_\lambda(10^{-15}$ erg s^{-1} cm^{-2})
Å

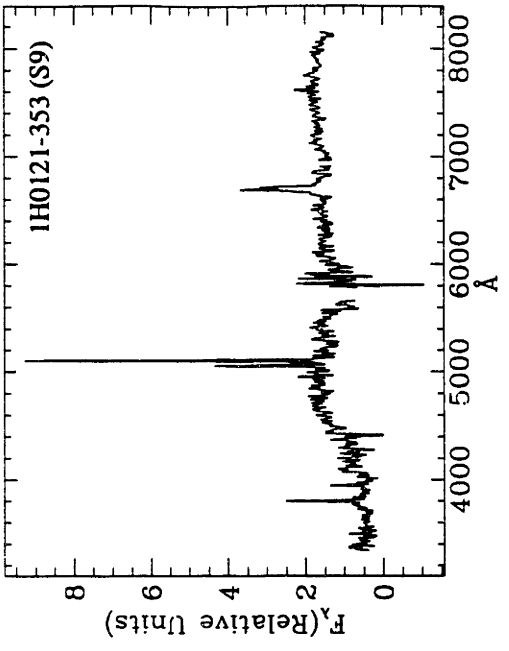
1H0121-353 (S9)
F_λ(Relative Units)
Å

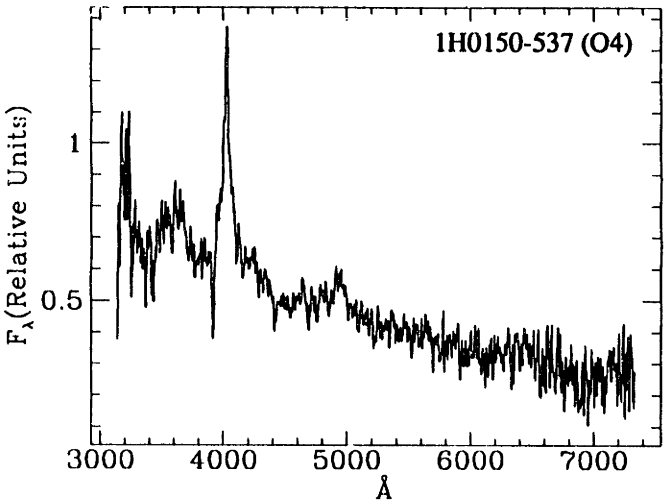
1H0150-537 (O4)
F_λ(Relative Units)
1
0.5
3000
4000
5000
6000
7000
Å

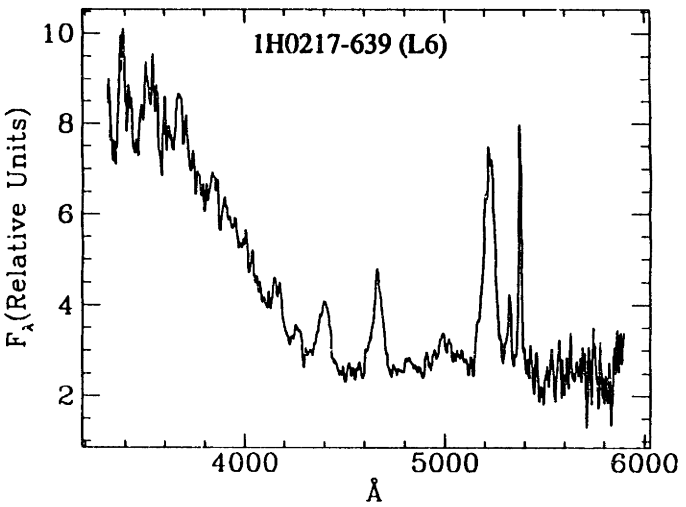
1H0217-639 (L6)
F_λ(Relative Units)
10
8
6
4
2
4000
5000
6000
Å

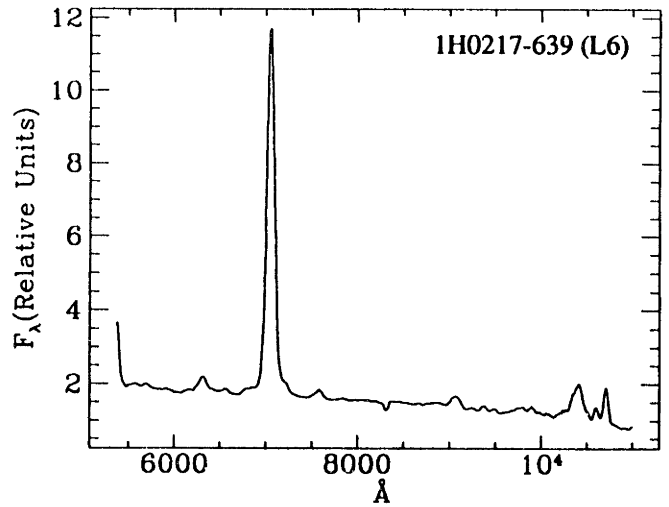
1H0217-639 (L6)
F_λ(Relative Units)
12
10
8
6
4
2
6000
8000
10^4
Å

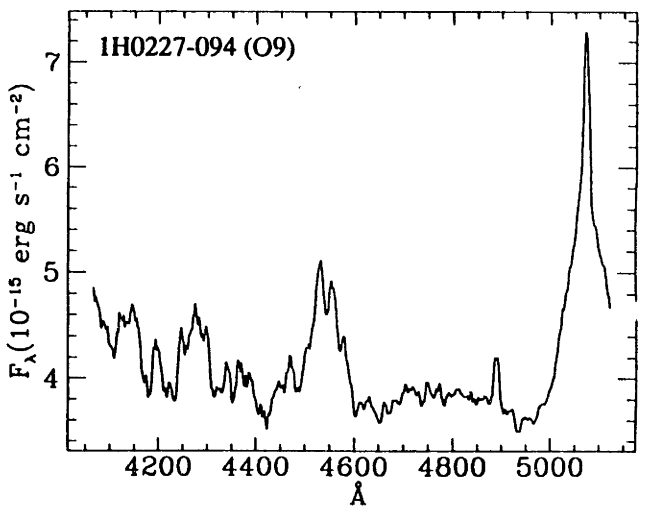
1H0227-094 (O9)
$F_\lambda(10^{-15}$ erg s^{-1} cm^{-2})
7
6
5
4
4200
4400
4600
4800
5000
Å

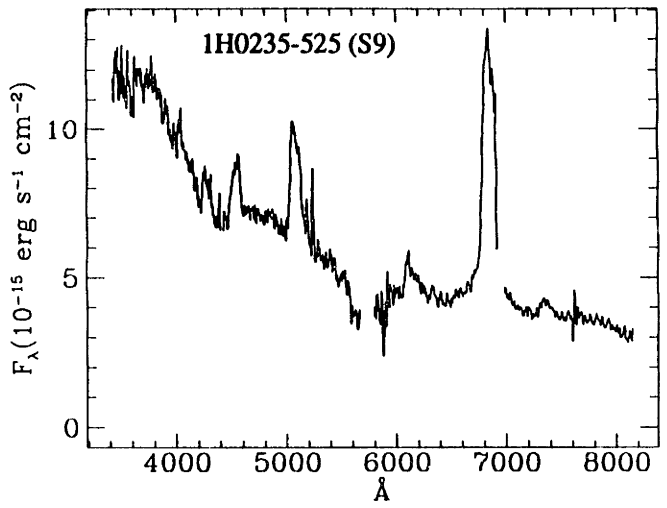
1H0235-525 (S9)
$F_\lambda(10^{-15}$ erg s^{-1} cm^{-2})
0
5
10
4000
5000
6000
7000
8000
Å

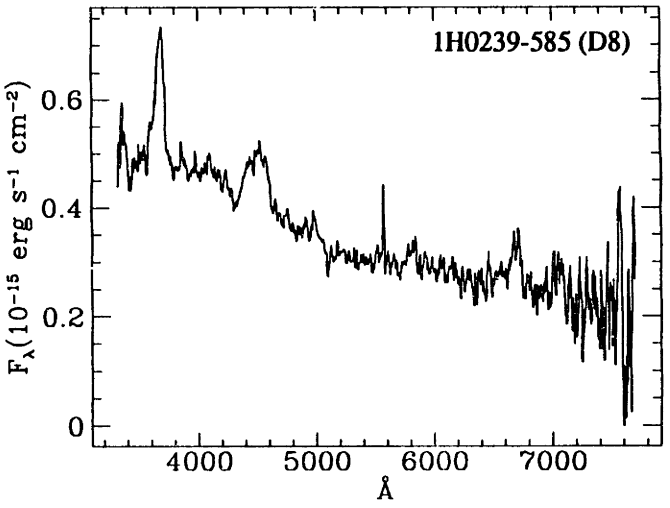
1H0239-585 (D8)
$F_\lambda(10^{-15}$ erg s^{-1} cm^{-2})
0
0.2
0.4
0.6
4000
5000
6000
7000
Å

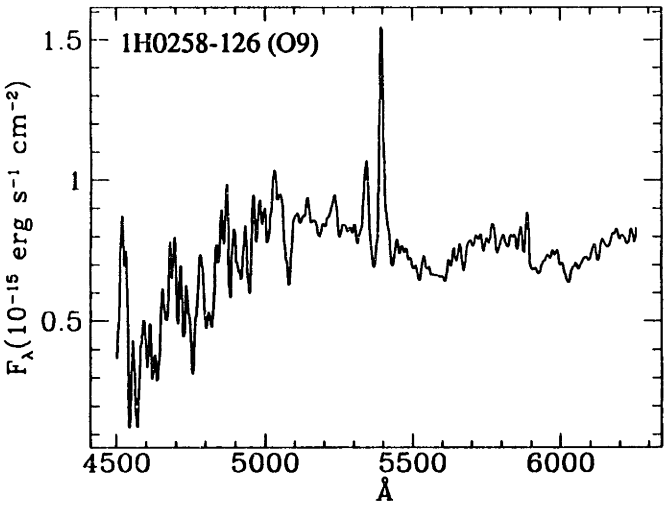
1H0258-126 (O9)
$F_\lambda(10^{-15}$ erg s^{-1} cm^{-2})
0.5
1
1.5
4500
5000
5500
6000
Å

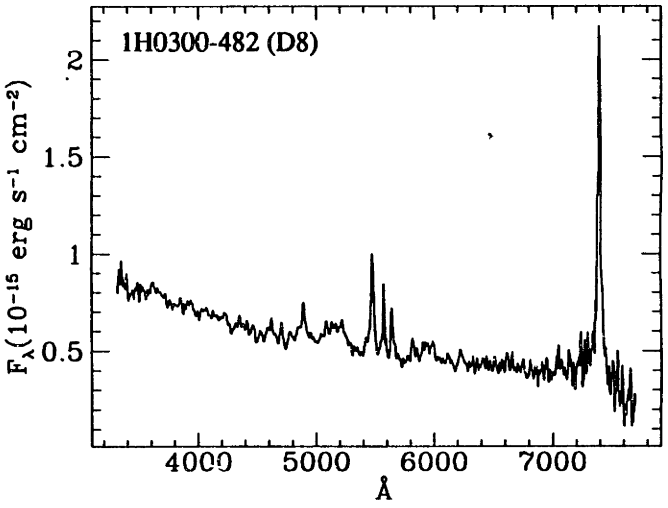
1H0300-482 (D8)
$F_\lambda(10^{-15}$ erg s^{-1} cm^{-2})
0.5
1
1.5
2
4000
5000
6000
7000
Å

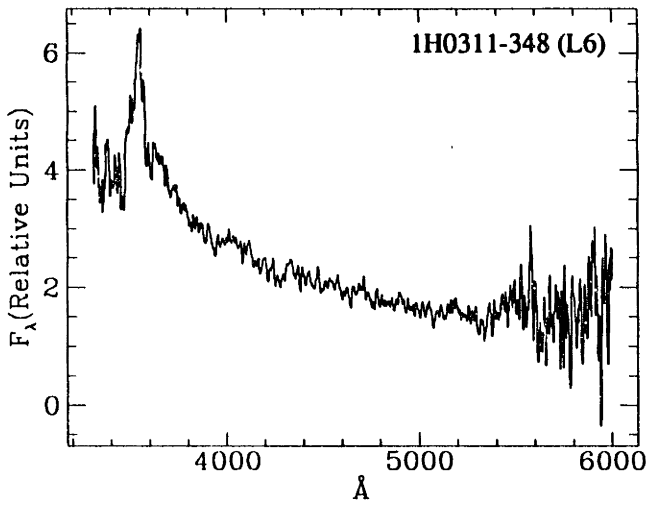
1H0311-348 (L6)
F_λ(Relative Units)
Å

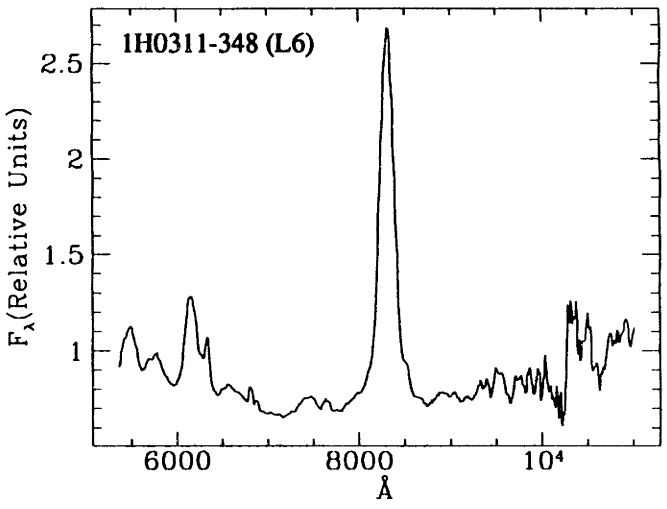
1H0311-348 (L6)
F_λ(Relative Units)
Å

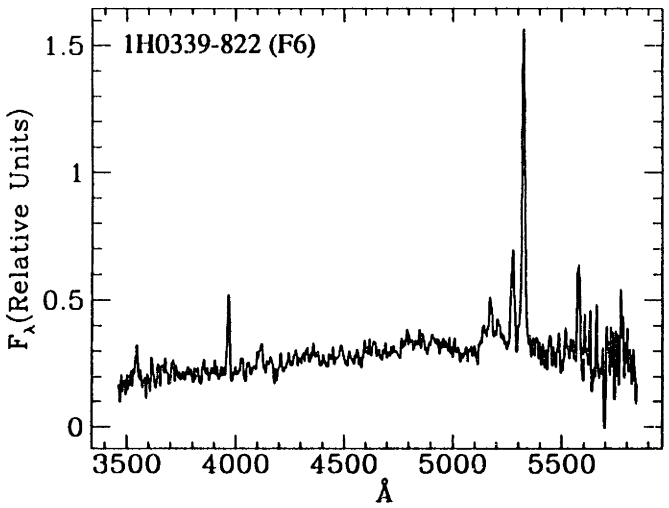
1H0339-822 (F6)
F_λ(Relative Units)
Å

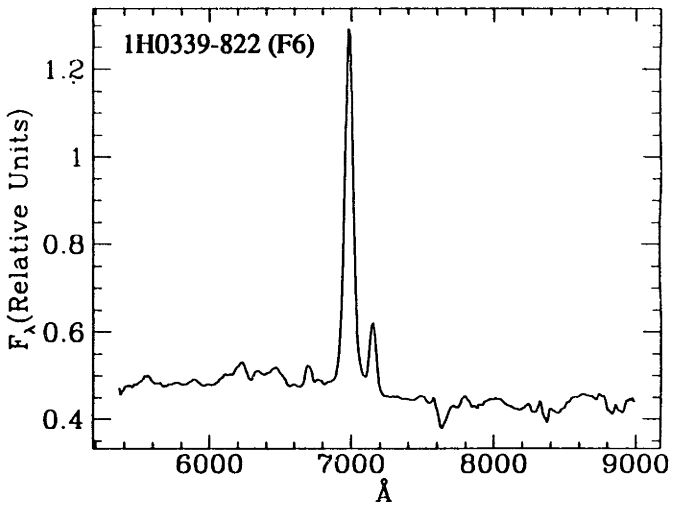
1H0339-822 (F6)
F_λ(Relative Units)
Å

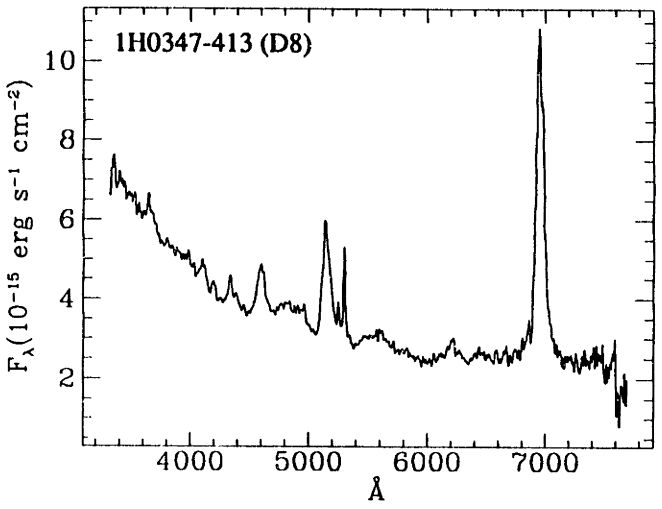
1H0347-413 (D8)
$F_\lambda(10^{-15}$ erg s^{-1} cm^{-2})
Å

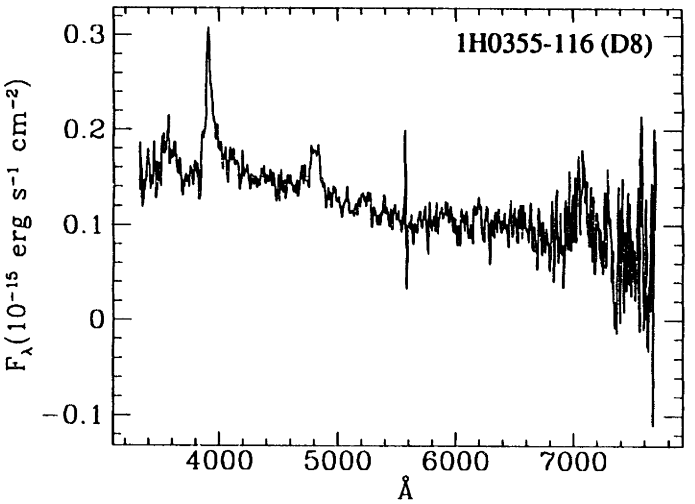
1H0355-116 (D8)
$F_\lambda(10^{-15}$ erg s^{-1} cm^{-2})
Å

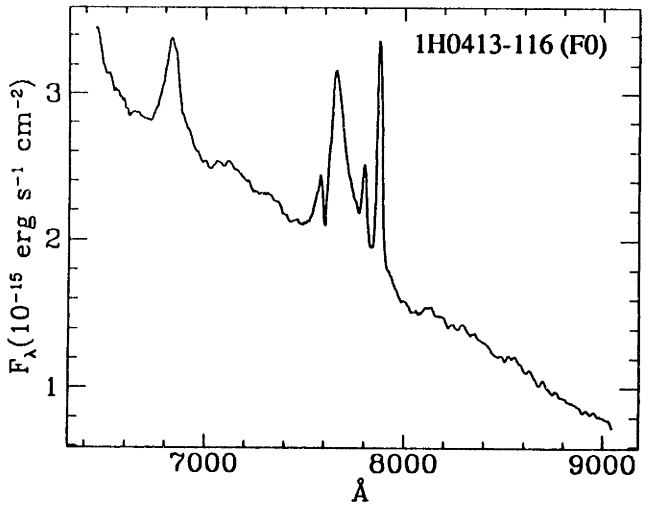
1H0413-116 (F0)
$F_\lambda(10^{-15}$ erg s^{-1} cm^{-2})
Å

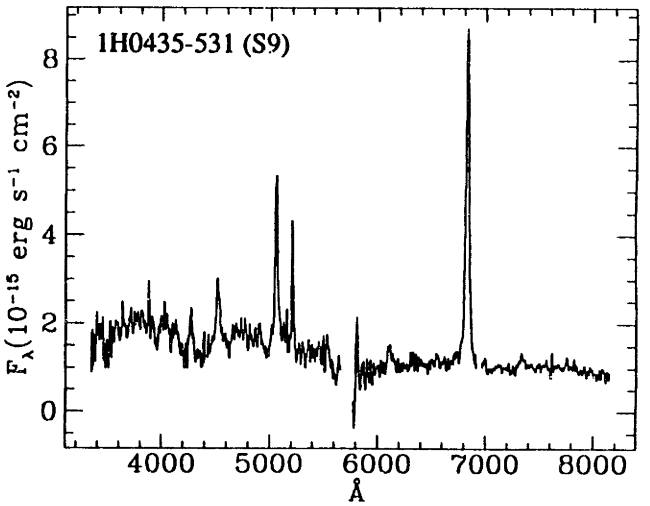
1H0435-531 (S9)
$F_\lambda(10^{-15}$ erg s^{-1} cm^{-2})
Å

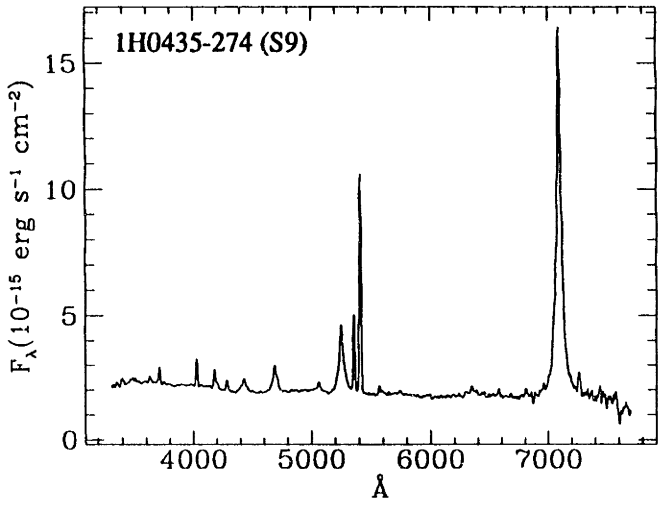
1H0435-274 (S9)
$F_\lambda(10^{-15}$ erg s^{-1} cm^{-2})
Å

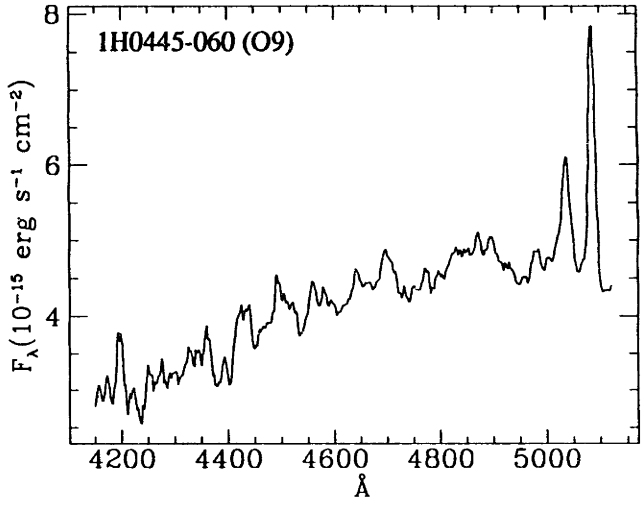
1H0445-060 (O9)
$F_\lambda(10^{-15}$ erg s^{-1} cm^{-2})
Å

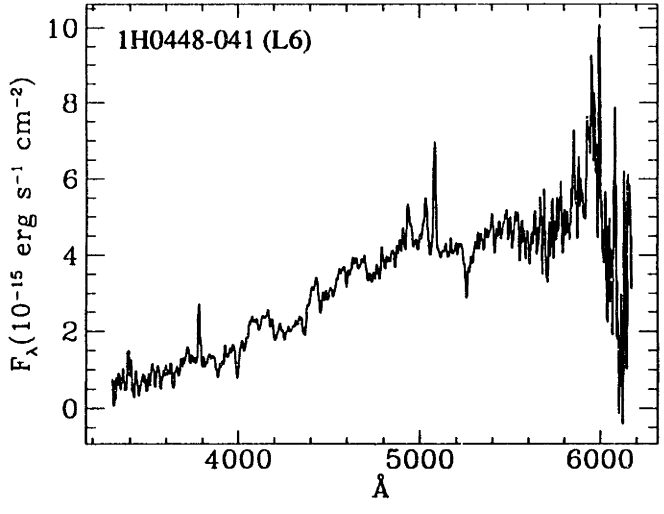
1H0448-041 (L6)
$F_\lambda(10^{-15}$ erg s^{-1} cm^{-2})
Å

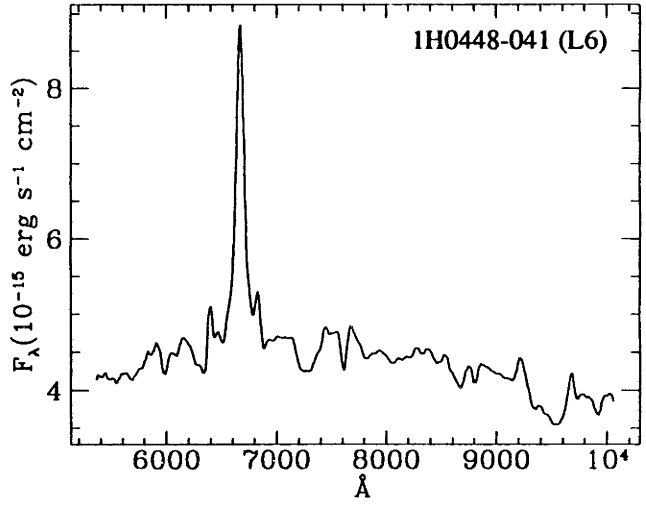
1H0448-041 (L6)
$F_\lambda(10^{-15}$ erg s^{-1} cm^{-2})
Å

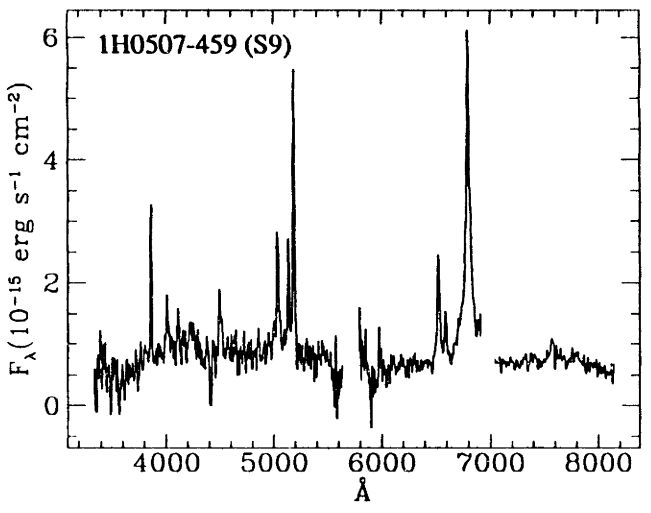
1H0507-459 (S9)
$F_\lambda(10^{-15}$ erg s^{-1} cm^{-2})
Å

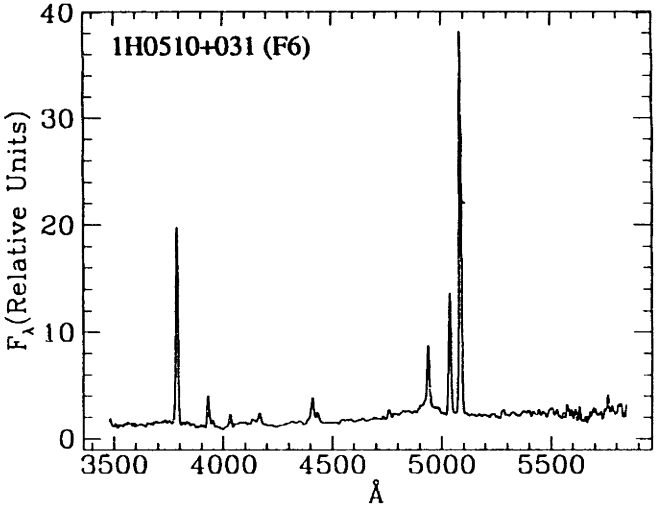
1H0510+031 (F6)
F_λ(Relative Units)
Å

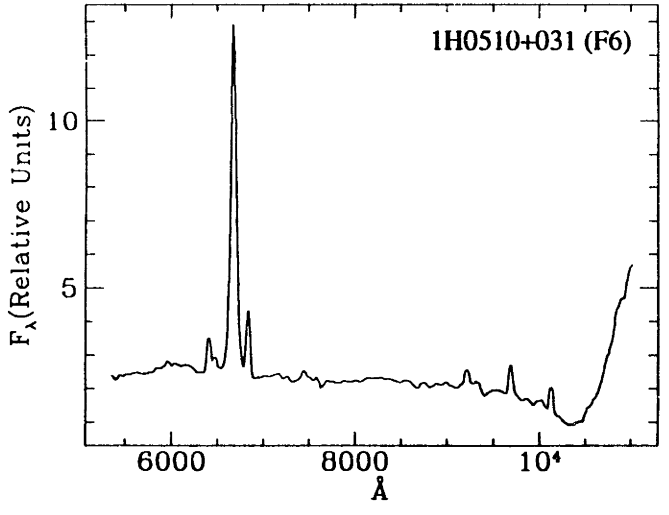
1H0510+031 (F6)
F_λ(Relative Units)
Å

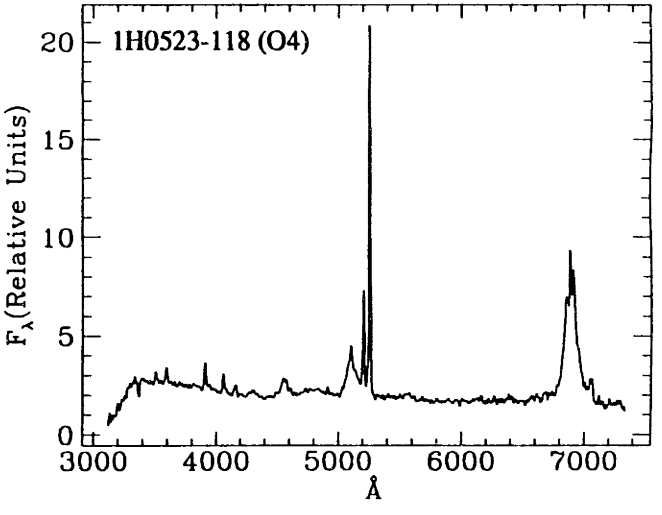
1H0523-118 (O4)
F_λ(Relative Units)
Å

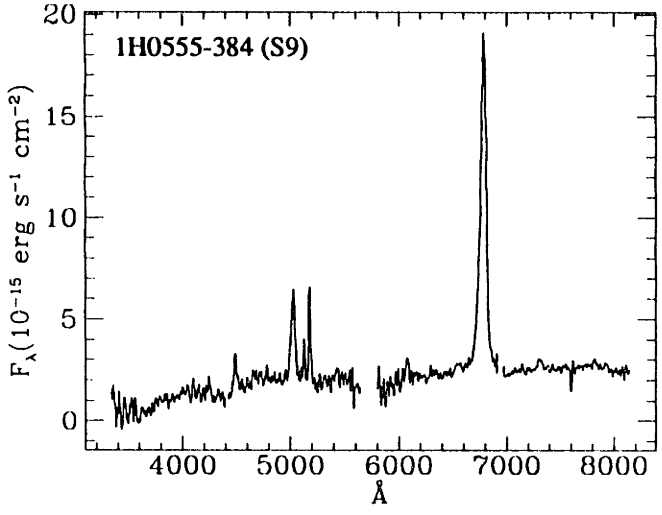
1H0555-384 (S9)
$F_\lambda(10^{-15}$ erg s^{-1} cm^{-2})
Å

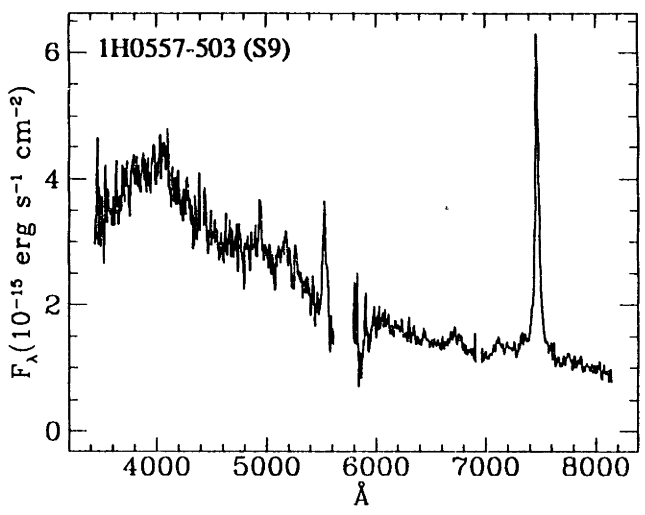
1H0557-503 (S9)
$F_\lambda(10^{-15}$ erg s^{-1} cm^{-2})
Å

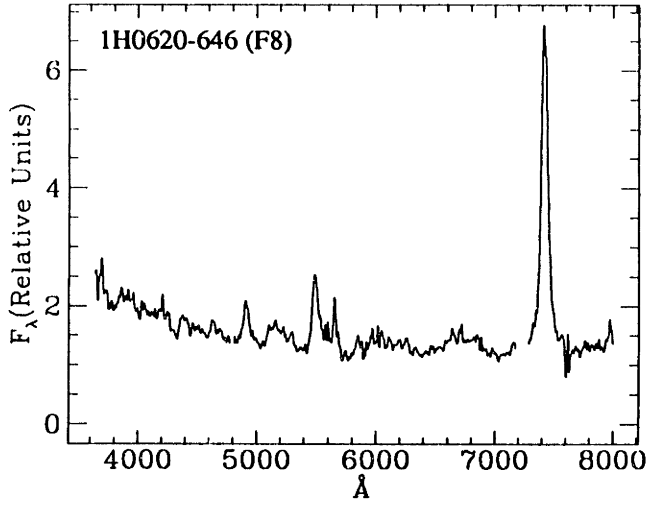
1H0620-646 (F8)
F_λ(Relative Units)
Å

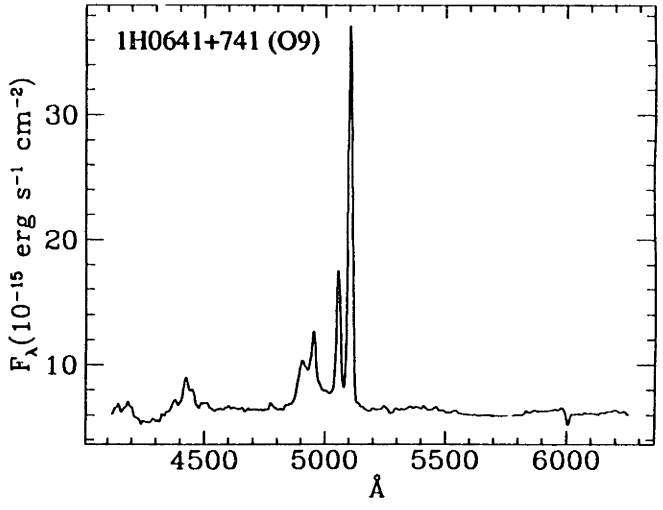
1H0641+741 (O9)
$F_\lambda(10^{-15}$ erg s^{-1} cm^{-2})
Å

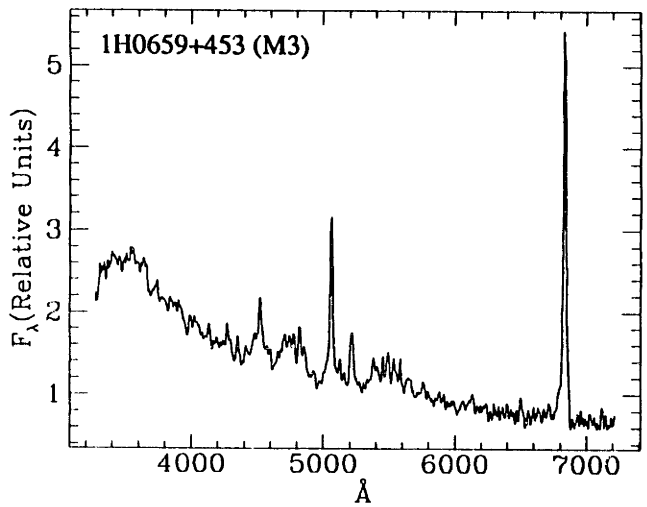
1H0659+453 (M3)
F_λ(Relative Units)
Å

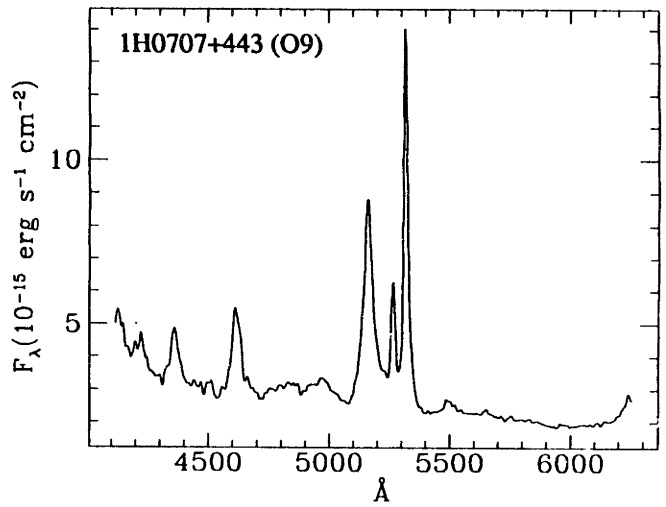
1H0707+443 (O9)
$F_\lambda(10^{-15}$ erg s^{-1} cm^{-2})
Å

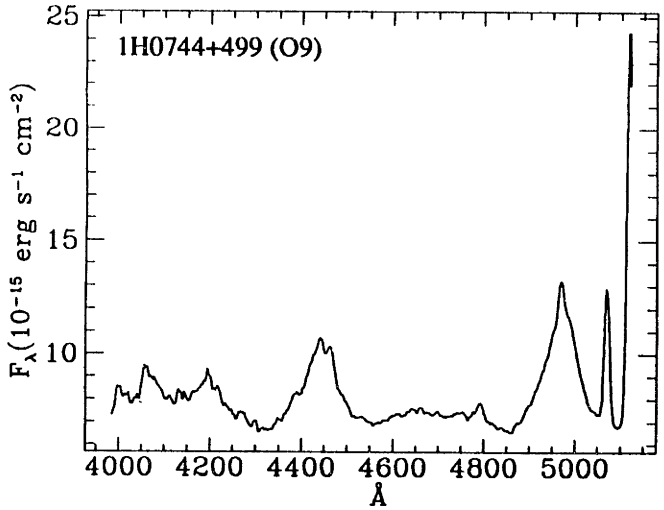
1H0744+499 (O9)
$F_\lambda(10^{-15}$ erg s^{-1} cm^{-2})
Å

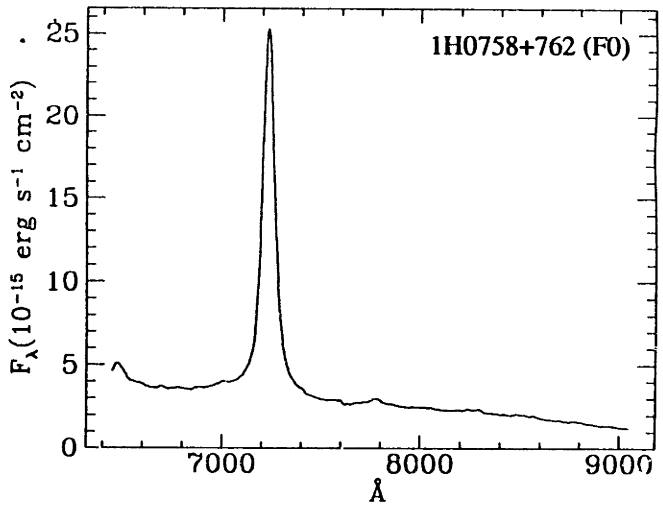
1H0758+762 (F0)
$F_\lambda(10^{-15}$ erg s^{-1} cm^{-2})
Å

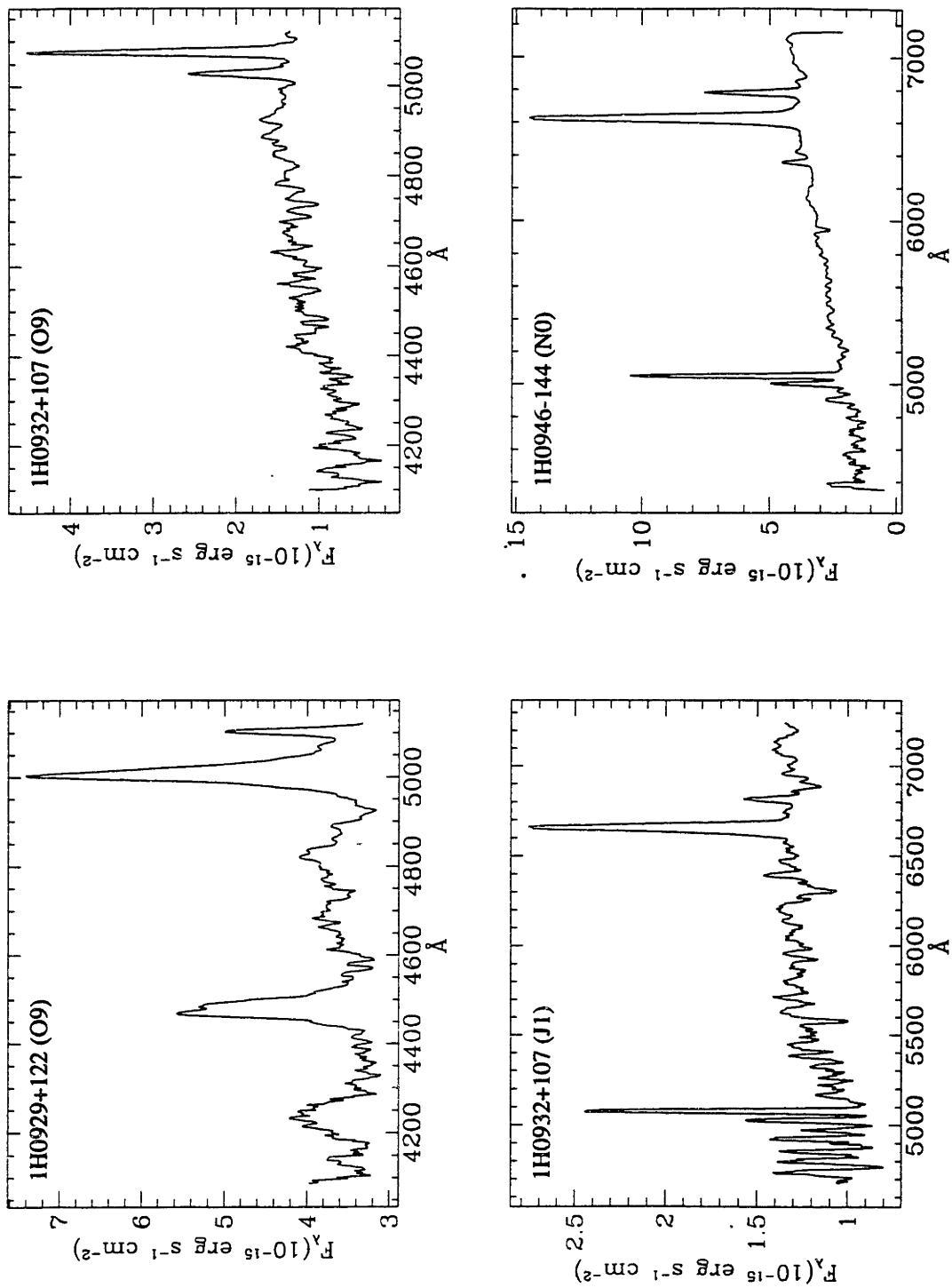
1H0932+107 (O9)
1H0946-144 (N0)
1H0929+122 (O9)
1H0932+107 (J1)
Å

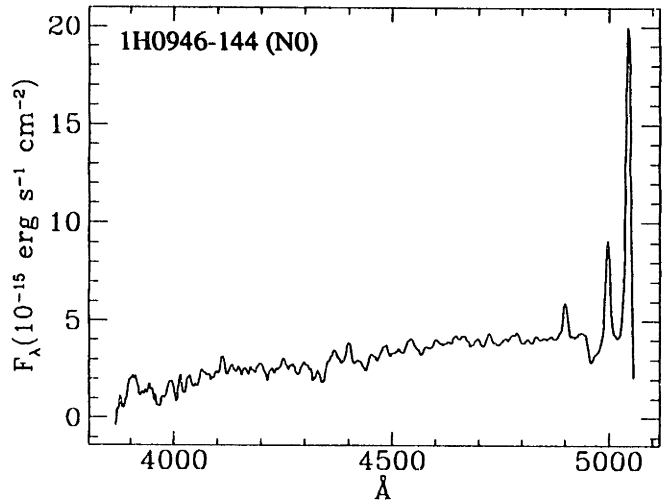
1H0946-144 (N0)
$F_\lambda(10^{-15}$ erg s^{-1} cm^{-2})
Å

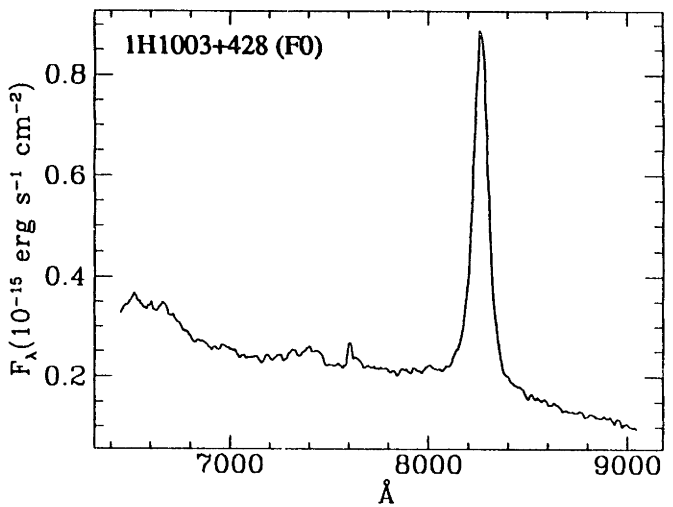
1H1003+428 (F0)
$F_\lambda(10^{-15}$ erg s^{-1} cm^{-2})
Å

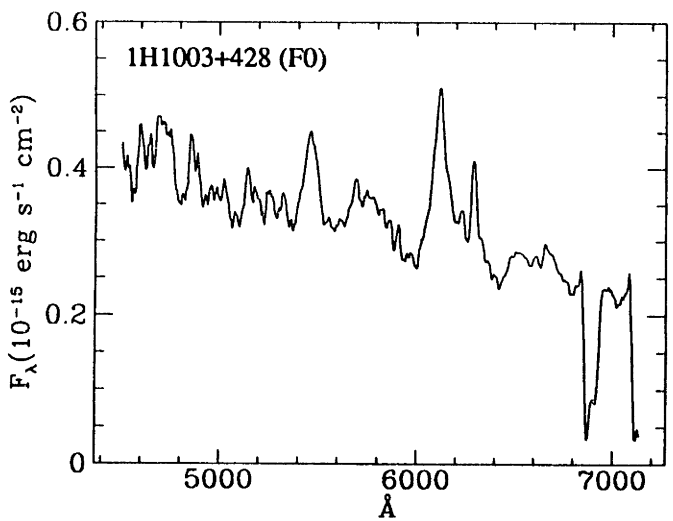
1H1003+428 (F0)
$F_\lambda(10^{-15}$ erg s^{-1} cm^{-2})
Å

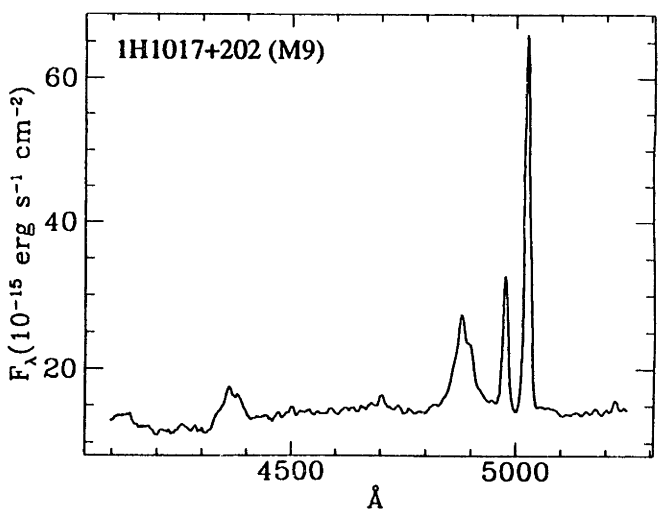
1H1017+202 (M9)
$F_\lambda(10^{-15}$ erg s^{-1} cm^{-2})
Å

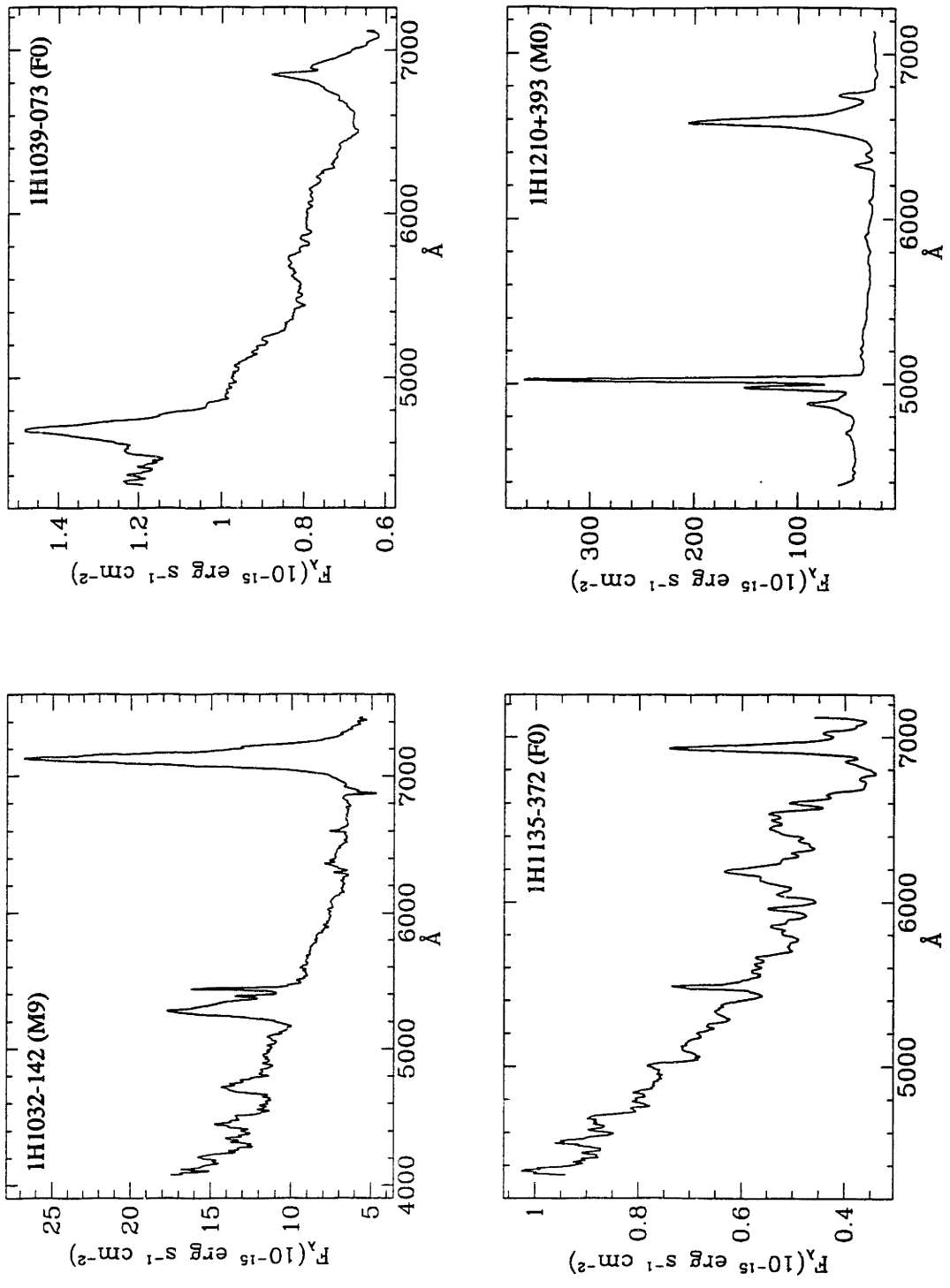
1H1039-073 (F0)
1H1210+393 (M0)
1H1032-142 (M9)
1H1135-372 (F0)
$F_\lambda(10^{-15}$ erg s^{-1} cm^{-2})
Å

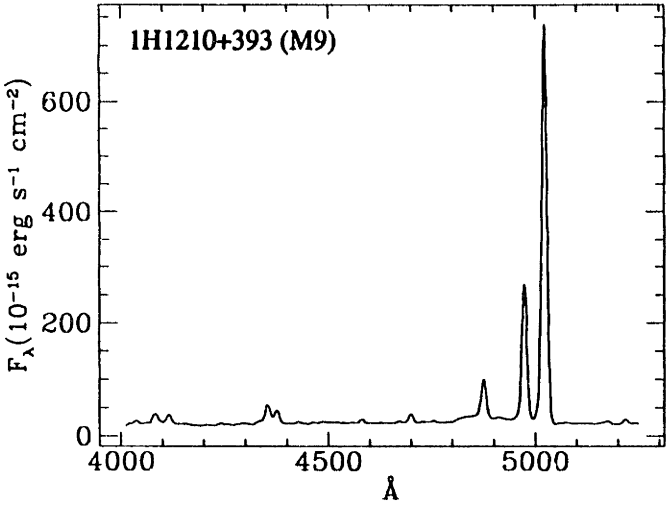
1H1210+393 (M9)
$F_\lambda(10^{-15}$ erg s^{-1} cm^{-2})
0
200
400
600
4000
4500
5000
Å

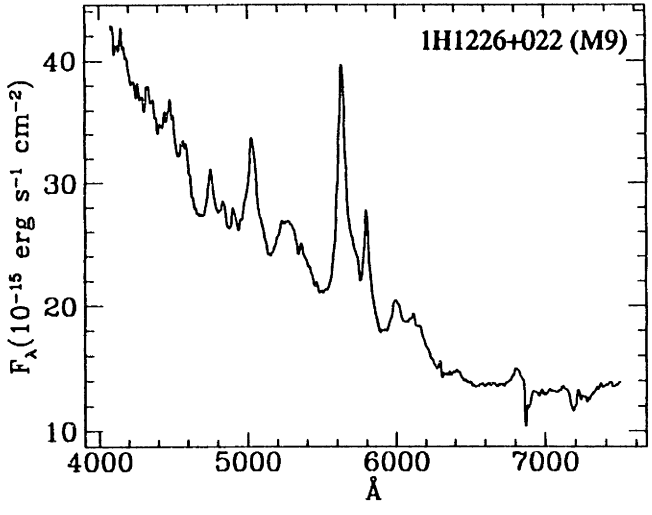
1H1226+022 (M9)
$F_\lambda(10^{-15}$ erg s^{-1} cm^{-2})
10
20
30
40
4000
5000
6000
7000
Å

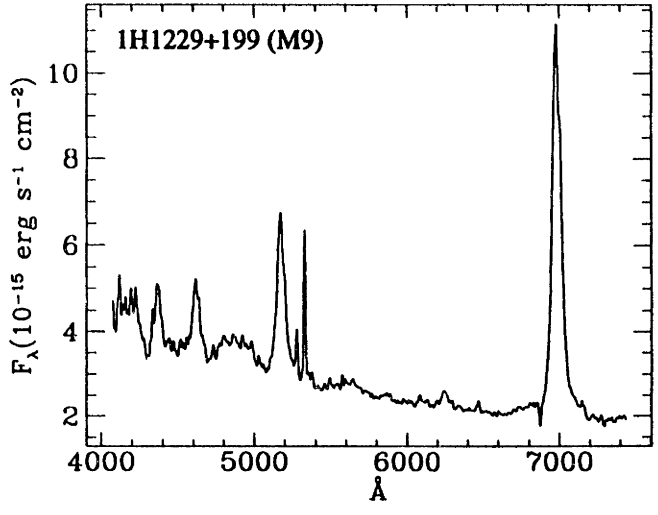
1H1229+199 (M9)
$F_\lambda(10^{-15}$ erg s^{-1} cm^{-2})
2
4
6
8
10
4000
5000
6000
7000
Å

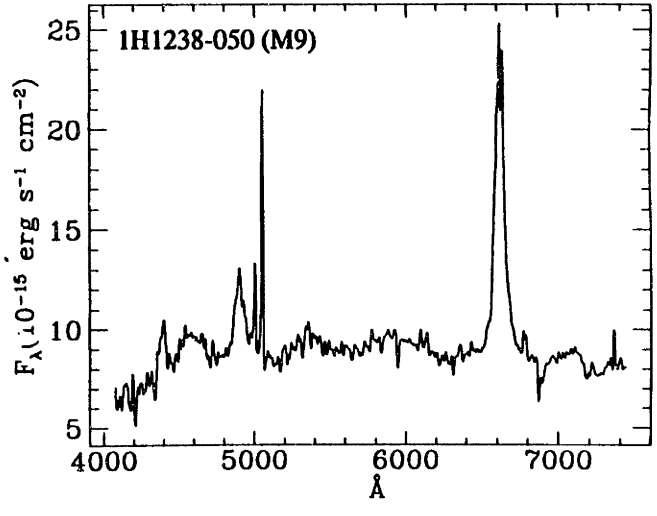
1H1238-050 (M9)
$F_\lambda(10^{-15}$ erg s^{-1} cm^{-2})
5
10
15
20
25
4000
5000
6000
7000
Å

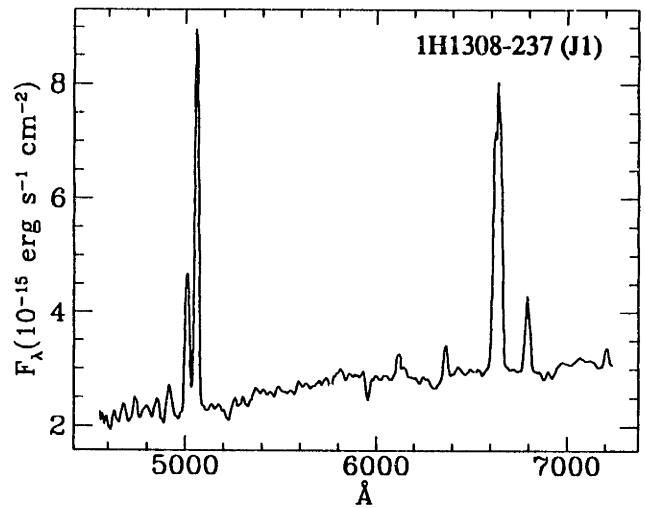
1H1308-237 (J1)
$F_\lambda(10^{-15}$ erg s^{-1} cm^{-2})
Å

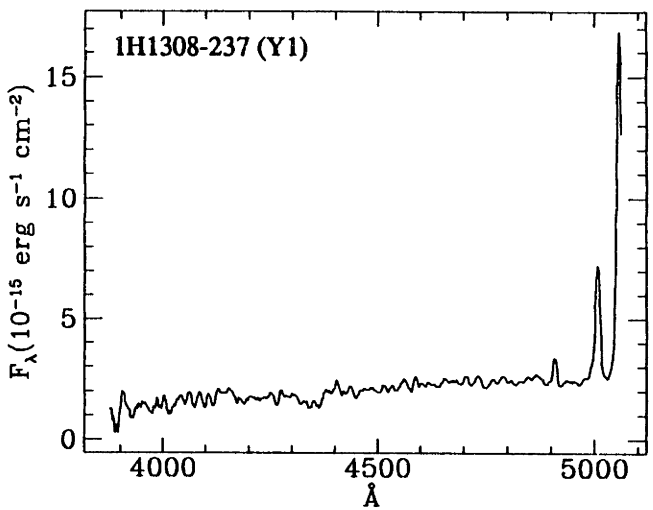
1H1308-237 (Y1)
$F_\lambda(10^{-15}$ erg s^{-1} cm^{-2})
Å

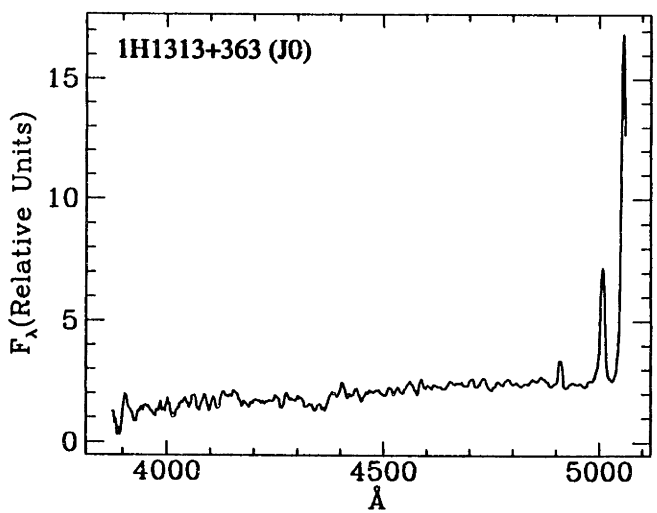
1H1313+363 (J0)
F_λ(Relative Units)
Å

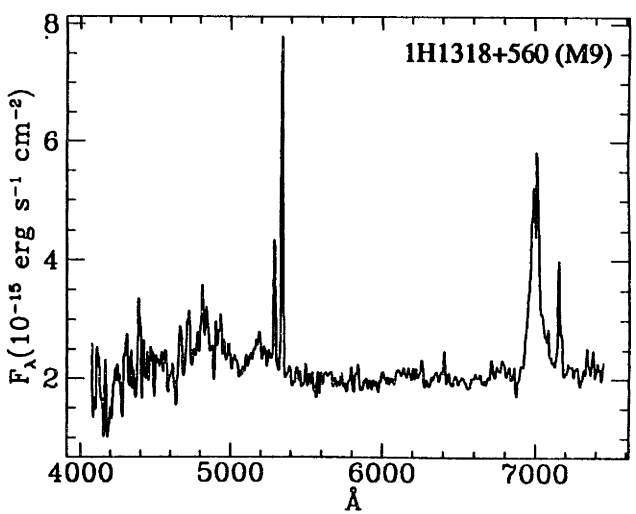
1H1318+560 (M9)
$F_\lambda(10^{-15}$ erg s^{-1} cm^{-2})
Å

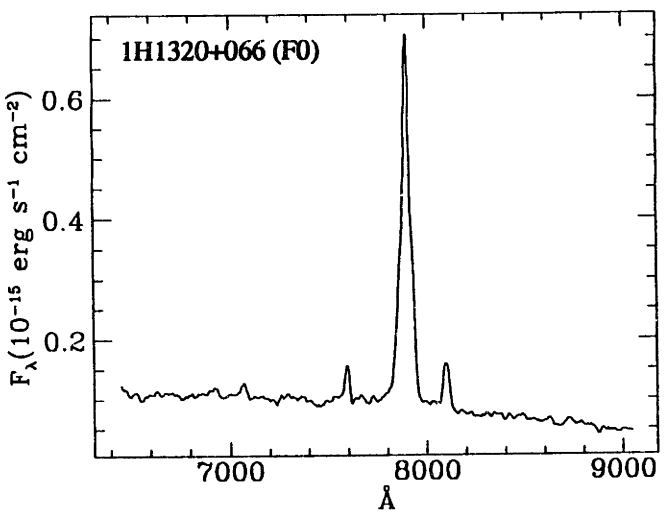
1H1320+066 (F0)
$F_\lambda(10^{-15}$ erg s^{-1} cm^{-2})
0.6
0.4
0.2
7000
8000
9000
Å

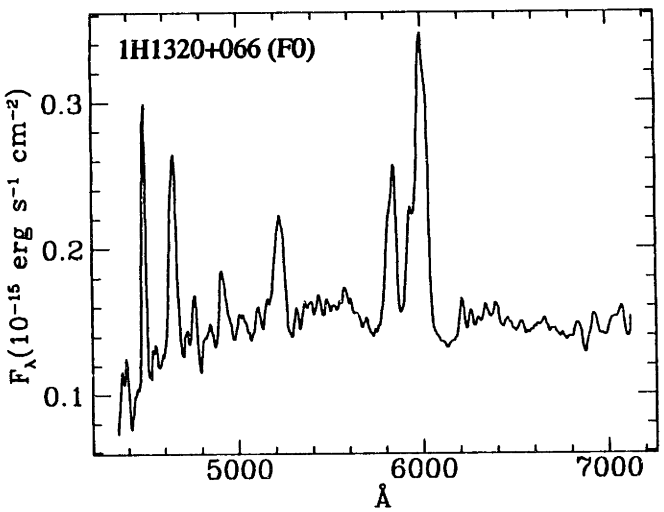
1H1320+066 (F0)
$F_\lambda(10^{-15}$ erg s^{-1} cm^{-2})
0.3
0.2
0.1
5000
6000
7000
Å

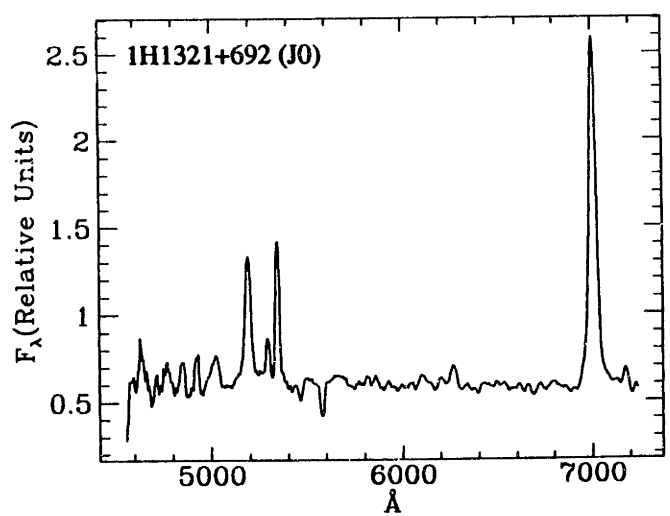
1H1321+692 (J0)
F_λ(Relative Units)
2.5
2
1.5
1
0.5
5000
6000
7000
Å

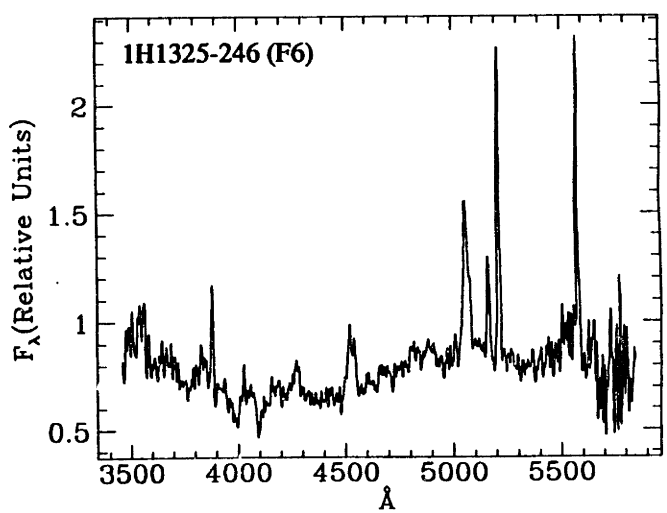
1H1325-246 (F6)
F_λ(Relative Units)
2
1.5
1
0.5
3500
4000
4500
5000
5500
Å

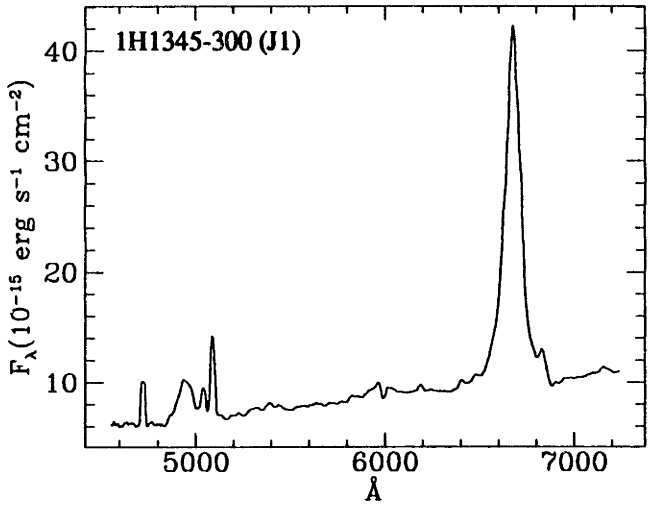
1H1345-300 (J1)
$F_\lambda(10^{-15}$ erg s^{-1} cm^{-2})
Å

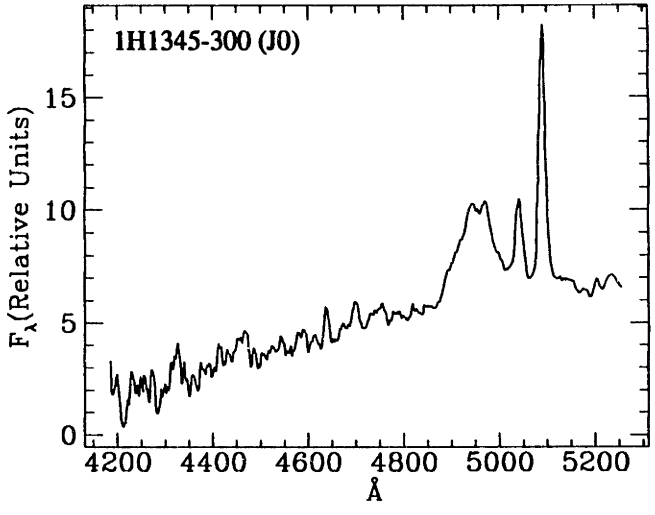
1H1345-300 (J0)
F_λ(Relative Units)
Å

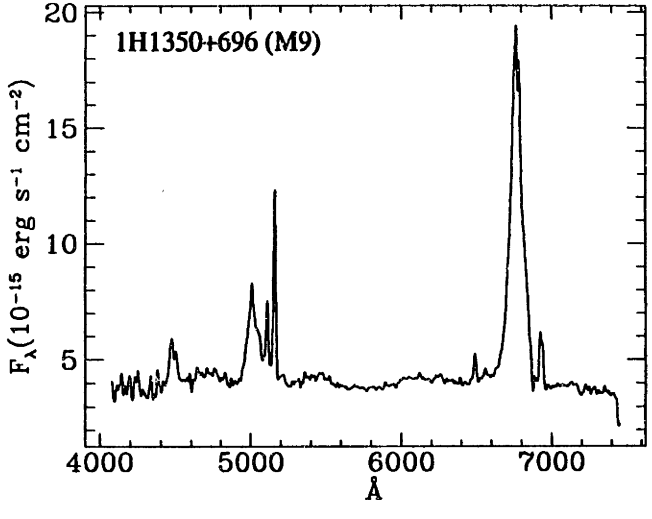
1H1350+696 (M9)
$F_\lambda(10^{-15}$ erg s^{-1} cm^{-2})
Å

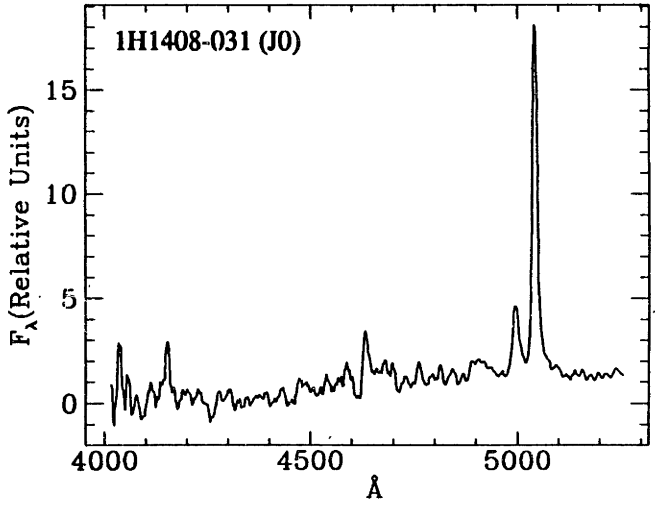
1H1408-031 (J0)
F_λ(Relative Units)
Å

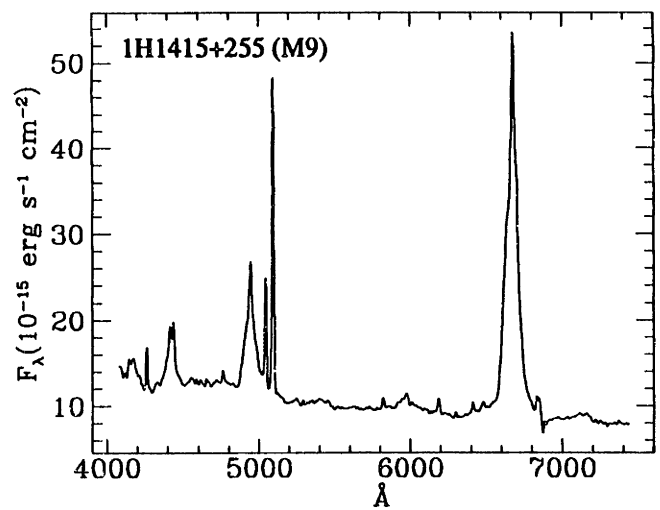
1H1415+255 (M9)
$F_\lambda(10^{-15}$ erg s^{-1} cm^{-2})
50
40
30
20
10
4000
5000
6000
7000
Å

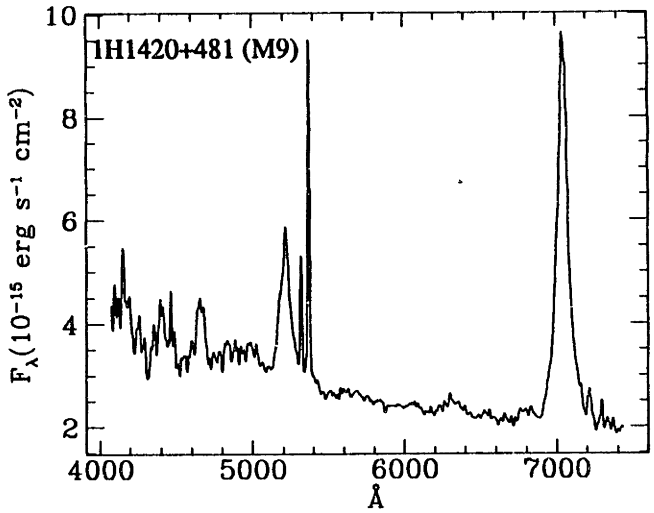
1H1420+481 (M9)
$F_\lambda(10^{-15}$ erg s^{-1} cm^{-2})
10
8
6
4
2
4000
5000
6000
7000
Å

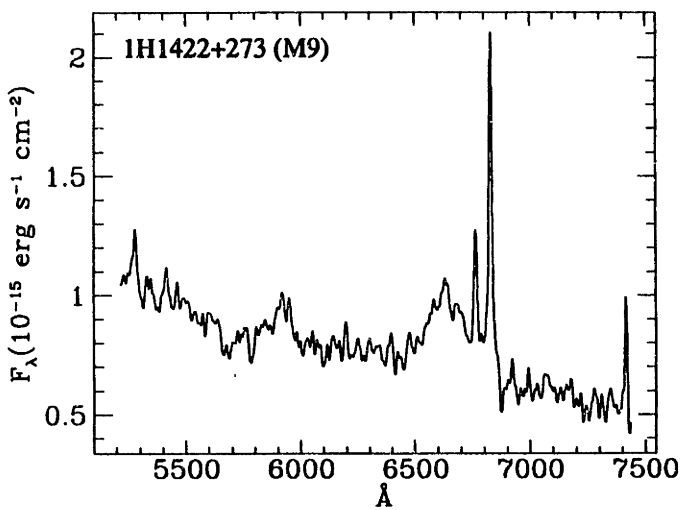
1H1422+273 (M9)
$F_\lambda(10^{-15}$ erg s^{-1} cm^{-2})
2
1.5
1
0.5
5500
6000
6500
7000
7500
Å

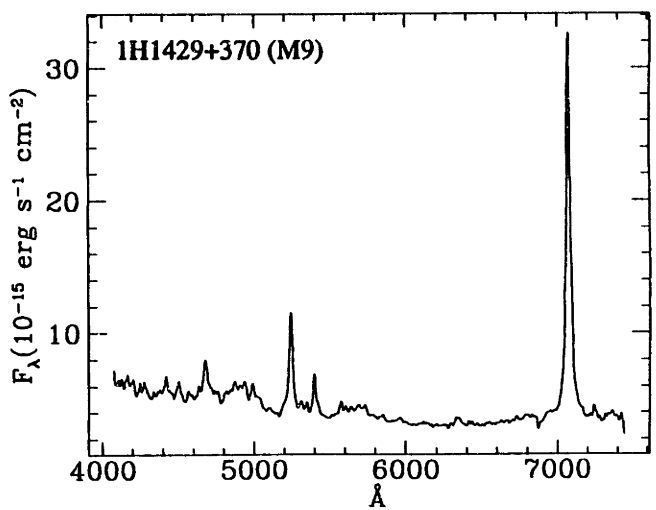
1H1429+370 (M9)
$F_\lambda(10^{-15}$ erg s^{-1} cm^{-2})
30
20
10
4000
5000
6000
7000
Å

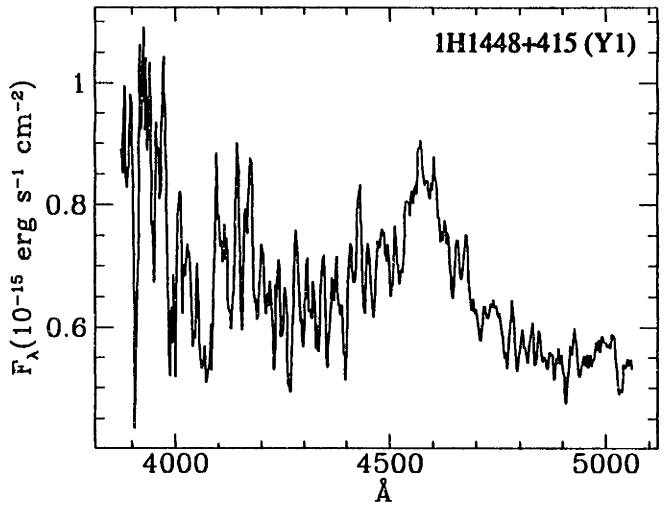
1H1448+415 (Y1)
$F_\lambda(10^{-15}$ erg s^{-1} cm^{-2})
1
0.8
0.6
4000
4500
5000
Å

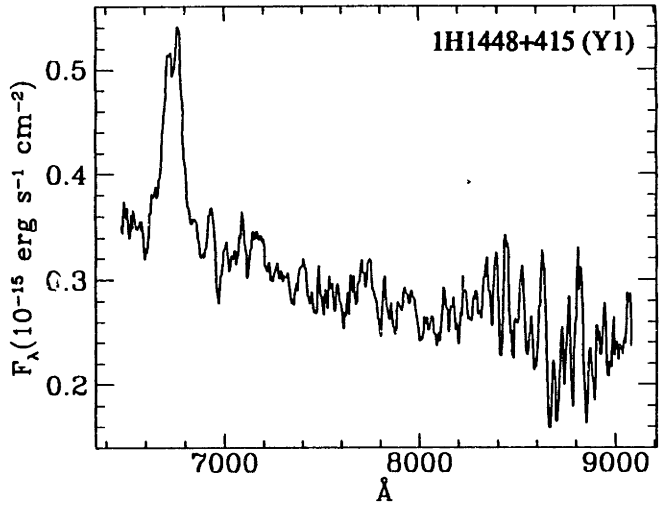
1H1448+415 (Y1)
$F_\lambda(10^{-15}$ erg s^{-1} cm^{-2})
0.5
0.4
0.3
0.2
7000
8000
9000
Å

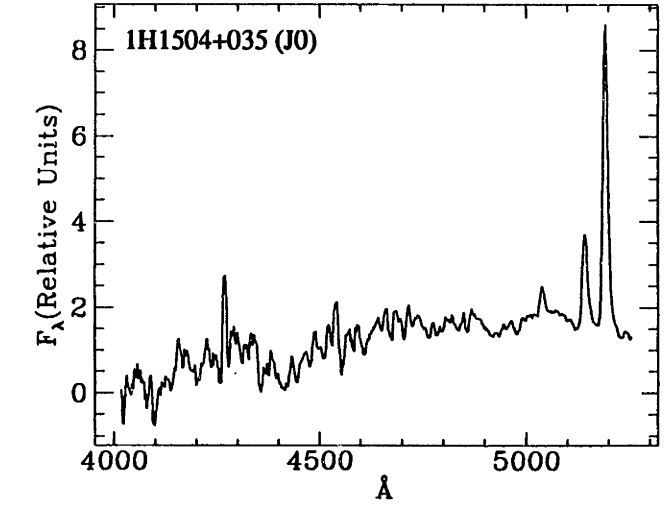
1H1504+035 (J0)
F_λ(Relative Units)
8
6
4
2
0
4000
4500
5000
Å

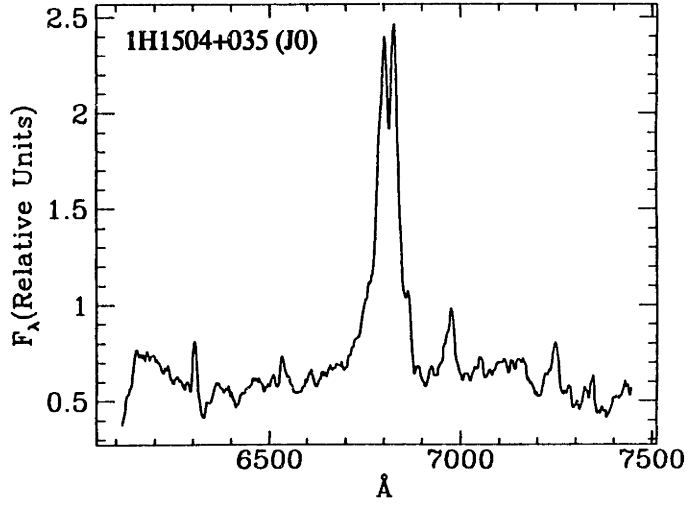
1H1504+035 (J0)
F_λ(Relative Units)
2.5
2
1.5
1
0.5
6500
7000
7500
Å

1H1538-182 (J1)
1H1540+338 (J9)
1H1530+585 (M9)
1H1540+338 (F0)
$F_\lambda(10^{-15}$ erg s^{-1} cm$^{-2})$
Å

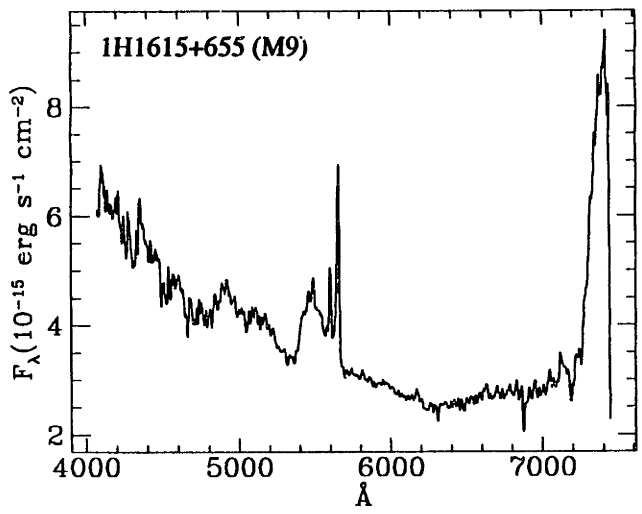
1H1615+655 (M9)
$F_\lambda(10^{-15}$ erg s^{-1} cm^{-2})
Å

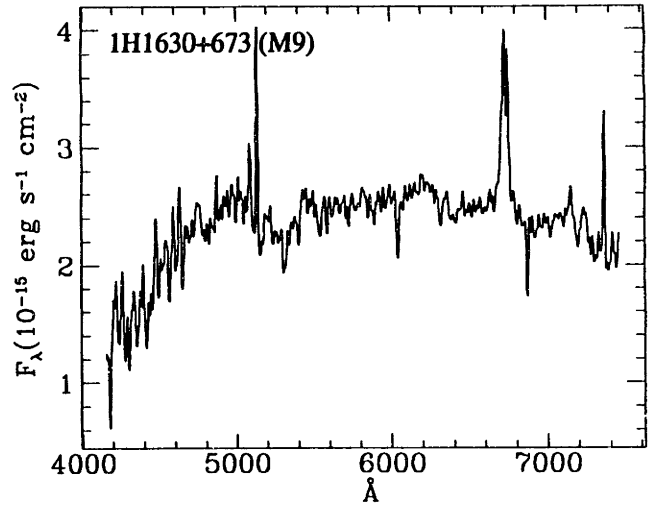
1H1630+673 (M9)
$F_\lambda(10^{-15}$ erg s^{-1} cm^{-2})
Å

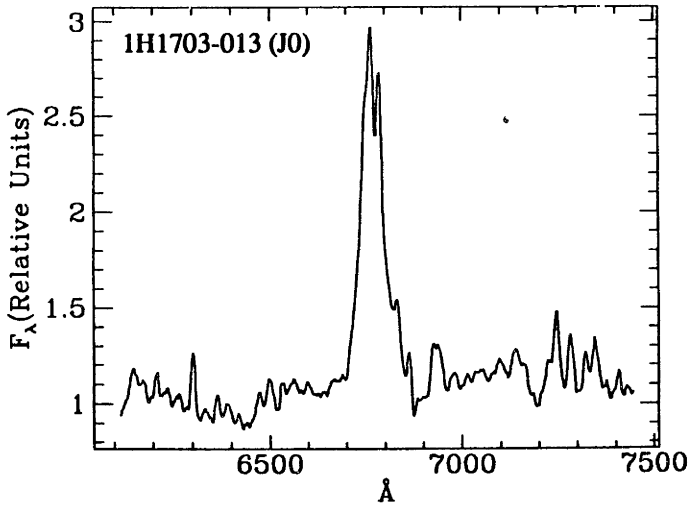
1H1703-013 (J0)
F_λ(Relative Units)
Å

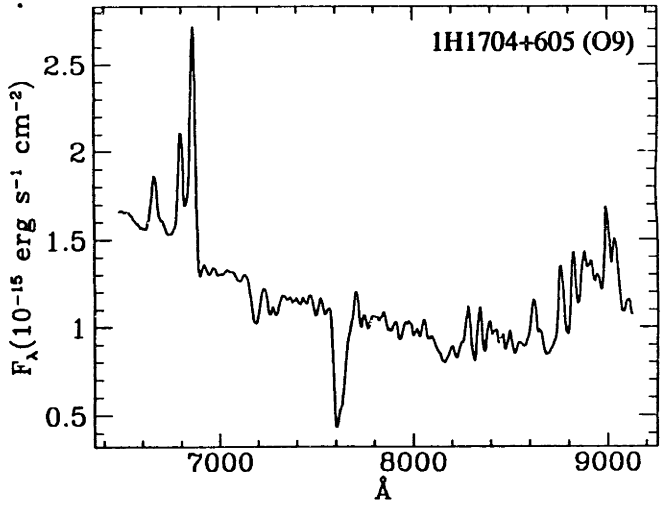
1H1704+605 (O9)
$F_\lambda(10^{-15}$ erg s^{-1} cm^{-2})
Å

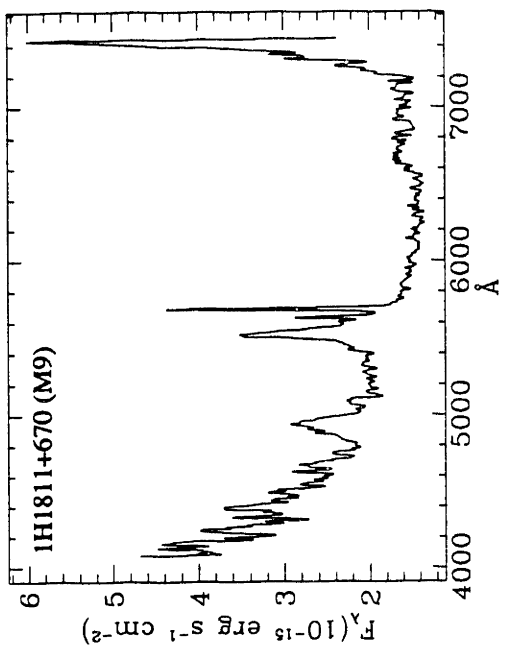
1H1811+670 (M9)
$F_\lambda(10^{-15}$ erg s^{-1} cm^{-2})
Å

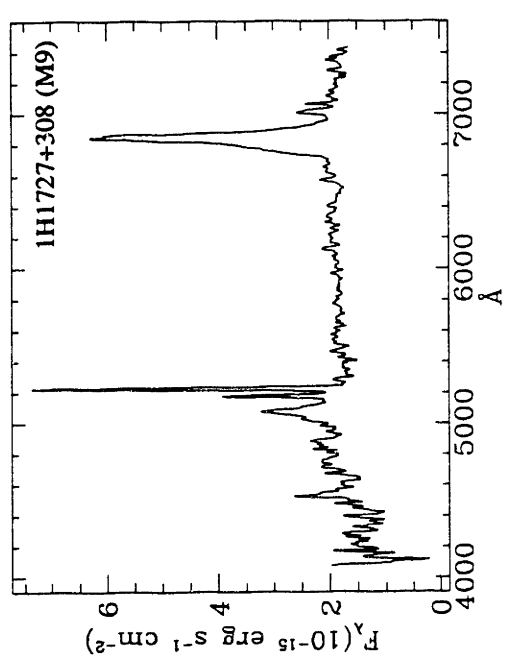
1H1727+308 (M9)
$F_\lambda(10^{-15}$ erg s^{-1} cm^{-2})
Å

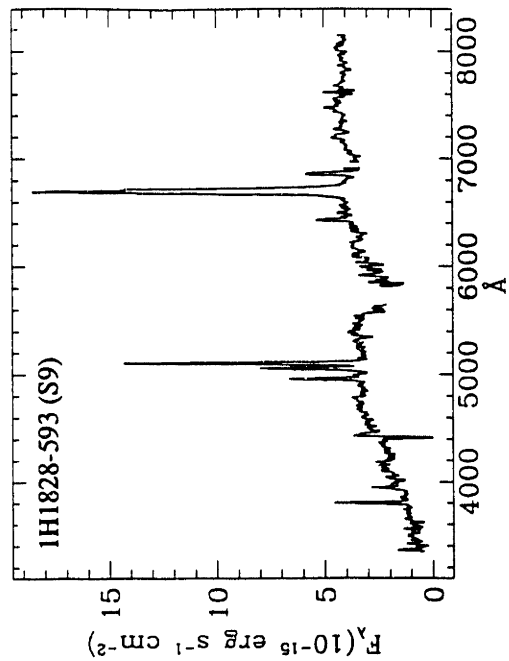
1H1828-593 (S9)
$F_\lambda(10^{-15}$ erg s^{-1} cm^{-2})
Å

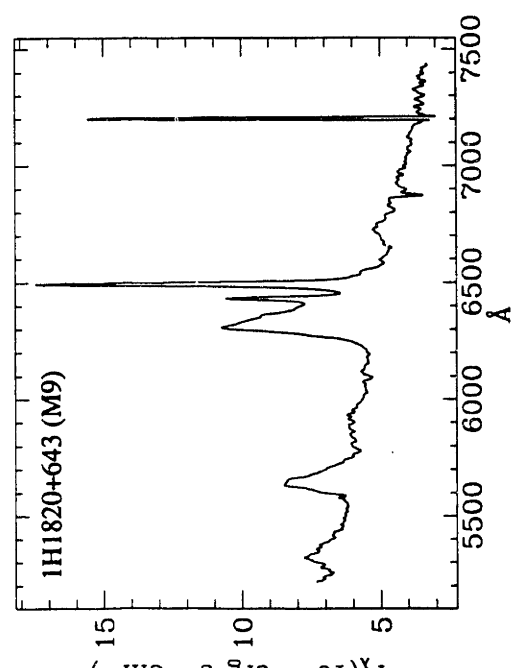
1H1820+643 (M9)
$F_\lambda(10^{-15}$ erg s^{-1} cm^{-2})
Å

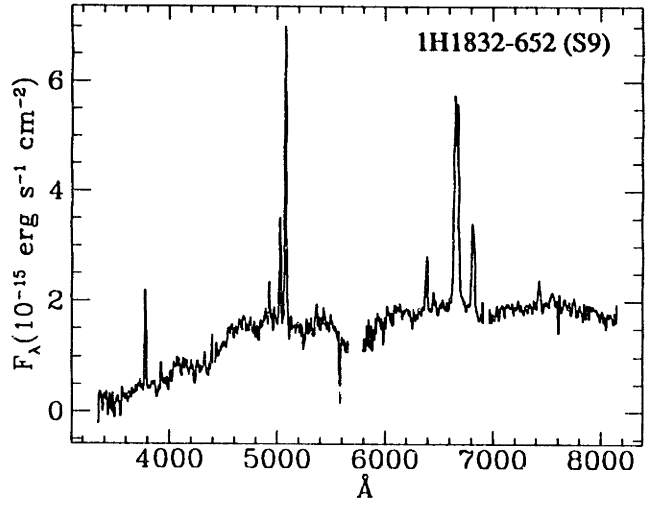
1H1832-652 (S9)
$F_\lambda(10^{-15}$ erg s^{-1} cm^{-2})
0
2
4
6
4000
5000
6000
7000
8000
Å

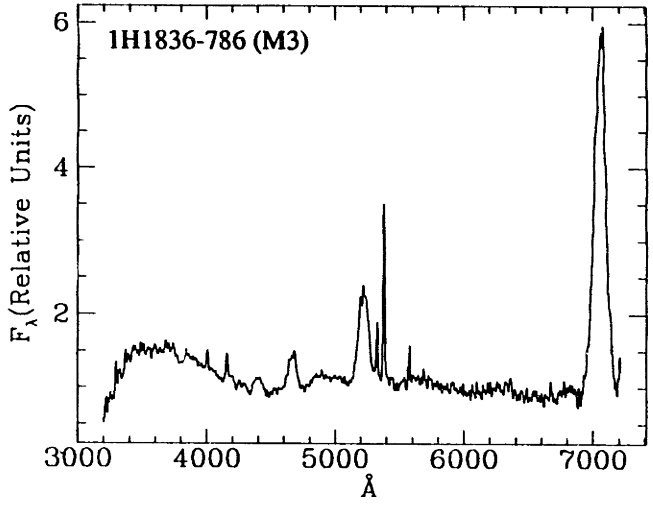
1H1836-786 (M3)
F_λ(Relative Units)
2
4
6
3000
4000
5000
6000
7000
Å

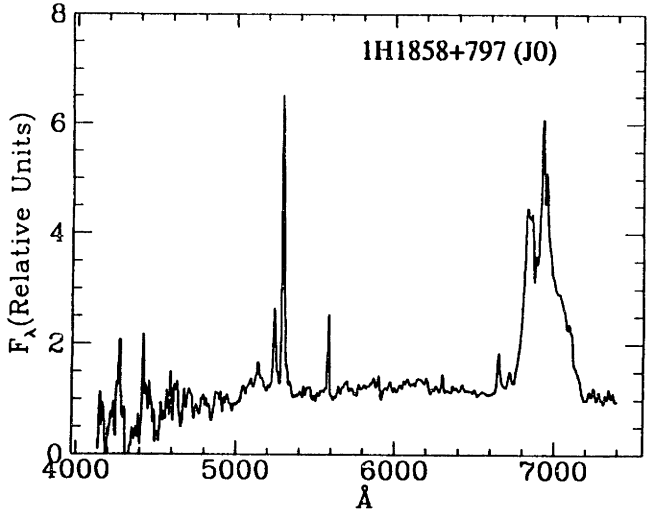
1H1858+797 (J0)
F_λ(Relative Units)
0
2
4
6
8
4000
5000
6000
7000
Å

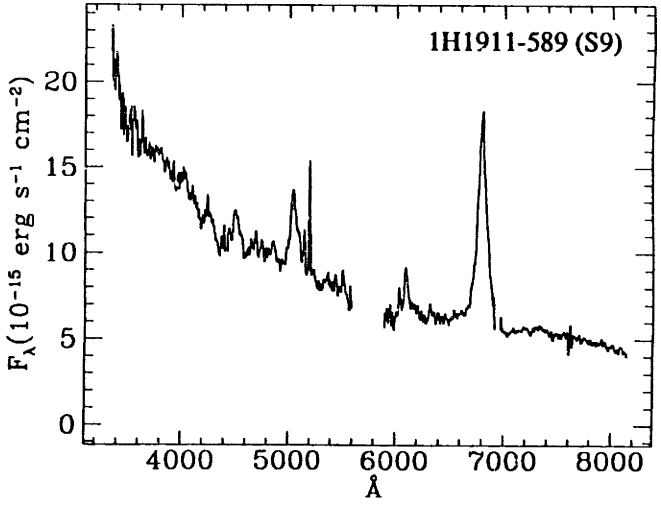
1H1911-589 (S9)
$F_\lambda(10^{-15}$ erg s^{-1} cm^{-2})
0
5
10
15
20
4000
5000
6000
7000
8000
Å

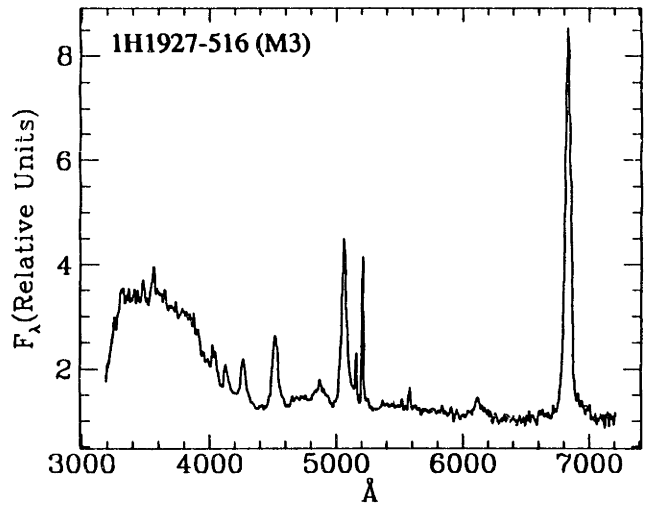
1H1927-516 (M3)
F_λ(Relative Units)
Å

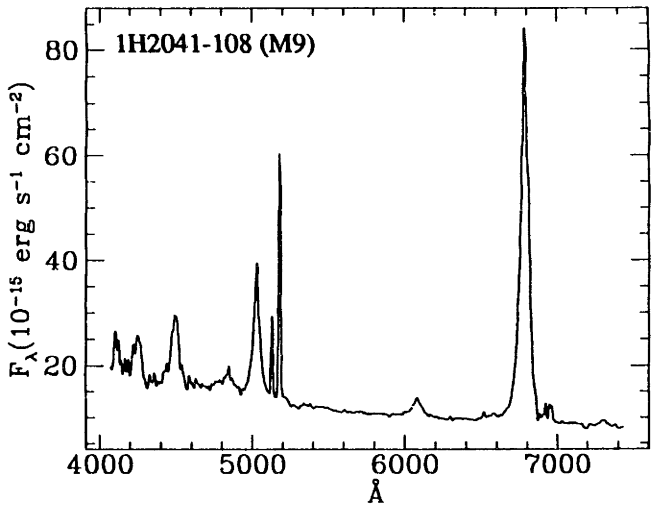
1H2041-108 (M9)
$F_\lambda(10^{-15}$ erg s^{-1} cm^{-2})
Å

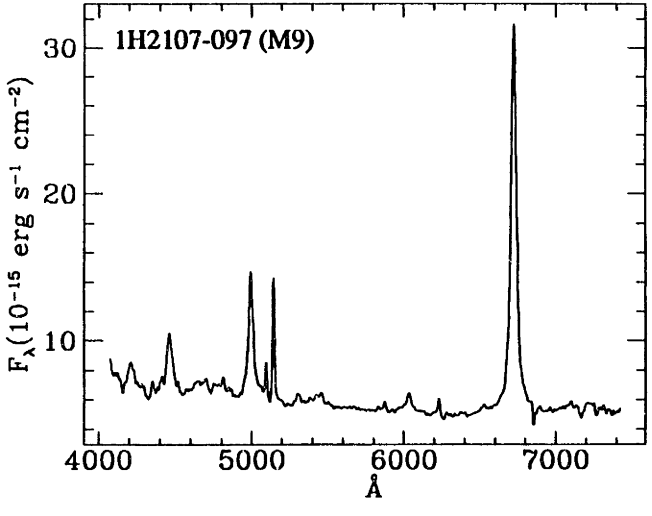
1H2107-097 (M9)
$F_\lambda(10^{-15}$ erg s^{-1} cm^{-2})
Å

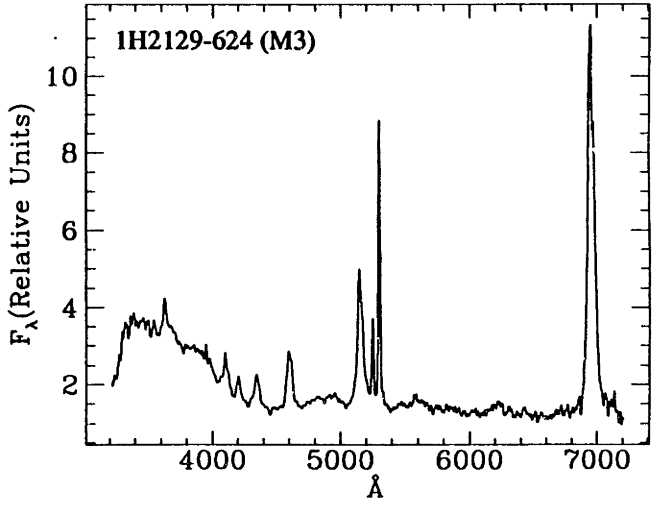
1H2129-624 (M3)
F_λ(Relative Units)
Å

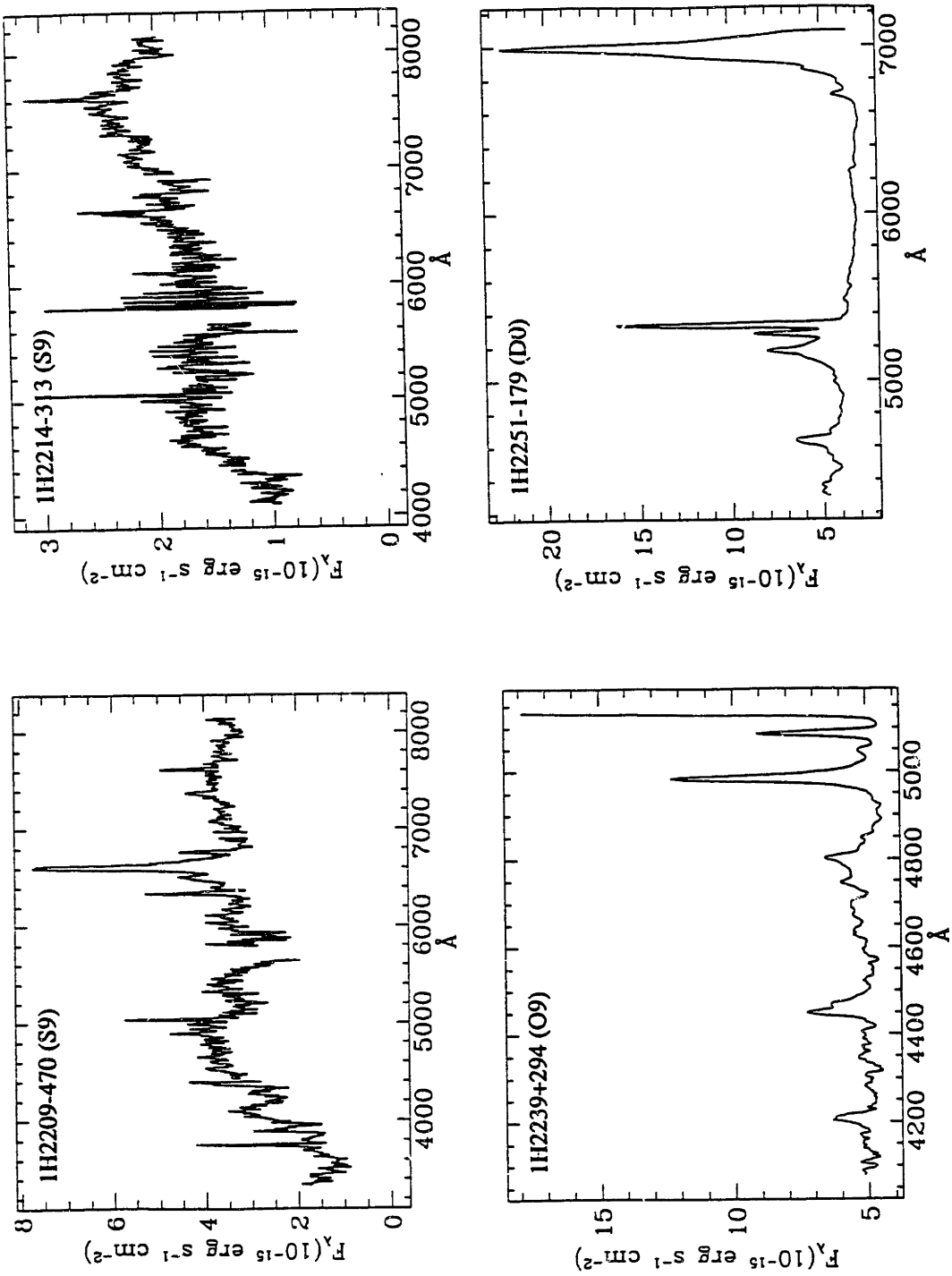
1H2214-313 (S9)
1H2251-179 (Dw)
1H2209-470 (S9)
1H2239+294 (O9)
$F_\lambda(10^{-15}$ erg s^{-1} cm^{-2})
Å

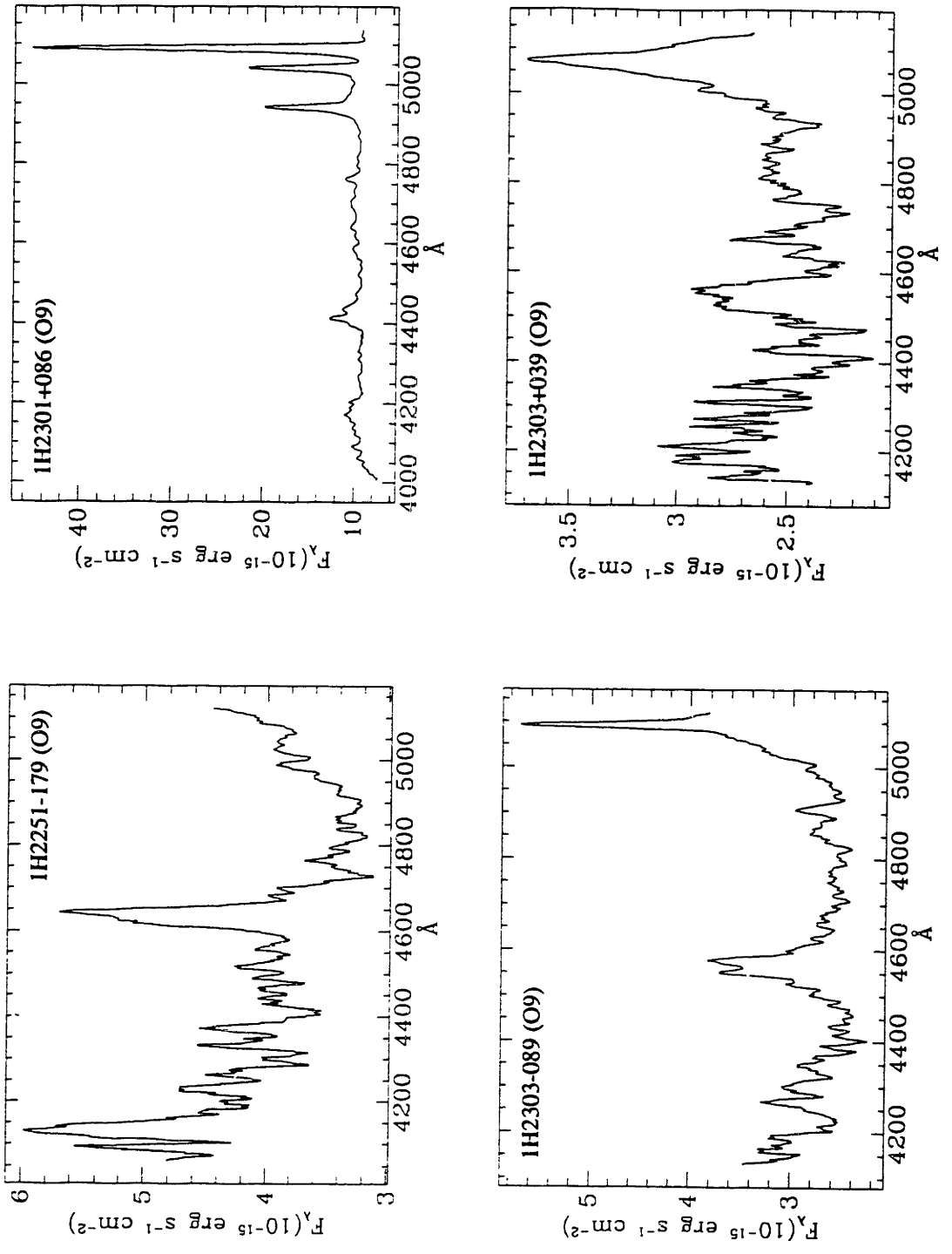
1H2301+086 (O9)
1H2303+039 (O9)
1H2251-179 (O9)
1H2303-089 (O9)
$F_\lambda(10^{-15}$ erg s^{-1} cm^{-2})
Å

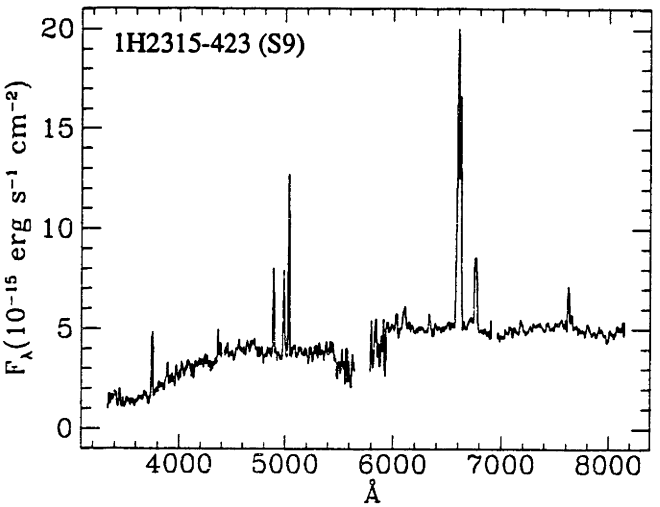
1H2315-423 (S9)
$F_\lambda(10^{-15}$ erg s^{-1} cm^{-2})
20
15
10
5
0
4000
5000
6000
7000
8000
Å